

Structural modeling of oxygen-fluorine ordering in transition metal inorganic oxyfluorides

Ouail Zakary

▶ **To cite this version:**

Ouail Zakary. Structural modeling of oxygen-fluorine ordering in transition metal inorganic oxyfluorides. Materials Science [cond-mat.mtrl-sci]. Le Mans Université, 2023. English. ⟨NNT : 2023LEMA1026⟩. ⟨tel-04412685⟩

HAL Id: tel-04412685

https://theses.hal.science/tel-04412685v1

Submitted on 23 Jan 2024

HAL is a multi-disciplinary open access archive for the deposit and dissemination of scientific research documents, whether they are published or not. The documents may come from teaching and research institutions in France or abroad, or from public or private research centers.

L'archive ouverte pluridisciplinaire **HAL**, est destinée au dépôt et à la diffusion de documents scientifiques de niveau recherche, publiés ou non, émanant des établissements d'enseignement et de recherche français ou étrangers, des laboratoires publics ou privés.



HAL Authorization

COLLEGE DOCTORAL PAYS DE LA LOIRE
ED MATIERE, MOLECULES MATERIAUX ET GEOSCIENCES

Le Mans Université

THESE DE DOCTORAT

DE
LE MANS UNIVERSITE
SOUS LE SCEAU DE
LA COMUE ANGERS – LE MANS

ECOLE DOCTORALE N° 596
Matière, Molécules, Matériaux et Géosciences
Spécialité : Physique de la Matière Condensée

Par
Ouail ZAKARY

“Structural modeling of oxygen-fluorine ordering in transition metal inorganic oxyfluorides”

Thèse présentée et soutenue à Le Mans – Salle d’innovation Pédagogique de la BU Le Mans Université, le 08 Décembre 2023 à 14h00
Unité de recherche : Institut des Molécules et Matériaux du Mans, UMR 6283 CNRS – Le Mans Université
Thèse N° : 2023LEMA1026

Rapporteurs avant soutenance :

Mathieu ALLIX	Directeur de Recherche au CNRS, Université d’Orléans
Christian BONHOMME	Professeur des Universités, Sorbonne Université

Composition du Jury :

Président :	Christel GERVAIS	Professeur des Universités, Sorbonne Université
Examinateurs :	Thibault CHARPENTIER	Directeur de Recherche au CEA, Université Paris-Saclay
	Damien DAMBOURNET	Maître de Conférences, Sorbonne Université
Dir. de thèse :	Monique BODY	Maître de Conférences, Le Mans Université
Co-dir. de thèse :	Christophe LEGEIN	Professeur des Universités, Le Mans Université

Acknowledgements

I extend my heartfelt gratitude to my esteemed thesis supervisors, Dr. Monique Body and Prof. Christophe Legein, for their unwavering support, invaluable guidance, and profound insights throughout the entirety of my research journey. Their dedication and mentorship have been instrumental in shaping this thesis.

A profound acknowledgment goes to Prof. Jens Dittmer (IMMM, Le Mans University), whose generosity in sharing his extensive knowledge and experience in the fundamentals of solid-state NMR spectroscopy and NQR experiments has been invaluable to my research.

Special thanks to researchers with whom we collaborated in the framework of the IR-RMN THC project. Dr. Franck Fayon (CEMHTI, Orléans) and Vincent Sarou-Kanian (CEMHTI, Orléans) played a pivotal role, assisting us in conducting high-resolution multidimensional NMR experiments of ^{23}Na, ^{87}Rb, and ^{93}Nb using state-of-the-art spectrometers operating at 750 and 850 MHz. Their expertise significantly contributed to the success of our project. I am truly grateful for the knowledge I have gained from their collaborative efforts.

I would like to express my appreciation to Dr. Thibault Charpentier (CEA, Paris-Saclay University) for his indispensable contributions in conducting computationally expensive first principle calculations. Additionally, gratitude is extended to Dr. Gwenaël Corbel (IMMM, Le Mans University) for his invaluable assistance and guidance in Rietveld structural refinements and variable temperature PXRD.

I am deeply thankful for the collaboration with Dr. Damien Dambournet (PHENIX, Sorbonne University) and Dr. Benjamin J. Morgan (University of Bath) in the study of the HTB phase of $TiOF_2$. Their expertise and collaboration have enriched the scope and depth of my work.

Heartfelt thanks to Engineer Cyrille Galven (IMMM, Le Mans University) for sharing his expertise and mentoring during the initial stages of my thesis, particularly in the synthesis processes used in preparing the studied materials. Additionally, my appreciation extends to Dr. Rémi Busselez (IMMM, Le Mans University) for his technical support in all matters related to the IMMM cluster.

I am profoundly grateful to my PhD student colleagues, Alexandra Pierron, Aurélie Poirier, and Zeinab Abdul-Hadi. Their friendship, camaraderie, and shared experiences have transformed this thesis

into a rewarding and enjoyable endeavor. They stood by me through the highs and lows, creating a stress-free and supportive environment.

Finally, I extend my deepest thanks to my family for their unwavering support. Their encouragement and understanding have been the foundation upon which this thesis stands. This journey would not have been possible without their love and belief in my abilities.

List of used abbreviations

Nuclear Magnetic Resonance

- **ssNMR**: **s**olid-**s**tate **N**uclear **M**agnetic **R**esonance
- **MAS**: **M**agic **A**ngle **S**pinning
- **NQR**: **N**uclear **Q**uadrupolar **R**esonance
- **CP-MAS**: **C**ross **P**olarization **M**agic **A**ngle **S**pinning
- **HETCOR**: **H**eteronuclear **C**orrelation
- **3QMAS**: **T**riple **Q**uantum **M**agic **A**ngle **S**pinning
- **J-HMQC**: ***J***-coupled **H**eteronuclear **M**ultiple **Q**uantum **C**oherence
- **TEDOR-MQMAS**: **T**ransferred **E**cho **D**ouble **R**esonance **M**ultiple **Q**uantum **M**agic **A**ngle **S**pinning
- **WURST**: **W**ideband, **U**niform, **R**ate, and **S**mooth **T**runcation
- **QCPMG**: **Q**uadrupolar **C**arr-**P**urcell-**M**eiboom-**G**ill
- **CW**: **C**ontinuous **W**ave
- **TPMP**: **T**wo **P**hase-**M**odulated **P**ulses
- **SPINAL-64**: **64**-**S**tep **S**mall-**P**hase **I**ncremental **A**lteration
- **XiX**: **X** **i**nverse-**X**
- **DQ-SQ**: **D**ouble **Q**uantum **S**ingle **Q**uantum
- **ZQ/3Q**: **Z**-**Q**uantum/**T**riple-**Q**uantum
- **1D**: one-dimensional
- **2D**: two-dimensional
- **TOP**: **T**wo-**D**imensional-**O**ne-**P**ulse
- **CT**: **C**entral **T**ransition
- **ST**: **S**atellite **T**ransition
- **n0-STSB**: **Z**eroth-**O**rder **S**atellite **S**pinning **S**ide**B**and
- **RF**: **R**adio**F**requency
- **FID**: **F**ree **I**nduction **D**ecay
- ***S/N***: **S**ignal-to-**N**oise ratio
- **LAB**: **L**aboratory frame
- **PAS**: **P**rinciple **A**xis **S**ystem
- **EFG**: **E**lectric **F**ield **G**radient
- **QIS**: **Q**uantum **I**nduced **S**hift
- **VTN**: **V**ariable **T**emperature **N**itrogen

Crystallography and first principle calculations

- **HAMs**: **H**etero**A**nionic **M**aterial**s**
- **TM**: **T**ransition **M**etal
- **NLO**: **N**on**L**inear **O**ptical
- **APO**: **A**tomic **P**osition **O**ptimization
- **FO**: **F**ull **O**ptimization
- **DFT**: **D**ensity **F**unctional **T**heory

- **HTB**: **H**exagonal-**T**ungsten-**B**ronze
- **XRPD**: **X**-**R**ay **P**owder **D**iffraction
- **TGA**: **T**hermo**G**ravimetric **A**nalysis
- **DTA**: **D**ifferential **T**hermal **A**nalysis
- **PDF**: **P**air **D**istribution **F**unction
- **RT**: **R**oom **T**emperature
- **HT**: **H**igh **T**emperature
- **VT**: **V**ariable **T**emperature
- **CASTEP**: **CA**mbridge **S**erial **T**otal **E**nergy **P**ackage
- **VASP**: **V**ienna **A**binitio **S**imulation **P**ackage
- **VESTA**: **V**isualization for **E**lectronic and **ST**ructural **A**nalysis
- **ICET**: **I**nteratomic **C**luster **E**xpansion **T**oolkit
- **BVS**: **B**ond **V**alence **S**um
- **SOF**: **S**ite **O**ccupancy **F**actor
- **SQS**: **S**pecial **Q**uasirandom **S**tructures
- **BBU**: **B**asic **B**uilding **U**nit
- **HomPUs**: **H**omoleptic **P**olyhedral **U**nits
- **HetPUs**: **H**eteroleptic **P**olyhedral **U**nits
- **SOJT**: **S**econd-**O**rder **J**ahn-**T**eller
- **NCS**: **N**on-Centro**S**ymmetric
- **ES**: **E**xperimental **S**tructure
- **IDPs**: **I**sotropic **D**isplacement **P**arameters
- **GIPAW**: **G**auge **I**ncluded **P**rojector Augmented Wave
- **PAW**: **P**rojector **A**ugmented **W**ave
- **BO**: **B**orn-**O**ppenheimer
- **HF**: **H**artree-**F**ock
- **HK**: **H**ohenberg-**K**ohn
- **KS**: **K**ohn-**S**ham
- **SCF**: **S**elf-**C**onsistent **F**ield
- **LDA**: **L**ocal **D**ensity **A**pproximation
- **LSDA**: **L**ocal **S**pin **D**ensity **A**pproximation
- **GGA**: **G**eneralized **G**radient **A**pproximation
- **BZ**: **B**rillouin **Z**one
- **AE**: **A**ll-**E**lectron
- **USPP**: **U**ltra-**S**oft **P**seudo**P**otentials
- **PBE**: **P**erdrew-**B**urke-**E**rnzerhof
- **vdW**: **v**an **d**er **W**aals
- **PBEsol**: **P**erdrew-**B**urke-**E**rnzerhof **s**olid
- **BFGS**: **B**royden-**F**letcher-**G**oldfarb-**S**hanno
- **BJ**: **B**ecke-**J**ohnson
- **CE**: **C**luster **E**xpansion
- **sdv**: **s**tandard **dev**iation
- **FP-LAPW**: **F**ull-**P**otential **L**inearized **A**ugmented **P**rojector **W**ave

Table of content

General Introduction 1

1. Heteroanionic Materials: Physicochemical Properties, Structural Features and the Challenges at Hand 1

2. Exploring Anion Ordering in Oxyfluorides 5

3. Thesis Objectives and Manuscript Outline 8

4. References 8

Chapter I: Deciphering O/F Ordering in Disordered Inorganic Oxyfluorides: A Multimodal Approach 23

I.1. Introduction 23

I.2. Solid-state NMR 25

I.2.1. Basic principle of NMR spectroscopy 25

I.2.2. Interactions in solid-state NMR 32

I.2.3. Experimental techniques in solid-state NMR 44

I.2.4. Fitting of NMR spectra using DMFit 62

I.3. Crystallography of disordered systems 65

I.3.1. Disorder in crystallography 65

I.3.2. Criteria for selecting structural models 69

I.4. First principle calculations 82

I.4.1. Quantum chemistry methods 83

I.4.2. First principle calculations of NMR parameters 93

I.4.3. Geometric relaxation 97

I.5. Conclusion 100

I.6. References 101

Chapter II: Ordered Oxyfluorides 109

II.1. Introduction 109

Multinuclear solid-state NMR, DFT calculations, and variable temperature PXRD of Nb and Ta isostructural oxyfluoride compounds revealing unexpected different structural features 111

II.2. Conclusion 147

Chapter III: Oxyfluorides Exhibiting Preferential O/F Ordering 149

III.1. Introduction 149

III.2. Structural modeling of O/F correlated disorder in $TaOF_3$ and $NbOF_{3-x}(OH)_x$ by coupling solid-state NMR and DFT calculations 151

III.2.1. Introduction 151

III.2.2. Conclusion 167

III.3. Hexagonal-Tungsten-Bronze $TiOF_2$: Synthesis, Crystal Structure and Short-Range Anion Ordering 169

III.3.1. Introduction 169

III.3.2. Average structure: X-ray and neutron diffractions 170

III.3.3. Short-range anion ordering 171
III.3.4. Modeling of ^{19}F NMR parameters 174
III.3.5. Conclusion 180
III.4. Conclusion 181
III.5. References 182
Chapter IV: "Disordered" Oxyfluorides 185
IV.1. Introduction 185
Preferential O/F Ordering in the Pyrochlore Oxyfluorides RbM_2O_5F (M = Nb, Ta) Revealed by Multimodal Structural Modeling Approach 187
IV.2. Conclusion 223
Chapter V: Magnetic Shielding to Chemical Shift Conversion 225
V.1. Introduction 225
V.2. Literature overview 226
V.3. Factors to consider when establishing a σ_{iso}–δ_{iso} correlation 229
V.3.1. Pseudopotentials 229
V.3.2. NMR calculation methods and exchange correlation functionals 230
V.3.2. Other factors 231
V.4. Conclusion 233
V.5. References 234
Conclusions and Perspectives 237
Appendix A: Ordered Oxyfluorides 241
Supplementary material: Multinuclear solid-state NMR, DFT calculations, and variable temperature PXRD of Nb and Ta isostructural oxyfluoride compounds revealing unexpected different structural features 243
Appendix B: Oxyfluorides Exhibiting Preferential O/F Ordering 277
Supporting information: Structural modeling of O/F correlated disorder in $TaOF_3$ and $NbOF_{3-x}(OH)_x$ by coupling solid state NMR and DFT calculations 279
Appendix C: Oxyfluorides Exhibiting Preferential O/F Ordering 331
Supporting information: Hexagonal-Tungsten-Bronze $TiOF_2$: Synthesis, Crystal Structure and Short-Range Anion Ordering 333
Appendix D: "Disordered" Oxyfluorides 353
Supporting information: Preferential O/F Ordering in the Pyrochlore Oxyfluorides RbM_2O_5F (M = Nb, Ta) Revealed by Multimodal Structural Modeling Approach 355
Résumé en Français 403

General Introduction

1. Heteroanionic Materials: Physicochemical Properties, Structural Features and the Challenges at Hand

Inorganic complex compounds with two or more anionic species are known as "*heteroanionic materials*" (HAMs), also commonly referred to as mixed-anion inorganic compounds. They present diverse physicochemical properties, such as high-temperature superconductivity,[1–6] ionic conductivity,[3,7,8] photocatalytic activity, [9–18] thermoelectricity[19,20] and nonlinear optical response,[21–26] and they find various applications, ranging from water splitting catalysts[9–11,14] to battery electrodes.[27–32] These characteristics make HAMs of particular interest to physicists and chemists, as they present an expansive chemical landscape, offering vast prospect for the creation of new materials tuned to specific physicochemical properties.[33–35] The incorporation of two or more anionic species with different charges, ionic radii, electronegativity and polarizability into the crystal structure introduces novel stoichiometric variations and degrees of freedom.[36,37] Through controlled synthesis, these aspects can be optimized, enabling the customization of material to meet targeted physicochemical properties. While HAMs encompass more than just oxide-derived compounds, oxides hold advantages due to their diverse chemistries, abundance, stability and ease of synthesis. Consequently, they serve as a logical foundation for designing novel HAMs with various stoichiometries, electronic and atomic structures and properties. Introducing different species of anions alongside oxygen in the structure of oxide-derived HAMs may result in properties that differ from those of their analogous oxides. For example, doping with F^- ions at the O^{2-} site in LaOFeAs results in superconducting $La[O_{1-x}F_x]FeAs$ with an estimated high temperature transition $T_C \simeq 26$ K at $x \simeq 0.11$.[5] Likewise, the incorporation of fluorine ions in Sr_2CuO_3 at ambient pressure resulted in a structural rearrangement, leading to the formation of superconducting $Sr_2CuO_2F_{2+\delta}$ with a maximum T_C of 46 K.[1] Equivalently, in the field of battery electrodes, the redox potential of the $LiFePO_4F$ tavorite phase surpasses that of the $LiFePO_4$ olivine phase by 750 mV.[30] In a similar vein, when combined to Mg-based electrolyte, $MoO_{2.8}F_{0.2}$ demonstrated a reversible capacity of approximately 80 mAh/g, which is nearly an order of magnitude

greater than that of the isostructural α-MoO_3 with a comparable particle size.[31] The properties of HAMs depend on various factors, including the type of anion specie, the relative stoichiometries of anions, and, most importantly, the arrangement of these anions within the crystal structure.

Mostly, all oxide-derived HAMs, such as oxyfluorides, oxynitrides, oxysulfides *etc.*, are built from metal-anion polyhedral units. Locally, these units interconnect through corners, edges or faces to form the crystal structure. The coordination and shape of the polyhedral units determine the manner in which they are connected. Depending on the compatibility between the anion and metal sizes, distinct coordination and shapes of these units can emerge giving rise to different crystal structures. Furthermore, depending on the type of the metal-anion ligands forming the polyhedral units, HAMs can be comprised of homoleptic polyhedral units, where single anionic specie coordinates one specific cation. This particular definition of HAMs permits the coordination of different cations by distinct anions, while ensuring that each individual cation is consistently coordinated by identical anions. On the other hand, HAMs can also be composed of heteroleptic polyhedral units, wherein a cation is coordinated by more than one anionic species. This alternative arrangement of HAMs allows for the coordination of different cations by multiple anion species, introducing a greater level of complexity and diversity in the bonding patterns within the crystal structure.

The short-range structure (polyhedral unit or unit cell) enables the assessment of the "*local arrangement*" of its anionic constituents, which is referred to here as "*short-range anion ordering*". Additionally, the "*overall arrangement*" of anions in the long-range structure, also known as the average structure (structure observed across multiple unit cells), is referred to here as "*long-range anion ordering*" (**Figure 1**). For HAMs mainly formed from metal-anion octahedra, short-range anion ordering is described by the different possible heteroleptic octahedral units $[MO_yX_{1-y}]^{n-}$ (or $[MO_{1-y}X_y]^{n-}$) (y = 1, 2, 3; X = F, N, S), including the different available geometric isomers (configurations) of the M–(O,X) ligands. Adjacent (*cis*) and opposite (*trans*) for $[MO_4X_2]^{n-}$ (or $[MO_2X_4]^{n-}$), and face (*fac*) and meridian (*mer*) for $[MO_3X_3]^{n-}$ (**Figure 1**). For HAMs exhibiting short-range anion order, their average structure incorporates either homoleptic octahedra or one heteroleptic octahedral configuration. In contrast, the average structure of HAMs demonstrating short-range anion disorder is primarily formed from multiple heteroleptic octahedral configurations or a combination of

homoleptic and heteroleptic octahedral configurations (**Figure 1**). Short-range anion order may give rise to long-range anion order, while short-range anion disorder always results in long-range anion disorder. Nevertheless, in some cases, short-range anion order lead to long-range anion disorder. This phenomenon, characterized by the interplay of order and disorder, is commonly referred to as "*correlated disorder"*.

The occurrence of long-range anion order or disorder in HAMs has been associated with the difference between the ionic radii of the different anions. For instance, oxysulfides demonstrate long-range anion order due to the considerably larger ionic radius of S^{2-} (1.84 Å) in comparison to O^{2-} (1.40 Å), even though they possess the same formal oxidation state. Conversely, oxyfluorides and oxynitrides, with quasi-similar ionic radii of N^{3-} (1.46 Å), O^{2-} (1.40 Å) and F^{-} (1.33 Å) anions, tend to exhibit long-range anion disorder, although they sometimes demonstrate some degree of short-range anion order. The level of long-range anion ordering in oxyfluorides and oxynitrides depends on the synthesis conditions employed.

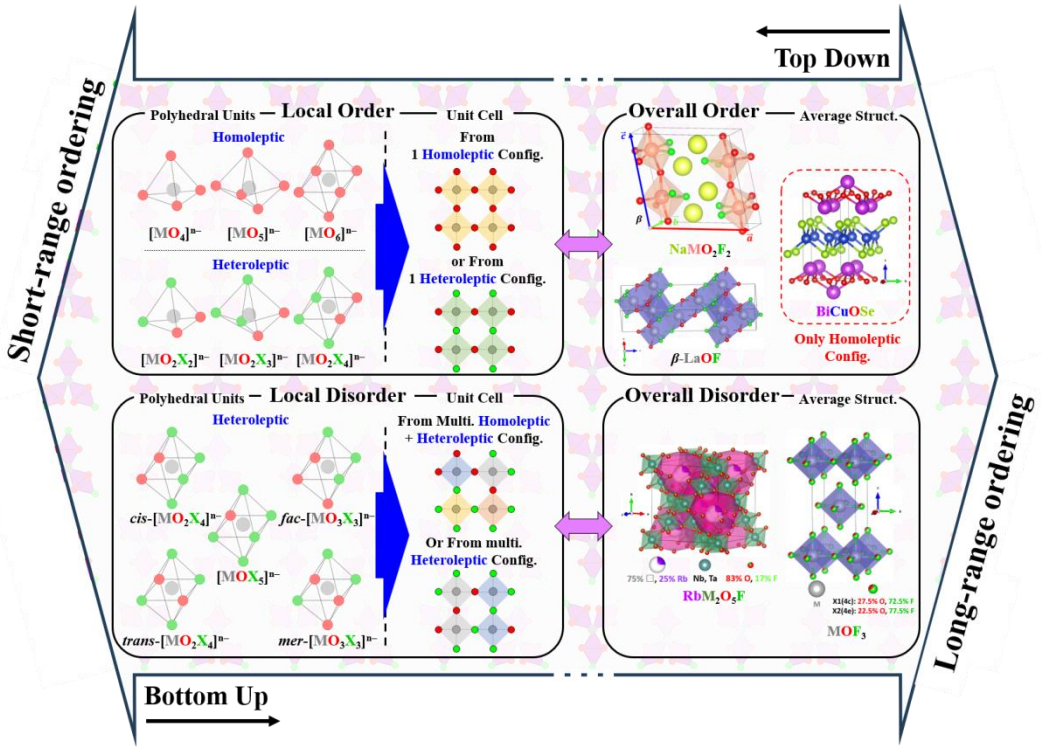


Figure 1. Anion ordering in heteroanionic materials

Heteroleptic octahedral configurations in oxide-derived HAMs are not all equivalent, as the π-hybridization in the M-anion bonds is maximized when anions with similar Pearson hardness[38] are in

close proximity, *cis* and *fac* configurations are favored,[39,40] especially if the M cation is a d^0 transition metal. Consequently, this allows atomic rearrangement toward characteristic bond lengths.[41–48] Except for the *trans* configuration, the arrangement of anions in the *cis*, *fac* and *mer* configurations and the unit $[MO_5X]^{n-}$ (or $[MOX_5]^{n-}$) reduces the local symmetry for the center metal d-orbitals. This symmetry breaking is seen as an out-of-center metal displacement towards the less electronegative anion(s) [34] and the acentric metal displacement is commonly observed among HAMs with heterolepic octahedra, including MO_2F[49–51] and MOF_3[52] (M = Nb, Ta), $A_2BB'O_3F_3$ (A, B = Na, K, Rb, Cs, Tl; B' = Mo, W),[53–57] AMO_2N (A = Er, Sr; M = Nb, Ta),[58] $Cd_2Nb_2O_6S$,[59] $KNaNbOF_5$,[60,61] $CsNaNbOF_5$[60] and Rb_2KTiOF_5.[62] For example, the B cations in the anion ordered units $[BOF_5]^{n-}$ from $KNaNbOF_5$,[60,61] $CsNaNbOF_5$[60] and Rb_2KTiOF_5[62] oxyfluorides are displaced toward O^{2-} anions, resulting in the formation of a polar unit with a local cation symmetry of 4*mm* (C_{2V}). Furthermore, *cis*-$[MO_4N_2]^{9-}$ octahedra forming the AMO_2N (A = Er, Sr; M = Nb, Ta)[58] oxynitrides demonstrate an acentric metal displacement directed toward N^{3-} anions, leading to a local metal symmetry of *mm*2 (C_{2V}) and unbalanced metal-anion bond lengths, *i.e.*, shorter M–N and longer M–O bond lengths. This acentric functionality of HAMs leads to the formation of local dipoles within the heteroleptic octahedra, which can be useful for designing noncentrosymmetric materials[63] exhibiting properties such as piezoelectricity, ferroelectricity and second harmonic generation.[34] Nonetheless, these properties are not only dependent on the acentric functionality of the material in the octahedral level, but also on the arrangement of anions within the heteroleptic octahedra in the short- and long-range structures. If anions are arranged in a disordered fashion the material may exhibit inversion symmetry as a result the electronic and magnetic desired responses are reduced. Therefore, it is critical to describe anion ordering both in the short- and long-range structures in order to understand the properties of HAMs.

2. Exploring Anion Ordering in Oxyfluorides

Among the family of oxide-derived HAMs, oxyfluorides occupy the largest space.[33] They are typically characterized with "*long-length-scale characterization techniques*", such as X-ray and neutron diffractions, which only provide a model of the average crystal structure. As O^{2-} and F^- have similar X-ray (or Neutron) scattering factors, relying solely on the diffraction data is insufficient to describe O/F ordering. Nevertheless, for oxyfluorides exhibiting short- and long-range O/F order, a complete structural description may be possible by diffraction data if combined to theoretical models that predict preferential short-range ordering, such as bond valence sum (BVS) calculations[64,65] and Pauling's second rule.[66] For instance, BVS calculation proved to be valuable for the determination of O^{2-} and F^- atomic positions of numerous oxyfluorides, where an O/F ordering was proposed, including, $Y_xO_yF_z$,[67] Cd_4F_6O,[68] TcO_2F_3,[69] $Bi_7F_{11}O_5$,[70] $Lu_3O_2F_5$,[71] $Te_2O_3F_2$,[72] $TeOF_2$,[73] FeOF,[39] NbO_2F,[49] NdOF,[74] $Nb^{V}_{1-x}Nb^{IV}_{x}O_{2-x}F_{1+x}$ ($0 \leq x \leq 0.48$),[75] $Nb_nO_{2n-1}F_{n+2}$ ($n = 3$),[52] $Er_3O_2F_5$,[76] and TaO_2F,[51] among others. Describing O/F ordering in oxyfluorides presenting short- and long-range disorders or correlated disorder with structural models reflecting unique preferential short-range ordering can, however, lead to an oversimplification of the overall structural complexity, thus, missing hidden models. In such cases, a multimodal structural solution approach, which requires using "*short-length-scale characterization techniques*", is necessary to determine the potentially existent various short-range O/F arrangements.

In this regard, solid-state NMR spectroscopy (ssNMR) is considered as a potent tool as it enables a direct probe of the local chemical environment (first coordination sphere) through space and through bond connectivities. It can also provide valuable structural characteristics such as the number and relative multiplicities of the crystallographic sites, and eventually the polyhedral distortion degree, among others. Describing O/F ordering in oxyfluorides is aided by the use of ^{19}F ssNMR, as this isotope possesses a nuclear spin of 1/2, a 100% natural abundance, a high gyromagnetic ratio and a broad range of chemical shifts (δ_{iso}, which is the most important quantity in the context of high resolution ssNMR).[77,78] However, interpretation of ^{19}F ssNMR magic angle spinning (MAS) spectra can often be challenging. This is due to the presence of interactions of anisotropic nature (orientation-

dependent) that frequently result in broad spectra, thereby sometimes hindering unambiguous spectral assignments. In such case, the application of two-dimensional (2D) NMR correlation experiments, which offer insights into the spatial proximity and bonding interactions among atoms, proves valuable for line assignment purposes. Diverse 2D heteronuclear correlation MAS experiments, including, CP-MAS HETCOR,[79] CP 3QMAS,[80] J-HMQC[81,82] and TEDOR-MQMAS,[83] have been employed to explore heteronuclear spatial proximities in multiple spin pairs, including, $^{19}F/^{1}H$,[84] $^{19}F/^{23}Na$,[85–88] $^{19}F/^{27}Al$,[88–92] $^{19}F/^{31}P$[89,93] and $^{19}F/^{207}Pb$,[94–96] resulting in both partial and complete experimental assignments of fluorine sites within numerous inorganic fluorides, such as β-Pb_2ZnF_6,[95] $Pb_5Ga_3F_{19}$,[96] β-$BaAlF_5$,[91,92] α-$CaAlF_5$,[91,92] $Ba_3Al_2F_{12}$,[91,92] α-$LaZr_2F_{11}$[97] and C_2F_x ($0.49 \leq x \leq 0.92$).[84] The utilization of 2D ^{19}F double-quantum single-quantum (DQ-SQ)[98] MAS correlation experiments has allowed for the assignments of ^{19}F resonances by revealing ($^{19}F/^{19}F$) proximities, in both inorganic fluorides, including (K,Na)MgF_3,[99] β-Pb_2ZnF_6,[95] $Pb_5Ga_3F_{19}$,[96] β-$BaAlF_5$,[91,92] α-$CaAlF_5$,[91,92] $Ba_3Al_2F_{12}$,[91,92] $Ba_5Al_3F_{19}$,[100] $RbLaF_4$,[101] Ba_5AlF_{13},[102] and oxyfluorides, including $[Ta_4F_{16}O_4]^{4-}$ and $[Ta_8F_{24}O_{12}]^{8-}$ clusters,[103] $4Mg_2SiO_4 \cdot Mg(OD_{1-x}F_x)_2$ ($x = 0.5$),[104] $UO_2F_2 \cdot 1.57H_2O$[105] and $Te_{0.47}Zr_{0.53}O_xF_y$.[106] Nevertheless, when confronted with distinct fluorine sites exhibiting similar connectivity patterns and inter-atomic distances, these 2D correlation techniques do not provide a direct means to assign the corresponding resonances.[91,107] Moreover, in oxyfluorides, both short-range and O/F correlated disorders give rise in ^{19}F MAS NMR spectra to distributions of resonance frequencies. The prediction of the spectroscopic responses by means of electronic structure calculations, such as density functional theory (DFT) methods with periodic boundary conditions, therefore plays an essential role not only to assign the different spectral contributions, but also to understand the structural origins of the experimental parameter distributions.[108–113]

Since its introduction by Mauri and Pickard in 2001, the gauge including projector augmented wave GIPAW approach[114,115], which allows for the calculation of the isotropic magnetic shielding values (σ_{iso}) of any atom in the periodic table, has proven to be critical in the process of ssNMR studying of solid materials. This approach allows for testing multiple structural model candidates, potentially describing O/F ordering in oxyfluorides. The validation of any of these models usually involves the simulation of their corresponding NMR spectra and subsequent direct comparison with

the available experimental data. This process requires converting the σ_{iso} values obtained from the calculations to δ_{iso} values that would be observed in the experiment. This conversion is achieved through correlating the calculated σ_{iso} values from a known ordered inorganic fluoride(s) to the experimental δ_{iso} values. The correlation results in a linear regression where the slope theoretically should be equal to 1 for ^{19}F in all existing inorganic fluorides (the same applies to other nuclei from other classes of inorganic compounds). However, previously established ^{19}F linear regressions, including those obtained from alkali, alkaline earth and rare earth fluorides,[116] TaF_5,[117] metal fluoride compounds in the 13th column,[118] alkali fluoroscandates,[119] ternary fluorido-zirconates,[120] TiF_4,[121] $CaTiF_6(H_2O)_2$,[122] among others, do not present a unity slope. Similarly, in this thesis, newly established linear regressions present slopes that deviate from unity. One of many suspected reasons explaining this slope discrepancy, which will be discussed later in **Chapter V** in-depth, is the identity of the cation species coordinated to fluorine. Given this reason, a precise prediction of ^{19}F δ_{iso} values in a given oxyfluoride requires a regression relation deduced from a known ordered inorganic fluoride containing similar cation species as the oxyfluoride.

Relying solely on ^{19}F δ_{iso} calculated values is often insufficient to model O/F ordering, as these values are dependent on the regression used. Therefore, it is necessary to calculate the quadrupolar NMR parameters of the ssNMR accessible quadrupolar nucleus(ei) present in the ^{19}F local environment. These parameters include the quadrupolar coupling constant (C_Q) and the asymmetry parameter (η_Q), they are calculated using the projector augmented wave[123–125] (PAW) approach. This step enables direct comparison with the experimental data and, thus, undoubtedly confirm the O/F ordering within the tested model(s). In other words, the presence of quadrupolar nucleus(ei) bonded to anions emphasizes the statement that an accurate model(s) should provide a perfect reconstruction of the experimental data, considering not only the ^{19}F δ_{iso} calculated values but also the calculated C_Q and η_Q values.

Throughout the last decade, the combination of X-ray (Neutron) diffraction, solid-state NMR and first principle calculations has been, initially, rigorously tested on inorganic ordered fluorides, resulting in resounding success.[95,97,100–102,116–121] Subsequently, its application was extended to describe the structure of numerous classes of disordered inorganic compounds.[126–147] The application of this

multimodal approach on oxyfluorides has remained limited, with only handful of studies exploring its potential, especially, for oxyfluorides exhibiting short-, correlated and long-range O/F disorder. Noteworthy instances include investigations on O/F ordered oxyfluorides, such as LaOF,[148] $UO_2F_2 \cdot 1.57H_2O$,[105] RbF-Al_2O_3,[149] $[H_2taz]_2 \cdot (Ti_5O_5F_{12})$,[150] ($K_5[Mo_3O_4F_9] \cdot XH_2O$ and $K_{16}[Mo_3O_4F_9]_2[TiF_6]_3 \cdot 2H_2O$ with X=2,3)[151] and $CaTiF_6(H_2O)_2$,[122] short- and long-range O/F disordered oxyfluorides, such as $4Mg_2SiO_4 \cdot Mg(OD_{1-x}F_x)_2$ (x = 0.5)[104] and β-$AlF_{3-x}(OH)_x$,[152] and oxyfluorides exhibiting O/F correlated and dynamical disorder, including MO_2F (M = Nb, Ta)[153] and $KNaNbOF_5$.[154,155]

3. Thesis Objectives and Manuscript Outline

The primary objective of this thesis is to meticulously describe O/F ordering in inorganic oxyfluorides, covering a spectrum of structural complexities that range from ordered and correlated disordered, to completely disordered structures. This objective will be attained through employing the multimodal approach described above, which encompasses a sequence of meticulous steps that entail:

- Characterizing the synthesized compounds using X-ray powder diffraction (XRPD), ssNMR of ^{1}H and ^{19}F nuclei and multidimensional high field ssNMR of ^{23}Na and ^{87}Rb and ^{93}Nb;
- Determining the average crystal structure by Rietveld refinements of the XRPD data;
- Constructing short-range models meeting specific criteria, *e.g.*, bond-valence sum calculations, preferential O/F ordering, Coulomb energy, *etc.*;
- Performing DFT optimizations on the selected models, then calculating quadrupolar NMR parameters and magnetic shielding constants using PAW and GIPAW approaches respectively;
- Selecting the final model(s) by comparing theoretical and experimental NMR parameters.

The thesis outline is as follows.

The **first chapter** delves into several key aspects. First, it covers the fundamental principles of NMR spectroscopy, elucidating the various interactions in ssNMR, and expounds upon the experimental methodologies applied in the investigation of inorganic oxyfluorides. Second, it briefly reviews the criteria used to identify structural models that potentially describe O/F ordering in

oxyfluorides. Third, the chapter explores the quantum chemistry fundamentals, and provides the underlying concepts of the PAW and the GIPAW approaches.

The **second chapter** is dedicated to studying the structure of niobium and tantalum di-oxyfluorides, $NaNbO_2F_2$ and $NaTaO_2F_2$, which exhibit short- and long-range O/F order, using XRPD, multinuclear ssNMR and first principle calculations. The main objectives of this chapter are twofold: firstly, to establish a ^{19}F σ_{iso}–δ_{iso} correlation to predict calculated δ_{iso} values in oxyfluorides compounds, such as $Na_2Nb_2O_5F_2$ and $Na_2Ta_2O_5F_2$; and secondly, to investigate the thermal behavior of both compounds using variable temperature XRPD. Additionally, this study provides, for the first time, the atomic positions in $NaTaO_2F_2$.

The **third chapter** comprises two sections. The first section involves an in-depth structural study of niobium and tantalum oxytrifluorides MOF_3 and their hydroxylated phases $MOF_{3-x}(OH)_x$ (M = Nb, Ta). Similarly, the second section deals with structural investigation of short-range O/F ordering in the hexagonal-tungsten-bronze phase of $TiOF_2$ oxyfluoride, HTB-$TiOF_2$. These compounds potentially present O/F correlated disorder, and their structures were investigated using XRPD, ^1H and ^{19}F MAS NMR, and DFT calculations.

The **fourth chapter** encompasses the structural study of short-range O/F ordering in RbM_2O_5F pyrochlore oxyfluorides (M = Nb, Ta) using XRPD, multinuclear high-field ssNMR and DFT calculations.

The **fifth** and last **chapter** addresses the σ_{iso}–δ_{iso} correlations discrepancy in an attempt to understand its origins and discusses the established correlations during the thesis and previously in the literature.

4. References

(1) AI-Mamouri, M.; Edwards, P. P.; Greaves, C.; Slaski, M. Synthesis and Superconducting Properties of the Strontium Copper Oxy-Fluoride $Sr_2CuO_2F_{2+\delta}$. *Nature* **1994**, *369* (6479), 382–384. https://doi.org/10.1038/369382a0.

(2) Hiroi, Z.; Kobayashi, N.; Takano, M. Probable Hole-Doped Superconductivity without Apical Oxygens in $(Ca, Na)_2CuO_2CI_2$. *Nature* **1994**, *371* (6493), 139–141. https://doi.org/10.1038/371139a0.

(3) Pöttgen, R.; Johrendt, D. Materials with ZrCuSiAs-Type Structure. *Zeitschrift für Naturforschung B* **2008**, *63* (10), 1135–1148. https://doi.org/10.1515/znb-2008-1001.

(4) Clarke, S. J.; Adamson, P.; Herkelrath, S. J. C.; Rutt, O. J.; Parker, D. R.; Pitcher, M. J.; Smura, C. F. Structures, Physical Properties, and Chemistry of Layered Oxychalcogenides and Oxypnictides. *Inorg. Chem.* **2008**, *47* (19), 8473–8486. https://doi.org/10.1021/ic8009964.

(5) Kamihara, Y.; Watanabe, T.; Hirano, M.; Hosono, H. Iron-Based Layered Superconductor $La[O_{1-x}F_x]FeAs$ (x = 0.05−0.12) with T_c = 26 K. *J. Am. Chem. Soc.* **2008**, *130* (11), 3296–3297. https://doi.org/10.1021/ja800073m.

(6) Yamanaka, S. Intercalation and Superconductivity in Ternary Layer Structured Metal Nitride Halides (MNX: M = Ti, Zr, Hf; X = Cl, Br, I). *J. Mater. Chem.* **2010**, *20* (15), 2922. https://doi.org/10.1039/b922149b.

(7) Imanaka, N.; Okamoto, K.; Adachi, G. Water-Insoluble Lanthanum Oxychloride-Based Solid Electrolytes with Ultra-High Chloride Ion Conductivity. *Angew. Chem. Int. Ed.* **2002**, *41* (20), 3890–3892. https://doi.org/10.1002/1521-3773(20021018)41:20<3890::AID-ANIE3890>3.0.CO;2-M.

(8) Kobayashi, G.; Hinuma, Y.; Matsuoka, S.; Watanabe, A.; Iqbal, M.; Hirayama, M.; Yonemura, M.; Kamiyama, T.; Tanaka, I.; Kanno, R. Pure H^- Conduction in Oxyhydrides. *Science* **2016**, *351* (6279), 1314–1317. https://doi.org/10.1126/science.aac9185.

(9) Scaife, D. E. Oxide Semiconductors in Photoelectrochemical Conversion of Solar Energy. *Solar Energy* **1980**, *25* (1), 41–54. https://doi.org/10.1016/0038-092X(80)90405-3.

(10) Hitoki, G.; Takata, T.; Kondo, J. N.; Hara, M.; Kobayashi, H.; Domen, K. An Oxynitride, TaON, as an Efficient Water Oxidation Photocatalyst under Visible Light Irradiation ($\lambda \leq$ 500 Nm). *Chem. Commun.* **2002**, No. 16, 1698–1699. https://doi.org/10.1039/B202393H.

(11) Ishikawa, A.; Takata, T.; Kondo, J. N.; Hara, M.; Kobayashi, H.; Domen, K. Oxysulfide $Sm_2Ti_2S_2O_5$ as a Stable Photocatalyst for Water Oxidation and Reduction under Visible Light Irradiation ($\lambda \leq$ 650 Nm). *J. Am. Chem. Soc.* **2002**, *124* (45), 13547–13553. https://doi.org/10.1021/ja0269643.

(12) Murase, T.; Irie, H.; Hashimoto, K. Ag^+-Inserted NbO_2F as a Novel Photocatalyst. *J. Phys. Chem. B* **2005**, *109* (28), 13420–13423. https://doi.org/10.1021/jp050423t.

(13) Idrees, F.; Cao, C.; Butt, F. K.; Tahir, M.; Tanveer, M.; Aslam, I.; Ali, Z.; Mahmood, T.; Hou, J. Facile Synthesis of Novel Nb_3O_7F Nanoflowers, Their Optical and Photocatalytic Properties. *CrystEngComm* **2013**, *15* (40), 8146. https://doi.org/10.1039/c3ce41210e.

(14) Maeda, K.; Lu, D.; Domen, K. Direct Water Splitting into Hydrogen and Oxygen under Visible Light by Using Modified TaON Photocatalysts with d^0 Electronic Configuration. *Chem. Eur. J.* **2013**, *19* (16), 4986–4991. https://doi.org/10.1002/chem.201300158.

(15) Xu, L.; Gong, H.; Deng, L.; Long, F.; Gu, Y.; Guan, J. Complex-Mediated Synthesis of Tantalum Oxyfluoride Hierarchical Nanostructures for Highly Efficient Photocatalytic Hydrogen Evolution. *ACS Appl. Mater. Interfaces* **2016**, *8* (14), 9395–9404. https://doi.org/10.1021/acsami.6b02622.

(16) Huang, F.; Zhao, H.; Yan, A.; Li, Z.; Liang, H.; Gao, Q.; Qiang, Y. In Situ Thermal Decomposition for Preparation of Nb_3O_7F/Nb_2O_5 Hybrid Nanomaterials with Enhanced Photocatalytic Performance. *Journal of Alloys and Compounds* **2017**, *695*, 489–495. https://doi.org/10.1016/j.jallcom.2016.11.113.

(17) Lange, M. A.; Khan, I.; Dören, R.; Ashraf, M.; Qurashi, A.; Prädel, L.; Panthöfer, M.; Von Der Au, M.; Cossmer, A.; Pfeifer, J.; Meermann, B.; Mondeshki, M.; Tahir, M. N.; Tremel, W. High-Speed Solid State Fluorination of Nb_2O_5 Yields NbO_2F and Nb_3O_7F with Photocatalytic Activity for Oxygen Evolution from Water. *Dalton Trans.* **2021**, *50* (19), 6528–6538. https://doi.org/10.1039/D1DT00533B.

(18) Lange, M. A.; Khan, I.; Opitz, P.; Hartmann, J.; Ashraf, M.; Qurashi, A.; Prädel, L.; Panthöfer, M.; Cossmer, A.; Pfeifer, J.; Simon, F.; Von Der Au, M.; Meermann, B.; Mondeshki, M.; Tahir, M. N.; Tremel, W. A Generalized Method for High-Speed Fluorination of Metal Oxides by Spark Plasma Sintering Yields Ta_3O_7F and TaO_2F with High Photocatalytic Activity for Oxygen Evolution from Water. *Adv. Mater.* **2021**, *33* (20), 2007434. https://doi.org/10.1002/adma.202007434.

(19) Zhao, L. D.; Berardan, D.; Pei, Y. L.; Byl, C.; Pinsard-Gaudart, L.; Dragoe, N. $Bi_{1-x}Sr_xCuSeO$ Oxyselenides as Promising Thermoelectric Materials. *Appl. Phys. Lett.* **2010**, *97* (9), 092118. https://doi.org/10.1063/1.3485050.

(20) Pei, Y.; Shi, X.; LaLonde, A.; Wang, H.; Chen, L.; Snyder, G. J. Convergence of Electronic Bands for High Performance Bulk Thermoelectrics. *Nature* **2011**, *473* (7345), 66–69. https://doi.org/10.1038/nature09996.

(21) Chen, C.; Xu, Z.; Deng, D.; Zhang, J.; Wong, G. K. L.; Wu, B.; Ye, N.; Tang, D. The Vacuum Ultraviolet Phase-matching Characteristics of Nonlinear Optical $KBe_2BO_3F_2$ Crystal. *Appl. Phys. Lett.* **1996**, *68* (21), 2930–2932. https://doi.org/10.1063/1.116358.

(22) McMillen, C. D.; Kolis, J. W. Hydrothermal Crystal Growth of $ABe_2BO_3F_2$ (A=K, Rb, Cs, Tl) NLO Crystals. *Journal of Crystal Growth* **2008**, *310* (7–9), 2033–2038. https://doi.org/10.1016/j.jcrysgro.2007.11.193.

(23) Huang, H.; Yao, J.; Lin, Z.; Wang, X.; He, R.; Yao, W.; Zhai, N.; Chen, C. Molecular Engineering Design to Resolve the Layering Habit and Polymorphism Problems in Deep UV NLO Crystals: New Structures in $MM'Be_2B_2O_6F$ (M═Na, M′═Ca; M═ K, M′═Ca, Sr). *Chem. Mater.* **2011**, *23* (24), 5457–5463. https://doi.org/10.1021/cm202870q.

(24) Yu, H.; Wu, H.; Pan, S.; Yang, Z.; Su, X.; Zhang, F. A Novel Deep UV Nonlinear Optical Crystal $Ba_3B_6O_{11}F_2$, with a New Fundamental Building Block, B_6O_{14} Group. *J. Mater. Chem.* **2012**, *22* (19), 9665. https://doi.org/10.1039/c2jm16058g.

(25) Wu, H.; Yu, H.; Yang, Z.; Hou, X.; Su, X.; Pan, S.; Poeppelmeier, K. R.; Rondinelli, J. M. Designing a Deep-Ultraviolet Nonlinear Optical Material with a Large Second Harmonic Generation Response. *J. Am. Chem. Soc.* **2013**, *135* (11), 4215–4218. https://doi.org/10.1021/ja400500m.

(26) Pan, Y.; Guo, S.-P.; Liu, B.-W.; Xue, H.-G.; Guo, G.-C. Second-Order Nonlinear Optical Crystals with Mixed Anions. *Coordination Chemistry Reviews* **2018**, *374*, 464–496. https://doi.org/10.1016/j.ccr.2018.07.013.

(27) Sorensen, E. M.; Izumi, H. K.; Vaughey, J. T.; Stern, C. L.; Poeppelmeier, K. R. $Ag_4V_2O_6F_2$: An Electrochemically Active and High Silver Density Phase. *J. Am. Chem. Soc.* **2005**, *127* (17), 6347–6352. https://doi.org/10.1021/ja050150f.

(28) Sauvage, F.; Bodenez, V.; Vezin, H.; Albrecht, T. A.; Tarascon, J.-M.; Poeppelmeier, K. R. $Ag_4V_2O_6F_2$ (SVOF): A High Silver Density Phase and Potential New Cathode Material for Implantable Cardioverter Defibrillators. *Inorg. Chem.* **2008**, *47* (19), 8464–8472. https://doi.org/10.1021/ic800793e.

(29) Sauvage, F.; Bodenez, V.; Tarascon, J.-M.; Poeppelmeier, K. R. Room-Temperature Synthesis Leading to Nanocrystalline $Ag_2V_4O_{11}$. *J. Am. Chem. Soc.* **2010**, *132* (19), 6778–6782. https://doi.org/10.1021/ja1009713.

(30) Julien, C. M.; Mauger, A.; Groult, H. Fluorosulfates and Fluorophosphates As New Cathode Materials for Lithium Ion Battery. In *Advanced Fluoride-Based Materials for Energy Conversion*; Elsevier, 2015; pp 77–101. https://doi.org/10.1016/B978-0-12-800679-5.00004-X.

(31) Incorvati, J. T.; Wan, L. F.; Key, B.; Zhou, D.; Liao, C.; Fuoco, L.; Holland, M.; Wang, H.; Prendergast, D.; Poeppelmeier, K. R.; Vaughey, J. T. Reversible Magnesium Intercalation into a Layered Oxyfluoride Cathode. *Chem. Mater.* **2016**, *28* (1), 17–20. https://doi.org/10.1021/acs.chemmater.5b02746.

(32) Lee, J.; Kitchaev, D. A.; Kwon, D.-H.; Lee, C.-W.; Papp, J. K.; Liu, Y.-S.; Lun, Z.; Clément, R. J.; Shi, T.; McCloskey, B. D.; Guo, J.; Balasubramanian, M.; Ceder, G. Reversible Mn^{2+}/Mn^{4+} Double Redox in Lithium-Excess Cathode Materials. *Nature* **2018**, *556* (7700), 185–190. https://doi.org/10.1038/s41586-018-0015-4.

(33) Kageyama, H.; Hayashi, K.; Maeda, K.; Attfield, J. P.; Hiroi, Z.; Rondinelli, J. M.; Poeppelmeier, K. R. Expanding Frontiers in Materials Chemistry and Physics with Multiple Anions. *Nat Commun* **2018**, *9* (1), 772. https://doi.org/10.1038/s41467-018-02838-4.

(34) Harada, J. K.; Charles, N.; Poeppelmeier, K. R.; Rondinelli, J. M. Heteroanionic Materials by Design: Progress Toward Targeted Properties. *Adv. Mater.* **2019**, *31* (19), 1805295. https://doi.org/10.1002/adma.201805295.

(35) Li, Y.; Zhang, Y.-F.; Deng, J.; Dong, W.-H.; Sun, J.-T.; Pan, J.; Du, S. Rational Design of Heteroanionic Two-Dimensional Materials with Emerging Topological, Magnetic, and Dielectric Properties. *J. Phys. Chem. Lett.* **2022**, *13* (16), 3594–3601. https://doi.org/10.1021/acs.jpclett.2c00620.

(36) Rajan, A. C.; Mishra, A.; Satsangi, S.; Vaish, R.; Mizuseki, H.; Lee, K.-R.; Singh, A. K. Machine-Learning-Assisted Accurate Band Gap Predictions of Functionalized MXene. *Chem. Mater.* **2018**, *30* (12), 4031–4038. https://doi.org/10.1021/acs.chemmater.8b00686.

(37) Li, R.; Cheng, Y.; Huang, W. Recent Progress of Janus 2D Transition Metal Chalcogenides: From Theory to Experiments. *Small* **2018**, *14* (45), 1802091. https://doi.org/10.1002/smll.201802091.

(38) Pearson, R. G. *Chemical Hardness*, 1st ed.; Wiley, 1997. https://doi.org/10.1002/3527606173.

(39) Brink, F. J.; Withers, R. L.; Thompson, J. G. An Electron Diffraction and Crystal Chemical Investigation of Oxygen/Fluorine Ordering in Rutile-Type Iron Oxyfluoride, FeOF. *Journal of Solid State Chemistry* **2000**, *155* (2), 359–365. https://doi.org/10.1006/jssc.2000.8925.

(40) Chevrier, V. L.; Hautier, G.; Ong, S. P.; Doe, R. E.; Ceder, G. First-Principles Study of Iron Oxyfluorides and Lithiation of FeOF. *Phys. Rev. B* **2013**, *87* (9), 094118. https://doi.org/10.1103/PhysRevB.87.094118.

(41) Pausewang, G.; Rüdorff, W. Über Alkali-oxofluorometallate der Übergangsmetalle. $A_3^IMeO_xF_{6-x}$-Verbindungen mit x = 1, 2, 3. *Z. Anorg. Allg. Chem.* **1969**, *364* (1–2), 69–87. https://doi.org/10.1002/zaac.19693640107.

(42) Christe, K. O.; Wilson, R. D. Cis- and Trans- Iodine (VII) Oxytetrafluoride Hypofluorite, OIF_4OF. *Inorganic and Nuclear Chemistry Letters* **1979**, *15* (9–10), 375–376. https://doi.org/10.1016/0020-1650(79)80114-2.

(43) Welk, M. E.; Norquist, A. J.; Arnold, F. P.; Stern, C. L.; Poeppelmeier, K. R. Out-of-Center Distortions in d^0 Transition Metal Oxide Fluoride Anions. *Inorg. Chem.* **2002**, *41* (20), 5119–5125. https://doi.org/10.1021/ic025622v.

(44) Fang, C. M.; De Wijs, G. A.; Orhan, E.; De With, G.; De Groot, R. A.; Hintzen, H. T.; Marchand, R. Local Structure and Electronic Properties of $BaTaO_2N$ with Perovskite-Type Structure. *Journal of Physics and Chemistry of Solids* **2003**, *64* (2), 281–286. https://doi.org/10.1016/S0022-3697(02)00296-2.

(45) Voit, E. I.; Voit, A. V.; Mashkovskii, A. A.; Laptash, N. M.; Kavun, V. Ya. Dynamic Disorder in Ammonium Oxofluorotungstates $(NH_4)_2WO_2F_4$ and $(NH_4)_3WO_3F_3$. *J Struct Chem* **2006**, *47* (4), 642–650. https://doi.org/10.1007/s10947-006-0351-3.

(46) Wolff, H.; Dronskowski, R. First-Principles and Molecular-Dynamics Study of Structure and Bonding in Perovskite-Type Oxynitrides ABO_2N (*A* = Ca, Sr, Ba; *B* = Ta, Nb). *J. Comput. Chem.* **2008**, *29* (13), 2260–2267. https://doi.org/10.1002/jcc.20895.

(47) Yang, M.; Oró-Solé, J.; Rodgers, J. A.; Jorge, A. B.; Fuertes, A.; Attfield, J. P. Anion Order in Perovskite Oxynitrides. *Nature Chem* **2011**, *3* (1), 47–52. https://doi.org/10.1038/nchem.908.

(48) Morelock, C. R.; Greve, B. K.; Cetinkol, M.; Chapman, K. W.; Chupas, P. J.; Wilkinson, A. P. Role of Anion Site Disorder in the Near Zero Thermal Expansion of Tantalum Oxyfluoride. *Chem. Mater.* **2013**, *25* (9), 1900–1904. https://doi.org/10.1021/cm400536n.

(49) Brink, F. J.; Withers, R. L.; Norén, L. An Electron Diffraction and Crystal Chemical Investigation of Oxygen/Fluorine Ordering in Niobium Oxyfluoride, NbO_2F. *Journal of Solid State Chemistry* **2002**, *166* (1), 73–80. https://doi.org/10.1006/jssc.2002.9562.

(50) Tao, J. Z.; Sleight, A. W. Very Low Thermal Expansion in TaO_2F. *Journal of Solid State Chemistry* **2003**, *173* (1), 45–48. https://doi.org/10.1016/S0022-4596(03)00077-X.

(51) Morelock, C. R.; Greve, B. K.; Cetinkol, M.; Chapman, K. W.; Chupas, P. J.; Wilkinson, A. P. Role of Anion Site Disorder in the Near Zero Thermal Expansion of Tantalum Oxyfluoride. *Chem. Mater.* **2013**, *25* (9), 1900–1904. https://doi.org/10.1021/cm400536n.

(52) Brink, F. J.; Withers, R. L.; Cordier, S.; Poulain, M. An Electron Diffraction and Bond Valence Sum Investigation of Oxygen/Fluorine Ordering in $Nb_nO_{2n-1}F_{n+2}$, n = 3. *Journal of Solid State Chemistry* **2006**, *179* (2), 341–348. https://doi.org/10.1016/j.jssc.2005.10.014.

(53) Peraudeau, G.; Ravez, J.; Hagenmuller, P.; Arend, H. Study of Phase Transitions in $A_3MO_3F_3$ Compounds (A = K, Rb, Cs; M = Mo, W). *Solid State Communications* **1978**, *27* (5), 591–593. https://doi.org/10.1016/0038-1098(78)90402-7.

(54) Chaminade, J. P.; Cervera-Marzal, M.; Ravez, J. $Na_3WO_3F_3$: A New Ferroelastic-Ferroelectric Oxyfluoride. *Materials Science and Engineering: B* **1989**, *3* (4), 497–500. https://doi.org/10.1016/0921-5107(89)90162-1.

(55) Ye, Z. G.; Ravez, J.; Rivera, J.-P.; Chaminade, J.-P.; Schmid, H. Optical and Dielectric Studies on Ferroelectric Oxyfluoride $K_3MoO_3F_3$ Single Crystals. *Ferroelectrics* **1991**, *124* (1), 281–286. https://doi.org/10.1080/00150199108209452.

(56) Gerasimova, Ju. V.; Vtyurin, A. N.; Ivanenko, A. A.; Shestakov, N. P. IR Spectroscopy Study of $A_2A'MO_3F_3$ Cryolites-Elpasolites. *Ferroelectrics* **2011**, *416* (1), 108–112. https://doi.org/10.1080/00150193.2011.577716.

(57) Atuchin, V. V.; Isaenko, L. I.; Kesler, V. G.; Lin, Z. S.; Molokeev, M. S.; Yelisseyev, A. P.; Zhurkov, S. A. Exploration on Anion Ordering, Optical Properties and Electronic Structure in $K_3WO_3F_3$ Elpasolite. *Journal of Solid State Chemistry* **2012**, *187*, 159–164. https://doi.org/10.1016/j.jssc.2011.12.037.

(58) Attfield, J. P. Principles and Applications of Anion Order in Solid Oxynitrides. *Crystal Growth & Design* **2013**, *13* (10), 4623–4629. https://doi.org/10.1021/cg4011168.

(59) Bernard, D.; Pannetier, J.; Moisan, J. Y.; Lucas, J. Influence des substitutions sur les transitions de phases de pyrochlores derivées de Cd2Nb2O6S. *Journal of Solid State Chemistry* **1973**, *8* (1), 31–36. https://doi.org/10.1016/0022-4596(73)90016-9.

(60) Marvel, M. R.; Lesage, J.; Baek, J.; Halasyamani, P. S.; Stern, C. L.; Poeppelmeier, K. R. Cation−Anion Interactions and Polar Structures in the Solid State. *J. Am. Chem. Soc.* **2007**, *129* (45), 13963–13969. https://doi.org/10.1021/ja074659h.

(61) Pinlac, R. A. F.; Stern, C. L.; Poeppelmeier, K. R. New Layered Oxide-Fluoride Perovskites: $KNaNbOF_5$ and $KNaMO_2F_4$ ($M = Mo^{6+}$, W^{6+}). *Crystals* **2011**, *1* (1), 3–14. https://doi.org/10.3390/cryst1010003.

(62) Udovenko, A. A.; Laptash, N. M. Dynamic Orientational Disorder in Crystals of Fluoroelpasolites, Structural Refinement of $(NH_4)_3AlF_6$, $(NH_4)_3TiOF_5$ and Rb_2KTiOF_5. *Acta Crystallogr B Struct Sci* **2011**, *67* (6), 447–454. https://doi.org/10.1107/S0108768111044867.

(63) *Functional Oxides | Wiley*. Wiley.com. https://www.wiley.com/en-us/Functional+Oxides-p-9781119972945 (accessed 2023-06-30).

(64) Brown, I. D.; Altermatt, D. Bond-Valence Parameters Obtained from a Systematic Analysis of the Inorganic Crystal Structure Database. *Acta Crystallogr B Struct Sci* **1985**, *41* (4), 244–247. https://doi.org/10.1107/S0108768185002063.

(65) Brese, N. E.; O'Keeffe, M. Bond-Valence Parameters for Solids. *Acta Crystallogr B Struct Sci* **1991**, *47* (2), 192–197. https://doi.org/10.1107/S0108768190011041.

(66) Pauling, L. THE PRINCIPLES DETERMINING THE STRUCTURE OF COMPLEX IONIC CRYSTALS. *J. Am. Chem. Soc.* **1929**, *51* (4), 1010–1026. https://doi.org/10.1021/ja01379a006.

(67) Bevan, D. J. M.; Mohyla, J.; Hoskins, B. F.; Steen, R. J. The Crystal Structures of Some Vernier Phases in the Yttrium Oxide-Fluoride System. *European Journal of Solid State and Inorganic Chemistry; (France)* **1990**, *27:3*.

(68) Aftati, A.; Champarnaud-Mesjard, J.-C.; Frit, B. Crystal Structure of a New Oxyfluoride, Cd_4F_6O: Relations to the Fluorite and the β-Bi_2O_3 Types. *Eur. j. solid state inorg. chem* **1993**, *30* (11), 1063–1073.

(69) Mercier, H. P. A.; Schrobilgen, G. J. Technetium(VII) Dioxotrifluoride, TcO_2F_3: Synthesis, x-Ray Structure Determination, and Raman Spectrum. *Inorg. Chem.* **1993**, *32* (2), 145–151. https://doi.org/10.1021/ic00054a006.

(70) Laval, J.-P.; Champarnaud-Mesjard, J.-C.; Frit, B.; Britel, A.; Mikou, A. $Bi_7F_{11}O_5$: A New Ordered Anion-Excess Fluorite-Related Structure with Columnar Clusters. *Eur. j. solid state inorg. chem* **1994**, *31* (10), 943–956.

(71) Laval, J. P.; Taoudi, A.; Abaouz, A.; Frit, B. $Lu_3O_2F_5$: A New Highly Densified Member (n = 3) of the M_nX_{2n+1} Series of Fluorite-Related Vernier Phases. *Journal of Solid State Chemistry* **1995**, *119* (1), 125–130. https://doi.org/10.1016/0022-4596(95)80018-K.

(72) Ider, A.; Laval, J. P.; Frit, B.; Carré, J.; Bastide, J. P. Crystal Structure of $Te_2O_3F_2$. *Journal of Solid State Chemistry* **1996**, *123* (1), 68–72. https://doi.org/10.1006/jssc.1996.0153.

(73) Guillet, L.; Ider, A.; Laval, J. P.; Frit, B. Crystal Structure of $TeOF_2$. *Journal of Fluorine Chemistry* **1999**, *93* (1), 33–38. https://doi.org/10.1016/S0022-1139(98)00271-1.

(74) Beaury, L.; Derouet, J.; Hölsä, J.; Lastusaari, M.; Rodriguez-Carvajal, J. Neutron Powder Diffraction Studies of Stoichiometric NdOF between 1.5 and 300 K. *Solid State Sciences* **2002**, *4* (8), 1039–1043. https://doi.org/10.1016/S1293-2558(02)01361-4.

(75) Brink, F. J.; Norén, L.; Withers, R. L. Electron Diffraction Evidence for Continuously Variable, Composition-Dependent O/F Ordering in the ReO_3 Type, $Nb^{V}_{1-x}Nb^{IV}_{x}O_{2-x}F_{1+x}$, $0 \leqslant x \leqslant 0.48$, Solid Solution. *Journal of Solid State Chemistry* **2004**, *177* (6), 2177–2182. https://doi.org/10.1016/j.jssc.2004.03.001.

(76) Müller-Bunz, H.; Janka, O.; Schleid, T. $Er_3O_2F_5$: Ein Erbiumoxidfluorid Mit Vernier-Struktur. *Zeitschrift für anorganische und allgemeine Chemie* **2007**, *633* (1), 37–39. https://doi.org/10.1002/zaac.200600274.

(77) Miller, J. M. Fluorine-19 Magic-Angle Spinning NMR. *Progress in Nuclear Magnetic Resonance Spectroscopy* **1996**, *28* (3–4), 255–281. https://doi.org/10.1016/0079-6565(95)01024-6.

(78) Harris, R. K.; Becker, E. D.; Cabral De Menezes, S. M.; Goodfellow, R.; Granger, P. NMR Nomenclature. Nuclear Spin Properties and Conventions for Chemical Shifts(IUPAC Recommendations 2001). *Pure and Applied Chemistry* **2001**, *73* (11), 1795–1818. https://doi.org/10.1351/pac200173111795.

(79) Caravatti, P.; Braunschweiler, L.; Ernst, R. R. Heteronuclear Correlation Spectroscopy in Rotating Solids. *Chemical Physics Letters* **1983**, *100* (4), 305–310. https://doi.org/10.1016/0009-2614(83)80276-0.

(80) Pruski, M.; Lang, D. P.; Fernandez, C.; Amoureux, J. P. Multiple-Quantum Magic-Angle Spinning NMR with Cross-Polarization: Spectral Editing of High-Resolution Spectra of Quadrupolar Nuclei. *Solid State Nuclear Magnetic Resonance* **1997**, *7* (4), 327–331. https://doi.org/10.1016/S0926-2040(96)01284-2.

(81) Lesage, A.; Sakellariou, D.; Steuernagel, S.; Emsley, L. Carbon−Proton Chemical Shift Correlation in Solid-State NMR by Through-Bond Multiple-Quantum Spectroscopy. *J. Am. Chem. Soc.* **1998**, *120* (50), 13194–13201. https://doi.org/10.1021/ja983048+.

(82) Massiot, D.; Fayon, F.; Alonso, B.; Trebosc, J.; Amoureux, J.-P. Chemical Bonding Differences Evidenced from J-Coupling in Solid State NMR Experiments Involving Quadrupolar Nuclei. *Journal of Magnetic Resonance* **2003**, *164* (1), 160–164. https://doi.org/10.1016/S1090-7807(03)00134-4.

(83) Amoureux, J. P.; Trébosc, J.; Tricot, G. Measurement of Through-Space Connectivities between Spin-1/2 and Quadrupolar Nuclei in Solid-State NMR: The TEDOR-MQMAS Method. *Magn. Reson. Chem.* **2007**, *45* (S1), S187–S191. https://doi.org/10.1002/mrc.2135.

(84) Vyalikh, A.; Bulusheva, L. G.; Chekhova, G. N.; Pinakov, D. V.; Okotrub, A. V.; Scheler, U. Fluorine Patterning in Room-Temperature Fluorinated Graphite Determined by Solid-State NMR and DFT. *J. Phys. Chem. C* **2013**, *117* (15), 7940–7948. https://doi.org/10.1021/jp4028029.

(85) Lim, K. H.; Grey, C. P. Triple Quantum Cross-Polarization NMR of $^{1}H/^{27}Al$ and $^{19}F/^{23}Na$ Spin Systems in Solids. *Chemical Physics Letters* **1999**, *312* (1), 45–56. https://doi.org/10.1016/S0009-2614(99)00884-2.

(86) Lim, K. H.; Grey, C. P. $^{19}F/^{23}Na$ Multiple Quantum Cross Polarization NMR in Solids. *The Journal of Chemical Physics* **2000**, *112* (17), 7490–7504. https://doi.org/10.1063/1.481347.

(87) Du, L.-S.; Samoson, A.; Tuherm, T.; Grey, C. P. $^{19}F/^{23}Na$ Double Resonance MAS NMR Study of Oxygen/Fluorine Ordering in the Oxyfluoride $Na_5W_3O_9F_5$. *Chem. Mater.* **2000**, *12* (12), 3611–3616. https://doi.org/10.1021/cm000355h.

(88) Dutour, J.; Guillou, N.; Huguenard, C.; Taulelle, F.; Mellot-Draznieks, C.; Férey, G. Chiolite, a Case Study for Combining NMR Crystallography, Diffraction and Structural Simulation. *Solid State Sciences* **2004**, *6* (10), 1059–1067. https://doi.org/10.1016/j.solidstatesciences.2004.07.031.

(89) Taulelle, F.; Pruski, M.; Amoureux, J. P.; Lang, D.; Bailly, A.; Huguenard, C.; Haouas, M.; Gérardin, C.; Loiseau, T.; Férey, G. Isomerization of the Prenucleation Building Unit during Crystallization of $AlPO_4$-CJ2: An MQMAS, CP-MQMAS, and HETCOR NMR Study. *J. Am. Chem. Soc.* **1999**, *121* (51), 12148–12153. https://doi.org/10.1021/ja991295n.

(90) Fechtelkord, M.; Behrens, H.; Holtz, F.; Bretherton, J. L.; Fyfe, C. A.; Groat, L. A.; Raudsepp, M. Influence of F Content on the Composition of Al-Rich Synthetic Phlogopite: Part II. Probing the Structural Arrangement of Aluminum in Tetrahedral and Octahedral Layers by ^{27}Al MQMAS and $^{1}H/^{19}F$-^{27}Al HETCOR and REDOR Experiments. *American Mineralogist* **2003**, *88* (7), 1046–1054. https://doi.org/10.2138/am-2003-0713.

(91) Martineau, C.; Legein, C.; Buzaré, J.-Y.; Fayon, F. On the Assignment of ^{19}F MAS NMR Spectra of Fluoroaluminates Using through-Space Spectral Edition of ^{19}F–^{27}Al and ^{19}F– ^{19}F Connectivities. *Phys. Chem. Chem. Phys.* **2009**, *11* (6), 950–957. https://doi.org/10.1039/B812091A.

(92) Wang, Q.; Hu, B.; Lafon, O.; Trébosc, J.; Deng, F.; Amoureux, J.-P. Homonuclear Dipolar Recoupling under Ultra-Fast Magic-Angle Spinning: Probing 19F−19F Proximities by Solid-State NMR. *Journal of Magnetic Resonance* **2010**, *203* (1), 113–128. https://doi.org/10.1016/j.jmr.2009.12.009.

(93) Taulelle, F. Clipping a Network into a Crystal. *Solid State Sciences* **2001**, *3* (7), 795–800. https://doi.org/10.1016/S1293-2558(01)01198-0.

(94) Martineau, C.; Fayon, F.; Legein, C.; Buzar?, J.-Y.; Silly, G.; Massiot, D. Accurate Heteronuclear J-Coupling Measurements in Dilute Spin Systems Using the Multiple-Quantum Filtered J-Resolved Experiment. *Chem. Commun.* **2007**, No. 26, 2720. https://doi.org/10.1039/b703321d.

(95) Martineau, C.; Fayon, F.; Legein, C.; Buzaré, J.-Y.; Body, M.; Massiot, D.; Goutenoire, F. Structure Determination of β-Pb_2ZnF_6 by Coupling Multinuclear Solid State NMR, Powder XRD and Ab Initio Calculations. *Dalton Trans.* **2008**, No. 44, 6150. https://doi.org/10.1039/b810863c.

(96) Martineau, C.; Fayon, F.; Legein, C.; Buzaré, J.-Y.; Goutenoire, F.; Suard, E. Neutron Powder Diffraction, Multinuclear, and Multidimensional NMR Structural Investigation of $Pb_5Ga_3F_{19}$. *Inorg. Chem.* **2008**, *47* (23), 10895–10905. https://doi.org/10.1021/ic801044j.

(97) Martineau, C.; Legein, C.; Body, M.; Péron, O.; Boulard, B.; Fayon, F. Structural Investigation of α-$LaZr_2F_{11}$ by Coupling X-Ray Powder Diffraction, ^{19}F Solid State NMR and DFT Calculations. *Journal of Solid State Chemistry* **2013**, *199*, 326–333. https://doi.org/10.1016/j.jssc.2012.12.016.

(98) Geen, H.; Titman, J. J.; Gottwald, J.; Spiess, H. W. Solid-State Proton Multiple-Quantum NMR Spectroscopy with Fast Magic Angle Spinning. *Chemical Physics Letters* **1994**, *227* (1–2), 79–86. https://doi.org/10.1016/0009-2614(94)00789-6.

(99) Martin, C. D. Effect of A-Site Cation Radius on Ordering of BX_6 Octahedra in (K,Na)MgF_3 Perovskite. *American Mineralogist* **2005**, *90* (10), 1522–1533. https://doi.org/10.2138/am.2005.1693.

(100) Martineau, C.; Fayon, F.; Suchomel, M. R.; Allix, M.; Massiot, D.; Taulelle, F. Structure Resolution of $Ba_5Al_3F_{19}$ and Investigation of Fluorine Ion Dynamics by Synchrotron Powder Diffraction, Variable-Temperature Solid-State NMR, and Quantum Computations. *Inorg. Chem.* **2011**, *50* (6), 2644–2653. https://doi.org/10.1021/ic102534d.

(101) Rollet, A.-L.; Allix, M.; Veron, E.; Deschamps, M.; Montouillout, V.; Suchomel, M. R.; Suard, E.; Barre, M.; Ocaña, M.; Sadoc, A.; Boucher, F.; Bessada, C.; Massiot, D.; Fayon, F. Synthesis and Structure Resolution of $RbLaF_4$. *Inorg. Chem.* **2012**, *51* (4), 2272–2282. https://doi.org/10.1021/ic202301e.

(102) Martineau, C.; Allix, M.; Suchomel, M. R.; Porcher, F.; Vivet, F.; Legein, C.; Body, M.; Massiot, D.; Taulelle, F.; Fayon, F. Structure Determination of Ba_5AlF_{13} by Coupling Electron, Synchrotron and Neutron Powder Diffraction, Solid-State NMR and Ab Initio Calculations. *Dalton Trans.* **2016**, *45* (39), 15565–15574. https://doi.org/10.1039/C6DT02454H.

(103) Alam, T. M.; Clawson, J. S.; Bonhomme, F.; Thoma, S. G.; Rodriguez, M. A.; Zheng, S.; Autschbach, J. A Solid-State NMR, X-Ray Diffraction, and Ab Initio Investigation into the Structures of Novel Tantalum Oxyfluoride Clusters. *Chem. Mater.* **2008**, *20* (6), 2205–2217. https://doi.org/10.1021/cm0717763.

(104) Griffin, J. M.; Yates, J. R.; Berry, A. J.; Wimperis, S.; Ashbrook, S. E. High-Resolution ^{19}F MAS NMR Spectroscopy: Structural Disorder and Unusual *J* Couplings in a Fluorinated Hydroxy-Silicate. *J. Am. Chem. Soc.* **2010**, *132* (44), 15651–15660. https://doi.org/10.1021/ja105347q.

(105) DeVore, M. A.; Klug, C. A.; Kriz, M. R.; Roy, L. E.; Wellons, M. S. Investigations of Uranyl Fluoride Sesquihydrate ($UO_2F_2 \cdot 1.57H_2O$): Combining ^{19}F Solid-State MAS NMR Spectroscopy and GIPAW Chemical Shift Calculations. *J. Phys. Chem. A* **2018**, *122* (34), 6873–6878. https://doi.org/10.1021/acs.jpca.8b04369.

(106) Laval, J.-P.; Duclère, J.-R.; Couderc, V.; Allix, M.; Genevois, C.; Sarou-Kanian, V.; Fayon, F.; Coulon, P.-E.; Chenu, S.; Colas, M.; Cornette, J.; Thomas, P.; Delaizir, G. Highly Transparent Fluorotellurite Glass-Ceramics: Structural Investigations and Luminescence Properties. *Inorg. Chem.* **2019**, *58* (24), 16387–16401. https://doi.org/10.1021/acs.inorgchem.9b01955.

(107) Wang, Q.; Hu, B.; Fayon, F.; Trébosc, J.; Legein, C.; Lafon, O.; Deng, F.; Amoureux, J.-P. Double-Quantum ^{19}F–^{19}F Dipolar Recoupling at Ultra-Fast Magic Angle Spinning NMR: Application to the Assignment of ^{19}F NMR Spectra of Inorganic Fluorides. *Phys. Chem. Chem. Phys.* **2009**, *11* (44), 10391. https://doi.org/10.1039/b914468d.

(108) Ashbrook, S. E.; McKay, D. Combining Solid-State NMR Spectroscopy with First-Principles Calculations – a Guide to NMR Crystallography. *Chem. Commun.* **2016**, *52* (45), 7186–7204. https://doi.org/10.1039/C6CC02542K.

(109) Charpentier, T. The PAW/GIPAW Approach for Computing NMR Parameters: A New Dimension Added to NMR Study of Solids. *Solid State Nuclear Magnetic Resonance* **2011**, *40* (1), 1–20. https://doi.org/10.1016/j.ssnmr.2011.04.006.

(110) Bonhomme, C.; Gervais, C.; Babonneau, F.; Coelho, C.; Pourpoint, F.; Azaïs, T.; Ashbrook, S. E.; Griffin, J. M.; Yates, J. R.; Mauri, F.; Pickard, C. J. First-Principles Calculation of NMR Parameters Using the Gauge Including Projector Augmented Wave Method: A Chemist's Point of View. *Chem. Rev.* **2012**, *112* (11), 5733–5779. https://doi.org/10.1021/cr300108a.

(111) Ashbrook, S. E.; Dawson, D. M. Exploiting Periodic First-Principles Calculations in NMR Spectroscopy of Disordered Solids. *Acc. Chem. Res.* **2013**, *46* (9), 1964–1974. https://doi.org/10.1021/ar300303w.

(112) Moran, R. F.; Dawson, D. M.; Ashbrook, S. E. Exploiting NMR Spectroscopy for the Study of Disorder in Solids. *International Reviews in Physical Chemistry* **2017**, *36* (1), 39–115. https://doi.org/10.1080/0144235X.2017.1256604.

(113) Ashbrook, S. E.; Griffin, J. M.; Johnston, K. E. Recent Advances in Solid-State Nuclear Magnetic Resonance Spectroscopy. *Annual Rev. Anal. Chem.* **2018**, *11* (1), 485–508. https://doi.org/10.1146/annurev-anchem-061417-125852.

(114) Pickard, C. J.; Mauri, F. All-Electron Magnetic Response with Pseudopotentials: NMR Chemical Shifts. *Phys. Rev. B* **2001**, *63* (24), 245101. https://doi.org/10.1103/PhysRevB.63.245101.

(115) Yates, J. R.; Pickard, C. J.; Mauri, F. Calculation of NMR Chemical Shifts for Extended Systems Using Ultrasoft Pseudopotentials. *Phys. Rev. B* **2007**, *76* (2), 024401. https://doi.org/10.1103/PhysRevB.76.024401.

(116) Sadoc, A.; Body, M.; Legein, C.; Biswal, M.; Fayon, F.; Rocquefelte, X.; Boucher, F. NMR Parameters in Alkali, Alkaline Earth and Rare Earth Fluorides from First Principle Calculations. *Phys. Chem. Chem. Phys.* **2011**, *13* (41), 18539. https://doi.org/10.1039/c1cp21253b.

(117) Biswal, M.; Body, M.; Legein, C.; Sadoc, A.; Boucher, F. NbF_5 and TaF_5: Assignment of ^{19}F NMR Resonances and Chemical Bond Analysis from GIPAW Calculations. *Journal of Solid State Chemistry* **2013**, *207*, 208–217. https://doi.org/10.1016/j.jssc.2013.09.001.

(118) Sadoc, A.; Biswal, M.; Body, M.; Legein, C.; Boucher, F.; Massiot, D.; Fayon, F. NMR Parameters in Column 13 Metal Fluoride Compounds (AlF_3, GaF_3, InF_3 and TlF) from First Principle Calculations. *Solid State Nuclear Magnetic Resonance* **2014**, *59–60*, 1–7. https://doi.org/10.1016/j.ssnmr.2014.01.001.

(119) Rakhmatullin, A.; Polovov, I. B.; Maltsev, D.; Allix, M.; Volkovich, V.; Chukin, A. V.; Boča, M.; Bessada, C. Combined Approach for the Structural Characterization of Alkali Fluoroscandates: Solid-State NMR, Powder X-Ray Diffraction, and Density Functional Theory Calculations. *Inorg. Chem.* **2018**, *57* (3), 1184–1195. https://doi.org/10.1021/acs.inorgchem.7b02617.

(120) Rakhmatullin, A.; Boča, M.; Mlynáriková, J.; Hadzimová, E.; Vasková, Z.; Polovov, I. B.; Mičušík, M. Solid State NMR and XPS of Ternary Fluorido-Zirconates of Various Coordination

Modes. *Journal of Fluorine Chemistry* **2018**, *208*, 24–35. https://doi.org/10.1016/j.jfluchem.2018.01.010.

(121) Murakami, M.; Noda, Y.; Takegoshi, K. Terminal and Bridging Fluorine Ligands in TiF_4 as Studied by ^{19}F NMR in Solids. *Solid State Nuclear Magnetic Resonance* **2019**, *101*, 82–88. https://doi.org/10.1016/j.ssnmr.2019.05.007.

(122) Legein, C.; Body, M.; Lhoste, J.; Li, W.; Charpentier, T.; Dambournet, D. Synthesis, Crystal Structure and ^{19}F NMR Parameters Modelling of $CaTiF_6(H_2O)_2$ Yielding to a Revision of the Bond-Valence Parameters for the Ti^{4+}/F^- Ion Pair. *Journal of Solid State Chemistry* **2023**, *319*, 123793. https://doi.org/10.1016/j.jssc.2022.123793.

(123) Blöchl, P. E. Projector Augmented-Wave Method. *Phys. Rev. B* **1994**, *50* (24), 17953–17979. https://doi.org/10.1103/PhysRevB.50.17953.

(124) Petrilli, H. M.; Blöchl, P. E.; Blaha, P.; Schwarz, K. Electric-Field-Gradient Calculations Using the Projector Augmented Wave Method. *Phys. Rev. B* **1998**, *57* (23), 14690–14697. https://doi.org/10.1103/PhysRevB.57.14690.

(125) Kresse, G.; Joubert, D. From Ultrasoft Pseudopotentials to the Projector Augmented-Wave Method. *Phys. Rev. B* **1999**, *59* (3), 1758–1775. https://doi.org/10.1103/PhysRevB.59.1758.

(126) Florian, P.; Veron, E.; Green, T. F. G.; Yates, J. R.; Massiot, D. Elucidation of the Al/Si Ordering in Gehlenite $Ca_2Al_2SiO_7$ by Combined ^{29}Si and ^{27}Al NMR Spectroscopy/Quantum Chemical Calculations. *Chem. Mater.* **2012**, *24* (21), 4068–4079. https://doi.org/10.1021/cm3016935.

(127) Véron, E.; Garaga, M. N.; Pelloquin, D.; Cadars, S.; Suchomel, M.; Suard, E.; Massiot, D.; Montouillout, V.; Matzen, G.; Allix, M. Synthesis and Structure Determination of $CaSi_{1/3}B_{2/3}O_{8/3}$: A New Calcium Borosilicate. *Inorg. Chem.* **2013**, *52* (8), 4250–4258. https://doi.org/10.1021/ic302114t.

(128) Ferrara, C.; Tealdi, C.; Pedone, A.; Menziani, M. C.; Rossini, A. J.; Pintacuda, G.; Mustarelli, P. Local versus Average Structure in $LaSrAl_3O_7$: A NMR and DFT Investigation. *J. Phys. Chem. C* **2013**, *117* (45), 23451–23458. https://doi.org/10.1021/jp403022j.

(129) Playford, Helen. Y.; Hannon, A. C.; Tucker, M. G.; Dawson, D. M.; Ashbrook, S. E.; Kastiban, R. J.; Sloan, J.; Walton, R. I. Characterization of Structural Disorder in γ-Ga_2O_3. *J. Phys. Chem. C* **2014**, *118* (29), 16188–16198. https://doi.org/10.1021/jp5033806.

(130) Ashbrook, S. E.; Mitchell, M. R.; Sneddon, S.; Moran, R. F.; De Los Reyes, M.; Lumpkin, G. R.; Whittle, K. R. New Insights into Phase Distribution, Phase Composition and Disorder in $Y_2(Zr,Sn)_2O_7$ Ceramics from NMR Spectroscopy. *Phys. Chem. Chem. Phys.* **2015**, *17* (14), 9049–9059. https://doi.org/10.1039/C4CP05827E.

(131) Flemming, R. L.; Terskikh, V.; Ye, E. Aluminum Environments in Synthetic Ca-Tschermak Clinopyroxene ($CaAlAlSiO_6$) from Rietveld Refinement, ^{27}Al NMR, and First-Principles Calculations. *American Mineralogist* **2015**, *100* (10), 2219–2230. https://doi.org/10.2138/am-2015-5348.

(132) Moran, R. F.; McKay, D.; Pickard, C. J.; Berry, A. J.; Griffin, J. M.; Ashbrook, S. E. Hunting for Hydrogen: Random Structure Searching and Prediction of NMR Parameters of Hydrous Wadsleyite. *Phys. Chem. Chem. Phys.* **2016**, *18* (15), 10173–10181. https://doi.org/10.1039/C6CP01529H.

(133) Diez-Gómez, V.; Arbi, K.; Sanz, J. Modeling Ti/Ge Distribution in $LiTi_{2-x}Ge_x(PO_4)_3$ NASICON Series by ^{31}P MAS NMR and First-Principles DFT Calculations. *J. Am. Chem. Soc.* **2016**, *138* (30), 9479–9486. https://doi.org/10.1021/jacs.6b03583.

(134) Fernandes, A.; McKay, D.; Sneddon, S.; Dawson, D. M.; Lawson, S.; Veazey, R.; Whittle, K. R.; Ashbrook, S. E. Phase Composition and Disorder in $La_2(Sn,Ti)_2O_7$ Ceramics: New Insights from NMR Crystallography. *J. Phys. Chem. C* **2016**, *120* (36), 20288–20296. https://doi.org/10.1021/acs.jpcc.6b06962.

(135) Cadars, S.; Ahn, N. H.; Okhotnikov, K.; Shin, J.; Vicente, A.; Hong, S. B.; Fernandez, C. Modeling Short-Range Substitution Order and Disorder in Crystals: Application to the Ga/Si Distribution in a Natrolite Zeolite. *Solid State Nuclear Magnetic Resonance* **2017**, *84*, 182–195. https://doi.org/10.1016/j.ssnmr.2017.04.001.

(136) Girard, G.; Vasconcelos, F.; Montagne, L.; Delevoye, L. ^{31}P MAS NMR Spectroscopy with ^{93}Nb Decoupling and DFT Calculations: A Structural Characterization of Defects in a Niobium-Phosphate Phase. *Solid State Nuclear Magnetic Resonance* **2017**, *84*, 210–215. https://doi.org/10.1016/j.ssnmr.2017.05.003.

(137) Grüninger, H.; Armstrong, K.; Greim, D.; Boffa-Ballaran, T.; Frost, D. J.; Senker, J. Hidden Oceans? Unraveling the Structure of Hydrous Defects in the Earth's Deep Interior. *J. Am. Chem. Soc.* **2017**, *139* (30), 10499–10505. https://doi.org/10.1021/jacs.7b05432.

(138) Fernandez-Carrion, A. J.; Al Saghir, K.; Veron, E.; Becerro, A. I.; Porcher, F.; Wisniewski, W.; Matzen, G.; Fayon, F.; Allix, M. Local Disorder and Tunable Luminescence in $Sr_{1-x/2}Al_{2-x}Si_xO_4$ ($0.2 \leq x \leq 0.5$) Transparent Ceramics. *Inorg. Chem.* **2017**, *56* (23), 14446–14458. https://doi.org/10.1021/acs.inorgchem.7b01881.

(139) Fischer, M. Local Environment and Dynamic Behavior of Fluoride Anions in Silicogermanate Zeolites: A Computational Study of the AST Framework. *J. Phys. Chem. C* **2019**, *123* (3), 1852–1865. https://doi.org/10.1021/acs.jpcc.8b10770.

(140) McKay, D.; Moran, R. F.; Dawson, D. M.; Griffin, J. M.; Sturniolo, S.; Pickard, C. J.; Berry, A. J.; Ashbrook, S. E. A Picture of Disorder in Hydrous Wadsleyite—Under the Combined Microscope of Solid-State NMR Spectroscopy and *Ab Initio* Random Structure Searching. *J. Am. Chem. Soc.* **2019**, *141* (7), 3024–3036. https://doi.org/10.1021/jacs.8b11519.

(141) Serrano-Sevillano, J.; Carlier, D.; Saracibar, A.; Lopez Del Amo, J. M.; Casas-Cabanas, M. DFT-Assisted Solid-State NMR Characterization of Defects in Li_2MnO_3. *Inorg. Chem.* **2019**, *58* (13), 8347–8356. https://doi.org/10.1021/acs.inorgchem.9b00394.

(142) Moran, R. F.; McKay, D.; Tornstrom, P. C.; Aziz, A.; Fernandes, A.; Grau-Crespo, R.; Ashbrook, S. E. Ensemble-Based Modeling of the NMR Spectra of Solid Solutions: Cation Disorder in $Y_2(Sn,Ti)_2O_7$. *J. Am. Chem. Soc.* **2019**, *141* (44), 17838–17846. https://doi.org/10.1021/jacs.9b09036.

(143) Moran, R. F.; Fernandes, A.; Dawson, D. M.; Sneddon, S.; Gandy, A. S.; Reeves-McLaren, N.; Whittle, K. R.; Ashbrook, S. E. Phase Distribution, Composition, and Disorder in $Y_2(Hf,Sn)_2O_7$ Ceramics: Insights from Solid-State NMR Spectroscopy and First-Principles Calculations. *J. Phys. Chem. C* **2020**, *124* (31), 17073–17084. https://doi.org/10.1021/acs.jpcc.0c04542.

(144) Ashbrook, S. E.; Dawson, D. M.; Gan, Z.; Hooper, J. E.; Hung, I.; Macfarlane, L. E.; McKay, D.; McLeod, L. K.; Walton, R. I. Application of NMR Crystallography to Highly Disordered

Templated Materials: Extensive Local Structural Disorder in the Gallophosphate GaPO-34A. *Inorg. Chem.* **2020**, *59* (16), 11616–11626. https://doi.org/10.1021/acs.inorgchem.0c01450.

(145) Fischer, M. Fluoride Anions in All-Silica Zeolites: Studying Preferred Fluoride Sites and Dynamic Disorder with Density Functional Theory Calculations. *J. Phys. Chem. C* **2021**, *125* (16), 8825–8839. https://doi.org/10.1021/acs.jpcc.1c01440.

(146) Hancock, J. C.; Griffith, K. J.; Choi, Y.; Bartel, C. J.; Lapidus, S. H.; Vaughey, J. T.; Ceder, G.; Poeppelmeier, K. R. Expanding the Ambient-Pressure Phase Space of $CaFe_2O_4$-Type Sodium Postspinel Host–Guest Compounds. *ACS Org. Inorg. Au* **2022**, *2* (1), 8–22. https://doi.org/10.1021/acsorginorgau.1c00019.

(147) Leube, B. T.; Collins, C. M.; Daniels, L. M.; Duff, B. B.; Dang, Y.; Chen, R.; Gaultois, M. W.; Manning, T. D.; Blanc, F.; Dyer, M. S.; Claridge, J. B.; Rosseinsky, M. J. Cation Disorder and Large Tetragonal Supercell Ordering in the Li-Rich Argyrodite $Li_7Zn_{0.5}SiS_6$. *Chem. Mater.* **2022**, *34* (9), 4073–4087. https://doi.org/10.1021/acs.chemmater.2c00320.

(148) Dabachi, J.; Body, M.; Dittmer, J.; Fayon, F.; Legein, C. Structural Refinement of the RT LaOF Phases by Coupling Powder X-Ray Diffraction, ^{19}F and ^{139}La Solid State NMR and DFT Calculations of the NMR Parameters. *Dalton Trans.* **2015**, *44* (47), 20675–20684. https://doi.org/10.1039/C5DT04028K.

(149) Šimko, F.; Rakhmatullin, A.; Véron, E.; Allix, M.; Florian, P.; Kontrík, M.; Netriová, Z.; Korenko, M.; Kavečanský, V.; Bessada, C. Oxo- and Oxofluoroaluminates in the $RbF–Al_2O_3$ System: Synthesis and Structural Characterization. *Inorg. Chem.* **2018**, *57* (21), 13702–13712. https://doi.org/10.1021/acs.inorgchem.8b02275.

(150) Albino, M.; Body, M.; Legein, C.; Hémon-Ribaud, A.; Leblanc, M.; Maisonneuve, V.; Lhoste, J. NMR Crystallography, Hydrogen Bonding and Optical Properties of the Novel 2D Hybrid Oxyfluorotitanate $[H_2Taz]_2{\cdot}(Ti_5O_5F_{12})$. *Crystal Growth & Design* **2018**, *18* (11), 6873–6884. https://doi.org/10.1021/acs.cgd.8b01085.

(151) Ding, F.; Griffith, K. J.; Koçer, C. P.; Saballos, R. J.; Wang, Y.; Zhang, C.; Nisbet, M. L.; Morris, A. J.; Rondinelli, J. M.; Poeppelmeier, K. R. Multimodal Structure Solution with ^{19}F NMR Crystallography of Spin Singlet Molybdenum Oxyfluorides. *J. Am. Chem. Soc.* **2020**, *142* (28), 12288–12298. https://doi.org/10.1021/jacs.0c04019.

(152) Camus-Génot, V.; Guiet, A.; Lhoste, J.; Fayon, F.; Body, M.; Kodjikian, S.; Moury, R.; Leblanc, M.; Bobet, J. L.; Legein, C.; Maisonneuve, V. Controlled Morphology Synthesis of Nanostructured β-$AlF_{3-x}(OH)_x$ with Tunable Specific Surface Area. *Crystal Growth & Design* **2021**, *21* (10), 5914–5927. https://doi.org/10.1021/acs.cgd.1c00808.

(153) Dabachi, J.; Body, M.; Galven, C.; Boucher, F.; Legein, C. Preparation-Dependent Composition and O/F Ordering in NbO_2F and TaO_2F. *Inorg. Chem.* **2017**, *56* (9), 5219–5232. https://doi.org/10.1021/acs.inorgchem.7b00355.

(154) Chien, P.-H.; Harada, J. K.; Liu, H.; Patel, S.; Huang, C.; Rondinelli, J. M.; Poeppelmeier, K. R.; Hu, Y.-Y. Microscopic Insights into the Reconstructive Phase Transition of $KNaNbOF_5$ with ^{19}F NMR Spectroscopy. *Chem. Mater.* **2020**, *32* (13), 5715–5722. https://doi.org/10.1021/acs.chemmater.0c01439.

(155) Harada, J. K.; Chien, P.-H.; Liu, H.; Patel, S.; Chen, C.-H. A.; Charles, N.; Hu, Y.-Y.; Poeppelmeier, K. R.; Rondinelli, J. M. Phase Transitions and Potential Ferroelectricity in Noncentrosymmetric $KNaNbOF_5$. *Phys. Rev. Materials* **2021**, *5* (12), 124401. https://doi.org/10.1103/PhysRevMaterials.5.124401.

Chapter I

Deciphering O/F Ordering in Disordered Inorganic Oxyfluorides: A Multimodal Approach

I.1. Introduction

The general premise of this chapter is to provide an in-depth description of fundamentals regarding the approach used in this thesis for describing O/F ordering in disordered inorganic oxyfluorides. The chapter consists of three sections. The first section describes the general principles of Nuclear Magnetic Resonance (NMR) spectroscopy, the different interactions that are of importance in solid-state systems as well as NMR sequences of pertinence to this thesis. The second section covers basics of crystallography for both ordered and disordered crystals, with a focus on disordered crystals. It encompasses the criteria used to select structural models for subsequent first principle calculations. The third section covers the first principle approach used to test the structural models. It unveils the main concepts underlying the Projector Augmented Wave (PAW) and Gauge Including Projector Augmented Wave (GIPAW) methods within a Density Functional Theory (DFT) framework. The theory behind semi-empirical dispersion corrections to DFT, such as DFT-D3 is briefly mentioned.

I.2. Solid-state NMR

I.2.1. Basic principle of NMR spectroscopy[1]

NMR spectroscopy is a powerful technique that probes local magnetic fields around atomic nuclei by measuring the interaction between an oscillating radio-frequency wave and a collection of nuclei immersed in a relatively strong magnetic field. This technique is widely utilized in numerous fields ranging from organic to inorganic chemistry, and provides detailed information regarding the molecular and crystal structures and allows to investigate the local atomic arrangement surrounding the targeted nucleus. Additionally, it offers insights into the behavior of systems exhibiting chemical and dynamical processes. The basic principle underpinning NMR is as follows: when placed in an external magnetic field, atomic nuclei, which exist in specific nuclear spin states, align themselves with said field. A radio-frequency pulse is then applied to the sample, inducing nuclei to absorb energy and transition to higher energy states. Upon cessation of the pulse, nuclei revert to their original states, releasing energy in the form of electromagnetic radiation. The frequency of this radiation is measured and used to determine information about the sample.

I.2.1.1. Nuclear spin dynamics

In their ground state, numerous isotopes feature a spin angular momentum denoted as $\vec{I}$ and a magnetic dipole moment expressed as $\vec{\mu}$. This magnetic dipole moment is directly linked to the spin angular momentum, following a proportionality relationship described as:

$$\vec{\mu} = \gamma \hbar \vec{I} \tag{1.1}$$

where γ represents the nucleus magnetogyric ratio specific to each isotope which can be either positive or negative, and $\hbar$ represents the reduced Planck constant, equal to h divided by 2π.

I.2.1.2. Quantum description

From a classical physics stand point, an object exhibits angular momentum as a consequence of its rotational motion around a given axis. In the intricate tapestry of subatomic physics, the concept of spin emerges as an intrinsic property intrinsic to elementary particles, representing a distinctive manifestation of angular momentum. Nuclear spin result from a combination of individual contributions of spin

angular momentum originating from its constituting nucleons. Nuclear spin is quantized, and its total quantum number manifests as a discrete set comprising both integers and half-integers.

In a magnetic field, the components I_x, I_y and I_z of the angular momentum operator $\vec{I}$ are distinguished, and typically, I_z is chosen along the direction of $\vec{B}_0$. According to quantum mechanics, the properties of $\vec{I}$ are:

$$I^2|I,m\rangle = I(I+1)|I,m\rangle \tag{1.2}$$

$$I_z|I,m\rangle = m|I,m\rangle \tag{1.3}$$

with $|I,m\rangle$ representing the eigenvectors of I^2 and I_z, whose eigenvalues satisfy the following:

$$I^2 = \hbar\sqrt{I(I+1)} \tag{1.4}$$

$$I_z = \hbar m_I \tag{1.5}$$

where m_I is the magnetic quantum number, which takes on values $m_I = -I, -I+1, \ldots, I-1, I$. There are $(2I+1)$ possible values of m_I, and consequently, an equal number of possible orientations of the angular momentum.

I.2.1.3. Zeeman Effect

In the presence of a magnetic field $\vec{B}_0$, the nuclear magnetic moment undergoes precession around this magnetic field with an angular velocity $\Omega_0 = -\gamma B_0$ (1.6), which results in a lifting of degeneracy of spin states into $(2I+1)$ equally spaced energy levels (**Figure 1.1**) known as the Zeeman Effect. The energy levels are determined by the eigenvalue equation:

$$\widehat{\mathcal{H}}_Z|I,m\rangle = E_{m,I}|I,m\rangle \tag{1.7}$$

where $\widehat{\mathcal{H}}_Z$ represents the Zeeman Hamiltonian operator for a nuclear spin I in a magnetic field along the z-axis, with a magnitude of B_0. $\widehat{\mathcal{H}}_Z$ is proportional to $\hat{I}_z$ and expressed by:

$$\widehat{\mathcal{H}}_Z = -\gamma\hbar B_0\hat{I}_z \tag{1.8}$$

where $\hat{I}_z$ is an $\hat{I}$ operator component, parallel to the magnetic field $\vec{B}_0$.

The eigenvalue $E_{m,I}$ is the energy associated with the eigenvector $|I,m\rangle$, as follows:

$$E_{m,I} = -\gamma m_I \hbar B_0 \tag{1.9}$$

The Zeeman energy levels are separated by:

$$\Delta E = \hbar\gamma B_0 = h\nu_0 \tag{1.10}$$

where ν_0 is the Larmor frequency, specific to each isotope nucleus and related to the strength of the magnetic field B_0 by: $\nu_0 = \frac{|\gamma|B_0}{2\pi}$.

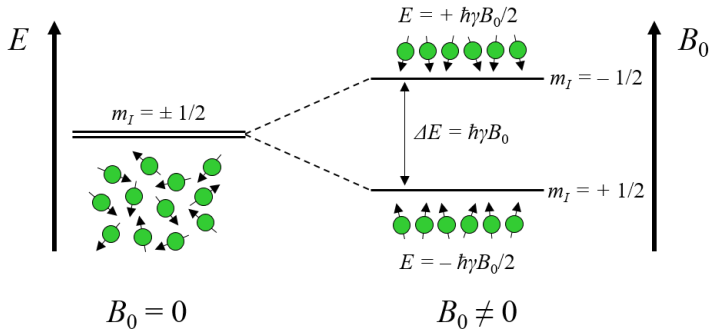


Figure 1.1. Illustration of the Zeeman Effect for spin-1/2 nuclei.

Some typical NMR properties of nuclei studied in this manuscript are gathered in **Table 1.1**.

Table 1.1. Nucleus, natural abundance (%), nuclear spin *I*, magnetogyric ratio γ (10^7 rad.T^{-1}.s^{-1}), quadrupolar moment *Q* (mbarn),[2] magnetic moment μ (μ_N) and Larmor frequency at 7, 17.6 and 20 T (MHz) for spin-1/2 and quadrupolar nuclei studied in the manuscript.[3]

Nucleus	Natural abundance	*I*	γ	*Q*	μ	Larmor frequency		
						7 T	17.6 T	20 T
^{1}H	100	1/2	26.75	n. a.	4.84	300.1	750.1	850.1
^{19}F	100	1/2	25.18	n. a.	4.55	282.4	705.8	799.9
^{23}Na	100	3/2	7.08	104	2.86	79.4	198.4	224.9
^{87}Rb	27.8	3/2	8.79	133.5	3.55	98.2	245.4	278.2
^{93}Nb	100	9/2	6.57	-320	6.82	73.5	183.6	208.1
^{181}Ta	100	7/2	3.24	3170	2.69	36	89.9	101.9

For spin-1/2 nuclei, the energy level splitting result in two distinct spin populations each occupying one of the two energy levels. These populations follow Boltzmann statistics and are expressed as follows:

$$\frac{N^{-1/2}}{N^{+1/2}} = exp\left(-\frac{\Delta E}{k_B T}\right) = exp\left(\frac{-\gamma \hbar B_0}{k_B T}\right) \quad (1.11)$$

where k_B is the Boltzmann constant (k_B = 1.38 × 10^{-23} J.K^{-1}) and T the absolute temperature.

I.2.1.4. A simple pulse sequence

In the absence of an external magnetic field, the orientations of the spin angular momentum vectors, exhibit a uniform distribution, pointing in all possible directions in space. Consequently, the total nuclear magnetic moment, *i.e.*, the macroscopic nuclear magnetization, M, expressed as $M = M_0 \exp(-t/T_2)$ (1.12) and derived from the cumulative contributions of the sample's constituent nuclei, is approximately zero. When the magnetic field $\vec{B}_0$ is applied, the nuclear spins begin to precess around $\vec{B}_0$ direction and the spin angular momentum vectors gradually align along this magnetic field. This gradual alignment is primarily a result of atomic thermal motion, which, in turn, disrupts the initial isotropic distribution of nuclear spins. After a time period, denoted as T_1 and referred to as spin-lattice relaxation time, a non-zero longitudinal magnetization, $M_{\parallel}$, is established and thermal equilibrium is reached (**Figure 1.2. (a)**).

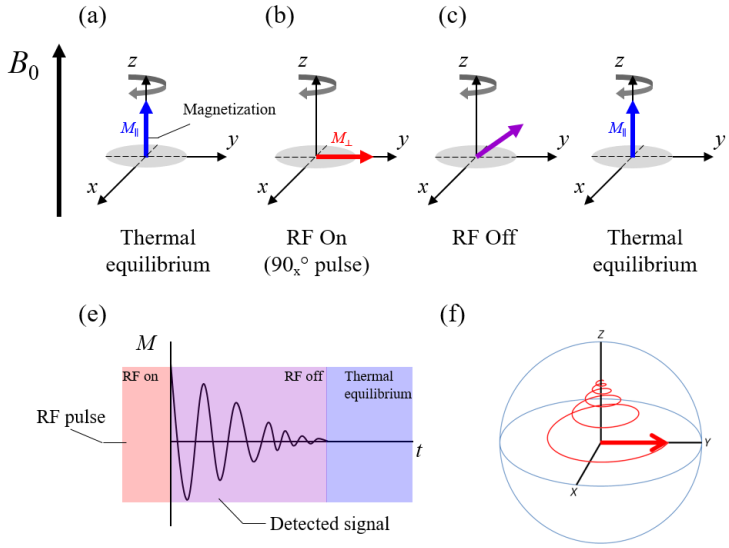


Figure 1.2. Illustration of M at thermal equilibrium (a), during (b) and after (c) RF pulse. Representation of the simple pulse sequence (e), return to thermal equilibrium and precession of M (f).

Given that the detection along the direction of the external field (conventionally, the *z*-axis) is unfeasible, the standard practice in NMR involves measuring the magnetization perpendicular to this field. This is accomplished by a flip of $M_{\parallel}$ using a radiofrequency (RF) pulse, characterized by the oscillating magnetic field $\vec{B}_{\mathrm{RF}}(t)$, with an appropriate frequency (ν_{RF}) and duration (τ_{RF}). The flip angle of $M_{\parallel}$ is given by $\theta_{\mathrm{P}} = \tau_{\mathrm{RF}}\gamma B_{\mathrm{RF}}(t)$ (1.13). A 90° pulse corresponds to a flip angle of $\theta_{\mathrm{P}} = \pi/2$. The resultant net magnetic moment, now in the (*x*,*y*) plane oriented perpendicular to $\vec{B}_0$, is referred to as transverse magnetization, $M_{\perp}$ (**Figure 1.2 (b)**). Subsequently, when the RF pulse is switched off, $M_{\perp}$ starts to precess in the (*x*,*y*) plane (**Figure 1.2 (c)**). To detect this precession, a wire coil is positioned near the sample. The $M_{\perp}$ precession induces an oscillating current in the coil, known as the Free Induction Decay (FID), which is then recorded as a function of time (**Figure 1.2 (e)**). The $M_{\perp}$ FID arises from two phenomena, (i), the re-alignment of *M* along the *z*-axis, characterized by T_1, and, (ii), the loss of coherence among the nuclear spins, denoted by the relaxation time (or the spin-spin relaxation time) T_2.

The Hamiltonian operator of the radiofrequency interaction is:

$$\hat{\mathcal{H}}_{\mathrm{RF}} = -B_{\mathrm{RF}}(t)cos[\nu_{\mathrm{RF}}t + \varphi(t)]\sum_i \gamma_n^i \hat{I}_x^i \qquad (1.14)$$

where ν_{RF} is the emitted frequency, and $\varphi(t)$ is the phase applied to the radiofrequency field. In the rotating frame of reference (along the *z*-axis), when the RF ($\nu_{\mathrm{RF}} \approx \nu_0$) pulse is applied, the effects of the static magnetic field $\vec{B}_0$ are reduced by a factor of $\frac{\nu_{\mathrm{RF}}}{\nu_0}$, and $\vec{B}_{\mathrm{RF}}(t)$ appears as a dominant magnetic field.

During the following T_1, the spin system re-establishes its thermal equilibrium state. This effect occurs as a relaxation of spin-level states through energy exchange with the surrounding environment. Consequently, the macroscopic magnetization gradually reverts to its equilibrium orientation, aligning parallel to $\vec{B}_0$.

I.2.1.5. Dynamic processes: relaxation

Longitudinal relaxation mechanisms are connected to fluctuations in local magnetic fields caused by thermal motion. These fluctuations can trigger transitions between quantum states within the spin

system, ultimately returning it to its thermal equilibrium state. This relaxation time, T_1, determines the recycle time between two acquisitions (often chosen as $5\times T_1$) during an NMR experiment. In liquid samples, proton T_1 relaxation times typically fall within the range of a few seconds.

Transverse relaxation is a result of interactions among spins. Indeed, interactions between neighboring magnetic dipoles generate a local magnetic field, known as $\vec{B}_L$, at each dipole. This local field fluctuates over time, for instance, due to changes in quantum states. As a result, fluctuations in the resonance frequency of the spins occur, which diminish the phase coherence of their precession. This loss of coherence constitutes the mechanism behind transverse relaxation. The transverse relaxation time, T_2, manifests as an exponential decay of the FID signal. In practice, an effective relaxation time T_2^* is observed. In solid-state NMR (ssNMR), T_2^* arises from inhomogeneous broadening caused by the static field, $\vec{B}_0$, inhomogeneities, chemical shift distribution and anisotropy, or even quadrupolar interactions.

I.2.1.6. Fourier transfer of an NMR signal

The FID signal is described by a time dependent function, which can be expressed as:

$$F(t) = A\ exp(i\omega_0 t)\ exp\left(-\frac{t}{T_2}\right) \tag{1.15}$$

with A representing the amplitude of the function, ω_0 the frequency of the spin considering the rotating frame of reference, and T_2 the relaxation time. This function can be transformed into a frequency dependent function through Fourier transformation. In the case of an NMR signal obtained in a single detection, we have:

$$F(\omega) = T\{F(t)\} = A\ \int_0^{+\infty} exp\big(i(\omega-\omega_0)\big)\ exp\left(-\frac{t}{T_2}\right) dt = \frac{AT_2}{1+T_2^2(\omega-\omega_0)^2} - i\frac{AT_2^2(\omega-\omega_0)}{1+T_2^2(\omega-\omega_0)^2} \tag{1.16}$$

The first term corresponds to the real part, and the second term to the imaginary part. Both parts are depicted in **Figure 1.3** as curves.

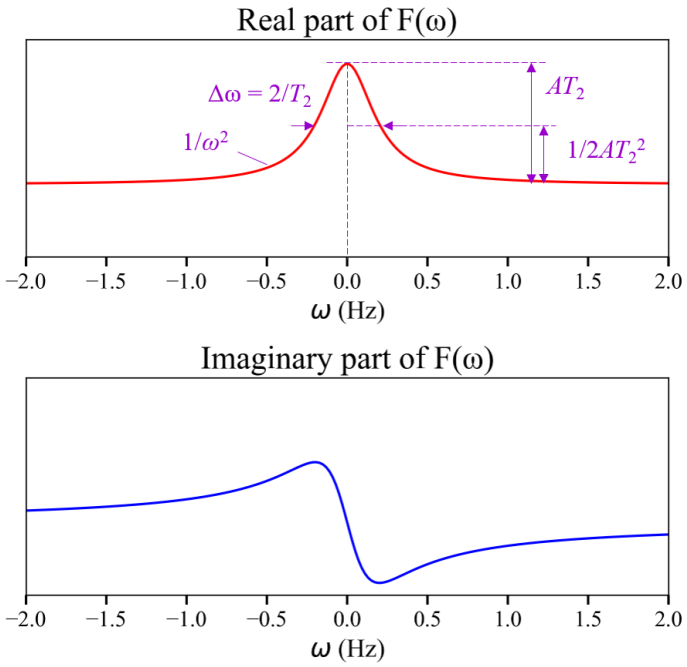


Figure 1.3. $F(\omega)$ function in the frequency domain, with the real and imaginary parts illustrated.

I.2.2. Interactions in solid-state NMR

To address NMR in solid-state systems, it becomes imperative to take into account the significant interactions affecting a nuclear spin within a solid-state medium. A standard representation for the Hamiltonian of a nuclear spin may take the form of:

$$\widehat{\mathcal{H}} = \widehat{\mathcal{H}}_{\mathrm{Z}} + \widehat{\mathcal{H}}_{\mathrm{RF}} + \widehat{\mathcal{H}}_{\mathrm{CS}} + \widehat{\mathcal{H}}_{\mathrm{DD}} + \widehat{\mathcal{H}}_{\mathrm{Q}} + \widehat{\mathcal{H}}_{\mathrm{J}} \quad (1.17)$$

with:

- $\widehat{\mathcal{H}}_{\mathrm{Z}}$, the Zeeman Hamiltonian describing the interaction between nuclear spins and the external magnetic field $\vec{B}_0$;
- $\widehat{\mathcal{H}}_{\mathrm{RF}}$, the RF Hamiltonian describing the interaction between nuclear spins and the applied time dependent magnetic field $\vec{B}_{\mathrm{RF}}$;
- $\widehat{\mathcal{H}}_{\mathrm{CS}}$, the chemical shift Hamiltonian describing the indirect interaction between nuclear spins and the local magnetic field created by the electrons surrounding the nucleus through their interaction with the external magnetic field;
- $\widehat{\mathcal{H}}_{\mathrm{DD}}$, the dipole-dipole coupling Hamiltonian describing the through-space spin-spin interaction;
- $\widehat{\mathcal{H}}_{\mathrm{Q}}$, the quadrupolar Hamiltonian describing the interaction between I>1/2 spins and the surrounding electric field gradient;
- $\widehat{\mathcal{H}}_{\mathrm{J}}$, the scalar coupling Hamiltonian describing the spin-spin interaction mediated by the bonding electrons.

The first two components, $\widehat{\mathcal{H}}_{\mathrm{Z}}$ and $\widehat{\mathcal{H}}_{\mathrm{RF}}$, are referred to as "*external*" interactions since they originate from externally generated $\vec{B}_0$ and $\vec{B}_{\mathrm{RF}}$ fields, whereas the remaining terms are categorized as "*internal*" interactions. These internal interactions are summarized in **Table 1.2**, which specifies the frequency range associated with each interaction and the structural insights they offer. Throughout this thesis, our research has primarily focused on chemical shift and quadrupolar interactions. In this section, we will provide a brief overview of these internal interactions.

Table 1.2. Magnitude (Hz), dependence to B_0 and structural information from each interaction.

Interaction	Frequency domain	Field dependence	Structural information
Quadrupolar coupling	0–10^7	1st order: independent 2nd order: $\propto 1/B_0$	geometry
Chemical shift	0–10^4	$\propto B_0$	first neighbors, coordination
Dipole coupling	0–10^4	independent	distances, spatial proximity
J-coupling	0–10^3	independent	distances, connectivity

I.2.2.1. Chemical shift

Electrons in the crystal structure (or molecules) induce localized variations in the magnetic fields over short distance scales. Nuclei located at two distinct crystallographic sites within the same crystal experience different magnetic fields when their electronic environments differ. For instance, fluorine atoms located in $[NbO_4F_2]^{5-}$ octahedra encounter slightly different magnetic fields compared to fluorine atoms located in $[NbO_5F]^{6-}$ octahedra. This phenomenon is known as "*chemical shift*" and holds significant importance in the context of NMR applications in chemistry.

The chemical shift mechanism involves a two-step process. First, the external magnetic field B_0 induces currents within the electron clouds surrounding the atoms. Second, these circulating currents, in turn, produce a magnetic field known as the induced field (B_{ind}) (**Figure 1.4**).

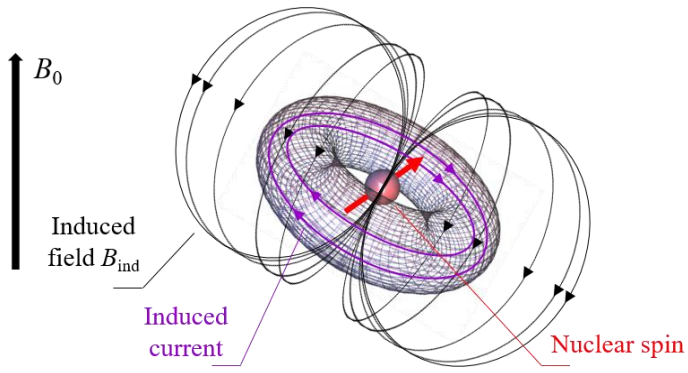


Figure 1.4. Mechanisms of the chemical shift

The nuclear spins sense the sum of the applied external field and the induced field generated by the electrons:

$$B_{\mathrm{loc}} = B_0 + B_{\mathrm{ind}} = B_0 - B_0\sigma = B_0(1-\sigma) \tag{1.18}$$

where σ represents the magnetic shielding tensor and is expressed as: $\sigma = \sigma_{\mathrm{d}} + \sigma_{\mathrm{p}}$ (1.19).

The origins of the induced currents stem from the quantum-mechanical behavior exhibited by electrons. These induced currents have been categorized into two distinct contributions: (i) the circulation of electrons in the electronic ground state induced by the magnetic field (diamagnetic term, σ_{d}) and (ii) electron circulation facilitated by participation in electronic excited states (paramagnetic term, σ_{p}).

The magnitude and sign of magnetic shielding rely on the chemical structure and its alignment with respect to $\vec{B}_0$. The magnetic shielding tensor, σ, is a second-rank tensor expressed as a diagonal matrix when represented in its principle axis system (PAS):

$$\sigma = \begin{bmatrix} \sigma_{\mathrm{xx}} & 0 & 0 \\ 0 & \sigma_{\mathrm{yy}} & 0 \\ 0 & 0 & \sigma_{\mathrm{zz}} \end{bmatrix} \tag{1.20}$$

and using the Haeberlen convention[4] $|\sigma_{\mathrm{zz}} - \sigma_{\mathrm{iso}}| \geq |\sigma_{\mathrm{xx}} - \sigma_{\mathrm{iso}}| \geq |\sigma_{\mathrm{yy}} - \sigma_{\mathrm{iso}}|$ (1.21).

The isotropic magnetic shielding, σ_{iso}, is calculated as the mean of the diagonal elements: $\sigma_{\mathrm{iso}} = \frac{1}{3}(\sigma_{\mathrm{xx}} + \sigma_{\mathrm{yy}} + \sigma_{\mathrm{zz}})$ (1.22). Likewise, the anisotropic component of the magnetic shielding and the asymmetry parameter are defined as:

$$\sigma_{\mathrm{CSA}} = (\sigma_{\mathrm{zz}} - \sigma_{\mathrm{iso}}) \tag{1.23}$$

$$\eta_{\mathrm{CSA}} = \frac{\sigma_{\mathrm{yy}} - \sigma_{\mathrm{xx}}}{\sigma_{\mathrm{iso}}} \tag{1.24}$$

The Hamiltonian operator describing the magnetic shielding is expressed as,

$$\widehat{\mathcal{H}}_{\mathrm{CS}} = \hbar\gamma \hat{I}_{\mathrm{z}} \sigma_{\mathrm{zz}}^{\mathrm{lab}} B_0 \tag{1.25}$$

where $\sigma_{\mathrm{zz}}^{\mathrm{lab}}$ represents the *z*-component of the magnetic shielding tensor in the laboratory (LAB) frame. It is determined by performing the appropriate sequence of rotations to transform from PAS to the LAB frame, and is given by:

$$\sigma_{zz}^{lab} = \sigma_{iso} + \frac{\sigma_{CSA}}{2}[(3cos^2\theta - 1) + \eta_{CSA}(sin^2\theta cos2\phi)] \quad (1.26)$$

where θ and ϕ represent the polar angles. In a powder sample, all possible orientations of crystallites exist, leading to various combinations of θ and ϕ angles. Consequently, each crystallite has a slightly different resonance frequency, resulting in a broadening of the resonance lines.

In NMR experiments, the frequency of spectral lines is determined in relation to a reference frequency, and is referred to as the chemical shift. The relationship between shielding and chemical shift, expressed in parts per million (ppm), is as follows:

$$\delta/\text{ppm} = \frac{\sigma_{ref} - \sigma}{1 - \sigma_{ref}} \times 10^6 \approx (\sigma_{ref} - \sigma) \times 10^6 \quad (1.27)$$

Henceforth, the isotropic chemical shift, δ_{iso}, is expressed equivalently as $\delta_{iso} = \frac{1}{3}(\delta_{xx} + \delta_{yy} + \delta_{zz})$ (1.28). This nomenclature aligns with the Haeberlen convention[4] regarding the principal components, which stipulates that $|\delta_{zz} - \delta_{iso}| \geq |\delta_{xx} - \delta_{iso}| \geq |\delta_{yy} - \delta_{iso}|$ (1.29). As for the magnetic shielding tensor, an anisotropic parameter, δ_{CSA}, and an asymmetry parameter, η_{CSA}, are defined as follows:

$$\delta_{CSA} = (\delta_{zz} - \delta_{iso}) \quad (1.30)$$

$$\eta_{CSA} = \frac{\delta_{yy} - \delta_{xx}}{\delta_{iso}} \quad (1.31)$$

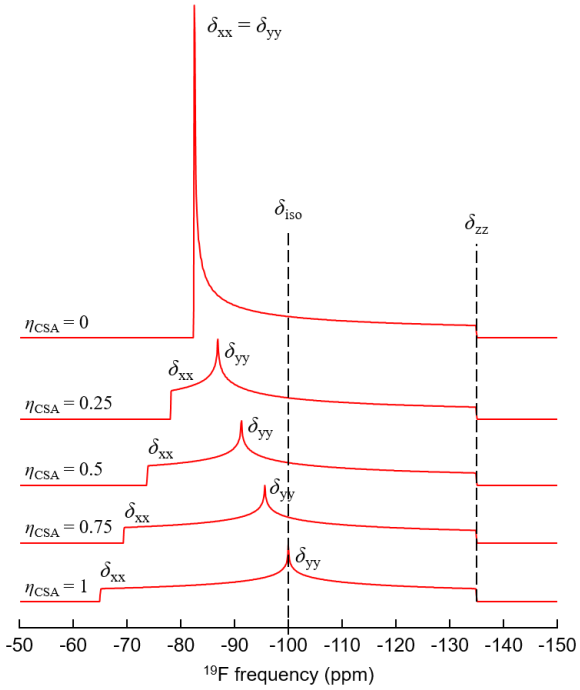


Figure 1.5. Simulated ^{19}F NMR static spectra, for fixed δ_{iso} and δ_{CSA} values, and different η_{CSA} values.

The chemical shift interaction provides valuable information about the short-range crystal structure, particularly regarding the coordination and nature of the nearest neighbors. Chemical shift anisotropy is sometimes the dominant interaction. The effect of chemical shift anisotropy asymmetry on the shape of resonance peaks in a powder spectrum is shown in **Figure 1.5**.

The following qualitative observations describe the influence on the chemical shift:

- The primary factor contributing to chemical shift typically arises from the impact of lower-energy electronic excited states. Heavier atoms typically possess more of these low-energy states compared to lighter atoms, resulting in a wider chemical shift range for heavier isotopes. For instance, while the chemical shift range for ^{1}H is typically around 15 ppm, it expands to approximately 400 ppm for ^{19}F. In the case of heavy nuclei like ^{93}Nb, chemical shifts can often exceed 1000 ppm.
- The chemical shift demonstrates a strong correlation with the electronegativity of neighboring functional groups. Electronegative ions such as O^{2-}, Cl^{-}, and F^{-} tend to withdraw electron density, thereby amplifying the local magnetic fields experienced by nearby nuclei. This, in turn, leads to increased δ values.
- In rigid molecules with well-defined three-dimensional structures, the chemical shift can be influenced by neighboring molecular units possessing significant magnetic susceptibility, even

when there is no direct chemical bond. For example, a benzene ring can readily support induced electron currents, causing a decrease in the local magnetic fields for nuclei situated close to the ring's axis of symmetry (resulting in a decrease in δ) and an increase in the local magnetic fields for nuclei positioned close to the plane of the ring (leading to an increase in δ) (**Figure 1.6**).

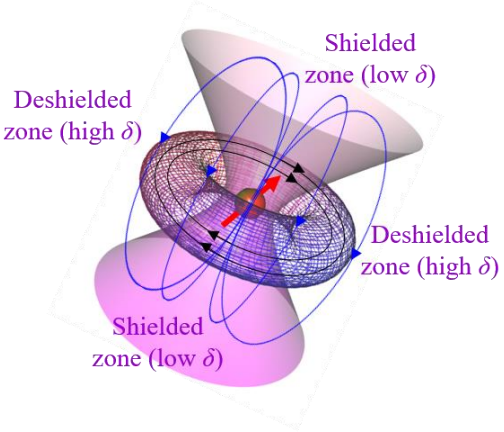


Figure 1.6. Ring current and chemical shift zones.

I.2.2.2. Direct dipole-dipole interaction

The dipole-dipole interaction arises from the interaction between a nuclear spin and the magnetic field generated by another nuclear spin across space, and vice versa. Dipolar coupling depends on the inter-nuclear distance, *r*, and on the magnetogyric ratios of the coupled nuclei. For two nuclei, *I* and *S*, of different types (*i.e.*, heteronuclear system), the dipolar Hamiltonian operator can be expressed as follows:

$$\hat{\mathcal{H}}_{\mathrm{DD}} = \frac{\mu_0}{4\pi}\hbar\gamma_I\gamma_S\left(\frac{\vec{I}.\vec{S}}{r_{IS}^3} - 3\frac{(\vec{I}.\vec{r}_{IS}).(\vec{I}.\vec{r}_{IS})}{r_{IS}^5}\right) \tag{1.32}$$

where r_{IS} represents the inter-nuclear distance, μ_0 the permeability in the vacuum, and γ_I and γ_S the magnetogyric ratios of *I* and *S* nuclei, respectively. Further derivations of (1.32) lead to:

$$\hat{\mathcal{H}}_{\mathrm{DD}} = \left(\frac{\mu_0}{4\pi}\right)\hbar\gamma_I\gamma_S[(1-3cos^2\theta)\hat{I}_z\hat{S}_z - \frac{1}{4}(1-3cos^2\theta)\left(\hat{I}_+\hat{S}_- + \hat{I}_+\hat{S}_-\right) - \frac{3}{2}sin\theta cos\theta \tag{1.33}$$

$$e^{-i\phi}\left(\hat{I}_z\hat{S}_+ + \hat{I}_+\hat{S}_z\right) - \frac{3}{2}sin\theta cos\theta e^{i\phi}\left(\hat{I}_z\hat{S}_- + \hat{I}_-\hat{S}_z\right) - \frac{3}{4}sin^2\theta e^{-2i\phi}\hat{I}_+\hat{S}_+ -$$

$$\frac{3}{4}sin^2\theta e^{2i\phi}\hat{I}_-\hat{S}_-]$$

with θ representing the polar angle describing the orientation of $\vec{r}_{IS}$ relative to the $\vec{B}_0$ field, and ϕ representing the azimuthal angle (**Figure 1.7**). $\hat{I}_z$ and $\hat{S}_z$ denote the *z*-axis components of the angular

momentum operators $\hat{I}$ and $\hat{S}$, respectively. $\hat{I}_+$ and $\hat{I}_-$ ($\hat{S}_+$ and $\hat{S}_-$) stand for the spin creation and annihilation operators for spin *I* (*S*).

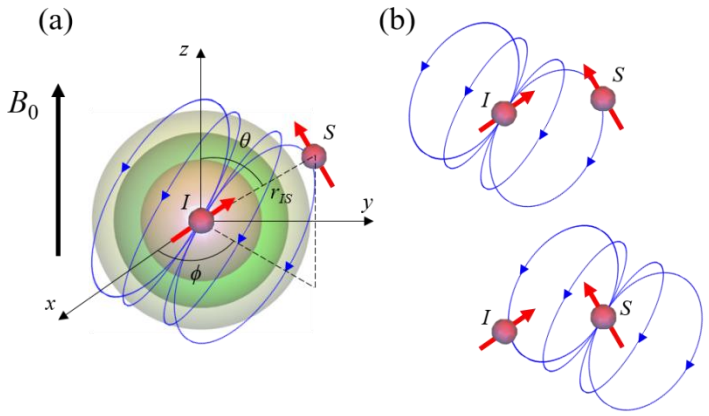


Figure 1.7. Magnetic field generated by spin *I* at the site of spin *S* (a). The dipole-dipole interaction is mutual (b).

In the case of a heteronuclear dipolar interaction, only the part $(1 - 3cos^2\theta)\hat{I}_z\hat{S}_z$ commutes with the Zeeman Hamiltonian, and the secular component of the Hamiltonian is written as follows:[5]

$$\hat{\mathcal{H}}_{DD}^{hetero} = d(1 - 3cos^2\theta)\hat{I}_z\hat{S}_z \tag{1.34}$$

with $d = \left(\frac{\mu_0}{4\pi}\right)\frac{\gamma_I\gamma_S}{r_{IS}^3}\hbar$ (1.35), often called the dipolar coupling constant.

An analogous type of coupling also occurs among similar spins, known as homonuclear dipolar coupling. In this case only the terms $(1 - 3cos^2\theta)\hat{I}_z\hat{S}_z$ and $-\frac{1}{4}(1 - 3cos^2\theta)\left(\hat{I}_+\hat{S}_- + \hat{I}_+\hat{S}_-\right)$ commute with the Zeeman Hamiltonian, and the secular component for homonuclear dipolar coupling is expressed as follows:

$$\hat{\mathcal{H}}_{DD}^{homo} = -d'\frac{(3cos^2\theta - 1)}{2}\left(3\hat{I}_{1z}\hat{I}_{2z} - \hat{I}_1.\hat{I}_2\right) \tag{1.36}$$

with $d = \left(\frac{\mu_0}{4\pi}\right)\frac{\gamma_I^2}{r_{IS}^3}\hbar$ (1.37), often called the homonuclear dipolar coupling constant.

In ssNMR, the homonuclear dipolar coupling interaction is characterized by a uniform broadening of resonance lines. Its strength primarily depends on the distance between the two nuclei and their magnetogyric ratios.

I.2.2.3. Quadrupolar interaction

Nuclei with nuclear spin $I > 1/2$ exhibit an asymmetric distribution of nuclear charges, which gives rise to an electric quadrupole moment Q. The quadrupole interaction originates from the coupling between this electric quadrupole moment Q and the local electric field gradient (EFG) around the nucleus (**Figure 1.8**). Typically, the EFG is generated by the distribution of electronic charges surrounding the nucleus. This local interaction reflects the asymmetry in the observed nucleus's electric environment. In the case of solid materials, the quadrupole interaction can reach several MHz and lead to the appearance of singularities in the line shapes and significant broadening of the spectrum.

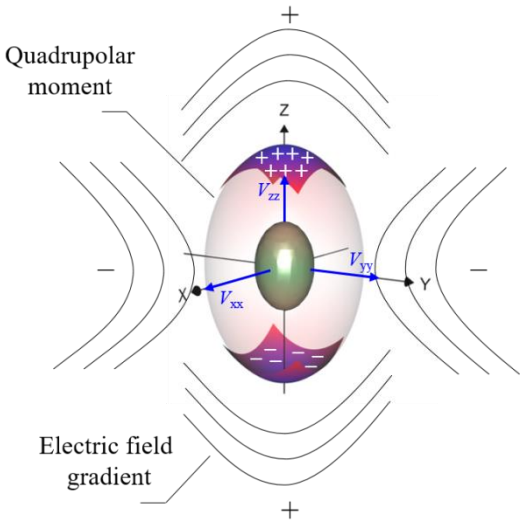


Figure 1.8. Illustration of the EFG surrounding the quadrupolar nucleus and the diagonal component of the EFG tensor

The coupling between the electric quadrupole moment Q of a nucleus I and the local EFG tensor is expressed by the Hamiltonian operator as follows:

$$\hat{\mathcal{H}}_{\mathrm{Q}} = \frac{eQ}{2I(2I-1)\hbar}\hat{I}V\hat{I} \tag{1.38}$$

where e is the electron charge, and V is the EFG tensor, which corresponds to the second derivative of the electrostatic potential, of rank 2. In its own set of principal axes, the EFG tensor is described by the following matrix:

$$V = \begin{bmatrix} V_{\mathrm{xx}} & 0 & 0 \\ 0 & V_{\mathrm{yy}} & 0 \\ 0 & 0 & V_{\mathrm{zz}} \end{bmatrix} \tag{1.39}$$

where the three diagonal components respect the following convention:

$$|V_{xx}| \leq |V_{yy}| \leq |V_{zz}| \tag{1.40}$$

The Laplace equation enforces a zero trace condition on the tensor, which is expressed as follows:

$$V_{xx} + V_{yy} + V_{zz} = 0 \tag{1.41}$$

Two parameters are then sufficient to describe the *V* tensor. The principal component of the electric field gradient tensor, V_{zz}, is proportional to the quadrupolar coupling constant C_Q, which is a parameter with a frequency dimension given by:

$$C_Q = \frac{eQV_{zz}}{\hbar} \tag{1.42}$$

The quadrupolar frequency, ν_Q, and the quadrupolar product P_Q are expressed in terms of C_Q as follows:

$$\nu_Q = \frac{3C_Q}{2I(2I-1)} \tag{1.43}$$

$$P_Q = C_Q\sqrt{1+\frac{\eta_Q^2}{3}} \tag{1.44}$$

where η_Q is the asymmetry parameter defined by the component of the EFG tensor:

$$\eta_Q = \frac{V_{xx}-V_{yy}}{V_{zz}}\,(0 \leq \eta_Q \leq 1) \tag{1.45}$$

The quadrupolar parameters characterize the local symmetry of a nucleus. If the observed nucleus occupies a site with cubic symmetry, then $V_{xx} = V_{yy} = V_{zz} = 0$, $C_Q = 0$ and $\eta_Q = 0$. For high symmetry sites, such as $\overline{3}m$, 3*m*, 4*mm*, *etc.*, $V_{xx} = V_{yy}$, $C_Q \neq 0$ and $\eta_Q = 0$.

Typically, the Hamiltonian operator for the quadrupole interaction contains both a first-order term and a second-order term:

$$\hat{\mathcal{H}}_Q = \hat{\mathcal{H}}_Q^{(1)} + \hat{\mathcal{H}}_Q^{(2)} \tag{1.46}$$

In cases where the Zeeman interaction greatly exceeds the quadrupole interaction, the latter is treated in quantum-mechanical perturbation theory framework, and the first-order quadrupole Hamiltonian operator is introduced as follows:

$$\widehat{\mathcal{H}}_{\mathrm{Q}}^{(1)} = \frac{C_{\mathrm{Q}}}{8I(2I-1)}\left(3cos^2\theta - 1 \pm \eta_{\mathrm{Q}} sin^2\theta cos2\phi(3\hat{I}_z^2 - \hat{I}^2)\right) \quad (1.47)$$

The first-order quadrupolar frequency is given by:

$$\omega_{m,m-1}^{(1)} = -\omega_0 - \frac{1}{4}(2m-1)\left[(3cos^2\theta - 1 + \eta_{\mathrm{Q}} sin^2\theta cos2\phi)\right] \quad (1.48)$$

with (θ,ϕ) being the polar angles that orient the EFG tensor relative to the LAB reference frame.

Strong quadrupolar couplings require treatment using second-order perturbation theory. For a 1/2↔–1/2 transition, the second-order quadrupolar frequency is given by:[6]

$$\omega_{\frac{1}{2}\leftrightarrow-\frac{1}{2}}^{(2)} = -\frac{1}{6\omega_0}\omega_{\mathrm{Q}}^2[\hat{I}(\hat{I}+1) - \frac{3}{4}][(-\frac{27}{8} + \frac{9}{4}\eta cos2\phi - \frac{3}{8}\eta^2 cos^2 2\phi)cos^4\beta + (-\frac{30}{8} \quad (1.49)$$

$$+ \frac{\eta^2}{2} - 2\eta cos2\phi)cos^2\theta + -\frac{3}{8} + \frac{\eta^2}{2} - \frac{\eta}{4}cos2\phi - \frac{3}{8}\eta^2 cos^2 2\phi]$$

Second-order quadrupole interaction affects both the central transition (CT) and satellite transitions (ST). In equation (1.49), the term $\frac{1}{\omega_0}$ indicates that the second-order interaction is inversely proportional to the static magnetic field. The effects of first and second-order quadrupole interactions on energy levels for a nucleus with spin 3/2 are illustrated in **Figure 1.9**. The CT is not affected by the first-order quadrupole interaction, while all ST are.

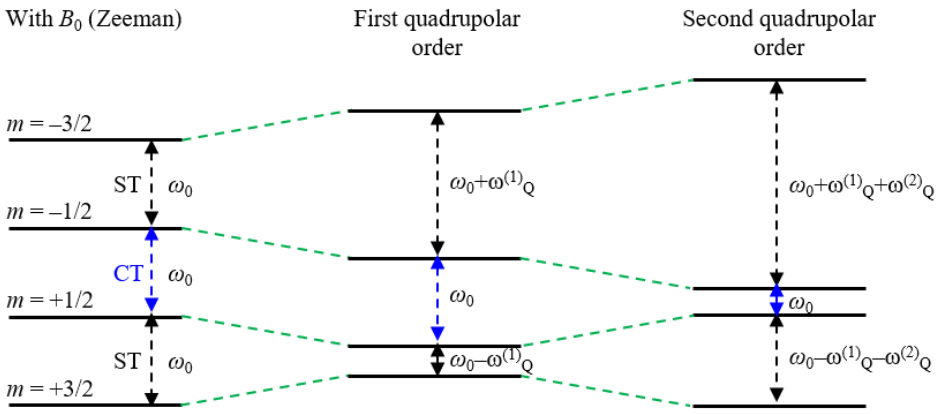


Figure 1.9. Energy levels of a 3/2-spin system influenced by the Zeeman interaction and first- and second-order quadrupole interactions.

I.2.2.4. Indirect spin-spin interaction (*J*-coupling)

Scalar coupling, also known as *J*-coupling, is regarded as a through-bond interaction that emerges from the interplay of nuclear spins connected by chemical bonds. While *J*-coupling is typically associated with through-bond interactions, there have been instances of hydrogen-bond-mediated *J*-couplings[7,8] and even "*through-space*" ^{19}F-^{19}F *J*-couplings.[9] This phenomenon results in the splitting of NMR resonances. In ssNMR spectra, *J*-coupling is infrequently observed as it is considerably smaller in magnitude when compared to other ssNMR interactions, such as dipolar coupling and quadrupolar interactions. Nevertheless, it provides vital structural insights into interatomic connections. Given that the *J*-coupling interaction relies on chemical bonds, it is primarily detectable in compounds featuring covalent bonds. The spin Hamiltonian for the *J*-coupling interaction between spins I_j and I_k is expressed as follows:

$$\hat{\mathcal{H}}_j = 2\pi \hat{I}_j J_{jk} \hat{I}_k \tag{1.50}$$

where J_{jk} represents the *J*-coupling tensor, which typically encompasses both isotropic and anisotropic components. The isotropic *J*-coupling is specifically defined as:

$$J_{jk}^{iso} = \frac{1}{3}(J_{xx}^{jk} + J_{yy}^{jk} + J_{zz}^{jk}) \tag{1.51}$$

The magnitude of the *J*-coupling primarily relies on factors such as the quantity and type of bonds connecting the nuclei involved, the magnetogyric ratios γ, and the degree of overlap among atomic

orbitals. Compounds that incorporate heavier atoms tend to exhibit higher *J*-coupling values due to the larger spatial extent of the orbitals associated with these atoms.

I.2.2.5. Euler angles[10]

As mentioned earlier, both the quadrupolar interaction and the chemical shift interaction exhibit anisotropy. In cases where both of these interactions coexist, the NMR spectrum is influenced by the relative orientations of these two tensors.

The Euler angles (α, β, γ) establish the connections between the coordinate systems of the corresponding tensors, V and δ, as well as their origins **(Figure 1.10**). Among these angles, β, which represents the angle between V_{zz} and δ_{zz}, exerts a more pronounced influence on the shape of the resonance line than the two others. There are different conventions[11] for the Euler angles relating the coordinate systems, the one used in this thesis corresponds to the "ZYZ order" convention used by Spiess,[12] Narita and co-workers,[13] Freude and Haase.[14]

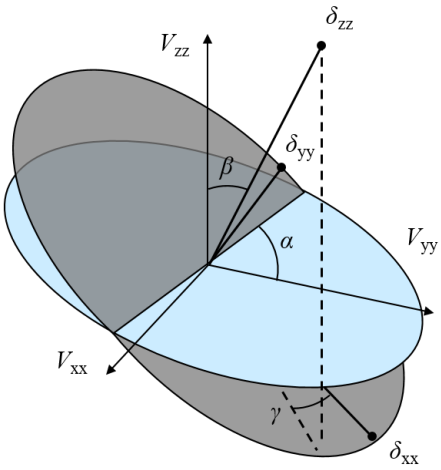


Figure 1.10. Illustration of the relative orientation of two tensors expressed by Euler angles (α, β, γ). The principal axes of the chemical shift tensor (δ_{xx}, δ_{yy}, δ_{zz}) are positioned relative to those of the EFG tensor (V_{xx}, V_{yy}, V_{zz}).

I.2.3. Experimental techniques in solid-state NMR

This section provides a detailed description of the various ssNMR experiments employed throughout this thesis to investigate the studied inorganic oxyfluorides. These experiments were conducted across a range of field strengths, on the Bruker Avance III spectrometer operating at 300 MHz (7 T) located in the "*Institut des Molécules et Matériaux du Mans*" (IMMM), as well as several Bruker Avance III spectrometers operating at 200 MHz (4.7 T), 750 MHz (17.6 T) and 850 MHz (20 T) located at the "*Conditions Extrêmes et Matériaux : Haute Température et Irradiation*" (CEMHTI) laboratory in Orléans, as part of a TGIR-RMN-THC project in collaboration with F. Fayon and V. Sarou-Kanian. The probed nuclei include ^{1}H, ^{19}F, ^{23}Na, ^{87}Rb, and ^{93}Nb. Additionally, Nuclear Quadrupolar Resonance (NQR) experiments were conducted in an attempt to probe ^{181}Ta, which are also reported at the end of this section.

I.2.3.1. Sensitivity and signal-to-noise ratio (*S*/*N*)

Sensitivity in NMR is limited when compared to other analytical methods, primarily due to the low energy difference between nuclear spin states at room temperature. This limited sensitivity is further influenced by various factors pertaining to the sample, such as interaction anisotropy, dipolar and quadrupolar couplings, as well as factors associated with the probe, including electronic noise, coil geometry, and temperature, among others. The signal intensity from spin-1/2 in a one-dimensional (1D) NMR experiment is directly proportional to:

$$M = N\gamma^2 \frac{\hbar^2 B_0}{4k_B T} \tag{1.52}$$

The signal-to-noise ratio (*S*/*N*) is a valuable metric for assessing the quality of a measurement at the signal location (within the signal bandwidth, not the entire acquisition bandwidth). It is calculated as the ratio of the NMR signal amplitude (*A*) to the standard deviation (σ_t) arising from random signal fluctuations:

$$\frac{S}{N} = \frac{A}{\sigma_t} \tag{1.53}$$

The enhancement of the signal-to-noise ratio (*S*/*N*) can be achieved by modifying several factors, including:

- Using a large quantity of the sample, particularly for compounds containing elements with low sensitivity, low natural abundance, and/or low magnetogyric ratio;
- Increasing the number of scans (as shown in **Figure 1.11 (a)**), since the *S*/*N* is directly proportional to the square root of the number of scans, n_S;
- Using very high magnetic fields: High fields offer improved spectral resolution and polarization sensitivity. Furthermore, for quadrupolar nuclei, the impact of second-order quadrupolar interactions is reduced (refer to section 1.2.2.3), resulting in enhanced spectral resolution of the central transition (as illustrated in **Figure 1.11 (b)**).

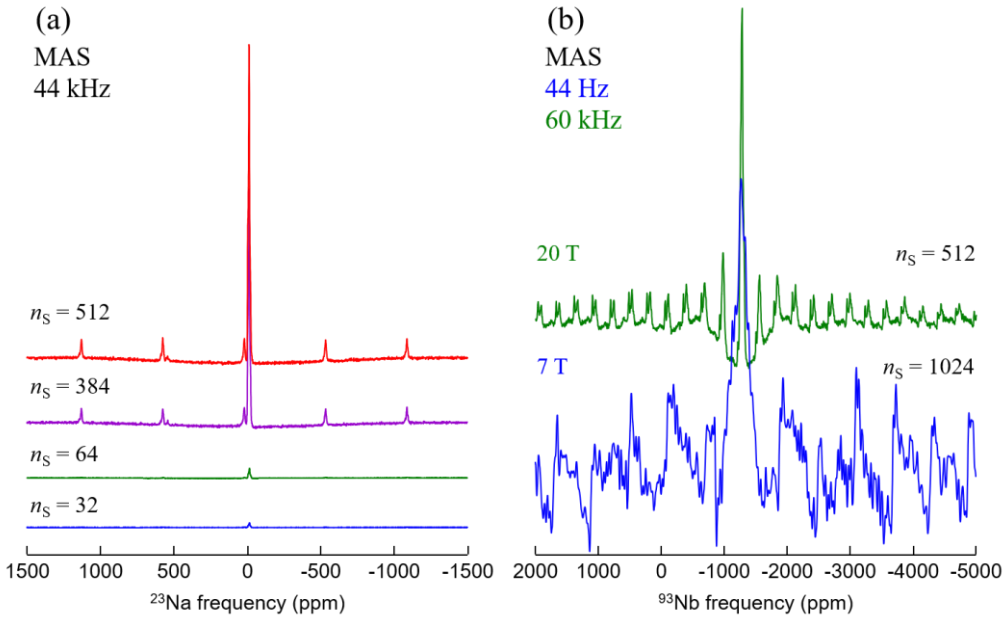


Figure 1.11. Experimental ^{23}Na MAS NMR spectra (7 T, 44 kHz) of $NaNbO_2F_2$ recorded using different numbers of scans, n_S (a). Experimental ^{93}Nb MAS NMR spectra of $NaNbO_2F_2$ recorded at different magnetic fields 7 T (44 kHz) and 20 T (60 kHz) (b).

I.2.3.2. The recycling delay effect on the *S*/*N*

In NMR spectroscopy, the recycling delay (d_1) refers to the time period between successive pulse sequences during data acquisition. This delay is necessary to allow the nuclear spins to return to their equilibrium states before the next pulse sequence is applied. The duration of d_1 is typically determined

by the spin-lattice relaxation time (T_1, refer to section I.2.1.5) of the nucleus being probed. An NMR signal with optimal d_1 value presents a significantly enhanced *S*/*N*, as illustrated in **Figure 1.12**.

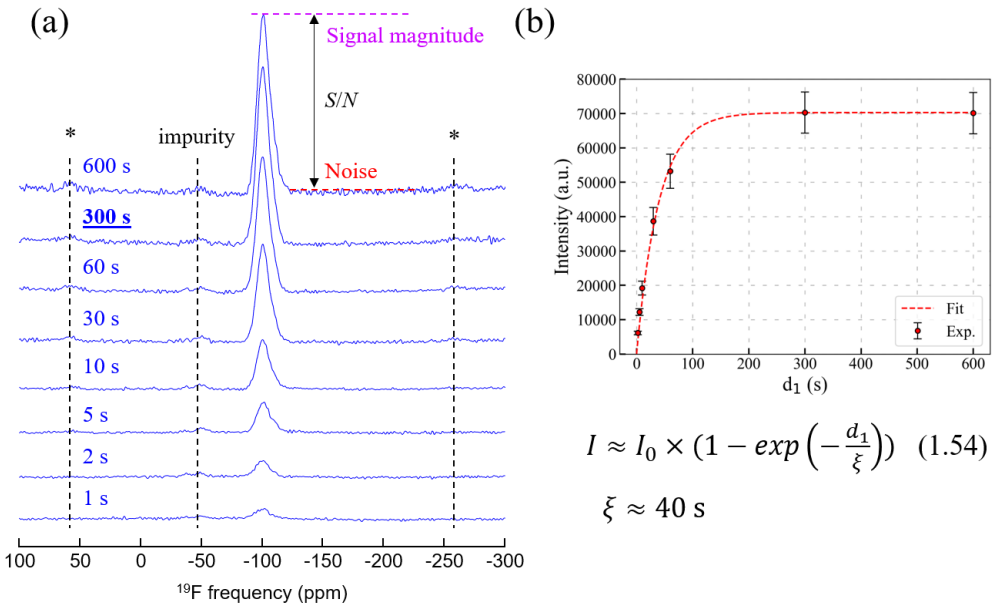


Figure 1.12. Experimental ^{19}F MAS NMR (44 kHz, 7 T) spectra of $RbNb_2O_5F$ recorded at different d_1 values (a). Experimental (red dots) and fit (dashed red curve) of the evolution of the absolute intensity of the ^{19}F main line with respect to d_1 (b). The approximate relation used to fit the points is given.

Various techniques, including MAS, decoupling, QCPMG, and more, are employed to reduce the NMR line broadening and enhance the *S*/*N*. Some of these techniques serve to fine-tune signals by partially or entirely mitigating the effects of the anisotropy of interactions. These NMR techniques are elaborated upon in the following sections.

I.2.3.3. The MAS experiment

In the liquid phase, rapid motions of molecules (correlation times on the order of 10^{-9} to 10^{-12} s) lead to the suppression of the anisotropic component of NMR interactions. Consequently, NMR spectra exhibit very narrow lines. Conversely, in the solid phase, these interactions persist and contribute to the heterogeneous broadening of NMR lines, thereby constraining spectral resolution. To overcome this challenge, substantial technological advancements have been made in dedicated solid-state NMR instrumentation.

Magic angle spinning[15–17] is a commonly employed technique in the solid-state NMR community. This technique significantly enhances the resolution of NMR resonances in solids by partially averaging

the effects of anisotropic interactions, particularly shielding anisotropy, dipolar coupling, and quadrupolar interactions, which contain the angular factor $(3cos^2\theta - 1)$, where θ represents the angle between the principal *z*-axis of the respective interaction tensor and the applied magnetic field (as illustrated in **Figure 1.13**). As the sample rotates about an axis inclined at an angle α to B_0, averaging of orientation-dependent interactions takes place, and this process is expressed by the equation:

$$\langle 3cos^2\theta - 1\rangle = \frac{1}{2}(3cos^2\alpha - 1)(cos^2\beta - 1) \quad (1.55)$$

where β represents the angle between the principal *z*-axis of the relevant interaction tensor and the rotation axis. When $\alpha = 54.74°$, it results in $(3cos^2\alpha - 1) = 0$, consequently rendering the average, $\langle 3cos^2\theta - 1\rangle$, also equal to zero.

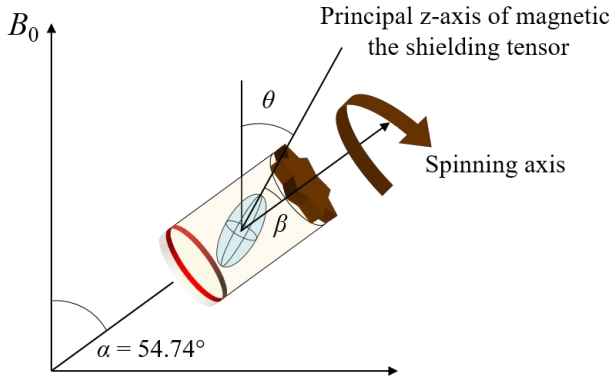


Figure 1.13. Rotor spinning around an axis at an angle α relative to the applied magnetic field. The chemical shift tensor is represented as an ellipsoid, with its principal *z*-axis depicted.

The resonance frequency ω of nuclei in a rotating powder experiencing various NMR interactions can be expanded as a Legendre polynomial according to the following equation:

$$\omega = \omega_0 + \omega_1 P_1(cos\theta) \quad (1.56)$$

$$P_1(cos\theta) = \frac{3cos^2\theta - 1}{2} \quad (1.57)$$

where ω_1 is a quantity whose expression depends on the specific interaction being considered.

In MAS, the anisotropic part $P_1(cos\theta)$ is averaged, which reduces anisotropic effects and enhances spectral resolution. To fully average the anisotropic component of NMR interactions, the spinning frequency must exceed the distribution of NMR interaction frequencies, *i.e.*, the width of the static line.

The refocusing of nuclear spin magnetization at the end of each rotor rotation period enhances spin echoes in the time domain (referred to as rotational echoes on the FID), resulting in the appearance of

rotational sidebands on both sides of the isotropic lines (**Figure 1.14**). These rotational sidebands are separated by multiples of the spinning frequency ($\omega_R/2\pi$). The higher the spinning frequency, the farther these rotational sidebands are from the isotropic line. At low spinning speeds, the intensities of the rotational sidebands replicate the shape of the line observed in the corresponding static spectrum and depend both on the strength of various anisotropic NMR interactions and the spinning frequency.

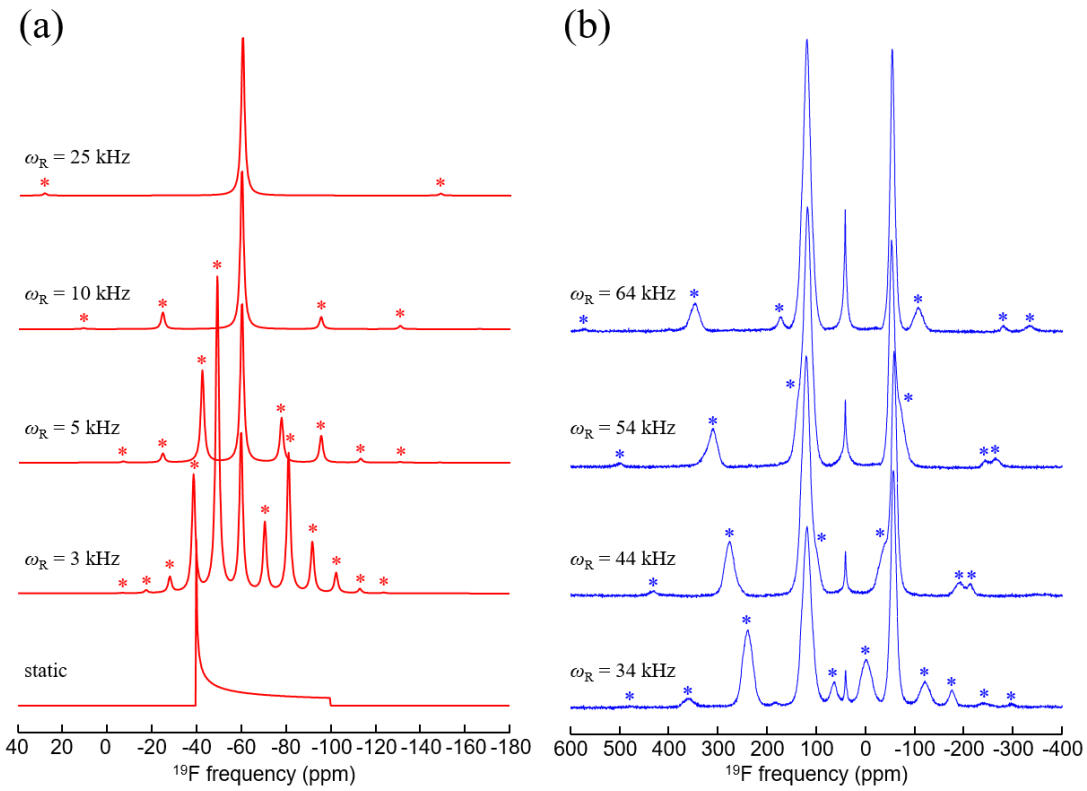


Figure 1.14. Simulated static and MAS ^{19}F NMR spectra with δ_{iso} = -60 ppm, δ_{CSA} = -40 ppm and η_{CSA} = 0 (a) and experimental MAS ^{19}F NMR spectra recorded at 7 T of $TaOF_3$ (b). The stars indicate spinning sidebands.

I.2.3.4. The importance of low-field NMR for spin-1/2 nuclei

For disordered systems involving spin-1/2 nuclei, such as ^{19}F spectra recorded on low-field spectrometers (e.g. 200 MHz) exhibit sidebands well separated from their corresponding main resonances (**Figure 1.15**). The lower the strength of the magnetic field, the wider the gap between the main resonances and its corresponding sidebands ($\Delta\delta$). For a recorded ^{19}F MAS NMR spectrum at 60 kHz with a 200 MHz spectrometer (where 1 ppm corresponds to 200 and 188 Hz for ^{1}H and ^{19}F, respectively), the resulting gap is $\Delta\delta$ = (60 kHz)/(188 Hz) = 319 ppm. However, for the same spectrum recorded with a 300 MHz spectrometer (where 1 ppm corresponds to 282 Hz for ^{19}F), the gap $\Delta\delta$ decreases to 212 ppm. It is crucial to avoid, or at least limit, the overlap between the isotropic (main resonances) and the sideband lines as this hampers the determination of the NMR parameter values and increases the associated uncertainties.

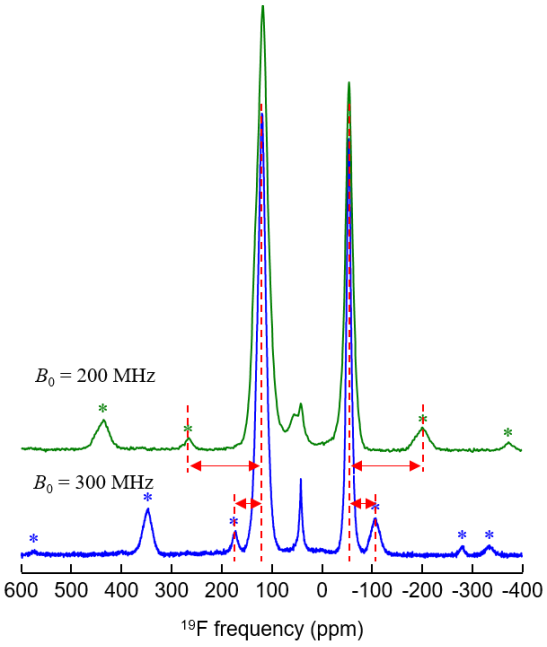


Figure 1.15. ^{19}F MAS NMR spectra of $TaOF_3$, recorded at 200 MHz (green) and 300 MHz (blue) spectrometers. They were recorded at a MAS frequency of 60 and 64 kHz for the green and blue spectra, respectively.

I.2.3.5. The Hahn echo experiment

In a so-called "*single-pulse*" NMR experiment, the nuclear spins observed in the (*x*,*y*) plane precess at slightly different rates, leading to phase differences (see section I.2.1.5). These phase differences, during the pulse and the subsequent relaxation period, result in baseline imperfections. The Hahn echo[18] is an experiment that overcomes these imperfections. Following the initial π/2 radiofrequency pulse, which tips the magnetization into the transverse plane, a second radiofrequency pulse π, after a certain

time, τ, refocuses the transverse magnetization at the end of the (2τ) time. At the end of this period, the spins are once again in phase (**Figure 1.16**). The acquisition of the NMR signal begins after the refocusing period. For all NMR experiments where the sample is spinning at the magic angle, the evolution times must be synchronized with the rotor's rotation period.

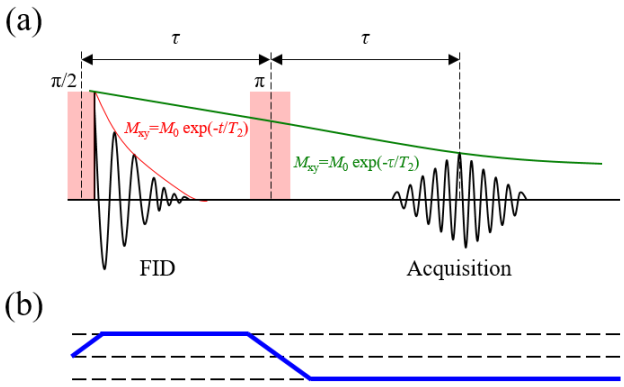


Figure 1.16. Pulse sequence (a) and coherence pathway (b) of the Hahn echo experiment. The delays τ represent the evolution and refocusing times of the transverse magnetization.

The ^{1}H and ^{19}F 1D NMR spectra presented in this manuscript were recorded using the Hahn echo sequence to obtain NMR spectra with a proper baseline. The effect of the Hahn echo sequence on the spectrum baseline is represented in **Figure 1.17**.

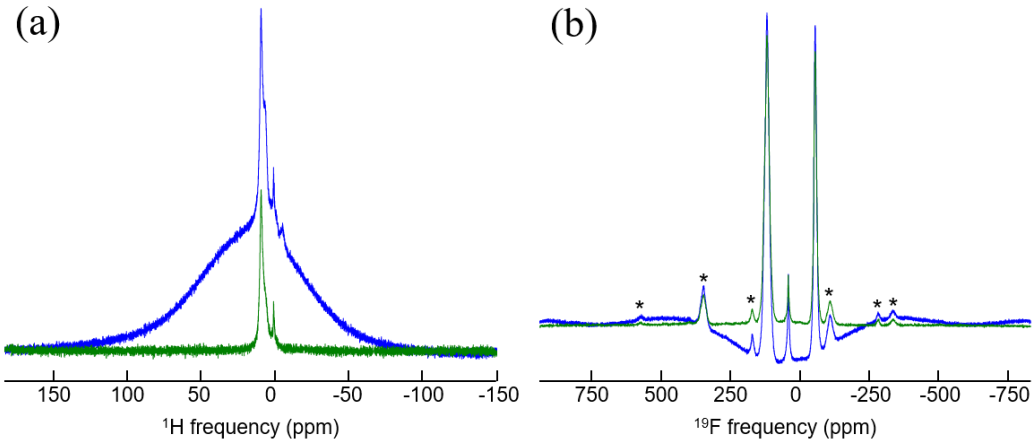


Figure 1.17. Experimental MAS NMR spectra, recorded using the simple pulse sequence (blue) and the Hahn echo sequence (green), of ^{1}H (a) and ^{19}F (b) from $TaOF_3$. The stars indicate spinning sidebands.

I.2.3.6. The Heteronuclear decoupling experiments

Often, the dipolar coupling interaction is responsible for broadening NMR peaks and a loss of *S*/*N*. This interaction is averaged out by MAS. However, when strong, the dipolar coupling interaction is not completely eliminated. Heteronuclear decoupling techniques, which consist of exciting one nucleus

during excitation and acquisition of a signal from the other coupled nucleus, are then employed to improve spectral resolution in solid-state NMR and prevent magnetization losses during pulse sequences. It has been shown that the MAS frequency and decoupling power are interdependent parameters. For low rotation speeds (5-20 kHz), high-power decoupling is necessary to eliminate the effects of both dipolar and *J*-couplings, whereas for high rotation speeds, low-power decoupling is sufficient. Several types of decoupling techniques exist, with the simplest being continuous wave (CW) decoupling.[19,20] This type of decoupling is not optimal, even at the highest currently achievable speeds (> 100 kHz). Methods have been proposed to enhance its performance. The first one utilizes two phase-modulated pulses (TPMP), also known as pulse train decoupling.[21] Other decoupling sequences, such as 64-step small-phase incremental alteration (SPINAL-64)[22] and X inverse-X (XiX),[23] have also been developed.

For instance, the main lines of the ^{19}F MAS NMR spectrum of $NaNbO_2F_2$ exhibit asymmetrical shapes, possibly attributable to heteronuclear coupling. To address this issue, we utilized ^{19}F–^{93}Nb heteronuclear decoupling using the XiX, CW and SPINAL-64 sequences. **Figure 1.18** illustrates the impact of these heteronuclear decoupling on the main line. The best decoupling—applied at an RF of ~106 kHz and resulted in perfectly symmetrical main lines—is the SPINAL-64 decoupling sequence whereas the XiX and CW ones did not result in fully decoupled spectra, probably due to the high MAS frequency (44 kHz).

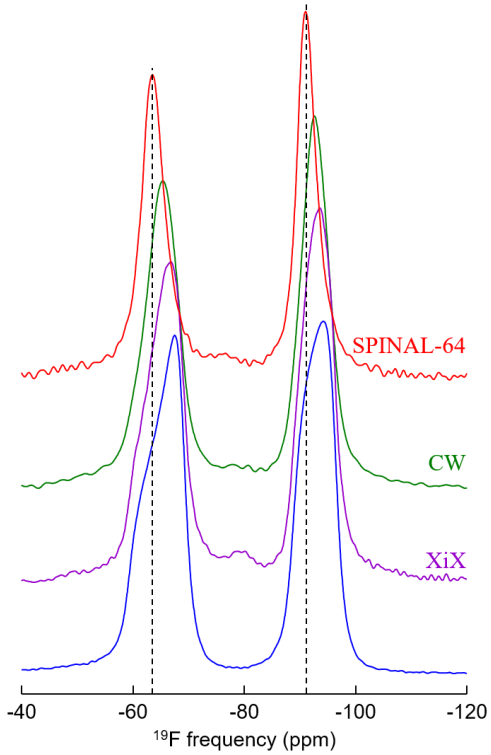


Figure 1.18. Experimental ^{19}F MAS NMR spectra of $NaNbO_2F_2$ recorded using a simple pulse sequence (blue) and using different heteronuclear decoupling sequences, including XiX, CW and SPINAL-64.

I.2.3.7. The Quadrupolar-Carr-Purcell-Meiboom-Gill (QCPMG) experiment

The CPMG pulse sequence (Carr-Purcell-Meiboom-Gill)[24,25] (pulse train and echo train) is used to significantly enhance the signal-to-noise ratio of echo spectra,[26–28] both in static[29,30] and MAS experiments. It has been demonstrated that, following a Fourier transformation of all the echoes, a spectrum is obtained containing a series of peaks, often referred to as "*spikelets*" or a comb-like pattern. These spikelets form an envelope that replicates a powder spectrum. Consequently, this envelope contains information about inhomogeneous interactions, including anisotropic chemical shift, quadrupolar and heteronuclear dipolar coupling.

In 1989, Cheng and Ellis[30] employed the CPMG experiment to observe the central transition of a half-integer quadrupolar nucleus. This sequence, known as the Quadrupolar-CPMG (QCPMG) sequence, is similar to the CPMG one. The enhancement of the signal-to-noise ratio in this case is attributed to the increased frequency separation between the spikelets. This experiment is particularly well-suited for nuclei with a low magnetogyric ratio.

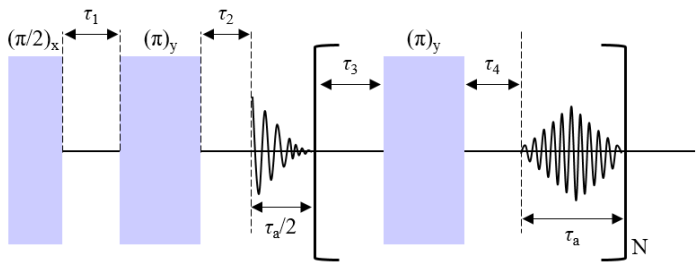


Figure 1.19. Illustration of the QCPMG pulse sequence.

The QCPMG pulse sequence resembles that of the Hahn echo but incorporates a series of refocusing pulses and acquisition periods (**Figure 1.19**). This experiment allows chemical shift interactions, heteronuclear dipolar coupling and second-order quadrupolar coupling to be refocused at each echo. However, it should be noted that direct homonuclear spin-spin interactions (dipolar coupling) and indirect coupling (*J*-coupling) are not refocused. In the context of MAS, the entire QCPMG cycle must be synchronized with the rotor rotation period ($\tau_{\mathrm{R}} = 1/\omega_{\mathrm{R}}$), such as:

$$2N\tau_{\mathrm{R}} = 2\tau_2 + P_2 + \tau_{\mathrm{a}} \tag{1.58}$$

where N is an integer, τ_2 represents a delay during which artifact effects are minimized, P_2 denotes the π refocusing pulse, and τ_{a} signifies the acquisition time for a single echo.

I.2.3.8. The WURST-QCPMG experiment

The Wideband Uniform Rate Smooth Truncation (WURST) QCPMG experiment has been employed for acquiring NMR spectra when the quadrupolar coupling is significantly large, such as with ^{137}Ba,[31] and ^{209}Bi nuclei.[32] Shurko and O'Dell[33] demonstrated the effectiveness of the WURST-QCPMG sequence for obtaining NMR spectra of ^{14}N, an abundant integer spin isotope (I = 1). WURST pulses enable efficient excitation of broad signals. In the WURST-QCPMG experiment (**Figure 1.20**), two WURST pulses with identical amplitude, phase profile, and sweep direction are used.

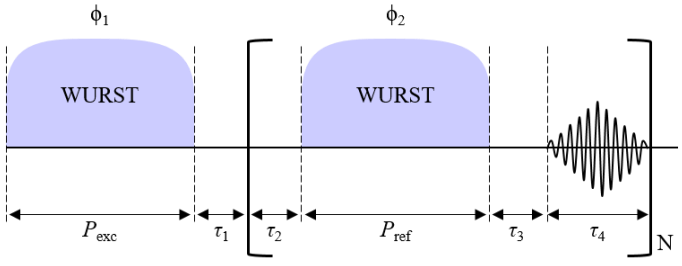


Figure 1.20. Illustration of the WURST-QCPMG pulse sequence.

The QCPMG and WURST-QCPMG pulse sequences have been employed for the NMR investigation of ^{93}Nb in $NaNbO_2F_2$, which features one niobium site with a C_Q value about 40 MHz. As illustrated in **Figure 1.21**, the spectrum obtained using the WURST-QCPMG sequence is more comprehensive compared to that obtained with MAS, owing to the broader irradiation.

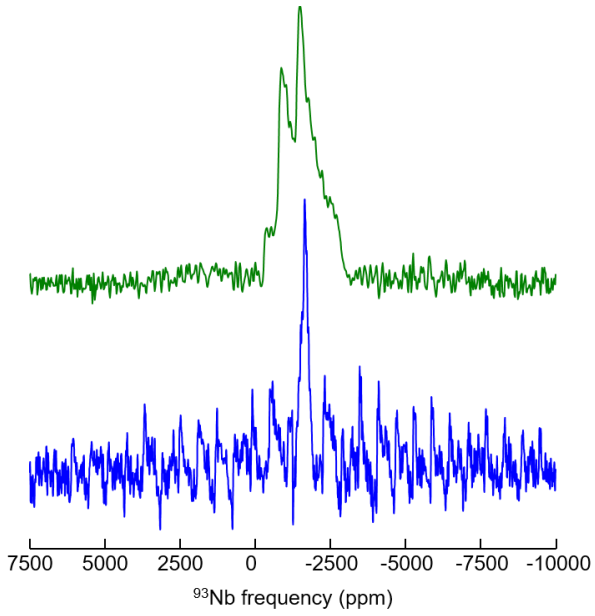


Figure 1.21. Experimental ^{93}Nb NMR spectra (7 T) recorded with, a simple pulse sequence at a MAS frequency of 44 kHz (blue), and the WURST-QCPMG pulse sequence at static mode (green).

I.2.3.9. Two-dimensional solid-state NMR

Analyzing 1D MAS spectra of quadrupolar nuclei can be a complex task, primarily due to the quadrupolar broadening of spectral lines. This challenge becomes more pronounced when dealing with either correlated disordered or fully disordered crystal materials, as they tend to exhibit a high distribution of NMR parameters. Two-dimensional solid-state NMR (2D ssNMR), coupled with advanced high-resolution methods, allow for deep insights into the nature of disorder in the short-range scale of these disordered systems.

i. Lineshapes in 2D experiments for Spin ½ nuclei

For spins ½ nuclei, NMR peak shapes typically manifest as Gaussian, or sometimes as a combination of Gaussian and Lorentzian. On 2D NMR spectra, "*star*" and "*round*" shapes are observed for Lorentzian and Gaussian peaks, respectively, as depicted in simulations in **Figure 1.22 (a)** and **(b)** [34] whereas the shape for a combination of Gaussian and Lorentzian is shown in **Figure 1.22 (c)**. However, in disordered compounds, a chemical shift dispersion, primarily arising from variations in the local magnetic field, can transform a symmetric 2D cross peak into an elongated ridge as explained in

ref [34], and can be simulated by introducing a shimming gradient to mimic distinct local magnetic fields in **Figure 1.22 (d)** and **(e)**.

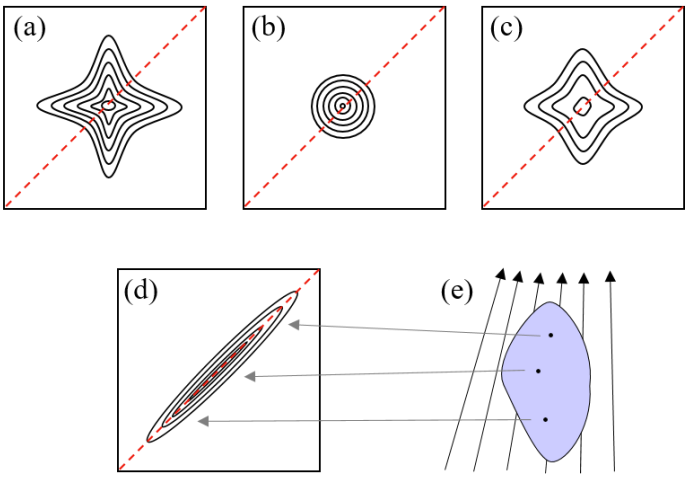


Figure 1.22. Lorentzian (a), Gaussian (a) Lorentzian-Gaussian (c) and Lorentzian-Gaussian with field gradient line-shapes in 2D spectra (d). (e) depicts three spins at distinct positions in the sample and their corresponding frequencies in the spectrum (d). (a)-(e) are reprinted from ref.[35]

ii. Basics of a 2D NMR sequence

The fundamental distinction between 2D and 1D NMR experiments is that in a 1D experiment, the signal is recorded as a function of a single time variable, whereas for 2D experiment the signal is recorded as a function of two time variables, namely t_1 and t_2. Typically, 2D experiments comprise four sequential stages, as illustrated in **Figure 1.23**: preparation, evolution, mixing, and detection. During the preparation phase, magnetization is generated through the application of a single or series of RF pulses. Subsequently, this magnetization evolves during the t_1 period, which serves as the evolution phase. In the mixing period, one or more RF pulses are applied to attain transverse magnetization. Finally, the signal is detected during the t_2 time. These four periods form the 2D pulse sequence.

The pulse sequence is iterated multiple times, with incremental adjustments to the duration of the evolution period t_1. For each t_1 value, a distinct FID is recorded as a function of t_2. This process accumulates a range of FIDs, constructing a dataset dependent on the two time variables, t_1 and t_2. Subsequently, a double Fourier Transformation is applied to convert the time-domain signals into their corresponding frequency domains, designated as F_1 and F_2. Finally, the resulting 2D spectrum is visualized through a contour plot.

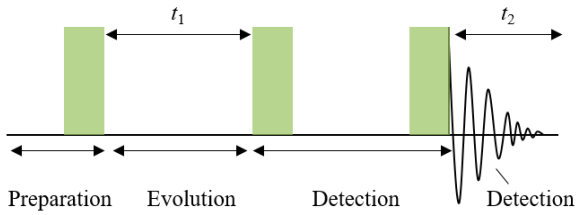


Figure 1.23. Illustration of a 2D NMR experiment pulse sequence

iii. The MQMAS experiment

The multiple quantum MAS (MQMAS) method introduced by Frydman *et al*.[36] is a two-dimensional technique that allows for the separation of isotropic interactions from second-order anisotropic interactions induced by the quadrupolar effect. The resulting spectrum comprises a "*classic*" MAS dimension and an isotropic dimension where the quadrupolar effect is suppressed, and only chemical shift and second-order quadrupolar-induced displacement influence the spectral lines.

In the present manuscript, the z-filter triple-quantum MAS (3QMAS)[37] experiment was used to record NMR spectra of the half-integer quadrupolar nuclei, including ^{87}Rb and ^{93}Nb. This experiment is composed of three pulses (**Figure 1.24**). The first pulse accomplishes the Z-quantum/triple-quantum (ZQ/3Q) transfer, the second one facilitates the reverse path (after a 3Q evolution time of t_1), and the final pulse is a selective 90° pulse on the central transition for the purpose of acquisition. Furthermore, the difference in excitation for large C_Q values is small, which enables the acquisition of spectra for nuclei with a broad quadrupolar distribution.

For ordered compounds, this sequence allows for the separation of inequivalent sites along F_1 projection and on the 2D spectra, allowing precise determination of NMR parameter values for each site. For disordered compounds, the shape of the NMR peaks on the 2D spectra provides information on the type of distribution experienced by the chemical shift and quadrupolar interactions.

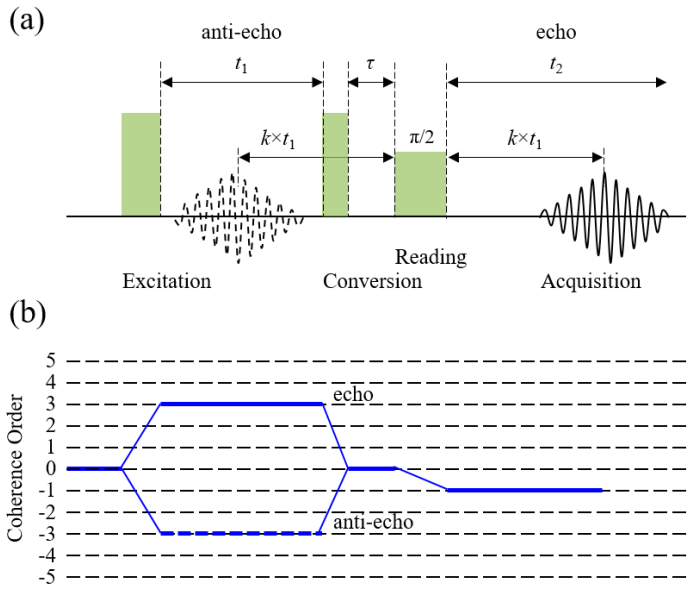


Figure 1.24. The z-filter 3QMAS pulse sequence (a) and its coherence pathway (b).

iv. Short-range ordering observed by MQMAS experiments

The MQMAS experiment offers a promising avenue for unraveling the distributions of δ_{iso} and EFG in disordered compounds. This EFG distribution, in turn, leads to distributions of C_Q, the quadrupole-induced shift δ_{qis}, and η_Q. Upon examining all parameters influencing MQMAS spectroscopy line shapes, three main factors emerge: the distribution of δ_{iso}, the magnitude of C_Q, and the distribution of C_Q. A summary of common MQMAS line shape features is presented and categorized into four scenarios in **Table 1.3**, based on the prominence (denoted as P) or not (denoted as NP) of these factors. When the magnitude of C_Q is considered as non-prominent, the C_Q value is small compared to the distribution of δ_{iso} and/or the magnetic field strength is sufficiently high to minimize quadrupolar broadening. Indeed, given that second-order quadrupolar broadening is inversely proportional to B_0^2 in ppm, the quadrupolar effects on the lineshape tend to diminish as magnetic field strength increases as evidenced in **Figure 1.25 (a)** and **(b)**. Although δ_{qis} is undoubtedly a crucial parameter, it is not explicitly included in **Table 1.3** for the sake of simplicity, as it is inherently a function of C_Q.

Table 1.3. Combinations of the distributions of δ_{iso}, C_Q and the magnitude of C_Q and the associated typical line shape in MQMAS experiments. "P" and "NP" stand for prominent and non-prominent, respectively

Cases	δ_{iso}	C_Q		Features of line shape
	Distribution	Magnitude	Distribution	
(1)	P	P	NP	Narrow ridge along diagonal
(2)	P	P	NP	Wide ridge parallel to diagonal
(3)	NP	P	NP	Nearly horizontal ridge
(4)	NP	P	NP	Horizontal ridge

Figure 1.25 showcases experimental MQMAS spectra, from the oxyfluorides studied during this thesis that illustrate the four cases summarized in **Table 1.3**. While comprehensive theoretical aspects and foundational principles of MQMAS have been extensively addressed in prior literature,[36–39] here the primary focus centers on the analysis of line shapes.

Within each spectrum in **Figure 1.25**, the diagonal represents the chemical shift line and serves as a pivotal reference for identifying individual resonances. A consistent trend can be found within MQMAS spectra as a function of the value of C_Q. For small C_Q values, the 2D peak is observed closer to the chemical shift line (diagonal). Conversely, for larger C_Q values, the peak shifts farther away, and presents a broader lineshape along the F_2 dimension (see section ii). The center of gravity for a given resonance along the F_2 dimension is given by $\delta_{\mathrm{center}} = \delta_{\mathrm{iso}} + \delta_{\mathrm{qis}}$ (1.59), where δ_{qis} has a negative sign, and its magnitude is directly proportional to C_Q. As the shift in the isotropic dimension (F_1) is defined as $\delta_{\mathrm{F1}} = \delta_{\mathrm{iso}} - 10/17\delta_{\mathrm{qis}}$ (1.60), an increase in C_Q results in an increase $|\delta_{qis}|$ so that δ_{F1} becomes larger, the width of the peak increases in the F_2 dimension and the peak shifts away (downward) from the chemical shift line, notably following the Quadrupole Induced Shift (QIS) line.

Figures 1.25 (a) corresponds to scenario (1), where the quadrupolar effect is either non-prominent or even negligible due to the strength of the magnetic field. The line shape appears as a stretched narrow ridge aligned with the diagonal, similar to the "*stretch effect*" observed in spin-1/2 nuclei, and is primarily determined by the distribution of δ_{iso}. However, for the same compound, but recorded at a lower field strength, quadrupole coupling is no longer negligible, leading to scenario (2) of **Table 1.3**.

As a result, the line shape of the corresponding MQMAS spectrum, in **Figure 1.25 (b)**, is broader and slightly off the diagonal.

In scenario (3), the local environment surrounding the probed nucleus is largely distributed, the influence of second-order quadrupolar broadening is significant and impacts the line shape. However, the chemical shift distribution is negligible and the line shape appears as a nearly, close to the line shape obtained for ordered compounds. On the MQMAS spectrum of **Figure 1.25 (c)**, the line shape is a nearly horizontal ridge which also exhibits broadening in the isotropic dimension, likely due to a combination of slight variations in both chemical shift and C_Q distributions.

Finally, in scenario (4), the C_Q value is either small or negligible due to the B_0 field strength, and the chemical shift distribution is also small, leading to a horizontal ridge, as shown in **Figure 1.25 (d)**.

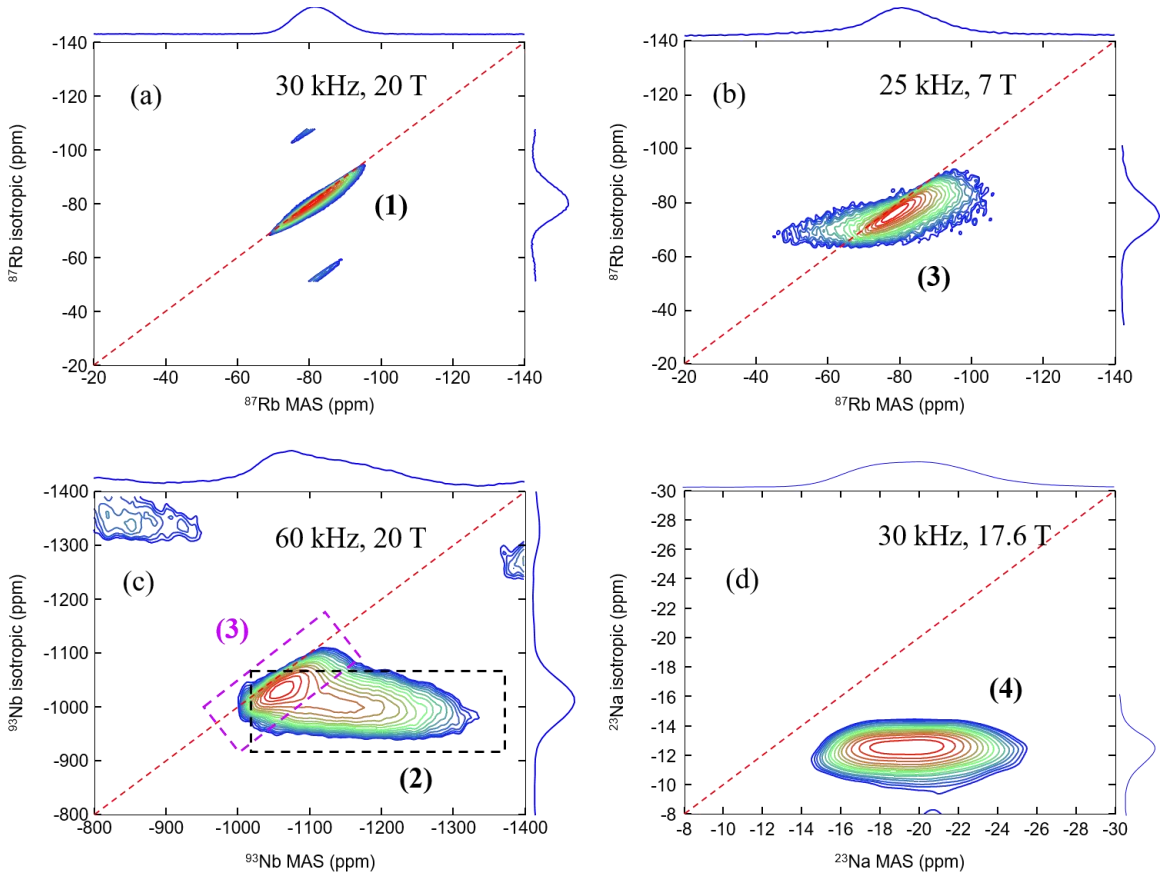


Figure 1.25. Experimental ^{87}Rb (a) and (b), ^{93}Nb (c) and ^{23}Na (d) and MQMAS NMR spectra from $RbNb_2O_5F$ (a, b and c) and $Na_2Ta_2O_5F_2$ (d), recorded using the z-filter 3QMAS sequence. The MAS frequency and magnetic field are indicated on each spectrum. The scenario from **Table 1.3** are indicated as (1), (2), (3) and (4) in bold and outlined by the dashed rectangles.

I.2.3.10. Nuclear Quadrupolar Resonance of ^{181}Ta

Nuclear quadrupolar resonance (NQR) is a useful tool to determine local electronic environments around nuclei with "*very*" large quadrupole moment (*Q*). The ^{181}Ta nucleus possesses the second-largest *Q* value, aside from rare-earth and actinide elements, and even minor local variations or nonstoichiometry in the composition can readily lead to broadening of the NQR spectrum. In an ordered compound such as $NaTaO_2F_2$ (refer to **Chapter II**) with only one Ta crystallographic site, three ^{181}Ta NQR resonances should be detected, corresponding to the transitions ±1/2↔±3/2, ±3/2↔±5/2 and ±5/2↔±7/2. When $\eta_Q = 0$, each one of these transitions is defined by the resonance frequency $\nu_{m\leftrightarrow m-1}$, given by:

$$\nu_{m\leftrightarrow m-1} = (m - \frac{1}{2})\frac{3eQV_{zz}}{2I(2I-1)} \quad (1.61)$$

and they are equally separated. This is not the case for non-zero η_Q values, and the ±1/2↔±3/2 transition frequency can even be higher than that of ±3/2↔±5/2 for $\eta_Q \geq 0.6$. In $NaTaO_2F_2$, as we will demonstrate later in **Chapter II**, the Ta site experiences a distorted local environment, resulting in an expectedly high C_Q value (~155 MHz from first principle calculations). We have attempted to record an ^{181}Ta-NQR spectrum (**Figure 1.29**). The experiment was carried out at RT on a 4 mm VTN CP-MAS probe-head with a minimum frequency value of 25 MHz. Multiple signal acquisitions were carried out by varying manually the frequency carrier from 28 to 80 MHz with an increment of 1 MHz. As shown in **Figure 1.29**, the expected spectrum shows two main resonance clusters (highlighted in orange). We speculate that the third group might appear at lower frequencies (≤25 MHz) that are not accessible with the available probes.

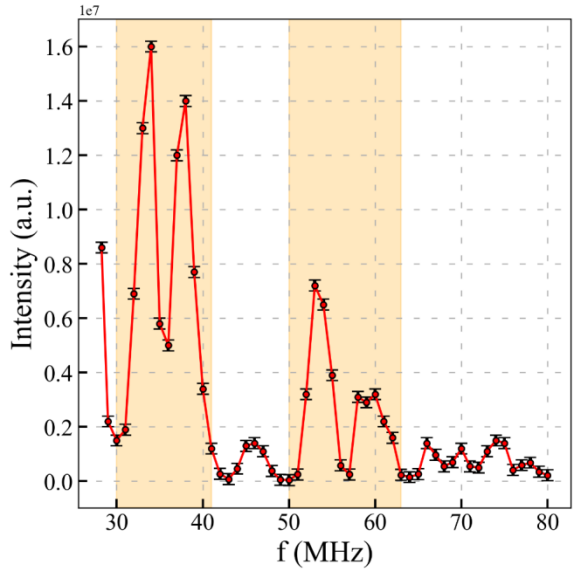


Figure 1.29. ^{181}Ta NQR spectrum of $NaTaO_2F_2$.

I.2.4. Fitting of NMR spectra using DMFit

I.2.4.1. 1D spectra of spin-1/2 nuclei

The ^{1}H and ^{19}F MAS NMR spectra were fitted using the Dmfit software[40] to extract the experimental NMR parameter values, including δ_{iso}, the amplitude (related to integrated intensity), the shape of the isotropic line (a mixture of Gaussian and Lorentzian shapes), and the chemical shift anisotropy tensor (δ_{CSA} and η_{CSA}). The "*csa mas*" model is used to take into account the spinning sidebands in the reconstructions. As the dipolar interaction is not explicitly considered, the amplitude and line width vary with the MAS frequency used and are readjusted accordingly. **Figure 1.26** illustrates an example of a ^{19}F MAS NMR fit of $NbOF_3$.

Within this manuscript, we adhere to a methodology that prioritizes the quality of the fit while keeping flexibility regarding the number of contributions employed. In our pursuit of modeling disordered crystals, obtaining highly precise experimental values for the NMR parameters is crucial in the process of modeling short-range ordering.

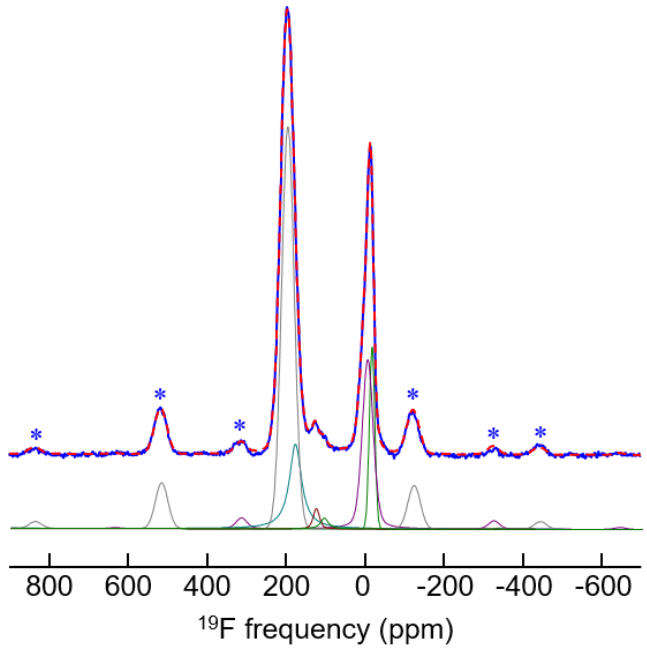


Figure 1.26. Experimental (blue) and fitted (dashed red) ^{19}F MAS (60 kHz, 4.7 T) NMR spectra of $NbOF_3$. The individual resonances used for the fit are shown below. The stars indicate spinning sidebands.

I.2.4.2. The Two-Dimensional-One-Pulse procedure

The two-dimensional-one-pulse (TOP) procedure,[41] implemented in Dmfit, was employed during the study of MOF_3 (M = Nb, Ta), which features two disordered anionic sites. It enables the generation

of an isotropic spectrum at "*infinite MAS frequency*". The ^{19}F MAS NMR spectrum of $NbOF_3$ was simulated using this procedure (**Figure 1.27**) to determine the relative intensities of the isotropic lines with high precision.

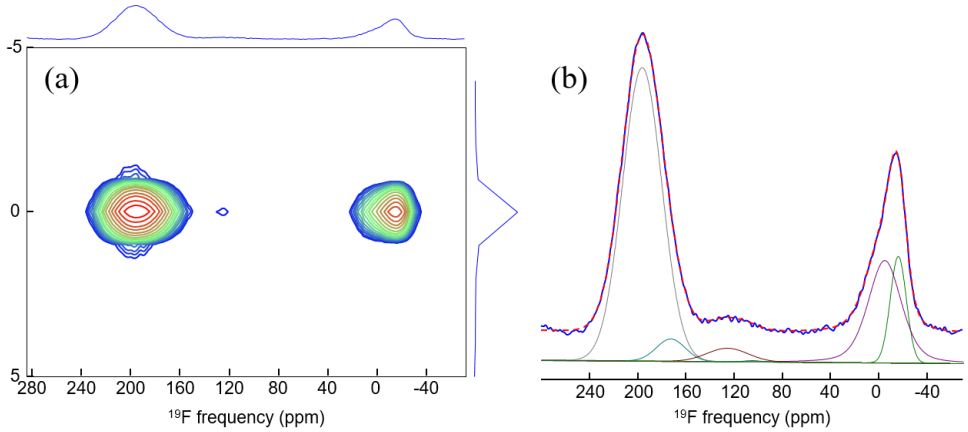


Figure 1.27. TOP (a) and infinite MAS frequency (b) ^{19}F NMR (4.7 T) spectra of $NbOF_3$. For spectrum (a), the individual resonances used to fit (dashed red) the experimental spectrum (blue) are shown below.

I.2.4.3. Quadrupolar nuclei

In addition to the NMR parameters previously mentioned, the C_Q and η_Q values as well as the Euler angles (α, β, γ) that describe the orientation of the EFG tensor relative to the chemical shift tensor (see section I.2.2.5) have to be determined. In the case of ordered crystals, the NMR lines are simulated using the "*int2QUAD*" model.

In disordered crystals, where both C_Q and δ_{iso} parameters are distributed, the "*Czjzek*" model[42,43] offers a potential avenue to derive the root mean-square quadrupolar product, $\sqrt{C_Q^2}$, by treating C_Q and δ_{iso} as normal (Gaussian) distributions.[44] This "*Czjzek*" model considers a statistical distribution of the quadrupolar interaction (C_Q, η_Q), whereas the "*CzSimple*" model includes a rapid version of the "*Czjzek*" model with an uncoupled Gaussian distribution of δ_{iso} values. Both models enable the retrieval of the average δ_{iso} ($<\delta_{iso}>$) and C_Q ($<C_Q>$) values, as well as $\Delta\delta_{iso}$. In a given disordered solid, the average asymmetry parameter ($<\eta_Q>$) value is estimated as ≈ 0.61 with an approximate standard deviation of σ_η ≈ 0.24.[43] **Figure 1.28** represents fits of ^{87}Rb MAS and z-filter 3QMAS NMR spectra obtained from the "*Czjzek*" model (or GIM, d=5) and the "*CzSimple*" model, respectively. In this manuscript, the experimental ^{23}Na, ^{87}Rb and ^{93}Nb spectra were fitted using either the "*Czjzek*" or the "*CzSimple*" model.

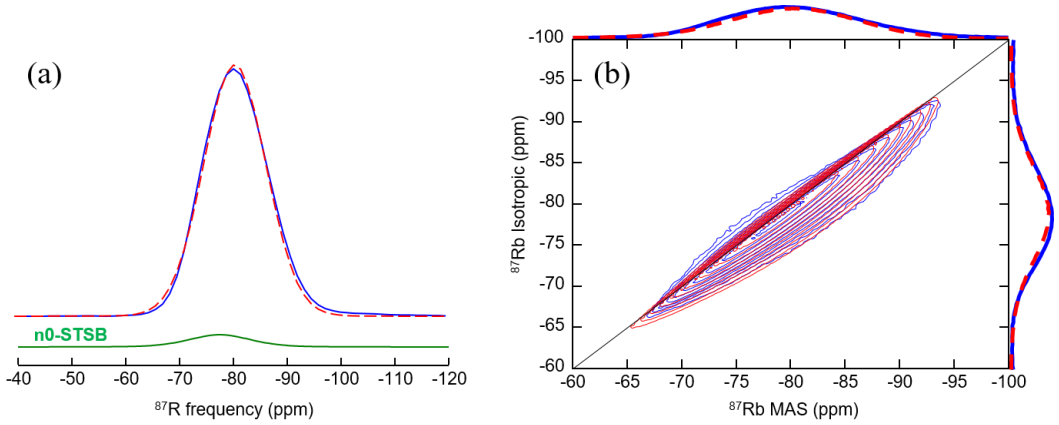


Figure 1.28. Experimental (blue) fitted (dashed red) ^{87}Rb CT MAS (a) and z-filter 3QMAS (b) NMR spectra (30 kHz, 20 T) of $RbNb_2O_5F$. The zeroth-order satellite transition spinning sideband (n0-STSB) is shown below the spectrum (a) in green.

I.3. Crystallography of disordered systems

The concepts and physical quantities discussed in this chapter are a part of the field of crystallography. A thorough understanding of these concepts is essential to follow the approach outlined in this manuscript seamlessly. The first section introduces various types of disorder and discusses concepts related to the structural modeling of disordered structures. The second and final section provides a detailed presentation of the criteria used in discerning models selected for subsequent first principle calculations.

I.3.1. Disorder in crystallography

The study of crystal materials has played a significant role in the development of solid-state physics. Crystallinity does not only introduce considerable simplifications in structural descriptions of these materials but also provide a foundation for theories governing their physicochemical properties. Therefore, it is only natural that the field of solid-state physics emerged from crystallography, with foundational theories originally tailored for crystal compounds.[45] However, practical applications often involve materials exhibiting varying degrees of disorder. For instance, semiconductor doping, commonly employed in microelectronics, can be viewed as a deviation from perfect crystallinity. Consequently, there is a growing need for a more profound understanding of the properties of disordered materials across various technological applications. Simultaneously, the effects of disorder are extensively explored from the perspective of fundamental physics. Many of the contemporary challenges in solid-state physics are, in one way or another, connected to disorder.

I.3.1.1. Different types of disorder

A low-level disorder can be defined as a disturbance of perfect crystalline order. This category includes defects, vacancies, and dislocations that are frequently observed in real materials. In polycrystalline materials, grain boundaries exhibit a more disordered atomic configuration than the grains.[46]

High-level disorder denotes a pronounced deviation from crystalline order. The fundamental property of amorphous materials is that they lack any long-range translational order. There is an element of randomness in atomic positions. The length scales over which order or disorder persists are also of

interest. Many materials exhibit local order over short length scales of a few atoms or molecules but are disordered over larger length scales.

Disorder in crystals can correspond to extremely varied cases, as illustrated in **Figure 1.30**:[47]

- **Structural or topological disorder:** characterized by the absence of long-range order and translational periodicity, with atoms located at interstitial sites.
- **Magnetic (orientation-based) disorder:** spins have different values at each point in a lattice. This situation occurs in solids and dipolar liquids where dipole moments exhibit orientation disorder.
- **Vibrational disorder:** refers to the instantaneous changes in atomic positions at lattice sites due to the thermal vibration of atoms.
- **Chemical or compositional disorder:** characterizes a broad class of materials such as alloys, mixtures, composites, and porous materials. In this category of disorder, crystallographic sites are shared by two or multiple atomic species or vacancies.

This manuscript focuses on the study of oxyfluoride structures that exhibit chemical disorder.

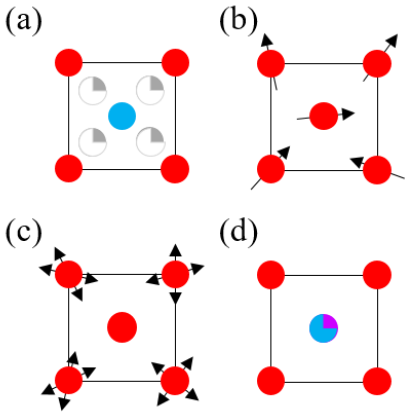


Figure 1.30. Illustration of the diverse types of disorder, (a) topological, (b) orientation-based, (c) vibrational and (d) chemical.

I.3.1.2. The concept of "*length-scale*" in crystal materials

As discussed in the **General Introduction**, the structure of crystal materials can be described from two different "*length-scales*", the "*long-range structure*" one, also referred to as the average structure (*i.e.*, structure that is observed across multiple unit cells), and the "*short-range structure*" one (*i.e.*, polyhedral unit, unit cell and/or supercell). In ordered crystals, such as ordered oxyfluorides, O/F arrangement in the short-range structure remains unchanged in the long-range structure. However, in

disordered oxyfluorides, the short-range O/F arrangements translate into a medium-range arrangement in the long-range structure (**Figure 1.31**).

The long-range structure, which is referred to in this manuscript as the experimental structure (ES), is experimentally determined by X-ray and neutron diffraction techniques. Although O and F atoms exhibit quasi-similar scattering factors, they can, however, be distinguishable by these techniques if each anion totally occupies a distinct crystallographic site, as is the case in ordered oxyfluorides. Nevertheless, for disordered oxyfluorides, O and F atoms, which occupy the same crystallographic site, are indistinguishable by X-ray and neutron diffraction techniques.

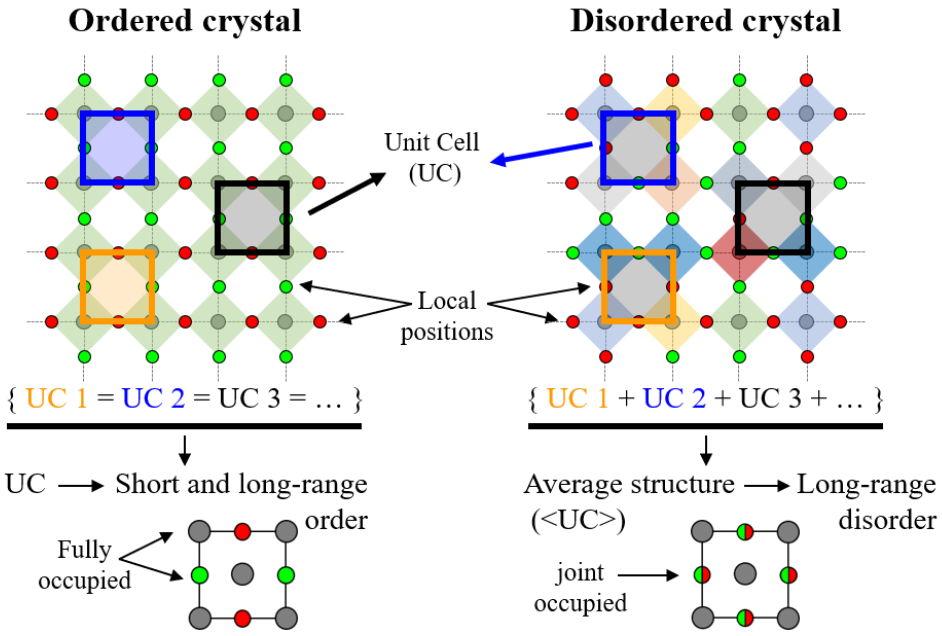


Figure 1.31. Representation of ordered (left) and disordered (right) oxyfluorides. The metal, O and F atoms are represented in gray, red and green, respectively. The unit cells are outlined by colored rectangles.

As described in the **General Introduction**, the structure of oxyfluorides exhibiting symmetry-dependent physicochemical properties should be described by both their long-range and short-range structures. By relying solely on ES, for instance, in the case of oxyfluorides exhibiting correlated O/F disorder (as discussed in **Chapter III**), leads to an oversimplification of the overall structural complexity, thus missing hidden models. In such cases, a multimodal structural solution approach, which requires combining ssNMR (section I.2 of this chapter) with the "*supercell approach*" (refer to I.3.1.6.), is necessary to precisely describe O/F arrangement in the short-range structure.

I.3.1.3. Supercells and disorder

In crystallography, a crystalline compound is described by a unit cell. This unit cell is defined by three cell parameters (a, b, c), the angles between them (α, β, γ), and the positions of the atoms in the crystal system, given by their coordinates (x, y, z) in the coordinate system ($\vec{a}$, $\vec{b}$, $\vec{c}$). Wyckoff positions are defined by the number of equivalent points generated in the unit cell by applying all the symmetry elements of the space group. There are general and special Wyckoff positions, distinguished by their symmetry and multiplicity (number of atoms present in a unit cell on a fully occupied site).

One of the most common approaches used to connect "*periodic*" structures with the local environment probed by spectroscopies in disordered solids is the "*supercell approach*". The idea is to create a supercell composed of *n* unit cells (with *n* being an integer), which within its boundaries, closely reflects the local structural properties of a disordered system: composition, nearest neighbors, *etc.* This atomic-level similarity between the real compound and the (though still periodic) model raises hopes that the calculated physical properties will also reflect the real properties of the materials.[48]

One of the challenges in constructing supercells is related to the interactions among structural defects. Several factors must be considered, including the size of the supercell, its total charge, as well as the distribution of local charges, the probabilities of different possible configurations, their total energies, and more.

I.3.2. Criteria for selecting structural models

In disordered oxyfluorides, the random distribution of anions in their respective disordered sites often results in a large number of combinations that exceed the limits of nowadays computational hardware. Since testing all possible combinations is rarely feasible, it is crucial to establish a set of defined criteria to obtain a manageable number of combinations. These criteria help to select models that potentially describe O/F ordering in the short- and long-range structures of disordered oxyfluorides, they include the following:

- Assessment of anion Site Occupancy Factors (SOF) values of the joint occupied crystallographic sites using bond valence sum (BVS) calculations;
- Calculation of the Coulomb energy using the Ewald method;
- Probability of occurrence of polyhedral environments (MX_n), possibility of correlated disorder.

I.3.2.1. The bond valence sum method

The concept of bond valence has proven it significance in the field of solid-state chemistry. Its historical development can be traced back to the concept of bond number, initially applied to metals and intermetallic compounds by Pauling in 1947. It was subsequently extended to oxides by Byström and Wilhelmi in 1951, as well as by Zachariasen in 1963. One of the primary advantages of this approach is that, to a generally excellent approximation, bond length can be uniquely determined from bond valence. Consequently, it serves as a robust method for predicting and interpreting bond lengths in crystalline materials.[49] For a bond between two atoms *i* and *j*, the valence is denoted as v_{ij}. The sum of all v_{ij} valences originating from a given atom *i* is noted V_i and satisfies the following equation:

$$\sum_j v_{ij} = V_i \tag{1.62}$$

The most widely accepted empirical expression for describing the relationship between bond length (d_{ij}) and v_{ij} valence is as follows:

$$v_{ij} = \exp\left(\frac{R_{ij} - d_{ij}}{b}\right) \tag{1.63}$$

where the parameter *b* is conventionally regarded as a constant with a widely accepted value of 0.37 Å.[50]

Equations (1.62) and (1.63) provide a framework for determining the parameters R_{ij}, which represent the bond lengths between pairs of atoms in known crystal (and molecular) structures, and referred to as the "*bond-valence parameter*". In this manuscript, the R_{ij} values used are 1.911, 1.920,[50] 1.87, 1.88,[51] 1.756,[52] 2.263, 1.677,[50] and 2.16 Å[51] for the pairs Nb^{5+}/O^{2-}, Ta^{5+}/O^{2-}, Nb^{5+}/F^{-}, Ta^{5+}/F^{-}, Na^{+}/O^{2-}, Rb^{+}/O^{2-}, Na^{+}/F^{-}, and Rb^{+}/F^{-}, respectively. These parameters serve various purposes. In crystallography, they are useful in predicting bond lengths based on given bond valences,[53,54] they are also employed to verify the reliability of determined structures from Rietveld refinements, and most importantly, they predict the SOF of each co-occupied crystallographic site, as thoroughly described in the MOF_3 (M = Nb, Ta) paper in **Chapter III** (refer to section 4.4. and **Table 4**). In this regard, the BVS method proves to be more robust than using sums of radii in most cases. On a more fundamental level, approximate bond-valence parameters aid in assessing the significance of bonding interactions between pairs of atoms.

I.3.2.2. Methods for constructing supercells

Various methods have been developed for constructing supercells from unit cells containing disordered sites (partially occupied or mixed sites). One of the effective methods is called "*Special Quasirandom Structures*" (SQS).[55] It involves building a limited number of supercells with possible atomic configurations in a random manner. Other methods have been described in various articles,[56–58] outlining optimization procedures for generating unique configurations (*i.e.*, symmetrically independent). Most of these methods are applicable to a limited category of solids (metallic alloys and semiconductors) and come with technical challenges, limitations regarding the types of disorder (number of substitutions and disordered crystallographic sites), and/or impractical input and output formats. A program, named "*Supercell*",[59] which is used in this manuscript, addresses these constraints present in previous software solutions.

I.3.2.3. "*Supercell*" program[59]

A disordered structure is described as a regular periodic structure with well-defined cell parameters, a space group, and a set of crystallographic sites. However, unlike ordered crystals where each

crystallographic site is entirely occupied by a single atomic specie, disordered structures have crystallographic sites that are partially occupied or of mixed composition. At the local level, this description lacks physical sense: a position cannot be simultaneously occupied by two or more atoms, or partially. These mixed compositions and partial occupancies mean that the same crystallographic site in a supercell can be occupied by different types of atoms or remain vacant. The key question is how to efficiently investigate the possible configurations. The approach implemented by the "*Supercell*" program is an exhaustive exploration where all individual configurations satisfying the conditions are generated and processed.

ii. Combinatorics of Atoms

For a supercell with several disordered crystallographic sites, the number of possible atomic configurations is based on enumerative combinatorial methods. The distribution of atoms on these sites has been reformulated as multinomial permutations.

Considering a system containing a disordered crystallographic site with a multiplicity, *K*, and a number of atoms, *N*, of different types occupying this site. The number of atoms of each type (including vacancy) is denoted as k_i, with i = 1, …, *N*, which satisfies $K = \sum_{i=1}^{N} k_i$. The total number of combinations is then given by:

$$P(k_1, k_2, \ldots, k_N) = \frac{(k_1 + k_2 + \cdots + k_N)!}{k_1!\, k_2! \ldots k_N!} = \frac{(\sum_{i+1}^{N} k_i)!}{\prod_{i=1}^{N} k_i!} \tag{1.64}$$

This equation is a generalization of the binomial distribution formula, obtained for $N = 2$. In most cases, the studied supercells have multiple disordered sites. Assuming that permutations within different sites are independent, the total number of structures will therefore be:

$$C = \prod_{i=1}^{M} P_i \tag{1.65}$$

where P_i represents the number of permutations for a disordered site i, and M represents the total number of independent disordered sites.

iii. The "*Supercell*" program algorithm

The algorithm of the "*Supercell*" program consists of four main steps, as shown in **Figure 1.32**.

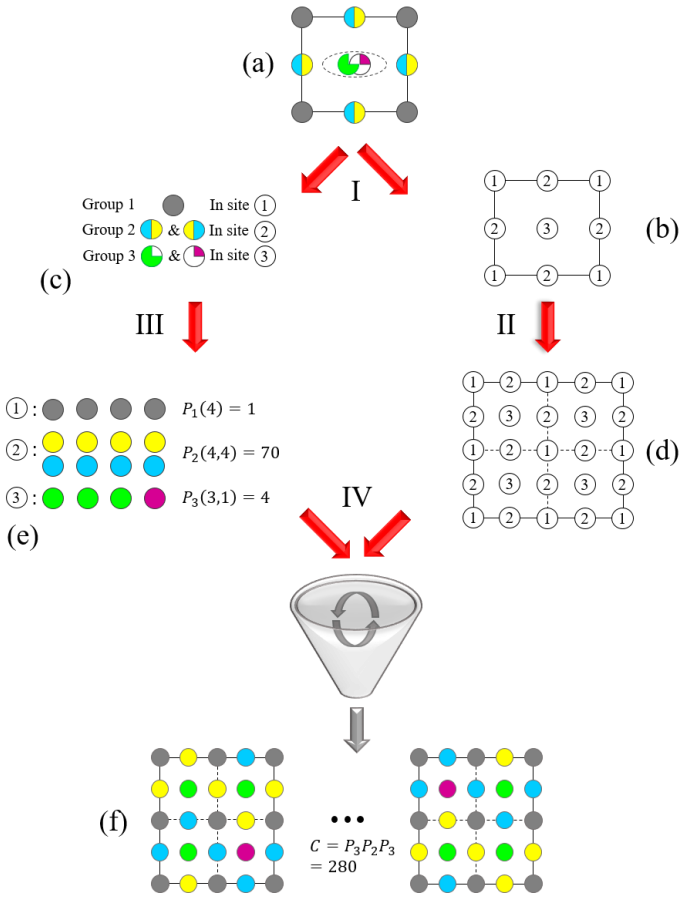


Figure 1.32. Illustration of the key concepts and steps involved in the workflow of the "*Supercell*" algorithm using a hypothetical disordered 2D crystal as an example with (a) the input structure, (b) crystallographic sites grouped into categories 1, 2, and 3. (c) Atom types and their occupancies assigned to one of these groups. (d) 2×2 supercell created from the cell shown in (b). (e) Atoms (gray, purple, green, yellow and blue) and vacancies (white) are used for permutations within the groups. (f) A subset of the possible structures with full occupancy (or vacancy) of all sites. Stages I–IV are explained in detail in the text, and the numbers of permutations P_i were calculated using formula (1.64).[59]

- **Step I: Assignment of crystallographic sites and atoms to groups**

All atoms present in the initial structure (**Figure 1.31**) are sorted into different groups. These groups are constructed in such a way that the application of permutation theory is independent for each group. Each group consists of a set of positions and a set of atoms that can occupy all these positions with equal probability and without any restriction. Crystallographic sites and atoms are counted in groups according to the following rules:

- Each atom type must be strictly assigned to a single group;
- Each group must be associated with at least one atom type;
- Each crystallographic position strictly belongs to one group;
- A group must be associated with at least one position;
- All atom types in a group occupy all positions assigned to the group with the same probability;
- Each position cannot be occupied by more than one atom.

- **Step II: Supercell generation**

A supercell is produced by replicating the unit cell along the three lattice vectors ($\vec{a}, \vec{b}, \vec{c}$), and the new supercell is characterized by a size ($l\vec{a}, m\vec{b}, n\vec{c}$), where *l*, *m*, and *n* are positive integers. Each crystallographic site "*p*" in the initial unit cell with Cartesian coordinates ($\overrightarrow{q_p}$) will have a total number of *l*×*m*×*n* images in the supercell with Cartesian coordinates:

$$\overrightarrow{q_p^{i,j,k}} = \overrightarrow{q_p} + i\vec{a} + j\vec{b} + k\vec{c} \tag{1.66}$$

where $i = 0, 1, \ldots, (l-1)$, $j = 0, 1, \ldots, (m-1)$, and $k = 0, 1, \ldots, (n-1)$. The choice of factors *l*, *m*, and *n* depends on the shape of the unit cell. In some lattices, the cell parameters *a*, *b*, and *c* are different, as in the case of a hexagonal or orthorhombic lattice. In such cases, the values for *l*, *m*, and *n* are chosen to approach an "*isotropic supercell*".

- **Step III: Occupation correction**

In this step, the occupation values of all atoms (represented by their labels) in each group are transformed into integer numbers of atoms distributed over all allowed positions in that group (**Figure 1.32**). In the supercell, these positions include all images of the sites assigned to the group by symmetry

and by translation of the initial unit cell. The implemented algorithm minimizes the χ^2 defined below with some restrictions:

$$\chi^2 = \sum_{i \in G} \sum_{j \in L_i} (R_i^j - \frac{N_i^j}{S_i})^2 \quad (1.67)$$

In this equation, the first summation (index i) extends over all groups (G), and the second (index j) over all atom labels (L_i) associated with group i. The N_i^j are variables (numbers of atoms) used to minimize equation (1.67), with R_i^j being the occupation value provided in the input file and S_i the number of allowed positions in group i.

One initial constraint is that the sum of occupations of all atoms within the same group must be less than or equal to the number of possible positions in that group: $\sum_j N_i^j \leq S_i$. The second constraint arises from charge balance. If the corresponding option is enabled, combinations of N_i^j that do not satisfy the system's charge balance condition $\sum_{ij} q_i^j N_i^j = 0$ will be rejected. An additional restriction is applied to fully occupied groups, meaning those where $\sum_j R_i^j = 1$. In such cases, the group must remain fully occupied after the procedure, which is enforced by the condition $\sum_j N_i^j = S$. Finally, it is possible to manually set some of the N_i^j values, which will then remain fixed during the minimization procedure. Here, vacancies are treated differently from atoms. Thus, N_i^j represents the number of actual atoms in group i, and the number of vacancies in group i is given by:

$$V_i = S_i - \sum_j N_i^j \quad (1.68)$$

- **Step IV: Processing and storage of resulting structures**

After determining the occupations for all sites, it becomes possible to construct supercells with atoms and vacancies (**Figure 1.32**). Permutations occur independently for each of the groups, so the resulting structures correspond to all possible combinations of all the groups.

As the number of combinations can be very large, the "*Supercell*" program includes several options. The first, "*-m*", reduces the total number of resulting structures by eliminating equivalently symmetric or translated supercells, resulting in a final set of unique supercell combinations. The second option, "-

q", allows for the calculation of Coulomb energy for each generated structure, providing information about their stability. It is then possible to rank these structures based on this energy and select a certain number of them using the "*-n*" option. The number *N* of combinations to be saved can be chosen in one of the following ways: randomly, the first and/or last *N* generated combinations, and/or the *N* combinations with the lowest or highest Coulomb energy.

I.3.2.4. Calculation of Coulomb energy for a supercell

The determination of the electrostatic potential and energy of an idealized crystal containing positive and negative point charges is a classical problem that has been addressed for nearly a century, starting with the work of Madelung (1918) and Ewald (1921).[60,61] The Ewald summation method is also the standard technique used to evaluate the repulsive internuclear electrostatic energy, $U_{n-n'}$, in electronic structure calculations, and it is employed for real crystals in the presence of thermal vibrations. The "*Supercell*" program applies this method for the numerical calculation of the Coulomb energy of supercells.

Consider a system consisting of N electric charges, both positive and negative, located within a box of volume L^3. The electrostatic interaction between the charges is significant at short distances. In this case, the system is considered globally electrically neutral, meaning that $\sum_i q_i = 0$. The aim is to numerically compute the potential energy of this N-particle system, which is given by the formula:

$$U_c = \frac{1}{2}\sum_{i=1}^{N} q_i \phi(r_i) \tag{1.69}$$

where $\phi(r_i)$ is the electrostatic potential at the position r_i of the ion with charge q_i:

$$\phi(\mathrm{r_i}) = \sum_{j,n}^{'} \frac{q_j}{|r_{ij} + nL|'} \tag{1.70}$$

where the "*prime*" in this summation indicates the sum of all periodic images *n* and all atoms *j*, except for $j = i$ if $n = 0$. In this situation, particle *i* interacts with all particles in its image, but not with itself. Equation (1.70) cannot be used to compute the electrostatic energy through computer simulation because it contains a poorly convergent sum (actually, the sum is only conditionally convergent). To address this constraint, another scenario must be considered, in which. each particle *i* with charge q_i is surrounded

by a diffuse charge distribution of opposite sign, so that the total charge of this cloud exactly cancels q_i. In this case, the electrostatic potential due to particle i is solely due to the fraction of q_i that is not shielded. At a great distance, this fraction rapidly approaches zero, the rate depending on the functional form of the shielding charge distribution. In the following, the distribution of the shielding charge cloud is assumed to be Gaussian.

The contribution of the electrostatic potential at a point r_i due to the set of shielded charges can be easily calculated through direct summation because the electrostatic potential due to a shielded charge decreases rapidly with r. However, the goal was not to evaluate the potential due to a set of shielded charges but rather due to a point charge. Therefore, a correction is needed. This is schematically represented in the **Figure 1.33**. Calculating the electrostatic energy at the ion i site requires initially excluding the electrostatic interaction of the ion with itself and to consider three contributions to the electrostatic potential:

- The contribution due to the point charge (q_i);
- The contribution due to the shielding charge cloud (Gaussian distribution) ($-q_i$);
- The contribution due to the compensating charge cloud (q_i).

To exclude the interaction of the ion with itself, none of these contributions to the electrostatic potential should be included at the ion's position i. However, it turns out to be convenient to retain the contribution from the compensating charge distribution and then correct for the resulting spurious interaction as it is a periodic function. Such a function can be represented by Fourier series, which will be essential for numerical implementation.

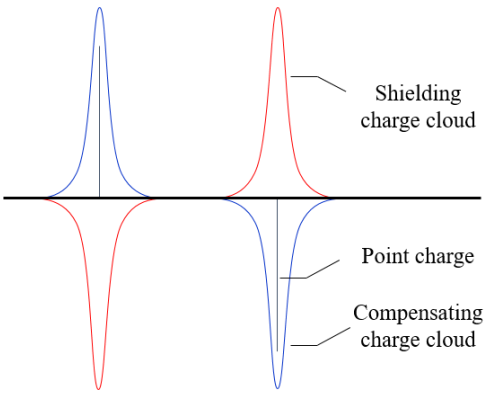


Figure 1.33. Illustration of point charge with compensating charge clouds (q_i) and shielding ($-q_i$).

This approach constitutes the essence of the Ewald summation method. Therefore, the Ewald formula for calculating Coulomb energy is expressed as follows:

$$U = U^{(r)} + U^{(k)} + U^{(self)} + U^{(Dipolar)} \tag{1.71}$$

where $U^{(r)}$ is called the real-space contribution (shielding charge cloud), $U^{(k)}$ is the reciprocal-space contribution (compensating charge cloud), $U^{(self)}$ is the self-energy, and $U^{(Dipolar)}$ accounts for the dipolar correction.

To determine the Coulomb energy expressions for each contribution, it is necessary first to find the electrostatic potential, which can be accomplished by solving the Poisson equation using the Fourier transform method.

According to the calculations, the Coulomb energies for each contribution are given by:

$$U^{(r)} = \frac{1}{2}\sum_{i}^{N}\sum_{j}^{N}\sum_{n\in\mathbb{Z}^3}^{\dagger} q_i q_j \frac{erfc(\alpha|r_{ij}+nL|)}{|r_{ij}+nL|} \tag{1.72}$$

$$U^{(k)} = \frac{1}{2L^3}\sum_{k\in\mathbb{K}^3;k\neq 0}\frac{4\pi}{k^2}exp\left(-\frac{k^2}{4\alpha^2}\right)\sum_{i}^{N}\sum_{j}^{N} q_i q_j exp\left(-iK.r_{ij}\right) \tag{1.73}$$

$$U^{(self)} = -\frac{\alpha}{\sqrt{\pi}}\sum_{i}^{N} q_i^2 \tag{1.74}$$

$$U^{(Dipolar)} = \frac{2\pi}{(1+2\epsilon')L^3}\left(\sum_{i}^{N} q_i r_i\right)^2 \tag{1.75}$$

where ϵ' is the dielectric constant and $\mathbb{K}^3 = \left\{\frac{2\pi n}{L} : n \in \mathbb{Z}^3\right\}$.

The electrostatic potential and energy of point charges in a real crystal, in the presence of thermal vibrations, are obtained as a particular case of the Fourier method. The Ewald summation method determines the electrostatic potential and energy of point charges in a crystal at a temperature obtained from the width of the Gaussian, not at 0 K. For commonly recommended Gaussian width values for computational convenience, the temperatures are very high.

I.3.2.4. Statistics and preferential short-range O/F ordering

Once supercells are generated, symmetry-equivalent combinations are eliminated, and the Coulomb energy is calculated, the next step is to identify which supercells among these combinations are suited for first principle calculations. There are two methods for finding these potential supercells. The first method involves performing a statistical analysis of the weight of each polyhedral environment in the supercell with respect to the experimental composition of the studied oxyfluoride, and, among the generated combinations, supercells with the lowest energies that follows these statistics are retained. The second method, which is more challenging, is to search for biases in the structure, such as preferential short-range O/F ordering.

i. Statistical analysis

In this manuscript, we have managed to derive a formalism allowing statistical analysis of any disordered crystal formed from polyhedral units. Consider a disordered oxyfluoride with the composition $A_tM_uO_vF_w$, where the ions A^n and M^m are surrounded by k anions, we define p as an integer value that corresponds to a certain polyhedral configuration, $p = \{0, \dots, k+1\}$. The number of possible combinations of each polyhedral configuration is given by:

$$C_p^k = \frac{k!}{P!\,(k-p)!} \tag{1.76}$$

The total statistical probability of the polyhedral configuration in the oxyfluoride $A_tM_uO_vF_w$, is given by:

$$P = \sum_{i=0}^{p} \sum_{j=k}^{0} C_i^k \left(\frac{v}{v+w}\right)^j \left(\frac{w}{v+w}\right)^i = 1 \tag{1.77}$$

where $i = \{0, 1, \dots, p\}$ and $j = \{k, (k-1, (k-2), \dots, 0\}$. In each increment of the i summation the probability of a polyhedral configuration is calculated. For instance, in RbM_2O_5F (M = Nb, Ta) oxyfluorides, M atoms form octahedral configurations $[MX_6]^{n-}$ (X = O, F). In this case, the equation (1.77) is expressed as:

$$P = \left\{1 \times \left(\frac{5}{6}\right)^{6} \times \left(\frac{1}{6}\right)^{0}\right\}_{[MO_6]^{7-}} + \left\{6 \times \left(\frac{5}{6}\right)^{5} \times \left(\frac{1}{6}\right)^{1}\right\}_{[MO_5F]^{6-}} + \left\{15 \times \left(\frac{5}{6}\right)^{4} \times \left(\frac{1}{6}\right)^{2}\right\}_{[MO_4F_2]^{5-}} + \left\{20 \times \left(\frac{5}{6}\right)^{3} \times \left(\frac{1}{6}\right)^{3}\right\}_{[MO_3F_3]^{4-}} + \left\{15 \times \left(\frac{5}{6}\right)^{2} \times \left(\frac{1}{6}\right)^{4}\right\}_{[MO_2F_4]^{3-}} + \left\{6 \times \left(\frac{5}{6}\right)^{1} \times \left(\frac{1}{6}\right)^{5}\right\}_{[MOF_5]^{2-}} + \left\{1 \times \left(\frac{5}{6}\right)^{0} \times \left(\frac{1}{6}\right)^{6}\right\}_{[MF_6]^{-}} = 1 \quad (1.78)$$

Equation (1.78) contain seven parts, each representing the probability of an octahedral configuration. **Figure 1.34** illustrates comprehensive charts of the probability of each octahedral conformation (**Figure 1.34** red histograms) and of the selected supercells that respect this probability (**Figure 1.34** blue histograms).

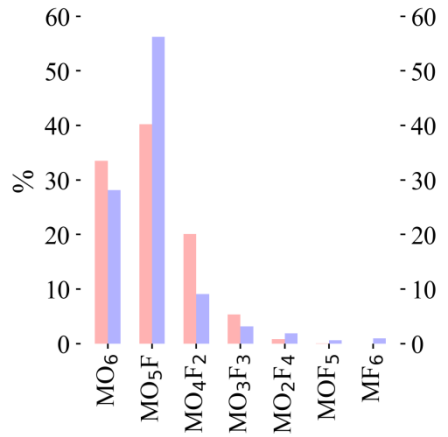


Figure 1.34. MX_6 population of RbM_2O_5F (M = Nb, Ta), from the statistics of composition (red chart), and the chosen sample of supercells (blue chart).

ii. Preferential short-range O/F ordering

As discussed in the **General Introduction**, within a given disordered oxyfluoride formed from octahedral units, π-hybridization in the M-anion bonds is maximized when anions with similar Pearson hardness[62] are in close proximity. Consequently, *cis*- and *fac*-$[MO_4F_2]^{5-}$ (or $[MO_2F_4]^{5-}$) configurations are favored, especially if the M cation is a d^0 transition metal.[63,64] This allows for atomic rearrangement towards characteristic bond lengths, leading to metal displacement towards the less electronegative anion.[65] These preferred configurations may result in preferential short-range O/F ordering, and/or O/F correlated disorder. Once the existence of correlated O/F disorder is confirmed, for instance, through experimental observation of metal displacements via electron diffraction,[66] the construction of supercells that exhibit this correlated disorder can be performed manually (as shown in the MOF_3 (M = Nb, Ta) paper in **Chapter III**). These supercells do not necessarily follow the statistics described above.

Up to this point, we have explored the process of constructing and sorting supercells. However, when O and F atoms are distributed on a same site in these supercells, the M–O and M–F bond lengths are equal, whereas in oxyfluorides compounds, M–O are expected to be shorter than M–F. As a solution, the selected supercells undergo relaxation through first-principle calculations, primarily using solid-state Density Functional Theory (DFT) with periodic boundary conditions. This leads to relaxed supercells with realistic bond lengths and the NMR parameters issued from these supercells become suitable for comparison to the experimental ones. This comparison serves as a decisive step in determining whether a supercell effectively describes O/F ordering or not.

An in-depth description of DFT relaxation and the PAW and GIPAW approach is provided in the following section.

I.4. First principle calculations

First principle calculations of solid-state NMR parameters (chemical shift, and quadrupolar interaction for nuclear spin nuclei $I > 1/2$) are crucial in modeling O/F ordering in oxyfluorides. Due to its sensitivity to local environments, ssNMR offers complementary information in terms of structural characterization compared to X-ray and neutron diffraction techniques. However, an additional tool for connecting experimental ssNMR data to structural models is needed to fully exploit short-range O/F ordering. First principle calculations provide this link.

In the case of solid-state NMR, it is important to consider the crystalline nature of the studied material. The preferred approach is to employ methods using periodic boundary conditions. Among the various existing methods, the PAW[67,68] and GIPAW[69,70] approaches, implemented in the CAmbridge Serial Total Energy Package (CASTEP)[71,72] and the Vienna Ab initio Simulation Package (VASP),[73,74] prove to be highly relevant for calculating EFG and magnetic shielding tensors in inorganic materials, including fluorides and oxyfluorides. These approaches are based on DFT and utilize plane waves and pseudopotentials.

In this section, fundamentals of DFT are described and the theory behind the PAW and GIPAW approaches is briefly mentioned.

I.4.1. Quantum chemistry methods

The objective of first principle calculations is to describe the properties of materials based on their crystalline structure, using quantum mechanical approximations. At the microscopic level, the problem can be straightforwardly formulated as solving the Schrödinger equation in a periodic crystalline system consisting of *A* atomic nuclei with mutual interactions and *N* electrons with spin σ_i positioned at $\vec{R}_I = \{\vec{R}_I; I = 1, \dots, A\}$ and at $\vec{r}_i = \{(\vec{r}_i, \sigma_i); i = 1, \dots, N\}$, respectively:

$$\hat{\mathcal{H}}\psi(\vec{R}, \vec{r}) = E\psi(\vec{R}, \vec{r}) \tag{1.79}$$

where ψ is the electronic wave function, E the energy of the system and $\hat{\mathcal{H}}$ the Hamiltonian of the system given by:

$$\hat{\mathcal{H}} = -\sum_{i}^{N} \frac{\hbar^2}{2m}\nabla_i^2 - \sum_{I}^{A} \frac{\hbar^2}{2M}\nabla_I^2 - \sum_{i,I} \frac{Z_I e^2}{|\vec{r}_i - \vec{R}_I|} + \sum_{i<j} \frac{e^2}{|\vec{r}_i - \vec{r}_j|} + \sum_{I<J} \frac{Z_I Z_J e^2}{|\vec{R}_I - \vec{R}_J|} \tag{1.80}$$

The first two terms of the Hamiltonian represent the kinetic energy operators of the *N* electrons and the *A* atomic nuclei, respectively. The last three terms represent the various interaction potentials: electron-nucleus, electron-electron, and nucleus-nucleus, respectively. Therefore, the Hamiltonian involves the interaction of *A* + *N* particles, and its solving is a very difficult, if not impossible, task due to the limited memory of the nowadays computational tools. However, it is possible to simplify it by introducing approximations.

I.4.1.1. The Born-Oppenheimer (BO) approximation

The Born-Oppenheimer approximation is considered as a first-level approach by fixing the positions of the atomic nuclei. Indeed, the mass of electrons is significantly lower than that of the nuclei, which means that electrons are much more mobile than nuclei. The kinetic energy of nuclei can then be neglected, and the term of interaction between nuclei is considered as a constant.

This initial approximation reduces the problem of *A* + *N* bodies to a problem with *N* electrons (referred to as "*the poly-electronic problem*"). The Schrödinger equation is simplified to:

$$\hat{\mathcal{H}}^{elect} = -\sum_{i}^{N} \frac{\hbar^2}{2m} \nabla_i^2 + \sum_{i<j} \frac{e^2}{|\vec{r}_i - \vec{r}_j|} + \sum_{\lambda} \frac{Z_\lambda}{|\vec{r}_i - \vec{R}_\lambda|} \quad (1.81)$$

Despite this approximation, solving the Schrödinger equation remains challenging. Other approximations, such as the Hartree-Fock approach and DFT, are necessary.

I.4.1.2. The Hartree-Fock approach

In the framework of the Hartree-Fock approach, it is assumed that each electron only interacts with the average field created by the other electrons in the system. It takes into account the one-electron terms (kinetic energy, nuclear attraction) and only considers the average electrostatic repulsion field created by the electrons in the system.[75]

The wave function ψ used is a product of one-electron wave functions $g_i(r_i, \theta_i, \varphi_i)$:

$$\psi = g_1(r_1, \theta_1, \varphi_1) \times g_2(r_2, \theta_2, \varphi_2) \times \ldots \times g_N(r_N, \theta_N, \varphi_N) \quad (1.82)$$

The major issue with this wave function is that it is not antisymmetric, meaning it does not adhere to the Pauli Exclusion Principle. To address this problem, this function is expanded in the form of a Slater determinant or a linear antisymmetric combination of spin orbitals.[75] The Slater determinant has the following form:

$$\psi(1,2,\ldots,N) = \frac{1}{\sqrt{N!}} \begin{vmatrix} \chi_1(1) & \chi_2(1) & \ldots & \chi_N(1) \\ \chi_1(2) & \chi_2(2) & \ldots & \chi_N(2) \\ \chi_1(3) & \chi_3(3) & \ldots & \chi_N(3) \end{vmatrix} \quad (1.83)$$

where $\chi_N(N) = g_N(r_N, \theta_N, \varphi_N)\sigma(m_s)$. The first term corresponds to a spatial function, and the second term to a spin function $\sigma(m_s) = \alpha(m_s)$ or $\sigma(m_s) = \beta(m_s)$.

The Hartree-Fock energy, E_{HF}, is greater than that of the ground state, E_0, due to the variational principle. In particular, it completely neglects the effects of electron correlation. The difference between this electronic energy E_{HF} and the exact value of the electronic energy ε_e is called the correlation energy E_{C} and is defined by:

$$E_{\mathrm{C}} = \varepsilon_e - E_{\mathrm{HF}} \quad (1.84)$$

Other methods, known as Post-Hartree-Fock methods, have since been developed to account for electronic correlations, such as Møller-Plesset perturbation theory[76] or the Multi-Configuration method.[77] These methods often provide results in very good agreement with experimental observations but require very long computation times, limiting their applicability.

I.4.1.3. Density Functional Theory (DFT)

Density functional theory (DFT) is one of the most widely used methods for solving the Schrödinger equation, enabling the study of infinite systems, *i.e.*, crystals.

i. Basic principle

In the Hartree-Fock approach, the energy of a system can be expanded as a functional of its wave function, ψ. In the case of DFT, the energy is a functional of the electronic charge density, $\rho(\vec{r})$, of the system. DFT is based on a model developed by Thomas[78] and Fermi[79] in 1927.

The basic idea of DFT is that the electronic charge density, $\rho_0(\vec{r})$, of the ground state completely determines observables such as energy, within the framework of non-relativistic quantum mechanics and taking into account electronic correlation effects. Thus, any electronic property of a system of *N* particles subject to an external potential, v_{ext}, can be calculated as long as its electronic charge density is known.

ii. Hohenberg-Kohn theorems

In 1962, Hohenberg and Kohn developed two theorems that form the foundations of DFT.[80,81]

- **First theorem**

Any physical property of a system with *N* electrons subjected to the influence of a static external potential v_{ext} can be expressed, in its ground state, as a functional of the electron density $\rho_0(\vec{r})$. In other words, a unique correspondence exists between the density of the ground state $\rho_0(\vec{r})$ and the external potential $v_{ext}(\vec{r})$, and therefore between $\rho_0(\vec{r})$ and the wave function of the ground state ψ_0.

For a given system, the energy is expressed as follows:

$$E[\rho(\vec{r})] = T[\rho(\vec{r})] + V_{ee}[\rho(\vec{r})] + V_{ne}[\rho(\vec{r})] \quad (1.85)$$

where the first term corresponds to the kinetic energy of the electrons, and the second and third terms correspond to the electron-electron and electron-nucleus potential energies.

By defining,

$$V_{ne}[\rho(\vec{r})] = \int \rho(\vec{r}) v_{ext}[\rho(\vec{r})] d\vec{r} \tag{1.86}$$

$$F_{\mathrm{HK}}[\rho(\vec{r})] = T[\rho(\vec{r})] + V_{ee}[\rho(\vec{r})] \tag{1.87}$$

The energy functional is written as:

$$E[\rho(\vec{r})] = F_{\mathrm{HK}}[\rho(\vec{r})] + \int \rho(\vec{r}) v_{ext}[\rho(\vec{r})] d\vec{r} \tag{1.88}$$

where F_{HK} is the universal functional of Hohenberg and Kohn, which encompasses all terms independent of the external potential. This functional includes electronic kinetic energy and repulsive electron-electron potential energy.

- **Second theorem**

The energy functional $E[\rho(\vec{r})]$ is minimized when the electron density $\rho(\vec{r})$ corresponds to the electron density of the ground state $\rho_0(\vec{r})$:

$$E_{\mathrm{Min}}[\rho(\vec{r})] = E[\rho_0(\vec{r})] \tag{1.89}$$

$$\frac{\partial E[\rho(\vec{r})]}{\partial \rho(\vec{r})} = 0 \tag{1.90}$$

The electron density of the ground state completely determines the properties of the N-electron system in an external potential v_{ext}.

iii. The Kohn-Sham equation

In 1965, Kohn and Sham developed an efficient method for calculating the ground state energy based on the electron density of this ground state because the theorems of Hohenberg and Kohn do not provide a procedure for calculating it. Their idea is to use a fictitious system of *n* independent electrons but with the same electron density as the real system,[81] that is: $\rho(\vec{r})_{fict} = \rho_0(\vec{r})$.

In this approximation, the Hamiltonian of the system is written as:

$$\hat{\mathcal{H}}^{\mathrm{KS}} = \sum_{i=1}^{N} \left[-\frac{\nabla_i^2}{2} + v(\vec{r})_{fict} \right] = \sum_{i=1}^{N} h_i^{\mathrm{KS}} \tag{1.91}$$

The goal is to provide an expression for the kinetic energy of the real system $T[\rho(\vec{r})]$ as a function of the kinetic energy of the fictitious system $T_{fict}[\rho(\vec{r})]$. The difference in kinetic energy between the real and fictitious systems, denoted as ΔT, is given by the relation:

$$\Delta T[\rho(\vec{r})] = T[\rho(\vec{r})] - T_{fict}[\rho(\vec{r})] \tag{1.92}$$

Similarly, the difference between the potential energy of the real system and the Coulomb repulsion energy between two point charge distributions, ΔV, is expressed as:

$$\Delta V[\rho(\vec{r})] = V_{ee}[\rho(\vec{r})] - \frac{1}{2}\iint \frac{\rho(\vec{r}_1)\rho(\vec{r}_2)}{\vec{r}_{12}} d\vec{r}_1\vec{r}_2 \tag{1.93}$$

The density functional $E[\rho(\vec{r})]$ can then be expanded as a sum:

$$E[\rho(\vec{r})] = T_{fict}[\rho(\vec{r})] + E_H[\rho(\vec{r})] + V_{ne}[\rho(\vec{r})] + E_{xc}[\rho(\vec{r})] \tag{1.94}$$

where:

- $T_{fict}[\rho(\vec{r})]$ is the kinetic energy of the fictitious system;
- $E_H[\rho(\vec{r})]$ is the classical Coulomb interaction between electrons (Hartree term), with:

$$E_H[\rho(\vec{r})] = \frac{1}{2}\iint \frac{\rho(\vec{r}_1)\rho(\vec{r}_2)}{\vec{r}_{12}} d\vec{r}_1\vec{r}_2 \tag{1.95}$$

- $V_{ne}[\rho(\vec{r})]$ is an external potential acting on the particles such as:

$$V_{ne}[\rho(\vec{r})] = \int \rho(\vec{r}) v_{ext}[\rho(\vec{r})] d\vec{r} \tag{1.96}$$

- $E_{xc}[\rho(\vec{r})]$ is the exchange-correlation functional, with:

$$E_{xc}[\rho(\vec{r})] = \Delta T[\rho(\vec{r})] - \Delta V[\rho(\vec{r})] \tag{1.97}$$

The exchange-correlation functional $E_{xc}[\rho(\vec{r})]$ accounts for the many-body effects that are not described in the other terms. This term contains all the differences between the fictitious system and the real system. Equation (1.94) takes on a new form after summing the last three terms:

$$E[\rho(\vec{r})] = T_{fict}[\rho(\vec{r})] + V_{eff}[\rho(\vec{r})] \tag{1.98}$$

with:

$$V_{eff}[\rho(\vec{r})] = \frac{1}{2}\iint \frac{\rho(\vec{r}_1)\rho(\vec{r}_2)}{\vec{r}_{12}} d\vec{r}_1\vec{r}_2 + \int \rho(\vec{r}) v_{ext}[\rho(\vec{r})] d\vec{r} + E_{xc}[\rho(\vec{r})] \quad (1.99)$$

The method used to solve the Kohn-Sham equations is an iterative process, involving the variable *k* defining the number of successive self-consistent field (SCF) cycles. The initial density $\rho(\vec{r})_{(k=1)}$ is used to determine $V_{eff(k=1)}$. This potential is then introduced into the "*n*" one-electron Schrödinger equations to obtain the ψ_i^{KS}.

$$\hat{\mathcal{H}}^{\mathrm{KS}}\psi_i^{\mathrm{KS}}(\vec{r}) = \left[\frac{-\hbar^2}{2m}\nabla^2 + V_{eff}(\vec{r})\right]\psi_i^{\mathrm{KS}}(\vec{r}) = \varepsilon_i^{\mathrm{KS}}\psi_i^{\mathrm{KS}}(\vec{r}) \quad (1.100)$$

This last equation indicates how to obtain the density from the *n* one-electron wave functions and defines a new density $\rho(\vec{r})_{(k+1)}$:

$$\rho(\vec{r})_{(k+1)} = \sum_{i=1}^{N} |\psi_i^{\mathrm{KS}}(\vec{r})|^2 \quad (1.101)$$

The process is repeated until the density and energy, ε_i, converge, meaning that the eigenfunctions $\psi_i^{\mathrm{KS}}(\vec{r})$ and eigenvalues ε_i are practically unchanged compared to the previous cycle $(k-1)$.

Following the Kohn and Sham scheme, the challenge in DFT lies in finding a suitable approximation for the exchange-correlation energy. There are several approximations for this exchange-correlation potential, and some of them are presented in the following paragraphs.

iv. Exchange-correlation functionals

- **Local Density Approximation (LDA)**

In this approximation, the electron density is treated locally as a uniform electron gas. The slow variation of $\rho(\vec{r})$ in the system allows for a functional that depends on the local value of the density:

$$E_{xc}^{\mathrm{LDA}}[\rho] = \int \rho(\vec{r})\varepsilon_{xc}[\rho(\vec{r})] d^3\vec{r} \quad (1.102)$$

where ε_{xc} is the exchange and correlation density per electron of an electron gas with density $\rho(\vec{r})$. Therefore, we can write:

$$V_{xc}^{\mathrm{LDA}}(\vec{r}) = \frac{\delta E_{xc}^{\mathrm{LDA}}}{\delta \rho(\vec{r})} = \varepsilon_{xc} + \rho(\vec{r}) \frac{d\varepsilon_{xc}}{d\rho(\vec{r})} \quad (1.103)$$

The exchange-correlation functional decomposes into an exchange term ε_x and a correlation term ε_c. In other words, the exchange-correlation energy can be expanded as a sum of small volume elements dr with a constant environment.

$$E_{xc}^{\mathrm{LDA}}[\rho] = \int \rho(\vec{r}) \varepsilon_x[\rho(\vec{r})] d^3\vec{r} + \int \rho(\vec{r}) \varepsilon_c[\rho(\vec{r})] d^3\vec{r} \quad (1.104)$$

In the case of systems with unpaired electrons, it is necessary to consider spins. For this purpose, the Local Spin Density Approximation (LSDA) is employed. The Kohn-Sham equations take on their polarized form:

$$E_{xc}^{\mathrm{LSDA}}[\rho] = \int (\rho^{\uparrow}(\vec{r}) + \rho^{\downarrow}(\vec{r})) \varepsilon_x\left[\rho^{\uparrow}(\vec{r}), \rho^{\downarrow}(\vec{r})\right] d\vec{r} \quad (1.105)$$

with $\uparrow = spin\ up$ and $\downarrow = spin\ down$.

- **The Generalized Gradient Approximation (GGA)**

To go beyond the LDA and LSDA and account for the non-homogeneity of the actual charge density, the gradient of the charge density $\nabla\rho(\vec{r})$ is introduced into the calculation of the exchange-correlation energy:

$$E_{xc}^{\mathrm{GGA}} = \int \rho(\vec{r}) f_{xc}[\rho(\vec{r}), \nabla\rho(\vec{r})] d^3\vec{r} \quad (1.106)$$

Several exchange-correlation functional, f_{xc}, have been developed. In this manuscript, we used the PBE functional proposed by Perdew, Burke, and Ernzerhof in 1996,[82] commonly used for solids.

I.4.1.4. Modeling periodic systems

i. Plane wave basis

- **Periodic system and Brillouin zone**

In crystalline solids, the total number of electrons is very large. However, the existence of translation symmetry allows for the consideration of the unit cell using periodic boundary conditions (**Figure 1.35**), known as the Born-von Karman cyclic conditions. These conditions enable the quantification of wave

vectors $\vec{k}$ in reciprocal space and introduce the concept of density of states. Boundary effects are thus eliminated, and the electrons are confined within a constant potential.

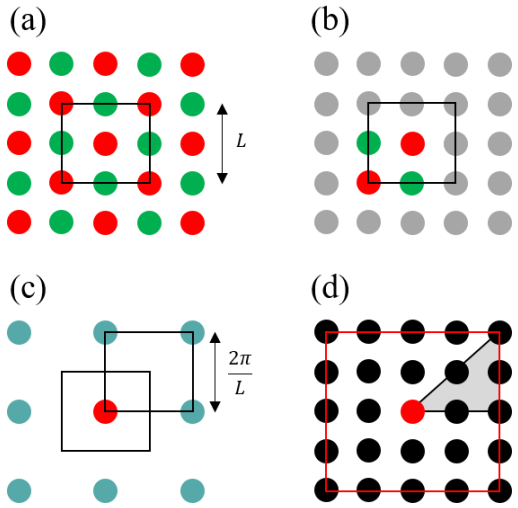


Figure 1.35. (a) Unit cell (black rectangle). (b) Atoms considered in the modeling (red and green). (c) Reciprocal lattice with the origin (gamma point) in red. (d) 1st Brillouin zone divided by a uniform k-point mesh with only the points in the gray triangle modeled (adapted from ref.[83]).

In solving the single-electron Schrödinger equation, the symmetry elements of the space group are considered to simplify the search for eigenvectors and eigenvalues. However, while the charge density has the periodicity of the lattice $\rho(\vec{r}+\vec{G}) = \rho(\vec{r})$, regardless of the lattice vector $\vec{G}$, the wave function must be handled in a precise manner.

For a given system, the Bloch's theorem demonstrates that the wave function is the product of a plane wave with a function that has the periodicity of the crystal:

$$\psi_{n,\vec{k}}(\vec{r}) = u_{n,\vec{k}}(\vec{r})e^{i\vec{k}\vec{r}} = \frac{1}{V}\sum_{\vec{G}} c_n(\vec{k}+\vec{G})e^{i(\vec{k}+\vec{G})\vec{r}} \qquad (1.107)$$

with c_n being the Fourier coefficient, and $u_{n,\vec{k}}(\vec{r})$ a periodic function with the periodicity of the crystal, where n is the band index and $\vec{k}$ is a reciprocal vector of the first Brillouin zone. The single-electron Schrödinger equation becomes:

$$\left[-\frac{\hbar^2}{2m}\nabla^2 + V_{eff}(\vec{r})\right]\psi_i^{(k)}(\vec{r}) = \varepsilon_i^{(k)}\psi_i^{(k)}(\vec{r}) \qquad (1.108)$$

The electronic charge density is written as a double summation over all occupied states $(n, \vec{k})$ and is expanded in terms of the plane wave basis vectors $\vec{G}$.

$$\rho(\vec{r}) = \sum_{\vec{G},\vec{G}'} \sum_{n,\vec{k}} c_{n,(\vec{k}+\vec{G})}\, c^{*}_{n,(\vec{k}+\vec{G}')} e^{i(\vec{G}-\vec{G}')\vec{r}} \tag{1.109}$$

For large values of $|\vec{k}+\vec{G}|$, the Fourier coefficients $c_{n,(\vec{k}+\vec{G})}$ become small, so it is possible to sum over a finite number of $\vec{G}$ vectors. This summation is limited to a basis set of reciprocal space vectors within a sphere with a radius defined by the cutoff energy E_{cut}:

$$\frac{\hbar^2|\vec{k}+\vec{G}|}{2m} \leq E_{cut} \tag{1.110}$$

The quality of a calculation is linked to this parameter. As the value of the cutoff energy increases, the precision of the calculations improves, and the physical parameters converge. However, increasing E_{cut} often leads to an increase in the number of plane waves, and thus, in the calculation time.

- **Sampling of the Brillouin zone**

The first Brillouin zone corresponds to the primitive lattice in reciprocal space. It is reduced to an irreducible Brillouin zone (gray triangle in **Figure 1.35 (d)**) by applying symmetry operations. This zone is then sampled by a certain number of k-points.

Several methods have been proposed to choose these k-points, including the Monkhorst-Pack one[84] used in this manuscript. In this method, a $k_1 \times k_2 \times k_3$ sampling in the three directions of the Brillouin zone space is performed, with equal increment between k-points.

In summary, in a plane wave electronic calculation, the number of k-points and the cutoff energy are the most important parameters. In this manuscript, all calculations were performed with an increment between k-points lower than 0.04 $Å^{-1}$ and a cutoff energy of 550 eV.

ii. Pseudopotential approach

In solid materials, physicochemical properties primarily depend on valence electrons. Core electrons located near the nucleus are minimally influenced by the environment. A first approximation is to treat these core electrons as frozen. However, this approximation remains challenging to handle in a plane wave basis because valence wave functions oscillate rapidly in the region occupied by core electrons.

In the pseudopotential approach, beyond a cutoff radius r_c, the Coulomb potential (referred to as all-electron, AE) from the {nucleus + electrons} system is replaced by a pseudopotential acting on a set of

pseudo-wave functions ({[nucleus + core electrons] + valence electrons} = {"*ion*" + valence electrons}), rather than on the true valence wave functions (**Figure 1.36**). Beyond r_c, the AE potential and the pseudopotential must be identical.[85] The pseudo-wave functions, solutions of the Schrödinger equation with the pseudopotential, should not have radial nodes in the core region and must be continuous at the cutoff radius, along with their first and second derivatives.

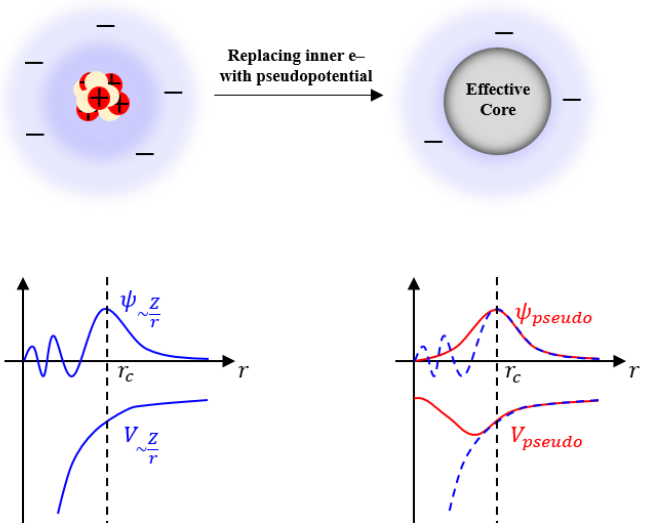


Figure 1.36. Illustration of the pseudopotential method. V and ψ are the actual potential and wave function, while V_{pseudo} and ψ_{pseudo} are the pseudopotential and pseudo-wave function, respectively.

I.4.2. First principle calculations of NMR parameters

In the previous section, we provided a brief description of some methods and approximations used to determine the electronic structure of periodic systems. This section presents the methods used to calculate NMR parameters. The magnetic shielding tensor is a parameter that depends on excited states, whereas the EFG tensor depends solely on the system's ground state, making the calculation simpler. The magnetic shielding tensors, σ, were calculated using the GIPAW approach,[69,70] implemented CASTEP[71,72] and VASP.[73,74] In the case of quadrupolar interactions, the EFG tensors, *V*, are calculated using the PAW approach[67,68] implemented in the same codes.

I.4.2.1. The Projector Augmented Wave (PAW) approach

In 1990, Blöchl introduced the PAW method,[67,68] which allows for the reconstruction of all-electron wave functions from calculations performed with pseudopotentials. The basic idea of this method is the introduction of a linear transformation operator, T, whose action on the pseudo-wave function, $|\tilde{\psi}\rangle$, also known as the pseudopotential function, allows for the reconstruction of the all-electron wave function, $|\psi\rangle$:

$$T|\tilde{\psi}\rangle = |\psi\rangle \tag{1.111}$$

T is constructed from partial wave functions $|\phi_{R,n}\rangle$ and $|\tilde{\phi}_{R,n}\rangle$, which are radial functions with angular momentum n. It is given by:

$$T = 1 + \sum_{R,n} \left[|\phi_{R,n}\rangle - |\tilde{\phi}_{R,n}\rangle\right]\langle\beta_{R,n}| \tag{1.112}$$

where $\langle\beta_{R,n}|$ are local projection functions.

The pseudopotential is constructed based on the all-electron wave function. In other words, it corresponds to the wave function of the isolated atom and not the atom in its chemical environment.

The total charge density obtained from the PAW method can be expressed in the following form:

$$\rho(r) = \rho_c(r) + \tilde{\rho}_v(r) + \rho_\Omega(r) \tag{1.113}$$

where $\rho_c(r)$ is the core charge density, $\tilde{\rho}_v(r)$ is the pseudo-valence electron density, and $\rho_\Omega(r)$ is the correction arising from the reconstruction of valence wave functions within the core region.

Using the all-electron potential obtained through the PAW method, Profeta *et al.*[86] derived the expression for the local EFG as follows:

$$G_{ij}(r) = \frac{\partial E_i(r)}{\partial r_j} - \frac{1}{3}\delta_{ij}\sum_k \frac{\partial E_k(r)}{\partial r_k} \tag{1.114}$$

The local electric field $E_i(r)$ can be calculated from the electron density $\rho(r)$ as follows:

$$E_i(r) = \int \frac{\rho(r')}{|r-r'|^3}(r_i - r'_i)d^3r \tag{1.115}$$

Hence, the local EFG can be expressed as:

$$G_{ij}(r) = \int \frac{\rho(r')}{|r-r'|^3}\left[\delta_{ij} - 3\frac{(r_i - r'_i)(r_j - r'_j)}{|r-r'|^2}\right]d^3r' \tag{1.116}$$

According to equations (1.113) and (1.116), EFG is then given by the following expression:

$$G_{ij}(r) = G_{ij}^c(r) + \tilde{G}_{ij}^v(r) + G_{ij}^{\Omega}(r) \tag{1.117}$$

I.4.2.2. The Gauge Including Projector Augmented Wave (GIPAW) approach

i. Electron current density and gauge problem in a periodic system

When a sample is placed in a uniform external magnetic field, B_0, electronic currents flow throughout the material. In the case of diamagnetic insulating materials, only the orbital motion of electrons contributes to this current. The response of the electrons to the external magnetic field, $B_0(r)$, can be represented by an induced electronic current density, $j(r)$, associated with an operator, $J(r)$.[87] The induced magnetic field, $B_{ind}(r)$, is given by the law of Biot-Savart:

$$B_{ind}(r) = \frac{\mu_0}{4\pi}\int d^3r' j(r')\frac{r-r'}{|r-r'|^3} \tag{1.118}$$

The magnetic shielding tensor is defined as the ratio between this induced field and the applied external field:

$$B_{ind}(r) = -\sigma(r)B_{ext} \tag{1.119}$$

Calculating the magnetic shielding tensor involves computing the induced electronic current. Generally, perturbation methods are used. Since the induced magnetic fields are weak, we can calculate the induced current within the framework of perturbation theory with:[87]

$$j^{(1)}(r') = 2\sum_s \left[\left\langle \psi_s^{(0)} \middle| J^{\mathrm{p}}(r') \middle| \psi_s^{(1)} \right\rangle + \left\langle \psi_s^{(1)} \middle| J^{\mathrm{p}}(r') \middle| \psi_s^{(1)} \right\rangle\right] + 2\sum_s \left\langle \psi_s^{(0)} \middle| J^{\mathrm{d}}(r') \middle| \psi_s^{(1)} \right\rangle \quad (1.120)$$

where the factor 2 accounts for spin degeneracy and the current operator $J(r')$ has been expanded as a sum of a paramagnetic and diamagnetic terms:

$$J(r') = J^{\mathrm{p}}(r') + J^{\mathrm{d}}(r') \quad (1.121)$$

$$J^{\mathrm{p}}(r') = -\frac{e^2}{2m_e}\mathrm{p}|r'\rangle\langle r'| + |r'\rangle\langle r'|\mathrm{p} \quad (1.122)$$

$$J^{\mathrm{d}}(r') = \frac{e^2}{2m_e}A(r')|r'\rangle\langle r'| \quad (1.123)$$

with $\mathrm{p}|r'\rangle\langle r'| + |r'\rangle\langle r'|\mathrm{p}$ the anticommutator of the momentum, p, and $|r'\rangle\langle r'|$ the projection operators. $A(r')$ is the vector potential related to the magnetic field B_0 by:

$$B_0 = \nabla \wedge A(r') \quad (1.124)$$

$$A(r') = \frac{1}{2}B_0 \times (r' - r'_0) \quad (1.125)$$

with r'_0 being the gauge origin. In classical physics, the momentum of a charged particle in a uniform magnetic field is not solely determined by its momentum. It involves a vector potential, $A(r')$, related to the magnetic field, which is not uniquely defined because the value of the magnetic field, B_0, remains unchanged under the transformation:

$$A(r') \rightarrow A(r') + \nabla f_{ind} \quad (1.126)$$

where f represents an arbitrary function. This is the gauge invariance problem. If the magnetic field is invariant whatever the choice of gauge, the same should hold for any observable. The GIPAW method makes this possible for the calculation of magnetic shielding tensors in periodic systems.

ii. GIPAW

It has been proven that in the PAW approach, and in the presence of a uniform magnetic field, the eigenvectors are not translationally invariant. In 2001, the GIPAW method was proposed as a solution by Pickard and Mauri[69,70] to calculate the "*all-electron*" response to a uniform magnetic field, using a transformation operator, T_B, that depends on the magnetic field, B_0. This operator is written as follows:

$$T_B = 1 + \sum_{R,n} e^{\frac{ier(R\times B)}{2h}} \left[|\tilde{\phi}_{R,n}\rangle - |\phi_{R,n}\rangle \right] \langle \beta_{R,n}| e^{\frac{-ier(R\times B)}{2h}} \quad (1.127)$$

It allows for the recovery of the all-electron wave functions, $|\psi\rangle$, from the pseudo-wave function, $|\tilde{\psi}\rangle$.

In CASTEP, the GIPAW method has been developed for so-called norm-conserving pseudopotentials (wherein the charge obtained by the pseudo-functions in the core region is the same as that given by the all-electron wave functions) and for Vanderbilt ultra-soft pseudopotentials (USPP).[88] As for VASP, this method has been developed for the so-called PAW potentials. As we will discuss later in **Chapter V**, PAW potentials can often provide greater accuracy compared to USPP.

I.4.3. Geometric relaxation

As discussed at the end of Section I.3, the geometric relaxation of experimental structures (ES) is a particularly necessary procedure when dealing with ordered/disordered oxyfluorides. The available algorithms for geometric relaxation involve minimizing residual forces acting on atoms. In this manuscript, two types of optimizations were performed on the studied oxyfluorides: (i) relaxation of atomic positions only (Atomic Position Optimization – APO), (ii) simultaneous relaxation of atomic positions and cell parameters (Full Optimization – FO). NMR parameters are highly sensitive to even slight variations in the structure. In most cases, structure relaxation (APO or FO) helps achieve a better agreement between calculated and experimental NMR parameters.

Throughout the course of this thesis, we employed the GGA with the PBE functional for DFT optimizations. In the case of fully optimized structures, this approximation is known for its tendency to overestimate or underestimate interatomic distances, cell parameters, and volume. To address this issue, there are two possibilities. The first one involves re-scaling the cell/supercell volume to its initial value while retaining the atomic positions from the final FO structure. The second approach entails applying semi-empirical dispersion corrections to DFT, namely DFT-D(2,3,4). These corrections are particularly effective in systems characterized by weak interactions, such as van der Waals (vdW) interactions.

Geometry relaxations were carried out using the Broyden-Fletcher-Goldfarb-Shanno (BFGS) method[89] with CASTEP[69,70] and the Hellmann-Feynman method with VASP.[73,74]

I.4.3.1. Semi-empirical dispersion correction to conventional DFT

Due to intrinsic limitations, the semi-local and hybrid exchange-correlation functionals fall short in accurately characterizing vdW interactions arising from dynamic correlations among fluctuating charge distributions, commonly referred to as London dispersion forces. To address this challenge and enhance the reliability of results for vdW systems, an alternative approach is employed by introducing an additional dispersion correction term, denoted as E_{disp}, to the conventional Kohn-Sham DFT (KS-DFT) total energy $E_{\mathrm{tot}}^{\mathrm{KS-DFT}}$:

$$E_{tot}^{\mathrm{KS-DFT}-disp} = E_{\mathrm{tot}}^{\mathrm{KS-DFT}} + E_{disp} \tag{1.128}$$

E_{disp} can be computed using various approximations, including:

- DFT-D2 method of Grimme[90];
- DFT-D3 method of Grimme *et al.*[91] with zero-damping function;
- DFT-D3 method of Becke-Johnson[92] damping function;
- DFT-D4 method,[93] which the extension of the D3 dispersion coefficient model;
- Tkatchenko-Scheffler method[94];
- Tkatchenko-Scheffler method with iterative Hirshfeld partitioning[95];
- Many-body dispersion energy method[96,97];
- Many-body dispersion energy with fractionally ionic model for polarizability method[98];
- dDsC dispersion correction method[99,100];
- DFT-ulg method[101].

In this manuscript, DFT-D3, which is included in VASP,[73,74] was used for oxyfluorides presenting vdW interactions, namely MOF_3 and $MOF_{3-x}(OH)_x$ (M = Nb, Ta) (**Chapter III**).

I.4.3.2. The DFT-D3(zero) method

In the DFT-D3 method of Grimme *et al.*[91] the vdW-dispersion energy-correction is expressed as follows:

$$E_{disp} = -\frac{1}{2}\sum_{i=1}^{N_{at}}\sum_{j=1}^{N_{at}}\sum_{\mathrm{L}}{}'\left(f_{d,6}(r_{ij,\mathrm{L}})\frac{C_{6ij}}{r_{ij,\mathrm{L}}^{6}} + f_{d,8}(r_{ij,\mathrm{L}})\frac{C_{8ij}}{r_{ij,\mathrm{L}}^{8}}\right) \quad (1.129)$$

In contrast to the DFT-D2 method, the dispersion coefficients C_{6ij} in the DFT-D3 method are influenced by the local geometry, specifically the coordination number around atoms i and j. In the zero-damping variant of the DFT-D3 method, denoted as DFT-D3(zero), the damping function is described as follows:

$$f_{d,n}(r_{ij,\mathrm{L}}) = \frac{s_n}{1 + 6\left(\frac{r_{ij}}{s_{R,n}R_{0ij}}\right)^{-\alpha_n}} \quad (1.130)$$

Here, $R_{0ij} = \sqrt{\frac{C_{8ij}}{C_{6ij}}}$, with fixed values assigned to the parameters α_6, α_8, $s_{R,8}$ and s_6, set at 14, 16, 1, and 1, respectively. On the other hand, the values of s_8 and $s_{R,6}$ are adjustable and contingent upon the choice of the exchange-correlation functional.

Alternatively, the Becke-Johnson (BJ) damping approach can be used in the DFT-D3 method:[92]

$$f_{d,n}(r_{ij,\mathrm{L}}) = \frac{s_n r_{ij}^n}{r_{ij}^n + \left(a_1 R_{0ij} + a_2\right)^n} \tag{1.131}$$

where $s_n = 1$ and a_1, a_2 and s_8 are adjustable parameters.

I.5. Conclusion

In this chapter, we have presented a comprehensive description of the theoretical framework that underpins our thesis approach.

The initial section provided fundamentals of the core principles governing the major NMR interactions in solid materials such as chemical shift interaction, dipole-dipole coupling, quadrupolar interaction, and *J*-coupling. Additionally, we elucidated the experimental intricacies and sequences used for oxyfluorides.

The subsequent section delved into the fundamental principles characterizing ordered and disordered crystals, expounding upon the algorithm of the "*supercell*" program. Furthermore, we described in-depth the criteria used in the selection of models for subsequent testing via first principle calculations. These criteria encompassed bond valence sum, Coulomb energy, correlated disorder, and statistical analyses.

The last section elucidated the main concepts underlying first principle calculations, outlining the PAW and GIPAW approaches that are used calculating the magnetic shielding and electric field gradient tensors, respectively. Additionally, we briefly mentioned the zero-damping semi-empirical dispersion correction to DFT, known as DFT-D3, which serves as a crucial tool for addressing weak interactions, such as van der Waals interactions.

I.6. References

(1) Levitt, M. H. *Spin Dynamics: Basics of Nuclear Magnetic Resonance*; John Wiley & Sons, 2013.

(2) Pyykkö, P. Year-2008 Nuclear Quadrupole Moments. *Molecular Physics* **2008**, *106* (16–18), 1965–1974. https://doi.org/10.1080/00268970802018367.

(3) Harris, R. K.; Becker, E. D.; Cabral De Menezes, S. M.; Goodfellow, R.; Granger, P. NMR Nomenclature. Nuclear Spin Properties and Conventions for Chemical Shifts(IUPAC Recommendations 2001). *Pure and Applied Chemistry* **2001**, *73* (11), 1795–1818. https://doi.org/10.1351/pac200173111795.

(4) Haeberlen, U. In Advances in Magnetic Resonance. *Suppl. 1; J. S. Waugh, Ed.; Academic Press* **1976**.

(5) Duer, M. J. *Introduction to Solid-State NMR Spectroscopy | Wiley*. Wiley.com. https://www.wiley.com/en-us/Introduction+to+Solid+State+NMR+Spectroscopy-p-9781405109147 (accessed 2023-09-14).

(6) MacKenzie, K. J. D.; Smith, M. E. *Multinuclear Solid-State Nuclear Magnetic Resonance of Inorganic Materials*; Elsevier, 2002.

(7) Brown, S. P.; Pérez-Torralba, M.; Sanz, D.; Claramunt, R. M.; Emsley, L. Determining Hydrogen-Bond Strengths in the Solid State by NMR: The Quantitative Measurement of Homonuclear J Couplings. *Chem. Commun.* **2002**, No. 17, 1852–1853. https://doi.org/10.1039/B205324A.

(8) Pham, T. N.; Griffin, J. M.; Masiero, S.; Lena, S.; Gottarelli, G.; Hodgkinson, P.; Filip, C.; Brown, S. P. Quantifying Hydrogen-Bonding Strength: The Measurement of $^{2h}J_{NN}$ Couplings in Self-Assembled Guanosines by Solid-State ^{15}N Spin-Echo MAS NMR. *Phys. Chem. Chem. Phys.* **2007**, *9* (26), 3416. https://doi.org/10.1039/b703513f.

(9) Griffin, J. M.; Yates, J. R.; Berry, A. J.; Wimperis, S.; Ashbrook, S. E. High-Resolution ^{19}F MAS NMR Spectroscopy: Structural Disorder and Unusual *J* Couplings in a Fluorinated Hydroxy-Silicate. *J. Am. Chem. Soc.* **2010**, *132* (44), 15651–15660. https://doi.org/10.1021/ja105347q.

(10) Mehring, M. *Principles of High Resolution NMR in Solids*; Springer Science & Business Media, 2012.

(11) Man, P. P. *Quadrupolar Interactions*; Wiley Chichester, 2012.

(12) Spiess, H. W. NMR Basic Principles and Progress. *Diehl, P., Fluck, E., Kosfeld, R., Eds* **1978**, 55–214.

(13) Narita, K.; Umeda, J.; Kusumoto, H. Nuclear Magnetic Resonance Powder Patterns of the Second-Order Nuclear Quadrupole Interaction in Solids with Asymmetric Field Gradient. *The Journal of Chemical Physics* **1966**, *44* (7), 2719–2723. https://doi.org/10.1063/1.1727118.

(14) Freude, D.; Haase, J. NMR Basic Principles and Progress. *Diehl, P., Fluck, E., Guenther, H., Kosfeld, R., Seelig, J., Eds* **1993**, 1–90.

(15) Andrew, E. R.; Bradbury, A.; Eades, R. G. Removal of Dipolar Broadening of Nuclear Magnetic Resonance Spectra of Solids by Specimen Rotation. *Nature* **1959**, *183* (4678), 1802–1803. https://doi.org/10.1038/1831802a0.

(16) Andrew, E. R.; Richards, R. E.; Packer, K. J. Magic Angle Spinning in Solid State n.m.r. Spectroscopy. *Philosophical Transactions of the Royal Society of London. Series A, Mathematical and Physical Sciences* **1997**, *299* (1452), 505–520. https://doi.org/10.1098/rsta.1981.0032.

(17) Lowe, I. J. Free Induction Decays of Rotating Solids. *Phys. Rev. Lett.* **1959**, *2* (7), 285–287. https://doi.org/10.1103/PhysRevLett.2.285.

(18) Hahn, E. L. Spin Echoes. *Phys. Rev.* **1950**, *80* (4), 580–594. https://doi.org/10.1103/PhysRev.80.580.

(19) Reich, H. J.; Jautelat, M.; Messe, M. T.; Weigert, F. J.; Roberts, J. D. Nuclear Magnetic Resonance Spectroscopy. Carbon-13 Spectra of Steroids. *J. Am. Chem. Soc.* **1969**, *91* (26), 7445–7454. https://doi.org/10.1021/ja01054a037.

(20) Ernst, R. R.; Bodenhausen, G.; Wokaun, A.; Redfield, A. G. Principles of Nuclear Magnetic Resonance in One and Two Dimensions. *Physics Today* **1989**, *42* (7), 75–76. https://doi.org/10.1063/1.2811094.

(21) Bennett, A. E.; Rienstra, C. M.; Auger, M.; Lakshmi, K. V.; Griffin, R. G. Heteronuclear Decoupling in Rotating Solids. *The Journal of Chemical Physics* **1995**, *103* (16), 6951–6958. https://doi.org/10.1063/1.470372.

(22) Fung, B. M.; Khitrin, A. K.; Ermolaev, K. An Improved Broadband Decoupling Sequence for Liquid Crystals and Solids. *Journal of Magnetic Resonance* **2000**, *142* (1), 97–101. https://doi.org/10.1006/jmre.1999.1896.

(23) Detken, A.; Hardy, E. H.; Ernst, M.; Meier, B. H. Simple and Efficient Decoupling in Magic-Angle Spinning Solid-State NMR: The XiX Scheme. *Chemical Physics Letters* **2002**, *356* (3), 298–304. https://doi.org/10.1016/S0009-2614(02)00335-4.

(24) Carr, H. Y.; Purcell, E. M. Effects of Diffusion on Free Precession in Nuclear Magnetic Resonance Experiments. *Phys. Rev.* **1954**, *94* (3), 630–638. https://doi.org/10.1103/PhysRev.94.630.

(25) Meiboom, S.; Gill, D. Modified Spin-Echo Method for Measuring Nuclear Relaxation Times. *Review of Scientific Instruments* **1958**, *29* (8), 688–691. https://doi.org/10.1063/1.1716296.

(26) Solomon, I. Multiple Echoes in Solids. *Phys. Rev.* **1958**, *110* (1), 61–65. https://doi.org/10.1103/PhysRev.110.61.

(27) Weisman, I. D.; Bennett, L. H. Quadrupolar Echoes in Solids. *Phys. Rev.* **1969**, *181* (3), 1341–1350. https://doi.org/10.1103/PhysRev.181.1341.

(28) Davis, J. H.; Jeffrey, K. R.; Bloom, M.; Valic, M. I.; Higgs, T. P. Quadrupolar Echo Deuteron Magnetic Resonance Spectroscopy in Ordered Hydrocarbon Chains. *Chemical Physics Letters* **1976**, *42* (2), 390–394. https://doi.org/10.1016/0009-2614(76)80392-2.

(29) Bloom, M.; Sternin, E. Transverse Nuclear Spin Relaxation in Phospholipid Bilayer Membranes. *Biochemistry* **1987**, *26* (8), 2101–2105. https://doi.org/10.1021/bi00382a007.

(30) Cheng, J. T.; Ellis, P. D. Adsorption of Rubidium(1+) to .Gamma.-Alumina as Followed by Solid-State Rubidium-87 NMR Spectroscopy. *J. Phys. Chem.* **1989**, *93* (6), 2549–2555. https://doi.org/10.1021/j100343a061.

(31) Hamaed, H.; Ye, E.; Udachin, K.; Schurko, R. W. Solid-State ^{137}Ba NMR Spectroscopy: An Experimental and Theoretical Investigation of ^{137}Ba Electric Field Gradient Tensors and Their

Relation to Structure and Symmetry. *J. Phys. Chem. B* **2010**, *114* (18), 6014–6022. https://doi.org/10.1021/jp102026m.

(32) Hamaed, H.; Laschuk, M. W.; Terskikh, V. V.; Schurko, R. W. Application of Solid-State ^{209}Bi NMR to the Structural Characterization of Bismuth-Containing Materials. *J. Am. Chem. Soc.* **2009**, *131* (23), 8271–8279. https://doi.org/10.1021/ja901347k.

(33) O'Dell, L. A.; Schurko, R. W. Fast and Simple Acquisition of Solid-State ^{14}N NMR Spectra with Signal Enhancement via Population Transfer. *J. Am. Chem. Soc.* **2009**, *131* (19), 6658–6659. https://doi.org/10.1021/ja901278q.

(34) Brown, S. P.; Wimperis, S. Inhomogeneous Broadening of Two-Dimensional NMR Lineshapes. *Chemical Physics Letters* **1995**, *237* (5–6), 509–515. https://doi.org/10.1016/0009-2614(95)00330-7.

(35) Chen, K. A Practical Review of NMR Lineshapes for Spin-1/2 and Quadrupolar Nuclei in Disordered Materials. *IJMS* **2020**, *21* (16), 5666. https://doi.org/10.3390/ijms21165666.

(36) Medek, A.; Harwood, J. S.; Frydman, L. Multiple-Quantum Magic-Angle Spinning NMR: A New Method for the Study of Quadrupolar Nuclei in Solids. *J. Am. Chem. Soc.* **1995**, *117* (51), 12779–12787. https://doi.org/10.1021/ja00156a015.

(37) Amoureux, J.-P.; Fernandez, C.; Steuernagel, S. ZFiltering in MQMAS NMR. *Journal of Magnetic Resonance, Series A* **1996**, *123* (1), 116–118. https://doi.org/10.1006/jmra.1996.0221.

(38) Frydman, L.; Harwood, J. S. Isotropic Spectra of Half-Integer Quadrupolar Spins from Bidimensional Magic-Angle Spinning NMR. *J. Am. Chem. Soc.* **1995**, *117* (19), 5367–5368. https://doi.org/10.1021/ja00124a023.

(39) Brown, S. P.; Heyes, S. J.; Wimperis, S. Two-Dimensional MAS Multiple-Quantum NMR of Quadrupolar Nuclei. Removal of Inhomogeneous Second-Order Broadening. *Journal of Magnetic Resonance, Series A* **1996**, *2* (119), 280–284. https://doi.org/10.1006/jmra.1996.0088.

(40) Massiot, D.; Fayon, F.; Capron, M.; King, I.; Le Calvé, S.; Alonso, B.; Durand, J.-O.; Bujoli, B.; Gan, Z.; Hoatson, G. Modelling One- and Two-Dimensional Solid-State NMR Spectra. *Magnetic Resonance in Chemistry* **2002**, *40* (1), 70–76. https://doi.org/10.1002/mrc.984.

(41) Massiot, D.; Hiet, J.; Pellerin, N.; Fayon, F.; Deschamps, M.; Steuernagel, S.; Grandinetti, P. J. Two-Dimensional One Pulse MAS of Half-Integer Quadrupolar Nuclei. *Journal of Magnetic Resonance* **2006**, *181* (2), 310–315. https://doi.org/10.1016/j.jmr.2006.05.007.

(42) Czjzek, G.; Fink, J.; Götz, F.; Schmidt, H.; Coey, J. M. D.; Rebouillat, J.-P.; Liénard, A. Atomic Coordination and the Distribution of Electric Field Gradients in Amorphous Solids. *Phys. Rev. B* **1981**, *23* (6), 2513–2530. https://doi.org/10.1103/PhysRevB.23.2513.

(43) Caër, G. L.; Brand, R. A. General Models for the Distributions of Electric Field Gradients in Disordered Solids. *J. Phys.: Condens. Matter* **1998**, *10* (47), 10715–10774. https://doi.org/10.1088/0953-8984/10/47/020.

(44) d'Espinose De Lacaillerie, J.-B.; Fretigny, C.; Massiot, D. MAS NMR Spectra of Quadrupolar Nuclei in Disordered Solids: The Czjzek Model. *Journal of Magnetic Resonance* **2008**, *192* (2), 244–251. https://doi.org/10.1016/j.jmr.2008.03.001.

(45) Cusack, N. E.; Stein, D. L. *The Physics of Structurally Disordered Matter: An Introduction*. *Physics Today* **1988**, *41* (12), 110–112. https://doi.org/10.1063/1.2811678.

(46) Freer, R. *The Physics and Chemistry of Carbides, Nitrides and Borides*; Springer Science & Business Media, 2012.

(47) Paufler, P. S. R. Elliott. Physics of Amorphous Materials. Longman Group Ltd., London, New York, 1984. Pp X + 386. Price: £ 25.00. ISBN 0–582–44636–8. *Cryst. Res. Technol.* **1985**, *20* (9), 1238–1238. https://doi.org/10.1002/crat.2170200922.

(48) Freysoldt, C.; Grabowski, B.; Hickel, T.; Neugebauer, J.; Kresse, G.; Janotti, A.; Van De Walle, C. G. First-Principles Calculations for Point Defects in Solids. *Rev. Mod. Phys.* **2014**, *86* (1), 253–305. https://doi.org/10.1103/RevModPhys.86.253.

(49) Brown, I. D. *Structure and Bonding in crystals - 1st Edition*. https://shop.elsevier.com/books/structure-and-bonding-in-crystals/nsvrotsky/978-0-12-525102-0 (accessed 2023-09-20).

(50) Brown, I. D.; Altermatt, D. Bond-Valence Parameters Obtained from a Systematic Analysis of the Inorganic Crystal Structure Database. *Acta Crystallogr B Struct Sci* **1985**, *41* (4), 244–247. https://doi.org/10.1107/S0108768185002063.

(51) Brese, N. E.; O'Keeffe, M. Bond-Valence Parameters for Solids. *Acta Crystallogr B Struct Sci* **1991**, *47* (2), 192–197. https://doi.org/10.1107/S0108768190011041.

(52) Wood, R. M.; Palenik, G. J. Bond Valence Sums in Coordination Chemistry. Sodium−Oxygen Complexes. *Inorg. Chem.* **1999**, *38* (17), 3926–3930. https://doi.org/10.1021/ic9903331.

(53) Brown, I. D. Predicting Bond Lengths in Inorganic Crystals. *Acta Crystallogr B Struct Crystallogr Cryst Chem* **1977**, *33* (5), 1305–1310. https://doi.org/10.1107/S0567740877005998.

(54) O'Keeffe, M. A Method Calculating Bond Valences in Crystals. *Acta Crystallogr A Found Crystallogr* **1990**, *46* (2), 138–142. https://doi.org/10.1107/S0108767389011104.

(55) Zunger, A.; Wei, S.-H.; Ferreira, L. G.; Bernard, J. E. Special Quasirandom Structures. *Phys. Rev. Lett.* **1990**, *65* (3), 353–356. https://doi.org/10.1103/PhysRevLett.65.353.

(56) Grau-Crespo, R.; Hamad, S.; Catlow, C. R. A.; Leeuw, N. H. D. Symmetry-Adapted Configurational Modelling of Fractional Site Occupancy in Solids. *J. Phys.: Condens. Matter* **2007**, *19* (25), 256201. https://doi.org/10.1088/0953-8984/19/25/256201.

(57) Rosenbrock, C. W.; Morgan, W. S.; Hart, G. L. W.; Curtarolo, S.; Forcade, R. W. Numerical Algorithm for Pólya Enumeration Theorem. *ACM J. Exp. Algorithmics* **2016**, *21*, 1–17. https://doi.org/10.1145/2955094.

(58) Mustapha, S.; D'Arco, P.; De La Pierre, M.; Noël, Y.; Ferrabone, M.; Dovesi, R. On the Use of Symmetry in Configurational Analysis for the Simulation of Disordered Solids. *J. Phys.: Condens. Matter* **2013**, *25* (10), 105401. https://doi.org/10.1088/0953-8984/25/10/105401.

(59) Okhotnikov, K.; Charpentier, T.; Cadars, S. Supercell Program: A Combinatorial Structure-Generation Approach for the Local-Level Modeling of Atomic Substitutions and Partial Occupancies in Crystals. *J Cheminform* **2016**, *8* (1), 17. https://doi.org/10.1186/s13321-016-0129-3.

(60) Madelung, E. Das Elektrische Feld in Systemen von Regelmäßig Angeordneten Punktladungen. *Phys. Z* **1918**, *19* (524), 32.

(61) Ewald, P. P. Die Berechnung optischer und elektrostatischer Gitterpotentiale. *Ann. Phys.* **1921**, *369* (3), 253–287. https://doi.org/10.1002/andp.19213690304.

(62) Pearson, R. G. *Chemical Hardness*, 1st ed.; Wiley, 1997. https://doi.org/10.1002/3527606173.

(63) Brink, F. J.; Withers, R. L.; Thompson, J. G. An Electron Diffraction and Crystal Chemical Investigation of Oxygen/Fluorine Ordering in Rutile-Type Iron Oxyfluoride, FeOF. *Journal of Solid State Chemistry* **2000**, *155* (2), 359–365. https://doi.org/10.1006/jssc.2000.8925.

(64) Chevrier, V. L.; Hautier, G.; Ong, S. P.; Doe, R. E.; Ceder, G. First-Principles Study of Iron Oxyfluorides and Lithiation of FeOF. *Phys. Rev. B* **2013**, *87* (9), 094118. https://doi.org/10.1103/PhysRevB.87.094118.

(65) Harada, J. K.; Charles, N.; Poeppelmeier, K. R.; Rondinelli, J. M. Heteroanionic Materials by Design: Progress Toward Targeted Properties. *Adv. Mater.* **2019**, *31* (19), 1805295. https://doi.org/10.1002/adma.201805295.

(66) Brink, F. J.; Withers, R. L.; Cordier, S.; Poulain, M. An Electron Diffraction and Bond Valence Sum Investigation of Oxygen/Fluorine Ordering in $Nb_nO_{2n-1}F_{n+2}$, n = 3. *Journal of Solid State Chemistry* **2006**, *179* (2), 341–348. https://doi.org/10.1016/j.jssc.2005.10.014.

(67) Blöchl, P. E. Projector Augmented-Wave Method. *Phys. Rev. B* **1994**, *50* (24), 17953–17979. https://doi.org/10.1103/PhysRevB.50.17953.

(68) Petrilli, H. M.; Blöchl, P. E.; Blaha, P.; Schwarz, K. Electric-Field-Gradient Calculations Using the Projector Augmented Wave Method. *Phys. Rev. B* **1998**, *57* (23), 14690–14697. https://doi.org/10.1103/PhysRevB.57.14690.

(69) Pickard, C. J.; Mauri, F. All-Electron Magnetic Response with Pseudopotentials: NMR Chemical Shifts. *Phys. Rev. B* **2001**, *63* (24), 245101. https://doi.org/10.1103/PhysRevB.63.245101.

(70) Yates, J. R.; Pickard, C. J.; Mauri, F. Calculation of NMR Chemical Shifts for Extended Systems Using Ultrasoft Pseudopotentials. *Phys. Rev. B* **2007**, *76* (2), 024401. https://doi.org/10.1103/PhysRevB.76.024401.

(71) Segall, M. D.; Lindan, P. J. D.; Probert, M. J.; Pickard, C. J.; Hasnip, P. J.; Clark, S. J.; Payne, M. C. First-Principles Simulation: Ideas, Illustrations and the CASTEP Code. *J. Phys.: Condens. Matter* **2002**, *14* (11), 2717–2744. https://doi.org/10.1088/0953-8984/14/11/301.

(72) Clark, S. J.; Segall, M. D.; Pickard, C. J.; Hasnip, P. J.; Probert, M. I. J.; Refson, K.; Payne, M. C. First Principles Methods Using CASTEP. *Zeitschrift für Kristallographie - Crystalline Materials* **2005**, *220* (5–6), 567–570. https://doi.org/10.1524/zkri.220.5.567.65075.

(73) Kresse, G.; Furthmüller, J. Efficiency of Ab-Initio Total Energy Calculations for Metals and Semiconductors Using a Plane-Wave Basis Set. *Computational Materials Science* **1996**, *6* (1), 15–50. https://doi.org/10.1016/0927-0256(96)00008-0.

(74) Kresse, G.; Furthmüller, J. Efficient Iterative Schemes for *Ab Initio* Total-Energy Calculations Using a Plane-Wave Basis Set. *Phys. Rev. B* **1996**, *54* (16), 11169–11186. https://doi.org/10.1103/PhysRevB.54.11169.

(75) Szabo, A.; Ostlund, N. S. *Modern Quantum Chemistry: Introduction to Advanced Electronic Structure Theory*; Courier Corporation, 2012.

(76) Møller, Chr.; Plesset, M. S. Note on an Approximation Treatment for Many-Electron Systems. *Phys. Rev.* **1934**, *46* (7), 618–622. https://doi.org/10.1103/PhysRev.46.618.

(77) Meyer, H.-D.; Manthe, U.; Cederbaum, L. S. The Multi-Configurational Time-Dependent Hartree Approach. *Chemical Physics Letters* **1990**, *165* (1), 73–78. https://doi.org/10.1016/0009-2614(90)87014-I.

(78) Thomas, L. H. The Calculation of Atomic Fields. *Math. Proc. Camb. Phil. Soc.* **1927**, *23* (5), 542–548. https://doi.org/10.1017/S0305004100011683.

(79) Fermi, E. Un Metodo Statistico per La Determinazione Di Alcune Priorieta Dell'atome. *Rend. Accad. Naz. Lincei* **1927**, *6* (602–607), 32.

(80) Hohenberg, P.; Kohn, W. Inhomogeneous Electron Gas. *Phys. Rev.* **1964**, *136* (3B), B864–B871. https://doi.org/10.1103/PhysRev.136.B864.

(81) Kohn, W.; Sham, L. J. Self-Consistent Equations Including Exchange and Correlation Effects. *Phys. Rev.* **1965**, *140* (4A), A1133–A1138. https://doi.org/10.1103/PhysRev.140.A1133.

(82) Perdew, J. P.; Burke, K.; Ernzerhof, M. Generalized Gradient Approximation Made Simple. *Phys. Rev. Lett.* **1996**, *77* (18), 3865–3868. https://doi.org/10.1103/PhysRevLett.77.3865.

(83) Bonhomme, C.; Gervais, C.; Babonneau, F.; Coelho, C.; Pourpoint, F.; Azaïs, T.; Ashbrook, S. E.; Griffin, J. M.; Yates, J. R.; Mauri, F.; Pickard, C. J. First-Principles Calculation of NMR Parameters Using the Gauge Including Projector Augmented Wave Method: A Chemist's Point of View. *Chem. Rev.* **2012**, *112* (11), 5733–5779. https://doi.org/10.1021/cr300108a.

(84) Monkhorst, H. J.; Pack, J. D. Special Points for Brillouin-Zone Integrations. *Phys. Rev. B* **1976**, *13* (12), 5188–5192. https://doi.org/10.1103/PhysRevB.13.5188.

(85) Troullier, N.; Martins, J. L. Efficient Pseudopotentials for Plane-Wave Calculations. *Phys. Rev. B* **1991**, *43* (3), 1993–2006. https://doi.org/10.1103/PhysRevB.43.1993.

(86) Profeta, M.; Benoit, M.; Mauri, F.; Pickard, C. J. First-Principles Calculation of the ^{17}O NMR Parameters in Ca Oxide and Ca Aluminosilicates: The Partially Covalent Nature of the Ca−O Bond, a Challenge for Density Functional Theory. *J. Am. Chem. Soc.* **2004**, *126* (39), 12628–12635. https://doi.org/10.1021/ja0490830.

(87) Yates, J. R.; Pickard, C. J. *Computation of Magnetic Resonance Parameters for Crystalline Systems: Principles*; John Wiley and Sons: Chichester, 2009.

(88) Vanderbilt, D. Soft Self-Consistent Pseudopotentials in a Generalized Eigenvalue Formalism. *Phys. Rev. B* **1990**, *41* (11), 7892–7895. https://doi.org/10.1103/PhysRevB.41.7892.

(89) Pfrommer, B. G.; Côté, M.; Louie, S. G.; Cohen, M. L. Relaxation of Crystals with the Quasi-Newton Method. *Journal of Computational Physics* **1997**, *131* (1), 233–240. https://doi.org/10.1006/jcph.1996.5612.

(90) Grimme, S. Semiempirical GGA-Type Density Functional Constructed with a Long-Range Dispersion Correction. *J. Comput. Chem.* **2006**, *27* (15), 1787–1799. https://doi.org/10.1002/jcc.20495.

(91) Grimme, S.; Antony, J.; Ehrlich, S.; Krieg, H. A Consistent and Accurate *Ab Initio* Parametrization of Density Functional Dispersion Correction (DFT-D) for the 94 Elements H-Pu. *The Journal of Chemical Physics* **2010**, *132* (15), 154104. https://doi.org/10.1063/1.3382344.

(92) Grimme, S.; Ehrlich, S.; Goerigk, L. Effect of the Damping Function in Dispersion Corrected Density Functional Theory. *J. Comput. Chem.* **2011**, *32* (7), 1456–1465. https://doi.org/10.1002/jcc.21759.

(93) Caldeweyher, E.; Bannwarth, C.; Grimme, S. Extension of the D3 Dispersion Coefficient Model. *The Journal of Chemical Physics* **2017**, *147* (3), 034112. https://doi.org/10.1063/1.4993215.

(94) Tkatchenko, A.; Scheffler, M. Accurate Molecular Van Der Waals Interactions from Ground-State Electron Density and Free-Atom Reference Data. *Phys. Rev. Lett.* **2009**, *102* (7), 073005. https://doi.org/10.1103/PhysRevLett.102.073005.

(95) Bultinck, P.; Van Alsenoy, C.; Ayers, P. W.; Carbó-Dorca, R. Critical Analysis and Extension of the Hirshfeld Atoms in Molecules. *The Journal of Chemical Physics* **2007**, *126* (14), 144111. https://doi.org/10.1063/1.2715563.

(96) Tkatchenko, A.; DiStasio, R. A.; Car, R.; Scheffler, M. Accurate and Efficient Method for Many-Body van Der Waals Interactions. *Phys. Rev. Lett.* **2012**, *108* (23), 236402. https://doi.org/10.1103/PhysRevLett.108.236402.

(97) Ambrosetti, A.; Reilly, A. M.; DiStasio, R. A.; Tkatchenko, A. Long-Range Correlation Energy Calculated from Coupled Atomic Response Functions. *The Journal of Chemical Physics* **2014**, *140* (18), 18A508. https://doi.org/10.1063/1.4865104.

(98) Gould, T.; Lebègue, S.; Ángyán, J. G.; Bučko, T. A Fractionally Ionic Approach to Polarizability and van Der Waals Many-Body Dispersion Calculations. *J. Chem. Theory Comput.* **2016**, *12* (12), 5920–5930. https://doi.org/10.1021/acs.jctc.6b00925.

(99) Steinmann, S. N.; Corminboeuf, C. A Generalized-Gradient Approximation Exchange Hole Model for Dispersion Coefficients. *The Journal of Chemical Physics* **2011**, *134* (4), 044117. https://doi.org/10.1063/1.3545985.

(100) Steinmann, S. N.; Corminboeuf, C. Comprehensive Benchmarking of a Density-Dependent Dispersion Correction. *J. Chem. Theory Comput.* **2011**, *7* (11), 3567–3577. https://doi.org/10.1021/ct200602x.

(101) Kim, H.; Choi, J.-M.; Goddard, W. A. Universal Correction of Density Functional Theory to Include London Dispersion (up to Lr, Element 103). *J. Phys. Chem. Lett.* **2012**, *3* (3), 360–363. https://doi.org/10.1021/jz2016395.

Chapter II

Ordered Oxyfluorides

II.1. Introduction

In the preceding chapter, a comprehensive overview of the fundamental principles underlying the multimodal approach was presented. This chapter presents the initial implementation of this approach to investigate ordered $NaMO_2F_2$ (M = Nb, Ta) oxyfluorides. A thorough analysis of the room temperature (RT) structure of these oxyfluorides was conducted using a combination of powder X-ray diffraction (PXRD), ^{19}F, ^{23}Na, and ^{93}Nb solid-state NMR techniques, along with DFT calculations of NMR parameters.

In the context of ordered structures, despite their nearly identical X-ray and neutron scattering factors, differentiation between oxide and fluoride anions is feasible when they occupy distinct crystallographic sites. The BVS method, widely used to assess variations in formal charge and size, effectively facilitates this distinction. Although niobium and tantalum isotopes typically show highly similar cell parameters due to their matching ionic radii values (~0.78 Å for sixfold coordination), the compounds $NaNbO_2F_2$ and $NaTaO_2F_2$ exhibit noticeable dissimilarities in their respective cell parameters. Additionally, an effort to optimize the synthesis conditions of these compounds using thermogravimetric analysis (TGA) and differential thermal analysis (DTA) revealed that $NaNbO_2F_2$ exhibits a very low amplitude endothermic event upon heating, whereas for its tantalum isotype no event was detected. Insights into the differing behaviors of the two compounds were obtained through variable temperature XRPD (VT XRPD) experiments.

Multinuclear solid-state NMR, DFT calculations, and variable temperature PXRD of Nb and Ta isostructural oxyfluoride compounds revealing unexpected different structural features

Ouail Zakary[a,*], Monique Body[a], Franck Fayon[b], Vincent Sarou-Kanian[b],

Gwenaël Corbel[a,*] Christophe Legein[a]

[a] Institut des Molécules et Matériaux du Mans (IMMM) – UMR 6283 CNRS, Le Mans Université, Avenue Olivier Messiaen, 72085 Le Mans Cedex 9, France

[b] CNRS, CEMHTI UPR3079, Université d'Orléans, 45071 Orléans, France

e-mail address of each author:

Ouail.Zakary@univ-lemans.fr; monique.body@univ-lemans.fr; franck.fayon@cnrs-orleans.fr; vincent.sarou-kanian@cnrs-orleans.fr; gwenael.corbel@univ-lemans.fr; christophe.legein@univ-lemans.fr

Corresponding Authors:

Ouail.Zakary@univ-lemans.fr (Ouail Zakary); gwenael.corbel@univ-lemans.fr (Gwenaël Corbel)

Abstract

An in-depth investigation of the structure of $NaNbO_2F_2$ and $NaTaO_2F_2$ oxyfluorides combining powder X-Ray diffraction (PXRD), ^{19}F solid-state NMR (ssNMR), and high-field ^{23}Na and ^{93}Nb ssNMR, and DFT calculations, confirmed that these oxyfluorides are ordered and isotypic. The experimental structure (ES) at RT, derived from Rietveld refinement of the PXRD data, exclusively incorporates *cis*-MO_4F_2 (M = Nb, Ta) heteroleptic octahedra, in which cations are displaced from their ideal centered positions toward oxygen atoms. ES atomic position optimization (APO) was performed and the NMR parameters were calculated for both the APO and ES models, and then compared to the experimental data. The best agreement was obtained for the APO model. Due to the equal values of ionic radii of sixfold coordinated Nb^{5+} and Ta^{5+}, niobium and tantalum isotypes have usually very close cell parameters, however those of $NaNbO_2F_2$ and $NaTaO_2F_2$ differ in unusual proportions. Moreover, when seeking to optimize the synthesis conditions of these compounds using thermal analyses, $NaNbO_2F_2$ appeared to exhibit very low amplitude endothermic event upon heating, whereas its tantalum isotype apparently does not. An extensive analysis of the structural parameters issued from VT PXRD was carried out, revealing that these parameters do not evolve in the same way for the two compounds.

Keywords

HAMs; oxyfluoroniobiates and oxyfluorotantalates; VT PXRD; Multinuclear solid-state NMR; DFT calculations

1. Introduction

Inorganic oxyfluorides are heteroanionic materials (HAMs) containing two anionic species with different characteristics, such as charge, ionic radii, electronegativity, and polarizability, which thus offer opportunities to control and tune the electronic and atomic structure and to develop new materials with targeted functionalities [1,2]. In HAMs, a metal cation is often bonded to two anionic ligands to form a heteroleptic polyhedron acting as the basic-building unit (BBU) of the structure. In recent years, early transition metal (TM) d^0 cation (Ti^{4+}, V^{5+}, Nb^{5+}, Ta^{5+}, Mo^{6+} and W^{6+}) oxyfluorides have been investigated for their properties and applications as nonlinear optical (NLO) [3–6], ferroelectric [7,8], photocatalytic [9,10] and battery [11–13] materials.

The closeness of the ionic radii for oxide and fluoride anions [14] allows them to occupy the same site(s) in a crystal, as for instance in the pyrochlores $RbNb(Ta)_2O_5F$ [15,16]. However, the different anionic characteristics lead to distinct bonding interactions in the heteroleptic polyahedra: M–O bonds are more covalent and thus shorter compared to the more ionic M–F bonds. The differences in bond lengths result in displacements of the M cation towards the oxide ions [3,17,18]. They produce *cis* rather than *trans* configurations for $[MO_2F_4]^{n-}$ and $[MO_4F_2]^{n-}$ octahedra and *fac* rather than *mer* configurations for $[MO_3F_3]^{n-}$ octahedra are favored. These different bond lengths and preferential configurations for early d^0 TM $[MO_xF_{6-x}]^{n-}$ octahedra can lead to structures without anion-site disorder [1], as observed in compounds based on $[MOF_5]^{2-}$ (M = V^{5+}, Nb^{5+}, Ta^{5+} [3,4,17,19–21]), $[MO_2F_4]^{2-}$ (M = Mo^{6+}, W^{6+} [20,22]), $[MoO_3F_3]^{3-}$ [8,23,24], $[NbO_4F_2]^{5-}$ [6] and $[MO_5F]^{5-}$ (M = Mo^{6+}, W^{6+}) [5,25]. Such distorted octahedra, because of their directing properties, anion ordering and greater probability to crystallize in non-centrosymmetric (NCS) space group are of interest for designing new second harmonic generation (SHG) NLO materials [3,26]. Nevertheless, more often than not, the anion-site order is only partial. Between the limits of fully ordered and randomly disordered anions, there are many cases of intermediate anion-site orders with local clustering or extended correlations that may give rise to nonrandom site occupancies in the averaged crystal structure [1,2]. Among oxyfluoroniobiates and oxyfluorotantalates, correlated disorder manifesting as O/F-ordered strings has been evidenced and modeled in MO_2F [27,28] and MOF_3 [29] resulting, for the latter, from

favored *cis*-$[MO_2F_4]^{3-}$ octahedra. Partial orderings are also likely, as observed, for example, in Bi_2NbO_5F [30].

$NaMO_2F_2$ (M = Nb, Ta) are part of the rich families of sodium oxyfluoroniobiates and oxyfluorotantalates [31], which include for the former, $NaNbO_2F$ [32], $NaNb_6O_{15}F$ [33], Na_3NbOF_6 [34], Na_2NbOF_5 [35], $NaNb_3O_5F$ [36], $Na_3Nb_{12}O_{31}F$ [37,38] and $Na_2Nb_2O_5F_2$ [39], and for the latter, $Na_2Ta_2O_5F_2$ [39], $Na_2Ta_2O_5F_2$-β [40] and $NaTa_2O_5F$ [41]. Moreover, $Na_2Ta_3O_6F_5$, $Na_4Ta_5O_{10}F_9$, $NaTa_3O_7F_2$, $Na_2Ta_6O_{15}F_2$, $Na_2Ta_8O_{19}F_4$, $NaTa_6O_{15}F$ (isotype with $NaNb_6O_{15}F$) and $NaTa_4O_8F_5$ [42,43] have been reported but their structures have not been determined. Among the sodium oxyfluoroniobiates and oxyfluorotantalates whose crystal structures have been determined, only three, $NaMO_2F_2$ (M = Nb [44], Ta), $NaNb_6O_{15}F$ [33] and Na_3NbOF_6 [34], are ordered. $NaNbO_2F_2$ [42,44] and $NaTaO_2F_2$ [42,43], whose atomic positions have not been determined, are isotype and crystallize in the monoclinic system ($P2_1/c$ space group (no. 14)). $NaMO_2F_2$ structures are built up from $[MO_4F_2]^{5-}$ octahedra. As $P2_1/c$ is centrosymmetric, this is redhibitory for NLO properties but does not detract from the interest of this study.

In this work, we combine PXRD (for consistency both crystal structures have been refined), ^{19}F, ^{23}Na and ^{93}Nb solid-state NMR and DFT calculations of NMR parameters to characterize the RT structures of $NaMO_2F_2$. In the case of ordered structures, despite oxide and fluoride anions have very similar X-ray and neutron scattering factors, their different structural environments allow them to be distinguished.. Differences in formal charge and size are captured by the popular bond valence sum (BVS) method [45,46]. Whereas, and in agreement with equal values of ionic radii of Ta^{5+} and Nb^{5+} cations (0.78 Å if sixfold coordinated) [14], niobium and tantalum isotypes have usually very close cell parameters (**Table S1**), those of $NaNbO_2F_2$ and $NaTaO_2F_2$ differ in unusual proportions. Furthermore, in seeking to optimize the synthesis conditions for these compounds thanks to TGA/DTA analyses, a very low amplitude endothermic event was found for $NaNbO_2F_2$ on heating, but not for its tantalum structural isotype. VT PXRD experiments finally revealed why the two compounds behaved differently when heated.

2. Materials and methods

2.1. Sample preparation

$NaNbO_2F_2$ was first synthesized in the form of plate-shaped crystals by Andersson and Galy [44] in the late 1960s by heating a stoichiometric mixture of NaF and NbO_2F at 600 °C. A few years later, single-crystals of $NaTaO_2F_2$ were synthesized by Chaminade et al. [42] who declared it to be an isotype of its niobium counterpart. In the present work, $NaMO_2F_2$ compounds were obtained through a two-step solid-state synthesis from a mixture of NaF and MO_2F (M = Nb, Ta) as done in ref. [44]. MO_2F compounds were prepared following the procedure reported in [28], and were subsequently mixed with NaF. As this sodium fluoride is moister sensitive, the steps of weighing, mixing and grinding were carried in a nitrogen-filled glove box. The mixtures were then loaded in platinum tubes, sealed and heated over two days at 550 °C and 600 °C for $NaNbO_2F_2$ and $NaTaO_2F_2$, respectively. The heating and cooling rates were set to 5 °C.min^{-1}.

2.2. Characterization techniques

2.2.1. Solid-state NMR spectroscopy

^{19}F (I = 1/2) magic angle spinning (MAS) NMR spectra were recorded with a Bruker Avance III spectrometer operating at 7 T (Larmor frequency of 282.4 MHz) using a 1.3 mm CP-MAS probe-head. The Hahn echo sequence was used with an interpulse delay of one rotor period and a recycle delay of 20 s. The 90° pulse was set to 1.56 µs (RF field of 160 kHz). For $NaNbO_2F_2$, a ^{93}Nb 64-step small-phase incremental alteration (SPINAL-64) [47] decoupling was employed during the acquisition process at a RF field of ~106 kHz.

^{23}Na (I = 3/2) and ^{93}Nb (I = 9/2) MAS NMR spectra were recorded with a Bruker Avance III spectrometer operating at 20 T (Larmor frequency of 224.9 and 208.1 MHz for ^{23}Na and ^{93}Nb, respectively) using 2.5 and 1.3 mm CP-MAS probe-heads for ^{23}Na and ^{93}Nb, respectively. For ^{23}Na, the spectra were recorded using a heteronuclear ^{23}Na–^{19}F SPINAL-64 decoupling sequence at a RF field of 132 kHz, a recycle delay of 1 s and 512 scans. The pulse duration was set to 0.35 µs corresponding to a small pulse flip angle of 10° to ensure a total excitation of the entire spin system. For the ^{93}Nb static spectrum, the Hahn echo sequence was used with a recycle delay of 1 s, the length of the CT 90° selective pulse was set to 2 µs (RF field of 125 kHz).

The ^{19}F, ^{23}Na and ^{93}Nb spectra were referenced to $CFCl_3$, 1 M NaCl aqueous solution and saturated $K[NbCl_6]/CH_3CN$ solution, respectively. All spectra were fitted using the DMFit software [48].

2.2.2. Thermal analysis

DTA and TGA analyses were carried on ~56 mg powder samples of $NaNbO_2F_2$ and $NaTaO_2F_2$ using a TGA/DTA Q600 SDT TA Instruments apparatus (Pt crucibles, α-Al_2O_3 as a reference) under argon atmosphere (flow rate of 100 $mL.min^{-1}$). The heating process was set from RT to 300 °C with heating and cooling rates of 10 $°C.min^{-1}$.

2.2.3. Powder X-ray diffraction

Both the RT and the temperature-controlled PXRD patterns were recorded with a PANalytical θ/θ Bragg–Brentano EMPYREAN diffractometer ($CuK\alpha_{1+2}$ radiations) equipped with a PIXcel^{1D} detector. The RT PXRD patterns were measured in a 2θ range of 5° to ~135° with a 0.0131° step size. The total acquisition time was approximately 7h30. The raw powders were dusted through a 63 µm sieve (Saulas) on a glass holder to avoid the strong preferential grain orientation. The temperature-controlled PXRD patterns were recorded under air in a temperature ranging from RT to 300 °C using a HTK 900 Anton Paar furnace attachment and a glass ceramic Macor sample holder. The PXRD patterns were collected at intervals of 20°C and 10°C over the temperature ranges [25–220°C] and [220–300°C], respectively. The temperature was stabilized for 4 minutes before each pattern was recorded. Each PXRD pattern was collected at a given temperature over a 2θ range from 10° to 100° with a 0.0131° step size and a total acquisition time of 3 h.

2.3. First principle calculations

The ground state electronic structure, the quadrupolar coupling NMR parameters and the magnetic shielding tensor were obtained using the Vienna *Ab Initio* Simulation Package (VASP, version 6.2.1) [49,50].

2.3.1. Tensor convention and preliminaries

The calculated magnetic shielding tensor and the experimental chemical shift parameters are defined by the Haeberlen convention [51]. The isotropic magnetic shielding (σ_{iso}), the anisotropy of the magnetic shielding (σ_{CSA}) and the asymmetry parameter (η_{CSA}), are respectively defined as $\sigma_{iso} = (\sigma_{xx} + \sigma_{yy} + \sigma_{zz})/3$, $\sigma_{CSA} = \sigma_{zz} - \sigma_{iso}$ and $\eta_{CSA} = (\sigma_{yy} - \sigma_{xx})/\sigma_{CSA}$, with the magnetic shielding tensor components σ_{ii} defined in the sequence $|\sigma_{zz} -$

$\sigma_{iso}| \geq |\sigma_{xx} - \sigma_{iso}| \geq |\sigma_{yy} - \sigma_{iso}|$. Similarly, the chemical shift tensor is defined by three parameters, the isotropic chemical shift (δ_{iso}), the anisotropy of the chemical shift (δ_{CSA}) and the asymmetry parameter (η_{CSA}), which are given by $\delta_{iso} = (\delta_{xx} + \delta_{yy} + \delta_{zz})/3$, $\delta_{CSA} = \delta_{zz} - \delta_{iso}$ and $\eta_{CSA} = (\delta_{yy} - \delta_{xx})/\delta_{CSA}$, with the chemical shift tensor components defined in the sequence $|\delta_{zz} - \delta_{iso}| \geq |\delta_{xx} - \delta_{iso}| \geq |\delta_{yy} - \delta_{iso}|$. σ_{iso} is related to δ_{iso} by the relation: $\delta_{iso} \simeq \sigma_{iso}(ref) - \sigma_{iso}$, with $\sigma_{iso}(ref)$ being the absolute isotropic magnetic shielding reference, that is determined by establishing a linear regression between the experimental δ_{iso} values and the calculated σ_{iso} values.

2.3.2. DFT relaxation

The electronic structure of the unit cells were determined through solid-state DFT calculations with periodic boundary conditions. The ionic relaxation scheme was set to conjugate-gradient algorithm. The Perdrew-Burke-Ernzerhof functional including the generalized gradient approximation (GGA-PBE) [52] was employed to obtain the ground state electronic structure. The projector augmented wave (PAW) potentials used for O, F, Na, Nb and Ta are respectively: O_s_GW, F_GW, Na_sv_GW, Nb_sv_GW and Ta_sv_GW. The wave function was expanded on a plane-wave basis set with a 550 eV kinetic energy cut-off and (4 × 6 × 4) shifted Monkhorst-Pack k-point mesh. The total energy was converged up to change below 10^{-8} eV.

2.3.3. NMR parameters calculation

The PAW [53,54] and the gauge including projector augmented wave (GIPAW) [55,56] approaches were used to calculate the quadrupolar coupling NMR parameters and the magnetic shielding values, respectively. The PAW potentials, plane-wave energy cut-off and the shifted Monkhorst-Pack k-point mesh were set the same as the DFT relaxation.

2.3.4. Magnetic shielding to chemical shift conversion

In the present work, ^{23}Na and ^{93}Nb δ_{iso} values were obtained using previously established linear regressions $\delta_{iso} = -0.811(13)\ \sigma_{iso} + 449(7)$ [57] and $\delta_{iso} = -\sigma_{iso} - 586.9$ [28], respectively. For ^{19}F δ_{iso} values, two new linear regressions established from NaF [58], $NaNbO_2F_2$ and $NaTaO_2F_2$ were used.

3. Results and discussion

3.1 RT PXRD data refinements

The experimental structures (ES) were obtained by refining the recorded RT PXRD diagrams using the structural Rietveld refinement method [59] implemented in the Fullprof software [60]. The crystal structure of $NaNbO_2F_2$ [44] was used as initial model for the refinements. Isotropic displacement parameters (IDPs, U_{iso}) were considered for all atoms. The background intensity was estimated from linear interpolation between points manually selected in regions free from Bragg reflections. The crystallographic data are gathered in **Table 1**. The atomic coordinates and U_{iso} values are gathered in **Table 2**. The observed, calculated and intensity difference patterns and reliability factors are given as **SM** (**Fig. S1** and **S2**). Crystal structures have been deposited via the joint CCDC/FIZ Karlsruhe deposition service. CSD [61] 2298195 and 2298195 (deposition number) contain the supplementary crystallographic data for $NaNbO_2F_2$ and $NaTaO_2F_2$, respectively. These data can be found free of charge from FIZ Karlsruhe via https://www.ccdc.cam.ac.uk/structures.

The cell parameters (**Table 1.**) are similar to those determined previously (a = 8.013 Å, b = 5.405 Å, c = 7.626 Å, β = 101.70 (°) for $NaNbO_2F_2$ [44] and a = 8.091 Å, b = 5.434 Å, c = 7.498 Å, β = 102.15 (°) and cell volumes of 325.44 $Å^3$ and 322.28 $Å^3$ for $NaNbO_2F_2$ and $NaTaO_2F_2$ [43], respectively). As mentioned in the introduction, the cell parameters of $NaNbO_2F_2$ and $NaTaO_2F_2$, whether determined more than 50 years ago or for this study, differ in unusual proportions compared with others niobium and tantalum isotypes (**Table S1**): –1.2 % and +1.7 % from Nb to Ta, for a and c, respectively. However, these differences almost perfectly compensate, since the volumes of the two cells are very close 0.1 %.

The BVS values gathered in **Table 3** were calculated using the following values of R_0 parameters: 1.756 [63], 1.677, 1.911, 1.92 [45], 1.87 and 1.88 Å [46] for Na^+/O^{2-}, Na^+/F^-, Nb^{5+}/O^{2-}, Ta^{5+}/O^{2-}, Nb^{5+}/F^- and Ta^{5+}/F^- ion pairs, respectively, and b = 0.37 Å. They support the refined crystal structures and then the ordering proposed previously for $NaNbO_2F_2$ [44].

Table 1. Crystal data for $NaNbO_2F_2$ and $NaTaO_2F_2$.

	$NaNbO_2F_2$	$NaTaO_2F_2$
Crystal system	monoclinic	monoclinic
SG	$P2_1/c$	$P2_1/c$
a (Å)	8.0026(3)	8.09997(3)
b (Å)	5.4072(3)	5.4391(1)
c (Å)	7.6243(3)	7.4982(3)
β (°)	101.916(2)	102.128(2)
V (Å^3)	322.81(2)	322.96(1)
Z	2	2
Formula weight (g.mol^{-1})	371.7656	547.8488
Density (calculated, g.cm^{-3})	3.825	5.634
T (K)	298	298
Wavelength (Å)	1.54056	1.54056
2θ range (°)	5–135	5–135
R_p/R_{wp} (%)	10.8/11.4	9.2/9.2
R_B/R_F (%)	6.2/5.2	5.0/5.3

Table 2. Atom, atomic coordinates (x, y, z) and isotropic displacement parameter (U_{iso}, Å^2) of $NaNbO_2F_2$ and $NaTaO_2F_2$. All atoms fully occupy 4e sites (symmetry 1).

	$NaNbO_2F_2$				$NaTaO_2F_2$			
Atom	***x***	***y***	***z***	U_{iso}	***x***	***y***	***z***	U_{iso}
Na1	0.3666(9)	0.780(3)	0.116(1)	0.014(3)	0.377(1)	0.793(3)	0.109(2)	0.014(5)
Nb1/Ta1	0.1549(3)	0.2644(9)	0.3180(4)	0.017(1)	0.1581(2)	0.2598(6)	0.2982(2)	0.0060(3)
O1	0.183(2)	0.156(2)	0.071(2)	0.018(4)	0.199(2)	0.154(3)	0.053(3)	0.007(5)
O2	0.043(2)	0.544(3)	0.212(2)	0.018(4)	0.037(3)	0.559(4)	0.216(3)	0.007(5)
F1	0.377(2)	0.444(2)	0.314(2)	0.023(4)	0.376(2)	0.472(3)	0.304(3)	0.014(4)
F2	0.310(2)	0.977(2)	0.378(2)	0.023(4)	0.330(2)	0.982(3)	0.377(3)	0.014(4)

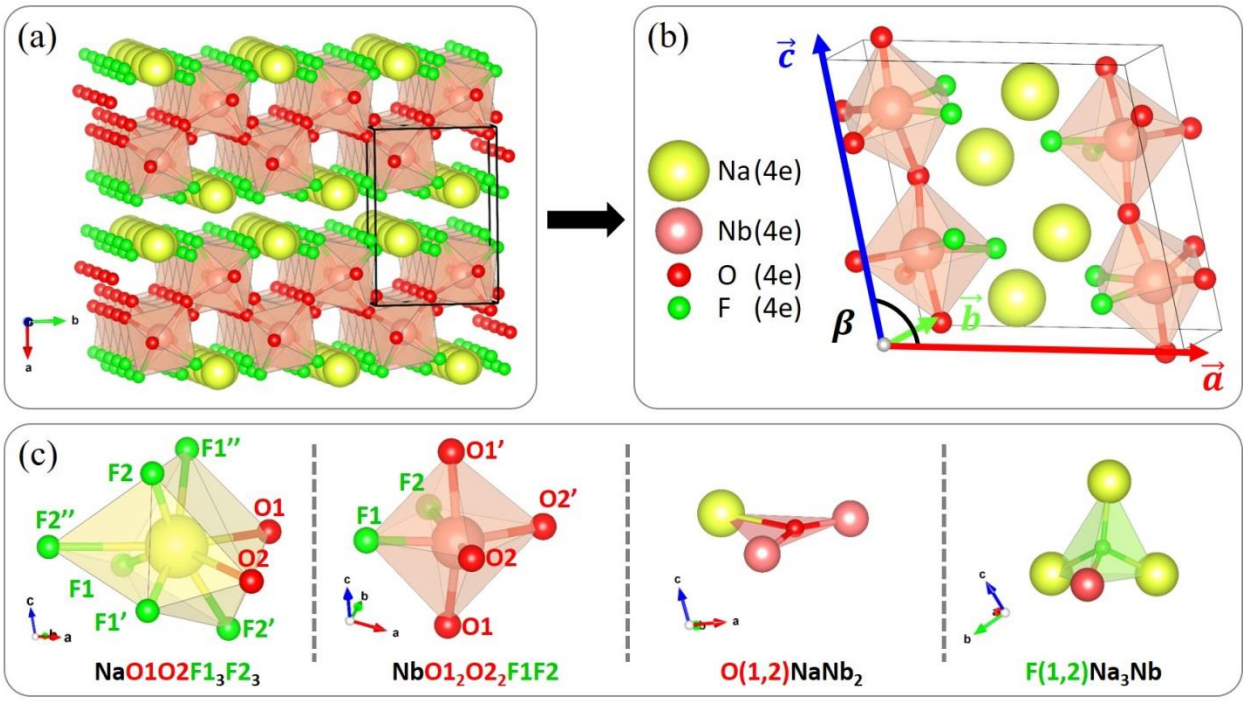


Fig. 1. Perspective views of the $NaNbO_2F_2$ structure (a), of the unit cell (b) and of the coordination polyhedra of Na^+, Nb^{5+}, O^{2-} and F^- ions (c), in which, atoms labeled X, X' and X'' (X = O1, O2, F1 and F2) are equivalent by symmetry operations. The drawings were created using VESTA [62].

Perspective views of the structure of $NaNbO_2F_2$ illustrating the $(NbO_2F_2)_n^-$ layers, the unit cell and the different local environments of Na^+, Nb^{5+}, O^{2-} and F^- ions are represented in **Fig. 1**. In $NaMO_2F_2$, the $[MO_4F_2]^{5-}$ octahedra adopt, as expected, a *cis* configuration and only share their four oxygen vertices to build infinite $[MO_2F_2]_n^-$ layers. The outward-facing fluorine vertices face outwards, i.e. towards the sodium atoms. This is consistent with the strong affinity between sodium (the most electropositive) and fluorine (the most electronegative) which results in strong electrostatic interactions between the sodium ions and the least polarizable fluoride ions. Concurrently, the Nb^{5+} ions are displaced from the octahedral center toward the oxide ions located *trans* opposite to the fluoride ones (**Fig. 1(c)**), enhancing the inherent distortions of the heteroleptic $[MO_4F_2]^{5-}$ octahedra (M–X bond lengths and X–M–X angles are reported in **Tables 4** and **S2,** respectively). These wavy $(NbO_2F_2)_n^-$ layers are stacked along the crystallographic *a* axis and separated from each

other by Na^+ ions located in an irregular environment consisting of six F^- and two O^{2-} ions (**Table S4** and **Fig. 1(c)**). It was described by Andersson *et al.* as a distorted octahedron considering only the F^- ions or as sevenfold coordinated considering in addition the nearest O^{2-} ion [44]. Na^+ conduction properties were investigated in both the stoichiometric and sodium-deficient $NaNbO_2F_2$ phases but the ionic conductivity of both samples «could not be measured because they were too porous» [64].

The longer *c* parameter observed for $NaNbO_2F_2$ is due to longer Nb–O1 bond-length (**Table 4** and **Fig. 1(c)**) and larger Nb–O1–Nb angle (~147.8 ° compared to ~143.9 ° for O1–Ta–O1) (**Fig. 1(b)**). The shorter *a* parameter observed for $NaNbO_2F_2$ is related to the smaller thickness of the $(NbO_2F_2)_n^-$ layer (~5.394 Å compared to ~5.599 Å for $(TaO_2F_2)_n^-$) (**Fig. 1(a)**), further details are discussed in section 3.4.

Table 3. Bond valence sum values from ES and APO models of $NaNbO_2F_2$ and $NaTaO_2F_2$

Model	V_i^{Na}	V_i^{Nb}	V_i^{O1}	V_i^{O2}	V_i^{F1}	V_i^{F2}
$NaNbO_2F_2$						
ES	1.003	5.069	1.783	2.070	1.107	1.112
APO	1.021	5.013	1.922	1.972	1.076	1.064
$NaTaO_2F_2$						
ES	1.103	4.926	1.915	2.027	1.067	1.021
APO	1.020	5.135	1.980	2.011	1.094	1.070

Table 4. Individual and average M–X bond lengths (X = O1, O1', O2, O2', F1 and F2, Å) in the MO_4F_2 octahedra in the ES and APO models of $NaMO_2F_2$ (M = Nb & Ta).

$NaMO_2F_2$	**M = Nb**		**M = Ta**	
Model	**ES**	**APO**	**ES**	**APO**
M–F1	2.031(15)	2.043	2.105(20)	2.051
M–O2'	1.955(19)	1.904	1.902(23)	1.916
M–F2	1.986(12)	2.017	2.056(17)	2.023
M–O2	1.857(18)	1.942	1.934(21)	1.927

M–O1	1.943(18)	1.832	1.929(22)	1.935
M–O1'	2.028(19)	2.140	2.015(23)	1.970
<M-X>	**1.967**	**1.980**	**1.990**	**1.970**

3.2 Multinuclear solid-state NMR

High-resolution solid-state NMR data are essential to support a structure determination through powder diffraction techniques. Indeed, for each nucleus with non-zero nuclear spin, NMR spectra provide information about the number of non-equivalent crystallographic sites and their relative multiplicity. Moreover, coupled with DFT calculations, NMR data allow assessing the accuracy of the structural models.

The experimental ^{19}F, ^{23}Na and ^{93}Nb NMR spectra are gathered in **Fig. 2**, their fits and corresponding fit parameters are given as supplementary material (**Fig. S3-S7** and **Tables S5-S9)**. **Table 5** gathers the experimental NMR parameters relevant for the discussion, including δ_{iso}, δ_{CSA}, η_{CSA}, the quadrupolar coupling constant (C_Q) and the asymmetry parameter (η_Q).

3.2.1 ^{19}F NMR

Two resonances, each having a relative intensity of 50%, are expected since there are two distinct F crystallographic sites with the same multiplicity (4e). Accordingly, both recorded ^{19}F MAS NMR spectra (**Fig. 2 (a)** and **(b)**) present two main resonances with similar intensities, as well as low intensity resonances assigned to NaF (δ_{iso} = –223.1 ppm [65]) and unidentified impurities. The ^{19}F δ_{iso} values (**Table 5**) are in between those of NaF in which F^- ions are sixfold coordinated to Na^+ ions (2.32 Å [58]) and those of the terminal F^- ions in NbF_5 (193-268 ppm [66]), $KNbF_6$ (100.0 ppm [67]) and $CsNbF_6$ (110.1 ppm [68]) and TaF_5 (106-174 ppm [66]) and $KTaF_6$ (37.1 ppm [67]), respectively. Accordingly, the ^{19}F δ_{iso} values of $NaNbO_2F_2$ are higher than the δ_{iso} values of $NaTaO_2F_2$. The significantly lower values for $NaNbO_2F_2$ and $NaTaO_2F_2$ compared with NbF_5 and TaF_5 can be explained by the presence of (two close) Na^+ ions (**Table 6**) and longer Nb–F and Ta–F bond lengths in $NaNbO_2F_2$ and $NaTaO_2F_2$ (the shortest the bond length, the highest the ^{19}F δ_{iso} value [66,69]). The same last argument and the larger δ_{iso} values of KF (–133.2 ppm [65]) and CsF (–11.2 ppm [65]) compared to NaF, explains the significantly lower values compared with

$KNbF_6$ (2 F sites, doubtful bond lengths: Nb–F1,2 = 2.124, 2.13 Å [70]) and $CsNbF_6$ (Nb-F = 1.876 Å [71]) and $KTaF_6$ (3 F sites, Ta–F1,2,3 = 1.905, 1.930, 1.905 Å [72]). The δ_{iso} gaps between the two main lines are similar: 27.8 and 21.5 ppm for $NaNbO_2F_2$ and $NaTaO_2F_2$, respectively. The main difference between the environments of F1 and F2 in $NaNbO_2F_2$ and $NaTaO_2F_2$ relies on the F–Nb and F–Ta bond lengths which are shorter for F2. From these bond lengths, for each compound, the main ^{19}F resonance with a lower δ_{iso} value is tentatively assigned to the F1 atoms whereas the main ^{19}F resonance with a higher δ_{iso} value is tentatively assigned to F2 atoms.

3.2.2 ^{23}Na and ^{93}Nb NMR

^{23}Na (I = 3/2) and ^{93}Nb (I = 9/2) are subjected to quadrupolar interaction. In that case, use of high magnetic fields allows to greatly enhance the resolution in MAS spectra, since the chemical shift dispersion increases with the magnetic field while second-order quadrupolar broadenings scale down [73]. The use of high magnetic fields are most beneficial for niobium compounds with large ^{93}Nb quadrupolar coupling constants (exceeding 20 MHz) [74]. The shape of the central transition (CT) of the high magnetic field (20 T) of the ^{23}Na and ^{93}Nb NMR spectra (**Fig. 2 (c)**, **(d)** and **(e)**) are indicative of high η_Q values consistent with these distorted sites.

For NbO_4F_2 octahedra, as for $NbOF_5$ octahedra, the out-of-center distortion results on large ^{93}Nb C_Q value (42.0 MHz in $NaNbO_2F_2$ (**Table 5**), 36.0 and 33.2 MHz in $Cdpy_4NbOF_5$ (py = C_5H_5N) and $[pyH]_2[Cdpy_4(NbOF_5)_2]$ [75]). Indeed, most of the ^{93}Nb C_Q values of sixfold-coordinated niobium oxides do not exceed 30 MHz [74] and ^{93}Nb C_Q values of sixfold-coordinated niobium fluorides are on the order of 10 MHz [67,68]. ^{93}Nb δ_{iso} values for $NbO_{6-x}F_x$ octahedra decrease as x increases. For most of the NbO_6 octahedra, they range between –900 and –1100 ppm [74], for NbO_4F_2, the value is close to –1200 ppm (**Table 5**), for $NbOF_5$ octahedra, they are close to –1300 (–1310 and –1320 ppm [75]) and for NbF_6 octahedra, they are close to –1600 ppm [67,68].

The NMR parameters of ^{23}Na in the two isotypes are, as expected since the Na^+ ion environments are similar, close (**Table 5**). The C_Q values are in the same order of magnitude than the values observed for eightfold-coordinated sodium fluorides in α-$NaCaAlF_6$ (Na1, C_Q

= 1.36 MHz) [76], $Na_5Al_3F_{14}$ (Na1 and Na2, C_Q = 1.48 and 3.18 MHz) and Na_3AlF_6 (Na2, C_Q = 1.43 MHz) [77].

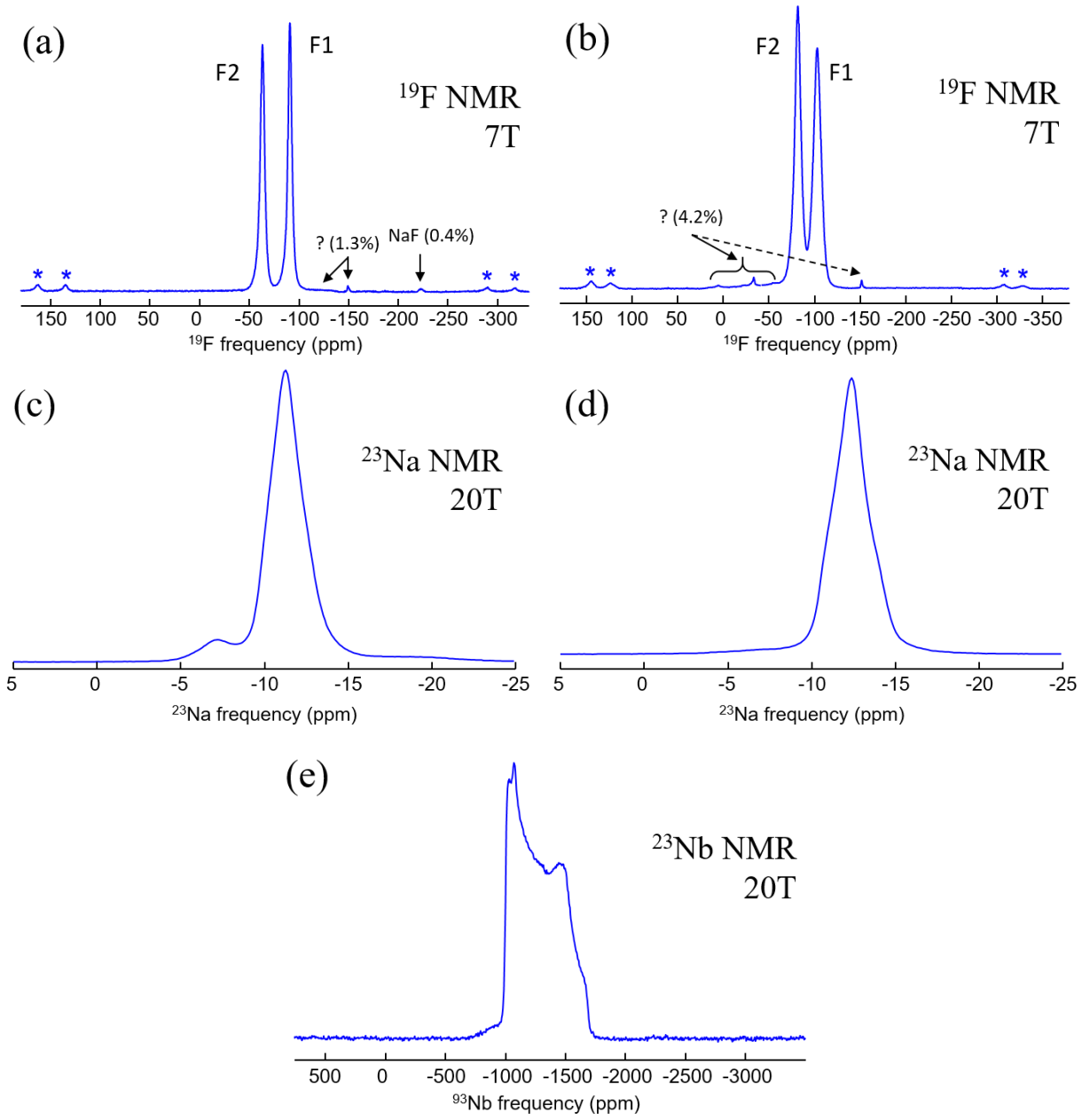


Fig. 2. MAS NMR spectrum of ^{19}F (64 kHz), central transition (CT) of ^{23}Na (30 kHz) and static NMR spectrum of ^{93}Nb of $NaNbO_2F_2$ ((a), (c) and (e)) and MAS NMR spectrum of ^{19}F (64 kHz) and CT of ^{23}Na (30 kHz) of $NaTaO_2F_2$ ((b) and (d)). The stars indicate spinning sidebands, the main resonances are assigned and additional resonances, one assigned to

NaF and the other to unidentified impurity, are outlined and their relative intensities are indicated on the ^{19}F spectra.

Table 5. Compound, nuclei, weighted average experimental δ_{iso}, δ_{CSA} and η_{CSA} values (<δ_{iso}>, <δ_{CSA}>, ppm and <η_{CSA}>), C_Q (MHz) and η_Q values, relative intensities (I, %) and corresponding assignments.

Compound	Nucleus	<δ_{iso}>	<δ_{CSA}>	<η_{CSA}>	C_Q	η_Q	I	Assignment
$NaNbO_2F_2$	**^{19}F**	-90.8	-125	0			49.0	F1
		-63.0	-130	0			49.4	F2
	^{23}Na	-9.8	8.9	0.30	1.60	0.71		
	^{93}Nb	-1206.1	-285.2	0.08	42.0	0.60		
$NaTaO_2F_2$	**^{19}F**	-102.8	-117.4	0			46.2	F1
		-81.3	-127.2	0			49.6	F2
	^{23}Na	-11.2	8.5	0.30	1.74	0.67		

Table 6. F–M bond lengths (X = F1 and F2, Å) from the ES and APO models of $NaMO_2F_2$ (M = Nb & Ta).

$NaMO_2F_2$	**M = Nb**		**M = Ta**	
Model	**ES**	**APO**	**ES**	**APO**
F1–M	2.031(15)	2.043	2.105(20)	2.051
F1–Na1	2.199(16)	2.256	2.196(22)	2.267
F1–Na1'	2.353(19)	2.292	2.277(26)	2.314
F2–M	1.986(14)	2.017	2.056(17)	2.023
F2–Na1	2.251(17)	2.263	2.270(23)	2.254
F2–Na1'	2.391(18)	2.348	2.353(24)	2.373

3.3 DFT relaxation

In order to assess the quality of the crystal structures and to confirm the ^{19}F resonance assignments, NMR parameters were modeled. Two sets of NMR parameters were

calculated for each compound, one set deduced from the experimental crystal structure (ES) and the other from the atomic position optimized (APO) model.

Table 7. Distortion index (*DI*), quadratic elongation (<λ>) and bond angle variance (σ_θ, deg.^{2}) for the [MO1$_2$O2$_2$F1F2] octahedron in $NaNbO_2F_2$ and $NaTaO_2F_2$ calculated from ES and APO models.

Model	*DI*	< λ>	σ_θ
$NaNbO_2F_2$			
ES	0.025	1.016	50.8
APO	0.044	1.015	42.8
$NaTaO_2F_2$			
ES	0.034	1.015	48.5
APO	0.023	1.008	26.0

Focussing now on the relaxation effects with respect to the ES, as is often the case for powder-refined crystal structures, significant atomic displacements (up to 0.11 Å for O in $NaNbO_2F_2$) are observed for $NaNbO_2F_2$ and $NaTaO_2F_2$. (**Table S2**). Nevertheless, the average bond lengths evolve little in the MO_4F_2 octahedra (**Table 4**) and in the Na^+ ions polyhedra (**Table S4**). The angular distortions $\alpha = \frac{1}{12}\sum_{i=1}^{n}|\alpha_i - 90°|$ and $\beta = \frac{1}{3}\sum_{i=1}^{n}|\beta_i - 180°|$ with α_i the twelve angles between two adjacent M-X bonds and β_i the three angles between two opposite M–X bonds (**Table S3**) are slightly reduced for $NaNbO_2F_2$. They are further reduced for $NaTaO_2F_2$ and are thus stronger in the APO structure of $NaNbO_2F_2$ than in that of $NaTaO_2F_2$. These observations are corroborated by the evolution of the values of the distortion index (*DI*) [78], the quadratic elongation (λ) and the bond angle variance (σ_θ)) [79] of the MO_4F_2 octahedra (**Table 7**).

As expected, for both the ES and APO models, the M–F bonds are longer than the M–O2 bonds (**Table 4**) and the angles O2–M–O2 are greater than 90° (~6 to 8°) and therefore the angles F1–M–F2 are smaller (~6 to 8°) than 90° (**Table S3**). In the APO structures, average M–F bond lengths on the one hand and average M–O2 bond lengths on the other hand are close. Finally, there is a markedly different structural feature in the two compounds; while

M–O1 bond lengths differ slightly and by the same amount (~0.09 Å) in both ES, they differ markedly (~0.31 Å) in $NaNbO_2F_2$ APO and almost equal in $NaTaO_2F_2$ APO (~0.03 Å). The *c* parameter is equal to the distance between two O1 atoms of two MO_4F_2 octahedra, and therefore depends on the lengths of the M–O1 bonds. The longer Nb–O1 bonds are consistent with a higher *c* value for $NaNbO_2F_2$ compared to $NaTaO_2F_2$. . This difference in *c* values of the two compounds is attributed to second-order Jahn-Teller distortion (SOJT) effect exhibited by Nb^{5+} ions. To ascertain whether the discrepancy in cell parameters arises from inaccuracies in structural refinements, they were relaxed, along with the atomic positions, using DFT calculations. This process yielded slightly altered cell parameters, yet the unusual proportions of *a* (–1.4%) and *c* (1.3%) parameters remained consistent.

3.4 PAW/GIPAW calculations

For ^{19}F in inorganic fluorides, several linear relationships between calculated isotropic magnetic shielding (σ_{iso}) values, using the GIPAW approach, and experimental isotropic chemical shift (δ_{iso}) values, $\delta_{iso} = \sigma_{ref} - a\,\sigma_{iso}$, have been established to convert calculated σ_{iso} values into "calculated" δ_{iso} values. As the absolute values of the slopes are dependent on the metal atom(s) constituting the fluoride(s) [29,65,66], two new linear regression relations have been established from NaF [58] and APO model of $NaNbO_2F_2$ ($\delta_{iso} = -0.706(15)\sigma_{iso} + 49.6(4.0)$) and NaF and APO model of $NaTaO_2F_2$ ($\delta_{iso} = -0.741(1)\sigma_{iso} + 63.5(2)$) and used to calculate the ^{19}F δ_{iso} values of $NaNbO_2F_2$ and $NaTaO_2F_2$, respectively. These relations could be useful in the future for the prediction of ^{19}F δ_{iso} values in ordered Na and (Nb/Ta)-based (oxy)fluorides and the structural modelling of disordered Na and (Nb/Ta)-based (oxy)fluorides.

The calculated NMR parameters from the ES and APO models are given in **Table 8** and represented through comprehensive radar charts in **Fig. 3**, showcasing the relative difference, denoted as $f\{G;\ N\}$, expressed as a percentage and defined by the relation $f\{G;N\} = 100 - \frac{|G_{exp} - G_{cal}|}{G_{exp}} \times 100$. G represents NMR parameters including, δ_{iso}, C_Q, and η_Q and N refer to ^{19}F, ^{23}Na and ^{93}Nb nuclei. These radar charts provide a concise visual representation of the agreement between the calculated and experimental NMR parameters.

For ^{19}F, the calculations confirm our tentative assignments and the agreement between the experimental and calculated δ_{iso} values from the APO models is almost perfect and slightly better to that from the ES models. Furthermore, in agreement with slightly more intense resonance spinning sidebands, the calculated σ_{CSA} values are higher for F2 atoms compared to F1 atoms (**Tables 5** and **8**).

With the exception of the η_Q value of ^{23}Na in $NaTaO_2F_2$, the agreement is also excellent for the quadrupolar nuclei from the APO models. The relaxation of the crystal structure of $NaNbO_2F_2$ especially improves C_Q and η_Q values of ^{93}Nb and ^{23}Na, respecively.

Table 8. δ_{iso} (ppm), σ_{CSA} (ppm), η_{CSA}, C_Q (MHz) and η_Q values calculated for ^{19}F, ^{23}Na and ^{93}Nb atoms from the ES and APO models of $NaNbO_2F_2$ and $NaTaO_2F_2$.

Model	Nucleus	Site	δ_{iso}	σ_{CSA}	η_{CSA}	C_Q	η_Q
$NaNbO_2F_2$							
ES	^{19}F	F1	-83.5	74.2	0.67		
		F2	-55.1	-109.7	0.86		
	^{23}Na	Na1	-11.2	11.5	0.22	1.82	0.12
	^{93}Nb	Nb1	-1172.5	258.9	0.42	65.0	0.65
APO	^{19}F	F1	-88.8	-84.1	0.87		
		F2	-64.7	-113.2	0.75		
	^{23}Na	Na1	-11.2	10.0	0.34	1.66	0.69
	^{93}Nb	Nb1	-1163.7	258.8	0.27	43.2	0.58
$NaTaO_2F_2$							
ES	^{19}F	F1	-103.3	67.6	0.97		
		F2	-67.7	-103.7	0.85		
	^{23}Na	Na1	-9.1	10.8	0.30	1.78	0.92
APO	^{19}F	F1	-102.9	70.8	0.67		
		F2	-81.2	-90.0	0.88		
	^{23}Na	Na1	-12.2	9.9	0.39	1.78	0.95

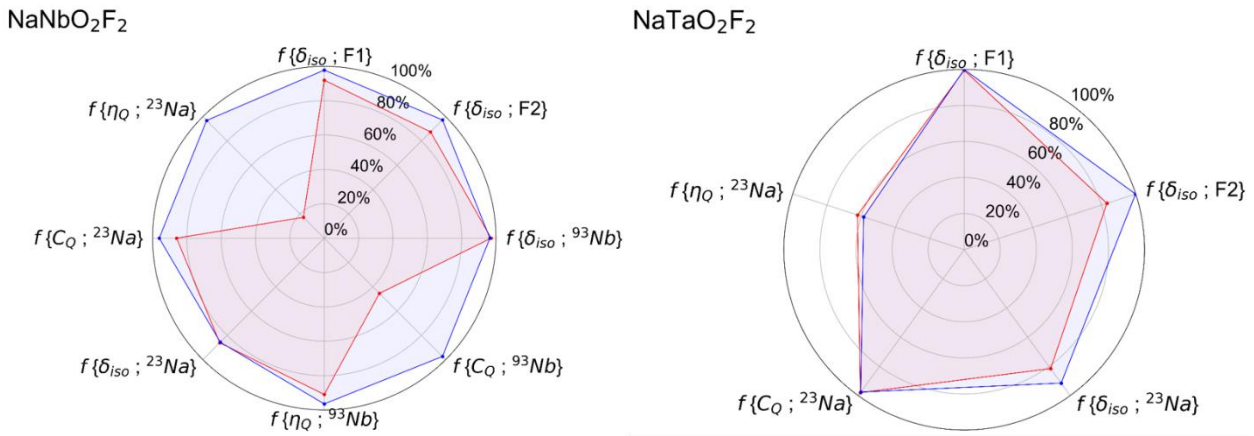


Fig. 3. Radar charts comparing experimental and calculated, from the ES (in red) and APO (in blue) models, NMR parameters of $NaNbO_2F_2$ (left) and $NaTaO_2F_2$ (right). The axes are scaled in % and features the scoring functions $f\{\delta_{iso}; F1\}$, $f\{\delta_{iso}; F2\}$, $f\{\delta_{iso}; {}^{23}Na\}$, $f\{\delta_{iso}; {}^{93}Nb\}$, $f\{C_Q; {}^{23}Na\}$, $f\{C_Q; {}^{93}Nb\}$, $f\{\eta_Q; {}^{23}Na\}$ and $f\{\eta_Q; {}^{93}Nb\}$.

3.4 Thermal and temperature-controlled PXRD analysis

The DTA-TGA was first used to determine the thermal stability of the two compounds studied and to determine the optimal annealing temperature to obtain the samples with the minimum amount of impurity. Once we had obtained the purest samples, we found that, $NaNbO_2F_2$ exhibits a very low amplitude endothermic event around 240 °C on heating up and one endothermic event with similar amplitude around 260 °C on cooling down (hysteresis of ~20 °C) whereas no similar event was detected for its tantalum structural isotype (**Fig. 4**). The TGA curves show no significant weight loss during the heating and cooling processes. As the amplitude of these events fall within the error margin, they could potentially due to instrumental/experiment perturbations. Hence, TDA and TGA experiments were repeated on the samples, and the results consistently unchanged (**Fig. S8**). Furthermore, additional experiments were performed on the $NaTaO_2F_2$ sample, spanning a broader temperature range (from RT to 600 °C) on the basis of ensuring whether the events observed in $NaNbO_2F_2$ do not occur at higher temperature in $NaTaO_2F_2$. As shown in **Fig. S8**, no events were detected at these higher temperatures. As no weight loss was detected, the two thermal events observed for $NaNbO_2F_2$ can only be attributed to a reversible structural transition that does not occur for $NaTaO_2F_2$ although it is isotype. A

comparative structural study was then undertaken by temperature-controlled PXRD to elucidate this singular difference of thermal behavior.

PXRD patterns were collected at several temperatures below and above the transition detected by DTA for $NaNbO_2F_2$. The same experiment was also carried out for $NaTaO_2F_2$ for comparison. After refining the data, plots of the thermal evolution of the cell parameters and of the different bond lengths and angles enabled us to understand what was happening during the heating of $NaNbO_2F_2$ and $NaTaO_2F_2$ powders. For each compound, **Fig. 5** shows the temperature dependence of the PXRD diagrams from RT to 300 °C in the 2θ range [32.5–35.5°] where significant changes in intensity and position of the peaks are observed**.** The (020) and (112) reflections overlap at RT for $NaNbO_2F_2$ (**Fig 5. (b)**), but are separated for $NaTaO_2F_2$ (**Fig. 5 (e)**). Conversely, the ($\bar{2}12$) and (300) reflections are separated for $NaNbO_2F_2$ (**Fig. 5 (c)**) but overlap for $NaTaO_2F_2$ (**Fig. 5 (f)**). These differences in reflection positions between the two compounds are related to the differences in cell parameters (**Table 1**). While the *a* and *b* cell parameters of $NaTaO_2F_2$ are longer than those of $NaNbO_2F_2$, the *c* parameter of $NaTaO_2F_2$ is shorter. Whatever the compound, all the diffraction peaks move towards the low 2θ angles with increasing temperature, thus reflecting an expansion of the monoclinic cell in all three crystallographic directions. The initially overlapped peaks start, gradually, separating upon reaching 300 °C, especially the (020) and (112) peaks for $NaNbO_2F_2$ and the ($\bar{2}12$) and (300) for $NaTaO_2F_2$. However, the displacement in position of the (300) peak with the temperature is greater for $NaNbO_2F_2$, than for $NaTaO_2F_2$, suggesting that the *a*-axis of the former has a greater expansion, which was confirmed by calculating the thermal expansion coefficients (TEC). **Fig. 6** displays the evolution against temperature of the cell parameters, *a*, *b*, *c* and *β* and volume *V* for both $NaNbO_2F_2$ (**Fig. 6** left) and $NaTaO_2F_2$ (**Fig. 6** right), obtained from Rietveld refinements of the temperature-controlled PXRD data (**Figures S9-S16**). The values of these different parameters as well as the corresponding reliability factors are gathered in **Tables S10** and **S11**. The thermal evolutions of the cell parameters of $NaNbO_2F_2$ show the same trend: they increase linearly up to ~220°C before expanding more strongly above this temperature. In contrast, no deviation from linearity is observed for $NaTaO_2F_2$, except for *β* but much lower than that observed for $NaNbO_2F_2$ (**Fig. 6**). For both compounds, the angle *β* and therefore

the monoclinic distortion increases with sample heating and the angle β exhibits the highest TEC (**Fig. 6**).

For the two compounds, the thermal analyses and the thermal evolutions of the cell parameters are in agreement with each other. Indeed, if no event is really perceptible for $NaTaO_2F_2$, the departure from linearity in the thermal expansion of the cell parameters for $NaNbO_2F_2$ at ~220°C (**Fig. 6**) is unquestionably correlated with the endothermic peak detected in the DTA curve at ~231°C (**Fig. 4**) To discern the underlying factors contributing to this difference in the thermal behavior of these isostructural compounds, a thorough examination of various structural attributes, including bond lengths and angles within M^{5+} and Na^+ polyhedra, inter-octahedral angles within M^{5+} octahedra, distances between $(MO_2F_2)_n^{n-}$ layers, layer thickness, as well as polyhedral volumes, was carried out.

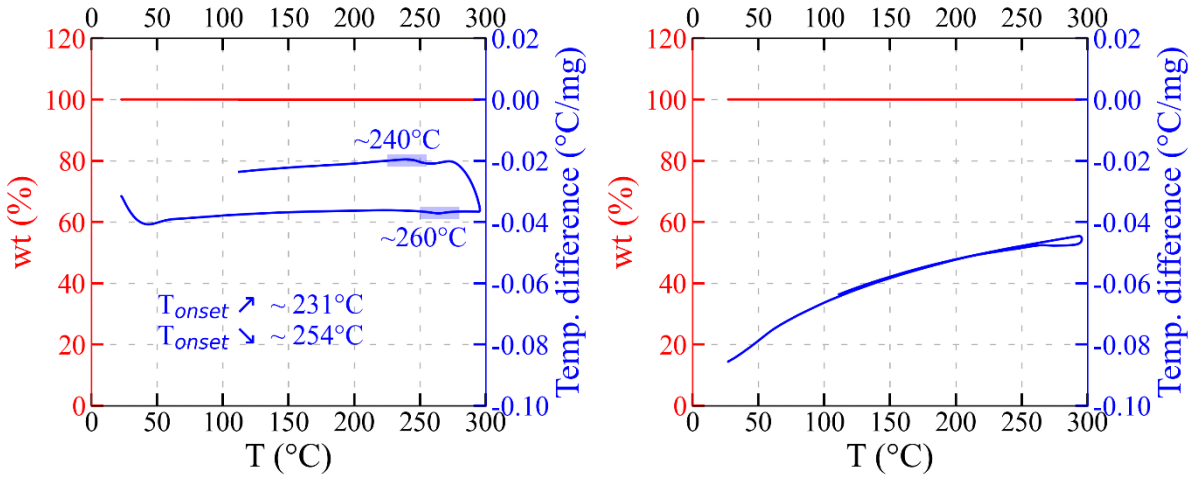


Fig. 4. DTA (blue) and TGA (red) curves of $NaNbO_2F_2$ (left) and $NaTaO_2F_2$ (right) recorded, under argon atmosphere (flow rate of 100 mL.min^{-1}), from RT to 300 °C, with heating/cooling rate of 10 °C.min^{-1}. The thermal accidents observed for $NaNbO_2F_2$ are highlighted in blue and their temperature values are indicated.

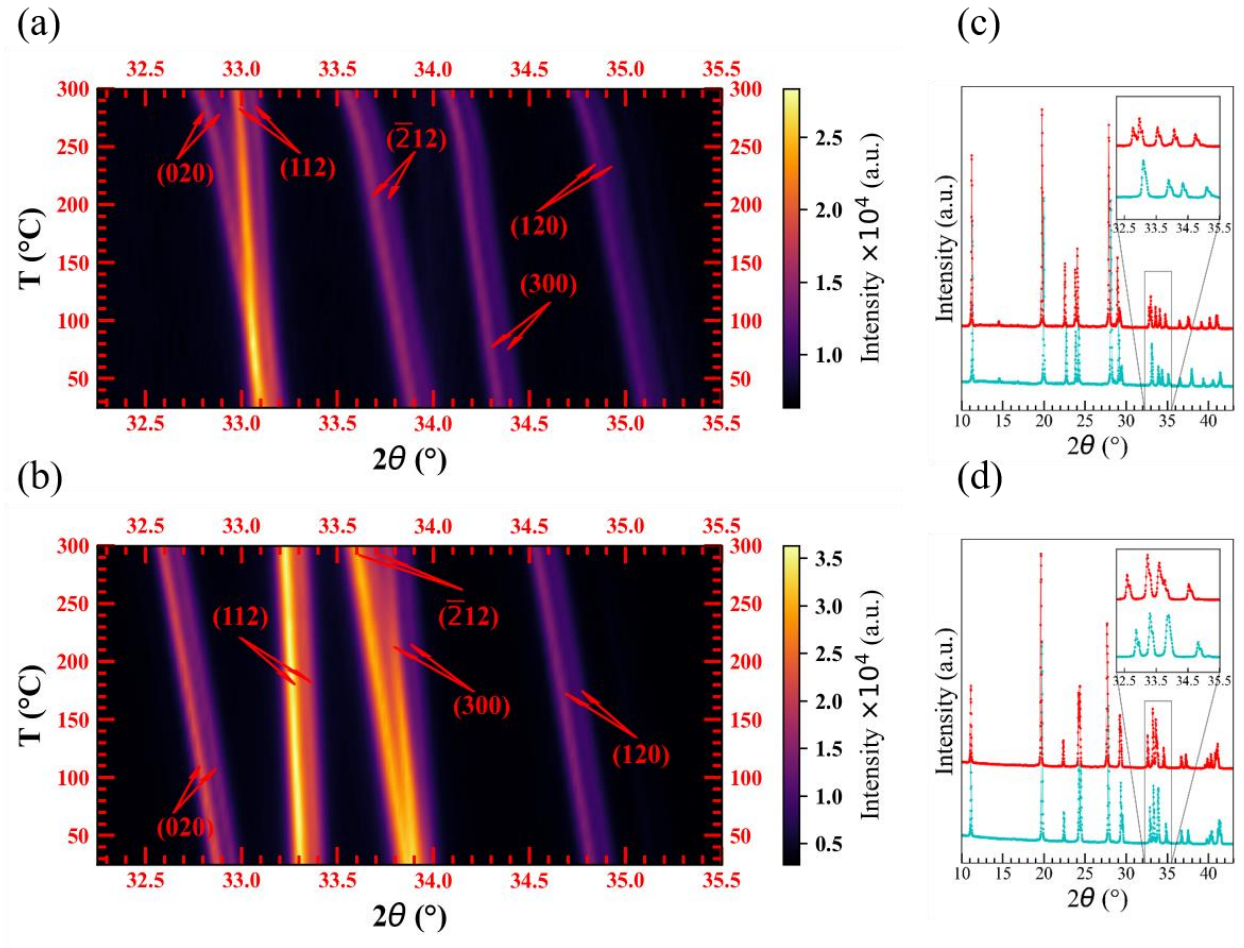


Fig. 5. Maps showing the temperature evolution of the (020), (112), ($\bar{2}$12), (300) and (120) peaks upon heating from RT to 300 °C of $NaNbO_2F_2$ (a) and $NaTaO_2F_2$ (b). PXRD patterns recorded at RT (blue) and 300 °C (red) of $NaNbO_2F_2$ (c) and $NaTaO_2F_2$ (d).

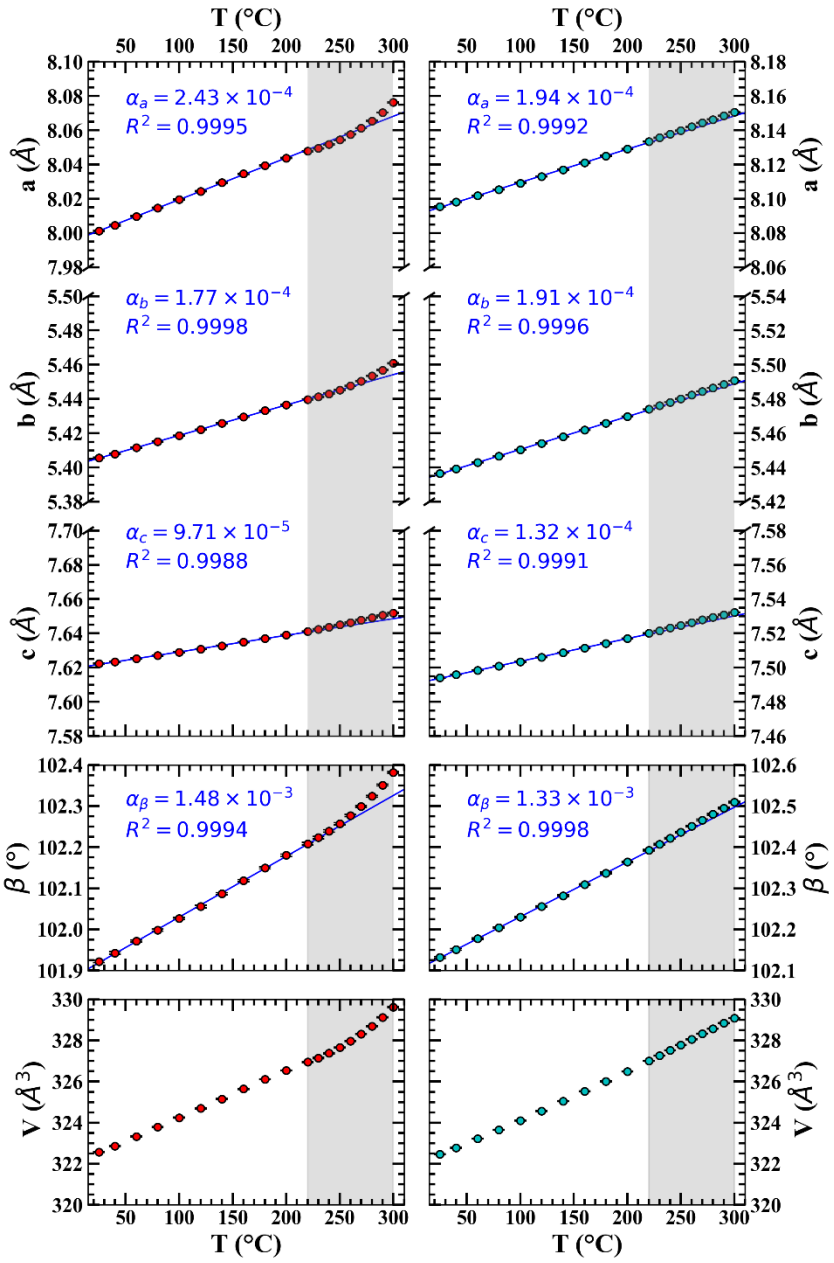


Fig. 6. Temperature dependence of the cell parameters *a*, *b*, *c*, *β* and *V* for $NaNbO_2F_2$ (left) and $NaTaO_2F_2$ (right) determined from Rietveld refinement of temperature-controlled PXRD data (**Tables S10** and **S11**). TECs (α_a, α_b, α_c and α_β, $°C^{-1}$), which were calculated from linear regression in the [25–220°C] temperature range (blue line), are given as well as the R-squared values.

Fig. 7 (b) summarizes the evolution against temperature of M–F1 and M–O1 bond lengths and F1–M–O1 and O2–M–O1 angles from $MO1_2O2_2F1F2$ octahedra (**Fig. 7 (a)**), the rest of the bond lengths and angles as well as those from $NaO1O2F1_3F2_3$ are given as **SM** (**Fig. S17-S22)**. In the [25–220°C] temperature range, the evolutions against temperature of M–F1 (constant), M–O1 (decreasing), M–O1' (increasing, **Fig. S19**), F1–M–O1 (constant) and O2'–M–O1 (increasing), are similar for both compounds with, however, different amplitudes; Nb–O1 (~0.11 Å decrease) higher than Ta–O1 (~0.04 Å decrease), Nb–O1' (~0.09 Å increase, **Fig. S19**) higher than Ta–O1' (~0.05 Å increase, **Fig. S19**), and O2'–Nb–O1 (~1.4 ° increase) lower than O2'–Ta–O1 (~3 ° increase). In the grey region (**Fig. 7 (b)**), these evolutions take different trends for both compounds, particularly for $NaNbO_2F_2$, where these trends are more pronounced. The trends of M–F1 and M–O1 are different; Nb–F1 decreases while Ta–F1 increases, and Nb–O1 increases while Ta–O1 remains the same. These differences in bond lengths between the compounds are not only present at the polyhedral level but also between polyhedra. Indeed, as observed in **Fig. 8**, there are significantly different evolutions of the inter-octahedral angles against temperature.

In the [25–220°C] temperature range, the evolutions against temperature of Φ (increasing), Ψ (decreasing), Ω (decreasing), are similar for both compounds with, however, different amplitudes, ~2.2 ° increase for Φ and ~2.5 and ~1.2 ° decrease for Ψ and Ω, respectively, in $NaNbO_2F_2$, compared to, ~4.8 ° increase for Φ and ~3.3 and ~4.3 ° decrease for Ψ and Ω, respectively, in $NaTaO_2F_2$. In the grey region (**Fig. 8 (b)**), these evolution trends change for Φ, constant in $NaNbO_2F_2$ and increasing in $NaTaO_2F_2$. Similarly, for Ω, the evolution trends change: constant in $NaNbO_2F_2$ while it remains the same for $NaTaO_2F_2$. In contrast, for Ψ, the evolution trends change similarly for both compounds. Since the angles Φ and Ω are opposite (**Fig. 9 (a)**), an increase in Φ should be coupled with a decrease in Ω and vice versa, which is the case for both compounds (**Fig. 8 (b)**). From the $(NbO_2F_2)_n^{n-}$ layer perspective, this increase (decrease) in Φ (Ω) stretches the zigzag form of the layers along the *b* direction. Especially for $NaTaO_2F_2$, where the amplitude of the Φ (Ω) increase (decrease) is ~2-3 times higher than that of $NaNbO_2F_2$. This stretching is further reinforced in $NaTaO_2F_2$ by the evolution against temperature of χ (**Fig. 9**), which is approximately constant for $NaNbO_2F_2$, while increasing by ~4° for $NaTaO_2F_2$. As for the distances between layers (d_2) and layer thickness (d_1) (**Fig. 9**), their evolutions against temperature are

approximately constant in both compounds in the [25–220°C] temperature range. In the grey region, d_2 slightly increases in $NaNbO_2F_2$ while decreases in $NaTaO_2F_2$, and d_1 remains approximately constant in $NaNbO_2F_2$ while increases in $NaTaO_2F_2$. This d_1 increase is coupled with an increase in χ (**Fig. 9 (b)**). For both compounds, in the [25–220°] temperature range, the polyhedral volume (V_p) increases with temperature (~0.8-0.9 Å^3) for $NaO1O2F1_3F2_3$ (**Fig. S17**) while decreases (~0.1-0.2 Å^3) for $MO1_2O2_2F1F2$ (**Fig. 7**). In the grey region, V_p of $NaO1O2F1_3F2_3$ stabilizes for $NaNbO_2F_2$ while approximately maintains its increasing for $NaTaO_2F_2$ (**Fig. S17**). Similarly, for $MO1_2O2_2F1F2$, V_p stabilizes for $NaNbO_2F_2$, while increases for $NaTaO_2F_2$ (**Fig. 7**).

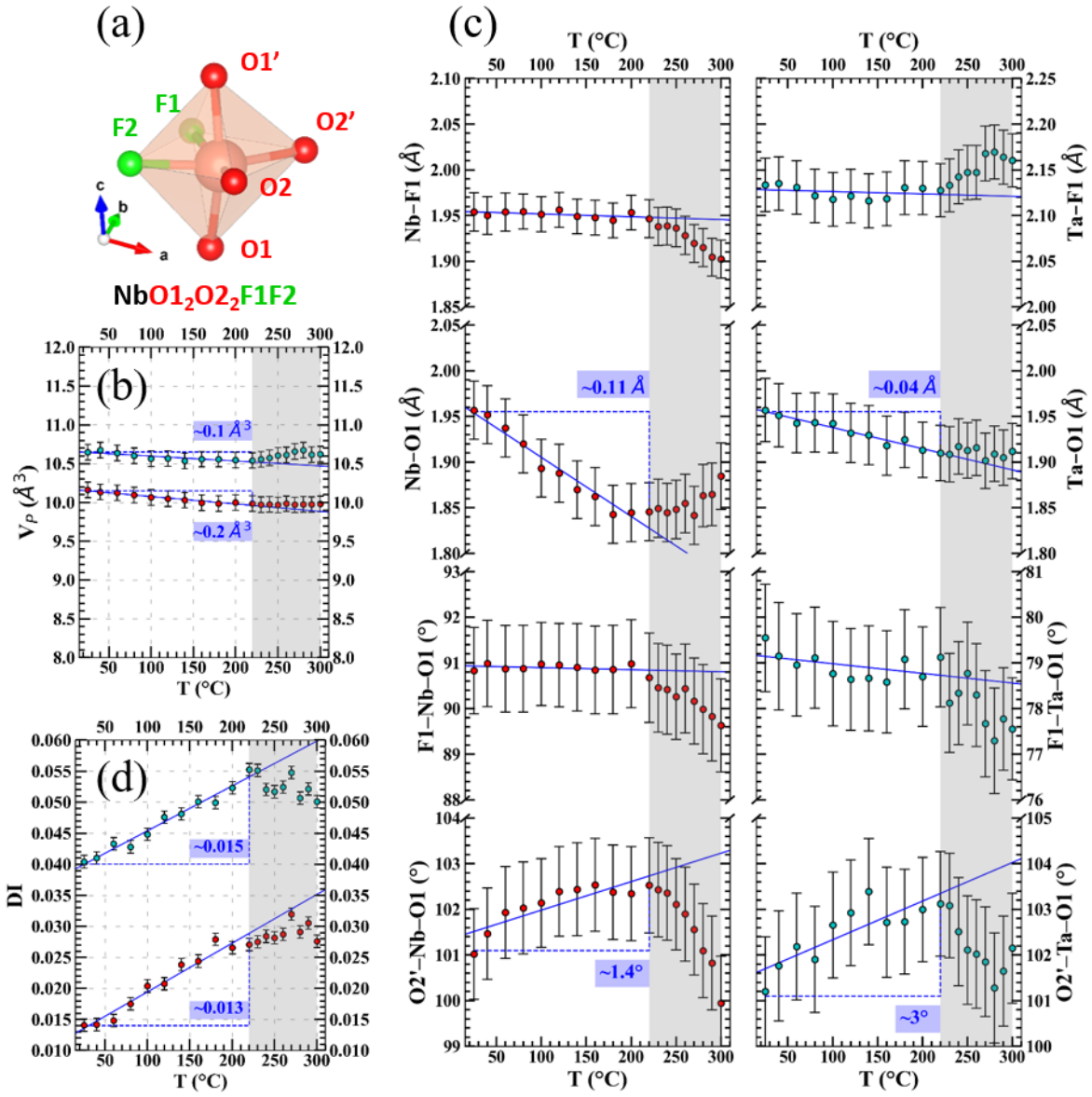


Fig. 7. Perspective view of Nb^{5+} octahedron (a), in which, atoms labeled X and X' (X = O1 and O2) are equivalent by symmetry operations. Temperature dependence of M^{5+} octahedron volume (b), bond lengths and angles (c) and distortion index (d) of $NaNbO_2F_2$ (red dots) and $NaTaO_2F_2$ (blue dots). Linear regressions (blue lines) are plotted in the [25–220°C] temperature range guiding the evolution of each quantity. The amplitude of significant evolutions is given and highlighted in blue.

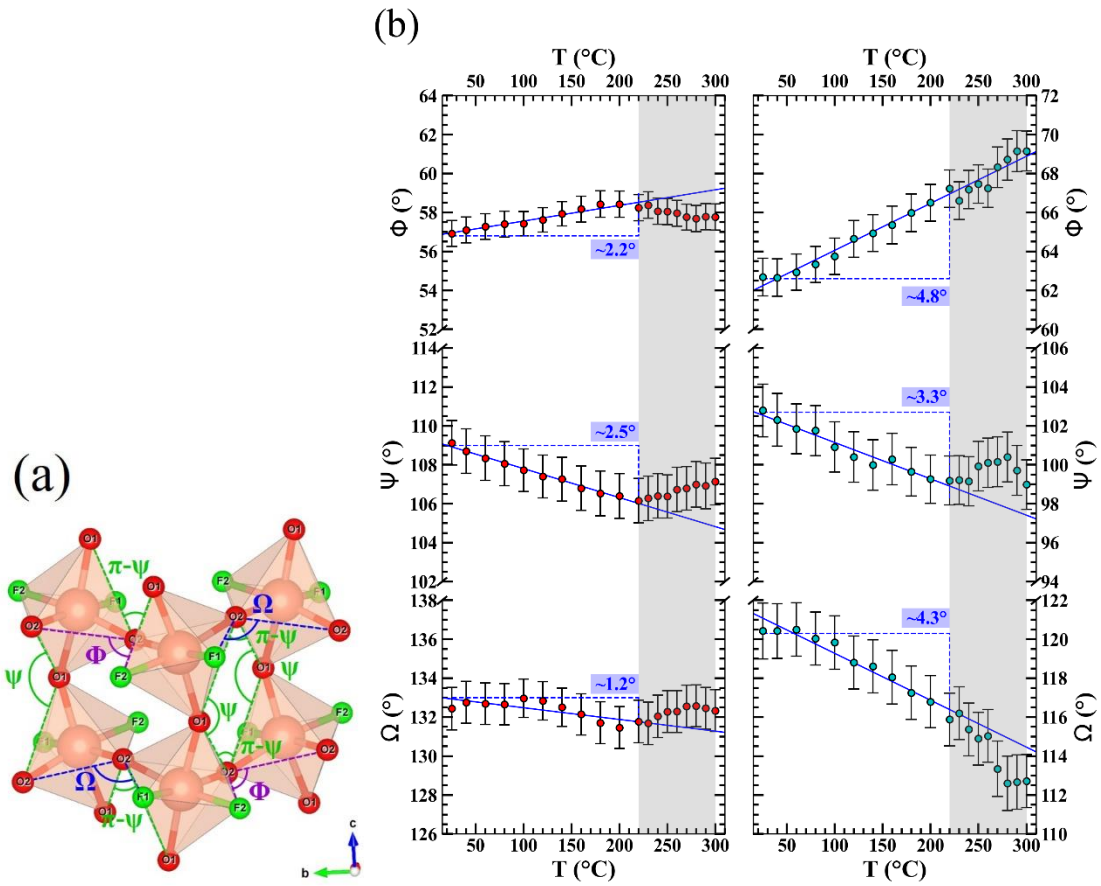


Fig. 8. Perspective view of the smallest octahedra unit describing the $NaNbO_2F_2$ framework with the inter-octahedral angles (*Φ*, *Ψ*, and *Ω*) (a). Temperature dependence of the inter-octahedral angles from $NaNbO_2F_2$ (left (b)) and $NaTaO_2F_2$ (right (b)). Linear regressions (blue lines) are plotted in the [25–220°C] temperature range guiding the evolution of each quantity. The amplitude of significant evolutions is given and highlighted in blue.

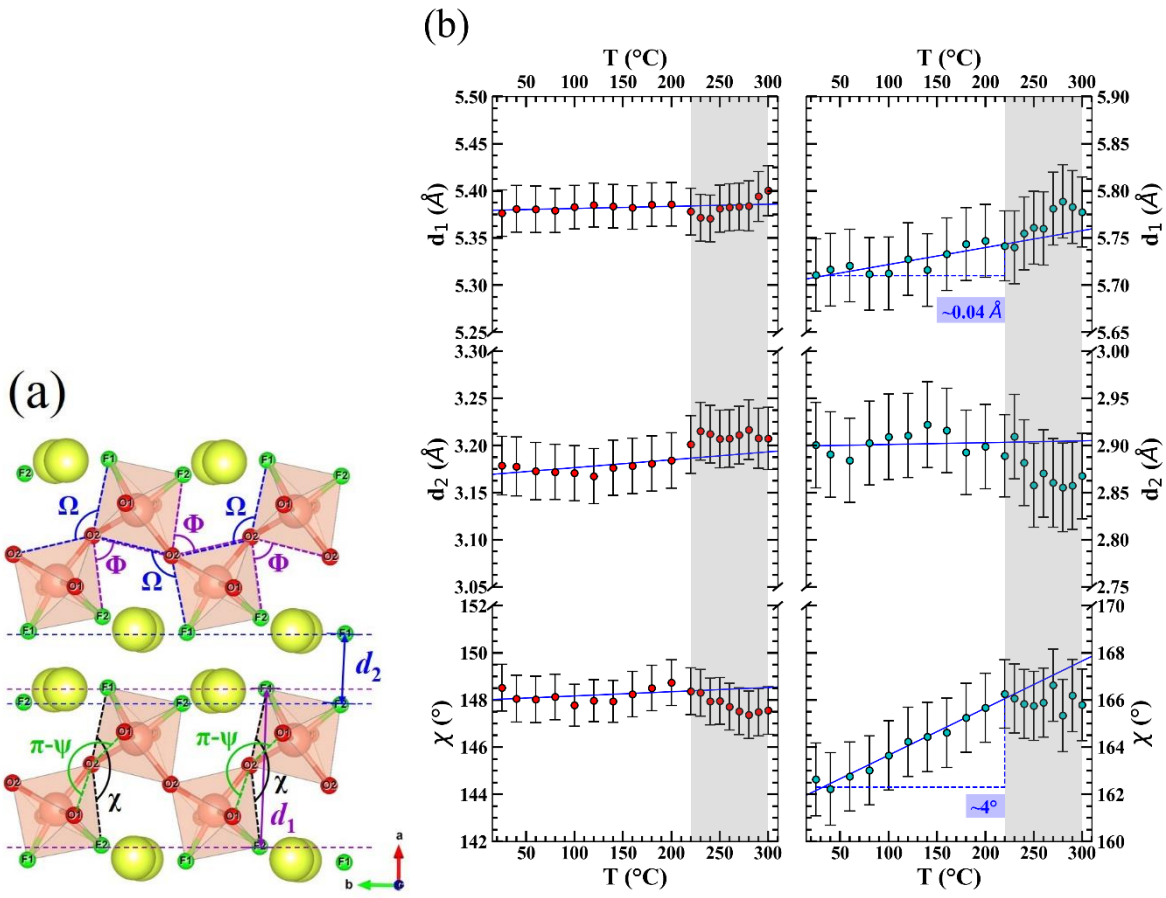


Fig. 9. Illustration of two $(NbO_2F_2)_n^{n-}$ layers with indicated inter-octahedral angles (χ, Ψ and Ω, °), distance between layers (d_2) and layer thickness (d_1) (a). Temperature dependence of χ, d_1 and d_2 from $NaNbO_2F_2$ (left (b)) and $NaTaO_2F_2$ (right (b)). Linear regressions (blue lines) are plotted in the [25–220°C] temperature range guiding the evolution of each quantity. The amplitude of significant evolutions is given and highlighted in blue.

From analyzing the evolution against temperature of the structural characteristics of both compounds, it seems that in the [25–220°C] temperature range $NaTaO_2F_2$ experiences higher amplitude of inter-polyhedral increase (or decrease, **Fig. 8** and **9**) hinting a stretching along the *b* direction of the $(NbO_2F_2)_n^{n-}$ layer. The amplitudes of bond length increase (or decrease, **Fig. 7**) are higher in $NaNbO_2F_2$. Except for d_1, all analyzed structural characteristics from $NaNbO_2F_2$ experience a sudden trend change in the [220–300°C] temperature range, while in $NaTaO_2F_2$, not all structural characteristics experienced this

trend change, among these, Ta–F1, F1–Ta–O1 and O2–Ta–O1 (**Fig. 7**),Ψ (**Fig. 8**), χ, and d_2 (**Fig. 9**).

4. Conclusion

$NaNbO_2F_2$ and $NaTaO_2F_2$ compounds were prepared using solid-state synthesis, and characterized using PXRD, ^{19}F NMR, and high-field ^{23}Na and ^{93}Nb NMR. For each compound, the atomic positions in ES were optimized and the NMR parameters, including δ_{iso}, δ_{CSA}, η_{CSA}, C_Q and η_Q, were calculated for ES and the ES with optimized positions (APO). These parameters were subsequently compared to the experimental data, revealing that the APO model is more precise than the ES one. Furthermore, these structural models revealed that $NaNbO_2F_2$ experienced the second-order Jahn-Teller distortion, explaining the unusual observed disparity between the cell parameters, particularly *c*, which is associated to the bond length Nb–O1. The observed low amplitude endothermic event was confirmed by the evolution against temperature of the cell parameters derived from Rietveld refinement of the VT PXRD data. For $NaNbO_2F_2$, the evolution of these parameters remained linear until reaching ~220 °C, a temperature close to that at which the endothermic event was observed, after which they deviated from linearity. In contrast, for $NaTaO_2F_2$, and except for β, cell parameters exhibited linear evolution with no deviation observed above ~220 °C. A thorough analysis of structural parameters at different temperatures revealed distinct behaviors in their evolution between the two compounds. Notably, $NaTaO_2F_2$ exhibit significant evolutions of the angles between polyhedra, especially Φ and Ω, while $NaNbO_2F_2$ display strong evolutions of the bond lengths, especially Nb–O1.

References

[1] H. Kageyama, K. Hayashi, K. Maeda, J.P. Attfield, Z. Hiroi, J.M. Rondinelli, K.R. Poeppelmeier, Expanding frontiers in materials chemistry and physics with multiple anions, Nat Commun. 9 (2018) 772. https://doi.org/10.1038/s41467-018-02838-4.

[2] J.K. Harada, N. Charles, K.R. Poeppelmeier, J.M. Rondinelli, Heteroanionic Materials by Design: Progress Toward Targeted Properties, Adv. Mater. 31 (2019) 1805295. https://doi.org/10.1002/adma.201805295.

[3] H.K. Izumi, J.E. Kirsch, C.L. Stern, K.R. Poeppelmeier, Examining the Out-of-Center Distortion in the $[NbOF_5]^{2-}$ Anion, Inorg. Chem. 44 (2005) 884–895. https://doi.org/10.1021/ic048766d.

[4] H. Lu, R. Gautier, M.D. Donakowski, T.T. Tran, B.W. Edwards, J.C. Nino, P.S. Halasyamani, Z. Liu, K.R. Poeppelmeier, Nonlinear Active Materials: An Illustration of Controllable Phase Matchability, J. Am. Chem. Soc. 135 (2013) 11942–11950. https://doi.org/10.1021/ja4050604.

[5] Y. Hu, C. Wu, X. Jiang, Z. Wang, Z. Huang, Z. Lin, X. Long, M.G. Humphrey, C. Zhang, Giant Second-Harmonic Generation Response and Large Band Gap in the Partially Fluorinated Mid-Infrared Oxide $RbTeMo_2O_8F$, J. Am. Chem. Soc. 143 (2021) 12455–12459. https://doi.org/10.1021/jacs.1c06061.

[6] M. Yan, R.-L. Tang, W. Liu, S.-P. Guo, From $Ba_3Nb_2O_2F_{12}(H_2O)_2$ to $Ba_{0.5}NbO_2F_2(H_2O)$: Achieving Balanced Nonlinear Optical Performance by O/F Ratio Regulation, Inorg. Chem. 61 (2022) 20709–20715. https://doi.org/10.1021/acs.inorgchem.2c03842.

[7] V.V. Atuchin, T.A. Gavrilova, V.G. Kesler, M.S. Molokeev, K.S. Aleksandrov, Low-temperature synthesis and structural properties of ferroelectric $K_3WO_3F_3$ elpasolite, Chemical Physics Letters. 493 (2010) 83–86. https://doi.org/10.1016/j.cplett.2010.05.023.

[8] A.M. Fry, P.M. Woodward, Structures of α-$K_3MoO_3F_3$ and α-$Rb_3MoO_3F_3$: Ferroelectricity from Anion Ordering and Noncooperative Octahedral Tilting, Crystal Growth & Design. 13 (2013) 5404–5410. https://doi.org/10.1021/cg401342q.

[9] L. Xu, H. Gong, L. Deng, F. Long, Y. Gu, J. Guan, Complex-Mediated Synthesis of Tantalum Oxyfluoride Hierarchical Nanostructures for Highly Efficient Photocatalytic Hydrogen Evolution, ACS Appl. Mater. Interfaces. 8 (2016) 9395–9404. https://doi.org/10.1021/acsami.6b02622.

[10] K. Aihara, R. Mizuochi, M. Okazaki, S. Nishioka, S. Yasuda, T. Yokoi, F. Ishiwari, A. Saeki, M. Inada, K. Maeda, Low-Temperature Microwave-Assisted Hydrothermal Synthesis of $Pb_2Ti_2O_{5.4}F_{1.2}$ Photocatalyst for Improved H_2 Evolution under Visible Light, ACS Materials Lett. 5 (2023) 2355–2360. https://doi.org/10.1021/acsmaterialslett.3c00574.

[11] J.C. Pérez-Flores, R. Villamor, D. Ávila-Brande, J.M. Gallardo Amores, E. Morán, A. Kuhn, F. García-Alvarado, VO_2F: a new transition metal oxyfluoride with high specific capacity for Li ion batteries, J. Mater. Chem. A. 3 (2015) 20508–20515. https://doi.org/10.1039/C5TA05434F.

[12] J.T. Incorvati, L.F. Wan, B. Key, D. Zhou, C. Liao, L. Fuoco, M. Holland, H. Wang, D. Prendergast, K.R. Poeppelmeier, J.T. Vaughey, Reversible Magnesium Intercalation into a Layered Oxyfluoride Cathode, Chem. Mater. 28 (2016) 17–20. https://doi.org/10.1021/acs.chemmater.5b02746.

[13] D. Deng, Transition Metal Oxyfluorides for Next-Generation Rechargeable Batteries, ChemNanoMat. 3 (2017) 146–159. https://doi.org/10.1002/cnma.201600342.

[14] R.D. Shannon, Revised effective ionic radii and systematic studies of interatomic distances in halides and chalcogenides, Acta Cryst A. 32 (1976) 751–767. https://doi.org/10.1107/S0567739476001551.

[15] D. Babel, G. Pausewang, W. Viebahn, Notizen: Die Struktur einiger Fluoride, Oxide und Oxidfluoride AMe $_2X_6$: Der $RbNiCrF_6$-Typ, Zeitschrift Für Naturforschung B. 22 (1967) 1219–1220. https://doi.org/10.1515/znb-1967-1126.

[16] J.B. Goodenough, H.Y.-P. Hong, J.A. Kafalas, Fast Na+-ion transport in skeleton structures, Materials Research Bulletin. 11 (1976) 203–220. https://doi.org/10.1016/0025-5408(76)90077-5.

[17] M.E. Welk, A.J. Norquist, F.P. Arnold, C.L. Stern, K.R. Poeppelmeier, Out-of-Center Distortions in d^0 Transition Metal Oxide Fluoride Anions, Inorg. Chem. 41 (2002) 5119–5125. https://doi.org/10.1021/ic025622v.

[18] N. Charles, R.J. Saballos, J.M. Rondinelli, Structural Diversity from Anion Order in Heteroanionic Materials, Chem. Mater. 30 (2018) 3528–3537. https://doi.org/10.1021/acs.chemmater.8b01336.

[19] M.R. Marvel, J. Lesage, J. Baek, P.S. Halasyamani, C.L. Stern, K.R. Poeppelmeier, Cation–Anion Interactions and Polar Structures in the Solid State, J. Am. Chem. Soc. 129 (2007) 13963–13969. https://doi.org/10.1021/ja074659h.

[20] R.A.F. Pinlac, C.L. Stern, K.R. Poeppelmeier, New Layered Oxide-Fluoride Perovskites: $KNaNbOF_5$ and $KNaMO_2F_4$ (M = Mo^{6+}, W^{6+}), Crystals. 1 (2011) 3–14. https://doi.org/10.3390/cryst1010003.

[21] M. Holland, N. Charles, J.M. Rondinelli, K.R. Poeppelmeier, Reconstructive Transitions from Rotations of Rigid Heteroanionic Polyhedra, J. Am. Chem. Soc. 138 (2016) 11882–11889. https://doi.org/10.1021/jacs.6b06813.

[22] H. Jo, M.H. Lee, K.M. Ok, Order and Disorder: Toward the Thermodynamically Stable α-$BaMoO_2F_4$ from the Metastable Polymorph, Chem. Mater. 33 (2021) 1875–1882. https://doi.org/10.1021/acs.chemmater.1c00074.

[23] F.J. Brink, L. Norén, D.J. Goossens, R.L. Withers, Y. Liu, C.-N. Xu, A combined diffraction (XRD, electron and neutron) and electrical study of $Na_3MoO_3F_3$, Journal of Solid State Chemistry. 174 (2003) 450–458. https://doi.org/10.1016/S0022-4596(03)00303-7.

[24] A.M. Fry, H.A. Seibel, I.N. Lokuhewa, P.M. Woodward, $Na_{1.5}Ag_{1.5}MO_3F_3$ (M = Mo, W): An Ordered Oxyfluoride Derivative of the $LiNbO_3$ Structure, J. Am. Chem. Soc. 134 (2012) 2621–2625. https://doi.org/10.1021/ja208587e.

[25] H.-X. Tang, R.-B. Fu, Z.-J. Ma, X.-T. Wu, A Potassium Tungsten Oxyfluoride with Strong Second-Harmonic Generation Response Derived from Anion-Ordered Functional Motif, Inorg. Chem. 60 (2021) 17364–17370. https://doi.org/10.1021/acs.inorgchem.1c02861.

[26] S. Bai, D. Wang, H. Liu, Y. Wang, Recent advances of oxyfluorides for nonlinear optical applications, Inorg. Chem. Front. 8 (2021) 1637–1654. https://doi.org/10.1039/D0QI01156H.

[27] R.L. Withers, F.J. Brink, Y. Liu, L. Norén, Cluster chemistry in the solid state: Structured diffuse scattering, oxide/fluoride ordering and polar behaviour in transition metal oxyfluorides, Polyhedron. 26 (2007) 290–299. https://doi.org/10.1016/j.poly.2006.05.021.

[28] J. Dabachi, M. Body, C. Galven, F. Boucher, C. Legein, Preparation-Dependent Composition and O/F Ordering in NbO_2F and TaO_2F, Inorg. Chem. 56 (2017) 5219–5232. https://doi.org/10.1021/acs.inorgchem.7b00355.

[29] O. Zakary, M. Body, T. Charpentier, V. Sarou-Kanian, C. Legein, Structural Modeling of O/F Correlated Disorder in $TaOF_3$ and $NbOF_{3-x}(OH)_x$ by Coupling Solid-State NMR and DFT Calculations, Inorg. Chem. 62 (2023) 16627–16640. https://doi.org/10.1021/acs.inorgchem.3c02844.

[30] E.E. McCabe, I.P. Jones, D. Zhang, N.C. Hyatt, C. Greaves, Crystal structure and electrical characterisation of Bi_2NbO_5F: an Aurivillius oxide fluoride, J. Mater. Chem. 17 (2007) 1193. https://doi.org/10.1039/b613970a.

[31] A. Agulyansky, Chemistry of Tantalum and Niobium Fluoride Compounds, Elsevier, 2004. https://doi.org/10.1016/B978-0-444-51604-6.X5000-9.

[32] W. Rüdorff, D. Krug, Alkaliniob(IV)-dioxidfluoride, Z. Anorg. Allg. Chem. 329 (1964) 211–217. https://doi.org/10.1002/zaac.19643290124.

[33] S. Andersson, R. Ottinger, S.J. Cyvin, I. Fedorcsák, R.A. Hoffman, A. Westerdahl, The Crystal Structure of $NaNb_6O_{15}F$ and $NaNb_6O_{15}OH$, Acta Chem. Scand. 19 (1965) 2285–2290. https://doi.org/10.3891/acta.chem.scand.19-2285.

[34] R. Stomberg, K.-M. Marstokk, H. Møllendal, H. Priebe, D.L. Powell, R. Suchi, The Crystal Structure of alpha-Sodium Hexafluorooxoniobate(V), alpha-$Na_3[NbF_6O]$., Acta Chem. Scand. 37a (1983) 453–459. https://doi.org/10.3891/acta.chem.scand.37a-0453.

[35] R. Stomberg, S. Jagner, A.F. Andresen, M. Maeda, H. Ohtaki, The Crystal Structure of Sodium Pentafluorooxoniobate(2–), $Na_2[NbF_5O]$., Acta Chem. Scand. 38a (1984) 603–607. https://doi.org/10.3891/acta.chem.scand.38a-0603.

[36] J. Köhler, A. Simon, $NaNb_3O_5F$ – eine Niob-Niob-Dreifachbindung mit „side-on"-Koordination durch Nb-Atome, Angew. Chem. 98 (1986) 1011–1012. https://doi.org/10.1002/ange.19860981118.

[37] D.X. Li, The crystal structure of $Na_3Nb_{12}O_{31}F$, Journal of Solid State Chemistry. 73 (1988) 1–4. https://doi.org/10.1016/0022-4596(88)90045-X.

[38] D.X. Li, S. Hovmöller, The crystal structure of $Na_3Nb_{12}O_{31}F$ determined by HREM and image processing, Journal of Solid State Chemistry. 73 (1988) 5–10. https://doi.org/10.1016/0022-4596(88)90046-1.

[39] E. Boivin, F. Pourpoint, S. Saitzek, P. Simon, P. Roussel, H. Kabbour, An unusual O^{2-}/F^- distribution in the new pyrochlore oxyfluorides: $Na_2B_2O_5F_2$ (B = Nb, Ta), Chem. Commun. 58 (2022) 2391–2394. https://doi.org/10.1039/D1CC06760E.

[40] M. Vlasse, J.-P. Chaminade, J.-C. Massies, M. Pouchard, Structure de l'oxyfluorure de tantale et de sodium $Na_2Ta_2O_5F_2\beta$, Journal of Solid State Chemistry. 12 (1975) 102–109. https://doi.org/10.1016/0022-4596(75)90184-X.

[41] J.B. Goodenough, H.Y.-P. Hong, J.A. Kafalas, Fast Na^+-ion transport in skeleton structures, Materials Research Bulletin. 11 (1976) 203–220. https://doi.org/10.1016/0025-5408(76)90077-5.

[42] J.-P. Chaminade, M. Pouchard, P. Hagenmuller, Tantalates et oxyfluorotantalates de sodium, Revue de Chimie Minérale. 9 (1972) 381–402.

[43] J.-P. Chaminade, M. Pouchard, Cristallochimie des composés oxygénés, oxyfluorés et fluorés du tantale et des alcalins ou de l'argent, Annales de Chimie. 10 (1975) 75–99.

[44] S. Andersson, J. Galy, The crystal structure of $NaNbO_2F_2$, Acta Crystallogr B Struct Sci. 25 (1969) 847–850. https://doi.org/10.1107/S056774086900313X.

[45] I.D. Brown, D. Altermatt, Bond-valence parameters obtained from a systematic analysis of the Inorganic Crystal Structure Database, Acta Crystallographica Section B Structural Science. 41 (1985) 244–247. https://doi.org/10.1107/S0108768185002063.

[46] N.E. Brese, M. O'Keeffe, Bond-valence parameters for solids, Acta Crystallographica Section B Structural Science. 47 (1991) 192–197. https://doi.org/10.1107/S0108768190011041.

[47] B.M. Fung, A.K. Khitrin, K. Ermolaev, An Improved Broadband Decoupling Sequence for Liquid Crystals and Solids, Journal of Magnetic Resonance. 142 (2000) 97–101. https://doi.org/10.1006/jmre.1999.1896.

[48] D. Massiot, F. Fayon, M. Capron, I. King, S. Le Calvé, B. Alonso, J.-O. Durand, B. Bujoli, Z. Gan, G. Hoatson, Modelling one- and two-dimensional solid-state NMR spectra: Modelling 1D and 2D solid-state NMR spectra, Magn. Reson. Chem. 40 (2002) 70–76. https://doi.org/10.1002/mrc.984.

[49] G. Kresse, J. Furthmüller, Efficiency of ab-initio total energy calculations for metals and semiconductors using a plane-wave basis set, Computational Materials Science. 6 (1996) 15–50. https://doi.org/10.1016/0927-0256(96)00008-0.

[50] G. Kresse, J. Furthmüller, Efficient iterative schemes for *ab initio* total-energy calculations using a plane-wave basis set, Phys. Rev. B. 54 (1996) 11169–11186. https://doi.org/10.1103/PhysRevB.54.11169.

[51] U. Haeberlen, In Advances in Magnetic Resonance, Suppl. 1; J. S. Waugh, Ed.; Academic Press. (1976).

[52] J.P. Perdew, K. Burke, M. Ernzerhof, Generalized Gradient Approximation Made Simple, Phys. Rev. Lett. 77 (1996) 3865–3868. https://doi.org/10.1103/PhysRevLett.77.3865.

[53] P.E. Blöchl, Projector augmented-wave method, Phys. Rev. B. 50 (1994) 17953–17979. https://doi.org/10.1103/PhysRevB.50.17953.

[54] G. Kresse, D. Joubert, From ultrasoft pseudopotentials to the projector augmented-wave method, Phys. Rev. B. 59 (1999) 1758–1775. https://doi.org/10.1103/PhysRevB.59.1758.

[55] C.J. Pickard, F. Mauri, All-electron magnetic response with pseudopotentials: NMR chemical shifts, Phys. Rev. B. 63 (2001) 245101. https://doi.org/10.1103/PhysRevB.63.245101.

[56] J.R. Yates, C.J. Pickard, F. Mauri, Calculation of NMR chemical shifts for extended systems using ultrasoft pseudopotentials, Phys. Rev. B. 76 (2007) 024401. https://doi.org/10.1103/PhysRevB.76.024401.

[57] M. Biswal, M. Body, C. Legein, G. Corbel, A. Sadoc, F. Boucher, Structural Investigation of α- and β-Sodium Hexafluoroarsenate, $NaAsF_6$, by Variable Temperature X-ray Powder Diffraction and Multinuclear Solid-State NMR, and DFT Calculations, J. Phys. Chem. C. 116 (2012) 11682–11693. https://doi.org/10.1021/jp3040727.

[58] V.T. Deshpande, Thermal expansion of sodium fluoride and sodium bromide, Acta Cryst. 14 (1961) 794–794. https://doi.org/10.1107/S0365110X61002357.

[59] H.M. Rietveld, A profile refinement method for nuclear and magnetic structures, J Appl Crystallogr. 2 (1969) 65–71. https://doi.org/10.1107/S0021889869006558.

[60] J. Rodriguez-Carvajal, MAGNETIC STRUCTURE DETERMINATION FROM POWDER DIFFRACTION USING THE PROGRAM *FullProf*, in: Applied Crystallography, WORLD SCIENTIFIC, Wisla, Poland, 2001: pp. 30–36. https://doi.org/10.1142/9789812811325_0005.

[61] C.R. Groom, I.J. Bruno, M.P. Lightfoot, S.C. Ward, The Cambridge Structural Database, Acta Crystallogr B Struct Sci Cryst Eng Mater. 72 (2016) 171–179. https://doi.org/10.1107/S2052520616003954.

[62] K. Momma, F. Izumi, *VESTA* : a three-dimensional visualization system for electronic and structural analysis, J Appl Crystallogr. 41 (2008) 653–658. https://doi.org/10.1107/S0021889808012016.

[63] R.M. Wood, G.J. Palenik, Bond Valence Sums in Coordination Chemistry. Sodium–Oxygen Complexes, Inorg. Chem. 38 (1999) 3926–3930. https://doi.org/10.1021/ic9903331.

[64] W.L. Roth, O. Muller, Study, selection, and preparation of solid cationic conductors. Final report, 13 November 1972--12 November 1973, General Electric Co., Schenectady, N.Y. (USA), 1974. https://www.osti.gov/biblio/5083602 (accessed August 21, 2023).

[65] A. Sadoc, M. Body, C. Legein, M. Biswal, F. Fayon, X. Rocquefelte, F. Boucher, NMR parameters in alkali, alkaline earth and rare earth fluorides from first principle calculations, Phys. Chem. Chem. Phys. 13 (2011) 18539. https://doi.org/10.1039/c1cp21253b.

[66] M. Biswal, M. Body, C. Legein, A. Sadoc, F. Boucher, NbF_5 and TaF_5: Assignment of ^{19}F NMR resonances and chemical bond analysis from GIPAW calculations, Journal of Solid State Chemistry. 207 (2013) 208–217. https://doi.org/10.1016/j.jssc.2013.09.001.

[67] M. Boča, A. Rakhmatullin, J. Mlynáriková, E. Hadzimová, Z. Vasková, M. Mičušík, Differences in XPS and solid state NMR spectral data and thermo-chemical properties of iso-structural compounds in the series $KTaF_6$, K_2TaF_7 and K_3TaF_8 and $KNbF_6$, K_2 NbF_7 and K_3NbF_8, Dalton Trans. 44 (2015) 17106–17117. https://doi.org/10.1039/C5DT02560E.

[68] D. Massiot, F. Fayon, M. Deschamps, S. Cadars, P. Florian, V. Montouillout, N. Pellerin, J. Hiet, A. Rakhmatullin, C. Bessada, Detection and use of small J couplings in solid state NMR experiments, Comptes Rendus Chimie. 13 (2010) 117–129. https://doi.org/10.1016/j.crci.2009.05.001.

[69] M. Murakami, Y. Noda, K. Takegoshi, Terminal and bridging fluorine ligands in TiF_4 as studied by ^{19}F NMR in solids, Solid State Nuclear Magnetic Resonance. 101 (2019) 82–88. https://doi.org/10.1016/j.ssnmr.2019.05.007.

[70] H. Bode, H. Von Döhren, Die Kristallstruktur des Kaliumhexafluoroniobats und des Kaliumhexafluorotantalats, Acta Cryst. 11 (1958) 80–82. https://doi.org/10.1107/S0365110X58000220.

[71] R.W. Berg, J.H. von Barner, E. Christensen, K. Nielsen, The Crystal Structure and IR and Raman Spectra of alpha-$CsNbF_6$, in: Progress in Molten Salt Chemistry 1, Prof. Niels J. Bjerrum Special Volume, Ed. R.W. Berg and H.A. Hjuler, Elsevier, n.d.: pp. 75–94. https://orbit.dtu.dk/en/publications/the-crystal-structure-and-ir-and-raman-spectra-of-alpha-csnbf6.

[72] S.D. Griesemer, L. Ward, C. Wolverton, High-throughput crystal structure solution using prototypes, Phys. Rev. Materials. 5 (2021) 105003. https://doi.org/10.1103/PhysRevMaterials.5.105003.

[73] Z. Gan, P. Gor'kov, T.A. Cross, A. Samoson, D. Massiot, Seeking Higher Resolution and Sensitivity for NMR of Quadrupolar Nuclei at Ultrahigh Magnetic Fields, J. Am. Chem. Soc. 124 (2002) 5634–5635. https://doi.org/10.1021/ja025849p.

[74] O.B. Lapina, D.F. Khabibulin, A.A. Shubin, V.V. Terskikh, Practical aspects of 51V and 93Nb solid-state NMR spectroscopy and applications to oxide materials, Progress in Nuclear Magnetic Resonance Spectroscopy. 53 (2008) 128–191. https://doi.org/10.1016/j.pnmrs.2007.12.001.

[75] L.-S. Du, R.W. Schurko, N. Kim, C.P. Grey, Solid-State ^{93}Nb, ^{19}F, and ^{113}Cd Nuclear Magnetic Resonance Study of Niobium Oxyfluorides: Characterization of Local Distortions and Oxygen/Fluorine Ordering, J. Phys. Chem. A. 106 (2002) 7876–7886. https://doi.org/10.1021/jp020457q.

[76] C. Martineau, M. Body, C. Legein, G. Silly, J.-Y. Buzaré, F. Fayon, Multinuclear High-Resolution NMR Study of Compounds from the Ternary System $NaF–CaF_2–AlF_3$: from Determination to Modeling of NMR Parameters, Inorganic Chemistry. 45 (2006) 10215–10223. https://doi.org/10.1021/ic061348j.

[77] G. Silly, C. Legein, J.Y. Buzaré, F. Calvayrac, Electric field gradients in fluoride crystalline powders: correlation of NMR measurements with ab initio calculations, Solid State Nuclear Magnetic Resonance. 25 (2004) 241–251. https://doi.org/10.1016/j.ssnmr.2003.09.001.

[78] W.H. Baur, The geometry of polyhedral distortions. Predictive relationships for the phosphate group, Acta Crystallogr B Struct Sci. 30 (1974) 1195–1215. https://doi.org/10.1107/S0567740874004560.

[79] K. Robinson, G.V. Gibbs, P.H. Ribbe, Quadratic Elongation: A Quantitative Measure of Distortion in Coordination Polyhedra, Science. 172 (1971) 567–570. https://doi.org/10.1126/science.172.3983.567.

II.2. Conclusion

In this chapter, the structure of $NaNbO_2F_2$ and $NaTaO_2F_2$ was thoroughly investigated combining XRPD, ^{19}F ssNMR, and high-field ssNMR of ^{23}Na and ^{93}Nb, and DFT calculations.

For each compound, the atomic positions in the experimental structure (ES) were optimized, and NMR parameters such as δ_{iso}, δ_{CSA}, η_{CSA}, C_Q, and η_Q were computed for both ES and the structure with optimized positions (APO). Comparison of these parameters with experimental data revealed the greater accuracy of the APO model over the ES one. Additionally, these structural models allowed for a precise assessment their structural features, revealing that $NaNbO_2F_2$ experienced second-order Jahn-Teller distortions, explaining the significant difference of cell parameters *a* and *c*, bond lengths M–O1 and angles O1–M–O1 from those of $NaTaO_2F_2$. Using VT XRPD, the observed low amplitude endothermic event was confirmed by the evolution against temperature of the cell parameters. An extensive analysis of structural parameters at different temperatures unveiled distinct trends between the two compounds. Notably, $NaTaO_2F_2$ displayed significant alterations in the angles between polyhedra, while $NaNbO_2F_2$ exhibited substantial variations in bond lengths.

The multimodal approach described in **Chapter I** effectively captured the ordered structure of these oxyfluorides. Subsequently, the application of this approach to oxyfluorides with a higher level of structural complexity is discussed in the following chapter, investigating O/F ordering within oxyfluorides with disordered average structures.

Chapter III

Oxyfluorides Exhibiting Preferential O/F Ordering

III.1. Introduction

In the preceding chapter, NMR parameters were modeled, novel ^{19}F σ_{iso}–δ_{iso} correlations were introduced, and a thorough analysis of the thermal behavior was conducted for the ordered oxyfluorides $NaNbO_2F_2$ and $NaTaO_2F_2$. The structure of these oxyfluorides contain exclusively *cis*-MO_4F_2 octahedra, a rarity in the broad oxyfluoride class of compounds. Most inorganic oxyfluorides, due to the similar ionic radii of O^{2-} and F^- ions, exhibit mixed anion crystallographic site occupancies, leading to a combination of multiple heteroleptic polyhedral units. As discussed in the first section of the **General Introduction**, oxyfluorides with structures comprised of heteroleptic polyhedral units, where anions are arranged in a disordered fashion in both short- and long-range structures, exhibit a decrease in the desired physicochemical properties. However, some oxyfluorides, while disordered in the long-range structure, may exhibit short-range O/F order and even "*O/F correlated disorder*". Understanding the underlying factors that help preventing complete randomness of O/F arrangement, thereby facilitates the engineering of new oxyfluorides with tailored physicochemical properties.

In this context, this chapter comprises two sections, both addressing oxyfluorides exhibiting O/F local order. In the first section, The multimodal approach described previously is applied to model O/F correlated disorder in niobium and tantalum oxytrifluorides, MOF_3, and their hydroxylated phases $MOF_{3-x}(OH)_x$ (M = Nb, Ta). Similarly, in the second section, we explore short-range O/F ordering in the Hexagonal-Tungsten-Bronze phase of $TiOF_2$, noted HTB-$TiOF_2$.

III.2. Structural modeling of O/F correlated disorder in $TaOF_3$ and $NbOF_{3-x}(OH)_x$ by coupling solid-state NMR and DFT calculations

III.2.1. Introduction

In this section, we present the structural modeling of MOF_3 oxyfluorides by combining PXRD, ssNMR spectroscopy and DFT calculations. The resonance assignments of ^{19}F NMR spectra have been revised and the occupancy rates of the anionic crystallographic sites have been reevaluated. Additionally, new ^{19}F σ_{iso}–δ_{iso} correlations from the two binary pentafluorides NbF_5 and TaF_5 were established using DFT-D3 and GIPAW approach to calculate σ_{iso} values. We demonstrate that the exclusive presence of *cis*-MO_2F_4 octahedra results in O/F correlated disorder that is defined by one-dimensional –F–M–O–M– strings along <100> and <010> directions. Taking into account these characteristics and 2×2×1 supercells, there are ten possible models describing short-range O/F ordering in these MOF_3 oxyfluorides. Moreover, the hydroxylated phase of niobium oxyfluoride, $NbOF_{3-x}(OH)_x$, is modeled by generating new supercells that incorporate OH groups. Strong and weak O−H···F bonds are formed in these new supercells, and their effect on ^{19}F δ_{iso} values is studied in-depth.

Inorganic Chemistry

pubs.acs.org/IC

Article

Structural Modeling of O/F Correlated Disorder in $TaOF_3$ and $NbOF_{3-x}(OH)_x$ by Coupling Solid-State NMR and DFT Calculations

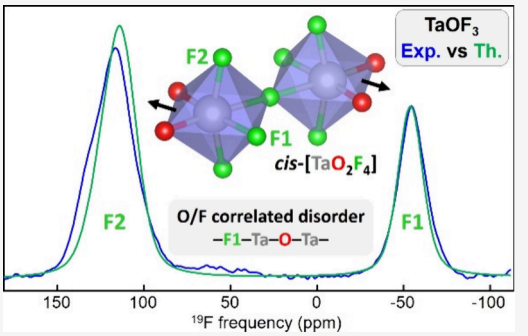
Ouail Zakary,* Monique Body,* Thibault Charpentier, Vincent Sarou-Kanian, and Christophe Legein

Cite This: *Inorg. Chem.* 2023, 62, 16627−16640

Read Online

ACCESS | Metrics & More | Article Recommendations | Supporting Information

ABSTRACT: The structure of MOF_3 (M = Nb, Ta) compounds was precisely modeled by combining powder X-ray diffraction, solid-state NMR spectroscopy, and semiempirical dispersion-corrected DFT calculations. It consists of stacked $_\infty(MOF_3)$ layers along the $\vec{c}$ direction formed by heteroleptic corner-connected MX_6 (X = O, F) octahedra. ^{19}F NMR resonance assignments and occupancy rates of the anionic crystallographic sites have been revised. The bridging site is shared equally by the anions, and the terminal site is occupied by F only. An O/F correlated disorder is expected since *cis*-MO_2F_4 octahedra are favored, resulting in one-dimensional −F−M−O−M− strings along the <100> and <010> directions. Ten different 2 × 2 × 1 supercells per compound, fulfilling these characteristics, were built. Using DFT calculations and the GIPAW approach, the supercells were relaxed and the ^{19}F isotropic chemical shift values were determined. The agreement between the experimental and calculated ^{19}F spectra is excellent for $TaOF_3$. The ^1H and ^{19}F experimental NMR spectra revealed that some of the bridging F atoms are substituted by OH groups, especially in $NbOF_3$. New supercells involving OH groups were generated. Remarkably, the best agreement is obtained for the supercells with the composition closest to that estimated from the ^{19}F NMR spectra, i.e., $NbOF_{2.85}(OH)_{0.15}$.



Downloaded via BIBCNRS INC on October 9, 2023 at 13:26:58 (UTC).
See https://pubs.acs.org/sharingguidelines for options on how to legitimately share published articles.

1. INTRODUCTION

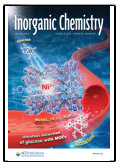
Heteroanionic materials, such as oxyhalides, offer opportunities for developing new materials with targeted functionalities.[1] Understanding their properties requires complete structural characterization. When these materials contain anions with similar X-ray or neutron scattering factors, such as oxides and fluorides, diffraction data alone are often insufficient to fully predict the anionic substructure. In these cases, if the anions are well-ordered, then a complete structural model may be proposed by combining long-range diffraction data with bond valence sum analysis. However, for those in which the different anions have joint occupancy of equivalent crystallographic sites, the structure cannot be fully described using a single-unit cell, even if it does not necessarily imply a random distribution of the anions. Indeed, between the limits of fully ordered and randomly disordered anions, there are many cases of intermediate anion orders with local clustering or extended correlations that may give rise to nonrandom site occupancies in the averaged crystal structure.[1,2]

Pentavalent (Nb,Ta)-based inorganic oxyfluorides represent a rich family of compounds,[3] synthesized and structurally characterized from the 1950s to the 2000s, including NbO_2F,[4−7] TaO_2F,[4,8] Nb_3O_7F,[5,9,10] Ta_3O_7F,[8,11] $Nb_5O_{12}F$,[9] $Nb_{17}O_{42}F$ and $Nb_{31}O_{77}F$,[12,13] $Nb_3O_5F_5$,[14] and $NbOF_3$ and $TaOF_3$.[15] They exhibit interesting physical properties such as photocatalytic activity (MO_2F (M = Nb,[16,17] Ta[18,19]) and M_3O_7F (M = Ta,[19] Nb[17,20,21])), electrochromism (NbO_2F),[22] almost-zero thermal expansion (TaO_2F),[23−25] and Li^+ intercalation (NbO_2F,[7,26,27] Nb_3O_7F[27,28]). Except in $Nb_{17}O_{42}F$[13] and MOF_3 (M = Nb, Ta)[15] crystal structures, O^{2-} and F^- are randomly distributed on all anion sites.[4,6,7,9−11,13,14] In $Nb_{17}O_{42}F$, O^{2-} and F^- are randomly distributed on only two of the anion sites, and in MOF_3, O^{2-} and F^- are preferentially distributed.

In disordered oxyfluorides, the short-range structures must deviate from the average crystal structures to accommodate the different M−O and M−F bond lengths. This has been indeed shown for MO_2F (M = Nb, Ta) and $Nb_3O_5F_5$ in four studies using various techniques: electron diffraction study of NbO_2F[29] and $Nb_3O_5F_5$[30] and variable-temperature neutron diffraction[23] and total X-ray scattering[25] studies of TaO_2F.

NbO_2F and TaO_2F both adopt an average cubic ReO_3-type structure. Brink et al.[29] have shown the coexistence in NbO_2F of (i) uncorrelated with each other one-dimensional O/F-ordered strings of atoms, −Nb−O−Nb−O−Nb−F−, with significant displacements of Nb from the ideal cation site, along the three ⟨001⟩ directions, and (ii) correlated rigid unit

Received: August 15, 2023
Published: September 25, 2023



© 2023 American Chemical Society

model (RUM) rotation of NbX_6 octahedra. It was suggested that the high transverse anisotropic displacement parameters, evidenced in TaO_2F, likely result from the static tilting of the TaO_4F_2 octahedra and Ta−(O/F)−Ta angles inferior to 180°.[23] In addition, Morelock et al.[25] demonstrated that a cubic 3 × 3 × 3 supercell model featuring −Ta−O−Ta−O−Ta−F− chains along the three ⟨001⟩ directions, with different Ta−O and Ta−F distances and O/F off-axis displacements, gave much better agreement with PDFs. Finally, the structural modeling of NbO_2F and TaO_2F by DFT geometry-optimized supercells, supported by the very good agreement between experimental and calculated ^{19}F δ_{iso} values, leads to realistic disordered structures.[31]

$Nb_3O_5F_5$[14] is the $n = 3$ member of an $Nb_nO_{2n-1}F_{n+2}$ ($1 \leq n \leq \infty$) homologous series of oxyfluoride compounds. Their average structure consists of two-dimensional slabs regularly stacked along the c direction and shifted one from another by $(1/2\ a + 1/2\ b)$. The thickness of each slab is formed by octahedral layers of corner-linked $Nb(O,F)_6$ octahedra. The continuous planes of diffuse intensity observed by electron diffraction imply the existence of strings of ordered oxygen and fluorine atoms for equatorial anion sites along [100] and [010] albeit without correlation from one such string to the next, and octahedral rotation RUM modes of distortion, analogous to those observed in NbO_2F.[30] Additionally, a bond valence sum (BVS) argument has been used to derive a plausible site occupation model for the remaining apical and median anion sites.

MOF_3 (M = Nb, Ta), the $n = 1$ members of the $M_nO_{2n-1}F_{n+2}$ series, then adopts the SnF_4-type structure (tetragonal system, SG: $I4/mmm$ (139)). The slabs consist of one octahedral layer formed by $MX1_{4/2}X2_2$ corner-linked octahedra and are stacked, via van der Waals (vdW) interactions, along the $\vec{c}$ direction. According to Rietveld refinements of the powder X-ray diffraction (PXRD) data, O and F atoms are distributed on both the bridging (X1) and terminal (X2) sites with site occupancies significantly different for the two compounds: 0.725 F/0.275 O for X1 and 0.775 F/0.225 O for X2 in $NbOF_3$ and 0.90 F/0.10 O for X1 and 0.60 F/0.40 O for X2 in $TaOF_3$.[15] Furthermore, based on BVS calculations,[32,33] the authors conclude that F atoms should preferentially occupy the X2 site for both compounds. In contrast, their analysis of the ^{19}F NMR spectrum of $TaOF_3$ led them to conclude that the X2 site is preferentially occupied by O atoms. On the other hand, and in agreement with previous BVS calculations, Brink et al. predict that, in $NbOF_3$, the apical (terminal) X2 anion site is overwhelmingly occupied by F rather than O (0.523 F/0.477 O for X1 and 0.977 F/0.023 O for X2) along with a RUM rotation angle equal to 7.8°.[30]

To capture structural features of complex materials on various length scales and generate realistic models, the combination of complementary quantitative experimental measurements is crucial.[34] Both intermediate-range chemical disorder and short-range geometrical disorder give rise in local spectroscopies such as NMR to distributions of resonance frequencies. The prediction of the spectroscopic responses by means of electronic structure calculations therefore plays an essential role not only to assign the different spectral contributions but also to understand the structural origins of the experimental parameter distributions.[35−39] This has been successfully exploited in numerous studies of disordered inorganic crystalline materials by coupling solid-state NMR and DFT calculations on supercells.[31,40−62]

Herein, we describe the structural modeling of the $NbOF_3$ and $TaOF_3$. Based on BVS calculations,[33] and on experimental δ_{iso} and relative intensity values extracted from the ^{19}F NMR spectra, assignment of the resonances and occupancy rates of the two anion crystallographic sites has been revised.

The average structures issued from PXRD refinements were used to construct 2 × 2 × 1 supercells fulfilling the expected O/F correlated disorder. Three arrangements of O and F in the $(\vec{a},\vec{b})$ planes are possible, and combining them results in 10 possible models for each compound. All models were geometry optimized, and magnetic shielding values were calculated using the GIPAW[63,64] approach, converted to chemical shifts and then compared to the experimental data. Despite the MOF_3 compounds being prepared using solid-state synthesis, the ^1H and ^{19}F experimental NMR spectra revealed that some of the bridging F1 atoms are substituted by OH groups, leading to the general formulation $MOF_{1-x}(OH)_xF_2$. Due to the higher OH group content in $NbOF_3$, a satisfactory agreement between experimental and calculated ^{19}F spectra could not be obtained without introducing OH groups in the models. Then, new models were built considering different OH substitution rates and their influence on the calculated ^1H and ^{19}F spectra is evidenced.

2. EXPERIMENTAL DETAILS

2.1. Synthesis. $NbOF_3$ has been known since the second half of the nineteenth century.[65] A hundred years later, its presence as a byproduct was mentioned in two studies on NbO_2F[66] and NbF_3[67] and then in the gas state as a product of the decomposition of NbO_2F.[5] MOF_3 (M = Nb, Ta) have been previously synthesized by Nieder-Vahrenholz and Schäfer,[68] by reaction of MF_5 with oxide glass or M_2O_5 and by Köhler et al.[15] by reaction of MF_5 with MO_2F. The aqueous solution synthesis proposed by Frevel and Rinn,[4] which was used by Köhler et al., leads to compounds that both contain hydroxyl defects and metal vacancies.[31,69] Consequently, in the present work, MO_2F was prepared by solid-state synthesis from a mixture of MF_5 (Alfa Aesar, 99.9 and 99% for TaF_5 and NbF_5, respectively) and M_2O_5 (Alfa Aesar, 99.85 and 99.9% for Ta_2O_5 and Nb_2O_5, respectively) with an excess of MF_5 (5 and 10% for NbF_5 and TaF_5, respectively) relative to the ideal 2:1 molar ratio. M_2O_5 compounds were dried under secondary vacuum at 150 °C for 9 h with heating and cooling rates of 2 °C·min^{-1}, and then kept under a nitrogen atmosphere inside a glovebox before use. Considering the moisture sensitivity of MF_5, the steps of weighing, mixing, and grinding were carried under a nitrogen atmosphere using a glovebox. The mixtures were then put inside platinum tubes, sealed, and heated up to 210 °C for 18 h with a heating rate of 5 °C·min^{-1} and then quenched in water at room temperature. MOF_3 was prepared from a mixture of MF_5 and MO_2F. The steps of weighing, mixing, and grinding were carried out under a nitrogen atmosphere inside a glovebox. The mixtures were then loaded in platinum tubes, sealed, and heated at 210 °C for 18 h with heating and cooling rates of 5 °C·min^{-1}. An excess of 10% MF_5 relative to the molar 1:1 ratio is required to avoid the presence of unreacted MO_2F. The final products are sensitive to moisture.

2.2. Characterization Techniques. *2.2.1. PXRD.* The PXRD patterns were recorded at room temperature with a PANalytical Empyrean diffractometer equipped with a PIXcel1D X-ray detector using monochromatic Cu K_α radiation (λ = 1.5406 Å). The samples were loaded in a domed sample holder using a glovebox under a nitrogen atmosphere. The patterns were measured in a 2θ range of

https://doi.org/10.1021/acs.inorgchem.3c02844
Inorg. Chem. 2023, 62, 16627−16640

5° to ∼120° with a 0.0131° step size. The recording time was approximately 6 h.

2.2.2. Solid-State NMR Spectroscopy. Magic angle spinning (MAS) NMR spectra of ^{19}F and ^{1}H ($I = \frac{1}{2}$) were recorded with a Bruker Avance III spectrometer functioning at 4.7 T (^{19}F and ^{1}H Larmor frequencies of 188.3 and 200 MHz, respectively) using a 1.3 mm CP-MAS probe head. The Hahn echo sequence was used with an interpulse delay of one rotor period and a recycle delay of 10 and 5 s for ^{19}F and ^{1}H, respectively. For both nuclei, the 90° pulse was set to 1.5 μs, corresponding to a 167 kHz RF field. ^{19}F and ^{1}H spectra are referenced to $CFCl_3$ and tetramethylsilane, respectively. The ^{19}F chemical shift anisotropies were determined from the spinning sideband intensities according to Herzfeld and Berger.[70] ^{19}F "infinite spinning frequency" MAS spectra were obtained from the full projection (onto the frequency dimension) of a two-dimensional one-pulse (TOP) spectrum issued from the stacking of subspectra shifted by the spinning frequency from the conventional MAS spectrum.[71] These "infinite spinning frequency" isotropic spectra allow a direct quantification of the inequivalent fluorine sites (environments) in the structure and represent an alternative to simulation of the spinning sideband manifolds. The reconstructions of the one-dimensional MAS (including spinning sidebands) and the TOP processing spectra were performed with the DMFit software.[72]

3. AB INITIO CALCULATIONS

3.1. Definitions. The calculated magnetic shielding parameters are defined by the Haeberlen convention.[73] The isotropic magnetic shielding (σ_{iso}), the anisotropy of the magnetic shielding (σ_{CSA}), and the asymmetry parameter (η_{CSA}) are respectively defined as $\sigma_{iso} = (\sigma_{xx} + \sigma_{yy} + \sigma_{zz})/3$, $\sigma_{CSA} = \sigma_{zz} - \sigma_{iso}$, and $\eta_{CSA} = (\sigma_{yy} - \sigma_{xx})/\sigma_{CSA}$, with the magnetic shielding tensor components σ_{ii} defined in the sequence $|\sigma_{zz} - \sigma_{iso}| \geq |\sigma_{xx} - \sigma_{iso}| \geq |\sigma_{yy} - \sigma_{iso}|$. The chemical shift tensor is also defined by three parameters, the isotropic chemical shift (δ_{iso}), the anisotropy of the chemical shift (δ_{CSA}), and the asymmetry parameter (η_{CSA}), which are given by $\delta_{iso} = (\delta_{xx} + \delta_{yy} + \delta_{zz})/3$, $\delta_{CSA} = \delta_{zz} - \delta_{iso}$, and $\eta_{CSA} = (\delta_{yy} - \delta_{xx})/\delta_{CSA}$, with the chemical shift tensor components defined in the sequence $|\delta_{zz} - \delta_{iso}| \geq |\delta_{xx} - \delta_{iso}| \geq |\delta_{yy} - \delta_{iso}|$. The relation between the isotropic magnetic shielding and the isotropic chemical shift is $\delta_{iso} \approx \sigma_{ref} - \sigma_{iso}$.

3.2. DFT Calculations. Solid-state DFT calculations with periodic boundary conditions were performed on 2 × 2 × 1 supercells (from 40 to 42 atoms). The ground-state electronic structure was obtained by the generalized gradient approximation (GGA) using the Perdew–Burke–Ernzerhof (PBE) functional (GGA-PBE).[74] The atomic position optimization (APO) and the full optimization of the supercells (FO, relaxation of atomic positions and supercell parameters) were performed using VASP (6.2.1 version).[75,76] The projector augmented wave (PAW)[77,78] potentials used for Ta, Nb, F, O, and H are, respectively, Ta_sv_GW ($5s^2$ $5p^6$ $6s^2$ $5d^3$), Nb_sv_GW ($4s^2$ $4p^6$ $5s^1$ $4d^4$), F_GW ($2s^2$ $2p^5$), O_s_GW ($2s^2$ $2p^6$), and H_GW ($1s^1$). The wave functions were expanded on a plane-wave basis set with a 550 eV kinetic energy cutoff and (3 × 3 × 3) shifted Monkhorst–Pack *k*-point mesh. The total energy was converged up to a change below 10^{-8} eV. Terminal F from different $_{\infty}(MOF_3)$ layers are weakly bonded to each other via vdW interactions. Since this interaction is not included in the standard DFT-GGA algorithm, zero-damping semiempirical dispersion correction of Grimme et al.[79] called DFT-D3 was included to the calculations. The damping function parameters (α_6, α_8, s_6, s_8, $s_{R,6}$, and $s_{R,8}$) were kept at the default values as well as the cutoff radius for pair interactions and the cutoff coordination radius. For both compounds, two methods of relaxation were performed, APO and FO, respectively, referred to in the following as APO_DFT-D3 and FO_DFT-D3.

The GIPAW approach[63,64] was used to calculate the magnetic shielding for the different nuclei, using VASP.[75,76] The PAW potentials, plane-wave energy cutoff, and shifted Monkhorst–Pack *k*-point mesh were set to the same values as for the geometry optimization. NMR parameter calculations were performed on the APO_DFT-D3 and FO_DFT-D3 supercells.

For ^{19}F in inorganic fluorides, several linear relationships between calculated σ_{iso} values, using the GIPAW approach, and experimental δ_{iso} values, $\delta_{iso} = \sigma_{ref} - a\ \sigma_{iso}$, have been established to convert calculated σ_{iso} values into "calculated" δ_{iso} values. The absolute values of the slopes depend on the metal atom(s) constituting the fluoride(s) and are often significantly less than 1.[80−92] Then, in this paper, distinct $\delta_{iso} = \sigma_{ref} - a\ \sigma_{iso}$, equations determined by linearly correlating the calculated σ_{iso} values to the experimental δ_{iso} values[83] of NbF_5 and TaF_5, are used for $NbOF_3$ and $TaOF_3$, respectively, as previously done for NbO_2F and TaO_2F.[31] Since the previous $\delta_{iso} = \sigma_{ref} - a\ \sigma_{iso}$ equations[83] have been established using CASTEP,[93,94] to ensure the consistency of our calculations, new linear regressions were determined using VASP and keeping the conditions used for calculations on MOF_3 supercells. These linear regressions are discussed in further detail later on in the paper (see Section 4.5). The ^{1}H δ_{iso} calculated values were deduced using the equation: δ_{iso} (ppm) = $-\sigma_{iso} + 31$.[95]

4. RESULTS AND DISCUSSION

4.1. Structural Characterization: Solid-State NMR. For (oxy)fluorides, ^{19}F solid-state NMR is the ideal technique for determining the proportion of fluorine atoms in each crystallographic site (in each different environment) through the relative intensities of the NMR lines. The ^{19}F MAS NMR spectra of $NbOF_3$ and $TaOF_3$ are shown in Figure 1. Their fits, those of the corresponding ^{19}F "infinite spinning frequency" isotropic spectra, and the corresponding fit parameters are reported in the SI (Figures S1−S4 and Tables S1−S4). The parameters relevant to the discussion are gathered in Table 1. Both ^{19}F MAS NMR spectra present two main resonances, one more intense with higher δ_{iso} and δ_{CSA} values and one less intense with lower δ_{iso} and δ_{CSA} values, as well as additional low-intensity resonances located in-between these two main resonances but closer to the more intense. For both compounds, the less intense ^{19}F main resonance is assigned to the X1 (bridging) anion site, and the more intense ^{19}F main resonance, as well as the additional low-intensity resonances, are assigned to the X2 (terminal) anion site (Table 1). These assignments are the opposite of those published previously.[15] However, they are supported by the evolution of the ^{19}F δ_{iso} values with the number of surrounding cations. For a given cation, the higher the coordination number, the lower the ^{19}F δ_{iso} values,[31,96] as observed, for instance, in NbF_5 (bridging: −42 ppm; terminal: 193 to 268 ppm), TaF_5 (bridging: −70 ppm; terminal: 106 to 174 ppm),[83] and TiF_4 (bridging: −2 to 30 ppm; terminal: 422 to 479 ppm).[90] These assignment are also supported by the higher δ_{CSA} values of the resonances assigned to the terminal F atoms, as also observed for instance in NbF_5, TaF_5,[83] and TiF_4,[90] the environment of a

https://doi.org/10.1021/acs.inorgchem.3c02844
Inorg. Chem. 2023, 62, 16627−16640

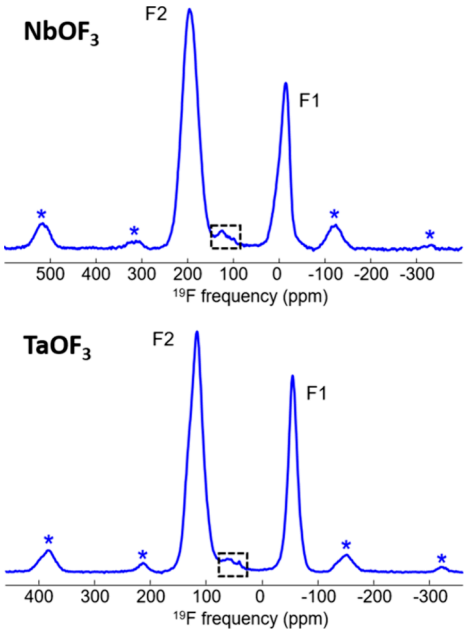


Figure 1. ^{19}F MAS NMR (4.7 T) spectra of $NbOF_3$ (60 kHz) and $TaOF_3$ (50 kHz). The stars indicate spinning sidebands. The main contributions are assigned, and additional resonances, assigned to F2 site, are outlined by the dashed rectangles.

Table 1. Compound, Weighted Average Experimental ^{19}F δ_{iso}, δ_{CSA}, and η_{CSA} Values ($<\delta_{iso,exp}>$, $<\delta_{CSA,exp}>$, ppm, and $<\eta_{CSA,exp}>$), Relative Intensities (I, %), and Corresponding Assignments

compound	$<\delta_{iso,exp}>$	$<\delta_{CSA,exp}>$	$<\eta_{CSA,exp}>$	I	assignment
$NbOF_3$	−8.2	−162.4	0.51	30.4	F1
	124.7	n. a.	n. a.	3.2	H-bonded F2
	195.1	−291.6	0.72	66.4	F2
$TaOF_3$	−54.9	−170.0	0.50	32.3	F1
	60.6	n. a.	n. a.	4.0	H-bonded F2
	118.1	−283.4	0.10	63.7	F2

terminal F atom being more anisotropic than the environment of a bridging F atom surrounded by two identical cations located approximately opposite each other.

If we assume that the X2 site is fully occupied by F, and thus that the X1 site is half occupied by F and O atoms, the relative intensities of the corresponding NMR lines should be 2/3 for the terminal F2 NMR line and 1/3 for the bridging F1 one. $NbOF_3$ and $TaOF_3$ are moisture sensitive, the most likely hypothesis to explain that the relative intensities of the bridging F1 NMR lines are less than 1/3 (Table 1) is the substitution of a part of the F atoms of the bridging X1 site by OH groups.

To confirm this hypothesis, ^{1}H MAS NMR spectra of $NbOF_3$ and $TaOF_3$ were recorded (Figure 2) and reconstructed (Figures S5 and S6 and Tables S5 and S6). They show similar features with two main contributions, one with δ_{iso} values ranging from 1 to 5 ppm and the other with δ_{iso} values ranging from 8 to 13 ppm (Table 2). Both are assigned to OH groups coordinated by Nb(Ta) atoms, but the latter are H-bonded, as evidenced by their higher ^{1}H δ_{iso} value (for an X−H···Y hydrogen bond, the shorter the H···Y distance, the lower the ^{1}H magnetic shielding and the higher the ^{1}H chemical shift[97−99]). Equivalently, for an X−H···F

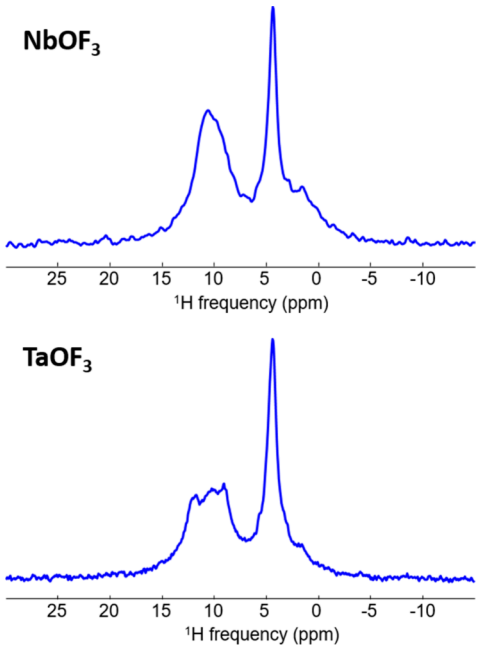


Figure 2. ^{1}H MAS NMR spectra of $NbOF_3$ (60 kHz) and $TaOF_3$ (50 kHz).

Table 2. Compound, Weighted Average Experimental ^{1}H δ_{iso} Values ($<\delta_{iso}>$, ppm), and Relative Intensities (I, %)

compound	$<\delta_{iso}>$	I
$NbOF_3$	3.2	44.6
	10.3	55.4
$TaOF_3$	4.4	55.0
	11.0	45.0

hydrogen bond, the shorter the H···F distance, the higher the ^{19}F magnetic shielding and the lower the ^{19}F chemical shift.[100] Therefore, the existence of intermediate NMR lines with lower ^{19}F δ_{iso} (higher σ_{iso}) values is explained by the formation of O−H···F2 bonds.

The substitution of F1 atoms by OH groups leads to the general formulation $MOF_{1-x}(OH)_xF_2$. From the relative intensities of the ^{19}F MAS NMR lines, the OH substitution rates (x) are estimated to be 0.15(2) and 0.05(1) for $NbOF_3$ and $TaOF_3$, respectively (Tables S7 and S8). Similarly to NbF_5 and TaF_5, $NbOF_3$ appears to be more hygroscopic than $TaOF_3$, resulting in a higher OH substitution rate for these niobium compounds.

4.2. Structural Characterization: XRPD. The crystal structures of $NbOF_3$ and $TaOF_3$, determined by Köhler et al. (*I4/mmm* space group (no. 139)),[15] have been revised. The recorded RT PXRD diagrams have been refined by using the Rietveld method[101] implemented in the FullProf software.[102] For both compounds, based on ^{19}F solid-state NMR, we assumed that the terminal X2 site is fully occupied by F atoms and that the bridging X1 site has an occupancy of 0.5 O and 0.5 F and we considered isotropic displacement parameters (IDPs) for all atoms. The cell parameters, atomic coordinates, and IDPs are gathered in Table 3. The observed, calculated, and intensity difference patterns and reliability factors are given as the SI (Figures S7 and S8 for $NbOF_3$ and $TaOF_3$, respectively).

Crystal structures were deposited via the joint CCDC/FIZ Karlsruhe deposition service. CSD[103] 2260474 and 2260475

https://doi.org/10.1021/acs.inorgchem.3c02844
Inorg. Chem. 2023, 62, 16627−16640

Table 3. Atom, Site Multiplicity and Wyckoff Symbol (Wyck.), Site Symmetry (Sym.), Atomic Coordinates (x, y, z), Site Occupancy Factor (sof), and Isotopic Displacement Parameters (U_{iso}, Å^2) in $NbOF_3$ ($a = b = 3.9739(1)$ Å, $c = 8.3612(2)$ Å) and $TaOF_3$ ($a = b = 3.9465(1)$ Å, $c = 8.4454(2)$ Å)

atom	Wyck.	Sym.	x	y	z	sof	U_{iso}
Nb	2a	4/*mmm*	0	0	0	1	0.05(8)
F1	4c	*mmm*	1/2	0	0	0.5	0.04(8)
O1	4c	*mmm*	1/2	0	0	0.5	0.04(8)
F2	4e	4*mm*	0	0	0.2175(2)	1	0.05(8)
Ta	2a	4/*mmm*	0	0	0	1	0.03(15)
F1	4c	*mmm*	1/2	0	0	0.5	0.04(15)
O1	4c	*mmm*	1/2	0	0	0.5	0.04(15)
F2	4e	4*mm*	0	0	0.2159(4)	1	0.04(15)

(deposition numbers) contain the supplementary crystallographic data for $NbOF_3$ and $TaOF_3$, respectively. These data can be obtained free of charge from FIZ Karlsruhe via www.cc dc.cam.ac.uk/structures.

The BVS calculations[32,33] (Table 4), despite slightly high bond valences for Nb and Ta, indicate quite clearly an occupation of the X1 sites by O and F and a preferential occupation of the X2 sites by F. Perspective views of the unit cell of $NbOF_3$ and of *cis*- and *trans*-NbO_2F_4 octahedra are presented in Figure 3a.

Table 4. Bond Valence Sum Values from the Experimental Structures (ES) and Average Bond Valence Sum Values (V_i) from the APO_DFT-D3 and FO_DFT-D3 Supercells of $NbOF_3$ and $TaOF_3$[a]

$NbOF_3$	V_i^{Nb}	V_i^{O1}	V_i^{F1}	V_i^{F2}
ES	5.385	1.629	1.458	1.149
APO_DFT-D3	5.176	2.131	1.101	0.972
FO_DFT-D3	5.183	2.142	1.099	0.971
$TaOF_3$	V_i^{Ta}	V_i^{O1}	V_i^{F1}	V_i^{F2}
ES	5.617	1.732	1.554	1.165
APO_DFT-D3	5.350	2.227	1.186	0.968
FO_DFT-D3	5.258	2.181	1.130	0.973

[a]The BVS values were obtained using the following values of R_0 parameters: 1.911, 1.920,[32] 1.87, and 1.88 Å[33] for Nb^{5+}/O^{2-}, Ta^{5+}/O^{2-}, Nb^{5+}/F, and Ta^{5+}/F^{-}, respectively, and $b = 0.37$ Å.

4.3. O/F Correlated Disorder. As mentioned in the introduction, O/F correlated disorder has been previously highlighted in $Nb_3O_5F_5$,[30] NbO_2F,[29,31] and TaO_2F[25,31] resulting in one-dimensional O/F-ordered strings of atoms and out-of-center displacement of metal cations. For $NbOF_3$, the presence of O/F correlated disorder in the $_\infty(MOF_3)$ layers, along <100> and <010> directions, has been predicted.[30] From our experimental results, in both MOF_3 compounds, the X1 site has an occupancy of 0.5 O and 0.5 F and the X2 site is occupied only by F leading to either *cis*- or *trans*-MO_2F_4 octahedra (Figure 3a). The former octahedral units are more favored, particularly when the cation is a d^0 transition metal. Indeed, having anions with similar Pearson hardness near each other maximizes the π-hybridization in the M-anion bonds by allowing atomic relaxations toward characteristic bond lengths (i.e., cation displacements toward the less electronegative anion).[2] This results in one-dimensional −F−M−O−M− chains along <100> and <010> directions.

4.4. Possible Models for $NbOF_3$ and $TaOF_3$ Using 2 × 2 × 1 Supercells. Considering a 2 × 2 × 1 supercell (Figure 3b), there are only three ways to construct a $_\infty(MOF_3)$ layer with *cis*-MO_2F_4 octahedra corner-connected by two O atoms and two F atoms (Figure 4a). Since each supercell consists of two stacked $_\infty(MOF_3)$ layers and excluding all symmetry equivalent combinations, 10 different 2 × 2 × 1 supercells have been built (Figure 4b). These 10 models were then geometry optimized. The structural characteristics of the 10 nonoptimized and APO_DFT-D3- and FO_DFT-D3-optimized supercells, for $NbOF_3$ and $TaOF_3$, are summarized in Tables 5 and 6 (details for each model are given as SI in Figure S9 and Tables S9−S22). For $NbOF_3$ and $TaOF_3$, each of the 10 APO_DFT-D3 and FO_DFT-D3 models exhibits similar structural characteristics.

When the supercells are fully optimized, the cell parameters a and b are more or less constant for $NbOF_3$ and increase for $TaOF_3$. For both, c decreases. The cell volume slightly decreases for $NbOF_3$ (1.2%) and remains almost constant for $TaOF_3$ (+0.2%), which seems to demonstrate the effectiveness of the dispersion correction. We observe, after APO and FO, atomic relaxations toward characteristic bond lengths, i.e., metal displacements toward oxygen, less electronegative than fluorine, as shown by the decrease of the average M−O1 (increase of the average M−F1) bond lengths (~0.1 Å, Table 5) and the increase of the average O1−M−O1 (decrease of

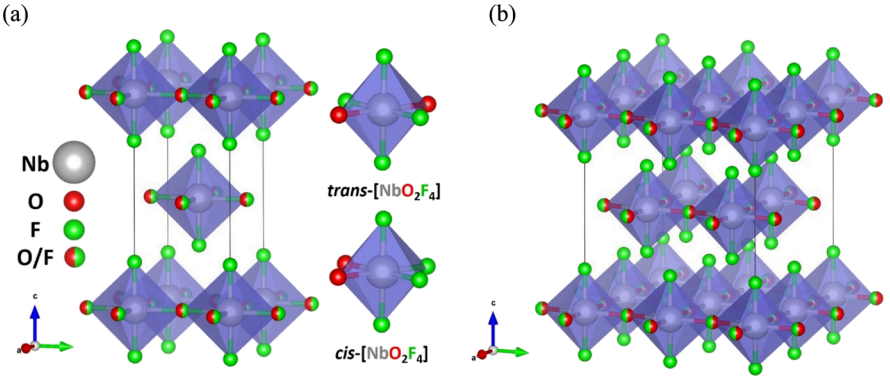


Figure 3. (a) Perspective views of the $NbOF_3$ unit cell (on the left) and of *cis*-and *trans*-NbO_2F_4 octahedra (on the right). (b) Perspective view of a 2 × 2 × 1 supercell. The NbO_2F_4 octahedra are displayed in purple.

https://doi.org/10.1021/acs.inorgchem.3c02844
Inorg. Chem. 2023, 62, 16627−16640

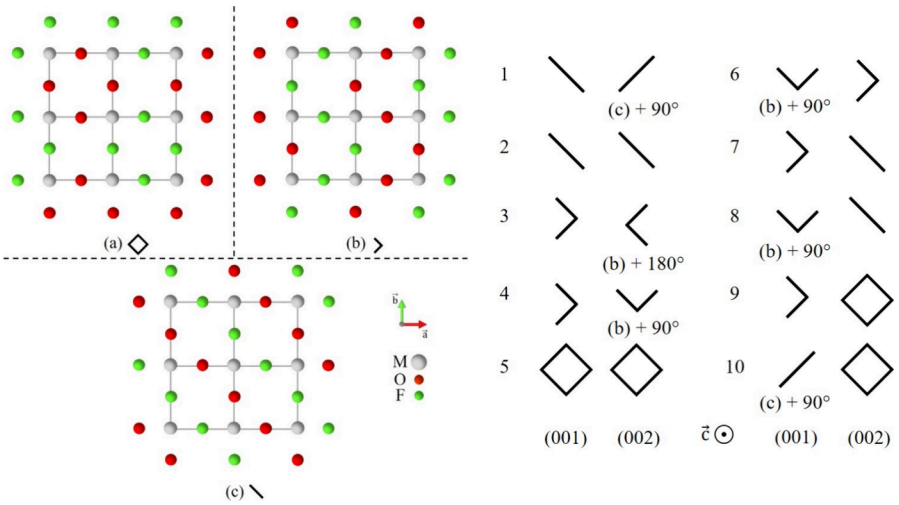


Figure 4. (Left) Representation of the three ways to construct a $_{\infty}(MOF_3)$ layer with *cis*-MO_2F_4 octahedra corner-connected by two O atoms and two F atoms, labeled as (a) diamond (◊), (b) zigzag (>), and (c) diagonal (\). (Right) Illustration of two successive ($\vec{a}$, $\vec{b}$) planes, (001) and (002), for each of the 10 constructed models. The rotational operation around $\vec{c}$ involved for five of the models is indicated.

Table 5. Average Cell Parameters (*a*, *b*, and *c*, Å), Average Supercell Volume (Å^3), and Average M−O1, M−F1, and M−F2 Bond Lengths (Å) from the 10 Non-Optimized (ES) and APO_DFT-D3- and FO_DFT-D3-Optimized Supercells of $NbOF_3$ and $TaOF_3$

supercell	*a*	*b*	*c*	*V*	M−O1	M−F1	M−F2
$NbOF_3$							
ES	7.948	7.948	8.361	528.2	1.987	1.987	1.819
APO_DFT-D3	7.948	7.948	8.361	528.2	1.888	2.092	1.881
FO_DFT-D3	7.945	7.944	8.266	521.7	1.886	2.093	1.881
$TaOF_3$							
ES	7.893	7.893	8.445	526.1	1.973	1.973	1.823
APO_DFT-D3	7.893	7.893	8.445	526.1	1.880	2.073	1.892
FO_DFT-D3	7.945	7.945	8.351	527.1	1.888	2.091	1.890

Table 6. Average X−M−X Angles (°) between Adjacent (X1−M−X1) and Opposite (F2−M−F2)) M−X Bonds and Average M−O1−M and M−F1−M Angles (°) of the 10 APO_DFT-D3- and 10 FO_DFT-D3-Optimized Supercells of $NbOF_3$ and $TaOF_3$

supercell	F1−M−F1	O1−M−O1	F2−M−F2	M−O1−M	M−F1−M
$NbOF_3$					
APO_DFT-D3	83.6	96.5	162.7	176.9	176.7
FO_DFT-D3	83.5	96.6	162.8	177.0	176.6
$TaOF_3$					
APO_DFT-D3	83.2	96.6	163.7	176.8	176.2
FO_DFT-D3	83.4	96.6	163.2	176.9	176.8

the average F1−M−F1) angles (~6°, Table 6 and Figure 5). The M−F2 bond lengths increase (~0.06 Å, Table 5) and the F2−M−F2 angles decrease (from 180 to ~ 163°, Table 6 and Figure 5). From the decrease of the F2−M−F2 angles, it can be estimated that in the average structure, the M−F2 bond lengths are underestimated by about 0.02 Å. $_{\infty}(MOF_3)$ layers are then getting closer in the optimized supercells since the decrease in angle values does not compensate for the increase in bond lengths. This is even more pronounced for the fully optimized supercells for which the cell parameters *c* are smaller.

After optimization, the values for bond lengths and bond angles not only deviate from the average values determined by diffraction but also are distributed, as expected in disordered compounds.

4.5. $\delta_{iso} = \sigma_{ref} - a\,\sigma_{iso}$ Equations for ^{19}F from NbF_5 and TaF_5. The equations used to convert the ^{19}F σ_{iso} values into δ_{iso} values were established from the two isomorph binary pentafluorides, NbF_5 and TaF_5. The calculations were done using the same conditions as for $NbOF_3$ and $TaOF_3$, i.e., on APO and FO structures, both including DFT-D3, for consistency and because NbF_5 and TaF_5 consist of tetrameric structural units $[M_4F_{20}]$ (M = Nb, Ta), built up from MF_6 octahedra linked to each other by corners, in a *cis*-configuration, and held together by vdW interactions. They seem perfectly suitable for establishing such predictive equations since they present several F crystallographic sites, including $NbOF_3$ and $TaOF_3$, bridging and terminal F atoms. The linear regressions between the calculated σ_{iso} values and experimental δ_{iso} values[83] of ^{19}F (Table S23) are reported in Figure 6. For NbF_5, the equations are δ_{iso} (ppm) = −1.031(6) σ_{iso} + 97.3(8) and δ_{iso} (ppm) = −1.034(17) σ_{iso} + 96.4(2.3) for APO_DFT-D3 and FO_DFT-D3, respectively. For TaF_5, the equations are δ_{iso} (ppm) = −0.968(15) σ_{iso} + 107.4(1.3) and δ_{iso} (ppm) = −0.968(7) σ_{iso} + 107.9(6) for APO_DFT-D3 and FO_DFT-D3, respectively. The slopes of the TaF_5 linear regressions, established using σ_{iso} values calculated with VASP, are closer to the theoretical −1 value in comparison to those (~−0.78 for APO structures)

https://doi.org/10.1021/acs.inorgchem.3c02844
Inorg. Chem. 2023, 62, 16627−16640

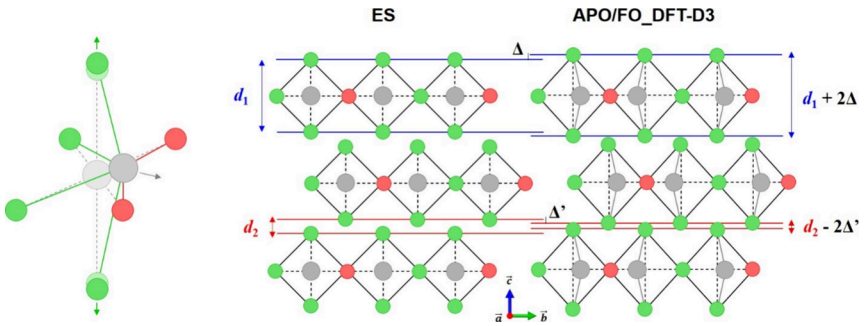


Figure 5. Illustration of the optimization effect on the MO_2F_4 octahedra (left) and on the thickness d_1 of the $_\infty(MOF_3)$ layers, as well as the distance d_2 between them (right). M, O, and F are represented in gray, red, and green, respectively.

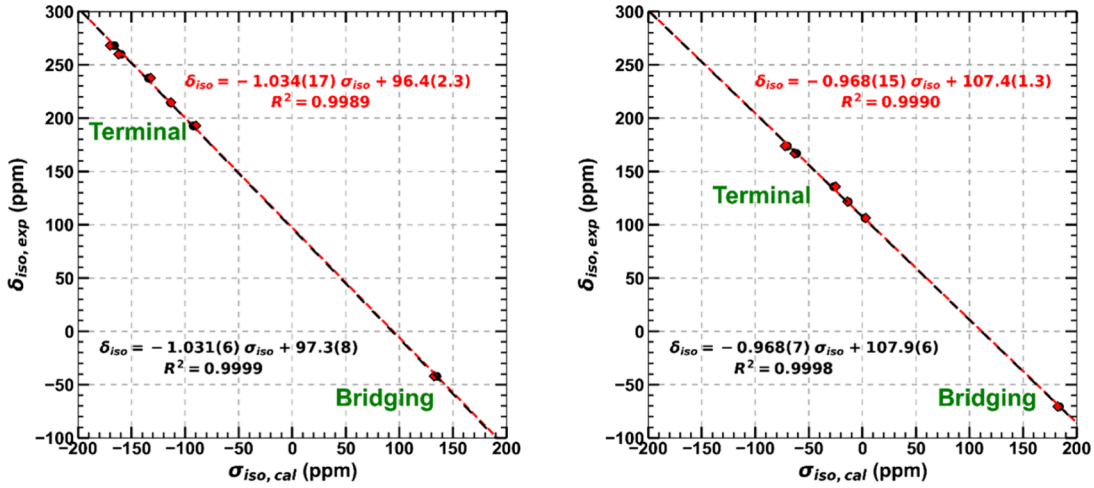


Figure 6. Calculated ^{19}F σ_{iso} values as a function of the experimental ^{19}F δ_{iso} values for NbF_5 (left) and TaF_5 (right). The red squares and the black dots correspond respectively to the values calculated from the FO_DFT-D3 and APO_DFT-D3 structures. The dashed red and black lines represent the linear regressions when considering the calculated σ_{iso} values from the FO_DFT-D3 and APO_DFT-D3 structures, respectively. Their equations are given in red and black, respectively.

Table 7. Average Calculated ^{19}F δ_{iso} (ppm), σ_{CSA} (ppm), and η_{CSA} Values for Each APO_DFT-D3- and FO_DFT-D3-Optimized Supercells of $NbOF_3$[a]

	APO_DFT-D3						FO_DFT-D3					
	F1			F2			F1			F2		
model	δ_{iso}	σ_{CSA}	η_{CSA}	δ_{iso}	σ_{CSA}	η_{CSA}	δ_{iso}	σ_{CSA}	η_{CSA}	δ_{iso}	σ_{CSA}	η_{CSA}
1	−17.6	147.6	0.71	213.9	330.7	0.12	−17.9	147.7	0.71	212.6	329.8	0.12
2	−17.5	143.3	0.91	209.1	330.1	0.03	−16.3	144.9	0.90	207.7	328.8	0.02
3	−14.0	141.7	0.79	211.5	327.7	0.29	−12.6	142.3	0.80	210.0	326.2	0.32
4	−18.1	139.9	0.79	215.5	331.4	0.12	−18.7	139.2	0.80	213.6	330.1	0.12
5	−7.0	151.2	0.91	212.8	332.2	0.06	−7.4	149.9	0.90	210.0	330.0	0.07
6	−17.3	141.4	0.85	211.0	331.0	0.08	−17.2	141.6	0.84	208.8	329.2	0.08
7	−17.4	144.9	0.79	211.6	330.7	0.08	−17.2	145.2	0.79	209.9	329.4	0.08
8	−18.0	143.7	0.73	215.6	331.0	0.11	−18.7	142.9	0.74	213.9	329.9	0.10
9	−8.6	147.2	0.79	210.7	327.3	0.25	−4.4	150.6	0.74	208.0	324.0	0.40
10	−12.2	150.6	0.78	213.7	331.4	0.08	−12.8	149.8	0.79	211.6	329.8	0.08

[a]The equations used to convert the calculated ^{19}F σ_{iso} values to calculated ^{19}F δ_{iso} values are those established from the APO_DFT-D3 and FO_DFT-D3 structures of NbF_5 (Figure 6).

established using σ_{iso} values calculated with CASTEP.[83] In contrast, the slopes of the NbF_5 linear regressions remain close whatever code is used to calculate the σ_{iso} values.

4.6. Theoretical ^{19}F Solid-State NMR Spectra of $NbOF_3$ and $TaOF_3$. The structural features of the APO_DFT-D3 and FO_DFT-D3 models being similar for each compound consistently, the calculated ^{19}F σ_{iso}, σ_{CSA}, and η_{CSA} values are similar as well (Tables S24−S35). Using the linear regression equations above (Figure 6), the calculated ^{19}F σ_{iso} values were converted into δ_{iso} values and the average δ_{iso}, σ_{CSA}, and η_{CSA} values from each model are gathered in Tables 7 and 8. The δ_{iso} values of the terminal F2 atoms decrease linearly as the F2 and M bond lengths increase (Figure S10).

https://doi.org/10.1021/acs.inorgchem.3c02844
Inorg. Chem. 2023, 62, 16627−16640

Table 8. Average Calculated ^{19}F δ_{iso}, σ_{CSA} (ppm), and η_{CSA} Values for Each APO_DFT-D3- and FO_DFT-D3-Optimized Supercells of $TaOF_3$[a]

	APO_DFT-D3						FO_DFT-D3					
	F1			F2			F1			F2		
model	$\delta_{iso,cal}$	σ_{CSA}	η_{CSA}	$\delta_{iso,cal}$	σ_{CSA}	η_{CSA}	$\delta_{iso,cal}$	σ_{CSA}	η_{CSA}	$\delta_{iso,cal}$	σ_{CSA}	η_{CSA}
1	−54.7	120.7	0.74	115.5	268.1	0.11	−53.8	123.2	0.75	119.6	272.6	0.11
2	−54.7	123.4	0.73	112.9	267.8	0.02	−52.8	125.4	0.79	116.8	272.4	0.00
3	−55.2	115.0	0.81	115.9	268.9	0.08	−54.2	117.7	0.84	119.2	272.7	0.08
4	−55.3	114.8	0.77	117.0	269.0	0.11	−54.7	117.7	0.79	120.3	272.9	0.11
5	−49.7	122.3	0.78	115.4	269.6	0.04	−48.6	123.5	0.87	118.1	272.8	0.05
6	−55.2	119.4	0.70	114.3	268.7	0.05	−53.8	120.8	0.78	117.6	272.6	0.05
7	−54.9	119.7	0.76	114.5	268.4	0.06	−53.5	122.3	0.78	118.1	272.6	0.06
8	−54.9	114.9	0.83	116.9	268.5	0.10	−54.3	117.8	0.83	120.5	272.7	0.10
9	−52.4	119.0	0.79	115.8	269.3	0.07	−51.4	121.4	0.83	118.8	272.8	0.07
10	−52.1	119.4	0.83	115.8	268.8	0.07	−51.0	122.8	0.84	119.0	272.7	0.07

[a]The equations used to convert the calculated ^{19}F σ_{iso} values into calculated ^{19}F δ_{iso} values are those established from the APO_DFT-D3 and FO_DFT-D3 structures of TaF_5 (Figure 6).

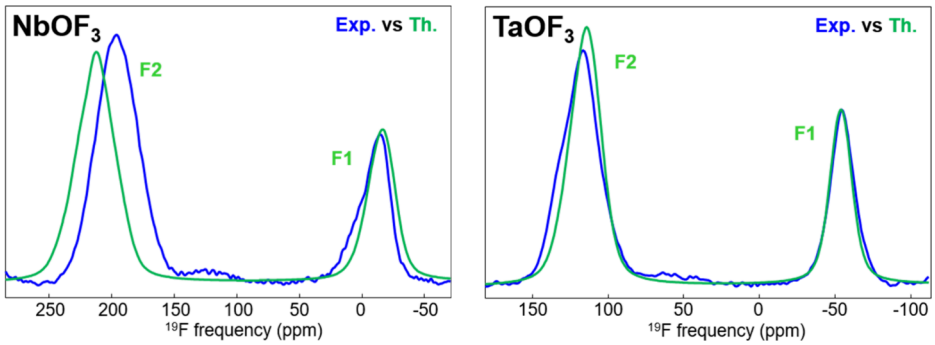


Figure 7. Experimental (blue) and theoretical (green) ^{19}F NMR spectra of $NbOF_3$ and $TaOF_3$. The experimental spectra were processed by using the TOP procedure.[71] The theoretical spectra were built by using the calculated ^{19}F δ_{iso} values from the APO_DFT-D3 models.

Table 9. ^{19}F Experimental Weighted Average $\delta_{iso,exp}$, δ_{CSA}, and η_{CSA} Values, and Calculated Average $\delta_{iso,cal}$, σ_{CSA}, and η_{CSA} Values from APO_DFT-D3 and FO_DFT-D3 Models, of F1 and F2 Atoms in $NbOF_3$ and $TaOF_3$ (ppm)

	experimental data			APO_DFT-D3			FO_DFT-D3		
F atoms	$\delta_{iso,exp}$	δ_{CSA}	η_{CSA}	$\delta_{iso,cal}$	σ_{CSA}	η_{CSA}	$\delta_{iso,cal}$	σ_{CSA}	η_{CSA}
$NbOF_3$									
F1	−8.2	−162.4	0.51	−14.8	145.1	0.81	−14.3	145.4	0.80
F2	194.3	−291.6	0.72	212.5	330.4	0.12	210.6	328.7	0.14
$TaOF_3$									
F1	−54.6	−170.0	0.50	−53.9	118.9	0.77	−52.8	121.3	0.81
F2	118.2	−283.4	0.10	115.4	268.7	0.07	118.8	272.7	0.07

For both compounds and in agreement with more intense spinning sidebands, the calculated σ_{CSA} values are higher for F2 atoms compared to F1 atoms. The η_{CSA} values show good agreement for both F1 and F2 atoms in $TaOF_3$ and a less satisfying agreement for F2 atoms in $NbOF_3$ (Tables 1, 7 and 8). For $TaOF_3$, the agreement between the calculated and experimental average ^{19}F δ_{iso} values is almost perfect for both F1 and F2 atoms. In contrast, for $NbOF_3$, this agreement is less satisfying for the F2 atoms. Furthermore, the dispersion of the calculated δ_{iso} values for each model is consistent with the widths of the NMR signals (Tables S1−S4, S27, S30, and S33). Therefore, since there is no significant difference between the total energy of each model (Table S10), there is no reason to rule out any particular model and we assume that they all contribute equally to the structural modeling of MOF_3. Theoretical ^{19}F NMR spectra were then plotted considering the 240 (80 F1 and 160 F2) calculated δ_{iso} values. These spectra being similar, we present only those from the APO_DFT-D3 models (Figure 7). The agreement between the experimental and theoretical spectra is excellent for $TaOF_3$ but less satisfactory for $NbOF_3$ in particular for the NMR line corresponding to the F2 atoms (Table 9). Assuming that it is related to the higher OH group content in $NbOF_3$, we studied the effect of the substitution of F1 atoms by OH groups on the structure and on the NMR parameters.

4.7. Modeling Hydroxylated $NbOF_3$. New supercells $NbO1F1_{1-x}(OH)1_xF2_2$ were then built with two different OH substitution rates, $x = 1/8$ and $x = 1/4$. For each of the 10 models, the substitution of one or two F1 atoms by OH groups was performed using the "Supercell" program[104] and led to multiple possible configurations. Testing all possible configurations for all models is beyond the limits of our

https://doi.org/10.1021/acs.inorgchem.3c02844
Inorg. Chem. 2023, 62, 16627−16640

Table 10. Weighted Average ^{19}F Experimental δ_{iso} Values (in Italic) and Average Theoretical δ_{iso} Values for F2, Strongly H-Bonded F2 and F1 Atoms ($<\delta_{iso}>$, ppm), and Corresponding Relative Intensities (I, %) from the Studied Sample and $NbOF_{1-x}(OH)_xF_2$ Models

	$<\delta_{iso}>$			I		
	F2	H-bonded F2	F1	F2	H-bonded F2	F1
$NbOF_{2.85}(OH)_{0.15}$	*194.3*	*120.3*	*−8.2*	*67.2*	*2.9*	*29.9*
$NbOF_3$	212.5	n. a.	−14.8	66.7	n. a.	33.3
$NbOF_{0.875}(OH)_{0.125}F_2$	205.1	112.6	−14.8	67.8	1.8	30.4
$NbOF_{0.75}(OH)_{0.25}F_2$	199.9	97.2	−15.9	67.3	5.4	27.3

computational hardware. Therefore, only the supercell with the lowest Coulomb energy was chosen for each $NbOF_3$ model and substitution rate. The atomic positions of the selected supercells were then optimized, and the structural characteristics are gathered as SI in Tables S36−S43. The NMR parameters are then calculated, and the ^{19}F σ_{iso} values are converted into ^{19}F δ_{iso} values by using the linear regression equations established on NbF_5 (Tables S44−S49). Average values are gathered in Table 10, and the two new theoretical ^{19}F NMR spectra are presented in Figure 8.

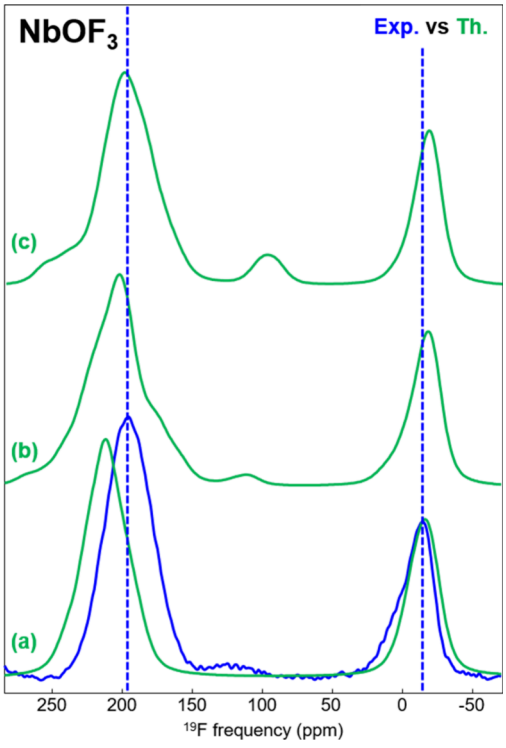


Figure 8. Experimental (blue) and theoretical (green) ^{19}F NMR spectra of $NbOF_3$ (a), $NbOF_{0.875}(OH)_{0.125}F_2$ (b), and $NbOF_{0.75}(OH)_{0.25}F_2$ (c). The experimental spectra were processed by using the TOP procedure.[71] The theoretical spectra are constructed with the calculated ^{19}F δ_{iso} from the APO_DFT-D3 models.

The agreement between the experimental and theoretical spectra is improved. Substituting F1 atoms by OH groups results in a decrease of the average F2 δ_{iso} value and thus of the gap between the calculated and experimental F2 resonances, without significant variation of the average F1 δ_{iso} values. Moreover, some F2 atoms have significantly lower δ_{iso} values (Figure 9 and Table 10) and they are distinguishable when plotted against F2−M bond lengths (Figure S11). A combined analysis of the structural data and calculated ^{1}H and ^{19}F δ_{iso} values shows that each OH group is involved in either one strong O−H···F bond or four weak O−H···F bonds or contacts (Tables 11 and Tables S50 and S51). Usually, O−H···F contacts with angles (°) larger than 115° and H···F distances (Å) smaller than the sum of H (1.20 Å) and F (1.47 Å) vdW radii are considered as H-bonds. The ^{19}F δ_{iso} values of the F2 atoms involved in O−H···F weak O−H···F bonds or contacts are only slightly lower than those of the remaining F2 atoms and contribute to the decrease of the δ_{iso} value of the main F2 resonance. The calculated ^{1}H δ_{iso} values of the H atoms forming weak O−H···F bonds or contact are only slightly less than those of H atoms forming a unique and strong H bond. Overall, the ^{1}H calculated δ_{iso} values are close to those of the NMR line assigned to H-bonded OH (Table 2). The experimental spectrum shows a second contribution assigned to non-H-bonded OH. Indeed, at room temperature and in the course of time, the rotational movement of OH groups enables the formation and breaking of these H-bonds, whereas these effects cannot be captured by the inherently static DFT optimized structure at 0 K.

5. CONCLUSIONS

The average crystal structures of $NbOF_3$ and $TaOF_3$, especially the occupancy rates of the anion crystallographic sites based on the correct assignment of the ^{19}F NMR resonances, have been revised. The nonbridging site is fully occupied by F while the bridging site has an occupancy of 0.5 O and 0.5 F. The structure consists of stacked $_\infty(MOF_3)$ layers along the $\vec{c}$ direction, formed by MO_2F_4 octahedra, corner-connected by two F and two O atoms. An O/F correlated disorder is then expected, since *cis*-MO_2F_4 octahedra are favored. Ten different 2 × 2 × 1 supercells per compound, fulfilling these characteristics, were built and DFT optimized, and the ^{19}F isotropic chemical shift values were determined. The agreement between the experimental and theoretical ^{19}F spectra is excellent for $TaOF_3$ but less satisfactory for $NbOF_3$ in relation to its higher OH group content. New supercells involving OH groups were then generated. A good agreement between the experimental and theoretical ^{19}F and ^{1}H calculated δ_{iso} values is obtained for the supercells with the composition closest to that estimated, i.e., $NbOF_{2.85}(OH)_{0.15}$. All of these results confirm the correlated disorder and show that the 10 possible 2 × 2 × 1 supercells present a good structural model of $NbOF_3$ and $TaOF_3$. The short-range structures deviate markedly from the average crystal structures to accommodate the different, by ∼0.2 Å, M−O and M−F bond lengths. The building unit of MOF_3, the *cis*-MO_2F_4 octahedra, is especially distorted with average angle values between adjacent and opposite M−X bonds away from the values of the average structure. The values for bond lengths and bond angles not only deviate

https://doi.org/10.1021/acs.inorgchem.3c02844
Inorg. Chem. 2023, 62, 16627−16640

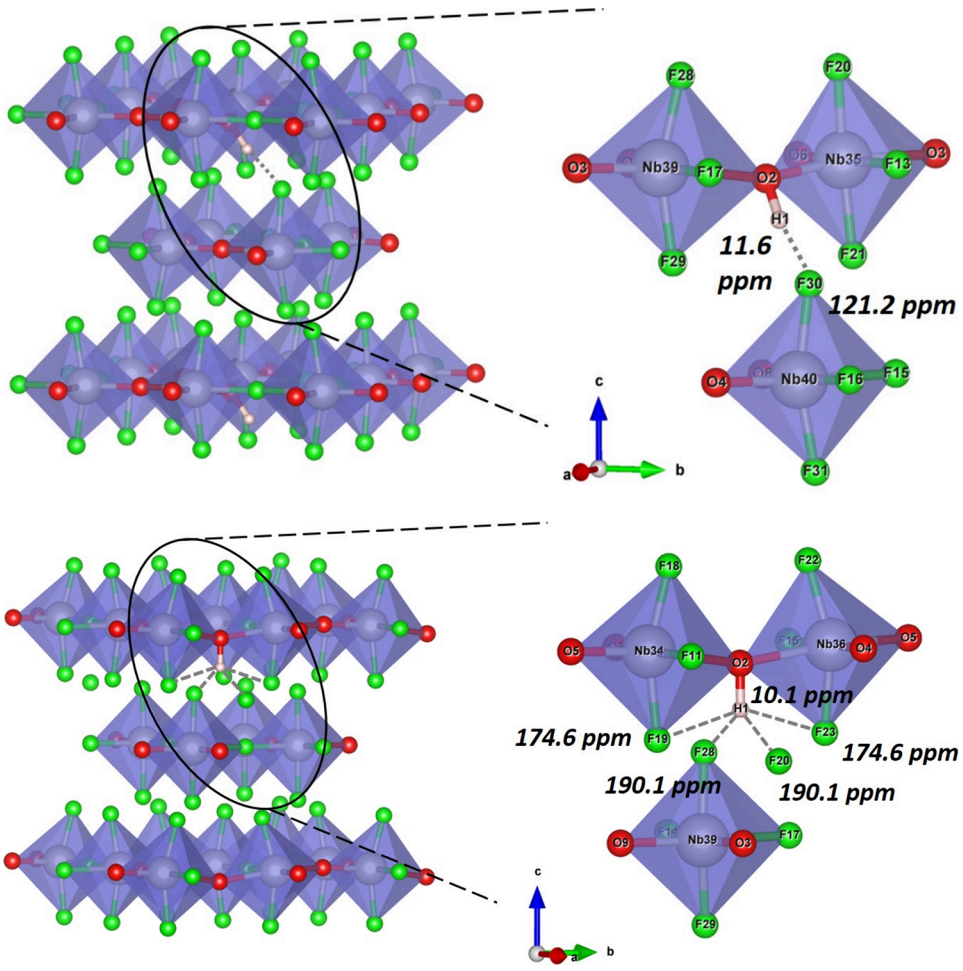


Figure 9. Perspective view of APO_DFT-D3 models 10 (top left) and 1 (bottom left) from $NbOF_{0.875}(OH)_{0.125}F_2$. Enlargement showing a strong O−H···F bond (top right) and O−H···F contacts (bottom right). ^1H and ^{19}F δ_{iso} values are indicated. Nb, O, F, and H atoms are represented in gray, red, green, and white, respectively. The MX_6 octahedra are represented in purple.

Table 11. Geometries of the O−H···F Contacts (Average H−O Bond Length (Å), H···F Distance (Å), and O−H···F Angle (°)) and Corresponding Calculated ^1H and ^{19}F δ_{iso} Values (ppm) for the 10 Supercells $NbOF_{0.875}(OH)_{0.125}F_2$ and $NbOF_{0.75}(OH)_{0.25}F_2$

H−O	H···F	O−H···F	^1H δ_{iso}	^{19}F δ_{iso}
$NbOF_{0.875}(OH)_{0.125}F_2$				
0.999	1.662	174.1	11.8	112.6
0.985	2.184	111.6	10.0	182.2
$NbOF_{0.75}(OH)_{0.25}F_2$				
1.000	1.661	172.1	12.0	97.1
0.988	2.126	113.3	10.5	182.2

from the average values determined by diffraction but are, as expected in disordered compounds, distributed. Finally, the structural modeling of hydroxylated $NbOF_3$ highlights that each H atom is strongly H-bonded to one F2 atom or in contact with four F2 atoms. This study proves the efficiency of combining theoretical calculations and solid-state NMR to model O/F correlated disorder in oxyfluorides as well as their hydroxylation.

■ ASSOCIATED CONTENT

Supporting Information

The Supporting Information is available free of charge at https://pubs.acs.org/doi/10.1021/acs.inorgchem.3c02844.

^{19}F and ^1H MAS NMR spectra and their fits; determination of the OH substitution rate in $NbOF_3$ and $TaOF_3$; Rietveld refinements; $NbOF_3$, $TaOF_3$, and hydroxylated $NbOF_3$ structural features; new NbF_5 and TaF_5 correlations ^{19}F σ_{iso} vs δ_{iso} established with VASP; $NbOF_3$, $TaOF_3$, and hydroxylated $NbOF_3$ calculated δ_{iso}, σ_{CSA}, and η_{CSA} values; geometries of the O−H···F contacts and calculated δ_{iso} values in hydroxylated $NbOF_3$ (PDF)

CIF files for ES structures of $NbOF_3$ and $TaOF_3$, the 10 APO_DFT-D3 and the 10 FO_DFT-D3 models of $NbOF_3$ and $TaOF_3$, and the 10 APO_DFT-D3 models of $NbOF_{0.875}(OH)_{0.125}F_2$ and $NbOF_{0.75}(OH)_{0.25}F_2$ (ZIP)

Accession Codes

CCDC 2260474−2260475 contain the supplementary crystallographic data for this paper. These data can be obtained free of charge via www.ccdc.cam.ac.uk/data_request/cif, or by emailing data_request@ccdc.cam.ac.uk, or by contacting The Cambridge Crystallographic Data Centre,

https://doi.org/10.1021/acs.inorgchem.3c02844
Inorg. Chem. 2023, 62, 16627−16640

12 Union Road, Cambridge CB2 1EZ, UK; fax: +44 1223 336033.

AUTHOR INFORMATION

Corresponding Authors

Ouail Zakary − *Institut des Molécules et Matériaux du Mans (IMMM) - UMR 6283 CNRS, Le Mans Université, 72805 Le Mans Cedex 9, France;* orcid.org/0000-0002-7793-3306; Email: Ouail.Zakary@univ-lemans.fr

Monique Body − *Institut des Molécules et Matériaux du Mans (IMMM) - UMR 6283 CNRS, Le Mans Université, 72805 Le Mans Cedex 9, France;* orcid.org/0000-0002-5895-3731; Email: Monique.Body@univ-lemans.fr

Authors

Thibault Charpentier − *Université Paris-Saclay, CEA, CNRS, NIMBE, Gif-sur-Yvette Cedex 91191, France;* orcid.org/0000-0002-3034-1389

Vincent Sarou-Kanian − *CEMHTI CNRS UPR3079, Université d'Orléans, Orléans 45071, France;* orcid.org/0000-0001-9611-8377

Christophe Legein − *Institut des Molécules et Matériaux du Mans (IMMM) - UMR 6283 CNRS, Le Mans Université, 72805 Le Mans Cedex 9, France;* orcid.org/0000-0001-7426-8817

Complete contact information is available at: https://pubs.acs.org/10.1021/acs.inorgchem.3c02844

Author Contributions

The manuscript was written through contributions of all authors. All authors have given approval to the final version of the manuscript.

Notes

The authors declare no competing financial interest.

ACKNOWLEDGMENTS

The authors acknowledge Cyrille Galven (IMMM − UMR 6283 CNRS, Le Mans Université) for his support with the synthesis.

REFERENCES

(1) Kageyama, H.; Hayashi, K.; Maeda, K.; Attfield, J. P.; Hiroi, Z.; Rondinelli, J. M.; Poeppelmeier, K. R. Expanding Frontiers in Materials Chemistry and Physics with Multiple Anions. *Nat. Commun.* **2018**, *9* (1), 772.

(2) Harada, J. K.; Charles, N.; Poeppelmeier, K. R.; Rondinelli, J. M. heteroanionic Materials by Design: Progress Toward Targeted Properties. *Adv. Mater.* **2019**, *31* (19), 1805295.

(3) Agulyansky, A. *Chemistry of Tantalum and Niobium Fluoride Compounds*; Elsevier, 2004.

(4) Frevel, L. K.; Rinn, H. W. The Crystal Structure of NbO_2F and TaO_2F. *Acta Crystallogr.* **1956**, *9* (8), 626−627.

(5) Andersson, S.; Åström, A.; Issidorides, C.; Kallner, A. The Thermal Decomposition of NbO_2F. *Acta Chem. Scand.* **1965**, *19*, 2136−2138.

(6) Carlson, S.; Larsson, A.-K.; Rohrer, F. E. High-Pressure Transformations of NbO_2F. *Acta Crystallogr. B Struct Sci.* **2000**, *56* (2), 189−196.

(7) Reddy, M. V.; Madhavi, S.; Subba Rao, G. V.; Chowdari, B. V. R. Metal oxyfluorides $TiOF_2$ and NbO_2F as Anodes for Li-Ion Batteries. *J. Power Sources* **2006**, *162* (2), 1312−1321.

(8) Jahnberg, L.; Andersson, S.; Fischer, P.; Stoll, E.; Eriksson, G.; Blinc, R.; Paušak, S.; Ehrenberg, L.; Dumanović, J. Studies on Pentavalent Tantalum Oxide Fluorides and the Thermal Decomposition of TaO_2F. *Acta Chem. Scand.* **1967**, *21*, 615−619.

(9) Andersson, S.; Åström, A.; Weedon, B. C. L. Phase Analysis Studies on Niobium Oxide Fluorides. *Acta Chem. Scand.* **1964**, *18*, 2233−2236.

(10) Andersson, S.; Åsbrink, S.; Reistad, T.; Sparrow, D. R. The Crystal Structure of Nb_3O_7F. *Acta Chem. Scand.* **1964**, *18*, 2339−2344.

(11) Vlasse, M.; Morilière, C.; Chaminade, J.-P.; Pouchard, M. Structure cristalline de l'oxyfluorure de tantale Ta_3O_7F α. *Bull. Soc. Fr. Minéral. Cristallogr.* **1975**, *98* (6), 325−330.

(12) Andersson, S.; Nord, S.; Sjöberg, B.; Mellander, O.; Hinton, M. Two New Niobium Oxide Fluorides Formed at High Temperature. *Acta Chem. Scand.* **1965**, *19*, 1401−1404.

(13) Åström, A.; Sletten, E.; Sletten, J.; Kulonen, E.; Brunvoll, J.; Bunnenberg, E.; Djerassi, C.; Records, R. The Crystal Structures of $Nb_{31}O_{77}F$ and $Nb_{17}O_{42}F$. *Acta Chem. Scand.* **1966**, *20*, 969−982.

(14) Cordier, S.; Roisnel, T.; Poulain, M. Synthesis and Characterization of the Novel $Nb_3O_5F_5$ Niobium oxyfluoride: The Term N = 3 of the $Nb_nO_{2n-1}F_{n+2}$ Series. *J. Solid State Chem.* **2004**, *177* (9), 3119−3126.

(15) Köhler, J.; Simon, A.; Van Wüllen, L.; Cordier, S.; Roisnel, T.; Poulain, M.; Somer, M. Structures and Properties of $NbOF_3$ and $TaOF_3$ — With a Remark to the O/F Ordering in the SnF_4 Type Structure. *Z. Anorg. Allg. Chem.* **2002**, *628* (12), 2683−2690.

(16) Murase, T.; Irie, H.; Hashimoto, K. Ag^+-Inserted NbO_2F as a Novel Photocatalyst. *J. Phys. Chem. B* **2005**, *109* (28), 13420−13423.

(17) Lange, M. A.; Khan, I.; Dören, R.; Ashraf, M.; Qurashi, A.; Prädel, L.; Panthöfer, M.; von der Au, M.; Cossmer, A.; Pfeifer, J.; Meermann, B.; Mondeshki, M.; Tahir, M. N.; Tremel, W. High-Speed Solid State Fluorination of Nb_2O_5 Yields NbO_2F and Nb_3O_7F with Photocatalytic Activity for Oxygen Evolution from Water. *Dalton Trans.* **2021**, *50* (19), 6528−6538.

(18) Xu, L.; Gong, H.; Deng, L.; Long, F.; Gu, Y.; Guan, J. Complex-Mediated Synthesis of Tantalum oxyfluoride Hierarchical Nanostructures for Highly Efficient Photocatalytic Hydrogen Evolution. *ACS Appl. Mater. Interfaces* **2016**, *8* (14), 9395−9404.

(19) Lange, M. A.; Khan, I.; Opitz, P.; Hartmann, J.; Ashraf, M.; Qurashi, A.; Prädel, L.; Panthöfer, M.; Cossmer, A.; Pfeifer, J.; Simon, F.; von der Au, M.; Meermann, B.; Mondeshki, M.; Tahir, M. N.; Tremel, W. A Generalized Method for High-Speed Fluorination of Metal Oxides by Spark Plasma Sintering Yields Ta_3O_7F and TaO_2F with High Photocatalytic Activity for Oxygen Evolution from Water. *Adv. Mater.* **2021**, *33* (20), 2007434.

(20) Idrees, F.; Cao, C.; Butt, F. K.; Tahir, M.; Tanveer, M.; Aslam, I.; Ali, Z.; Mahmood, T.; Hou, J. Facile Synthesis of Novel Nb_3O_7F Nanoflowers, Their Optical and Photocatalytic Properties. *CrystEngComm* **2013**, *15* (40), 8146.

(21) Huang, F.; Zhao, H.; Yan, A.; Li, Z.; Liang, H.; Gao, Q.; Qiang, Y. In Situ Thermal Decomposition for Preparation of Nb_3O_7F/Nb_2O_5 Hybrid Nanomaterials with Enhanced Photocatalytic Performance. *J. Alloys Compd.* **2017**, *695*, 489−495.

(22) Mizoguchi, H.; Orita, M.; Hirano, M.; Fujitsu, S.; Takeuchi, T.; Hosono, H. NbO_2F: An oxyfluoride Phase with Wide Band Gap and Electrochromic Properties. *Appl. Phys. Lett.* **2002**, *80* (25), 4732−4734.

(23) Tao, J. Z.; Sleight, A. W. Very Low Thermal Expansion in TaO_2F. *J. Solid State Chem.* **2003**, *173* (1), 45−48.

(24) Sawhill, S.; Savrun, E. A near Zero Coefficient of Thermal Expansion Ceramic: Tantalum oxyfluoride. *Ceram. Int.* **2012**, *38* (3), 1981−1989.

(25) Morelock, C. R.; Greve, B. K.; Cetinkol, M.; Chapman, K. W.; Chupas, P. J.; Wilkinson, A. P. Role of Anion Site Disorder in the Near Zero Thermal Expansion of Tantalum oxyfluoride. *Chem. Mater.* **2013**, *25* (9), 1900−1904.

(26) Bohnke, C.; Fourquet, J. L.; Randrianantoandro, N.; Brousse, T.; Crosnier, O. Electrochemical Intercalation of Lithium into the

Perovskite-Type NbO_2F: Influence of the NbO_2F Particle Size. *J. Solid State Electrochem.* **2001**, *5* (1), 1−7.
(27) Bashian, N. H.; Preefer, M. B.; Milam-Guerrero, J.; Zak, J. J.; Sendi, C.; Ahsan, S. A.; Vincent, R. C.; Haiges, R.; See, K. A.; Seshadri, R.; Melot, B. C. Understanding the Role of Crystallographic Shear on the Electrochemical Behavior of Niobium oxyfluorides. *J. Mater. Chem. A* **2020**, *8* (25), 12623−12632.
(28) Permér, L. Li-Inserted Nb_3O_7F and Its Thermal Decomposition Products Studied by High-Resolution Electron Microscopy and X-Ray Powder Diffraction. *J. Solid State Chem.* **1992**, *97* (1), 105−114.
(29) Brink, F. J.; Withers, R. L.; Norén, L. An Electron Diffraction and Crystal Chemical Investigation of Oxygen/Fluorine Ordering in Niobium oxyfluoride, NbO_2F. *J. Solid State Chem.* **2002**, *166* (1), 73−80.
(30) Brink, F. J.; Withers, R. L.; Cordier, S.; Poulain, M. An Electron Diffraction and Bond Valence Sum Investigation of Oxygen/Fluorine Ordering in $NbnO_{2n-1}F_{n+2}$. *J. Solid State Chem.* **2006**, *179* (2), 341−348.
(31) Dabachi, J.; Body, M.; Galven, C.; Boucher, F.; Legein, C. Preparation-Dependent Composition and O/F Ordering in NbO_2F and TaO_2F. *Inorg. Chem.* **2017**, *56* (9), 5219−5232.
(32) Brown, I. D.; Altermatt, D. Bond-Valence Parameters Obtained from a Systematic Analysis of the Inorganic Crystal Structure Database. *Acta Crystallogr., Sect. B: Struct. Sci.* **1985**, *41* (4), 244−247.
(33) Brese, N. E.; O'Keeffe, M. Bond-Valence Parameters for Solids. *Acta Crystallogr., Sect. B: Struct. Sci.* **1991**, *47* (2), 192−197.
(34) Goodwin, A. L. Opportunities and Challenges in Understanding Complex Functional Materials. *Nat. Commun.* **2019**, *10* (1), 4461.
(35) Charpentier, T. The PAW/GIPAW Approach for Computing NMR Parameters: A New Dimension Added to NMR Study of Solids. *Solid State Nucl. Magn. Reson.* **2011**, *40* (1), 1−20.
(36) Bonhomme, C.; Gervais, C.; Babonneau, F.; Coelho, C.; Pourpoint, F.; Azaïs, T.; Ashbrook, S. E.; Griffin, J. M.; Yates, J. R.; Mauri, F.; Pickard, C. J. First-Principles Calculation of NMR Parameters Using the Gauge Including Projector Augmented Wave Method: A Chemist's Point of View. *Chem. Rev.* **2012**, *112* (11), 5733−5779.
(37) Ashbrook, S. E.; Dawson, D. M. Exploiting Periodic First-Principles Calculations in NMR Spectroscopy of Disordered Solids. *Acc. Chem. Res.* **2013**, *46* (9), 1964−1974.
(38) Moran, R. F.; Dawson, D. M.; Ashbrook, S. E. Exploiting NMR Spectroscopy for the Study of Disorder in Solids. *Int. Rev. Phys. Chem.* **2017**, *36* (1), 39−115.
(39) Ashbrook, S. E.; Griffin, J. M.; Johnston, K. E. Recent Advances in Solid-State Nuclear Magnetic Resonance Spectroscopy. *Annual Rev. Anal. Chem.* **2018**, *11* (1), 485−508.
(40) Florian, P.; Veron, E.; Green, T. F. G.; Yates, J. R.; Massiot, D. Elucidation of the Al/Si Ordering in Gehlenite $Ca_2Al_2SiO_7$ by Combined ^{29}Si and ^{27}Al NMR Spectroscopy/Quantum Chemical Calculations. *Chem. Mater.* **2012**, *24* (21), 4068−4079.
(41) Ferrara, C.; Tealdi, C.; Pedone, A.; Menziani, M. C.; Rossini, A. J.; Pintacuda, G.; Mustarelli, P. Local versus Average Structure in $LaSrAl_3O_7$: A NMR and DFT Investigation. *J. Phys. Chem. C* **2013**, *117* (45), 23451−23458.
(42) Véron, E.; Garaga, M. N.; Pelloquin, D.; Cadars, S.; Suchomel, M.; Suard, E.; Massiot, D.; Montouillout, V.; Matzen, G.; Allix, M. Synthesis and Structure Determination of $Ca\text{-}Si_{1/3}B_{2/3}O_{8/3}$: A New Calcium Borosilicate. *Inorg. Chem.* **2013**, *52* (8), 4250−4258.
(43) Ashbrook, S. E.; Mitchell, M. R.; Sneddon, S.; Moran, R. F.; De Los Reyes, M.; Lumpkin, G. R.; Whittle, K. R. New Insights into Phase Distribution, Phase Composition and Disorder in $Y_2(Zr,Sn)_2O_7$ Ceramics from NMR Spectroscopy. *Phys. Chem. Chem. Phys.* **2015**, *17* (14), 9049−9059.
(44) Playford, Helen. Y.; Hannon, A. C.; Tucker, M. G.; Dawson, D. M.; Ashbrook, S. E.; Kastiban, R. J.; Sloan, J.; Walton, R. I. Characterization of Structural Disorder in $\gamma\text{-}Ga_2O_3$. *J. Phys. Chem. C* **2014**, *118* (29), 16188−16198.
(45) Flemming, R. L.; Terskikh, V.; Ye, E. Aluminum Environments in Synthetic Ca-Tschermak Clinopyroxene ($CaAlAlSiO_6$) from Rietveld Refinement, ^{27}Al NMR, and First-Principles Calculations. *Am. Mineral.* **2015**, *100* (10), 2219−2230.
(46) Diez-Gómez, V.; Arbi, K.; Sanz, J. Modeling Ti/Ge Distribution in $LiTi_{2-x}Ge_x(PO_4)_3$ NASICON Series by ^{31}P MAS NMR and First-Principles DFT Calculations. *J. Am. Chem. Soc.* **2016**, *138* (30), 9479−9486.
(47) Fernandes, A.; McKay, D.; Sneddon, S.; Dawson, D. M.; Lawson, S.; Veazey, R.; Whittle, K. R.; Ashbrook, S. E. Phase Composition and Disorder in $La_2(Sn,Ti)_2O_7$ Ceramics: New Insights from NMR Crystallography. *J. Phys. Chem. C* **2016**, *120* (36), 20288−20296.
(48) Moran, R. F.; McKay, D.; Pickard, C. J.; Berry, A. J.; Griffin, J. M.; Ashbrook, S. E. Hunting for Hydrogen: Random Structure Searching and Prediction of NMR Parameters of Hydrous Wadsleyite. *Phys. Chem. Chem. Phys.* **2016**, *18* (15), 10173−10181.
(49) Fernandez-Carrion, A. J.; Al Saghir, K.; Veron, E.; Becerro, A. I.; Porcher, F.; Wisniewski, W.; Matzen, G.; Fayon, F.; Allix, M. Local Disorder and Tunable Luminescence in $Sr_{1-x/2}Al_{2-x}Si_xO_4$ ($0.2 \leq x \leq 0.5$) Transparent Ceramics. *Inorg. Chem.* **2017**, *56* (23), 14446−14458.
(50) Cadars, S.; Ahn, N. H.; Okhotnikov, K.; Shin, J.; Vicente, A.; Hong, S. B.; Fernandez, C. Modeling Short-Range Substitution Order and Disorder in Crystals: Application to the Ga/Si Distribution in a Natrolite Zeolite. *Solid State Nucl. Magn. Reson.* **2017**, *84*, 182−195.
(51) Girard, G.; Vasconcelos, F.; Montagne, L.; Delevoye, L. 31P MAS NMR Spectroscopy with 93Nb Decoupling and DFT Calculations: A Structural Characterization of Defects in a Niobium-Phosphate Phase. *Solid State Nucl. Magn. Reson.* **2017**, *84*, 210−215.
(52) Grüninger, H.; Armstrong, K.; Greim, D.; Boffa-Ballaran, T.; Frost, D. J.; Senker, J. Hidden Oceans? Unraveling the Structure of Hydrous Defects in the Earth's Deep Interior. *J. Am. Chem. Soc.* **2017**, *139* (30), 10499−10505.
(53) Fischer, M. Local Environment and Dynamic Behavior of Fluoride Anions in Silicogermanate Zeolites: A Computational Study of the AST Framework. *J. Phys. Chem. C* **2019**, *123* (3), 1852−1865.
(54) McKay, D.; Moran, R. F.; Dawson, D. M.; Griffin, J. M.; Sturniolo, S.; Pickard, C. J.; Berry, A. J.; Ashbrook, S. E. A Picture of Disorder in Hydrous Wadsleyite—Under the Combined Microscope of Solid-State NMR Spectroscopy and *Ab Initio* Random Structure Searching. *J. Am. Chem. Soc.* **2019**, *141* (7), 3024−3036.
(55) Moran, R. F.; McKay, D.; Tornstrom, P. C.; Aziz, A.; Fernandes, A.; Grau-Crespo, R.; Ashbrook, S. E. Ensemble-Based Modeling of the NMR Spectra of Solid Solutions: Cation Disorder in $Y_2(Sn,Ti)_2O_7$. *J. Am. Chem. Soc.* **2019**, *141* (44), 17838−17846.
(56) Serrano-Sevillano, J.; Carlier, D.; Saracibar, A.; Lopez Del Amo, J. M.; Casas-Cabanas, M. DFT-Assisted Solid-State NMR Characterization of Defects in Li_2MnO_3. *Inorg. Chem.* **2019**, *58* (13), 8347−8356.
(57) Moran, R. F.; Fernandes, A.; Dawson, D. M.; Sneddon, S.; Gandy, A. S.; Reeves-McLaren, N.; Whittle, K. R.; Ashbrook, S. E. Phase Distribution, Composition, and Disorder in $Y_2(Hf,Sn)_2O_7$ Ceramics: Insights from Solid-State NMR Spectroscopy and First-Principles Calculations. *J. Phys. Chem. C* **2020**, *124* (31), 17073−17084.
(58) Ashbrook, S. E.; Dawson, D. M.; Gan, Z.; Hooper, J. E.; Hung, I.; Macfarlane, L. E.; McKay, D.; McLeod, L. K.; Walton, R. I. Application of NMR Crystallography to Highly Disordered Templated Materials: Extensive Local Structural Disorder in the Gallophosphate GaPO-34A. *Inorg. Chem.* **2020**, *59* (16), 11616−11626.
(59) Camus-Génot, V.; Guiet, A.; Lhoste, J.; Fayon, F.; Body, M.; Kodjikian, S.; Moury, R.; Leblanc, M.; Bobet, J. L.; Legein, C.;

Maisonneuve, V. Controlled Morphology Synthesis of Nanostructured β-$AlF_{3-x}(OH)_x$ with Tunable Specific Surface Area. *Cryst. Growth Des.* **2021**, *21* (10), 5914−5927.
(60) Fischer, M. Fluoride Anions in All-Silica Zeolites: Studying Preferred Fluoride Sites and Dynamic Disorder with Density Functional Theory Calculations. *J. Phys. Chem. C* **2021**, *125* (16), 8825−8839.
(61) Hancock, J. C.; Griffith, K. J.; Choi, Y.; Bartel, C. J.; Lapidus, S. H.; Vaughan, J. T.; Ceder, G.; Poeppelmeier, K. R. Expanding the Ambient-Pressure Phase Space of $CaFe_2O_4$ -Type Sodium Postspinel Host−Guest Compounds. *ACS Org. Inorg. Au* **2022**, *2* (1), 8−22.
(62) Leube, B. T.; Collins, C. M.; Daniels, L. M.; Duff, B. B.; Dang, Y.; Chen, R.; Gaultois, M. W.; Manning, T. D.; Blanc, F.; Dyer, M. S.; Claridge, J. B.; Rosseinsky, M. J. Cation Disorder and Large Tetragonal Supercell Ordering in the Li-Rich Argyrodite $Li_7Zn_{0.5}SiS_6$. *Chem. Mater.* **2022**, *34* (9), 4073−4087.
(63) Pickard, C. J.; Mauri, F. All-Electron Magnetic Response with Pseudopotentials: NMR Chemical Shifts. *Phys. Rev. B* **2001**, *63*(24) 245101.
(64) Yates, J. R.; Pickard, C. J.; Mauri, F. Calculation of NMR Chemical Shifts for Extended Systems Using Ultrasoft Pseudopotentials. *Phys. Rev. B* **2007**, *76* (2) 024401.
(65) Galissard de Marignac, J.-C. Untersuchungen Über Die Verbindungen Des Niobiums. *J. Prakt. Chem.* **1866**, *97*, 449−465.
(66) Schäfer, H. Der Transport Anorganischer Stoffe Über Die Gasphase Und Seine Anwendungen. *Chemische Transportreaktionen* 1962.
(67) Schäfer, H.; Schnering, H. G.; Niehues, K.-J.; Nieder-Vahrenholz, H. G. Beiträge zur chemie der elemente niob und tantal. *J. Less Common Metals* **1965**, *9* (2), 95−104.
(68) Nieder-Vahrenholz, H.-G.; Schäfer, H. Die Oxidfluoride des Niobs und Tantals. *Z. Anorg. Allg. Chem.* **1987**, *544* (1), 122−126.
(69) Wilkinson, A. P.; Josefsberg, R. E.; Gallington, L. C.; Morelock, C. R.; Monaco, C. M. History-Dependent Thermal Expansion in NbO_2F. *J. Solid State Chem.* **2014**, *213*, 38−42.
(70) Herzfeld, J.; Berger, A. E. sideband Intensities in NMR Spectra of Samples Spinning at the Magic Angle. *J. Chem. Phys.* **1980**, *73* (12), 6021−6030.
(71) Massiot, D.; Hiet, J.; Pellerin, N.; Fayon, F.; Deschamps, M.; Steuernagel, S.; Grandinetti, P. J. Two-Dimensional One Pulse MAS of Half-Integer Quadrupolar Nuclei. *J. Magn. Reson.* **2006**, *181* (2), 310−315.
(72) Massiot, D.; Fayon, F.; Capron, M.; King, I.; Le Calvé, S.; Alonso, B.; Durand, J.-O.; Bujoli, B.; Gan, Z.; Hoatson, G. Modelling One- and Two-Dimensional Solid-State NMR Spectra. *Magn. Reson. Chem.* **2002**, *40* (1), 70−76.
(73) Haeberlen, U. *Adv. Magn. Reson.; Suppl. 1*; Academic Press: New York, 1976.
(74) Perdew, J. P.; Burke, K.; Ernzerhof, M. Generalized Gradient Approximation Made Simple. *Phys. Rev. Lett.* **1996**, *77* (18), 3865−3868.
(75) Kresse, G.; Furthmüller, J. Efficiency of Ab-Initio Total Energy Calculations for Metals and Semiconductors Using a Plane-Wave Basis Set. *Comput. Mater. Sci.* **1996**, *6* (1), 15−50.
(76) Kresse, G.; Furthmüller, J. Efficient Iterative Schemes for *Ab Initio* Total-Energy Calculations Using a Plane-Wave Basis Set. *Phys. Rev. B* **1996**, *54* (16), 11169−11186.
(77) Blöchl, P. E. Projector Augmented-Wave Method. *Phys. Rev. B* **1994**, *50* (24), 17953−17979.
(78) Kresse, G.; Joubert, D. From Ultrasoft Pseudopotentials to the Projector Augmented-Wave Method. *Phys. Rev. B* **1999**, *59* (3), 1758−1775.
(79) Grimme, S.; Antony, J.; Ehrlich, S.; Krieg, H. A Consistent and Accurate *Ab Initio* Parametrization of Density Functional Dispersion Correction (DFT-D) for the 94 Elements H-Pu. *J. Chem. Phys.* **2010**, *132* (15), 154104.
(80) Griffin, J. M.; Yates, J. R.; Berry, A. J.; Wimperis, S.; Ashbrook, S. E. High-Resolution ^{19}F MAS NMR Spectroscopy: Structural Disorder and Unusual *J* Couplings in a Fluorinated Hydroxy-Silicate. *J. Am. Chem. Soc.* **2010**, *132* (44), 15651−15660.
(81) Sadoc, A.; Body, M.; Legein, C.; Biswal, M.; Fayon, F.; Rocquefelte, X.; Boucher, F. NMR Parameters in Alkali, Alkaline Earth and Rare Earth Fluorides from First Principle Calculations. *Phys. Chem. Chem. Phys.* **2011**, *13* (41), 18539.
(82) Pedone, A.; Charpentier, T.; Menziani, M. C. The Structure of Fluoride-Containing Bioactive Glasses: New Insights from First-Principles Calculations and Solid State NMR Spectroscopy. *J. Mater. Chem.* **2012**, *22* (25), 12599.
(83) Biswal, M.; Body, M.; Legein, C.; Sadoc, A.; Boucher, F. NbF_5 and TaF_5: Assignment of ^{19}F NMR Resonances and Chemical Bond Analysis from GIPAW Calculations. *J. Solid State Chem.* **2013**, *207*, 208−217.
(84) Sadoc, A.; Biswal, M.; Body, M.; Legein, C.; Boucher, F.; Massiot, D.; Fayon, F. NMR Parameters in Column 13 Metal Fluoride Compounds (AlF_3, GaF_3, InF_3 and TlF) from First Principle Calculations. *Solid State Nucl. Magn. Reson.* **2014**, *59*−*60*, 1−7.
(85) Rakhmatullin, A.; Boča, M.; Mlynáriková, J.; Hadzimová, E.; Vasková, Z.; Polovov, I. B.; Mičušík, M. Solid State NMR and XPS of Ternary Fluorido-Zirconates of Various Coordination Modes. *J. Fluorine Chem.* **2018**, *208*, 24−35.
(86) Rakhmatullin, A.; Polovov, I. B.; Maltsev, D.; Allix, M.; Volkovich, V.; Chukin, A. V.; Boča, M.; Bessada, C. Combined Approach for the Structural Characterization of Alkali Fluoroscandates: Solid-State NMR, Powder X-Ray Diffraction, and Density Functional Theory Calculations. *Inorg. Chem.* **2018**, *57* (3), 1184−1195.
(87) Martel, L.; Capelli, E.; Body, M.; Klipfel, M.; Beneš, O.; Maksoud, L.; Raison, P. E.; Suard, E.; Visscher, L.; Bessada, C.; Legein, C.; Charpentier, T.; Kovács, A. Insight into the Crystalline Structure of ThF_4 with the Combined Use of Neutron Diffraction, ^{19}F Magic-Angle Spinning-NMR, and Density Functional Theory Calculations. *Inorg. Chem.* **2018**, *57* (24), 15350−15360.
(88) DeVore, M. A.; Klug, C. A.; Kriz, M. R.; Roy, L. E.; Wellons, M. S. Investigations of Uranyl Fluoride Sesquihydrate (UO_2F_2·$1.57H_2O$): Combining ^{19}F Solid-State MAS NMR Spectroscopy and GIPAW Chemical Shift Calculations. *J. Phys. Chem. A* **2018**, *122* (34), 6873−6878.
(89) Dabachi, J.; Body, M.; Dittmer, J.; Rakhmatullin, A.; Fayon, F.; Legein, C. Insight into the Factors Influencing NMR Parameters in Crystalline Materials from the KF−YF_3 Binary System. *Dalton Trans.* **2019**, *48* (2), 587−601.
(90) Murakami, M.; Noda, Y.; Takegoshi, K. Terminal and Bridging Fluorine Ligands in TiF_4 as Studied by ^{19}F NMR in Solids. *Solid State Nucl. Magn. Reson.* **2019**, *101*, 82−88.
(91) Ding, F.; Griffith, K. J.; Koçer, C. P.; Saballos, R. J.; Wang, Y.; Zhang, C.; Nisbet, M. L.; Morris, A. J.; Rondinelli, J. M.; Poeppelmeier, K. R. Multimodal Structure Solution with ^{19}F NMR Crystallography of Spin Singlet Molybdenum oxyfluorides. *J. Am. Chem. Soc.* **2020**, *142* (28), 12288−12298.
(92) Legein, C.; Body, M.; Lhoste, J.; Li, W.; Charpentier, T.; Dambournet, D. Synthesis, Crystal Structure and ^{19}F NMR Parameters Modelling of $CaTiF_6(H_2O)_2$ Yielding to a Revision of the Bond-Valence Parameters for the Ti^{4+}/F - ion pair. *J. Solid State Chem.* **2023**, *319*, 123793.
(93) Segall, M. D.; Lindan, P. J. D.; Probert, M. J.; Pickard, C. J.; Hasnip, P. J.; Clark, S. J.; Payne, M. C. First-Principles Simulation: Ideas, Illustrations and the CASTEP Code. *J. Phys.: Condens. Matter* **2002**, *14* (11), 2717−2744.
(94) Clark, S. J.; Segall, M. D.; Pickard, C. J.; Hasnip, P. J.; Probert, M. I. J.; Refson, K.; Payne, M. C. First Principles Methods Using CASTEP. *Z. fur Krist. - Cryst. Mater* 2005, *220* (5/6) 567.
(95) Gervais, C.; Profeta, M.; Lafond, V.; Bonhomme, C.; Azaïs, T.; Mutin, H.; Pickard, C. J.; Mauri, F.; Babonneau, F. Combined Ab Initio Computational and Experimental Multinuclear Solid-State Magnetic Resonance Study of Phenylphosphonic Acid. *Magn. Reson. Chem.* **2004**, *42* (5), 445−452.

https://doi.org/10.1021/acs.inorgchem.3c02844
Inorg. Chem. 2023, 62, 16627−16640

(96) Li, W.; Corradini, D.; Body, M.; Legein, C.; Salanne, M.; Ma, J.; Chapman, K. W.; Chupas, P. J.; Rollet, A.-L.; Julien, C.; Zhagib, K.; Duttine, M.; Demourgues, A.; Groult, H.; Dambournet, D. High Substitution Rate in TiO_2 Anatase Nanoparticles with Cationic Vacancies for Fast Lithium Storage. *Chem. Mater.* **2015**, *27* (14), 5014−5019.
(97) Berglund, B.; Vaughan, R. W. Correlations between Proton Chemical Shift Tensors, Deuterium Quadrupole Couplings, and Bond Distances for Hydrogen Bonds in Solids. *J. Chem. Phys.* **1980**, *73* (5), 2037−2043.
(98) Eckert, H.; Yesinowski, J. P.; Silver, L. A.; Stolper, E. M. Water in Silicate Glasses: Quantitation and Structural Studies by Proton Solid Echo and Magic Angle Spinning NMR Methods. *J. Phys. Chem.* **1988**, *92* (7), 2055−2064.
(99) Harris, R. K.; Jackson, P.; Merwin, L. H.; Say, B. J.; Hägele, G. Perspectives in High-Resolution Solid-State Nuclear Magnetic Resonance, with Emphasis on Combined Rotation and Multiple-Pulse Spectroscopy. *J. Chem. Soc., Faraday Trans. 1* **1988**, *84* (11), 3649.
(100) Dalvit, C.; Vulpetti, A. Fluorine-Protein Interactions and ^{19}F NMR Isotropic Chemical Shifts: An Empirical Correlation with Implications for Drug Design. *ChemMedChem.* **2011**, *6* (1), 104−114.
(101) Rietveld, H. M. A Profile Refinement Method for Nuclear and Magnetic Structures. *J. Appl. Crystallogr.* **1969**, *2* (2), 65−71.
(102) Rodriguez-Carvajal, J. Magnetic Structure Determination from Powder Diffraction Using the Program *FullProf*. In *Applied Crystallography*; WORLD SCIENTIFIC: Wisla, Poland, 2001; pp 30−36.
(103) Groom, C. R.; Bruno, I. J.; Lightfoot, M. P.; Ward, S. C. The Cambridge Structural Database. *Acta Crystallogr. B Struct Sci. Cryst. Eng. Mater.* **2016**, *72* (2), 171−179.
(104) Okhotnikov, K.; Charpentier, T.; Cadars, S. Supercell Program: A Combinatorial Structure-Generation Approach for the Local-Level Modeling of Atomic Substitutions and Partial Occupancies in Crystals. *J. Cheminform* **2016**, *8* (1), 17.

https://doi.org/10.1021/acs.inorgchem.3c02844
Inorg. Chem. 2023, 62, 16627−16640

III.2.2. Conclusion

For both $NbOF_3$ and $TaOF_3$ oxyfluorides, O/F correlated disorder results directly from the anionic site occupancies, which were based on ^{19}F NMR resonance assignments, and the presence of exclusively *cis*-MO_2F_4 octahedra. This correlated disorder, defined by –F–M–O–M–strings along the <100> and <010> directions, was confirmed through the remarkable agreement observed between the calculated ^{19}F δ_{iso} values, derived from the ten 2×2×1 supercells, and the experimental ^{19}F δ_{iso} values. These supercells serve as robust structural models for $NbOF_3$ and $TaOF_3$. They, as expected, deviate from the average crystal structures to accommodate the different, by ∼0.2 Å, M−O and M−F bond lengths. The values for bond lengths and bond angles not only deviate from the average values determined by diffraction but are, as expected in disordered compounds, distributed. Finally, the structural modeling of hydroxylated $NbOF_3$ highlights that each H atom is strongly H-bonded to one F2 atom or in contact with four F2 atoms. This study proves the efficiency of combining theoretical calculations and solid-state NMR to model O/F correlated disorder in oxyfluorides as well as their hydroxylation.

III.3. Hexagonal-Tungsten-Bronze $TiOF_2$: Synthesis, Crystal Structure and Short-Range Anion Ordering

III.3.1. Introduction

In this section, we provides precise modeling of short-range O/F ordering in hydroxylated HTB-$TiOF_2$ by combining X-ray/neutron diffraction, Pair Distribution Function (PDF) analysis, ssNMR and DFT calculation methods. This study was conducted in collaboration with several researchers from various laboratories, both national and international, including:

a. CNRS, Université de Bordeaux, Bordeaux INP, ICMCB, UMR 5026, F-33600 Pessac, France
b. Department of Chemistry, University of Bath, BA2 7AY Bath, United Kingdom
c. The Faraday Institution, Quad One, Harwell Science and Innovation Campus, Didcot OX11 0RA, U.K
d. Sorbonne Université, CNRS, Physicochimie des Electrolytes et Nanosystèmes Interfaciaux, PHENIX, F-75005 Paris, France
e. Réseau sur le Stockage Electrochimique de l'Energie (RS2E), FR CNRS 3459, 80039 Amiens Cedex, France
f. NIMBE, CEA, CNRS, Université Paris-Saclay, CEA Saclay, 91191 Gif-sur-Yvette Cedex, France
g. X-ray Science Division, Advanced Photon Source, Argonne National Laboratory, Illinois 60439, United States
h. Thomas Young Centre, University College London, Gower Street, London, WC1E 6BT UK

Our role in this study involved modeling ^{19}F NMR parameters of the structural model issued from combining X-ray/neutron diffraction (performed by Alain Demourgues[a] and co-workers), PDF analysis (performed by Damien Dambournet[d,e] and co-workers) and Cluster Expansion (CE) technique (performed by Benjamin J. Morgan[b,c,h] and co-workers).

III.3.2. Average structure: X-ray and neutron diffractions (performed by Alain Demourgues[a] and co-workers)

The average structure adopts a hexagonal-tungsten-bronze (HTB)-type structure (SG: *Pnma* (62), with a = 7.558(1) Å, b = 7.392(1) Å and c = 12.789(1) Å), in which the hexagonal cavities along the $\vec{b}$ direction are occupied by water molecules. The structure consists of three Ti sites (4a, 4b and 4c Wyckoff sites) and six anionic sites (4c and 8d Wyckoff sites). The arrangement of oxygen and fluorine atoms was selected to match the ideal composition of $TiOF_2$, where O^{2-} ions occupy the three 4c sites and F^- (or OH^-) ions occupy the three 8d sites. This results in a structure formed from corner-shared TiX_6 (X = O, F) octahedra, featuring both three- and six-membered rings (**Figure 3.1**). Rietveld analysis of the X-ray data shows that Ti–X bond lengths exhibit relatively high estimated standard deviations (sdv). Even though the sdv values are somewhat reduced when using neutron data, they still remain considerably too high to differentiate between oxygen and fluorine/hydroxyl anions on the basis of bond valence sum calculations. The phase composition is estimated as $Ti_{0.99}\square_{0.01}O_{0.96}F_{1.53}(OH)_{0.51}\cdot 0.33H_2O$, it highlights a complex substructure built from up to three types of anions (O^{2-}, OH^-, F^-) and cationic vacancies ($\square$) arising from the presence of OH groups. This complex substructure and the large sdv values observed from diffraction analyses, suggest that anions are distributed across the different sites.

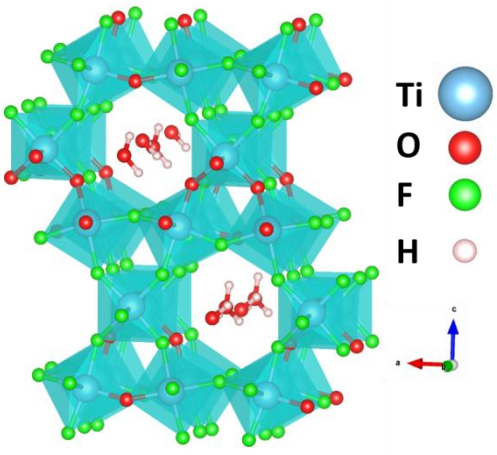


Figure 3.1. Perspective view of the unit cell of $TiOF_2$. TiX_6 (X = O, F) octahedra are displayed in blue.

III.3.3. Short-range anion ordering

III.3.3.1. PDF analysis (performed by Damien Dambournet[d,e] and co-workers)

To extend our investigation beyond the confines of average structural analysis, atomic short-range ordering was explored by means of PDF, which was obtained from the Fourier transformation of the scattering data. By analyzing a sequence of peaks associated with all inter-atomic distances, *r*, we can access various scales ranging from short- to long-range ordering. In this regard, two PDF refinement tests were conducted. The first test excluded inter-atomic distances that comprise the short-range structure (*i.e.*, distances where $1 < r < 5$ Å) and only values of *r* within the range [5–25] Å were considered. Meanwhile, the second test covered a wider range of inter-atomic distances, with a *r* range of [1–25] Å. The fit from the first test, *i.e.*, *r* within the range [5–25] Å, demonstrates a good reconstruction of the PDF data with a reliability factor R_w of 12.7% (**Figure 3.2 (a)**), confirming the average structure refinements from the diffraction data (i.e., *Pnma* SG and unit cell parameters). However, in the fit from the second test, *i.e.*, *r* within [1–25] Å, the refinement from the short-range structure (*i.e.*, *r* in [1–5] Å) does not reproduce well the local PDF features (**Figure 3.2 (b)**). This less satisfying fit suggests that the short-range structure differs from the average structure.

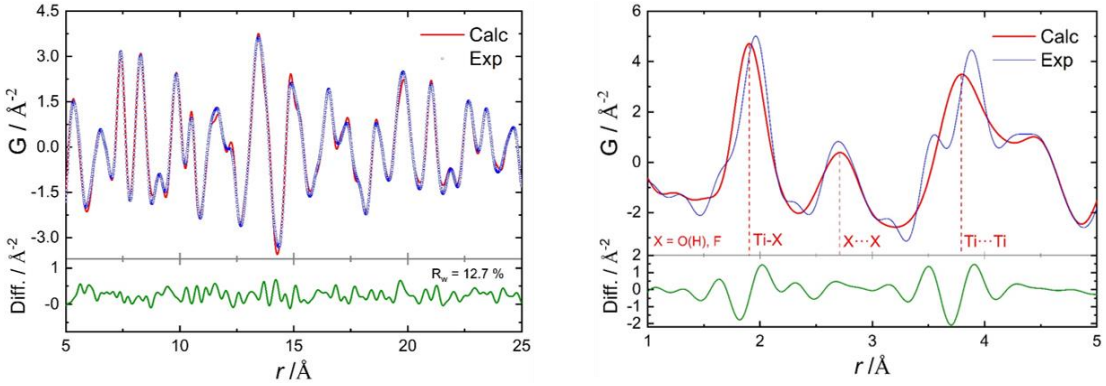


Figure 3.2. Real-space refinement of the PDF data of the sample synthetized in non-aqueous medium, (left) excluding and (right) including the short-range structure (zoom on the *r* in [1–5] Å)

III.3.3.2. DFT methods (performed by Benjamin J. Morgan[b,c,h] and co-workers)

To gain deeper insights into the short-range structure, Monte Carlo simulations were conducted at various temperatures. These simulations were based on an effective-Hamiltonian parameterized using a cluster expansion approach. We investigated the range of Ti coordination environments in a HTB-type

structural model with the $TiOF_2$ composition. **Figure 3.3** represents histograms of the frequency distribution of the different Ti coordination environments derived from the Monte Carlo simulation. These histograms show clearly that *cis*-TiO_2F_4 and *fac*-TiO_3F_3 are much more frequent than *trans*-TiO_2F_4 and *mer*-TiO_3F_3 octahedra, indicating a preferential short-range O/F ordering of O and F in the octahedra. While an increase in simulation temperature causes an increase in non-ideal Ti coordination environments, it does not alter the qualitative coordination preference.

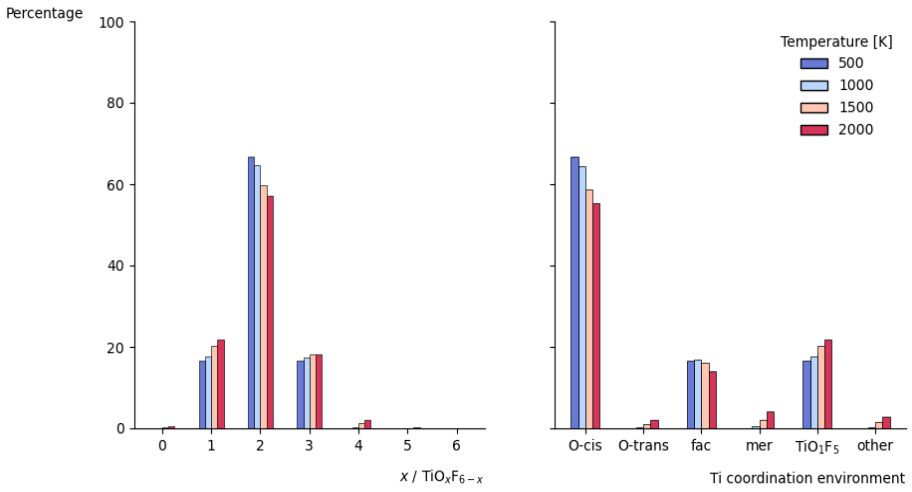


Figure 3.3. Histograms of Ti coordination environments from Monte Carlo simulations at various temperatures in HTB-$TiOF_2$. On the left, percentage of occurrence of (left) TiO_xF_{6-x} octahedra containing *x* O atoms and (right) of the different octahedral configurations.

At the octahedral level, and similarly to MX_6 octahedra from MOF_3 (M = Nb, Ta) discussed in the previous section, not all configurations of TiX_6 octahedra are equiprobable. They preferentially adopt configurations that minimize the opposite Ti–O bonds such as *cis*-TiO_2F_4 and *fac*-TiO_3F_3 octahedra. Indeed, having oxygen and fluorine, which have similar Pearson hardness, near each other maximizes the bonding energy in the Ti–X (X = O, F) bonds by allowing Ti displacement toward oxygen which is the less electronegative anion (**Figure 3.4**). Similar displacements were observed in numerous oxyfluorides with d^0 transition metals.[1–6]

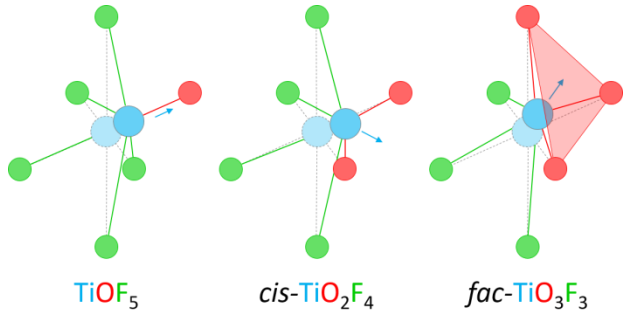


Figure 3.4. Illustration of Ti displacements (directed by blue arrows) in the configurations $TiOF_5$, *cis*-TiO_2F_4 and *fac*-TiO_3F_3.

To ascertain whether the observed patterns in the PDF analysis are indicative of O/F local order within the HTB-$TiOF_2$ compound, ground-state search functionality implemented in the Interatomic Cluster Expansion Toolkit (ICET) was employed. This computational approach was used to seek out the lowest energy arrangement of anions within the experimental unit cell. The outcome of this search revealed a structural configuration comprising ×8 *cis*-TiO_2F_4, ×2 *fac*-TiO_3F_3 and ×2 $TiOF_5$ octahedra, which is consistent with the results obtained from Monte Carlo simulations, as depicted in **Figure 3.3**.

III.3.3.3. Confirming the structural model issued from DFT computation

To confirm the structural model issued from DFT computation, PDF data was refined considering the structural features of this model, *i.e.*, ×8 *cis*-TiO_2F_4, ×2 *fac*-TiO_3F_3 and ×2 $TiOF_5$ octahedra. A first attempt of refining this data did not yield satisfactory results (**Figure 3.5 (a)**). We suspect that the absence of water molecules located within hexagonal cavities (**Figure 3.5 (b)**) could be the reason for this discrepancy. Incorporating water molecules in the previous model significantly enhanced the quality of the fit (**Figure 3.5 (c) and (d)**). This structural model, based on DFT computation and with added water molecules, is referred to here as PDF-DFT_1.

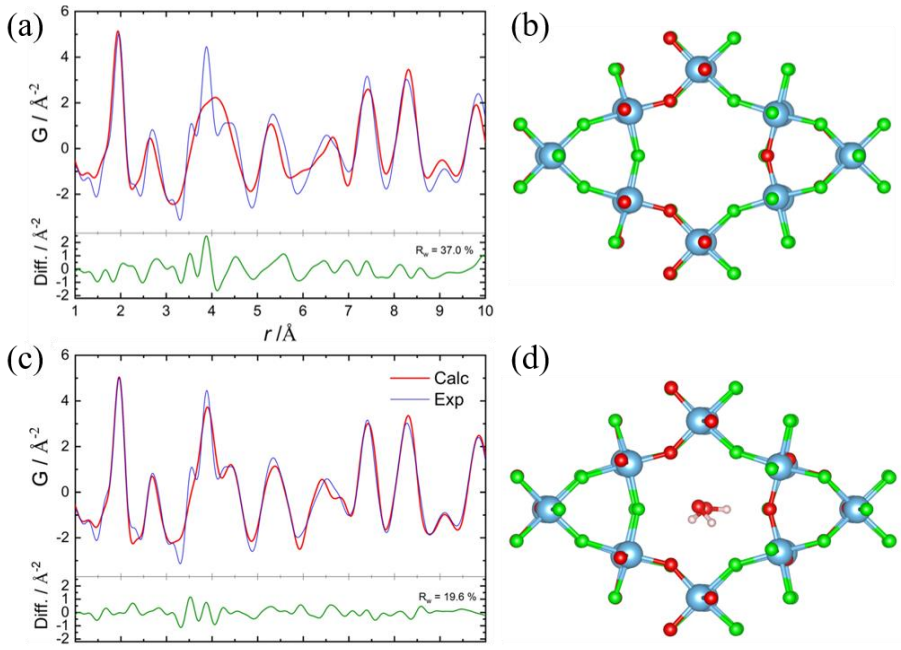


Figure 3.5. Representation of PDF data refinements from the HTB-$TiOF_2$ sample synthesized in non-aqueous medium using the model issued from DFT computation, (a) without and (c) with water molecules, along with the corresponding hexagonal cavities (b) and (d), respectively.

III.3.4. Modeling of ^{19}F NMR parameters

To obtain a more accurate picture of the environments of the ^{19}F and ^{1}H atoms, their NMR parameters were calculated using the DFT approach on the PDF-DFT_1 model. The resulting theoretical isotropic magnetic shielding values, σ_{iso}, were converted to isotropic chemical shift values, δ_{iso}, and then and compared with experimental δ_{iso} values extracted from previously recorded ^{1}H and ^{19}F MAS NMR spectra (**Figures S1 and S2 and Tables S1 and S2**).[7]

III.3.4.1. Calculation conditions

Solid-state DFT calculations with periodic boundary conditions were initially performed on the PDF-DFT_1 model including water molecules (60 atoms), and then on models with multiple OH groups (from 62 to 70 atoms). The ground-state electronic structure was obtained by the generalized gradient approximation (GGA) using the Perdew-Burke-Ernzerhof (PBE) functional (GGA-PBE).[8] Atomic position optimizations (APO) were performed on the PDF-DFT_1 model using VASP (6.2.1 version).[9,10] DFT-PDF_1 model with optimized atomic positions is referred to as PDF-DFT_2 in the following. The PAW[11,12] potentials used for Ti, F, O and H are respectively: Ti_sv_GW ($3s^2 3p^6 4s^2 3d^2$), F_GW ($2s^2 2p^5$), O_s_GW ($2s^2 2p^4$) and H_GW ($1s^1$). Valence electrons were described by a plane-wave basis with a 550

eV kinetic energy cut-off and (4 × 4 × 3) shifted Monkhorst-Pack k-point mesh. The total energy was converged up to a change below 10^{-8} eV. Since the structure contains water molecules located in the hexagonal cavities, which can potentially form H-bonds, DFT-D3 dispersion correction,[13] expected to be more efficient for non-covalent interactions, was included to the calculations. The gauge including projector augmented wave (GIPAW) approach,[14,15] implemented in VASP,[9,10] was used to calculate the magnetic shielding tensors.

III.3.4.2. Results and discussion

i. Structural features and σ_{iso}–δ_{iso} correlation for ^{19}F from TiF_4

The structural features of the PDF-DFT_1 and PDF-DFT_2 models are gathered in **Table 3.1**. For both models, as expected, Ti–O bond lengths are shorter than Ti–F ones. PDF-DFT_2 model exhibits slightly higher sdv for Ti–O (0.049 Å) and Ti–F (0.069 Å) bond lengths compared to PDF-DFT_1 (0.035 and 0.043 Å for Ti–O and Ti–F, respectively).

Table 3.1 Ti environment, average, shortest and longest Ti–X bond lengths (<Ti–X>, $Ti–X_{min}$ and $Ti–X_{max}$, Å; X = O, F; Å) and standard deviation (sdv, Å) values from the PDF refined DFT-models before (PDF-DFT_1) and after APO (PDF-DFT_2).

	TiX_6 Octahedra	<Ti–O>	$Ti–O_{min}$	$Ti–O_{max}$	sdv (Ti–O)	<Ti–F>	$Ti–F_{min}$	$Ti–F_{max}$	Sdv (Ti–F)
PDF-DFT_1	All	1.842	1.768	1.925	0.035	2.010	1.931	2.097	0.043
	$TiOF_5$ (x2)	1.770	1.768	1.773		1.978	1.931	2.044	
	TiO_2F_4 (x8)	1.837	1.808	1.865		2.015	1.943	2.097	
	TiO_3F_3 (x2)	1.879	1.842	1.925		2.038	1.989	2.088	
PDF-DFT_2	All	1.811	1.723	1.902	0.049	1.999	1.902	2.159	0.069
	$TiOF_5$ (x2)	1.723	1.723	1.723		1.965	1.905	2.062	
	TiO_2F_4 (x8)	1.808	1.771	1.884		2.003	1.902	2.159	
	TiO_3F_3 (x2)	1.848	1.819	1.902		2.031	1.927	2.085	

For ^{19}F, the linear regression equation depends not only on the nature of the metal(s) constituting the studied compound(s),[16,17] but also on the nature (bridging or terminal) of F atoms. Here, we consider the calculated ^{19}F σ_{iso} and experimental ^{19}F δ_{iso} values from TiF_4,[18] ordered fluoride (**Figure 3.6** and **Tables S3** and **S4**). The linear regression established considering both the bridging and terminal F atoms (**Figure 3.6 (a)**) deviates from those established considering only bridging F atoms (**Figure 3.6 (b)**) or terminal F atoms (**Figure 3.6 (c)**). The linear regression relation established on terminal F atoms presents errors associated with the slope, Δs = 0.068, and intersect, $\Delta\sigma_{iso}^{(ref)}$ = 22.8 ppm, significantly higher than those from both bridging and terminal F atoms (Δs = 0.007 and $\Delta\sigma_{iso}^{(ref)}$ = 1.7 ppm) and from bridging F atoms (Δs = 0.014, $\Delta\sigma_{iso}^{(ref)}$ = 0.6 ppm). Since the HTB-$TiOF_2$ structure incorporates exclusively

bridging F atoms, the linear regression equation established from bridging F atoms (**Figure 3.6 (b)**), *i.e.*, the equation δ_{iso} (ppm) = –0.828(14) σ_{iso} + 44.2(6), was used to convert the HTB-$TiOF_2$ calculated ^{19}F σ_{iso} values to calculated ^{19}F δ_{iso} values.

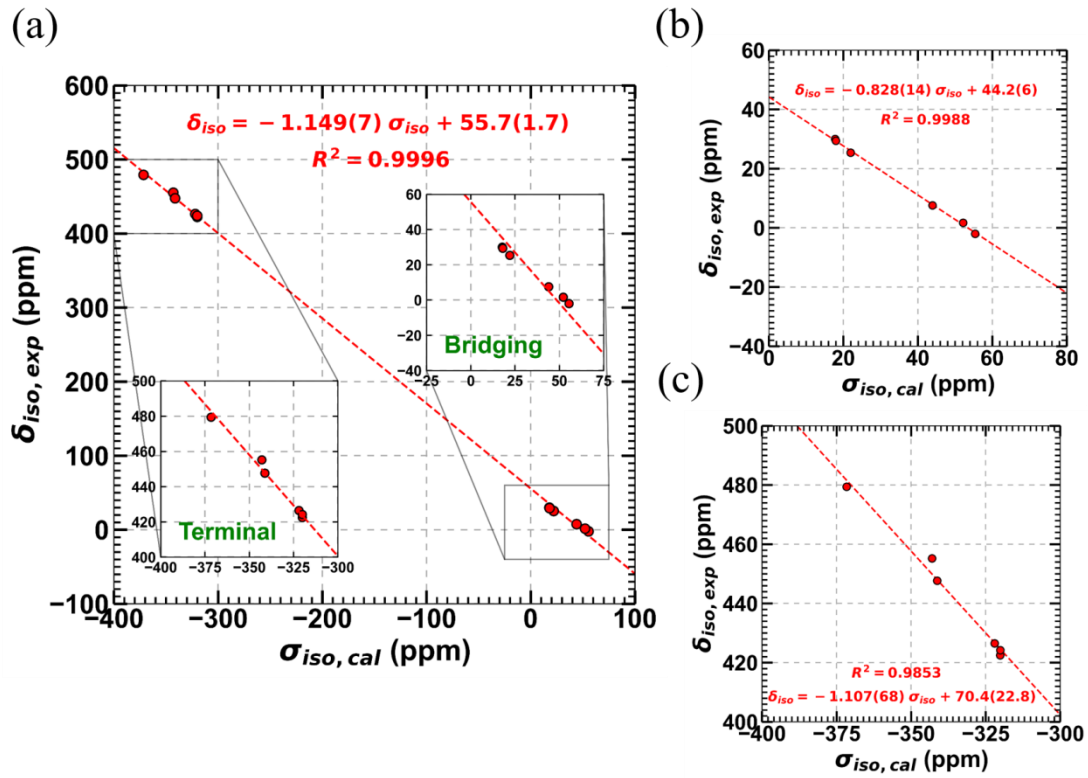


Figure 3.6. Calculated ^{19}F σ_{iso} values vs. experimental ^{19}F δ_{iso} values for bridging and terminal (a), for bridging (b) and for terminal (c) F atoms from TiF_4. In (a), enlargements of data points of the bridging and terminal F atoms are indicated. The dashed lines represent linear regressions, the corresponding equations and R-squared values are given in red.

ii. Theoretical ^{19}F solid-state NMR spectra of HTB-$TiOF_2$

Although the calculated ^{19}F δ_{iso} average values are closer to the weighted average experimental ^{19}F one (1.2 ppm) for PDF-DFT_2 (28.3 ppm) than for PDF-DFT_1 (36.4 ppm), the agreement is less than satisfactory. For both these models, theoretical ^{19}F NMR spectra were plotted considering the 24 calculated δ_{iso} values and compared to the experimental one (**Figure 3.7**). The agreement is unsatisfactory: not only are the NMR lines poorly positioned, but the range of calculated δ_{iso} values is wider than the experimental one. Given that the experimental composition is estimated with a high percentage of OH content, *i.e.*, $Ti_{0.99}\square_{0.01}O_{0.96}F_{1.53}(OH)_{0.51}\cdot 0.33H_2O$, we assume that this discrepancy

may be related to the OH presence in the HTB-$TiOF_2$ structure. Consequently, we studied the effect of the substitution of F by OH groups on the structure and on the ^{19}F δ_{iso} values.

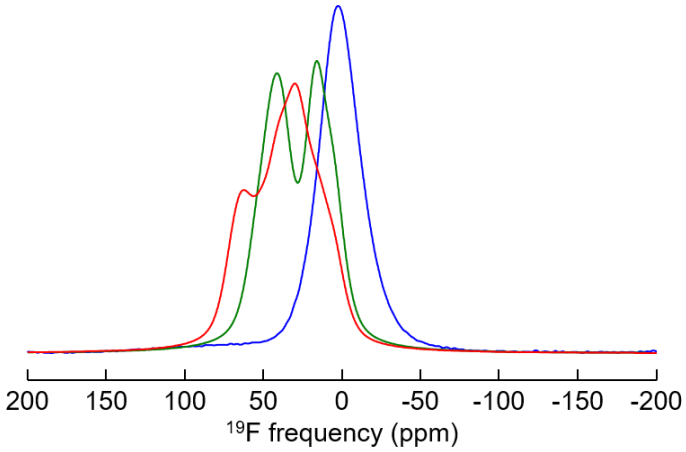


Figure 3.7. Experimental (blue) and theoretical ^{19}F NMR spectra of HTB-$TiOF_2$. The red and green spectra correspond to the PDF-DFT_1 and PDF-DFT_2 models, respectively.

III.3.4.3. Modeling hydroxylated HTB-$TiOF_2$

Five new models $TiOF_{2-x}(OH)_x \cdot 0.33H_2O$ were then built with OH substitution rates x = 1/6, 1/3, 1/2, 2/3 and 5/6 (**Table S5**). Similarly to $NbOF1F2_{2-x}(OH)_x$ compound in the previous section, the substitution of F atoms by OH groups was performed manually, and the distribution of these OH groups in the anionic sites was conducted using the "*Supercell*" program,[19] leading to high number of combinations, unmanageable with our computational hardware. Only the lowest Coulomb energy combination was chosen for each substitution rate. The atomic positions of the five selected combinations were then optimized, and the corresponding structural features are gathered in **Table S6**. The NMR parameters were then calculated, and the ^{19}F σ_{iso} values are converted to δ_{iso} values by using the linear regression equation discussed previously. The average ^{19}F δ_{iso} values are gathered in **Table 3.2**.

Table 3.2 Weighted average ^{19}F experimental δ_{iso} value (in italic) and average calculated ^{19}F δ_{iso} values from the different $TiOF_{2-x}(OH)_x \cdot 0.33H_2O$ compositions. The experimental composition is given in italic.

Model	Composition	$<\delta_{iso}>$	$\delta_{iso,\ min}$	$\delta_{iso,\ max}$
	$Ti_{0.99}\square_{0.01}O_{0.96}F_{1.53}(OH)_{0.51}\cdot 0.33H_2O$	*1.2*	n.a.	n.a.
PDF-DFT_2	$TiOF_2 \cdot 0.33H_2O$	28.3	3.5	55.8
PDF-DFT_3	$TiOF_{1.83}(OH)_{0.17} \cdot 0.33H_2O$	1.2	–66.4	48.1
PDF-DFT_4	$TiOF_{1.67}(OH)_{0.33} \cdot 0.33H_2O$	0.5	–35.4	22.0
PDF-DFT_5	$TiOF_{1.50}(OH)_{0.50} \cdot 0.33H_2O$	–3.2	–41.0	17.0
PDF-DFT_6	$TiOF_{1.33}(OH)_{0.67} \cdot 0.33H_2O$	–5.4	–25.3	27.6
PDF-DFT_7	$TiOF_{1.17}(OH)_{0.83} \cdot 0.33H_2O$	–10.4	–27.4	35.7

The substitution of F atoms by OH groups affects significantly the ^{19}F δ_{iso} calculated values (**Table 3.2 and Tables S7-S12**). The presence of two OH groups results in a decrease of the average ^{19}F δ_{iso} value from 28.3 ppm for $TiOF_2 \cdot 0.33H_2O$ to1.2 ppm (**Table 3.2**). A similar effect was observed and thoroughly exploited for $NbOF1F2_{2-x}(OH)_x$ in the previous section. A further increase of OH content in the structure leads to further decrease in ^{19}F δ_{iso} values (**Figure S3**). The best agreement between the experimental and calculated ^{19}F δ_{iso} was expected for the model with the composition the closest to the experimental one, *i.e.* $TiOF_{1.50}(OH)_{0.50} \cdot 0.33H_2O$. However, the agreement is not perfect. Instead, a resounding agreement is observed for the model with the $TiOF_{1.67}(OH)_{0.33} \cdot 0.33H_2O$ composition (**Figure 3.8**). This discrepancy might be due to H-bonds that OH groups form, and which are characterized by strong O–H···O bonds. The closer the F atoms are to these bonds, the greater their δ_{iso} value is affected. In a scenario where the calculations are conducted at temperatures similar to the experimental one, the effect of O–H···O bonds on ^{19}F δ_{iso} would be less pronounced, potentially leading to better agreement for the model with the composition $TiOF_{1.50}(OH)_{0.50} \cdot 0.33H_2O$. Indeed, at room temperature and in the course of time, the rotational movement of OH groups enables the formation and breaking of these H-bonds, whereas these effects cannot be captured by the inherently static DFT optimized structure at 0 K.

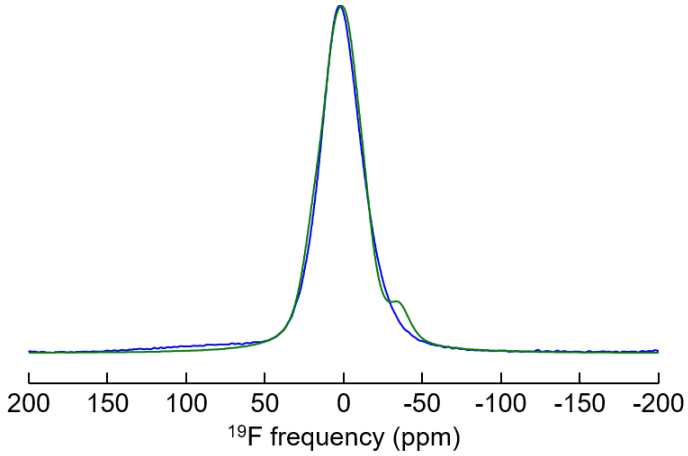


Figure 3.8. Experimental (blue) and theoretical (green) ^{19}F NMR spectra of HTB-$TiOF_2$. The green spectrum corresponds to model PDF-DFT_4 with the composition $TiOF_{1.67}(OH)_{0.33}\cdot 0.33H_2O$.

III.3.5. Conclusion

The average structure of titanium oxyfluoride $TiOF_2$ exhibiting the HTB-type structure was determined by Rietveld refinements of the X-ray and neutron diffraction data. The structure crystalizes in the orthorhombic system with the *Pnma* space group. Although the phase composition, estimated as $Ti_{0.99}\square_{0.01}O_{0.96}F_{1.53}(OH)_{0.51}\cdot 0.33H_2O$, along with refinements of the diffraction data, highlights a complex disordered average structure, PDF analysis, combined to DFT-parametrized cluster expansion methods conducted on a stoichiometric $TiOF_2$ system, revealed preferential short-range O/F ordering characterized by the strong preference for *cis*-TiO_2F_4 octahedra. The DFT model issued from this combination was further evaluated by modeling ^{19}F δ_{iso} values and comparing them to the experimental NMR data. A new linear regression equation, established from the experimental δ_{iso} and calculated σ_{iso} values for the bridging F atoms of TiF_4, was used. While some calculated ^{19}F δ_{iso} values fall within the experimental spectrum range, the agreement between the theoretical and experimental ^{19}F NMR spectra is not satisfactory. Given that the estimated compositions present a high content of OH groups substituting F atoms, new models, with the general composition $TiOF_{2-x}(OH)_x\cdot 0.33H2O$ and different OH substitution *x* rates were constructed. Notably, a resounding agreement between the theoretical and experimental ^{19}F NMR spectra was obtained for the model with the composition $TiOF_{1.67}(OH)_{0.33}\cdot 0.33H_2O$.

III.4. Conclusion

In this chapter, we have provided an in-depth investigation of the crystal structure of metal transition oxyfluorides, MOF_3 (M = Nb, Ta), and HTB-$TiOF_2$, and their hydroxylated phases, $NbOF_{2.85}(OH)_{0.15}$ and $Ti_{0.99}\square_{0.01}O_{0.96}F_{1.53}(OH)_{0.51}\cdot 0.33H_2O$. We have proved that this approach, first tested on MOF_3 and then extended upon the complex HTB-type structure of $TiOF_2$, allowed us to identify with high degree of certainty short-range O/F ordering. The structure of MOF_3 compounds consists exclusively of *cis*-MO_2F_4 octahedra, whereas in HTB-$TiOF_2$, these *cis*-TiO_2F_4 octahedra predominate, but are not exclusive.

Although the stoichiometric average structures are disordered, O/F correlated disorder was found in MOF_3, characterized by one-dimensional –F–M–O–M– strings along <100> and <010> directions. Surprisingly, this hidden short-range order arises from the exclusive presence of *cis*-MO_2F_4 octahedra.

Modeling the hydroxylated phases has allowed us to access more profound insights, such as the correlation between OH groups and ^{1}H and ^{19}F δ_{iso} values. We have successfully managed to identify the different types of hydrogen bonds formed in the hydroxylated phases $NbOF_{3-x}(OH)_x$, namely O–H···F, and $TiOF_{2-x}(OH)_x\cdot 0.33H_2O$, namely O–H···O, and to highlight the potential presence of dynamic processes experienced by these hydrogen bonds. When OH groups are present in the local environment of fluorine atoms, the corresponding ^{19}F δ_{iso} values decrease. As conventional DFT calculations are conducted at 0 K, differences between the experimental and calculated ^{1}H and ^{19}F δ_{iso} values can reveal the presence of dynamic processes at the hydrogen bond level. These processes are characterized by the rapid formation and breaking of the hydrogen bonds, in the course of time, enabled by the rotational movement of OH groups.

III.5. References

(1) Dabachi, J.; Body, M.; Galven, C.; Boucher, F.; Legein, C. Preparation-Dependent Composition and O/F Ordering in NbO_2F and TaO_2F. *Inorg. Chem.* **2017**, *56* (9), 5219–5232. https://doi.org/10.1021/acs.inorgchem.7b00355.

(2) Pausewang, G.; Rüdorff, W. Über Alkali-oxofluorometallate der Übergangsmetalle. $A_3^IMeO_xF_{6-x}$-Verbindungen mit x = 1, 2, 3. *Z. Anorg. Allg. Chem.* **1969**, *364* (1–2), 69–87. https://doi.org/10.1002/zaac.19693640107.

(3) Christe, K. O.; Wilson, R. D. Cis- and Trans- Iodine (VII) Oxytetrafluoride Hypofluorite, OIF_4OF. *Inorganic and Nuclear Chemistry Letters* **1979**, *15* (9–10), 375–376. https://doi.org/10.1016/0020-1650(79)80114-2.

(4) Welk, M. E.; Norquist, A. J.; Arnold, F. P.; Stern, C. L.; Poeppelmeier, K. R. Out-of-Center Distortions in d^0 Transition Metal Oxide Fluoride Anions. *Inorg. Chem.* **2002**, *41* (20), 5119–5125. https://doi.org/10.1021/ic025622v.

(5) Voit, E. I.; Voit, A. V.; Mashkovskii, A. A.; Laptash, N. M.; Kavun, V. Ya. Dynamic Disorder in Ammonium Oxofluorotungstates $(NH_4)_2WO_2F_4$ and $(NH_4)_3WO_3F_3$. *J Struct Chem* **2006**, *47* (4), 642–650. https://doi.org/10.1007/s10947-006-0351-3.

(6) Morelock, C. R.; Greve, B. K.; Cetinkol, M.; Chapman, K. W.; Chupas, P. J.; Wilkinson, A. P. Role of Anion Site Disorder in the Near Zero Thermal Expansion of Tantalum Oxyfluoride. *Chem. Mater.* **2013**, *25* (9), 1900–1904. https://doi.org/10.1021/cm400536n.

(7) Li, W.; Body, M.; Legein, C.; Dambournet, D. Sol–Gel Chemistry of Titanium Alkoxide toward HF: Impacts of Reaction Parameters. *Crystal Growth & Design* **2016**, *16* (9), 5441–5447. https://doi.org/10.1021/acs.cgd.6b00910.

(8) Perdew, J. P.; Burke, K.; Ernzerhof, M. Generalized Gradient Approximation Made Simple. *Phys. Rev. Lett.* **1996**, *77* (18), 3865–3868. https://doi.org/10.1103/PhysRevLett.77.3865.

(9) Kresse, G.; Furthmüller, J. Efficiency of Ab-Initio Total Energy Calculations for Metals and Semiconductors Using a Plane-Wave Basis Set. *Computational Materials Science* **1996**, *6* (1), 15–50. https://doi.org/10.1016/0927-0256(96)00008-0.

(10) Kresse, G.; Furthmüller, J. Efficient Iterative Schemes for *Ab Initio* Total-Energy Calculations Using a Plane-Wave Basis Set. *Phys. Rev. B* **1996**, *54* (16), 11169–11186. https://doi.org/10.1103/PhysRevB.54.11169.

(11) Blöchl, P. E. Projector Augmented-Wave Method. *Phys. Rev. B* **1994**, *50* (24), 17953–17979. https://doi.org/10.1103/PhysRevB.50.17953.

(12) Kresse, G.; Joubert, D. From Ultrasoft Pseudopotentials to the Projector Augmented-Wave Method. *Phys. Rev. B* **1999**, *59* (3), 1758–1775. https://doi.org/10.1103/PhysRevB.59.1758.

(13) Grimme, S.; Antony, J.; Ehrlich, S.; Krieg, H. A Consistent and Accurate *Ab Initio* Parametrization of Density Functional Dispersion Correction (DFT-D) for the 94 Elements H-Pu. *The Journal of Chemical Physics* **2010**, *132* (15), 154104. https://doi.org/10.1063/1.3382344.

(14) Pickard, C. J.; Mauri, F. All-Electron Magnetic Response with Pseudopotentials: NMR Chemical Shifts. *Phys. Rev. B* **2001**, *63* (24), 245101. https://doi.org/10.1103/PhysRevB.63.245101.

(15) Yates, J. R.; Pickard, C. J.; Mauri, F. Calculation of NMR Chemical Shifts for Extended Systems Using Ultrasoft Pseudopotentials. *Phys. Rev. B* **2007**, *76* (2), 024401. https://doi.org/10.1103/PhysRevB.76.024401.

(16) Biswal, M.; Body, M.; Legein, C.; Sadoc, A.; Boucher, F. NbF_5 and TaF_5: Assignment of ^{19}F NMR Resonances and Chemical Bond Analysis from GIPAW Calculations. *Journal of Solid State Chemistry* **2013**, *207*, 208–217. https://doi.org/10.1016/j.jssc.2013.09.001.

(17) Martel, L.; Capelli, E.; Body, M.; Klipfel, M.; Beneš, O.; Maksoud, L.; Raison, P. E.; Suard, E.; Visscher, L.; Bessada, C.; Legein, C.; Charpentier, T.; Kovács, A. Insight into the Crystalline Structure of ThF_4 with the Combined Use of Neutron Diffraction, ^{19}F Magic-Angle Spinning-NMR, and Density Functional Theory Calculations. *Inorg. Chem.* **2018**, *57* (24), 15350–15360. https://doi.org/10.1021/acs.inorgchem.8b02683.

(18) Murakami, M.; Noda, Y.; Takegoshi, K. Terminal and Bridging Fluorine Ligands in TiF_4 as Studied by ^{19}F NMR in Solids. *Solid State Nuclear Magnetic Resonance* **2019**, *101*, 82–88. https://doi.org/10.1016/j.ssnmr.2019.05.007.

(19) Okhotnikov, K.; Charpentier, T.; Cadars, S. Supercell Program: A Combinatorial Structure-Generation Approach for the Local-Level Modeling of Atomic Substitutions and Partial Occupancies in Crystals. *J Cheminform* **2016**, *8* (1), 17. https://doi.org/10.1186/s13321-016-0129-3.

Chapter IV

“Disordered” Oxyfluorides

IV.1. Introduction

In the previous chapter, O/F correlated disorder in $NbOF_3$ and $TaOF_3$, as well as preferential short-range O/F ordering in HTB-$TiOF_2$, were evidenced and thoroughly explored. The similarity among these oxyfluorides is the favored (or even exclusive) presence of *cis*-MO_2F_4 (M = Nb, Ta, Ti) octahedra, which do not align with the statistical distribution of MX_6 octahedra permitted by the experimental formulations (**Figure 4.1**). The tendency of anions in these oxyfluorides to form specific octahedral configuration, such as *cis*-MO_2F_4 in MOF_3 and HTB-$TiOF_2$, or *cis*-MO_4F_2 in MO_2F compounds, is not coincidental. Chemists have attempted to explain this behavior from an atomistic perspective. They propose that anions arrange in a way that maximizes the π-hybridization in the M-anion bonds, particularly if M is a d^0 transition metal. However, this explanation does not solely apply to *cis*-MO_2F_4 octahedra but also to *fac*-MO_3F_3 octahedra: the favored or exclusive presence of *cis*-MO_2F_4 octahedra over *fac*-MO_3F_3 ones remains a mystery that requires further investigations. This non-random short-range O/F ordering raises a critical yet unaddressed question within the inorganic chemistry community: can inorganic oxyfluorides ever exhibit complete random distribution of anions in the crystal substructure?

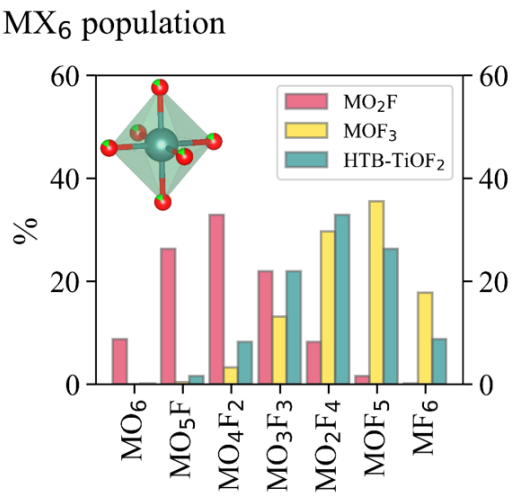


Figure 4.1. Statistical distribution of MX_6 octahedra.

In this context, O/F short-range arrangement should be studied in oxyfluorides with more complex structures. The cation- and anion-disordered pyrochlore oxyfluorides RbM_2O_5F (M = Nb, Ta), are a well suited candidates for the study of structural disorder, as three of the nuclei, ^{19}F, ^{87}Rb and ^{93}Nb, are easily observable by ssNMR. The first aim of this study is to assess whether anions can be randomly distributed in the crystal substructure.

Preferential O/F Ordering in the Pyrochlore Oxyfluorides RbM_2O_5F (M = Nb, Ta) Revealed by Multimodal Structural Modeling Approach

Ouail Zakary[a,], Monique Body[a], Christophe Legein[a,*], Vincent Sarou-Kanian[b], Frank Fayon[b], Aydar Rakhmatullin[b], Thibault Charpentier[c]*

[a] Institut des Molécules et Matériaux du Mans (IMMM) – UMR 6283 CNRS, Le Mans Université, avenue Olivier Messiaen, 72085 Le Mans Cedex 9, France

[b] Conditions Extrêmes et Matériaux, Haute Température et Irradiation (CEMHTI), UPR3079 CNRS, Orléans, France

[c] Université Paris-Saclay, CEA, CNRS, NIMBE, 91191, Gif-sur-Yvette cedex, France

KEYWORDS: Pyrochlores, Correlated Disorder, Multinuclear High Field Solid-State NMR, First Principle Calculations

ABSTRACT. The short-range structure of RbM_2O_5F (M = Nb, Ta) pyrochlore oxyfluorides was thoroughly investigated by combining X-ray powder diffraction (XRPD), multinuclear high field solid-state NMR and DFT calculations. The shapes of NMR spectra, carried out for ^{19}F, ^{87}Rb and ^{93}Nb (for $RbNb_2O_5F$) nuclei, confirm the existence of disordered local environments for those nuclei. From the average structure obtained by refining the XRPD data and using the supercell approach, two sets of 20 possible models were built, with Rb atoms in either the 8b or 32e sites. After DFT relaxation, all these Rb atoms were found to occupy low-symmetry (*x*,*y*,*z*) positions. Furthermore, when present, all $NbOF_5$ and NbF_6 octahedra evolved, during the DFT relaxation process, into to either NbO_2F_5, $NbOF_6$ or NbO_2F_6 polyhedra, underlining the preference of Nb atoms for oxygen atoms. NMR parameters were calculated using the PAW and GIPAW approaches. Among the tested models, only 8 with Rb initially in the 32e site (and the corresponding 8 models with Rb initially in the 8b site) present calculated C_Q values within the ^{87}Rb and ^{93}Nb (when present) average C_Q ranges extracted from NMR spectra. Instead of a statistical distribution of MX_6 octahedra, anions in the structure of $RbNb_2O_5F$ and $RbTa_2O_5F$ pyrochlores are locally ordered. This local anion order is defined by the exclusive presence of MOF_5 octahedra, as well as the presence of $RbO_{15}F_3$ cages and/or an equal proportion of $RbO_{14}F_4$, and $RbO_{16}F_2$ ones.

1. Introduction

Pyrochlores are well-known for their highly “tailorable” structures, which makes it possible to create materials with targeted physicochemical properties and functionalities.[1,2] Having the ideal stoichiometric formula $A_2B_2X_6Y$, the pyrochlore structure crystallizes in the isometric crystal system with centrosymmetric $Fd\bar{3}m$ (no. 227) space-group. This structure incorporates four possible distinct crystallographic sites, two for the cations A (32e and/or 16c and/or 8b Wyckoff positions) and B (16d Wyckoff position) and two for the anions, noted X (48f Wyckoff position) and Y (8b Wyckoff position). The eightfold coordinated A cation (AX_6Y_2 distorted cubes) sites are relatively large, whereas the sixfold coordinated B cation (trigonal antiprisms BX_6) sites are smaller. The extensive flexibility observed in the composition of pyrochlores emanates from the wide variety of possible site substitutions that may occur on the cationic sites, but also on the anionic sites.[3–6] Instead of the more commonly observed O^{2-} anion, these positions can be filled by anions such as OH^-, F^- and S^{2-}. For instance, there are at least 75 known pyrochlore oxyfluorides, whether ordered or disordered (**Tables S1** and **S2**), some of which possess intriguing properties. $CsTi_2O_{2.85}F_{3.15}$ is synthesized at relatively low temperature and turns out to exhibit excellent thermal stability and acid/alkali resistance.[7] The n-type semiconductors $Na_2B_2O_5F_2$ (B = Nb, Ta) have been shown to be photoactive[8]. Similarly, pyrochlores such as $Pb_2Ti_2O_{5.4}F_{1.2}$,[9] Sb_2TiNbO_6F[10] and $Na_{2-2x}Sn_xM_2O_5F_2$ (M = Nb, Ta and $1 \leq x \leq 0$)[11] exhibit interesting photocatalytic properties. Moreover, in some cases, the structure of pyrochlore oxyfluorides enables dynamic processes, particularly ionic transport[12] and conductivity.[13]

In oxide-derived heteroanionic pyrochlores, the coexistence of two (or more) anionic species with different charges, ionic radii, electronegativities and polarizabilities in the host crystal structure allows for modifying stoichiometry and local structure, resulting in properties distinct from those of analogous pyrochlore oxides. These properties depend not only on the

stoichiometry and identity of the constituent anions but also on their arrangement in the crystal structure. Therefore, a precise description of local order in these structures is of the utmost importance. Oxide-derived heteroanionic pyrochlores, such as oxyfluorides, are typically characterized with “long-length-scale characterization techniques”, such as X-ray and neutron diffraction, which, however, only provide a model of the average crystal structure, known as the “long-range structure”[14]. As O^{2-} and F^{-} have similar X-ray (or Neutron) scattering factors, relying solely on the diffraction data is insufficient to describe O/F ordering. In this context, solid-state NMR spectroscopy (ssNMR) combined to DFT calculations is regarded as a potent multimodal approach, as it can offer detailed insights into the local atomic environments. Indeed, over the past decade, multiple disordered oxyfluorides have been successfully described through the combination of X-ray powder diffraction (XRPD), ssNMR and DFT calculations.[15–17]

The pyrochlore oxyfluorides RbM_2O_5F (M = Nb, Ta) seem ideal to further assessing the efficiency of this multimodal approach in investigating local structures within such disordered compounds. This process is facilitated by the easy observation of the three out of the five nuclei through ssNMR. Initially synthesized and characterized by Babel *et al.*,[18] the average structure of these compounds was found to adopt the pyrochlore structure, wherein Rb and M cations are located in the 8b and 16c sites, respectively, while O and F co-occupy the 48f site with respective site occupancy factors of 83.3% and 16.7%. However, Follow-up investigations from Ory *et al.*[19] and Fourquet *et al.*[20] demonstrated that in $RbNb_2O_5F$, Rb atoms are statistically distributed in the 32e site, rather than totally occupying the 8b site. Later on, from single crystal data of $RbTa_2O_5F$ and in accordance with the initial model given by Babel *et al.*,[18] Goodenough *et al.*[12] conclude that the 32e site cannot be occupied and that Rb atoms indeed occupy the 8b site. From these studies, the positions of Rb atoms remain uncertain. Moreover, the co-occupation of the anionic site result in random configurations of MX_6 octahedra (X = O, F),

with possible homoleptic and/or heteroleptic polyhedral units (HomPUs and HetPUs, respectively).

Herein, we investigate the short-range structure of RbM_2O_5F pyrochlores and propose a set of models describing its O/F ordering. To achieve this, RbM_2O_5F compounds were synthesized and characterized by XRPD, ^{19}F ssNMR and high field ssNMR of ^{87}Rb and ^{93}Nb (for $RbNb_2O_5F$). The average structure was obtained by refining the XRPD data. Using the supercell approach along with Coulomb energy sorting and cation environment probabilities as selective criteria, 20 models were selected for $RbNb_2O_5F$, with Rb distributed on the 32e sites. To provide a basis for comparison, 20 similar models with Rb positioned on the 8b sites were tested. Subsequently, DFT relaxation was performed on these 40 models, and NMR parameters were calculated using the PAW and GIPAW approaches. These parameters were then compared to the experimental data. An overall agreement is reached for 16 models exclusively featuring MO_5F octahedra.

2. Experimental section

2.1 Synthesis. Pure RbM_2O_5F compounds were obtained by direct solid-state synthesis from a stoichiometric mixture of RbF (Alfa Produkte, 99.9%) and M_2O_5 (M = Nb, Ta) (Alfa Aesar, 99.85% and 99.9% for Ta_2O_5 and Nb_2O_5, respectively). Prior to synthesis, M_2O_5 compounds were dried under secondary vacuum at 150 °C for 9 hours, with heating and cooling occurring at a rate of 2 °C per minute and then stored in a glove box under nitrogen atmosphere. With RbF being moisture sensitive, the weighing, mixing and grinding steps were performed under nitrogen atmosphere in a glove box. The resulting mixtures were then placed inside platinum tubes, sealed and heated to 750 °C for four days with a heating rate of 5 °C.min^{-1}, after which they were left to cool down naturally.

2.2 X-ray powder diffraction. The PXRD diagrams were recorded using a PANalytical θ/θ Bragg–Brentano EMPYREAN diffractometer (CuKα_{1+2} radiations) equipped with a PIXcel^{1D} detector. The patterns were measured in a 2θ range of 5° to ~120° with a 0.0131° step size, the recording time was approximately 6 hours. The obtained data was refined employing the Rietveld structural refinement method[21] incorporated in the Fullprof software.[22] Alongside the usual refinement parameters, the preferred orientation parameter (G1) was refined. The background intensity was estimated from linear interpolation between points manually selected in regions free from Bragg reflections.

2.3 Solid-state NMR spectroscopy. The ^{19}F (*I = 1/2*) magic angle spinning (MAS) NMR spectra were recorded with a Bruker Avance III spectrometer functioning at 7.0 T (^{19}F Larmor frequency of 283.4 MHz) using a 1.3 mm CP-MAS probe-head, the spinning frequency was set to 44 kHz. The Hahn echo sequence was used with an interpulse delay of one rotor period and a recycle delay of 300 s and 30 s for $RbNb_2O_5F$ and $RbTa_2O_5F$, respectively. The 90° pulse was set to 1.56 μs (RF field of 160 kHz) and 1.25 μs (RF field of 200 kHz) for $RbNb_2O_5F$ and $RbTa_2O_5F$, respectively.

The ^{87}Rb (I = 3/2) and ^{93}Nb (I = 9/2) MAS and multiple-quantum MAS (MQMAS[23,24]) NMR spectra were acquired using a Bruker Avance III spectrometer operating at 20.0 T (^{87}Rb and ^{93}Nb Larmor frequencies of 278.2 and 208.1 MHz, respectively).

The ^{87}Rb MAS and MQMAS spectra were recorded using a 2.5 mm CP-MAS probe-head, at a 30 kHz spinning frequency. The ^{87}Rb one-pulse MAS NMR spectra was recorded with a recycle delay of 0.25 s and a pulse duration of 0.38 μs (RF field of 64 kHz), corresponding to a small flip angle of 10° to ensure a total excitation of the entire spin system. The ^{87}Rb two-dimensional z-filtered MQMAS spectra were recorded using a RF field strength of 64 kHz for the triple-quantum excitation and reconversion (3QMAS), with a z-filter duration of 33 μs,

recycle delay of 0.33 s and 128 t_1 increments with 1152 transients each. The duration of the central transition (CT) 90° selective pulse was set to 9.8 μs (RF field of 13 kHz).

The ^{93}Nb MAS and MQMAS NMR spectra were recorded using a 0.7 mm CP-MAS probe-head, at ultra-fast spinning frequency of 100 kHz. The Hahn echo sequence was used for the ^{93}Nb one-dimensional CT MAS NMR spectrum (CTMAS), with a recycle delay of 1 s and duration of the CT 90° selective pulse of 2 μs (RF field of 25 kHz). The ^{93}Nb 3QMAS spectrum was acquired with a RF field strength of 350 kHz for the triple-quantum excitation and reconversion, a CT selective pulse of 2 μs (RF field of 25 kHz), a z-filter duration of one rotor period and a recycle delay of 0.5 s. 40 t_1 increments of 4800 transients each were accumulated.

The recorded spectra of ^{19}F, ^{87}Rb and ^{93}Nb were referenced to $CFCL_3$ (using BaF_2 as secondary reference with δ_{iso} = –14.3 ppm),[25] 1 M aqueous solution of RbCl and $KNbCl_6$, respectively. All spectra were fitted using the DMFit software,[26] the baseline intensities of the ^{87}Rb MAS and ^{93}Nb CTMAS spectra were estimated from linear interpolation between points manually selected in regions free from resonances. The “Czjzek”[27] and “CzSimple” models were used to fit the MAS, CTMAS and 3QMAS spectra, respectively. The “Czjzek” model considers a statistical distribution of the quadrupolar interaction (C_Q and the asymmetry parameter, η_Q) induced by the distribution of the local environment of the probed nuclei, whereas the “CzSimple” model includes a rapid version of the “Czjzek” model with an uncoupled Gaussian distribution of δ_{iso} values. Both models are used with d = 5 and enable the retrieval of the average δ_{iso} ($<\delta_{iso}>$) and C_Q ($<C_Q>$) values, as well as the width of the Gaussian distribution of the average δ_{iso} value ($\Delta\delta_{iso}$). The average asymmetry parameter ($<\eta_Q>$) value is fixed at ~ 0.61 with an approximate standard deviation of σ_η ~ 0.24.[27]

3. First principle calculations

The ground state electronic structure, the electric field gradient and magnetic shielding tensors were all calculated using VASP (version 6.2.1).[28,29]

3.1 DFT relaxation. The electronic structure of the unit cell consisting of 72 atoms was determined through solid-state DFT calculations with periodic boundary conditions. Conjugate-gradient algorithm was used in ionic relaxation. The Perdew-Burke-Ernzerhof functional including the generalized gradient approximation (GGA-PBE)[30] was employed to obtain the ground state electronic structure. The projector augmented wave (PAW) potentials[31] used for Rb, Ta, Nb, F and O are respectively: Rb_sv_GW, Ta_sv_GW, Nb_sv_GW, F_GW and O_s_GW. The wave functions were expanded on a plane-wave basis set with a 550eV kinetic energy cut-off and a 3 × 3 × 3 shifted Monkhorst-Pack k-point mesh. The total energy was converged up to a change bellow 10^{-8} eV.

3.2 NMR parameters calculations. The PAW[32,33] and GIPAW[34,35] approaches were used to calculate the electric field gradient and the magnetic shielding tensors, respectively. The PAW potentials, plane-wave energy cut-off and the shifted Monkhorst-Pack k-point mesh were set the same as the DFT relaxation.

The magnetic shielding and chemical shift parameters are defined using the Haeberlen convention.[36] The isotropic magnetic shielding (σ_{iso}), anisotropy (σ_{csa}) and asymmetry (η_{csa}) parameters are respectively defined as $\sigma_{iso} = (\sigma_{xx} + \sigma_{yy} + \sigma_{zz})/3$, $\sigma_{csa} = \sigma_{zz} - \sigma_{iso}$ and $\eta_{csa} = (\sigma_{yy} - \sigma_{xx})/\sigma_{csa}$, with the magnetic shielding tensor components σ_{ii} defined in the sequence $|\sigma_{zz} - \sigma_{iso}| \geq |\sigma_{xx} - \sigma_{iso}| \geq |\sigma_{yy} - \sigma_{iso}|$. Similarly, the isotropic chemical shift (δ_{iso}), anisotropy (δ_{csa}) and asymmetry (η_{csa}) parameters are given by $\delta_{iso} = (\delta_{xx} + \delta_{yy} + \delta_{zz})/3$, $\delta_{csa} = \delta_{zz} - \delta_{iso}$ and $\eta_{csa} = (\delta_{yy} - \delta_{xx})/\delta_{csa}$, with the chemical shift tensor components δ_{ii} ordered in the sequence $|\delta_{zz} - \delta_{iso}| \geq |\delta_{xx} - \delta_{iso}| \geq |\delta_{yy} - \delta_{iso}|$.

σ_{iso} is related to δ_{iso} by the relation $\delta_{iso} \simeq \sigma_{iso,ref} - \sigma_{iso}$, where $\sigma_{iso,ref}$ represents the absolute isotropic magnetic shielding reference, that is determined by establishing a linear regression between experimental δ_{iso} and calculated σ_{iso} values. Multiple linear regressions for fluorine have been determined on a variable number of ordered fluorides.[37–43] In the present study, calculated ^{19}F δ_{iso} values were derived from linear regression equation established from RbF[44] and MF_5 (M = Nb, Ta)[45,46] fluorides, considering the cationic similarity of these fluorides to RbM_2O_5F. Furthermore, calculated ^{87}Rb δ_{iso} values were deduced from a new regression equation established in the present work. Further details about the ^{19}F and ^{87}Rb linear regressions are presented in the “NMR parameters calculation” section.

4. Results and discussion

4.1 Characterization. The experimental ^{19}F MAS NMR spectra, shown in **Figure 1**, display a broad and slightly asymmetric line and are both reconstructed using two contributions (**Figures S1** and **S2**, **Tables S3** and **S4**). The weighted average ^{19}F δ_{iso} values, around –101.5 and –109.5 ppm for $RbNb_2O_5F$ and $RbTa_2O_5F$, respectively, are within the δ_{iso} range of values identified for fluorine atoms surrounded by at least one alkaline and one niobium atoms (from –85.1 to –119.2 ppm for equatorial F sites in CS and HT $KNaNbOF_5$).[47] These NMR data are consistent with literature structural model, where the environment of the bridging fluorine site is distributed.[12,18]

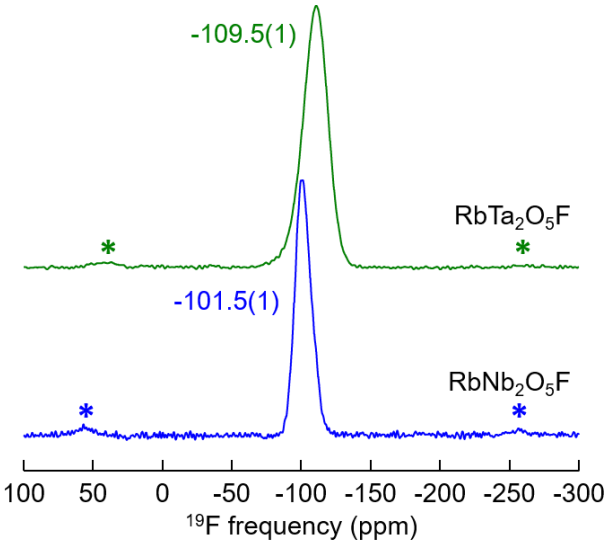


Figure 1. Experimental ^{19}F MAS (44 kHz) NMR (7 T) spectra of $RbNb_2O_5F$ and $RbTa_2O_5F$. The average weighted experimental chemical shift values are indicated. The asterisks refer to spinning sidebands.

Given that ^{87}Rb ($I = 3/2$) and ^{93}Nb ($I = 9/2$) nuclei are subject to the quadrupolar interaction, the use of ^{87}Rb and ^{93}Nb NMR enables insights on the distribution of their local environment. **Figure 2** presents ^{87}Rb MAS NMR spectra from $RbNb_2O_5F$ and $RbTa_2O_5F$. Both spectra display a broad asymmetric CT shape and an absence of singularities in the ST patterns. These features are consistent with a disordered local environment for ^{87}Rb. The line shapes observed on ^{87}Rb 3QMAS spectra (**Figure 3**) take the form of a ridge along the diagonal, confirming the presence of both chemical shift and quadrupolar interaction dispersions.[48] For both compound, an initial set of parameters was obtained by reconstructing the ^{87}Rb MAS spectrum using Gaussian distributions for both the chemical shift and quadrupolar interactions. These parameters were then used to construct the ^{87}Rb 3QMAS spectrum and were subsequently adjusted to achieve the best possible reconstruction of both 1D and 2D spectra. The resultant parameters are gathered in **Table 1**. Similar ^{87}Rb δ_{iso} and $\Delta\delta_{iso}$ values are obtained for both compounds, indicating similar environments. The C_Q value is slightly higher for $RbTa_2O_5F$,

which may be attributed to a greater sensibility of the quadrupolar interaction to small variations of these environments.

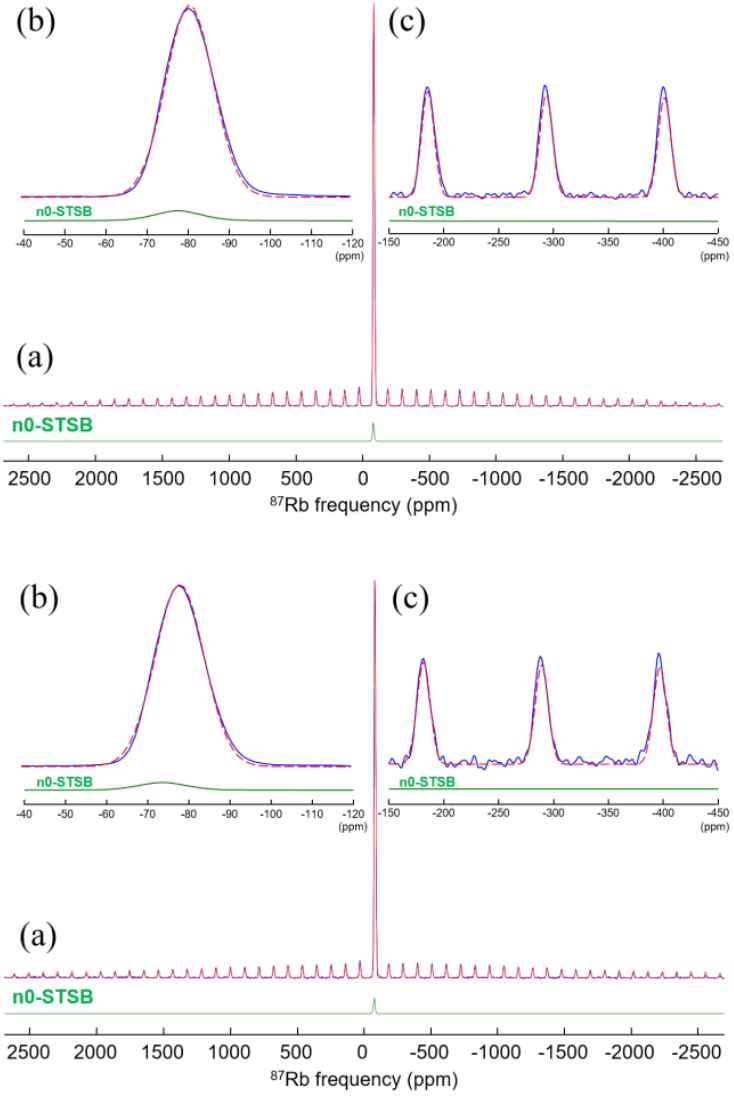


Figure 2. Experimental and fitted ^{87}Rb MAS (30 kHz at 20.0 T) NMR spectra (a) of $RbNb_2O_5F$ (left) and $RbTa_2O_5F$ (right). The insets present zooms of (b) the central transition and (c) the first-order satellite transitions. The zeroth-order satellite transition spinning sidebands (n0-STSB) are shown below the spectra, at –77.5 and –73.6 ppm for $RbNb_2O_5F$ and $RbTa_2O_5F$, respectively.

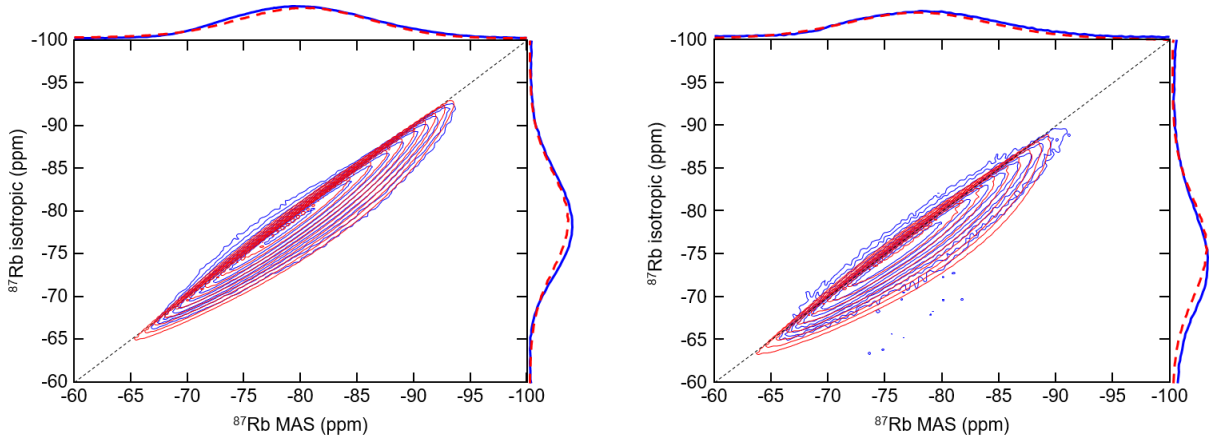


Figure 3. Experimental and fitted ^{87}Rb 3QMAS (30 kHz at 20.0 T) NMR spectra of $RbNb_2O_5F$ (a) and $RbTa_2O_5F$ (b).

Table 1. Compound, ^{87}Rb average δ_{iso} values (δ_{iso}, ppm), width of the distribution of the δ_{iso} values ($\Delta\delta_{iso}$, ppm) and average quadrupolar coupling constant (C_Q, MHz).

Compound	δ_{iso} (±0.2)	$\Delta\delta_{iso}$ (±0.2)	C_Q (±0.2)
$RbNb_2O_5F$	–79.5	13.3	1.7
$RbTa_2O_5F$	–76.5	13.5	2.0

^{93}Nb MAS and 3QMAS spectra were recorded for $RbNb_2O_5F$ at the ultra-high MAS frequency of 100 kHz. They were fitted using the same approach as for the ^{87}Rb spectra. The resulting parameters are gathered in **Table 2**. In comparison to ^{87}Rb MAS NMR spectra, ^{93}Nb CTMAS spectrum (**Figure 4**) from $RbNb_2O_5F$ exhibit broader asymmetric CT, indicating largely distributed ^{93}Nb local environment. This distribution is further confirmed by ^{93}Nb 3QMAS spectrum (**Figure 4**), which exhibit a combination of horizontal ridge and a wide ridge along the diagonal indicating largely distributed δ_{iso} and C_Q.

Table 2. Spectrum, ^{93}Nb average δ_{iso} value (δ_{iso}, ppm), width of the distribution of the δ_{iso} value ($\Delta\delta_{iso}$, ppm), average quadrupolar coupling constant (C_Q, MHz). Average values from CTMAS and 3QMAS spectra are given in bold italic.

Spectrum	δ_{iso} (±5)	$\Delta\delta_{iso}$ (±5)	C_Q (±5)
CTMAS	–1048.8	86.3	55.1
3QMAS	–1060.5	86.3	55.1
< >	***–1054.6***	***86.3***	***55.1***

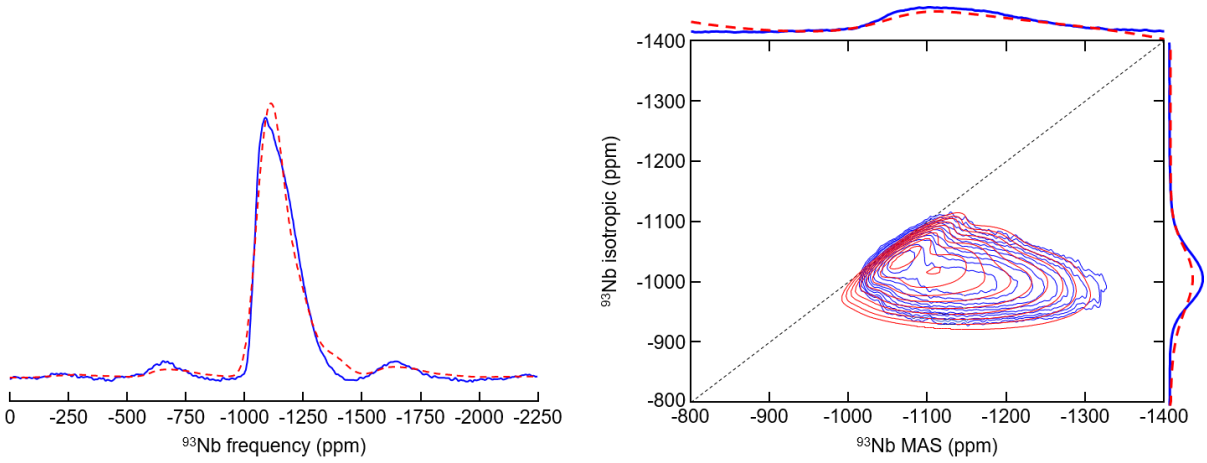


Figure 4. Experimental (blue) and fitted (red) ^{93}Nb MAS (left) and MQMAS (right) NMR (100 kHz at 20.0 T) spectra of $RbNb_2O_5F$.

4.2 Average structure. The experimental structure (ES) was derived by refining the XRPD patterns using the Rietveld refinement method. Two structural solutions were tested, the first solution involves considering Rb atoms in the 8b site, while the second solution considers Rb atoms partially occupying the 32e site. Realistic refinement parameters were obtained with the latter structural solution, considering isotropic displacement parameters (IDPs) for all atoms and constraining these IDPs for cations. The ES crystallographic features are gathered in **Table 3**. The experimental and calculated XRPD patterns, as well as their refinement reliability

parameters, are gathered in **Figures S3** and **S4**. The obtained ES fits the model proposed by Ory *et al.*[19] The structure consists of a 3D network of corner-shared MX_6 octahedra, forming ring-like shapes referred to hereafter as the subarray *sub*–MX_3, which collectively constitute the tridimensional framework. A large polyhedral cage, whose center hosts the 32e site that is partially occupied by Rb atoms, is formed by four *sub*–MX_3 (**Figure 5**). Both the cationic and anionic environments are distributed. Given the formulation of the compounds, MO_6, MO_5F and MO_4F_2 octahedra present the highest probabilities at ~30, ~40 and ~20 %, respectively (**Figure 5**). As Rb atoms are coordinated by 18 anions, various polyhedral configurations are possible, with the most likely ones being $RbO_{17}F$, $RbO_{16}F_2$, $RbO_{15}F_3$, $RbO_{14}F_4$ and $RbO_{13}F_5$, constituting ~14, ~23, ~25, ~18 and ~10%, respectively (**Figure 5**).

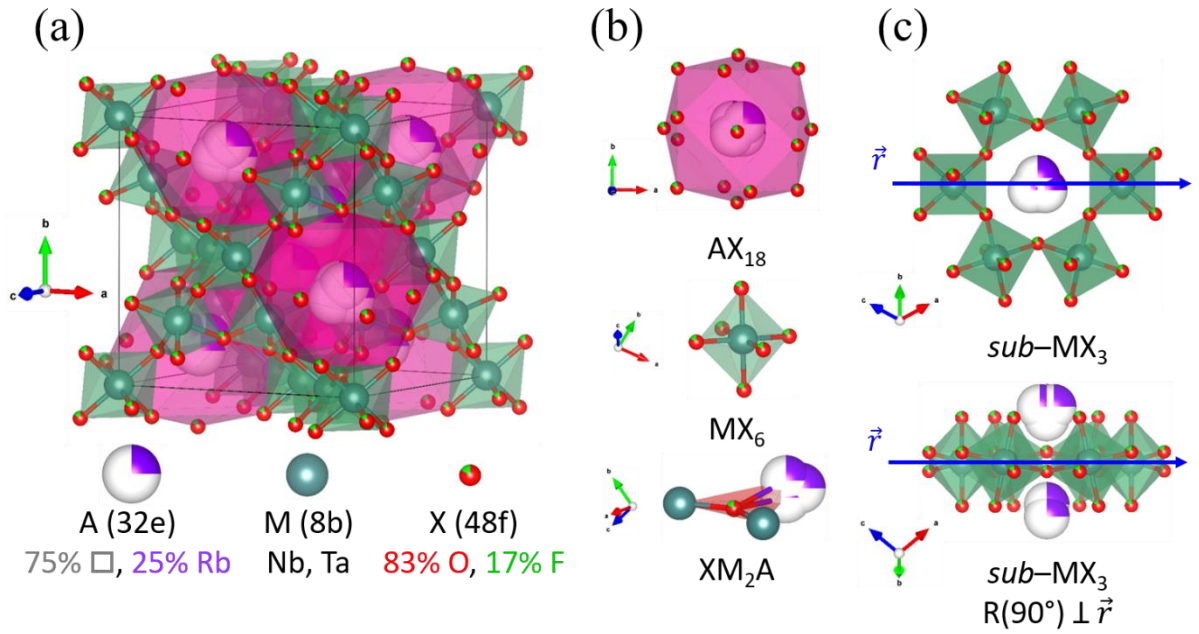


Figure 4. Perspective view of the average structure of RbM_2O_5F (a), first coordination sphere of anions, and A (A = □, Rb) and M (M = Nb, Ta) cations (b) and illustrative view of the subarray *sub*–MX_3 (top c) rotated 90° around the $\vec{r}$ axis (bottom c).

Table 2. Atom, Wyckoff multiplicity (Wyck.), site symmetry (Sym.), atomic coordinates (*x*,*y*,*z*), site occupancy factor (SOF) and IDPs (U_{iso}, Å^2). Uncertainties are indicated between brackets.

Atom	Wyck.	Sym.	*x*	*y*	*z*	SOF	U_{iso}
$RbNb_2O_5F$ (SG: *Fd*$\bar{3}$*m,* No. 227, *a* = *b* = *c* = 10.4956(1) Å, *V* = 1156.18(1) Å^3)							
Rb	32e	3m	0.3960(1)	0.3960(1)	0.3960(1)	0.250	0.0228(2)
Nb	16c	$\bar{3}$m	0	0	0	1.000	0.0228(2)
O	48f	2mm	0.3194(2)	0.125	0.125	0.833	0.0258(11)
F	48f	2mm	0.3194(2)	0.125	0.125	0.167	0.0258(11)
$RbTa_2O_5F$ (SG: *Fd*$\bar{3}$*m*, No. 227, *a* = *b* = *c* = 10.4774(1) Å, *V* = 1150.17(2) Å^3)							
Rb	32e	3m	0.3961(1)	0.3961(1)	0.3961(1)	0.250	0.0162(2)
Ta	16c	$\bar{3}$m	0	0	0	1.000	0.0162(2)
O	48f	2mm	0.3362(4)	0.125	0.125	0.833	0.0581(18)
F	48f	2mm	0.3362(4)	0.125	0.125	0.167	0.0581(18)

4.3 Modeling approach and DFT relaxation. Considering the ES issued from XRPD, anions and Rb cations were distributed in their corresponding disordered sites using the “Supercell” program.[49] This distribution led to considerable number of possible combinations (~10^{15}). To reduce these combinations to a manageable number, two criteria were used. The first favored models that follow the statistical distribution of the MX_6 octahedra and RbX_{18} cages (**Figure 5**), while the second involved choosing models with the lowest Coulomb energy value. Considering these criteria, 20 models were selected for DFT relaxation. The corresponding MX_6 and RbX_{18} distributions are compared to the initial ones in **Figure 5**. Ultimately, the most favored polyhedral in the 20 selected models were MO_5F and $RbO_{15}F_3$ polyhedra, comprising ~56 and ~44 %, respectively.

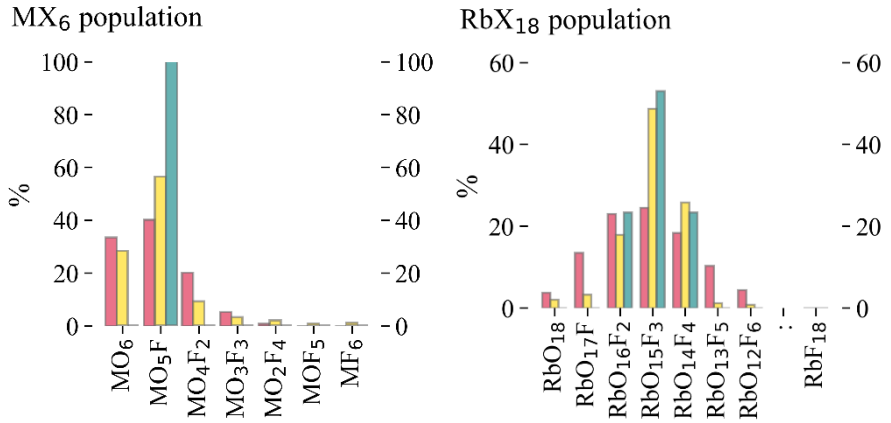


Figure 5. Statistical distributions of MX_6 and RbX_{18} polyhedra from experimental composition (red), tested (bleu) and selected (green) models.

Furthermore, 20 more models were built up from the preceding 20 models, with Rb atoms positioned in the 8b positions, even though these positions resulted in less satisfactory Rietveld refinement compared to the 32e positions. In total, 40 models were tested for $RbNb_2O_5F$, each containing 48 anion, 8 Rb and 16 Nb cations. In the following, models with Rb atoms positioned in the 32e and 8b positions are referred to as APO_32e and APO_8b, respectively. Regarding $RbTa_2O_5F$, and for the sake of computational efficiency, only the 20 best models, 10 with Rb in the 32e positions and 10 with Rb in the 8e positions, were considered.

For the 40 selected models from $RbNb_2O_5F$, the impact of APO on Nb and Rb polyhedral was analyzed. NbO_6, NbO_5F, NbO_4F_2 and NbO_3F_3 octahedra remained unchanged. However, for $NbOF_5$ and NbF_6 octahedra, one and/or two oxygen atoms relaxed toward Nb, leading to distorted unusual NbO_2F_5, $NbOF_6$ or NbO_2F_6 polyhedra (**Table S5**). Only two out of the four models presenting NbO_2F_4 octahedra experienced this effect, specifically, two out of the three initially present NbO_2F_4 octahedra in these two models changed after APO to NbO_3F_4 polyhedra (**Table S5**). In contrast, RbX_{18} cages experience no change after APO (**Table S6**). The values of the total free energy issued from DFT relaxation of each model are gathered in

Table S7. Unsurprisingly, models in which their fluorine-rich Nb octahedra experienced compositional changes exhibit the highest energies.

4.4 NMR parameters calculation.

The validation of any of these models involves the calculation of their NMR parameters and subsequent direct comparison with the available experimental data. Except C_Q and η_Q, calculated σ_{iso} values need to be converted to δ_{iso} values. This conversion is achieved through establishing a linear regression equation. For instance, many linear regression equations were established for ^{19}F.[25,38,40,41,50–58] In the present work, two linear regression equations, δ_{iso}(ppm) = –0.959(29) σ_{iso} + 106.1(4.3) and δ_{iso}(ppm) = –0.935(16) σ_{iso} + 108.9(1.8), used for $RbNb_2O_5F$ and $RbTa_2O_5F$, respectively, were established using the experimental and calculated data from RbF[44] and MF_5[40,43] fluorides (see **Table S8** and **Figure S5**). Similarly, for ^{87}Rb, a new linear regression equation was established from RbF,[44] $RbNO_3$,[59] $RbVO_3$,[60] $RbClO_4$,[61] $RbLaF_4$[62], Rb_2SO_4[63] and $RbSr_2Nb_3O_{10}$.[64] As the experimental ^{87}Rb δ_{iso} value of RbF fluoride is not provided in the literature, an ^{87}Rb MAS NMR spectrum of this fluoride was recorded and fitted (**Table S9** and **Figure S6**). The ^{87}Rb linear regression equation is determined as δ_{iso}(ppm) = –0.722(32) σ_{iso} + 2297(103), it was established using the experimental and calculated data from those seven compounds (**Tables S10** and **S11** and **Figure S7**). The ^{93}Nb calculated δ_{iso} values were deduced using the relation $\delta_{iso} = -586.9 - \sigma_{iso}$ previously established.[16]

The ^{87}Rb and ^{93}Nb NMR spectra were reconstructed using the "Czjzek" (GIM, d=5)[27] and “CzSimple” models, which consider a statistical distribution of the pair (C_Q, η_Q), described by the following probability distribution $P(C_Q, \eta_Q)$:

$$P(C_Q, \eta_Q) = \frac{C_Q^4 \eta_Q}{\sqrt{2\pi}\sigma^5}\left(1 - \frac{\eta_Q^2}{9}\right) exp\left(-\frac{C_Q^2}{2\sigma^2}\left(1 + \frac{\eta_Q^2}{3}\right)\right),$$

where σ is related to the strength of average experimental C_Q value and is given by $\sigma = C_Q/2$. This probability distribution $P(C_Q, \eta_Q)$ is represented as a function of the pair (C_Q, η_Q) in **Figure 6**. The graphs at the bottom and on the left side of each map illustrate $P(C_Q, \eta_Q)$ curve as a function of C_Q and η_Q, respectively. For ^{87}Rb, the possible experimental C_Q values range approximately from 0.5 MHz to 3 MHz, with the highest probabilities concentrated within the approximate range of [1.5-2] MHz (**Figure 6** (a)). Similarly, the range of possible C_Q values for ^{93}Nb extends approximately from 10 to 100 MHz, with the highest probabilities concentrated within the approximate range [40-70] MHz (**Figure 6** (b)). For both nuclei, η_Q values above 0.5 are the most probable.

The selection of the best models describing disorder in RbM_2O_5F pyrochlores is based on the overall agreement between the experimental and calculated NMR parameters, namely ^{19}F δ_{iso}, ^{87}Rb δ_{iso}, C_Q, and η_Q and ^{93}Nb δ_{iso}, C_Q, and η_Q. Particular emphasis is placed on the C_Q parameters for ^{87}Rb and ^{93}Nb nuclei. Indeed, a small discrepancy between experimental and calculated δ_{iso} values may not be significant as it could be due to the choice of the linear regression equation. Models with such discrepancies but with good agreement between experimental and calculated C_Q and η_Q values are retained. Conversely, models showing excellent agreement between experimental and calculated δ_{iso} values, but significant discrepancies between calculated and experimental C_Q and η_Q values for ^{87}Rb and/or ^{93}Nb are excluded.

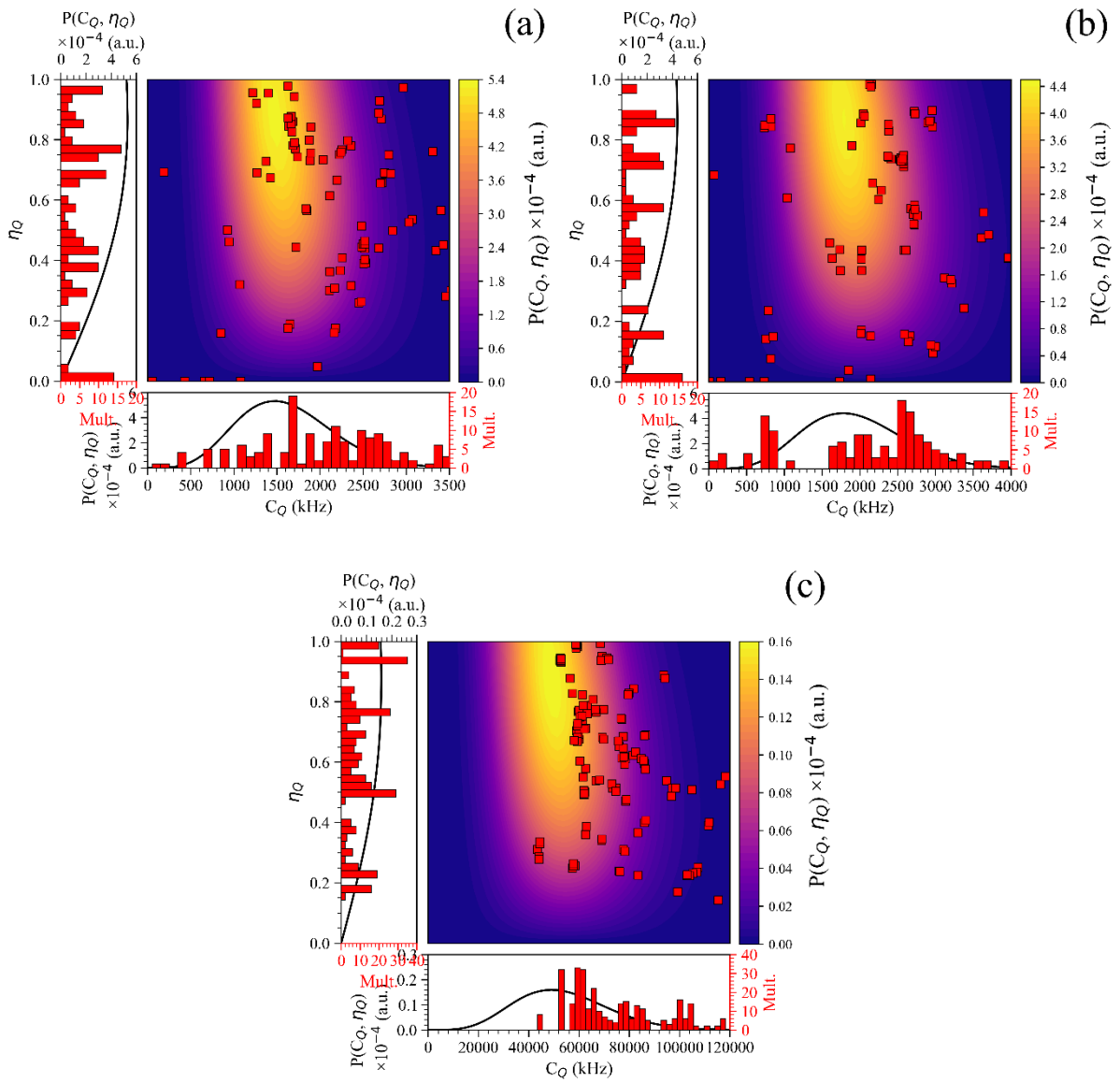


Figure 6. Maps of the GIM distribution $P(C_Q, \eta_Q)$ (in a.u.) used to fit the CT of the ^{87}Rb NMR spectra for (a) $RbNb_2O_5F$ and (b) $RbTa_2O_5F$, and the ^{93}Nb NMR spectra for $RbNb_2O_5F$ (c). For each map, the color bar on the right side indicate the intensity of $P(C_Q, \eta_Q)$, and each red square represent a calculated (C_Q, η_Q) pair value for an Rb or Nb atom from the selected models. The graphs at the bottom and the left side illustrate the probabilities associated with C_Q and η_Q values, respectively, whereas the histograms show the calculated C_Q and η_Q values from the selected models.

Calculated NMR parameters relevant for the discussion are summarized in **Tables 4** and **5**, further details on the values for each of the tested 40 models are gathered in **Tables S12-S23**. A first selection of models is easily made by comparing experimental and calculated C_Q values. APO_32e models 10 to 20 all present maximum ^{93}Nb C_Q values above the upper limit value of 120 MHz and/or both the average and maximum ^{87}Rb C_Q values above the experimental maximum value of 3 MHz (**Table 4**). These eleven models were therefore discarded. The same approach was used to investigate the APO_8b models. As with the APO_32e models, models 10 to 20 all present far overestimated calculated ^{87}Rb and/or ^{93}Nb C_Q values (**Tables S12-S15**). Note that all these discarded models contain octahedra with compositions other than NbO_5F (**Table S5**). MO_6 and MO_4F_2 octahedra are also present in the model 5 (APO_8b and APO_32e) and both the ^{87}Rb and ^{93}Nb C_Q values are also highly overestimated (4.3 and 142.3 MHz for ^{87}Rb and ^{93}Nb, respectively) compared to the experimental values (**Tables 4**, **S12** and **S14**). These two models were also excluded.

Table 4. ^{93}Nb and ^{87}Rb absolute calculated average (aver.), minimum (min.) and maximum (max.) C_Q (MHz) values and average η_Q values for the 20 APO_32e models of $RbNb_2O_5F$.

model	^{93}Nb C_Q			^{93}Nb η_Q	^{87}Rb C_Q			^{87}Rb η_Q
	aver.	min.	max.	aver.	aver.	min.	max.	aver.
1	52.7	52.4	53.0	0.94	2.51	2.48	2.52	0.45
2	66.4	44.1	79.9	0.51	2.42	1.84	3.07	0.54
3	89.6	69.3	115.5	0.49	2.51	1.63	3.52	0.63
4	60.5	58.7	62.3	0.74	1.67	1.63	1.74	0.83
5	85.2	36.0	142.3	0.48	3.19	1.91	4.26	0.61
6	64.6	57.4	78.2	0.59	1.98	0.19	2.82	0.65
7	77.0	59.4	118.4	0.67	2.39	1.63	3.43	0.55
8	65.1	56.6	74.8	0.66	1.80	0.93	2.84	0.58
9	90.8	75.8	105.4	0.50	1.74	1.22	2.24	0.67
10	112.3	52.0	152.4	0.52	3.85	2.61	5.12	0.86
11	90.1	42.3	159.7	0.51	3.13	1.10	5.00	0.63
12	71.1	20.6	189.6	0.55	3.71	1.80	5.80	0.50
13	86.8	31.1	158.5	0.52	3.08	1.40	7.50	0.56
14	87.5	43.1	140.3	0.40	5.13	2.80	8.60	0.33
15	74.5	26.6	160.6	0.61	4.46	1.70	8.60	0.45
16	81.5	41.0	133.5	0.57	6.65	2.70	11.40	0.51
17	85.7	30.8	127.9	0.57	4.68	1.50	9.70	0.60
18	76.9	30.6	140.0	0.56	5.38	2.50	8.30	0.27
19	71.1	43.6	125.0	0.63	4.84	1.60	7.20	0.43
20	77.4	30.2	142.9	0.55	5.68	0.50	10.10	0.46

For the remaining models, *i.e.* models 1 to 4 and 6 to 9, all calculated C_Q and η_Q values are within the range of possible values determined by the experimental distributions for both ^{93}Nb and ^{87}Rb nuclei (**Tables 4** and **S12-S15**). Analysis of the calculated δ_{iso} values does not allow us to select one model over another (**Tables 5** and **S20-S23**). For ^{19}F and ^{93}Nb, all average calculated δ_{iso} values are slightly higher than the experimental ones (~–101 ppm and ~–1050 ppm for ^{19}F and ^{93}Nb, respectively), however this could be due to the choice of the linear

regression equation. For ^{87}Rb, all average calculated δ_{iso} values are close to the experimental value (–79.5 ppm). For all three nuclei, the δ_{iso} range remains also compatible with the width of the distributions used to reconstruct the NMR spectra (~25 ppm LW for ^{19}F and ~13 and 86.3 ppm $\Delta\delta_{iso}$ for ^{87}Rb and ^{93}Nb, respectively).

Table 5. ^{19}F, ^{87}Rb and ^{93}Nb average calculated δ_{iso} values (δ_{iso}, ppm), and difference between minimum and maximum calculated δ_{iso} values ($\Delta\delta_{iso}$, ppm), for the APO_32e models from $RbNb_2O_5F$.

model	^{19}F δ_{iso}		^{87}Rb δ_{iso}		^{93}Nb δ_{iso}	
	aver.	$\Delta\delta_{iso}$	aver.	$\Delta\delta_{iso}$	aver.	$\Delta\delta_{iso}$
1	–84.4	0.2	–75.6	0.1	–964	0.8
2	–92.9	13.3	–77.8	3.9	–1012	26.6
3	–90.3	18.2	–80.3	9.6	–998	65.2
4	–99.3	0.4	–78.1	0.3	–1008	13.3
6	–91.6	24.1	–77.4	17.3	–1006	20.8
7	–86.6	27.3	–76.5	20.3	–992	55.3
8	–96.9	25.1	–79.9	5.9	–1018	22.5
9	–89.7	30.7	–81.3	11.4	–992	15.9

Concise representations of the relative differences between the calculated and experimental NMR parameters are given by radar charts in **Figure 7**. The relative difference, denoted as $f\{G; N\}$, is expressed as a percentage and defined as follows:

$$f\{G;N\} = 100 - \frac{|G_{exp} - |G_{cal}||}{G_{exp}} \times 100,$$

where G represents an average NMR parameter (either δ_{iso}, C_Q, or η_Q), and N is one of the nuclei (^{19}F, ^{87}Rb or ^{93}Nb). The calculated and experimental values are denoted as G_{cal} and G_{exp}, respectively. The percentage score indicates the closeness of the calculated values to the experimental values, with higher percentages representing a better match.

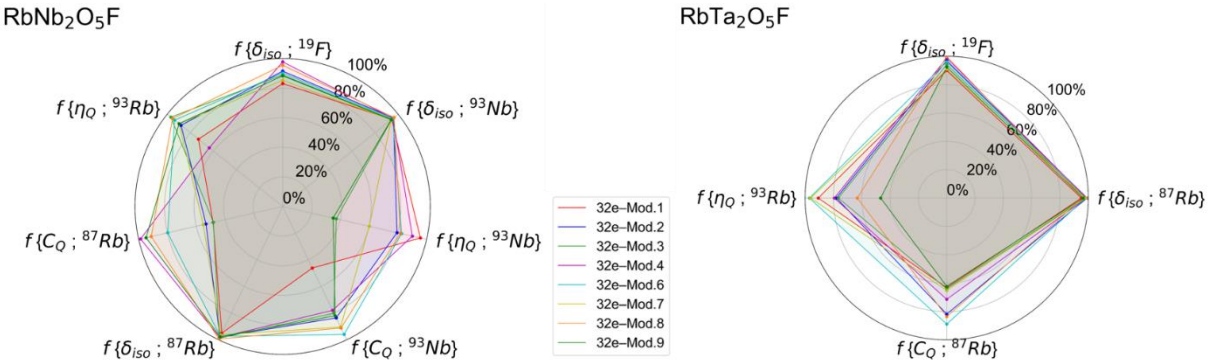


Figure 7. Relative differences between average experimental and calculated NMR parameters values for (a) $RbNb_2O_5F$ and (b) $RbTa_2O_5F$. The axes are scaled in % and features the scoring functions $f\{<\delta_{iso}>;\ ^{19}F\}$, $f\{<\delta_{iso}>;\ ^{87}Rb\}$, $f\{<\delta_{iso}>;\ ^{93}Nb\}$, $f\{<C_Q>;\ ^{87}Rb\}$, $f\{<C_Q>;\ ^{93}Nb\}$, $f\{<\eta_Q>;\ ^{87}Rb\}$ and $f\{<\eta_Q>;\ ^{93}Nb\}$. The color assigned to each selected model is indicated in the legend.

As illustrated by the radar chart, the δ_{iso} parameters do not allow us to select one model over another (**Figure 7** (a)). Particularly, models with $f\{<C_Q>;\ ^{87}Rb\}$, $f\{<C_Q>;\ ^{93}Nb\}$, $f\{<\eta_Q>;\ ^{87}Rb\}$ and $f\{<\eta_Q>;\ ^{93}Nb\}$ between 50% and 60% are still valid since the calculated C_Q and η_Q values are within the range of possible experimental values. The same conclusions were reached for the APO_8b models of $RbNb_2O_5F$: models 1 to 4 and 6 to 9 are also possible.

The same approach was applied to $RbTa_2O_5F$. Only models 1 to 10 were tested, with Rb atoms in either 32e or 8b positions before optimization. Calculated NMR parameter values are gathered in **Tables S24-S29**, and values relevant to the discussion are summarized in **Table 6**.

Table 6. ^{19}F and ^{87}Rb average calculated δ_{iso} values (δ_{iso}, ppm) and difference between minimum and maximum calculated δ_{iso} values ($\Delta\delta_{iso}$, ppm) and ^{87}Rb absolute calculated average (aver.), minimum (min.) and maximum (max.) C_Q (MHz) values and average η_Q values for APO_32e models 1 to 10 of $RbTa_2O_5F$.

model	^{19}F δ_{iso}		^{87}Rb δ_{iso}		^{87}Rb C_Q			^{87}Rb η_Q
	aver.	$\Delta\delta_{iso}$	aver.	$\Delta\delta_{iso}$	aver.	min	max	
1	–98.3	0.1	–72.7	0.1	2.72	2.70	2.76	0.55
2	–106.0	5.6	–75.9	8.2	2.35	2.02	3.00	0.48
3	–103.0	18.5	–78.2	11.9	2.71	1.04	3.96	0.47
4	–108.0	0.3	–77.4	0.2	2.56	2.53	2.58	0.74
5	–95.6	47.1	–71.4	9.0	3.68	2.74	4.59	0.62
6	–105.1	11.5	–75.2	19.4	2.21	0.07	2.96	0.63
7	–99.2	18.6	–75.3	11.0	2.68	2.05	3.71	0.59
8	–109.6	16.2	–79.2	8.6	1.66	0.74	2.73	0.83
9	–101.0	16.0	–79.3	6.6	1.24	0.76	1.74	0.28
10	–69.3	10.8	–68.5	14.4	3.55	2.28	4.81	0.82

Similar to $RbNb_2O_5F$, calculated ^{87}Rb C_Q from $RbTa_2O_5F$ values are too high for models 5 and 10, exceeding the limit value 4 MHz (**Tables 6** and **S24-S25**). Moreover, for models 10 (APO_32e and APO_8b), the average calculated ^{19}F δ_{iso} values are also significantly higher (–69.3 and –63.9 ppm) than the experimental value (∼–109.5 ppm). Models 5 and 10 were again discarded. For the remaining models, all average calculated ^{19}F and ^{87}Rb δ_{iso} values are close to the experimental values (∼–109.5 and –76.5 ppm for ^{19}F and ^{87}Rb, respectively), as evidenced on the radar chart (**Figure 7** (b)), and ^{87}Rb C_Q and η_Q values are within the range of the experimental values (**Tables S24** and **S26**). Similarly, APO_8b models 1 to 4 and 6 to 9 are also possible (**Tables S25**, **S27** and **S29**).

The calculated C_Q and η_Q values of each individual Rb and Nb atom from the selected sixteen models (corresponding to 128 Rb atoms and 256 Nb atoms) are plotted onto the $P(C_Q, \eta_Q)$ maps

as red squares in **Figure 6**. The histograms at the bottom and the left side of the maps show the corresponding calculated C_Q and η_Q values respectively, with the associated probabilities. For ^{87}Rb, the distributions of calculated C_Q and η_Q values span the entire range of possible values (**Figures 6** (a) and (b)), whereas for ^{93}Nb, the calculated C_Q values are mostly above 40 MHz (**Figure 6** (c)). A better agreement with the shape of the probability curves, especially the C_Q ones, could be obtained by varying the ratios of the different models. This suggests that the selected models are not equiprobable.

4.5 short range O/F ordering.

For both compounds, the selected models contain only MO_5F octahedra (M = Nb, Ta). Excluding MO_6 and MO_4F_2 octahedra, which does not comply with the statistics, indicates unexpected short-range preferential O/F ordering in these pyrochlore structures. After optimization, the metal atom moves towards the oxygens, away from the more electronegative anion, fluorine. Consequently, the M–F bond length is systematically greater than the M–O bond length in each of the MO_5F octahedra (**Tables 7**, **S30-S31** and **S34-S35**). This displacement of the metal from its ideal centered position towards the polyhedral corners/edges/faces occupied by oxygen atoms has previously been observed in other metal transition oxyfluorides, including MO_2F[16] and MOF_3[43] compounds.

Regarding Rb environments, the selected models contain either exclusively $RbO_{15}F_3$ cages or an equal proportion of $RbO_{14}F_4$, and $RbO_{16}F_2$ cages, or a mixt of these three cages. Once again, a deviation from the theoretical proportions of the RbX_{18} cages is observed (**Figure 5**). Before optimization and depending on the initial model, the positional coordinates of the Rb atoms are either (1/2,1/2,1/2) or (*x*,*x*,*x*), which define the 8b and 32e sites respectively. After optimization, these Rb atoms all occupy low-symmetry positions described by the coordinates (*x*,*y*,*z*). This displacement of Rb atoms is facilitated by the spacious dimensions of RbX_{18} cages, as

highlighted by the average bond lengths Rb–O and Rb–F (**Table 7**). Whatever the nature of the occupied Rb site (8b or 32e), the average Rb–X and M–X (X = O, F) bond lengths are similar in both models 32e and 8b after optimization (**Tables 7**, **S32-S33** and **S36-S37**).

Table 7. Bond lengths (M–O and M–F, Å), average bond lengths (<M–O>, <M–F>, <Rb–O> and <Rb–F>, Å) from the average ES, the 8 APO_32e and 8 APO_8b models of $RbNb_2O_5F$ and $RbTa_2O_5F$.

Cell	M–O or <M–O>	M–F or <M–F>	<Rb–O>	<Rb–F>
$RbNb_2O_5F$				
ES	1.993(1)	1.993(1)	3.587	3.587
APO_32e	1.961	2.162	3.615	3.588
APO_8b	1.956	2.144	3.608	3.588
$RbTa_2O_5F$				
ES	2.061(2)	2.061(2)	3.507	3.507
APO_32e	1.957	2.149	3.605	3.586
APO_8b	1.955	2.143	3.599	3.587

5. Conclusion

^{19}F, ^{87}Rb and ^{93}Nb MAS NMR spectra of pyrochlore oxyfluorides $RbNb_2O_5F$ and $RbTa_2O_5F$ all indicate that the local environments of the probed nuclei are distributed. For both compounds, average structures were determined by refining the XRPD patterns using the Rietveld structural refinement method. Improved refinement was achieved by considering the structural literature model, where O and F atoms occupy the 48f site with occupancies of 83.3% and 16.7%, respectively, and Rb atoms occupy the 32e site with an occupancy of 25%. Using supercell approach, 20 models were considered, having both the lowest Coulomb energy, and an overall alignment of the statistical distribution of MX_6 units and RbX_{18} cages. 20 similar models with Rb atoms located in the 8b positions also considered. After DFT relaxation, Rb

atoms deviate from their original sites (8b and 32e) towards less symmetrical positions (*x*,*y*,*z*). Moreover, underlining the preference of M atoms for less electronegative atoms, one to two oxygen atoms are added to the fluorine-rich MX_6 octahedra, such as MOF_5 and MF_6, leading to either MO_2F_5, MOF_6 or MO_2F_6 polyhedra. Of the 40 models tested, only 16 (8 APO_32e and the corresponding 8 APO_8b) have calculated C_Q values compatible with the ^{87}Rb and ^{93}Nb (when present) C_Q values extracted from NMR spectra. These 16 models present also satisfactory agreement between the calculated and experimental δ_{iso} values, for the three nuclei ^{19}F, ^{87}Rb and ^{93}Nb (when present). Instead of a statistical distribution of MX_6 octahedra, the pyrochlore structure of $RbNb_2O_5F$ and $RbTa_2O_5F$ presents a short-range O/F preferential ordering, defined by the exclusive presence of MOF_5 octahedra, whereas the Rb atoms are located in $RbO_{15}F_3$ cages and/or an equal proportion of $RbO_{14}F_4$, and $RbO_{16}F_2$ ones. Additionally, a displacement of M atoms towards O atoms is observed. Combining solid state NMR, XRDP and DFT calculations provides a powerful tool for investigating and describing local order in disordered compounds.

ASSOCIATED CONTENT

Supporting Information. The Supporting Information is available free of charge on the ACS Publications website at DOI:

The reported pyrochlore oxyfluorides (ordered and disordered); ^{19}F MAS, and ^{87}Rb and ^{93}Nb MAS and 3QMAS NMR spectra and their fits; Rietveld refinements; new ^{19}F and ^{87}Rb σ_{iso} vs δ_{iso} established with VASP; $RbNb_2O_5F$ and $RbTa_2O_5F$ NMR parameters, including ^{19}F σ_{iso}, and ^{87}Rb and ^{93}Nb C_Q and η_Q values; $RbNb_2O_5F$ and $RbTa_2O_5F$ structural features. (SI.pdf)

CIF files for ES structures of $RbNb_2O_5F$ and $RbTa_2O_5F$, the 8 APO_8b and 8 APO_32e models of $RbNb_2O_5F$ and $RbTa_2O_5F$ (CIF_files.zip).

AUTHOR INFORMATION

Corresponding Authors

*E-mail: Ouail.Zakary@univ-lemans.fr.

*E-mail: Christophe.Legein@univ-lemans.fr

ORCID

Ouail Zakary: 0000-0002-7793-3306

Monique Body: 0000-0002-5895-3731

Christophe Legein: 0000-0001-7426-8817

Vincent Sarou-Kanian: 0000-0001-9611-8377

Franck Fayon: 0000-0001-5086-5625

Aydar Rakhmatullin: 0000-0002-7328-5081

Thibault Charpentier: 0000-0002-3034-1389

Author Contributions

The manuscript was written through contributions of all authors. All authors have given approval to the final version of the manuscript.

Notes

The authors declare no competing financial interest.

(1) Jiang, B.; Bridges, C. A.; Unocic, R. R.; Pitike, K. C.; Cooper, V. R.; Zhang, Y.; Lin, D.-Y.; Page, K. Probing the Local Site Disorder and Distortion in Pyrochlore High-Entropy Oxides. *J. Am. Chem. Soc.* **2021**, *143* (11), 4193–4204. https://doi.org/10.1021/jacs.0c10739.

(2) Gayen, P.; Saha, S.; Ramani, V. Pyrochlores for Advanced Oxygen Electrocatalysis. *Acc. Chem. Res.* **2022**, *55* (16), 2191–2200. https://doi.org/10.1021/acs.accounts.2c00049.

(3) Vanderah, T. A.; Levin, I.; Lufaso, M. W. An Unexpected Crystal-Chemical Principle for the Pyrochlore Structure. *Eur J Inorg Chem* **2005**, *2005* (14), 2895–2901. https://doi.org/10.1002/ejic.200500234.

(4) Bosi, F.; Christy, A. G.; Hålenius, U. Crystal-Chemical Aspects of the Roméite Group, $A_2Sb_2O_6Y$, of the Pyrochlore Supergroup. *Mineral. mag.* **2017**, *81* (6), 1287–1302. https://doi.org/10.1180/minmag.2016.080.166.

(5) Talanov, M. V.; Talanov, V. M. Structural Diversity of Ordered Pyrochlores. *Chem. Mater.* **2021**, *33* (8), 2706–2725. https://doi.org/10.1021/acs.chemmater.0c04864.

(6) Belakovskiy, D. I.; Uvarova, Y. New Mineral Names,. *American Mineralogist* **2021**, *106* (7), 1186–1191. https://doi.org/10.2138/am-2021-NMN106714.

(7) Xu, Q.; Su, Y.; Tang, Y.; Wang, Z.; Lu, L.; Tang, L. Low Temperature Synthesis of Oxyfluoride $CsTi_2O_{2.85}F_{3.15}$ from a Layered Oxide $Cs_{0.68}Ti_{1.83}O_4$. *Journal of Solid State Chemistry* **2022**, *314*, 123368. https://doi.org/10.1016/j.jssc.2022.123368.

(8) Boivin, E.; Pourpoint, F.; Saitzek, S.; Simon, P.; Roussel, P.; Kabbour, H. An Unusual O^{2-}/F^- Distribution in the New Pyrochlore Oxyfluorides: $Na_2B_2O_5F_2$ (B = Nb, Ta). *Chem. Commun.* **2022**, *58* (14), 2391–2394. https://doi.org/10.1039/D1CC06760E.

(9) Kuriki, R.; Ichibha, T.; Hongo, K.; Lu, D.; Maezono, R.; Kageyama, H.; Ishitani, O.; Oka, K.; Maeda, K. A Stable, Narrow-Gap Oxyfluoride Photocatalyst for Visible-Light Hydrogen Evolution and Carbon Dioxide Reduction. *J. Am. Chem. Soc.* **2018**, *140* (21), 6648–6655. https://doi.org/10.1021/jacs.8b02822.

(10) Luo, Y.; Zhou, X.; Zhang, J.; Qi, Y.; Li, Z.; Zhang, F.; Li, C. Development of Sn^{2+}-Based Oxyfluoride Photocatalyst with Visible Light Response of ca. 650 Nm via Strengthened Hybridization of Sn 5s and O 2p Orbitals. *Journal of Energy Chemistry* **2021**, *63*, 385–390. https://doi.org/10.1016/j.jechem.2021.07.028.

(11) Boivin, E.; Saitzek, S.; Fauth, F.; Huvé, M.; Roussel, P.; Kabbour, H. New Pyrochlore-like Oxyfluorides $Na_{2-2x}Sn_xM_2O_5F_2$ (M = Nb^{5+} or Ta^{5+} and $1 \leq x \leq 0$) as Potential Candidates for Overall Water Splitting Photocatalysis. *Chem. Mater.* **2023**, *35* (2), 447–456. https://doi.org/10.1021/acs.chemmater.2c02801.

(12) Goodenough, J. B.; Hong, H. Y.-P.; Kafalas, J. A. Fast Na^+-Ion Transport in Skeleton Structures. *Materials Research Bulletin* **1976**, *11* (2), 203–220. https://doi.org/10.1016/0025-5408(76)90077-5.

(13) Phraewphiphat, T.; Iqbal, M.; Suzuki, K.; Hirayama, M.; Kanno, R. Synthesis and Lithium-Ion Conductivity of $LiSrB_2O_6F$ (B = Nb^{5+}, Ta^{5+}) with a Pyrochlore Structure. *J.*

Jpn. Soc. Powder Powder Metallurgy **2018**, *65* (1), 26–33. https://doi.org/10.2497/jjspm.65.26.

(14) Harada, J. K.; Charles, N.; Poeppelmeier, K. R.; Rondinelli, J. M. Heteroanionic Materials by Design: Progress Toward Targeted Properties. *Adv. Mater.* **2019**, *31* (19), 1805295. https://doi.org/10.1002/adma.201805295.

(15) Grüninger, H.; Armstrong, K.; Greim, D.; Boffa-Ballaran, T.; Frost, D. J.; Senker, J. Hidden Oceans? Unraveling the Structure of Hydrous Defects in the Earth’s Deep Interior. *J. Am. Chem. Soc.* **2017**, *139* (30), 10499–10505. https://doi.org/10.1021/jacs.7b05432.

(16) Dabachi, J.; Body, M.; Galven, C.; Boucher, F.; Legein, C. Preparation-Dependent Composition and O/F Ordering in NbO_2F and TaO_2F. *Inorg. Chem.* **2017**, *56* (9), 5219–5232. https://doi.org/10.1021/acs.inorgchem.7b00355.

(17) Ding, F.; Charles, N.; Harada, J. K.; Malliakas, C. D.; Zhang, C.; Dos Reis, R.; Griffith, K. J.; Nisbet, M. L.; Zhang, W.; Halasyamani, P. S.; Dravid, V. P.; Rondinelli, J. M.; Poeppelmeier, K. R. Perovskite-like K_3TiOF_5 Exhibits (3 + 1)-Dimensional Commensurate Structure Induced by Octahedrally Coordinated Potassium Ions. *J. Am. Chem. Soc.* **2021**, *143* (45), 18907–18916. https://doi.org/10.1021/jacs.1c05704.

(18) Babel, D.; Pausewang, G.; Viebahn, W. Notizen: Die Struktur Einiger Fluoride, Oxide Und Oxidfluoride AMe_2X_6 : Der $RbNiCrF_6$ -Typ. *Zeitschrift für Naturforschung B* **1967**, *22* (11), 1219–1220. https://doi.org/10.1515/znb-1967-1126.

(19) Ory, G.; Fourquet, J. L.; Jacoboni, C.; Miranday, J. P.; De Pape, R. *Localisation des cations monovalents dans les pyrochlores A’B_2X_6 (A’ = Rb, Cs, Tl) : mise en évidence de nouvelles positions cristallographiques dans le cas du thallium*. Gallica. https://gallica.bnf.fr/ark:/12148/bpt6k9822341w (accessed 2023-10-12).

(20) Fourquet, J. L.; Jacoboni, C.; De Pape, R. Les pyrochlores AIB_2X_6: Mise en evidence de l’occupation par le cation AI de nouvelles positions cristallographiques dans le groupe d’espace fd3m. *Materials Research Bulletin* **1973**, *8* (4), 393–403. https://doi.org/10.1016/0025-5408(73)90043-3.

(21) Rietveld, H. M. A Profile Refinement Method for Nuclear and Magnetic Structures. *J Appl Crystallogr* **1969**, *2* (2), 65–71. https://doi.org/10.1107/S0021889869006558.

(22) Rodriguez-Carvajal, J. FULLPROF: A Program for Rietveld Refinement and Pattern Matching Analysis. In *satellite meeting on powder diffraction of the XV congress of the IUCr*; Toulouse, France:[sn], 1990; Vol. 127.

(23) Medek, A.; Harwood, J. S.; Frydman, L. Multiple-Quantum Magic-Angle Spinning NMR: A New Method for the Study of Quadrupolar Nuclei in Solids. *J. Am. Chem. Soc.* **1995**, *117* (51), 12779–12787. https://doi.org/10.1021/ja00156a015.

(24) Amoureux, J.-P.; Fernandez, C.; Steuernagel, S. ZFiltering in MQMAS NMR. *Journal of Magnetic Resonance, Series A* **1996**, *123* (1), 116–118. https://doi.org/10.1006/jmra.1996.0221.

(25) Sadoc, A.; Body, M.; Legein, C.; Biswal, M.; Fayon, F.; Rocquefelte, X.; Boucher, F. NMR Parameters in Alkali, Alkaline Earth and Rare Earth Fluorides from First Principle Calculations. *Physical Chemistry Chemical Physics* **2011**, *13* (41), 18539. https://doi.org/10.1039/c1cp21253b.

(26) Massiot, D.; Fayon, F.; Capron, M.; King, I.; Le Calvé, S.; Alonso, B.; Durand, J.-O.; Bujoli, B.; Gan, Z.; Hoatson, G. Modelling One- and Two-Dimensional Solid-State NMR Spectra. *Magnetic Resonance in Chemistry* **2002**, *40* (1), 70–76. https://doi.org/10.1002/mrc.984.

(27) Caër, G. L.; Brand, R. A. General Models for the Distributions of Electric Field Gradients in Disordered Solids. *J. Phys.: Condens. Matter* **1998**, *10* (47), 10715–10774. https://doi.org/10.1088/0953-8984/10/47/020.

(28) Kresse, G.; Furthmüller, J. Efficiency of Ab-Initio Total Energy Calculations for Metals and Semiconductors Using a Plane-Wave Basis Set. *Computational Materials Science* **1996**, *6* (1), 15–50. https://doi.org/10.1016/0927-0256(96)00008-0.

(29) Kresse, G.; Furthmüller, J. Efficient Iterative Schemes for *Ab Initio* Total-Energy Calculations Using a Plane-Wave Basis Set. *Phys. Rev. B* **1996**, *54* (16), 11169–11186. https://doi.org/10.1103/PhysRevB.54.11169.

(30) Perdew, J. P.; Burke, K.; Ernzerhof, M. Generalized Gradient Approximation Made Simple. *Phys. Rev. Lett.* **1996**, *77* (18), 3865–3868. https://doi.org/10.1103/PhysRevLett.77.3865.

(31) Kresse, G.; Joubert, D. From Ultrasoft Pseudopotentials to the Projector Augmented-Wave Method. *Phys. Rev. B* **1999**, *59* (3), 1758–1775. https://doi.org/10.1103/PhysRevB.59.1758.

(32) Blöchl, P. E. Projector Augmented-Wave Method. *Phys. Rev. B* **1994**, *50* (24), 17953–17979. https://doi.org/10.1103/PhysRevB.50.17953.

(33) Petrilli, H. M.; Blöchl, P. E.; Blaha, P.; Schwarz, K. Electric-Field-Gradient Calculations Using the Projector Augmented Wave Method. *Phys. Rev. B* **1998**, *57* (23), 14690–14697. https://doi.org/10.1103/PhysRevB.57.14690.

(34) Pickard, C. J.; Mauri, F. All-Electron Magnetic Response with Pseudopotentials: NMR Chemical Shifts. *Phys. Rev. B* **2001**, *63* (24), 245101. https://doi.org/10.1103/PhysRevB.63.245101.

(35) Yates, J. R.; Pickard, C. J.; Mauri, F. Calculation of NMR Chemical Shifts for Extended Systems Using Ultrasoft Pseudopotentials. *Phys. Rev. B* **2007**, *76* (2), 024401. https://doi.org/10.1103/PhysRevB.76.024401.

(36) Haeberlen, U. In Advances in Magnetic Resonance. J. S. Waugh, Ed.; Academic Press. New York 1976.

(37) Zheng, A.; Liu, S.-B.; Deng, F. ^{19}F Chemical Shift of Crystalline Metal Fluorides: Theoretical Predictions Based on Periodic Structure Models. *J. Phys. Chem. C* **2009**, *113* (33), 15018–15023. https://doi.org/10.1021/jp904454t.

(38) Griffin, J. M.; Yates, J. R.; Berry, A. J.; Wimperis, S.; Ashbrook, S. E. High-Resolution ^{19}F MAS NMR Spectroscopy: Structural Disorder and Unusual *J* Couplings in a Fluorinated Hydroxy-Silicate. *J. Am. Chem. Soc.* **2010**, *132* (44), 15651–15660. https://doi.org/10.1021/ja105347q.

(39) Martineau, C.; Fayon, F.; Suchomel, M. R.; Allix, M.; Massiot, D.; Taulelle, F. Structure Resolution of $Ba_5Al_3F_{19}$ and Investigation of Fluorine Ion Dynamics by Synchrotron Powder Diffraction, Variable-Temperature Solid-State NMR, and Quantum Computations. *Inorg. Chem.* **2011**, *50* (6), 2644–2653. https://doi.org/10.1021/ic102534d.

(40) Biswal, M.; Body, M.; Legein, C.; Sadoc, A.; Boucher, F. NbF_5 and TaF_5: Assignment of ^{19}F NMR Resonances and Chemical Bond Analysis from GIPAW Calculations. *Journal of Solid State Chemistry* **2013**, *207*, 208–217. https://doi.org/10.1016/j.jssc.2013.09.001.

(41) Sadoc, A.; Biswal, M.; Body, M.; Legein, C.; Boucher, F.; Massiot, D.; Fayon, F. NMR Parameters in Column 13 Metal Fluoride Compounds (AlF_3, GaF_3, InF_3 and TlF) from First Principle Calculations. *Solid State Nuclear Magnetic Resonance* **2014**, *59–60*, 1–7. https://doi.org/10.1016/j.ssnmr.2014.01.001.

(42) Martineau, C.; Allix, M.; Suchomel, M. R.; Porcher, F.; Vivet, F.; Legein, C.; Body, M.; Massiot, D.; Taulelle, F.; Fayon, F. Structure Determination of Ba_5AlF_{13} by Coupling Electron, Synchrotron and Neutron Powder Diffraction, Solid-State NMR and Ab Initio Calculations. *Dalton Trans.* **2016**, *45* (39), 15565–15574. https://doi.org/10.1039/C6DT02454H.

(43) Zakary, O.; Body, M.; Charpentier, T.; Sarou-Kanian, V.; Legein, C. Structural Modeling of O/F Correlated Disorder in $TaOF_3$ and $NbOF_{3-x}(OH)_x$ by Coupling Solid-State NMR and DFT Calculations. *Inorg. Chem.* **2023**, *62* (40), 16627–16640. https://doi.org/10.1021/acs.inorgchem.3c02844.

(44) Goldschmidt, V. M. Die Gesetze der Krystallochemie. *Naturwissenschaften* **1926**, *14* (21), 477–485. https://doi.org/10.1007/BF01507527.

(45) Edwards, A. J. 717. The Structures of Niobium and Tantalum Pentafluorides. *J. Chem. Soc.* **1964**, 3714. https://doi.org/10.1039/jr9640003714.

(46) Brewer, S. A.; Brisdon, A. K.; Fawcett, J.; Holliman, P. J.; Holloway, J. H.; Hope, E. G.; Russell, D. R. Re-evaluation of the X-ray Crystal Structure of $[Ta_4F_{20}]$ and the Synthesis and Characterization of a Series of Mixed-Metal Pentafluorides of Niobium and Tantalum. *Z. anorg. allg. Chem.* **2006**, *632* (2), 325–329. https://doi.org/10.1002/zaac.200500374.

(47) Chien, P.-H.; Harada, J. K.; Liu, H.; Patel, S.; Huang, C.; Rondinelli, J. M.; Poeppelmeier, K. R.; Hu, Y.-Y. Microscopic Insights into the Reconstructive Phase Transition of $KNaNbOF_5$ with ^{19}F NMR Spectroscopy. *Chem. Mater.* **2020**, *32* (13), 5715–5722. https://doi.org/10.1021/acs.chemmater.0c01439.

(48) Chen, K. A Practical Review of NMR Lineshapes for Spin-1/2 and Quadrupolar Nuclei in Disordered Materials. *IJMS* **2020**, *21* (16), 5666. https://doi.org/10.3390/ijms21165666.

(49) Okhotnikov, K.; Charpentier, T.; Cadars, S. Supercell Program: A Combinatorial Structure-Generation Approach for the Local-Level Modeling of Atomic Substitutions

and Partial Occupancies in Crystals. *J Cheminform* **2016**, *8* (1), 17. https://doi.org/10.1186/s13321-016-0129-3.

(50) Pedone, A.; Charpentier, T.; Menziani, M. C. The Structure of Fluoride-Containing Bioactive Glasses: New Insights from First-Principles Calculations and Solid State NMR Spectroscopy. *J. Mater. Chem.* **2012**, *22* (25), 12599. https://doi.org/10.1039/c2jm30890h.

(51) Rakhmatullin, A.; Boča, M.; Mlynáriková, J.; Hadzimová, E.; Vasková, Z.; Polovov, I. B.; Mičušík, M. Solid State NMR and XPS of Ternary Fluorido-Zirconates of Various Coordination Modes. *Journal of Fluorine Chemistry* **2018**, *208*, 24–35. https://doi.org/10.1016/j.jfluchem.2018.01.010.

(52) Rakhmatullin, A.; Polovov, I. B.; Maltsev, D.; Allix, M.; Volkovich, V.; Chukin, A. V.; Boča, M.; Bessada, C. Combined Approach for the Structural Characterization of Alkali Fluoroscandates: Solid-State NMR, Powder X-Ray Diffraction, and Density Functional Theory Calculations. *Inorg. Chem.* **2018**, *57* (3), 1184–1195. https://doi.org/10.1021/acs.inorgchem.7b02617.

(53) Martel, L.; Capelli, E.; Body, M.; Klipfel, M.; Beneš, O.; Maksoud, L.; Raison, P. E.; Suard, E.; Visscher, L.; Bessada, C.; Legein, C.; Charpentier, T.; Kovács, A. Insight into the Crystalline Structure of ThF_4 with the Combined Use of Neutron Diffraction, ^{19}F Magic-Angle Spinning-NMR, and Density Functional Theory Calculations. *Inorganic Chemistry* **2018**, *57* (24), 15350–15360. https://doi.org/10.1021/acs.inorgchem.8b02683.

(54) DeVore, M. A.; Klug, C. A.; Kriz, M. R.; Roy, L. E.; Wellons, M. S. Investigations of Uranyl Fluoride Sesquihydrate ($UO_2F_2 \cdot 1.57H_2O$): Combining ^{19}F Solid-State MAS NMR Spectroscopy and GIPAW Chemical Shift Calculations. *J. Phys. Chem. A* **2018**, *122* (34), 6873–6878. https://doi.org/10.1021/acs.jpca.8b04369.

(55) Dabachi, J.; Body, M.; Dittmer, J.; Rakhmatullin, A.; Fayon, F.; Legein, C. Insight into the Factors Influencing NMR Parameters in Crystalline Materials from the $KF–YF_3$ Binary System. *Dalton Transactions* **2019**, *48* (2), 587–601. https://doi.org/10.1039/C8DT03241F.

(56) Murakami, M.; Noda, Y.; Takegoshi, K. Terminal and Bridging Fluorine Ligands in TiF_4 as Studied by ^{19}F NMR in Solids. *Solid State Nuclear Magnetic Resonance* **2019**, *101*, 82–88. https://doi.org/10.1016/j.ssnmr.2019.05.007.

(57) Ding, F.; Griffith, K. J.; Koçer, C. P.; Saballos, R. J.; Wang, Y.; Zhang, C.; Nisbet, M. L.; Morris, A. J.; Rondinelli, J. M.; Poeppelmeier, K. R. Multimodal Structure Solution with ^{19}F NMR Crystallography of Spin Singlet Molybdenum Oxyfluorides. *J. Am. Chem. Soc.* **2020**, *142* (28), 12288–12298. https://doi.org/10.1021/jacs.0c04019.

(58) Legein, C.; Body, M.; Lhoste, J.; Li, W.; Charpentier, T.; Dambournet, D. Synthesis, Crystal Structure and ^{19}F NMR Parameters Modelling of $CaTiF_6(H_2O)_2$ Yielding to a Revision of the Bond-Valence Parameters for the Ti^{4+}/F<sub>−</sup> ion pair. *Journal of Solid State Chemistry* **2023**, *319*, 123793. https://doi.org/10.1016/j.jssc.2022.123793.

(59) Larsen, F. H.; Nielsen, N. Chr. Effects of Finite Rf Pulses and Sample Spinning Speed in Multiple-Quantum Magic-Angle Spinning (MQ-MAS) and Multiple-Quantum

Quadrupolar Carr−Purcell−Meiboom−Gill Magic-Angle Spinning (MQ-QCPMG-MAS) Nuclear Magnetic Resonance of Half-Integer Quadrupolar Nuclei. *J. Phys. Chem. A* **1999**, *103* (50), 10825–10832. https://doi.org/10.1021/jp992798i.

(60) Vosegaard, T.; Skibsted, J.; Bildsøe, H.; Jakobsen, H. J. Solid-State NMR of $RbVO_3$. A Comparison of Experiments for Retrieving Chemical Shielding and Quadrupole Coupling Tensorial Interactions. *Solid State Nuclear Magnetic Resonance* **1999**, *14* (3–4), 203–210. https://doi.org/10.1016/S0926-2040(99)00021-1.

(61) Vosegaard, T.; Skibsted, J.; Bildsøe, H.; Jakobsen, H. J. Quadrupole Coupling and Anisotropic Shielding from Single-Crystal NMR of the Central Transition for Quadrupolar Nuclei. ^{87}Rb NMR of $RbClO_4$ and Rb_2SO_4. *Journal of Magnetic Resonance, Series A* **1996**, *122* (2), 111–119. https://doi.org/10.1006/jmra.1996.0186.

(62) Rollet, A.-L.; Allix, M.; Veron, E.; Deschamps, M.; Montouillout, V.; Suchomel, M. R.; Suard, E.; Barre, M.; Ocaña, M.; Sadoc, A.; Boucher, F.; Bessada, C.; Massiot, D.; Fayon, F. Synthesis and Structure Resolution of $RbLaF_4$. *Inorg. Chem.* **2012**, *51* (4), 2272–2282. https://doi.org/10.1021/ic202301e.

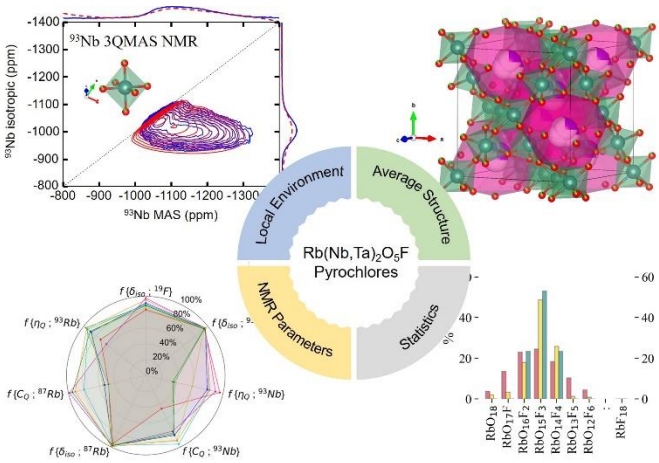
(63) Weber, H. J.; Schulz, M.; Schmitz, S.; Granzin, J.; Siegert, H. Determination and Structural Application of Anisotropic Bond Polarisabilities in Complex Crystals. *J. Phys.: Condens. Matter* **1989**, *1* (44), 8543–8547. https://doi.org/10.1088/0953-8984/1/44/025.

(64) Wang, X.; Adhikari, J.; Smith, L. J. An Investigation of Distortions of the Dion−Jacobson Phase $RbSr_2Nb_3O_{10}$ and Its Acid-Exchanged Form with ^{93}Nb Solid State NMR and DFT Calculations. *J. Phys. Chem. C* **2009**, *113* (40), 17548–17559. https://doi.org/10.1021/jp902318v.

Table of Contents Synopsis.

Thorough investigation of RbM_2O_5F (M = Nb, Ta) pyrochlore oxyfluorides involved XRPD, multinuclear high field solid-state NMR, and DFT calculations. NMR spectra of ^{19}F, ^{87}Rb, and ^{93}Nb confirmed disordered local environments. Refined XRPD data with DFT yielded 20 possible models showing Rb atoms at low-symmetry positions (*x*,*y*,*z*). DFT relaxation revealed preference of Nb for oxygen, converting $NbOF_5/NbF_6$ into $NbO_2F_5/NbOF_6/NbO_2F_6$ polyhedra. Preferential short-range O/F ordering is revealed, featuring exclusively MOF_5 octahedra, and $RbO_{15}F_3$, $RbO_{14}F_4$ and $RbO_{16}F_2$ cages.

Table of Contents Graphic.



IV.2. Conclusion

In this chapter, we have modeled, using the thesis multimodal approach, the structure of pyrochlore oxyfluorides RbM_2O_5F (M = Nb, Ta). The average structure, from Rietveld refinements of the XRPD data and from the literature, incorporates one co-occupied anionic site with site occupancy factors of 83.3% for O and 16.7% for F. The Rb site is occupied at 25%, and the M site is fully occupied. Using the supercell approach, 20 models were constructed. Additionally, 20 similar models with Rb atoms positioned at the 8b sites were considered. DFT relaxation confirms the affinity of Nb atoms for oxygen atoms, as the fluorine-rich octahedra, $NbOF_5$ and NbF_6, were converted to into NbO_2F_5/$NbOF_6$/NbO_2F_6 polyhedra.

In this study, the C_Q values proved to be the key parameters, rather than the calculated δ_{iso} values which were not sufficiently discriminating, to select or reject the different models. Among the 40 models tested, 16 present calculated C_Q values compatible with experimental ones for ^{87}Rb and ^{93}Nb (when present). Unexpectedly, the structure of the 16 selected models consists exclusively of MOF_5 octahedra, and $RbO_{15}F_3$, $RbO_{14}F_4$ and $RbO_{16}F_2$ cages. These results suggest the existence of a preferential O/F ordering in $RbNb_2O_5F$ and $RbTa_2O_5F$.

It is important to keep in mind that the results obtained from these pyrochlore oxyfluorides do not conclusively answer the question posed in the introduction. This chapter merely adds two compounds to the list of disordered inorganic oxyfluorides exhibiting short-range O/F order or correlated O/F disorder. To find out whether disordered inorganic oxyfluorides with a complete random distribution of anions exist, it would be necessary to study a statistically significant number of these compounds.

Chapter V

Magnetic Shielding to Chemical Shift Conversion

V.1. Introduction

The ^{19}F δ_{iso} range of inorganic materials, approximately 400-500 ppm, is relatively wide whereas ^{1}H shows a narrower δ_{iso} range of about 15 ppm. While a simple conversion relation, typically $\delta_{iso} = -\sigma_{iso} + 31$,[1] is sufficient for ^{1}H, due to the ^{19}F sensitivity to local environment, the development of an unified and efficient equation to convert the calculated ^{19}F σ_{iso} values into δ_{iso} values remains a challenge.

In this manuscript, we have employed linear regression equations to convert calculated σ_{iso} values into calculated δ_{iso} values for various nuclei, including, ^{19}F, ^{23}Na, ^{87}Rb and ^{93}Nb. These equations were established from ordered inorganic compounds and they take the form $\delta_{iso} = -a\,\sigma_{iso} + \sigma_{iso}^{ref}$, where a represents the slope and σ_{iso}^{ref} the intercept. Theoretically, the slope a should be equal to 1. However, while some of the linear regression equations established in this manuscript present slopes that are close to the theoretical value of 1, such as 1.034 and 0.968 for NbF_5 and TaF_5, respectively, others have slopes far from this value, such as 0.828 for the bridging F atoms in TiF_4. Furthermore, previous attempts of establishing universal ^{19}F linear regression equation from a broad range of ordered fluorides, including alkali, alkaline earth and rare earth fluorides, resulted in an equation with a slope of 0.70.[2] Despite the correction of the cationic localized empty orbitals of Ca^{2+}, Sc^{3+} (3d) and La^{3+} (4f), the slope remained far from theory, with a value of 0.80.[2] In light of these observations, it seems that the quest of a unique linear regression equation with a slope equal to 1, efficient for all nuclei is comparable to the quest of the Holy Grail. This Chapter serves as an attempt in finding and understanding the underlying factors contributing to the observed slope and intercept discrepancies. Additionally, we present our perspective, substantiated by quantitative evidence, on the factors that should be taken into account during the process of converting calculated σ_{iso} to calculated δ_{iso}.

V.2. Literature overview

A linear regression is assumed to be reliable if it is established from a series of ordered compounds. For ^{19}F in inorganic ordered fluorides, numerous linear regression equations, mostly using the GIPAW[3,4] approach,[2,5–22] but also a full-potential one, *i.e.* all electron augmented plane wave[23] (APW),[24–26] have been established to convert calculated σ_{iso} values to calculated δ_{iso} values (**Table 5.1**). Two different methods can be used in this conversion: either the slope is kept to the theoretical value, 1, and only the σ_{iso}^{ref} value is determined ($\delta_{iso} = -\sigma_{iso} + \sigma_{iso}^{ref}$), or both the slope and σ_{iso}^{ref} values are refined simultaneously ($\delta_{iso} = -a\,\sigma_{iso} + \sigma_{iso}^{ref}$). In the case of ^{19}F, the former approach was used only once, likely because, due to the generalized gradient approximation (GGA) to the exchange-correlation functional,[25] the values of the slope are often significantly below 1. For ^{19}F, out of 31 equations, 22 present slopes that deviate from 1, *i.e.*, with $a < 0.9$ or $a > 1$. Equations with slope close to 1 were established from one or at most five compounds, while equations that have slope values far from 1, except for TaF_5,[7] TiF_4,[18] $UO_2F_2 \cdot 1.57H_2O$,[14] Rb_3ScF_6,[21] and $CaTiF_6(H_2O)_2$,[27] are established from at least three compounds, with the majority established from a higher number of compounds. This observation further confirms that achieving a universal linear regression with a slope of 1 is not feasible for ^{19}F with the approaches used to date.

If we take a closer look on the equations established from compounds with transition metals, including Nb^{5+}, Ta^{5+} and Ti^{4+}, we found two equations established from compounds with Nb^{5+} and Ta^{5+}, and five ones established from compounds with Ti^{4+}. The pentafluorides NbF_5 and TaF_5 were used to establish the Nb^{5+} and Ta^{5+} equations. These fluorides contain only one bridging F site (M–F–M), but five terminal F sites. As for compounds with Ti^{4+}, (i) one equation is determined from only Ti-bounded F atoms,[19] (ii) two equations are determined from average σ_{iso} and δ_{iso} values for disordered hybrids,[15,20] (iii) one equation was established from the six F atoms of $CaTiF_6(H_2O)_2$,[27] and (iv) the last one is determined on TiF_4,[18] whose structure presents ten F sites.[28] However, for TiF_4, two groups of points are clearly observed in **Figure 3.6** (**chapter III**), one corresponding to the bridging F atoms and the second corresponding to the terminal F atoms, separated by more than 300 ppm. The two insets added to the graph provide an enlarged view of these two groups (**Figure 3.6 (a)**) and highlight the fact that the data

points are not very well aligned on the regression line. The two distinct linear regressions for bridging (**Figure 3.6 (b)**) and terminal (**Figure 3.6 (c)**) F atoms confirm that a unique regression equation cannot be effective in predicting the δ_{iso} values for both bridging and terminal F atoms in Ti compounds.

Based on the preceding analysis, it can be argued that in order to predict accurate ^{19}F δ_{iso} values in oxyfluorides, the related ^{19}F linear regression equation must be derived exclusively from a single ordered fluoride exhibiting multiple F sites with environments similar to those found in the studied oxyfluorides, and containing the same cation(s). For instance, the equation δ_{iso}(ppm) = –0.828(14) σ_{iso} + 44.2(6), derived from bridging F atoms in the ordered fluoride TiF_4, allows accurately predicting δ_{iso} values in the disordered oxyfluoride HTB-$TiOF_2$ whose structure exclusively presents bridging F atoms. Similarly, for $NbOF_3$ and $TaOF_3$ oxyfluorides, the ^{19}F δ_{iso} values of bridging and terminal F atoms were successfully predicted using linear regression equations from NbF_5 and TaF_5 which also contain terminal and bridging F atoms. Nevertheless, while this argument applies to HTB-$TiOF_2$, $NbOF_3$ and $TaOF_3$, it does not fully apply to NbO_2F and TaO_2F, where all F atoms are of bridging nature. Furthermore, the linear regression equation used, which predicts accurate ^{19}F δ_{iso} values, is established from NbF_5 and TaF_5, where only one bridging F site exists, with the rest being terminal F sites. Therefore, this argument remains circumstantial, and each case should be studied individually.

Table 5.1 Previously reported linear regression equations between the calculated σ_{iso} and the experimental δ_{iso} values for ^{19}F in inorganic fluorides.

Inorganic fluoride(s)	Equation(s)	Ref.
LiF, NaF, KF, RbF, $KF{\cdot}2H_2O$, $RbF{\cdot}H_2O$, CaF_2, SrF_2, CdF_2, HgF_2, Hg_2F_2, α-PbF_2, α-AlF_3, LaF_3, Na_3AlF_6, $Na_5Al_3F_{14}$, $KAlF_4$, Na_2SiF_6, *and two organic fluorides.*	$\delta_{iso} = -0.68\ (\sigma_{iso} - 81.39)$	[5]
MF (M = Li, Na, K, Rb), MF_2 (M = Ca, Sr, Ba), MF_3 (M = Sc, Y, La), CdF_2, HgF_2, Hg_2F_2, α-PbF_2, α-AlF_3, $Na_5Al_3F_{14}$, ZnF_2, GaF_3, InF_3, $BaLiF_3$, β-$BaAlF_5$ and $Ba_3Al_2F_{12}$	$\delta_{iso} = -0.80(3)\ \sigma_{iso} + 89(9)$	[2]
NaF, CaF_2, Na_2SiF_6, $Ca_4(Si_2O_7)F_2$, Fluoroapatite $Ca_5(PO_4)_3F$	$\delta_{iso} = -\sigma_{iso} + 170.5$ $\delta_{iso} = -0.963\ \sigma_{iso} + 159.6$	[6]
NbF_5	$\delta_{iso} = -1.028(6)\ \sigma_{iso} + 100.4(8)$	[7]
TaF_5	$\delta_{iso} = -0.777(11)\ \sigma_{iso} + 86.2(1.2)$	
MF (M = Li, Na, K, Rb, Cs), MF_2 (M = Ca, Sr, Ba) MF (M = Li, Na, K, Rb, Cs, Tl), MF_2 (M =Mg, Ca, Sr, Ba), MF_3 (M = Al, Ga, In)	$\sigma_{iso} = -1.26(4)\ \delta_{iso} + 123.2$ $\sigma_{iso} = -0.964(36)\ \delta_{iso} + 191.2$ $\sigma_{iso} = -0.817(36)\ \delta_{iso} + 236.3$ $\sigma_{iso} = -1.05(4)\ \delta_{iso} + 184.5$	[25]
MF (M = Li, Na, K, Rb), MF_2 (M = Ca, Sr, Ba), MF_3 (M = Sc, Y, La), α-AlF_3, β-AlF_3, η-AlF_3, GaF_3, TlF-II, TlF-I	$\delta_{iso} = -0.795(15)\ \sigma_{iso} + 89(4)$	[8]
Fluorinated imidazolium salts $[C_6H_4(CH_2(C_4H_6N_2)_2]_2+\ 2[A]^-$ (A = BF_4, PF_6)	$\delta_{iso} = -0.704\ (\sigma_{iso} - 105.1)$	[9]
BaF_2, β-$BaAlF_5$ and $Ba_5Al_3F_{19}$	$\delta_{iso} = -0.87\ \sigma_{iso} + 117$	[10]
MF (M = Li, Na, K, Rb, Cs, Tl), MF_2 (M = Mg, Ca, Sr, Ba), MF_3 (M = Al, Ga, In)	$\delta_{iso} = -0.7964(250)\ \sigma_{iso} + 86.47(7.08)$ $\delta_{iso} = -0.8056(257)\ \sigma_{iso} + 87.76(7.22)$ $\delta_{iso} = -0.8429(337)\ \sigma_{iso} + 101.64(9.54)$	[26]
ScF_3, Na_3ScF_6, Li_3ScF_6, $NaScF_4$, KSc_2F_7, $K_5Sc_3F_{14}$	$\delta_{iso} = -0.589\ \sigma_{iso} + 20.24$	[11]
M_2ZrF_6 (M = Li, K, Rb, Cs), K_3ZrF_7, Li_4ZrF_8, $Na_5Zr_2F_{13}$	$\delta_{iso} = -0.795(38)\ \sigma_{iso} + 82(3)$	[12]
ThF_4	$\delta_{iso} = -0.938\ \sigma_{iso} + 77.1$	[13]
$UO_2F_2{\cdot}1.57H_2O$	$\delta_{iso} = -0.4988\ (\sigma_{iso} + 11.34)$	[14]
$[H_2taz]_2{\cdot}(Ti_5O_5F_{12})$ & $[H_2gua]_2{\cdot}(Ti_5O_5F_{12})$	$\delta_{iso} = -0.97(9)\ \sigma_{iso} + 67(5)$	[15]
KF, γ-K_3YF_6, K_2YF_5, α-KY_3F_{10} and YF_3	$\delta_{iso} = -0.743(22)\ \sigma_{iso} + 68.5(4.5)$	[16]
LiF, NaF, KF, CsF, BaF_2	$\delta_{iso} = -1.233\ \sigma_{iso} + 127.7$; $\delta_{iso} = -1.177\ \sigma_{iso} + 126.0$; $\delta_{iso} = -1.014\ \sigma_{iso} + 192.3$; $\delta_{iso} = -1.005\ \sigma_{iso} + 183.1$	[17]
TiF_4	$\delta_{iso} = -1.13(1)\ \sigma_{iso} + 63(3)$	[18]
$K_5[Mo_3O_4F_9]{\cdot}3H_2O$, $K_5[Mo_3O_4F_9]{\cdot}2H_2O$ & $K_{16}[Mo_3O_4F_9]_2[TiF_6]_3{\cdot}2H_2O$	$\delta_{iso} = -0.824(26)\ \sigma_{iso} + 66(6)$	[19]
trans-$Zn_3TiF_7(H_2O)_2(taz)_3{\cdot}3H_2O$, trans-$Zn_3TiF_7(taz)_3$ & cis-$Zn_3TiF_7(H_2O)_2(taz)_3{\cdot}C_2H_5OH$	$\delta_{iso} = -0.82(1)\ \sigma_{iso} + 92(3)$	[20]
Rb_3ScF_6	$\delta_{iso} = -0.730\ \sigma_{iso} + 70.17$	[21]
$CaTiF_6\ (H_2O)_2$	$\delta_{iso} = -0.612(20)\ \sigma_{iso} + 100.6(1.1)$	[27]
NbF_5	$\delta_{iso} = -1.031(6)\ \sigma_{iso} + 97.3(8)$	[22]
TaF_5	$\delta_{iso} = -0.968(7)\ \sigma_{iso} + 107.9(6)$	

V.3. Factors to consider when establishing a σ_{iso}–δ_{iso} correlation

V.3.1. Pseudopotentials

The pseudopotentials used for the calculations significantly influence the calculated σ_{iso} values and subsequently, the linear regression equation. For instance, VASP uses the projector augmented wave (PAW) potentials.[29,30] Generally, these potentials exhibit greater accuracy compared to ultra-soft pseudopotentials (USPP) implemented in CASTEP due to two main reasons. Firstly, the radial cutoffs (core radii) are similar compared to the radii used for USPP. Secondly, the PAW potentials reconstruct the precise valence wave function, incorporating all nodes within the core region. Consequently, the slope of the established linear regression from TaF_5 using PAW potentials is closer to 1 (~0.97, **Chapter III**)[22] in comparison to that derived using USPP (~0.78).[7]

PAW potentials can be categorized into multiple types, and these types also affect the calculated values. There are PAW potentials used for standard DFT calculations and GW (Green's function with screened coulomb interaction) PAW potentials used for GW calculations. Among the standard PAW potentials, the harder potentials, labeled as '*h*', require a greater energy cutoff than the softer '*s*' potentials, whereas for the potentials '*pv*', '*sv*', and '*d*', the '*p*', '*s*', and '*d*' semi-core states respectively are treated as valence states. Similarly, for GW PAW potentials, '*h_GW*', '*s_GW*', '*pv_GW*', '*sv_GW*', and '*d_GW*' types exist. The GW PAW potentials can also be used for standard DFT calculations, with slightly better results. Consequently, four sets of calculations were performed to establish linear regressions from RbF and NbF_5 fluorides using various PAW potentials for F, Rb and Nb atoms: the '*F*', '*Rb_pv*' and '*Nb_pv*' ones in the first set (**Figure 5.1 (a)**); the '*F*', '*Rb_sv*' and '*Nb_sv*' potentials in the second set (**Figure 5.1 (b)**); '*F_GW*', '*Rb_sv_GW*' and '*Nb_sv_GW*' potentials in the third set (**Figure 5.1 (c)**); and '*F_GW_new*', '*Rb_sv_GW*' and '*Nb_sv_GW*' potentials in the fourth and final set (**Figure 5.1 (d)**). As depicted in **Figure 5.1**, the slope value significantly improved, increasing from ~0.89 to ~0.96, when using '*sv*' potentials for Rb and Nb. The improvement was even more pronounced when using '*GW_sv*' for Rb and Nb, in conjunction with '*GW*' and '*GW_new*' potentials for F. Furthermore, the average difference between the calculated and experimental ^{19}F δ_{iso} values, $\langle\Delta\delta_{iso}\rangle$, decreased by ~2.1 ppm.

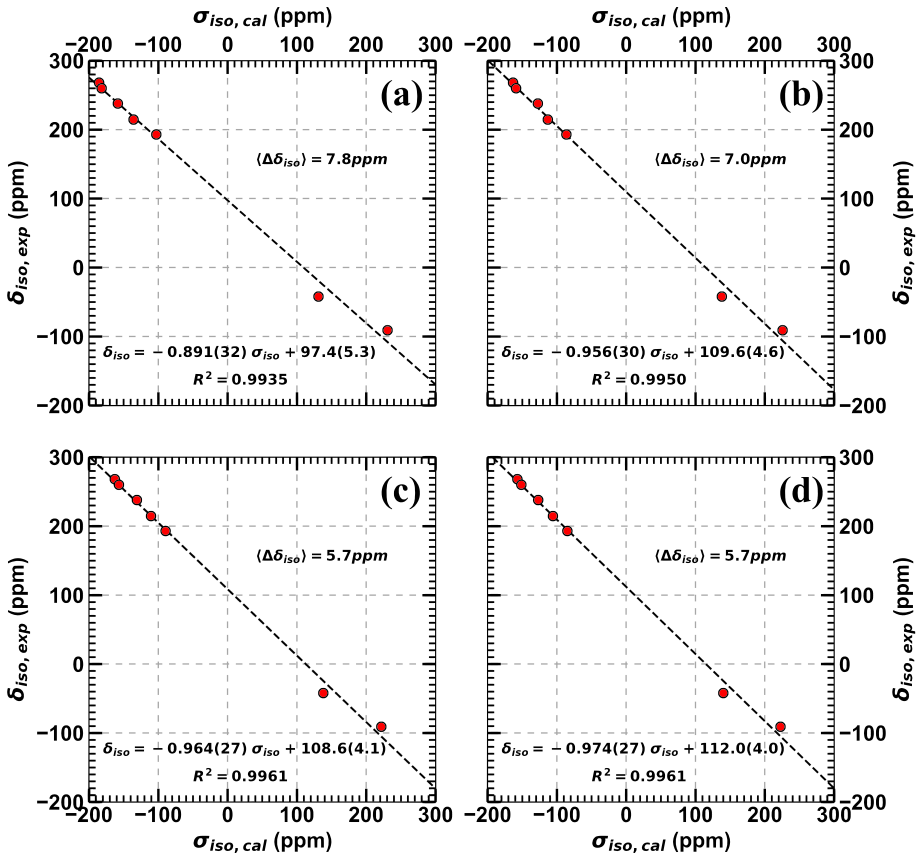


Figure 5.1. Calculated ^{19}F σ_{iso} values as a function of the experimental ^{19}F δ_{iso} values for RbF and NbF_5. The dashed lines represent linear regressions when considering σ_{iso} values calculated using the PAW potentials, '*F*', '*Rb_pv*' and '*Nb_pv*' (a), '*F*', '*Rb_sv*' and '*Nb_sv*' (b), '*F_GW*', '*Rb_sv_GW*' and '*Nb_sv_GW*' (c) and '*F_GW_new*', '*Rb_sv_GW*' and '*Nb_sv_GW*' (d). The linear regression equations, their R-squared as well as the average difference $\langle\Delta\delta_{iso}\rangle$ are given.

V.3.2. NMR calculation methods and exchange correlation functionals

Similar to pseudopotentials, the NMR calculation method, including the gauge including projector augmented wave (GIPAW) and the full-potentials linearized augmented plane wave (FP-LAPW), in conjunction with the exchange correlation functional, comprising the Perdrew-Burke-Ernzerhof (PBE) and the Becke-Johnson potential with local-density approximation (BJ-LDA), significantly impact the calculated σ_{iso} values. A series of calculations was conducted by Laskowski *et al.*[25] to refine the slope of linear regression equations deduced from various ordered fluorides to converge on the optimal value of 1. They employed GIPAW and FP-LAPW methods and PBE and BJ-LDA exchange correlation functionals. Subsequently, their analysis revealed that the calculated ^{19}F σ_{iso} values from FP-LAPW using BJ exchange correlation potentials yielded a slope of 1.05, whereas with PBE, the slope was estimated to be 1.26.[25] Furthermore, the calculated ^{19}F δ_{iso} values from BJ were found to be three times

closer to the experimental ^{19}F δ_{iso} values, with an average difference $\langle\Delta\delta_{iso}\rangle$ of ~11.2 ppm, compared to the values from PBE where $\langle\Delta\delta_{iso}\rangle$ was ~32.6 ppm.

V.3.3. Other factors

Other factors should also be considered when performing standard DFT NMR parameters calculations. These include the energy cutoff, E_{cut}, the break condition for the electronic self-consistency loop, E_{diff}, and the chosen k-point mesh. These factors were optimized with VASP for LiF and LaF_3 fluorides to demonstrate their influence on ^{7}Li, ^{19}F, and ^{139}La calculated σ_{iso} values (**Figure 5.2**). For LaF_3, the variation in the ^{19}F σ_{iso} values calculated as a function of E_{cut} is similar for all three F sites, with a ~2.2 ppm decrease (**Figure 5.2** F1, F2 and F3). Regarding ^{139}La, the σ_{iso} value fluctuated around –4646 ppm with a magnitude of ~2 ppm (**Figure 5.2** La1). For LiF, increasing the E_{cut} value from 500 to 900 eV resulted in a ^{19}F σ_{iso} decrease of ~3.9 ppm (**Figure 5.2** F4). As for ^{7}Li, the σ_{iso} value stabilizes at ~–88.7 ppm from an E_{cut} of 650 eV (**Figure 5.2** Li1). The effect of E_{diff} and the choice of the k-point mesh on the calculated ^{19}F and ^{7}Li σ_{iso} values is very small (~1 ppm variation at most, **Figure 5.2** F1 and Li1).

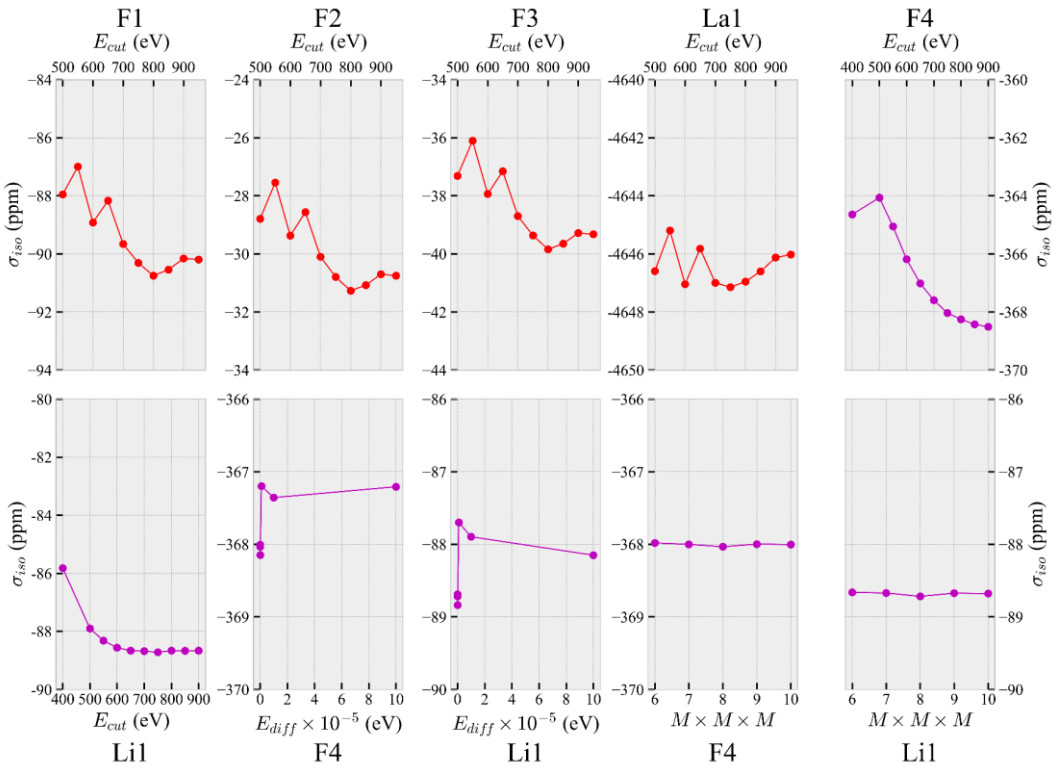


Figure 5.2. Calculated σ_{iso} values as a function of E_{cut}, E_{diff}, and the $M \times M \times M$ k-point mesh for F1, F2, F3 and La1 sites from LaF_3 (red) and for F4 and Li1 sites from LiF (purple).

The effect of the temperature on the experimental δ_{iso} values is another pertinent factor to consider. Even small temperature differences in MAS NMR experiments, which arise from low-to-high MAS frequencies (equivalently, low-to-high temperatures, ~40-70 °C), does result in a variation of the δ_{iso} value for a given resonance. This is due to the thermal expansion that the crystal structure of the studied sample experiences. Two possible methodologies are worth testing to approach this temperature-induced discrepancy. The first method is to record a sequence of NMR spectra, for instance ^{19}F MAS NMR spectra, at the largest possible range of temperature on a series of stables and known ordered fluorides. Then, establishing a correlation between these temperatures and their corresponding δ_{iso} values, and fitting the correlation using the appropriate method. Depending on the evolution of δ_{iso} with respect to temperature, *i.e.*, whether it is linear or non-linear, δ_{iso} values at very low temperatures can be estimated. The second method is to perform first principle calculations at temperatures equivalent to those from the NMR experiments. This can be achieved by conducting *ab initio* molecular dynamics at a given temperature and time interval. For each structure relaxed at the temperature T and time t_i, $\sigma_{iso}^{(i)}$ values are calculated. The calculated σ_{iso} value can be estimated as an average value calculated at T in the chosen time interval $[t_0, t_N]$ as $\langle\sigma_{iso}\rangle = \Sigma_{(i)}^{N} \sigma_{iso}^{(i)}/N$, where $i = 0, \ldots, N$.

V.4. Conclusion

In this chapter, we provided a brief overview of ^{19}F linear regression equations previously established in the literature and highlighted their discrepancies in slopes and intercepts and therefore the impossibility of establishing a universal linear regression equation with a slope of 1 for this nucleus. Furthermore, we conducted an analysis of the various parameters that need to be considered during the process of converting calculated σ_{iso} values to δ_{iso} values. These parameters include pseudopotentials (PAW, GW PAW and USPP), DFT relaxation parameters (E_{cut}, E_{diff} and the k-point mesh), the NMR parameters calculation method (GIPAW and FP-LAPW methods), and the exchange correlation functional (PBE and BJ-LDA). Depending on the compound under study, these parameters should be carefully chosen, and the DFT relaxation parameters should be optimized. Moreover, a speculative assessment of the temperature effect on δ_{iso} values has been provided.

Based on the established ^{19}F linear regressions in this thesis, the conversion of calculated ^{19}F σ_{iso} values into ^{19}F δ_{iso} values for a given oxyfluoride should be performed using a linear regression equation derived from one ordered fluoride with multiple F sites and the same cation(s). The goal is not to obtain an equation with a slope of 1, but well aligned points defined by a good R-squared value resulting in accurate calculated δ_{iso} values.

Finally, further calculation tests assessing the exchange correlation functional BJ-LDA should be considered for NbF_5, TaF_5, and TiF_4. Additionally, the temperature effect on δ_{iso} values should be thoroughly studied for alkali, alkaline earth, rare earth, and other ordered fluorides.

V.5. References

(1) Gervais, C.; Profeta, M.; Lafond, V.; Bonhomme, C.; Azaïs, T.; Mutin, H.; Pickard, C. J.; Mauri, F.; Babonneau, F. Combinedab Initio Computational and Experimental Multinuclear Solid-State Magnetic Resonance Study of Phenylphosphonic Acid. *Magn. Reson. Chem.* **2004**, *42* (5), 445–452. https://doi.org/10.1002/mrc.1360.

(2) Sadoc, A.; Body, M.; Legein, C.; Biswal, M.; Fayon, F.; Rocquefelte, X.; Boucher, F. NMR Parameters in Alkali, Alkaline Earth and Rare Earth Fluorides from First Principle Calculations. *Phys. Chem. Chem. Phys.* **2011**, *13* (41), 18539. https://doi.org/10.1039/c1cp21253b.

(3) Pickard, C. J.; Mauri, F. All-Electron Magnetic Response with Pseudopotentials: NMR Chemical Shifts. *Phys. Rev. B* **2001**, *63* (24), 245101. https://doi.org/10.1103/PhysRevB.63.245101.

(4) Yates, J. R.; Pickard, C. J.; Mauri, F. Calculation of NMR Chemical Shifts for Extended Systems Using Ultrasoft Pseudopotentials. *Phys. Rev. B* **2007**, *76* (2), 024401. https://doi.org/10.1103/PhysRevB.76.024401.

(5) Griffin, J. M.; Yates, J. R.; Berry, A. J.; Wimperis, S.; Ashbrook, S. E. High-Resolution ^{19}F MAS NMR Spectroscopy: Structural Disorder and Unusual *J* Couplings in a Fluorinated Hydroxy-Silicate. *J. Am. Chem. Soc.* **2010**, *132* (44), 15651–15660. https://doi.org/10.1021/ja105347q.

(6) Pedone, A.; Charpentier, T.; Menziani, M. C. The Structure of Fluoride-Containing Bioactive Glasses: New Insights from First-Principles Calculations and Solid State NMR Spectroscopy. *J. Mater. Chem.* **2012**, *22* (25), 12599. https://doi.org/10.1039/c2jm30890h.

(7) Biswal, M.; Body, M.; Legein, C.; Sadoc, A.; Boucher, F. NbF_5 and TaF_5: Assignment of ^{19}F NMR Resonances and Chemical Bond Analysis from GIPAW Calculations. *Journal of Solid State Chemistry* **2013**, *207*, 208–217. https://doi.org/10.1016/j.jssc.2013.09.001.

(8) Sadoc, A.; Biswal, M.; Body, M.; Legein, C.; Boucher, F.; Massiot, D.; Fayon, F. NMR Parameters in Column 13 Metal Fluoride Compounds (AlF_3, GaF_3, InF_3 and TlF) from First Principle Calculations. *Solid State Nuclear Magnetic Resonance* **2014**, *59–60*, 1–7. https://doi.org/10.1016/j.ssnmr.2014.01.001.

(9) Neouze, M.-A.; Kronstein, M.; Litschauer, M.; Puchberger, M.; Coelho, C.; Bonhomme, C.; Gervais, C.; Tielens, F. Exploring the Molecular Structure of Imidazolium-Silica-Based Nanoparticle Networks by Combining Solid-State NMR Spectroscopy and First-Principles Calculations. *Chem. Eur. J.* **2014**, *20* (46), 15188–15196. https://doi.org/10.1002/chem.201403730.

(10) Martineau, C.; Allix, M.; Suchomel, M. R.; Porcher, F.; Vivet, F.; Legein, C.; Body, M.; Massiot, D.; Taulelle, F.; Fayon, F. Structure Determination of Ba_5AlF_{13} by Coupling Electron, Synchrotron and Neutron Powder Diffraction, Solid-State NMR and Ab Initio Calculations. *Dalton Trans.* **2016**, *45* (39), 15565–15574. https://doi.org/10.1039/C6DT02454H.

(11) Rakhmatullin, A.; Polovov, I. B.; Maltsev, D.; Allix, M.; Volkovich, V.; Chukin, A. V.; Boča, M.; Bessada, C. Combined Approach for the Structural Characterization of Alkali Fluoroscandates: Solid-State NMR, Powder X-Ray Diffraction, and Density Functional Theory Calculations. *Inorg. Chem.* **2018**, *57* (3), 1184–1195. https://doi.org/10.1021/acs.inorgchem.7b02617.

(12) Rakhmatullin, A.; Boča, M.; Mlynáriková, J.; Hadzimová, E.; Vasková, Z.; Polovov, I. B.; Mičušík, M. Solid State NMR and XPS of Ternary Fluorido-Zirconates of Various Coordination Modes. *Journal of Fluorine Chemistry* **2018**, *208*, 24–35. https://doi.org/10.1016/j.jfluchem.2018.01.010.

(13) Martel, L.; Capelli, E.; Body, M.; Klipfel, M.; Beneš, O.; Maksoud, L.; Raison, P. E.; Suard, E.; Visscher, L.; Bessada, C.; Legein, C.; Charpentier, T.; Kovács, A. Insight into the Crystalline Structure of ThF_4 with the Combined Use of Neutron Diffraction, ^{19}F Magic-Angle Spinning-NMR, and Density Functional Theory Calculations. *Inorg. Chem.* **2018**, *57* (24), 15350–15360. https://doi.org/10.1021/acs.inorgchem.8b02683.

(14) DeVore, M. A.; Klug, C. A.; Kriz, M. R.; Roy, L. E.; Wellons, M. S. Investigations of Uranyl Fluoride Sesquihydrate ($UO_2F_2{\cdot}1.57H_2O$): Combining ^{19}F Solid-State MAS NMR Spectroscopy and GIPAW Chemical Shift Calculations. *J. Phys. Chem. A* **2018**, *122* (34), 6873–6878. https://doi.org/10.1021/acs.jpca.8b04369.

(15) Albino, M.; Body, M.; Legein, C.; Hémon-Ribaud, A.; Leblanc, M.; Maisonneuve, V.; Lhoste, J. NMR Crystallography, Hydrogen Bonding and Optical Properties of the Novel 2D Hybrid Oxyfluorotitanate $[H_2Taz]_2{\cdot}(Ti_5O_5F_{12})$. *Crystal Growth & Design* **2018**, *18* (11), 6873–6884. https://doi.org/10.1021/acs.cgd.8b01085.

(16) Dabachi, J.; Body, M.; Dittmer, J.; Rakhmatullin, A.; Fayon, F.; Legein, C. Insight into the Factors Influencing NMR Parameters in Crystalline Materials from the $KF–YF_3$ Binary System. *Dalton Trans.* **2019**, *48* (2), 587–601. https://doi.org/10.1039/C8DT03241F.

(17) Bartók, A. P.; Yates, J. R. Ultrasoft Pseudopotentials with Kinetic Energy Density Support: Implementing the Tran-Blaha Potential. *Phys. Rev. B* **2019**, *99* (23), 235103. https://doi.org/10.1103/PhysRevB.99.235103.

(18) Murakami, M.; Noda, Y.; Takegoshi, K. Terminal and Bridging Fluorine Ligands in TiF_4 as Studied by ^{19}F NMR in Solids. *Solid State Nuclear Magnetic Resonance* **2019**, *101*, 82–88. https://doi.org/10.1016/j.ssnmr.2019.05.007.

(19) Ding, F.; Griffith, K. J.; Koçer, C. P.; Saballos, R. J.; Wang, Y.; Zhang, C.; Nisbet, M. L.; Morris, A. J.; Rondinelli, J. M.; Poeppelmeier, K. R. Multimodal Structure Solution with ^{19}F NMR Crystallography of Spin Singlet Molybdenum Oxyfluorides. *J. Am. Chem. Soc.* **2020**, *142* (28), 12288–12298. https://doi.org/10.1021/jacs.0c04019.

(20) Albino, M.; Lhoste, J.; Body, M.; Legein, C.; Hémon-Ribaud, A.; Maisonneuve, V.; Leblanc, M. Topotactic Desolvation and Condensation Reactions of 3D $Zn_3TiF_7(H_2O)_2(Taz)_3{\cdot}S$ ($S = 3H_2O$ or C_2H_5OH). *Dalton Trans.* **2020**, *49* (48), 17758–17771. https://doi.org/10.1039/D0DT03391J.

(21) Rakhmatullin, A.; Molokeev, M. S.; King, G.; Polovov, I. B.; Maksimtsev, K. V.; Chesneau, E.; Suard, E.; Bakirov, R.; Šimko, F.; Bessada, C.; Allix, M. Polymorphs of Rb_3ScF_6: X-Ray and Neutron Diffraction, Solid-State NMR, and Density Functional Theory Calculations Study. *Inorg. Chem.* **2021**, *60* (8), 6016–6026. https://doi.org/10.1021/acs.inorgchem.1c00485.

(22) Zakary, O.; Body, M.; Charpentier, T.; Sarou-Kanian, V.; Legein, C. Structural Modeling of O/F Correlated Disorder in $TaOF_3$ and $NbOF_{3-x}(OH)_x$ by Coupling Solid-State NMR and DFT Calculations. *Inorg. Chem.* **2023**, *62* (40), 16627–16640. https://doi.org/10.1021/acs.inorgchem.3c02844.

(23) Blaha, P.; Schwarz, K.; Sorantin, P.; Trickey, S. B. Full-Potential, Linearized Augmented Plane Wave Programs for Crystalline Systems. *Computer Physics Communications* **1990**, *59* (2), 399–415. https://doi.org/10.1016/0010-4655(90)90187-6.

(24) Laskowski, R.; Blaha, P. Calculations of NMR Chemical Shifts with APW-Based Methods. *Phys. Rev. B* **2012**, *85* (3), 035132. https://doi.org/10.1103/PhysRevB.85.035132.

(25) Laskowski, R.; Blaha, P.; Tran, F. Assessment of DFT Functionals with NMR Chemical Shifts. *Phys. Rev. B* **2013**, *87* (19), 195130. https://doi.org/10.1103/PhysRevB.87.195130.

(26) De Wijs, G. A.; Laskowski, R.; Blaha, P.; Havenith, R. W. A.; Kresse, G.; Marsman, M. NMR Shieldings from Density Functional Perturbation Theory: GIPAW versus All-Electron Calculations. *The Journal of Chemical Physics* **2017**, *146* (6), 064115. https://doi.org/10.1063/1.4975122.

(27) Legein, C.; Body, M.; Lhoste, J.; Li, W.; Charpentier, T.; Dambournet, D. Synthesis, Crystal Structure and ^{19}F NMR Parameters Modelling of $CaTiF_6(H_2O)_2$ Yielding to a Revision of the Bond-Valence Parameters for the Ti^{4+}/F^- Ion Pair. *Journal of Solid State Chemistry* **2023**, *319*, 123793. https://doi.org/10.1016/j.jssc.2022.123793.

(28) Bialowons, H.; Müller, M.; Müller, B. G. Titantetrafluorid - Eine uberraschend einfache Kolumnarstruktur. *Z. Anorg. Allg. Chem.* **1995**, *621* (7), 1227–1231. https://doi.org/10.1002/zaac.19956210720.

(29) Blöchl, P. E. Projector Augmented-Wave Method. *Phys. Rev. B* **1994**, *50* (24), 17953–17979. https://doi.org/10.1103/PhysRevB.50.17953.

(30) Kresse, G.; Joubert, D. From Ultrasoft Pseudopotentials to the Projector Augmented-Wave Method. *Phys. Rev. B* **1999**, *59* (3), 1758–1775. https://doi.org/10.1103/PhysRevB.59.1758.

Conclusions and Perspectives

The research presented in this thesis aims to shed light on the structural complexities of transition metal inorganic oxyfluorides. By employing a multimodal approach that integrates various techniques, including XRPD, ssNMR, and DFT calculations, and in some instances, VT XRPD and PDF, each chapter has contributed significant insights into O/F ordering in both the short- and long-range structures. The following overarching conclusions can be drawn from the collective findings of this study.

The initial chapter laid the groundwork by providing detailed description of the robust theoretical framework, delineating the core principles governing NMR interactions in solid materials, and presenting the experimental sequences involved in the analysis of oxyfluorides. The incorporation of the PAW and GIPAW approaches in first principle calculations, coupled with the utilization of the DFT-D3 method for addressing weak interactions, proved critical in fundamentally understanding these oxyfluorides.

In **Chapter II**, the detailed investigation of $NaNbO_2F_2$ and $NaTaO_2F_2$ structures has uncovered valuable insights into the distinctive structural features of these compounds. The identification of second-order Jahn-Teller distortions in $NaNbO_2F_2$ and the distinct trends observed in structural parameters at different temperatures for $NaTaO_2F_2$ provide significant contributions to our understanding of their unique characteristics. These findings not only deepen our comprehension of the structural properties of these oxyfluorides but also highlight the effectiveness of the multimodal approach adopted in **Chapter I**, demonstrating its applicability in exploring compounds with diverse structural dynamics.

Chapter III, focusing on the crystal structures of $NbOF_3$, $TaOF_3$, $NbOF_{3-x}(OH)_x$, and $Ti_{0.99}\square_{0.01}O_{0.96}F_{1.53}(OH)_{0.51}\cdot 0.33H_2O$ oxyfluorides, has presented compelling evidence regarding the presence of preferential short-range O/F ordering and O/F correlated disorder within these compounds. The identification of O/F correlated disorder in $NbOF_3$ and $TaOF_3$, along with the insightful analysis of

the relationship between OH groups and ^{1}H and ^{19}F δ_{iso} values in the hydroxylated phases, provides valuable insights into the intricate interplay between structural features and their corresponding NMR parameters. Insights on dynamic processes at the hydrogen bond level further underscores the complexity of these compounds and paves the way for a deeper understanding of their structural dynamics.

Chapter IV's exploration of the pyrochlore oxyfluorides $RbNb_2O_5F$ and $RbTa_2O_5F$ has provided a meticulous analysis of the structural models, underscoring the significance of C_Q values in discerning the different models over the calculated δ_{iso} values. The exclusive presence of MOF_5 octahedra and $RbO_{15}F_3$, $RbO_{14}F_4$, and $RbO_{16}F_2$ cages in the selected models suggests the existence of preferential O/F ordering in these pyrochlores.

The comprehensive exploration of the conversion process from calculated σ_{iso} values to calculated δ_{iso} values, as discussed in the final chapters, has highlighted the intricacies involved in this crucial step. The recognition of the need for considering specific factors and the importance of the alignment of data points for accurate conversion, highlight the significance of this step in predicting accurate chemical shifts for disordered oxyfluorides.

In conclusion, this thesis represents a significant step forward in unraveling the complexities of the structure of oxyfluorides and provides a strong foundation for continued research in this field.

It is imperative to acknowledge that while this study has significantly contributed to the understanding of inorganic oxyfluorides and heteroanionic materials in general, there are still areas that require further investigation. While the results offer valuable insights into these specific compounds, the closing remarks of the thesis prompt a broader perspective, emphasizing the need for a more extensive exploration of a statistically significant number of purportedly disordered inorganic oxyfluorides. This exploration is necessary to determine whether compounds with a completely random distribution of anions exist, given that the compounds believed to be disordered and studied in this thesis were found to exhibit preferential short-range O/F ordering or O/F correlated disorder. Moreover, the identified challenges in the process of converting calculated σ_{iso} values to δ_{iso} values, the requirement for broader

temperature studies, and the necessity for an extensive examination of various exchange correlation functionals and pseudopotentials suggest promising avenues for future research endeavors.

Appendix A

Ordered Oxyfluorides

Multinuclear solid-state NMR, DFT calculations, and variable temperature PXRD of Nb and Ta isostructural oxyfluoride compounds revealing unexpected different structural features

Ouail Zakary[a,*], Monique Body[a], Franck Fayon[b], Vincent Sarou-Kanian[b]

Gwenaël Corbel[a,*] Christophe Legein[a]

[a] Institut de Molécules et Matériaux du Mans (IMMM) - UMR 6283 CNRS, Le Mans Université, Avenue Olivier Messiaen, 72805 Le Mans Cedex 9, France

[b] CNRS, CEMHTI UPR3079, Université d'Orléans, 45071 Orléans, France

Supplementary material

Table of content

1. Cell parameters of isotypes niobium (V) and tantalum (V) oxyfluorides, fluorides and oxides S246

Table S1. Formula, space group (SG), cell parameters a, b and c and volume, ICSD code and reference of isotypes of Nb(V) and Ta(V) oxyfluorides containing 3-, 4- and 5-elements and fluorides and oxides containing 2- and 3-elements S246

2. Rietveld refinements S249

Fig. S1. Observed, calculated and difference diffraction patterns of $NaNbO_2F_2$.. ..... S249

Fig. S2. Observed, calculated and difference diffraction patterns of $NaTaO_2F_2$. S249

3. Structural features S250

Table S2. Experimental and APO fractional atomic coordinates, differences between these fractional atomic coordinates and atomic displacements in $NaNbO_2F_2$ and $NaTaO_2F_2$ S250

Table S3. X–M–X and X–M–X' angles (M = Nb, Ta; X = O1, O2, F1 and F2) from the ES and APO models of $NaMO_2F_2$ (M = Nb, Ta) S251

Table S4. Na–X, Na–X' and Na–X'' bond lengths (X = F1, F2, O1, O2; X' = F1, F2; X'' = F1, F2) from the ES and APO models of $NaMO_2F_2$ (M = Nb, Ta) S251

4. ^{19}F MAS NMR spectra and their fits S252

Fig. S3. Experimental and fitted ^{19}F MAS (64 kHz) NMR spectra of $NaNbO_2F_2$. S252

Table S5. ^{19}F δ_{iso}, δ_{CSA}, η_{CSA}, line width and relative intensity of each individual resonance used to fit the ^{19}F MAS (64 kHz) NMR spectrum of $NaNbO_2F_2$, weighted average ^{19}F δ_{iso}, δ_{CSA}, η_{CSA}, sum of the corresponding relative intensities and assignments. S252

Fig. S4. Experimental and fitted ^{19}F MAS (64 kHz) NMR spectra of $NaTaO_2F_2$. S253

Table S6. ^{19}F δ_{iso}, δ_{CSA}, η_{CSA}, line width, relative intensity of each individual resonance used to fit the ^{19}F MAS (64 kHz) NMR spectrum of $NaTaO_2F_2$, weighted average ^{19}F δ_{iso}, δ_{CSA}, η_{CSA}, sum of the corresponding relative intensities and assignments. S253

5. ^{23}Na and ^{93}Nb NMR spectra and their fits S254

Fig. S5. (a) An overview of the experimental and fitted ^{23}Na MAS (30 kHz) NMR spectra of $NaNbO_2F_2$. Enlargements of the (b) central transition (CT) and (c) satellite transitions (ST).S S254

Table S7. ^{23}Na δ_{iso}, δ_{CSA}, η_{CSA}, C_Q and η_Q of the resonance used to fit the ^{23}Na MAS (30 kHz) NMR spectrum of $NaNbO_2F_2$. S254

Fig. S6. (a) An overview of the experimental and fitted ^{23}Na MAS (30 kHz) NMR spectra of $NaTaO_2F_2$. Enlargements of the (b) central transition (CT) and (c) satellite transitions (ST).S255

Table S8. ^{23}Na δ_{iso}, δ_{CSA}, η_{CSA}, C_Q nd η_Q of the individual resonances used to fit the ^{23}Na MAS (30 kHz) NMR spectrum of $NaTaO_2F_2$, weighted average ^{23}Na δ_{iso}, δ_{CSA}, η_{CSA}, C_Q and η_Q. S255

Fig. S7. Experimental and fitted ^{93}Nb static NMR spectra of $NaNbO_2F_2$. S256

Table S9. ^{93}Nb δ_{iso}, δ_{CSA}, η_{CSA}, C_Q and η_Q of the resonance used to fit the ^{93}Nb static NMR spectrum of $NaNbO_2F_2$. S256

6. Thermal and temperature controlled PXRD analysis S257

Fig. S8. DTA and TGA curves of $NaNbO_2F_2$ and $NaTaO_2F_2$ recorded, under argon atmosphere, from RT to 300/600 °C, with heating/cooling rate of 10 °C.min^{-1} S257

Fig. S9. Observed, calculated and difference temperature-controlled diffraction patterns in the [25–100°C] temperature range of $NaNbO_2F_2$. S258

Fig. S10. Observed, calculated and difference temperature-controlled diffraction patterns in the [100–200°C] temperature range of $NaNbO_2F_2$. S259

Fig. S11. Observed, calculated and difference temperature-controlled diffraction patterns in the [200–250°C] temperature range of $NaNbO_2F_2$. S260

Fig. S12. Observed, calculated and difference temperature-controlled diffraction patterns in the [260–300°C] temperature range of $NaNbO_2F_2$. S261

Fig. S13. Observed, calculated and difference temperature-controlled diffraction patterns in the [25–100°C] temperature range of $NaTaO_2F_2$ S262

Fig. S14. Observed, calculated and difference temperature-controlled diffraction patterns in the [100–200°C] temperature range of $NaTaO_2F_2$. S263

Fig. S15. Observed, calculated and difference temperature-controlled diffraction patterns in the [200–250°C] temperature range of $NaTaO_2F_2$. S264

Fig. S16. Observed, calculated and difference temperature-controlled diffraction patterns in the [260–300°C] temperature range of $NaTaO_2F_2$. S265

Table S10. Cell parameters and reliability factors of $NaNbO_2F_2$ from Rietveld refinements of the temperature-controlled PXRD data S266

Table S11. Cell parameters and reliability factors of $NaTaO_2F_2$ from Rietveld refinements of the temperature-controlled PXRD data.....S267

Fig. S17. Perspective view of Na^+ polyhedron, in which, atoms labeled X, X' and X'' (X = F1 and F2) are equivalent by symmetry operations. Temperature dependence of Na^+ polyhedron volume, bond lengths and distortion index of $NaNbO_2F_2$ and $NaTaO_2F_2$.. .....S268

Fig. S18. Temperature dependence of Na^+ polyhedra bond lengths from $NaNbO_2F_2$ and $NaTaO_2F_2$.. .....S269

Fig. S19. Temperature dependence of MO_4F_2 octahedra bond lengths from $NaNbO_2F_2$ and $NaTaO_2F_2$. S270

Fig. S20. Temperature dependence of MO_4F_2 octahedra angles from $NaNbO_2F_2$ and $NaTaO_2F_2$. S271

Fig. S21. Temperature dependence of MO_4F_2 octahedra angles from $NaNbO_2F_2$ and $NaTaO_2F_2$. S272

Fig. S22. Temperature dependence of MO_4F_2 octahedra angles from $NaNbO_2F_2$ and $NaTaO_2F_2$. S273

7. References.....S274

1. Cell parameters of isotypes niobium (V) and tantalum (V) oxyfluorides, fluorides and oxides

Table S1. Formula, space group (SG), cell parameters a, b and c (Å) and volume (Å^3), ICSD code (ICSD release 2023.1 [1]) and reference of isotypes of Nb(V) and Ta(V) oxyfluorides containing 3-, 4- and 5-elements and fluorides and oxides containing 2- and 3-elements. Below, ***in bold italic, cell parameters and volumes ratio***. ***Ratio below 0.99 or above 1.01 are highlighted in yellow.*** For consistency, only isotypes whose structures were refined in the same study (published in the same article) have been considered.

Formula	SG	a	b	c	v	ICSD-	Ref.
$NbOF_3$	*I4/mmm*	3.9675		8.4033	132.28	391169	[2]
$TaOF_3$		3.9448		8.4860	132.05	391168	
		1.0058		***0.9903***	***1.0014***		
$NbOF_3$	*I4/mmm*	3.9739		8.3612	132.05	n. a.	[3]
$TaOF_3$		3.9465		8.4454	131.53	n. a.	
		1.0069		***0.9900***	***1.0040***		
NbO_2F	*Pm$\bar{3}$m*	3.9031			59.461	n. a.	[4]
TaO_2F		3.8991			59.278	n. a.	
		1.0010			**1.0031**		
$CsNb_2O_5F$	*Fd$\bar{3}$m*	10.538			1170.2	421275	[5]
$CsTa_2O_5F$		10.480			1151.0	421277	
		1.006			***1.017***		
$(ClOF_2)(NbF_6)$	*Pna2$_1$*	30.189	5.2653	8.3588	1328.66	111377	[6]
$(ClOF_2)(TaF_6)$		30.2598	5.2923	8.3610	1338.96	111381	
		0.998	***0.995***	***1.000***	***0.992***		
$Ca_{1.5}Nb_2O_6F$	*P4$_3$32*	10.4506			1141.36	157313	[7]
$Ca_{1.5}Ta_2O_6F$		10.4321			1135.31	157315	
		1.002			***1.005***		
$Ca_{1.5}Nb_2O_6F$	*Fd$\bar{3}$m*	10.444			1139.2	157314	[7]
$Ca_{1.5}Ta_2O_6F$		10.43308			1135.63	157316	
		1.001			***1.003***		
$Hg_3(NbF_5)_2SO_4$	*Fdd2*	18.048	15.699	9.166	2597.05	60921	[8]
$Hg_3(TaF_5)_2SO_4$		18.078	15.705	9.153	2598.67	60922	
		0.998	***1.000***	***1.001***	***0.999***		
$LiSrNb_2O_6F$	*Fd$\bar{3}$m*	10.48171			1151.58	236009	[9]
$LiSrTa_2O_6F$		10.46401			1145.76	236010	
		1.002			***1.005***		
$LiSr_{0.9}Nb_2O_6F_{0.8}$	*Fd$\bar{3}$m*	10.4909			1154.62	236011	[9]
$LiSr_{0.9}Ta_2O_6F_{0.8}$		10.4687			1147.30	236012	
		1.002			***1.006***		
$Na_2Nb_2O_5F_2$	*Fd$\bar{3}$m*	10.5181			1163.62	n. a.	[10]
$Na_2Ta_2O_5F_2$		10.5231			1165.28	n. a.	
		0.9995			***0.999***		
$Hg_{2.881}NbF_6$	*I4$_1$/am*	7.692		12.679	750.18	30720	[11]
$Hg_{2.884}TaF_6$		7.711		12.714	755.97	30721	
		0.9975		***0.9972***	***0.9923***		
$NaNbF_6$	*Fm$\bar{3}$m*	8.26349			564.27	134083	[12]
$NaTaF_6$		8.2841			568.51	134084	
		0.9975			***0.9926***		
$LiNbF_6$	*R$\bar{3}$H*	5.3181		13.5861	332.77	165202	[13]
$LiTaF_6$		5.3206		13.6178	333.79	165205	
		0.9995		***0.9977***	***0.9969***		

Table S1. Continued

Formula	SG	a	b	c	v	ICSD-	Ref.
Eu_3NbO_7	$C222_1$	10.648	7.5064	7.5829	606.09	230392	[14]
Eu_3TaO_7		10.6655	7.5163	7.5822	607.83	230393	
		0.9984	***0.9987***	***1.0001***	***0.9971***		
Pr_3NbO_7	$Cmcm$	10.959	7.524	7.6676	632.24	78007	[15]
Pr_3TaO_7		10.973	7.523	7.6721	633.33	78008	
		0.9987	***1.0001***	***0.9994***	***0.9983***		
Y_3NbO_7	$Fm\bar{3}m$	5.245			144.29	109064	[16]
Y_3TaO_7		5.245			144.29	109057	
		1.000			***1.000***		
$NdNbO_4$	$I12/a1$	5.46272	11.2666	5.14029	315.37	122154	[17]
$NdTaO_4$		5.50402	11.2142	5.10419	313.47	122156	
		0.9925	***1.0047***	***1.0071***	***1.0061***		
$DyNbO_4$	$I12/a1$	5.320	11.000	5.074	295.99	109179	[18]
$DyTaO_4$		5.354	11.063	5.061	298.28	109188	
		0.9936	***0.9943***	***1.0026***	***0.9923***		
$ErNbO_4$	$I12/a1$	5.280	10.916	5.064	290.98	109180	[18]
$ErTaO_4$		5.306	10.893	5.042	289.96	109189	
		0.9951	***1.0021***	***1.0044***	***1.0035***		
$EuNbO_4$	$I12/a1$	5.393	11.133	5.113	306.01	109177	[18]
$EuTaO_4$		5.428	11.103	5.087	305.53	109185	
		0.9936	***1.0027***	***1.0051***	***1.0016***		
$SmNbO_4$	$I12/a1$	5.42064	11.17543	5.11994	309.11	32997	[19]
$SmTaO_4$		5.45879	11.14178	5.09332	308.21	32996	
		0.9930	***1.0030***	***1.0052***	***1.0029***		
$TbNbO_4$	$I12/a1$	5.349	11.036	5.085	299.20	109178	[18]
$TbTaO_4$		5.382	11.022	5.068	299.16	109187	
		0.9939	***1.0013***	***1.0034***	***1.0001***		
$TiNb_2O_7$	$I12/m1$	17.6719	3.8006	11.8924	795.33	251796	[20]
$TiTa_2O_7$		17.6624	3.8012	11.829	790.99	251797	
		1.0005	***0.9998***	***1.0054***	***1.0055***		
$NaNb_3O_8$	$Ibam$	7.2344	10.3100	7.0426	378.62	63203	[21]
$NaTa_3O_8$		7.242	10.462	7.001	379.82	63204	
		0.9990	***0.9855***	***1.0059***	***0.9969***		
$Hf_6Nb_2O_{17}$	$Ima2$	40.90975	4.94531	5.27123	68466.9	403369	[22]
$Hf_6Ta_2O_{17}$		40.83084	4.94345	5.26371	68071.4	403368	
		1.0019	***1.0004***	***1.0014***	***1.0058***		
Li_7NbO_6	$P\bar{1}$	5.3793	5.9194	5.3792	126.94	413371	[23]
Li_7TaO_6		5.38486	5.92014	5.38551	127.21	413372	
		0.9990	***0.9999***	***0.9988***	***0.9979***		
$ScNbO_4$	$P12/a1$	5.101	5.665	4.818	139.17	109191	[18]
$ScTaO_4$		5.118	5.67	4.809	139.49	109192	
		0.9967	***0.9991***	***1.0019***	***0.9977***		
$Eu_5Nb_4O_{15}$	$P\bar{3}m$	5.652		11.428	316.16	166561	[24]
$Eu_5Ta_4O_{15}$		5.652		11.469	317.29	166562	
		1.0000		***0.9964***	***0.9964***		
$CrNbO_4$	$P4_2/mnm$	4.6484		3.0113	65.067	72275	[25]
$CrTaO_4$		4.6445		3.0186	65.115	72276	
		1.0008		***0.9976***	***0.9993***		
$RhNbO_4$	$P4_2/mnm$	4.70186		3.01685	66.695	86826	[26]
$RhTaO_4$		4.6971		3.0303	66.857	86827	
		1.0010		***0.9956***	***0.9976***		
$TiNbO_4$	$P4_2/mnm$	4.743		2.9944	67.362	72277	[25]
$TiTaO_4$		4.709		3.0672	68.014	72278	
		1.0072		***0.9763***	***0.9904***		

Table S1. Continued

Formula	SG	a	b	c	v	ICSD-	Ref.
$MnNb_2O_6$	*Pbcn*	14.4236	5.7609	5.0839	422.44	15856	[27]
$MnTa_2O_6$		14.4219	5.7513	5.0816	421.49	15857	
		1.0001	***1.0017***	***1.0005***	***1.0022***		
$Sb(Sb_{0.5}Nb_{0.5})O_4$	$Pna2_1$	5.514	4.8761	11.7961	317.16	93865	[28]
$Sb(Sb_{0.5}Ta_{0.5})O_4$		5.5019	4.8762	11.8038	316.68	93866	
		1.0022	***1.0000***	***0.9993***	***1.0015***		
$BiNbO_4$	*Pnna*	5.6827	11.717	4.9854	331.95	97422	[29]
$BiTaO_4$		5.6384	11.773	4.9608	329.30	97423	
		1.0079	***0.9952***	***1.0050***	***1.0080***		
$LiNbO_3$	*R3cH*	5.13761		13.8497	316.59	35953	[30]
$LiTaO_3$		5.1459		13.78143	316.04	35954	
		0.9984		***1.0050***	***1.0017***		
$NaNbO_2F_2$	$P2_1/c$	8.0026	5.4072	7.6243	322.81	n. a.	This
$NaTaO_2F_2$		8.09997	5.4391	7.4982	322.96	n. a.	work
		0.988	***0.994***	***1.017***	***0.9995***		

2. Rietveld refinements

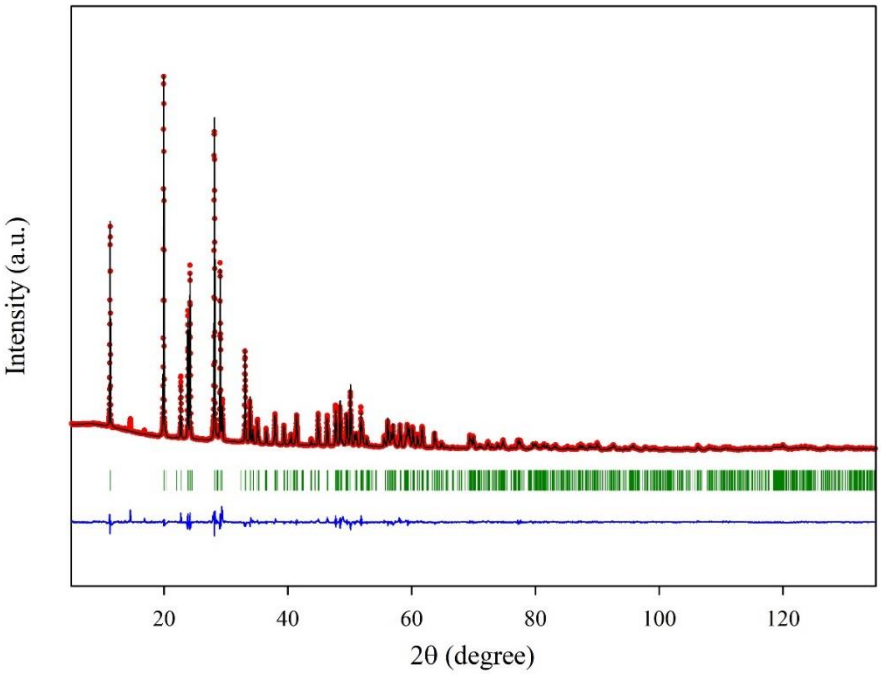


Fig. S1. Observed (red), calculated (black) and difference (blue) diffraction patterns of $NaNbO_2F_2$. The green vertical markers refer to the Bragg positions. The obtained refinement reliability factors are R_p = 10.8%, R_{wp} = 11.4%, R_{exp} = 2.3%, R_B = 6.2% and R_F = 5.2%.

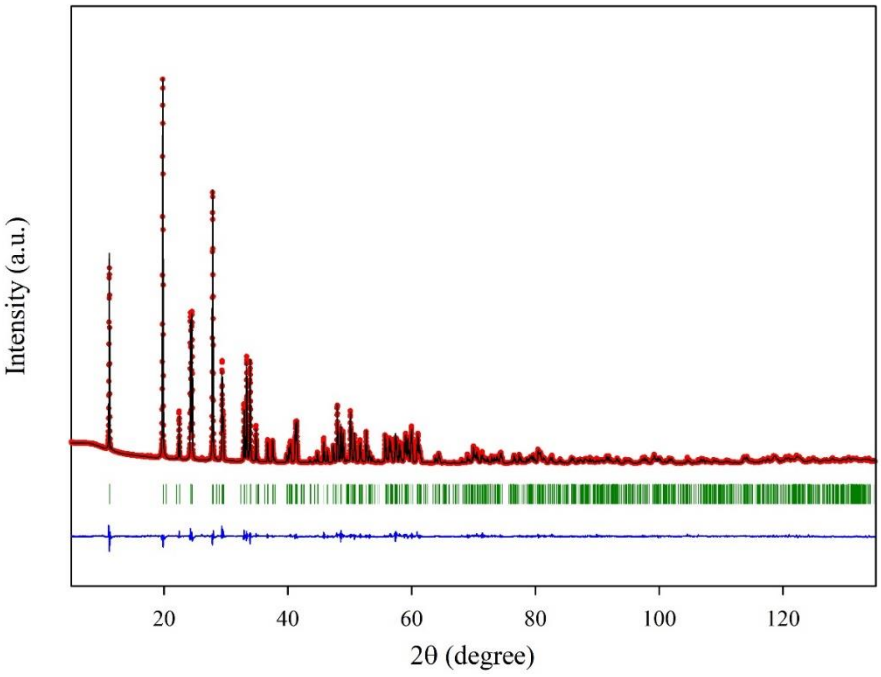


Fig. S2. Observed (red), calculated (black) and difference (blue) diffraction patterns of $NaTaO_2F_2$. The green vertical markers refer to the Bragg positions. The obtained refinement reliability factors are R_p = 9.2%, R_{wp} = 9.2%, R_{exp} = 2%, R_B = 5% and R_F = 5.3%.

3. Structural features

Table S2. Experimental (*x*, *y*, *z*) and APO (*x'*, *y'*, *z'*) fractional atomic coordinates, differences between these fractional atomic coordinates (*x-x'*, *y-y'*, *z-z'*) and atomic displacements in $NaNbO_2F_2$ and $NaTaO_2F_2$.

$NaNbO_2F_2$										
Atom	***x***	***y***	***z***	***x'***	***y'***	***z'***	***x - x'***	***y – y'***	***z – z'***	***d***
Na1	0.3666	0.780	0.116	0.3595	0.7804	0.1196	0.0071	-0.0004	-0.0040	0.070
Nb1	0.1549	0.2644	0.3180	0.1563	0.2685	0.3189	-0.0014	-0.0041	-0.0009	0.025
O1	0.183	0.156	0.071	0.1787	0.1527	0.0564	0.0038	0.0035	0.0145	0.110
O2	0.043	0.544	0.212	0.0414	0.5642	0.2107	0.0011	-0.0203	0.0010	0.110
F1	0.377	0.444	0.314	0.3782	0.4523	0.3131	-0.0013	-0.0083	0.0006	0.047
F2	0.310	0.977	0.378	0.3151	0.9773	0.3806	-0.0047	-0.0007	-0.0023	0.038
$NaTaO_2F_2$										
Atom	***x***	***y***	***z***	***x'***	***y'***	***z'***	***x - x'***	***y – y'***	***z – z'***	***d***
Na1	0.377	0.793	0.109	0.3675	0.7898	0.1102	0.0092	0.0034	-0.0010	0.079
Ta1	0.1581	0.2598	0.2982	0.1590	0.2631	0.2984	-0.0009	-0.0033	-0.0003	0.019
O1	0.199	0.154	0.053	0.1867	0.1590	0.0548	0.0118	-0.0047	-0.0015	0.102
O2	0.037	0.559	0.216	0.0338	0.5556	0.2106	0.0029	0.0036	0.0057	0.048
F1	0.376	0.472	0.304	0.3742	0.4676	0.3131	0.0022	0.0043	-0.0093	0.080
F2	0.330	0.982	0.377	0.3230	0.9842	0.3795	0.0074	-0.0019	-0.0028	0.068

Table S3. X–M–X and X–M–X' angles (M = Nb, Ta; X = O1, O2, F1 and F2, °) and angular distosions α and β (°) in the MO_4F_2 octahedra from the ES and APO models of $NaMO_2F_2$.

$NaMO_2F_2$	M = Nb		M = Ta	
Model	**ES**	**APO**	**ES**	**APO**
F1–M–O1	89.4(6)	90.0	83.2(8)	84.7
F1–M–O2	87.2(7)	85.9	85.0(8)	87.2
F1–M–O1'	81.9(6)	83.2	83.0(8)	86.8
F1–M–O2'	168.1(7)	169.7	177.2(9)	176.6
O1–M–O2	101.5(7)	99.8	94.6(9)	95.8
O1–M–F2	90.3(6)	91.3	86.0(7)	86.2
O1–M–O2'	100.0(7)	99.3	99.3(9)	95.0
O2–M–F2	164.3(7)	164.2	168.0(8)	170.6
O2–M–O1'	88.0(7)	88.1	96.9(8)	94.3
F2–M–O1'	78.8(6)	79.6	79.7(7)	82.4
F2–M–O2'	90.1(7)	92.4	95.8(8)	92.7
O1'–M–O2'	87.5(7)	87.0	94.4(9)	92.8
O1–M–O1'	166.9(7)	169.2	161.1(9)	166.5
O2–M–O2'	98.0(8)	96.8	96.0(9)	96.2
F1–M–F2	82.5(6)	82.9	83.1(8)	83.9
α	**5.4**	**5.2**	**6.4**	**4.6**
β	**13.3**	**12.3**	**11.2**	**8.8**

Table S4. Na–X, Na–X' and Na–X'' bond lengths (X = F1, F2, O1, O2; X' = F1, F2; X'' = F1, F2, Å) and their average in the ES and APO models of $NaMO_2F_2$ (M = Nb, Ta).

$NaMO_2F_2$	M = Nb		M = Ta	
Model	**ES**	**APO**	**ES**	**APO**
Na–F1	2.199(16)	2.256	2.196(22)	2.267
Na–F2	2.251(17)	2.263	2.270(22)	2.254
Na–O1	2.493(19)	2.468	2.421(22)	2.469
Na–O2	3.111(22)	3.011	3.283(28)	3.217
Na–F1'	2.353(19)	2.292	2.277(26)	2.314
Na–F1''	2.759(19)	2.778	2.622(26)	2.600
Na–F2'	2.391(17)	2.348	2.353(24)	2.373
Na–F2''	3.054(17)	3.077	2.897(23)	2.996
<Na-X>	**2.576**	**2.562**	**2.540**	**2.561**

4. ^{19}F MAS NMR spectra and their fits

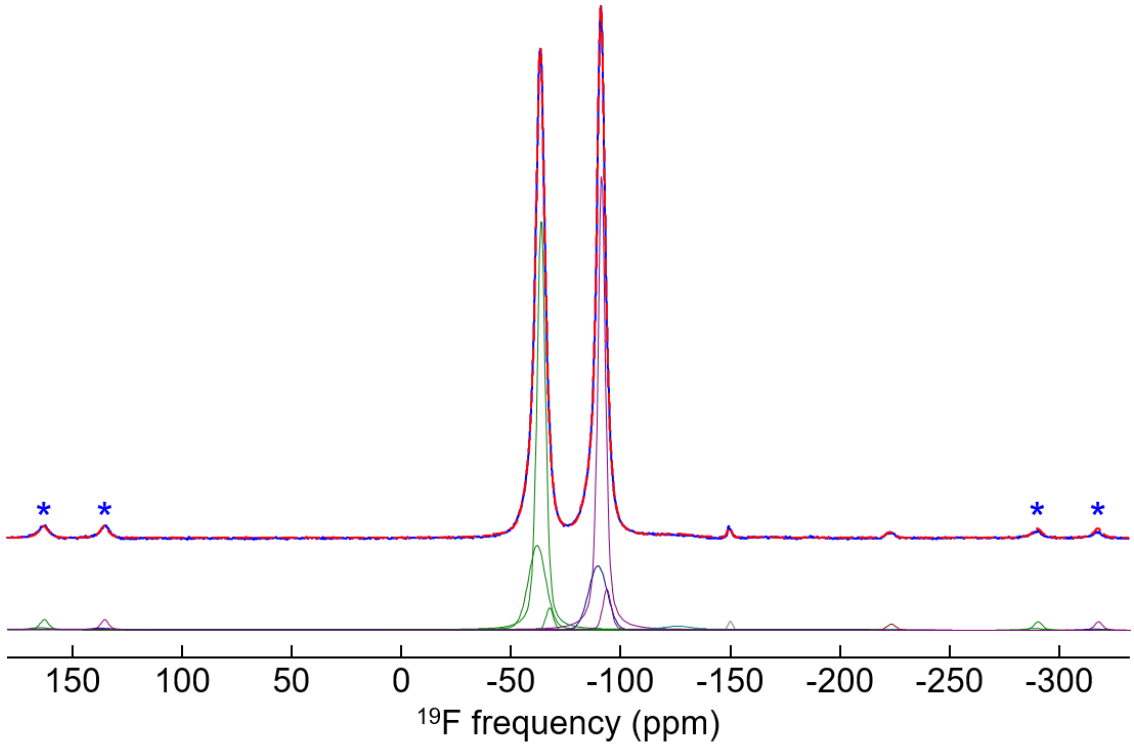


Fig. S3. Experimental (blue) and fitted (dashed red) ^{19}F MAS (64 kHz) NMR spectra of $NaNbO_2F_2$. The individual resonances used for the fit (**Table S5**) are shown below. The stars indicate spinning sidebands.

Table S5. ^{19}F δ_{iso} (ppm), δ_{CSA} (ppm), η_{CSA}, line width (LW, ppm) and relative intensity (I, %) of each individual resonance used to fit the ^{19}F MAS (64 kHz) NMR spectrum of $NaNbO_2F_2$, weighted average ^{19}F δ_{iso} (<δ_{iso}>, ppm), δ_{CSA} (<δ_{CSA}>, ppm), η_{CSA} (<η_{CSA}>), sum of the corresponding relative intensities (ΣI, %) and assignments.

δ_{iso}	δ_{CSA}	η_{CSA}	LW	I	<δ_{iso}>	<δ_{CSA}>	<η_{CSA}>	ΣI	Assignment
-91.0	-125.0	0	4.0	36.0	-90.8	-125.0	0.0	49.0	F1
-89.3	-125.0	0	9.9	9.9					
-93.4	-125.0	0	4.5	3.1					
-63.4	-130.0	0	4.5	34.7	-63.0	-130.0	0.0	49.3	F2
-61.6	-130.0	0	9.3	13.3					
-67.3	-130.0	0	3.9	1.3					
-125.8	0.0	0	16.0	1.0	n. a.	n. a.	n. a.	1.7	Impurities
-149.7	0.0	0	2.4	0.3					
-223.1	0.0	0	4.8	0.4					

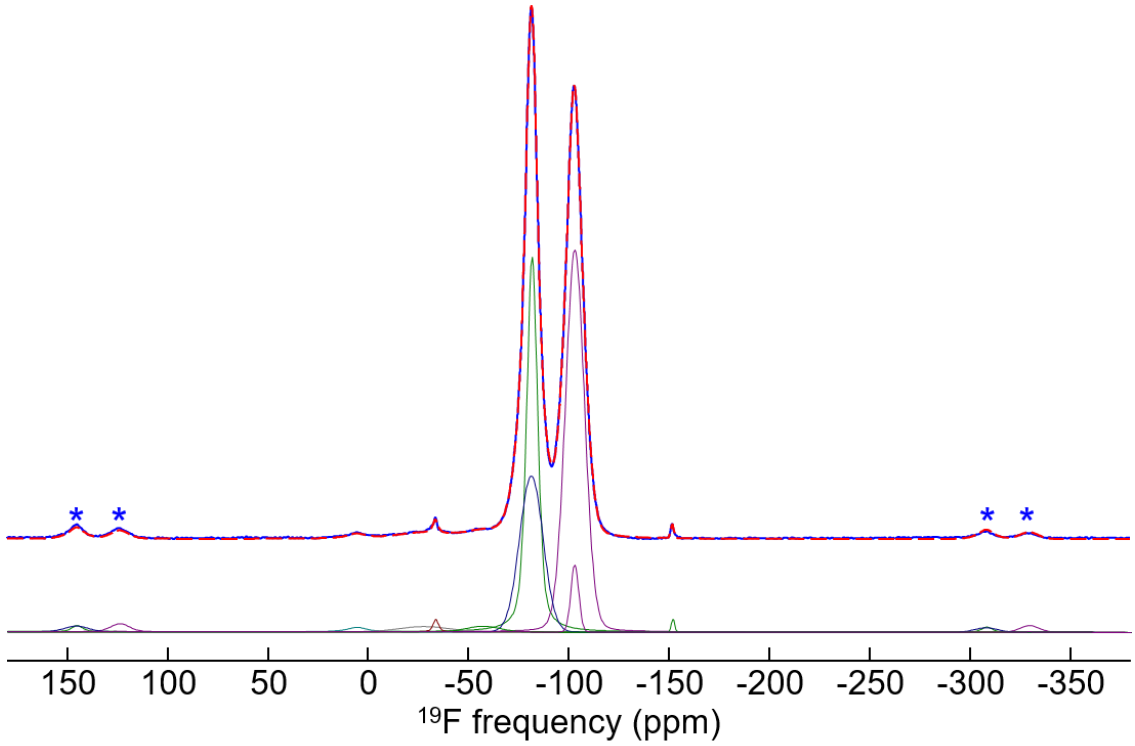


Fig. S4. Experimental (blue) and fitted (dashed red) ^{19}F MAS (64 kHz) NMR spectra of $NaTaO_2F_2$. The individual resonances used for the fit (**Table S6**) are shown below. The stars indicate spinning sidebands.

Table S6. ^{19}F δ_{iso} (ppm), δ_{CSA} (ppm), η_{CSA}, line width (LW, ppm) and relative intensity (I, %) of each individual resonance used to fit the ^{19}F MAS (64 kHz) NMR spectrum of $NaTaO_2F_2$, weighted average ^{19}F δ_{iso} (<δ_{iso}>, ppm), δ_{CSA} (<δ_{CSA}>, ppm), η_{CSA} (<η_{CSA}>), sum of the corresponding relative intensities (ΣI, %) and assignments.

δ_{iso}	δ_{CSA}	η_{CSA}	LW	I	<δ_{iso}>	<δ_{CSA}>	<η_{CSA}>	ΣI	Assignment
-102.8	-120.4	0	11.1	43.2	-102.8	-117.4	0.0	46.2	F1
-102.8	-73.6	0	4.7	3.0					
-81.5	-106.2	0	6.4	28.2	-81.3	-127.2	0.0	49.6	F2
-81.1	-154.9	0	13.7	21.3					
5.7	0.0	0	11.9	0.8	n. a.	n. a.	n. a.	4.2	Impurities
-27.6	0.0	0	29.8	1.6					
-33.6	0.0	0	3.1	0.5					
-151.7	0.0	0	1.9	0.3					
-57.0	0.0	0	19.9	1.1					

5. ^{23}Na and ^{93}Nb NMR spectra and their fits

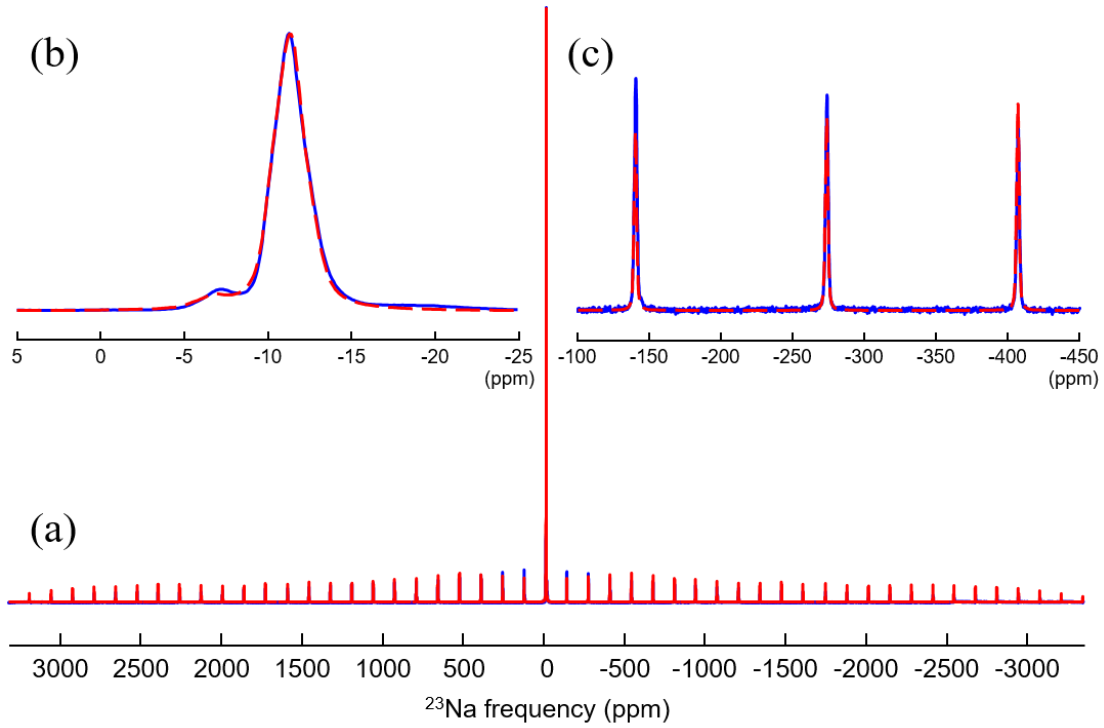


Fig. S5. (a) An overview of the experimental (blue) and fitted (dashed red, **Table S7**) ^{23}Na MAS (30 kHz) NMR spectra of $NaNbO_2F_2$. Enlargements of the (b) central transition (CT) and (c) satellite transitions (ST).

Table S7. ^{23}Na δ_{iso} (ppm), δ_{CSA} (ppm), η_{CSA}, C_Q (MHz) and η_Q of the resonance used to fit the ^{23}Na MAS (30 kHz) NMR spectrum of $NaNbO_2F_2$.

δ_{iso}	δ_{CSA}	η_{CSA}	C_Q	η_Q
-9.8	8.9	0.3	1.6	0.71

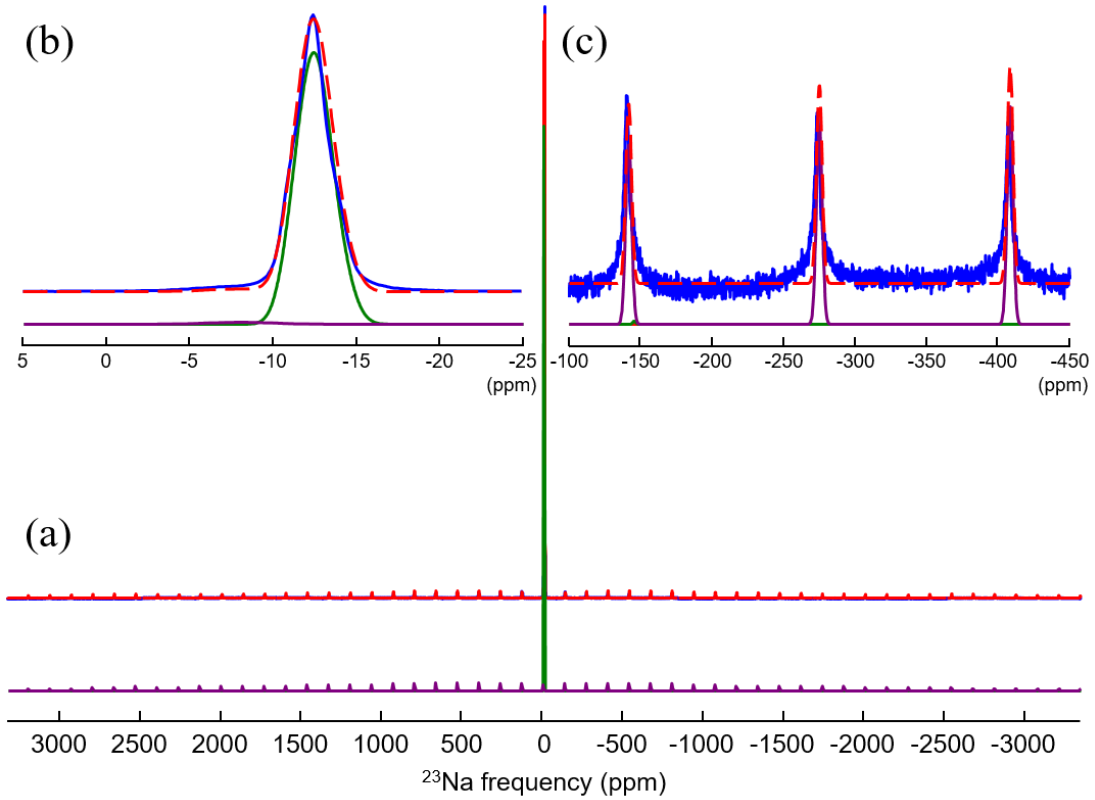


Fig. S6. (a) An overview of the experimental (blue) and fitted (dashed red, **Table S4**) ^{23}Na MAS (30 kHz) NMR spectra of $NaTaO_2F_2$. Enlargements of the (b) central transition (CT) and (c) satellite transitions (ST). The individual resonances used for the fit (**Table S4**) are shown below (green).

Table S8. ^{23}Na δ_{iso} (ppm), δ_{CSA} (ppm), η_{CSA}, C_Q (MHz) and η_Q of the individual resonances used to fit the ^{23}Na MAS (30 kHz) NMR spectrum of $NaTaO_2F_2$, weighted average ^{23}Na δ_{iso} (<δ_{iso}>, ppm), δ_{CSA} (<δ_{CSA}>, ppm), η_{CSA} (<η_{CSA}>), C_Q (<C_Q>, MHz) and η_Q (<η_Q>).

δ_{iso}	δ_{CSA}	η_{CSA}	C_Q	η_Q	I	<δ_{iso}>	<δ_{CSA}>	<η_{CSA}>	<C_Q>	<η_Q>
-10.8	8.5	0	1.74	0.67	56	-11.2	8.5	0.3	1.74	0.67
-11.8	8.5	0	1.74	0.67	44					

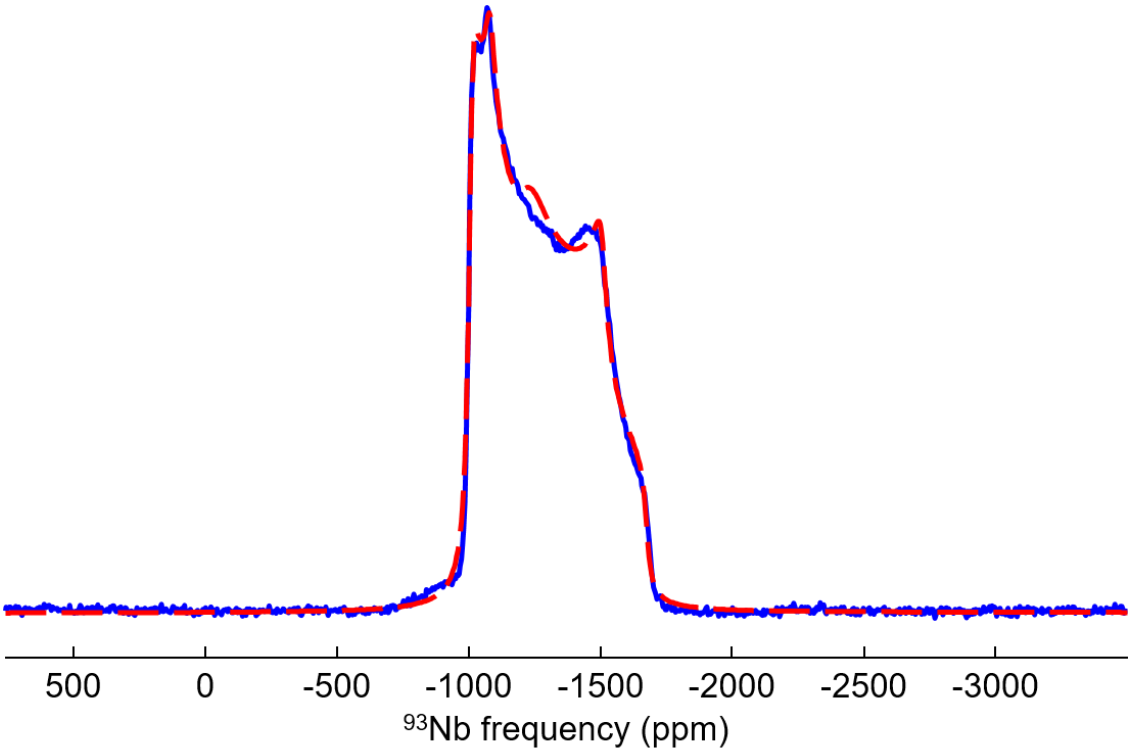


Fig. S7. Experimental (blue) and fitted (dashed red, **Table S9**) ^{93}Nb static NMR spectra of $NaNbO_2F_2$.

Table S9. ^{93}Nb δ_{iso} (ppm), δ_{CSA} (ppm), η_{CSA}, C_Q (MHz) and η_Q of the resonance used to fit the ^{93}Nb static NMR spectrum of $NaNbO_2F_2$.

δ_{iso}	δ_{CSA}	η_{CSA}	C_Q	η_Q
-1206.1	-285.2	0.08	42.04	0.6

6. Thermal and temperature controlled PXRD analysis

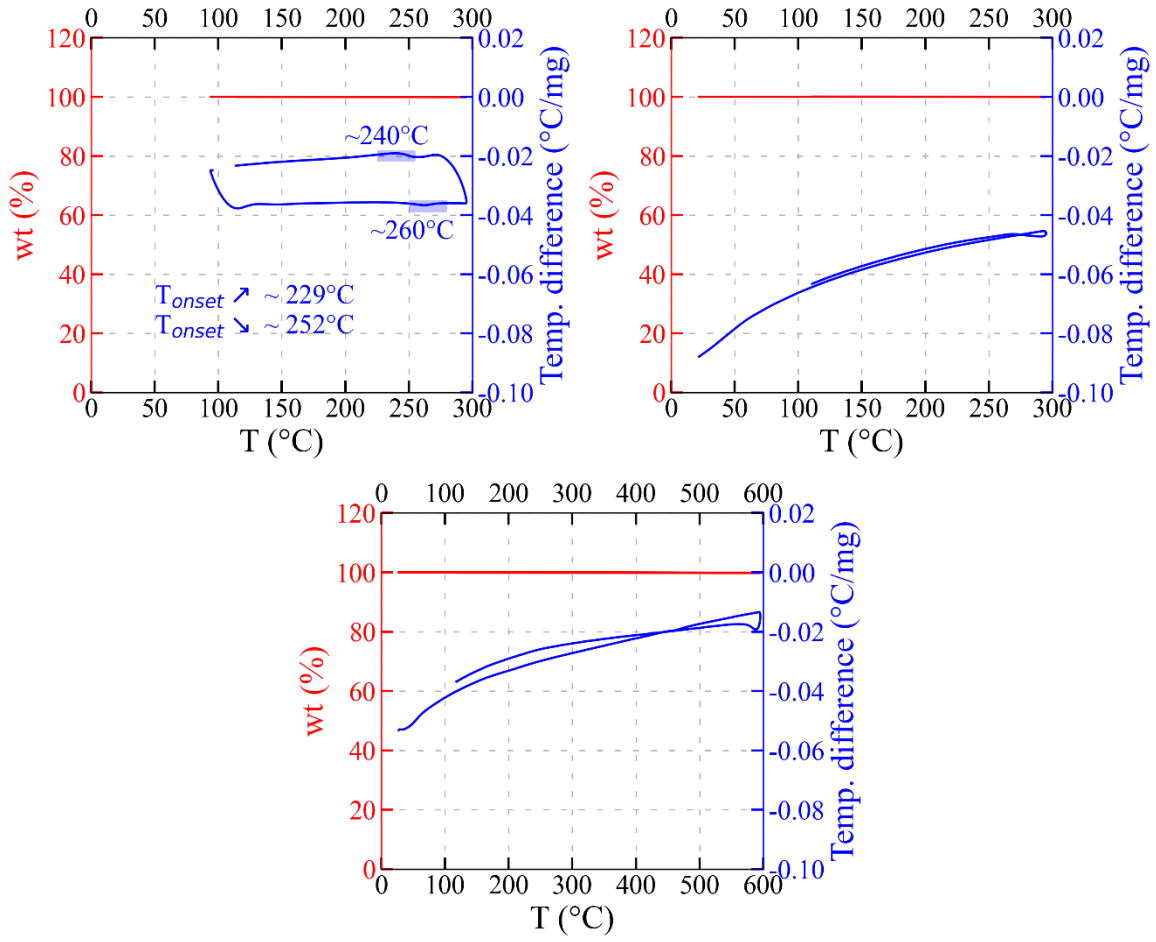


Fig. S8. DTA (blue) and TGA (red) curves of $NaNbO_2F_2$ (top left) and $NaTaO_2F_2$ (top right and bottom) recorded, under argon atmosphere (flow rate of 100 mL.min^{-1}), from RT to 300/600 °C, with heating/cooling rate of 10 °C.min^{-1}. The thermal accidents observed for $NaNbO_2F_2$ are highlighted in blue and their temperature values are indicated.

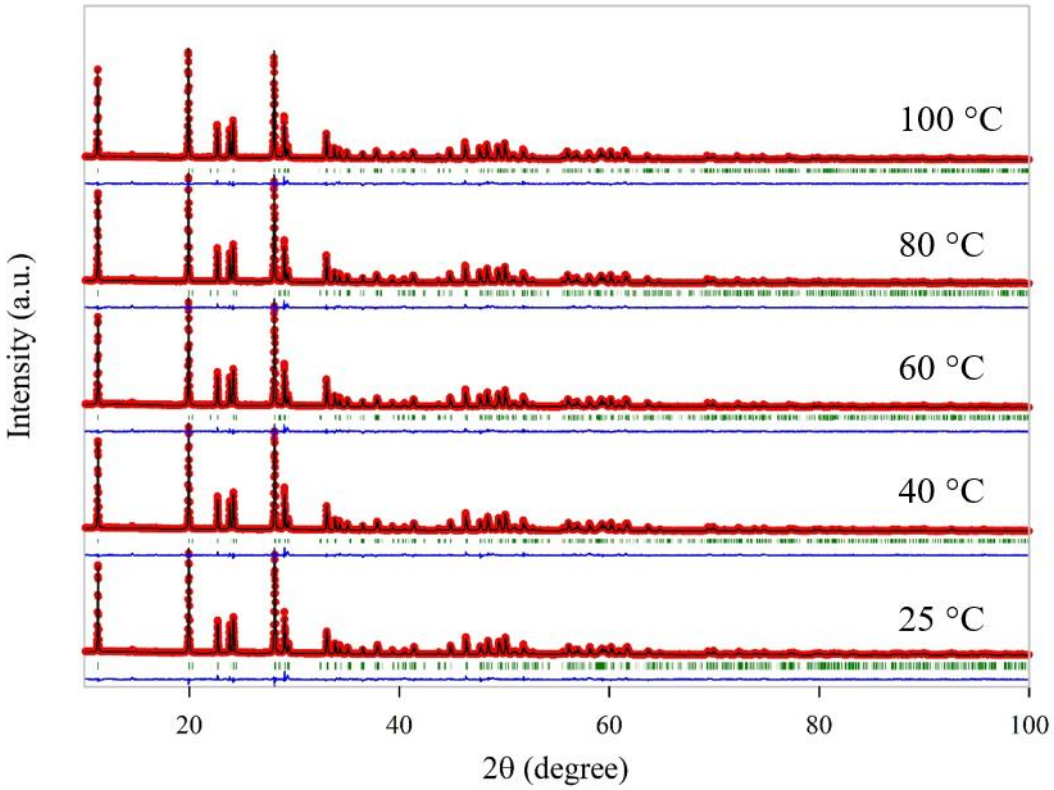


Fig. S9. Observed (red), calculated (black) and difference (blue) temperature-controlled diffraction patterns in the [25–100°C] temperature range of $NaNbO_2F_2$. The green vertical markers refer to the Bragg positions. The obtained refinement reliability factors are given in **Table S10**.

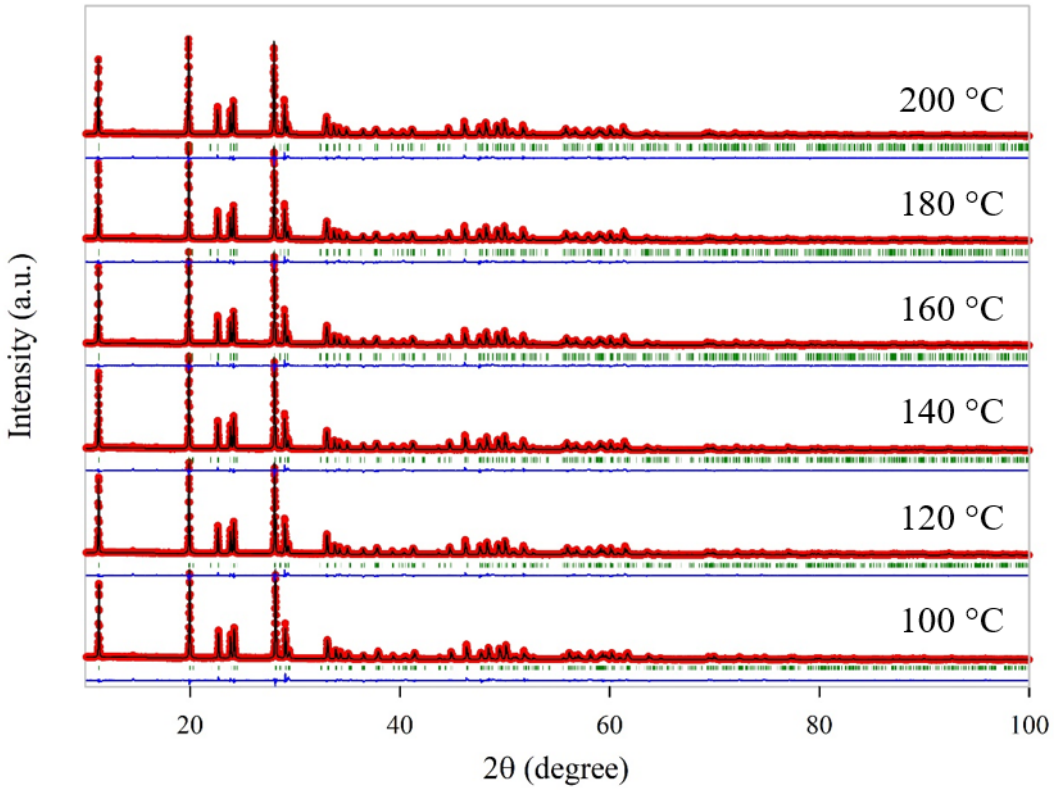


Fig. S10. Observed (red), calculated (black) and difference (blue) temperature-controlled diffraction patterns in the [100–200°C] temperature range of $NaNbO_2F_2$. The green vertical markers refer to the Bragg positions. The obtained refinement reliability factors are given in **Table S10**.

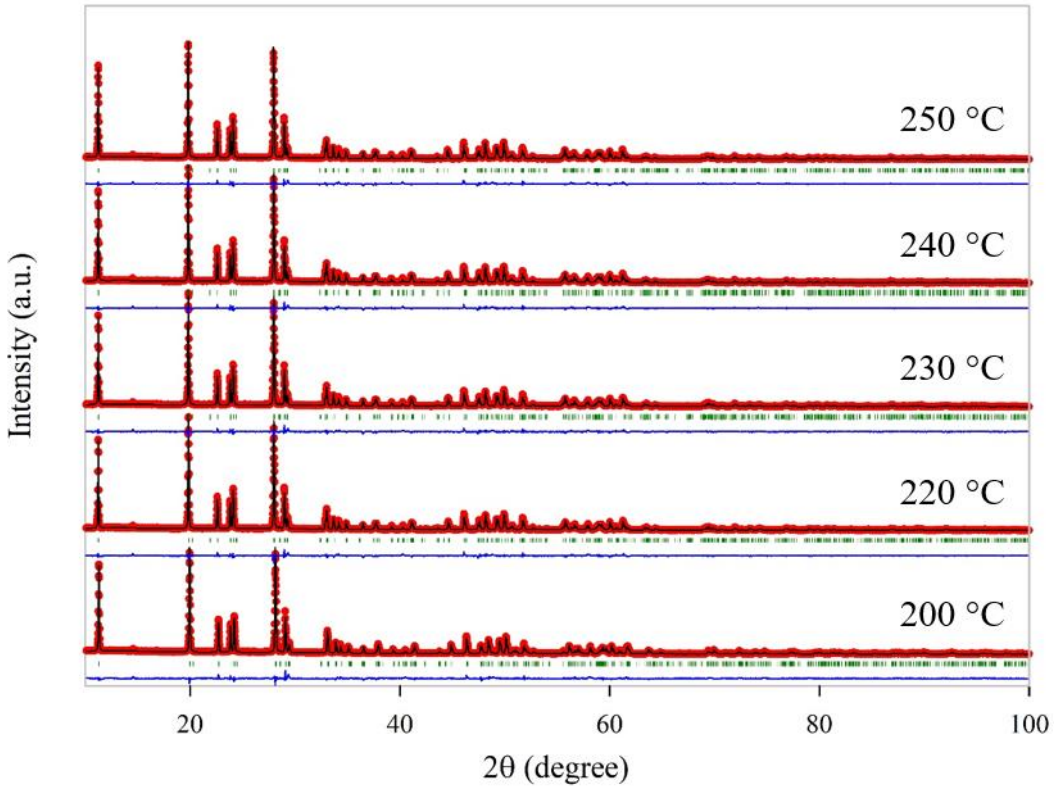


Fig. S11. Observed (red), calculated (black) and difference (blue) temperature-controlled diffraction patterns in the [200–250°C] temperature range of $NaNbO_2F_2$. The green vertical markers refer to the Bragg positions. The obtained refinement reliability factors are given in **Table S10**.

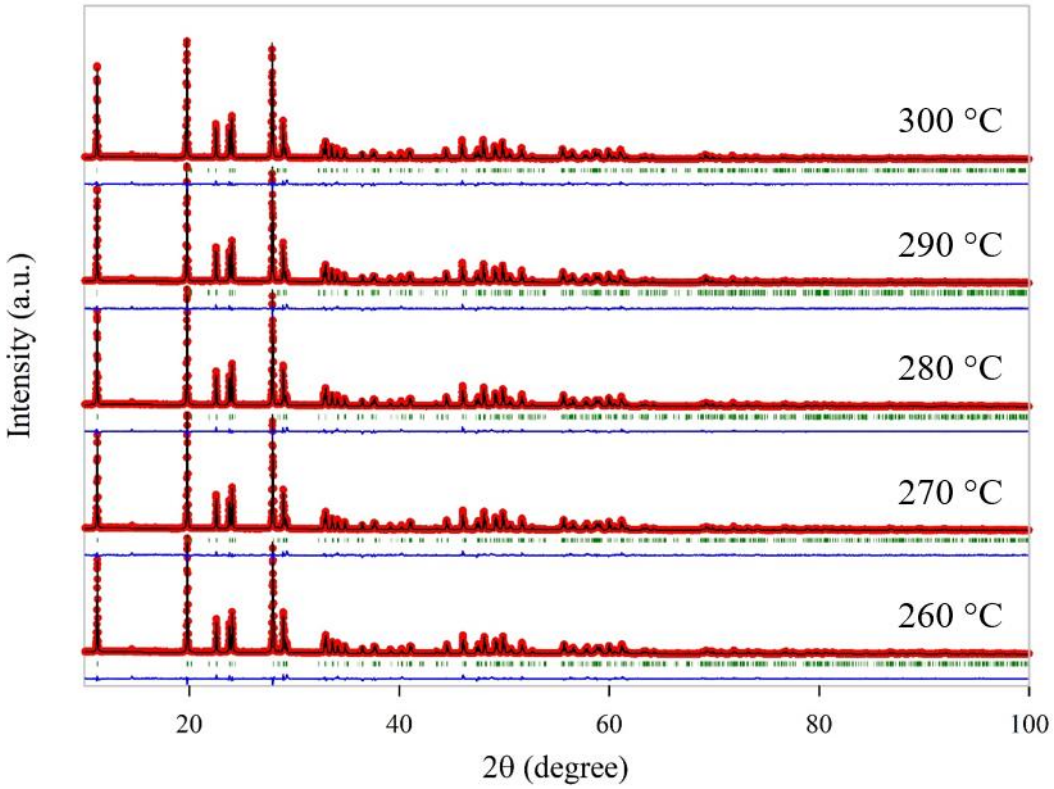


Fig. S12. Observed (red), calculated (black) and difference (blue) temperature-controlled diffraction patterns in the [260–300°C] temperature range of $NaNbO_2F_2$. The green vertical markers refer to the Bragg positions. The obtained refinement reliability factors are given in **Table S10**.

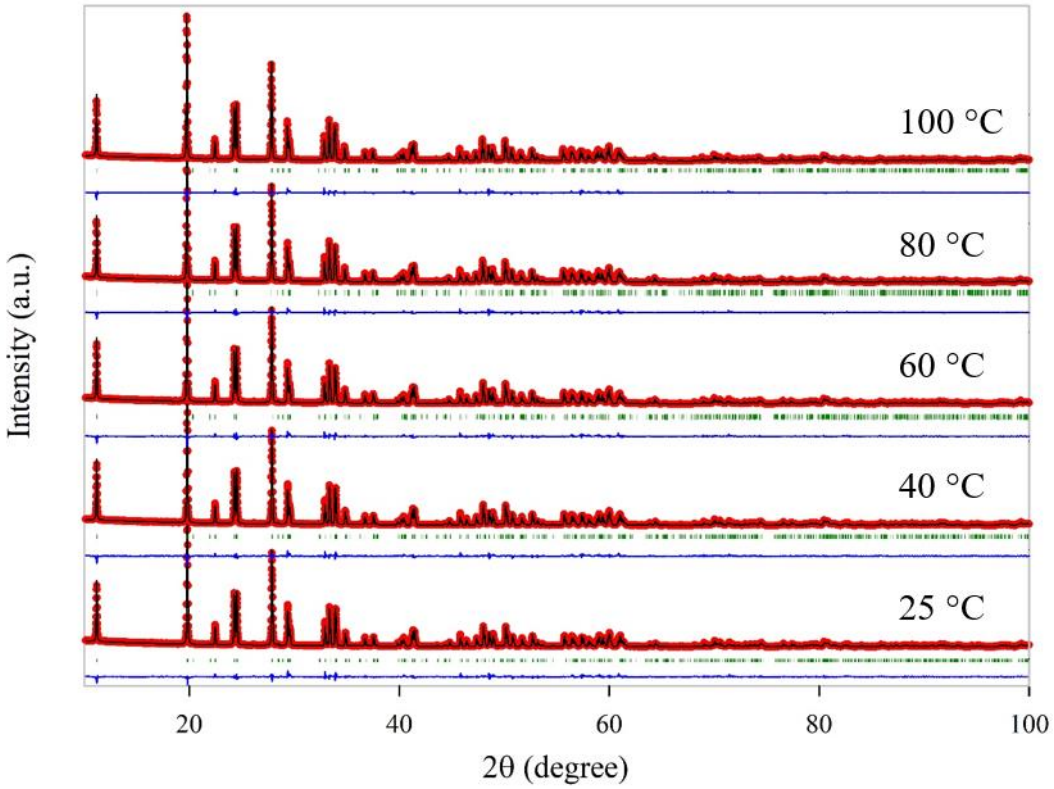


Fig. S13. Observed (red), calculated (black) and difference (blue) temperature-controlled diffraction patterns in the [25–100°C] temperature range of $NaTaO_2F_2$. The green vertical markers refer to the Bragg positions. The obtained refinement reliability factors are given in **Table S11**.

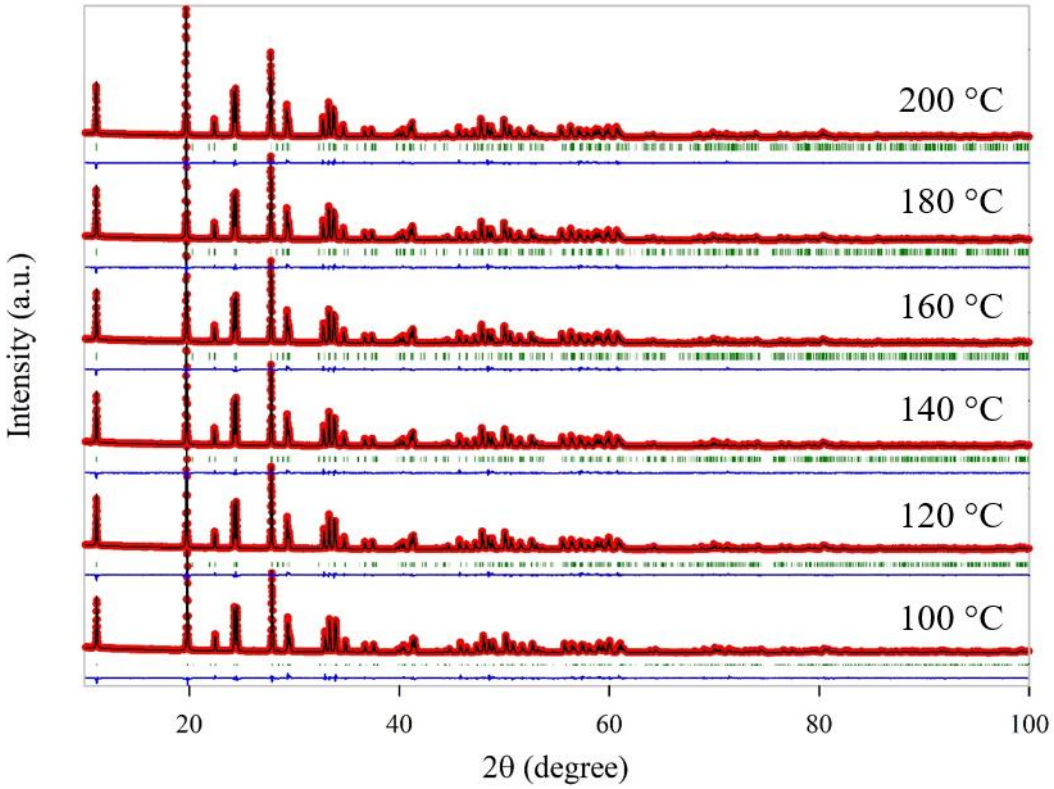


Fig. S14. Observed (red), calculated (black) and difference (blue) temperature-controlled diffraction patterns in the [100–200°C] temperature range of $NaTaO_2F_2$. The green vertical markers refer to the Bragg positions. The obtained refinement reliability factors are given in **Table S11**.

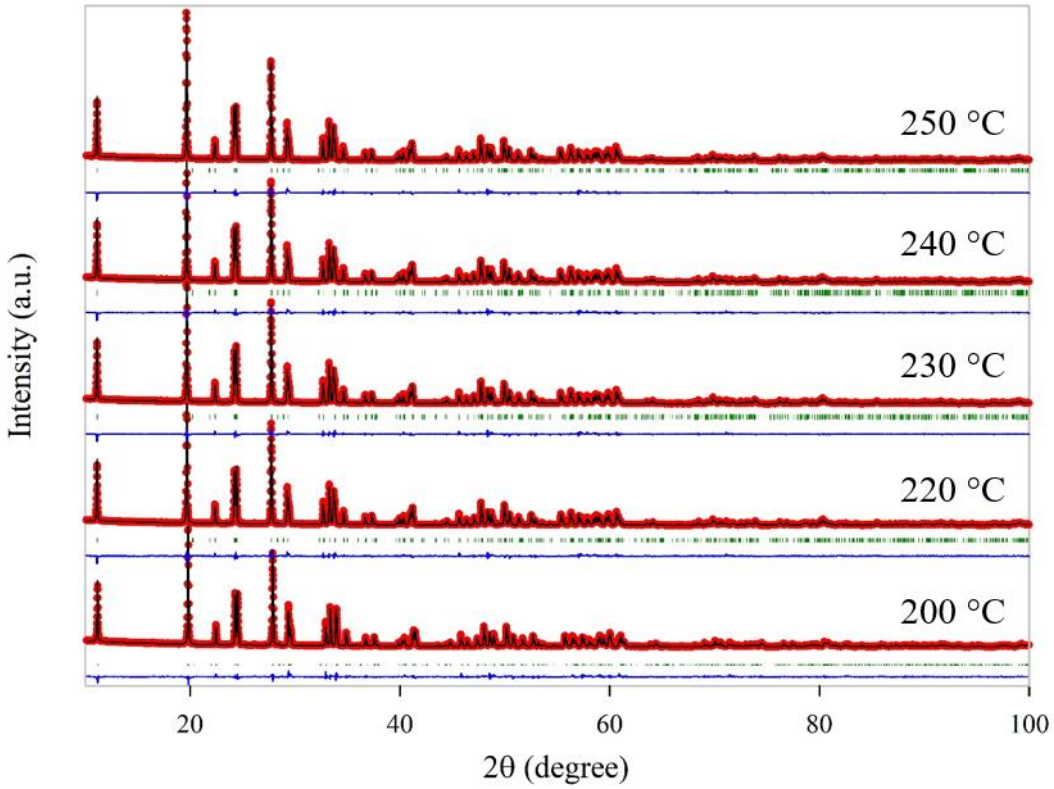


Fig. S15. Observed (red), calculated (black) and difference (blue) temperature-controlled diffraction patterns in the [200–250°C] temperature range of $NaTaO_2F_2$. The green vertical markers refer to the Bragg positions. The obtained refinement reliability factors are given in **Table S11**.

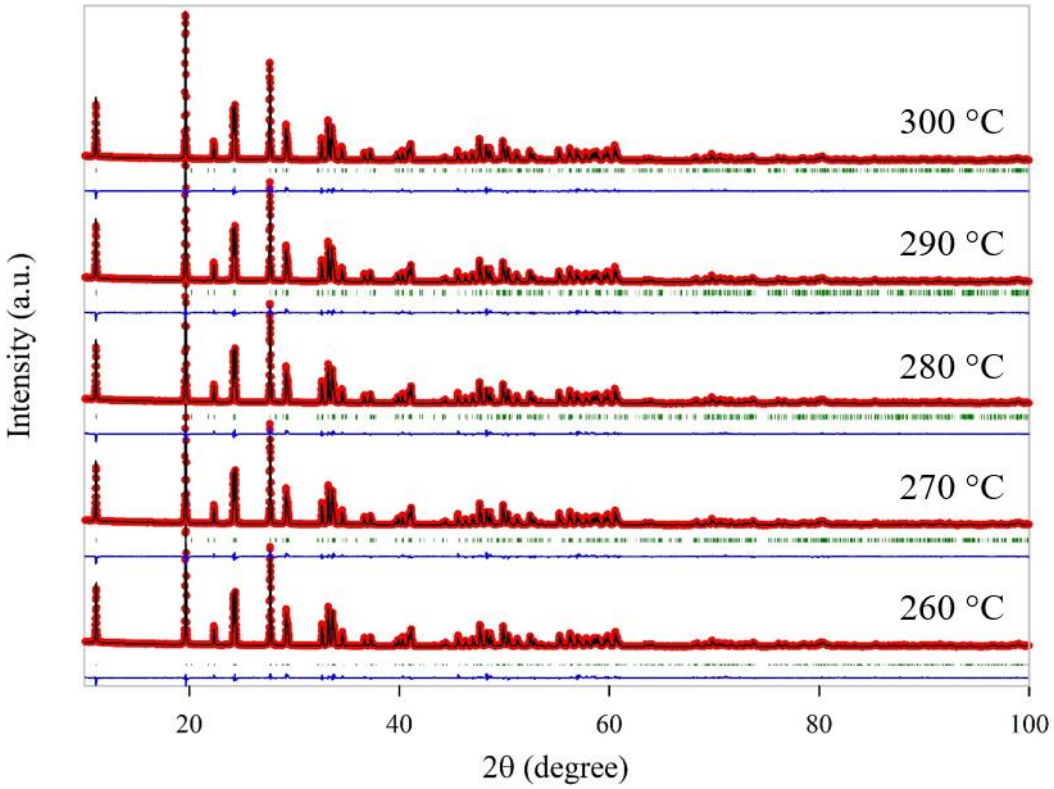


Fig. S16. Observed (red), calculated (black) and difference (blue) temperature-controlled diffraction patterns in the [260–300°C] temperature range of $NaTaO_2F_2$. The green vertical markers refer to the Bragg positions. The obtained refinement reliability factors are given in **Table S11**.

Table S10. Cell parameters and reliability factors of $NaNbO_2F_2$ from Rietveld refinements of the temperature-controlled PXRD data.

***T* (°C)**	**RT**	**40**	**60**	**80**	**100**	**120**	**140**
***a* (Å)**	8.0012(3)	8.0046(3)	8.0097(3)	8.0147(3)	8.0196(3)	8.0245(3)	8.0294(3)
***b* (Å)**	5.4057(3)	5.4080(3)	5.4116(3)	5.4151(2)	5.4186(2)	5.4222(2)	5.4258(3)
***c* (Å)**	7.6223(3)	7.6233(3)	7.6253(3)	7.6271(3)	7.6290(3)	7.6308(3)	7.6327(3)
***β* (°)**	101.922(3)	101.943(3)	101.972(3)	101.999(3)	102.026(3)	102.056(3)	102.087(3)
***V* (Å³)**	322.57(2)	322.86(2)	323.33(2)	323.78(2)	324.24(2)	324.69(2)	325.16(2)
R_{wp} **(%)**	12.4	12.2	12	12	11.7	11.7	11.8
R_p **(%)**	15.3	14.9	14.8	14.8	14.6	14.6	14.6
R_{exp} **(%)**	4.1	4.1	4.1	4.1	4.1	4.1	4
R_B **(%)**	8.7	8	7.9	8.1	8	8	8.1
***T* (°C)**	**160**	**180**	**200**	**220**	**230**	**240**	**250**
***a* (Å)**	8.0346(3)	8.0395(3)	8.0439(3)	8.0479(3)	8.0495(3)	8.0518(3)	8.0544(3)
***b* (Å)**	5.4296(3)	5.4332(3)	5.4365(3)	5.4398(3)	5.4413(3)	5.4431(3)	5.4452(3)
***c* (Å)**	7.6349(3)	7.6370(3)	7.6390(3)	7.6411(3)	7.6424(3)	7.6436(3)	7.6450(3)
***β* (°)**	102.119(3)	102.150(3)	102.180(3)	102.208(3)	102.223(3)	102.239(3)	102.257(3)
***V* (Å³)**	325.64(2)	326.11(2)	326.54(2)	326.95(3)	327.14(3)	327.38(3)	327.66(2)
R_{wp} **(%)**	11.8	12	12	12.2	12.2	12.2	12
R_p **(%)**	14.6	14.7	14.7	15	15	14.9	14.4
R_{exp} **(%)**	4	4	4	4	4.1	4	4
R_B **(%)**	8	8.2	8	8	7.8	7.9	7.8
***T* (°C)**	**260**	**270**	**280**	**290**	**300**		
***a* (Å)**	8.0576(3)	8.0613(3)	8.0655(3)	8.0704(3)	8.0763(3)		
***b* (Å)**	5.4477(2)	5.4505(2)	5.4534(2)	5.4569(2)	5.4608(2)		
***c* (Å)**	7.6464(3)	7.6478(3)	7.6492(3)	7.6506(3)	7.6519(3)		
***β* (°)**	102.277(2)	102.299(2)	102.324(2)	102.351(2)	102.382(2)		
***V* (Å³)**	327.97(2)	328.32(2)	328.69(2)	329.13(2)	329.63(2)		
R_{wp} **(%)**	12.1	12.1	12.2	12.3	12.3		
R_p **(%)**	14.5	14.4	14.3	14.2	14.4		
R_{exp} **(%)**	4	4	4	4	4		
R_B **(%)**	8	8	7.9	8	8.1		

Table S11. Cell parameters and reliability factors of $NaTaO_2F_2$ from Rietveld refinements of the temperature-controlled PXRD data.

***T* (°C)**	**RT**	**40**	**60**	**80**	**100**	**120**	**140**
***a* (Å)**	8.0956(3)	8.0982(3)	8.1019(3)	8.1054(3)	8.1092(3)	8.1131(3)	8.1170(3)
***b* (Å)**	5.4366(2)	5.4392(2)	5.4429(2)	5.4466(2)	5.4503(2)	5.4541(2)	5.4580(2)
***c* (Å)**	7.4942(2)	7.4959(2)	7.4984(2)	7.5009(2)	7.5034(2)	7.5060(2)	7.5088(2)
***β* (°)**	102.132(2)	102.151(2)	102.178(2)	102.204(2)	102.230(2)	102.256(2)	102.282(2)
***V* (Å³)**	322.47(2)	322.78(2)	323.22(2)	323.66(2)	324.11(2)	324.57(2)	325.04(2)
R_{wp} **(%)**	11.6	11.4	11.3	11.1	11	11	10.9
R_p **(%)**	11.1	11	10.8	10.6	10.5	10.5	10.4
R_{exp} **(%)**	3	3	3	3	3	3	3
R_B **(%)**	6.5	6.3	6.1	6.1	5.9	6	6
***T* (°C)**	**160**	**180**	**200**	**220**	**230**	**240**	**250**
***a* (Å)**	8.1210(3)	8.1251(3)	8.1292(2)	8.1335(2)	8.1356(2)	8.1378(2)	8.1398(2)
***b* (Å)**	5.4618(2)	5.4658(2)	5.4698(2)	5.4740(2)	5.4761(2)	5.4781(2)	5.4801(2)
***c* (Å)**	7.5115(2)	7.5142(2)	7.5171(2)	7.5201(2)	7.5216(2)	7.5231(2)	7.5247(2)
***β* (°)**	102.309(2)	102.337(2)	102.365(2)	102.393(2)	102.408(2)	102.422(2)	102.436(2)
***V* (Å³)**	325.52(2)	326.00(2)	326.49(2)	327.01(2)	327.27(2)	327.53(2)	327.78(2)
R_{wp} **(%)**	11	10.8	10.5	10.5	10.5	10.6	10.6
R_p **(%)**	10.4	10.2	10	10	10	10.1	10.2
R_{exp} **(%)**	3	3	3	3	3	3	3
R_B **(%)**	6.2	5.9	5.7	5.6	5.6	5.7	6.1
***T* (°C)**	**260**	**270**	**280**	**290**	**300**		
***a* (Å)**	8.1420(2)	8.1443(2)	8.1463(2)	8.1486(2)	8.1505(2)		
***b* (Å)**	5.4823(2)	5.4845(2)	5.4865(2)	5.4886(2)	5.4907(2)		
***c* (Å)**	7.5263(2)	7.5279(2)	7.5293(2)	7.5309(2)	7.5323(2)		
***β* (°)**	102.451(2)	102.466(2)	102.480(2)	102.495(2)	102.510(2)		
***V* (Å³)**	328.05(2)	328.33(2)	328.57(2)	328.84(2)	329.09(2)		
R_{wp} **(%)**	10.6	10.8	10.7	10.5	10.5		
R_p **(%)**	10.2	10.4	10.2	10.1	10.1		
R_{exp} **(%)**	3	3	3	3	3		
R_B **(%)**	6.2	6	6.3	6	6.1		

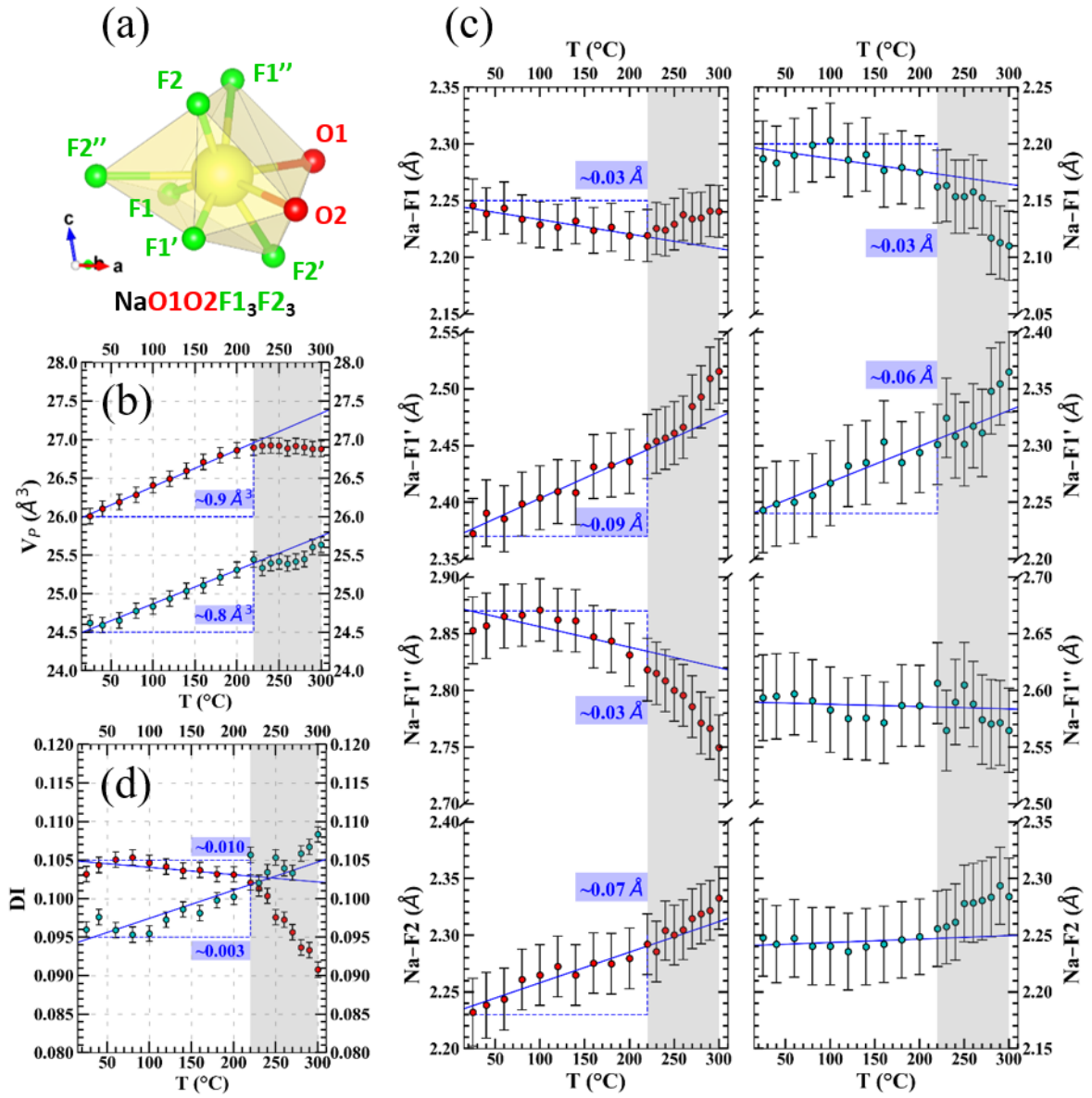


Fig. S17. Perspective view of Na^+ polyhedron (a), in which, atoms labeled X, X' and X'' (X = F1 and F2) are equivalent by symmetry operations. Temperature dependence of Na^+ polyhedron volume (b), bond lengths (c) and distortion index (d) of $NaNbO_2F_2$ (red dots) and $NaTaO_2F_2$ (blue dots). Linear regressions (blue lines) are plotted in the [25–220°C] temperature range guiding the variation of each quantity. The amplitudes of significant variations are given and highlighted in blue.

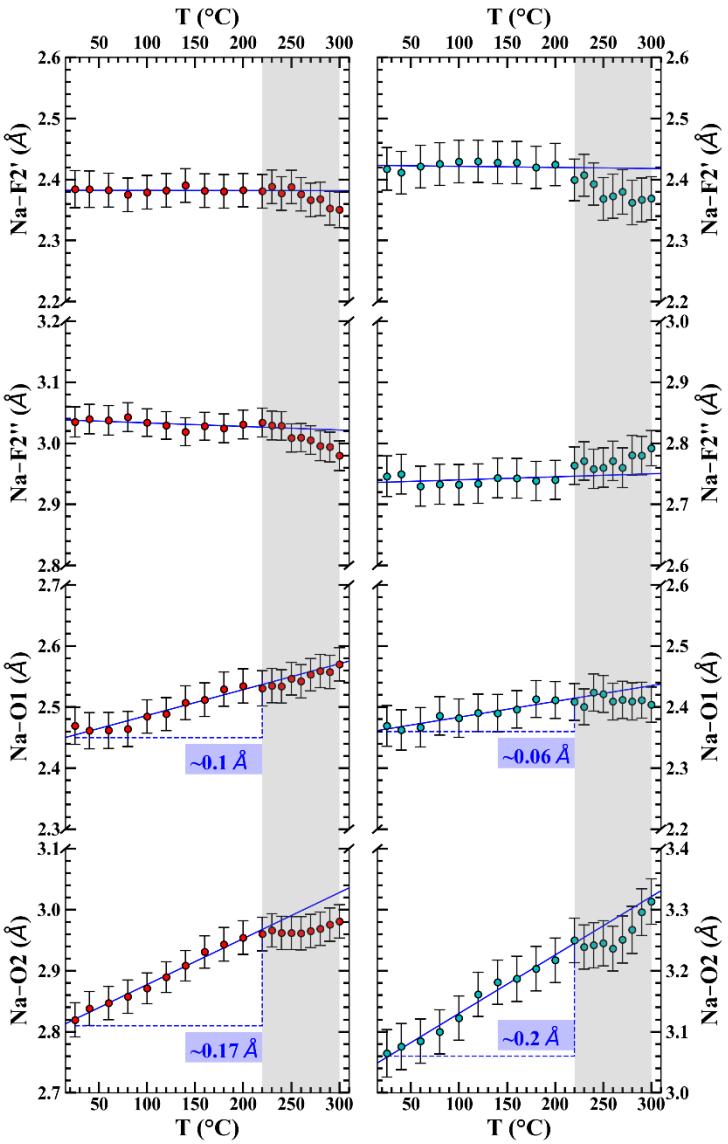


Fig. S18. Temperature dependence of Na^+ polyhedra bond lengths from $NaNbO_2F_2$ (left) and $NaTaO_2F_2$ (right). X, X' and X'' (X = F1 and F2) are atoms equivalent by symmetry operations. Linear regressions (blue lines) are plotted in the [25–220°C] temperature range guiding the variation of each quantity. The amplitudes of significant variations are indicated and highlighted in blue.

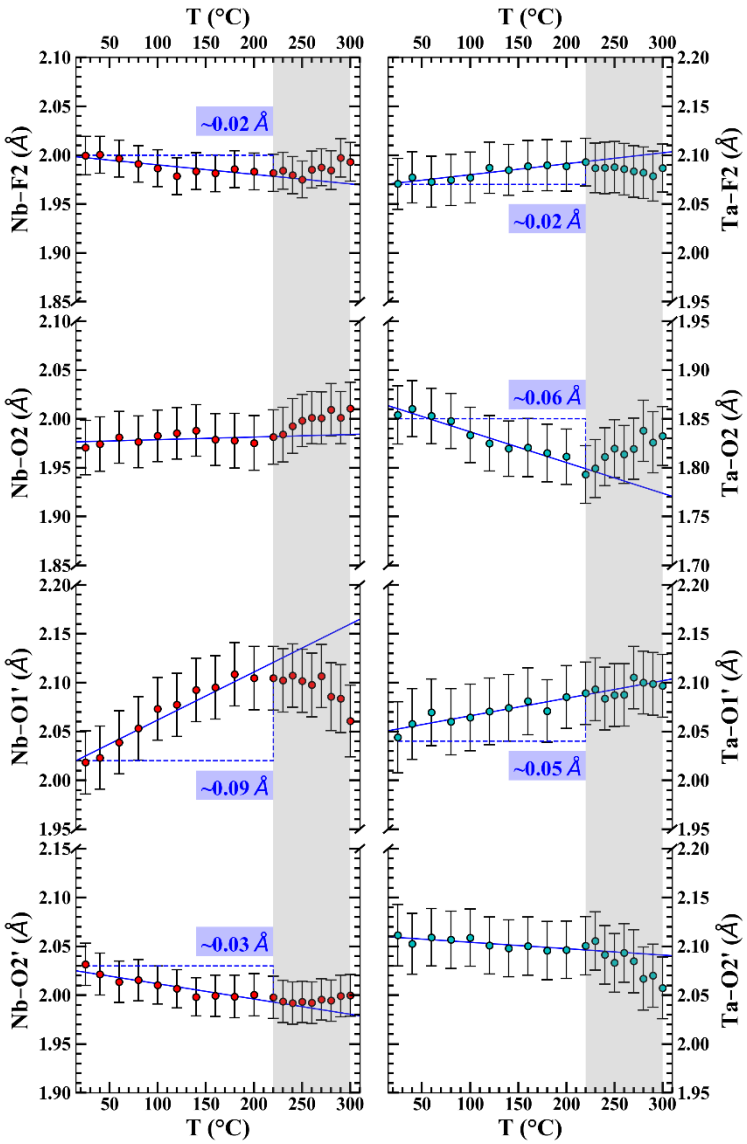


Fig. S19. Temperature dependence of MO_4F_2 octahedra bond lengths from $NaNbO_2F_2$ (left) and $NaTaO_2F_2$ (right). X and X' (X = O1 and O2) are atoms equivalent by symmetry operations. Linear regressions (blue lines) are plotted in the [25–220°C] temperature range guiding the variation of each quantity. The amplitudes of significant variations are indicated and highlighted in blue.

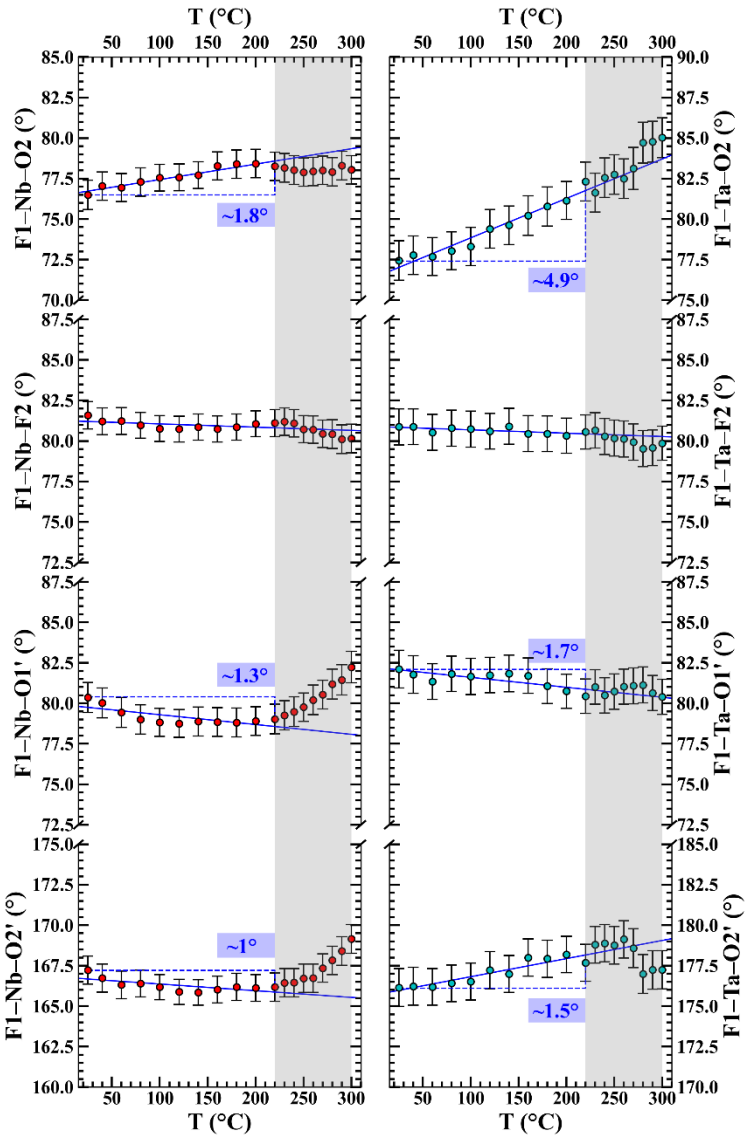


Fig. S20. Temperature dependence of MO_4F_2 octahedra angles from $NaNbO_2F_2$ (left) and $NaTaO_2F_2$ (right). X and X' (X = O1 and O2) are atoms equivalent by symmetry operations. Linear regressions (blue lines) are plotted in the [25–220°C] temperature range guiding the variation of each quantity. The amplitudes of significant variations are indicated and highlighted in blue.

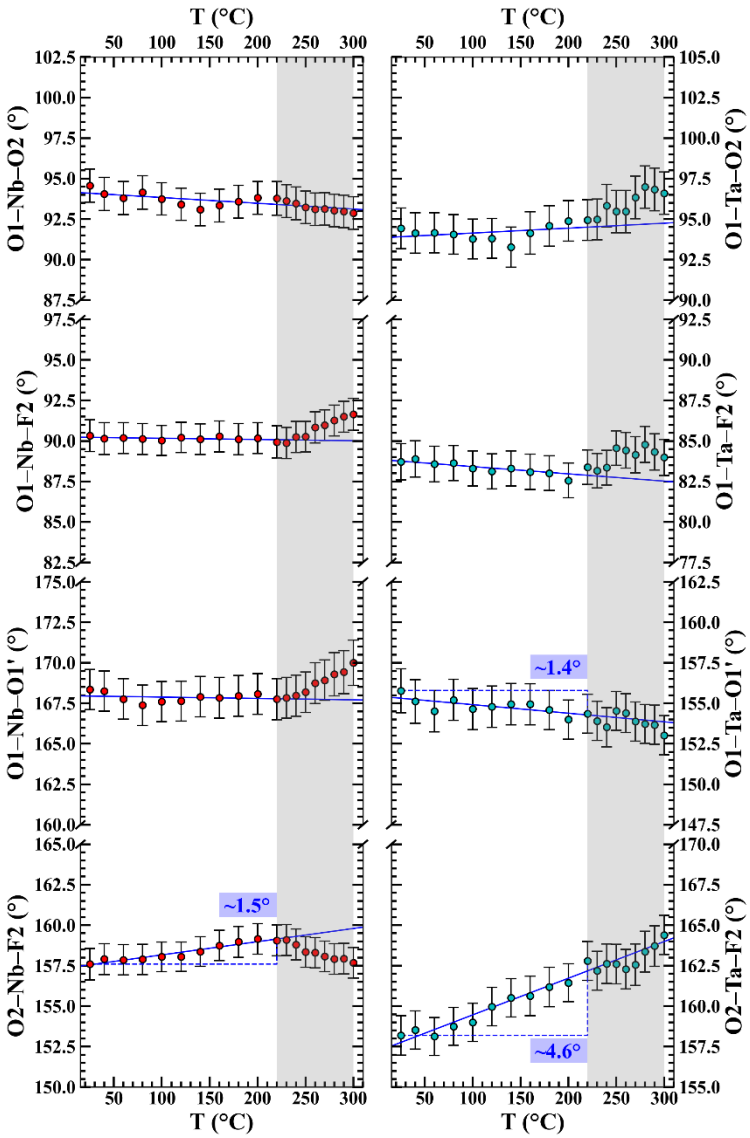


Fig. S21. Temperature dependence of MO_4F_2 octahedra angles from $NaNbO_2F_2$ (left (b)) and $NaTaO_2F_2$ (right (b)). X and X' (X = O1 and O2) are atoms equivalent by symmetry operations. Linear regressions (blue lines) are plotted in the [25–220°C] temperature range guiding the variation of each quantity. The amplitudes of significant variations are indicated and highlighted in blue.

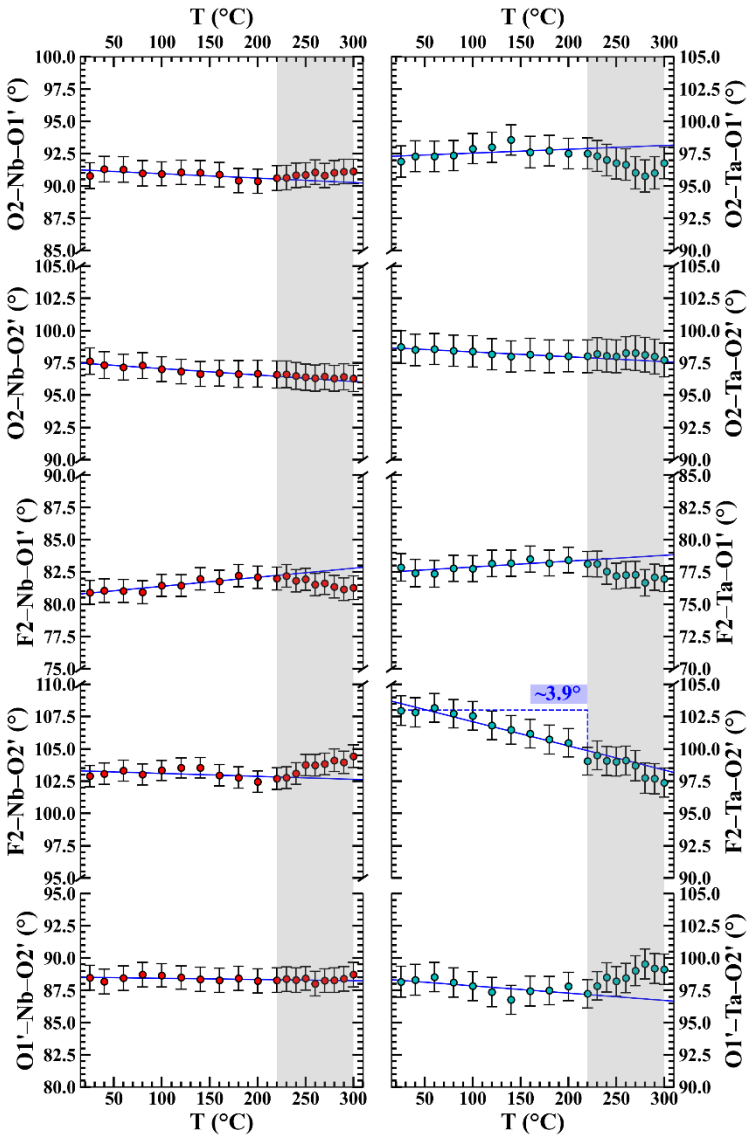


Fig. S22. Temperature dependence of MO_4F_2 octahedra angles from $NaNbO_2F_2$ (left) and $NaTaO_2F_2$ (right). X and X' (X = O1 and O2) are atoms equivalent by symmetry operations. Linear regressions (blue lines) are plotted in the [25–220°C] temperature range guiding the variation of each quantity. The amplitudes of significant variations are indicated and highlighted in blue.

7. References

[1] D. Zagorac, H. Müller, S. Ruehl, J. Zagorac, S. Rehme, Recent developments in the Inorganic Crystal Structure Database: theoretical crystal structure data and related features, J Appl Crystallogr. 52 (2019) 918–925. https://doi.org/10.1107/S160057671900997X.

[2] J. Köhler, A. Simon, L. Van Wüllen, S. Cordier, T. Roisnel, M. Poulain, M. Somer, Structures and Properties of $NbOF_3$ and $TaOF_3$ — With a Remark to the O/F Ordering in the SnF_4 Type Structure., Z. Anorg. Allg. Chem. 628 (2002) 2683–2690. https://doi.org/10.1002/1521-3749(200212)628:12<2683::AID-ZAAC2683>3.0.CO;2-E.

[3] O. Zakary, M. Body, T. Charpentier, V. Sarou-Kanian, C. Legein, Structural Modeling of O/F Correlated Disorder in $TaOF_3$ and $NbOF_{3-x}(OH)_x$ by Coupling Solid-State NMR and DFT Calculations, Inorg. Chem. 62 (2023) 16627–16640. https://doi.org/10.1021/acs.inorgchem.3c02844.

[4] J. Dabachi, M. Body, C. Galven, F. Boucher, C. Legein, Preparation-Dependent Composition and O/F Ordering in NbO_2F and TaO_2F, Inorganic Chemistry. 56 (2017) 5219–5232. https://doi.org/10.1021/acs.inorgchem.7b00355.

[5] S.N. Britvin, O.I. Siidra, A. Lotnyk, S.V. Krivovichev, W. Depmeier, Niobate and Tantalate Pyrochlores: Soft Synthesis by the Fluoride Route, Eur. J. Inorg. Chem. 2010 (2010) 1082–1088. https://doi.org/10.1002/ejic.200900999.

[6] B. Scheibe, A.J. Karttunen, F. Weigend, F. Kraus, Photochemistry with Chlorine Trifluoride: Syntheses and Characterization of Difluorooxychloronium(V) Hexafluorido(non)metallates(V), $[ClOF_2][MF_6]$ (M=V, Nb, Ta, Ru, Os, Ir, P, Sb), Chemistry A European J. 27 (2021) 2381–2392. https://doi.org/10.1002/chem.202003629.

[7] F. Le Berre, M.-P. Crosnier-Lopez, C. Galven, J.-L. Fourquet, C. Legein, M. Body, J.-Y. Buzaré, Ca^{2+}/vacancies and O^{2-}/F^- ordering in new oxyfluoride pyrochlores $Li_{2x}Ca_{1.5-x}\square_{0.5-x}M_2O_6F$ (M = Nb,Ta) for $0 \leq x \leq 0.5$, Dalton Trans. (2007) 2457–2466. https://doi.org/10.1039/B701863K.

[8] I.D. Brown, R.J. Gillespie, K.R. Morgan, J.F. Sawyer, K.J. Schmidt, Z. Tun, P.K. Ummat, J.E. Vekris, Preparation and crystal structure of $Hg_3(NbF_5)_2SO_4$, $Hg_3(TaF_5)_2SO_4$, and $Hg_4(Ta_2F_{11})_2$, Inorg. Chem. 26 (1987) 689–693. https://doi.org/10.1021/ic00252a012.

[9] T. Phraewphiphat, M. Iqbal, K. Suzuki, M. Hirayama, R. Kanno, Synthesis and Lithium-Ion Conductivity of $LiSrB_2O_6F$ (B = Nb^{5+}, Ta^{5+}) with a Pyrochlore Structure, J. Jpn. Soc. Powder Powder Metallurgy. 65 (2018) 26–33. https://doi.org/10.2497/jjspm.65.26.

[10] E. Boivin, F. Pourpoint, S. Saitzek, P. Simon, P. Roussel, H. Kabbour, An unusual O^{2-}/F^- distribution in the new pyrochlore oxyfluorides: $Na_2B_2O_5F_2$ (B = Nb, Ta), Chem. Commun. 58 (2022) 2391–2394. https://doi.org/10.1039/D1CC06760E.

[11] Z. Tun, D. Brown, P.K. Ummat, The room-temperature structures of mercury niobium fluoride, $Hg_{3-\delta}NbF_6$, and mercury tantalum fluoride, $Hg_{3-\delta}TaF_6$, Acta Crystallogr C Cryst Struct Commun. 40 (1984) 1301–1303. https://doi.org/10.1107/S0108270184007733.

[12] A.J. Lloyd, E.B. Masterson, S.J. Baxter, J.J. Molaison, A.M. Dos Santos, A.P. Wilkinson, Thermal Expansion and Response to Pressure of Double-ReO_3-Type Fluorides NaM^VF_6 (M = Nb, Ta), Inorg. Chem. 59 (2020) 13979–13987. https://doi.org/10.1021/acs.inorgchem.0c01693.

[13] O. Graudejus, A.P. Wilkinson, L.C. Chacón, N. Bartlett, M–F Interatomic Distances and Effective Volumes of Second and Third Transition Series MF_6^- and MF_6^{2-} Anions, Inorg. Chem. 39 (2000) 2794–2800. https://doi.org/10.1021/ic000041w.

[14] Y. Hinatsu, Y. Doi, M. Wakeshima, Magnetic Studies on Eu_3MO_7 (M = Nb, Ta, Ir) with Fluorite-related Structure by ^{151}Eu Mössbauer Spectroscopy and Magnetic Susceptibility Measurements, Journal of Solid State Chemistry. 262 (2018) 224–228. https://doi.org/10.1016/j.jssc.2018.03.024.

[15] J.F. Vente, R.B. Helmholdt, D.J.W. IJdo, The Structure and Magnetic Properties of Pr_3MO_7 with M = Nb, Ta, and Sb, Journal of Solid State Chemistry. 108 (1994) 18–23. https://doi.org/10.1006/jssc.1994.1003.

[16] H.P. Rooksby, E.A.D. White, Rare-Earth Niobates and TantaIates of Defect Fluorite- and Weberite-Type Structures, Journal of the American Ceramic Society. 47 (1964) 94–96. https://doi.org/10.1111/j.1151-2916.1964.tb15663.x.

[17] M. Saura-Múzquiz, B.G. Mullens, H.E. Maynard-Casely, B.J. Kennedy, Neutron diffraction study of the monoclinic – tetragonal phase transition in $NdNbO_4$ and $NdTaO_4$, Dalton Trans. 50 (2021) 11485–11497. https://doi.org/10.1039/D1DT01981C.

[18] C. Keller, Über ternäre Oxide des Niobs und Tantals vom Typ ABO_4, Zeitschrift Anorg Allge Chemie. 318 (1962) 89–106. https://doi.org/10.1002/zaac.19623180108.

[19] B.G. Mullens, M. Avdeev, H.E.A. Brand, S. Mondal, G. Vaitheeswaran, B.J. Kennedy, Insights into the structural variations in $SmNb_{1-x}Ta_xO_4$ and $HoNb_{1-x}Ta_xO_4$ combined experimental and computational studies, Dalton Trans. 50 (2021) 9103–9117. https://doi.org/10.1039/D1DT01051D.

[20] L. Perfler, V. Kahlenberg, C. Wikete, D. Schmidmair, M. Tribus, R. Kaindl, Nanoindentation, High-Temperature Behavior, and Crystallographic/Spectroscopic Characterization of the High-Refractive-Index Materials $TiTa_2O_7$ and $TiNb_2O_7$, Inorg. Chem. 54 (2015) 6836–6848. https://doi.org/10.1021/acs.inorgchem.5b00733.

[21] K. Range, M. Wildenauer, A.M. Heyns, Extrem kurze nichtbindende Sauerstoff-Sauerstoff-Abstände: Die Kristallstrukturen von $NbBO_4$, $NaNb_3O_8$ und $NaTa_3O_8$, Angewandte Chemie. 100 (1988) 973–975. https://doi.org/10.1002/ange.19881000721.

[22] S.J. McCormack, W.M. Kriven, Crystal structure solution for the $A_6B_2O_{17}$ (A = Zr, Hf ; B = Nb, Ta) superstructure, Acta Crystallogr B Struct Sci Cryst Eng Mater. 75 (2019) 227–234. https://doi.org/10.1107/S2052520619001963.

[23] C. Mühle, R.E. Dinnebier, L. Van Wüllen, G. Schwering, M. Jansen, New Insights into the Structural and Dynamical Features of Lithium Hexaoxometalates Li_7MO_6 (M = Nb, Ta, Sb, Bi), Inorg. Chem. 43 (2004) 874–881. https://doi.org/10.1021/ic030208w.

[24] J.P. Fayolle, B. Raveau, Synthèse et caractéristiques cristallographiques de nouveaux tantalates et niobates d'europium divalent de type $Ba_5Ta_4O_{15}$, Comptes Rendus Des Seances de l'Academie Des Sciences, Serie C: Sciences Chimiques. 279 (1974) 521–524.

[25] A. Petersen, Hk. Müller-Buschbaum, Ein Beitrag über Oxide vom Typ AMO_4 (A = Ti^{3+}, Cr^{3+}; M = Nb^{5+}, Ta^{5+}), Z. Anorg. Allg. Chem. 609 (1992) 51–54. https://doi.org/10.1002/zaac.19926090309.

[26] Ismunandar, B.J. Kennedy, B.A. Hunter, The Structure of Rh*M*O_4, M = Nb, Ta, and Sb, MSF. 278–281 (1998) 714–719. https://doi.org/10.4028/www.scientific.net/MSF.278-281.714.

[27] H. Weitzel, Kristallstrukturverfeinerung von Wolframiten und Columbiten, Zeitschrift Für Kristallographie - Crystalline Materials. 144 (1976) 238–258. https://doi.org/10.1524/zkri.1976.144.16.238.

[28] K.M. Ok, N.S.P. Bhuvanesh, P.S. Halasyamani, $SbSb_xM_{1-x}O_4$ (M=Nb^V or Ta^V): Solid Solution Behavior and Second-Harmonic Generating Properties, Journal of Solid State Chemistry. 161 (2001) 57–62. https://doi.org/10.1006/jssc.2001.9266.

[29] C.-Y. Lee, R. Macquart, Q. Zhou, B.J. Kennedy, Structural and spectroscopic studies of $BiTa_{1-x}Nb_xO_4$, Journal of Solid State Chemistry. 174 (2003) 310–318. https://doi.org/10.1016/S0022-4596(03)00225-1.

[30] Z.-G. Zhang, T. Abe, C. Moriyoshi, H. Tanaka, Y. Kuroiwa, Study of materials structure physics of isomorphic $LiNbO_3$ and $LiTaO_3$ ferroelectrics by synchrotron radiation X-ray diffraction, Jpn. J. Appl. Phys. 57 (2018) 11UB04. https://doi.org/10.7567/JJAP.57.11UB04.

Appendix B

Oxyfluorides Exhibiting Preferential O/F Ordering

Structural modeling of O/F correlated disorder in $TaOF_3$ and $NbOF_{3-x}(OH)_x$ by coupling solid state NMR and DFT calculations

Ouail Zakary[a,], Monique Body[a,*], Thibault Charpentier[b], Vincent Sarou-Kanian[c], Christophe Legein[a]*

[a] Institut de Molécules et Matériaux du Mans (IMMM) - UMR 6283 CNRS, Le Mans Université, Avenue Olivier Messiaen, 72805 Le Mans Cedex 9, France

[b] Université Paris-Saclay, CEA, CNRS, NIMBE, 91191, Gif-sur-Yvette cedex, France

[c] CNRS, CEMHTI UPR3079, Université d'Orléans, 45071 Orléans, France

Supporting information

Table of content

1. ^{19}F MAS NMR spectra and their fits S285

Figure S1. Experimental and fitted ^{19}F MAS NMR spectra of $NbOF_3$ S285

Table S1. Experimental ^{19}F δ_{iso}, δ_{CSA}, η_{CSA}, line width, relative intensity and assignment of each individual resonance used to fit the ^{19}F MAS NMR spectrum of $NbOF_3$, weighted average ^{19}F δ_{iso}, δ_{CSA} and η_{CSA} of the resonances assigned to the same F atom type and sum of the corresponding relative intensities. S285

Figure S2. Experimental and fitted ^{19}F TOP MAS NMR spectra of $NbOF_3$ S286

Table S2. Experimental ^{19}F δ_{iso}, line width, relative intensity and assignment of each individual resonance used to fit the ^{19}F TOP MAS NMR spectrum of $NbOF_3$, weighted average ^{19}F δ_{iso} of the resonances assigned to the same atom type and sum of the corresponding relative intensities S286

Figure S3. Experimental and fitted ^{19}F MAS NMR spectra of $TaOF_3$ S287

Table S3. Experimental ^{19}F δ_{iso}, δ_{CSA}, η_{CSA}, line width, relative intensity and assignment of each individual resonance used to fit the ^{19}F MAS NMR spectrum of $TaOF_3$, weighted average ^{19}F δ_{iso}, δ_{CSA} and η_{CSA} of the resonances assigned to the same atom type and sum of the corresponding relative intensities S287

Figure S4. Experimental and fitted ^{19}F TOP MAS NMR spectra of $TaOF_3$ S288

Table S4. Experimental ^{19}F δ_{iso}, line width, relative intensity and assignment of each individual resonance used to fit the ^{19}F TOP MAS NMR spectrum of $TaOF_3$, weighted average ^{19}F δ_{iso} of the resonances assigned to the same atom type and sum of the corresponding relative intensities..... S288

2. ^1H MAS NMR spectra and their fits..... S289

Figure S5. Experimental and fitted ^1H MAS NMR spectra of $NbOF_3$..... S289

Table S5. Experimental ^1H δ_{iso}, line width and relative intensity of each individual resonance used to fit the ^1H MAS NMR spectrum of $NbOF_3$. S289

Figure S6. Experimental and fitted ^1H MAS NMR spectra of $TaOF_3$.. ..... S290

Table S6. Experimental ^1H δ_{iso}, line width and relative intensity of each individual resonance used to fit the ^1H MAS NMR spectrum of $TaOF_3$..... S290

3. Determination of the OH substitution rate in $NbOF_3$ and $TaOF_3$..... S291

Table S7. Assignment, average experimental ^{19}F δ_{iso} and corresponding relative intensity, for $NbOF_3$ and $TaOF_3$. S291

Table S8. Relative intensity ratio (R), OH substitution rate (x) deduced from the ^{19}F MAS and the ^{19}F TOP MAS NMR spectra of $NbOF_3$ and $TaOF_3$, and average R and x value..S291

4. Rietveld refinements S292

Figure S7. Observed, calculated and difference diffraction patterns of $NbOF_3$.. ..... S292

Figure S8. Observed, calculated and difference diffraction patterns of $TaOF_3$.. ..... S293

5. $NbOF_3$ and $TaOF_3$ structural features. S294

Table S9. Formula, number of F atoms, number of OH groups and number and composition of the MX_6 octahedra in models 1 to 10. ..... S294

Figure S9. Supercell parameters a, b, c and volume V of each model from the FO_DFT-D3 structures for $NbOF_3$ and $TaOF_3$..... S294

Table S10. Total energy after relaxation from the 10 APO_DFT-D3 models of $NbOF_3$, $TaOF_3$, $NbOF_{0.875}(OH)_{0.125}F_2$ and $NbOF_{0.75}(OH)_{0.25}F_2$. S295

Table S11. Average, shortest and longest Nb–X (X = O, F1 & F2) bond lengths from the 10 APO_DFT-D3 models of $NbOF_3$. S295

Table S12. Average, minimal and maximal X–Nb–X (X = O, F1 & F2) angle values from the 10 APO_DFT-D3 models of $NbOF_3$. S296

Table S13. Average, minimal and maximal Nb–X–Nb (X = O & F1) angle values from the 10 APO_DFT-D3 models of $NbOF_3$. S296

Table S14. Average, shortest and longest Nb–X (X = O, F1 & F2) bond lengths from the 10 FO_DFT-D3 models of $NbOF_3$. S297

Table S15. Average, minimal and maximal X–Nb–X (X = O, F1 & F2) angle values from the 10 FO_DFT-D3 models of $NbOF_3$. S297

Table S16. Average, minimal and maximal Nb–X–Nb (X = O & F) angle values from the 10 FO_DFT-D3 models of $NbOF_3$. S298

Table S17. Average, shortest and longest Ta–X (X = O, F1 & F2) bond lengths from the 10 APO_DFT-D3 models of $TaOF_3$. S298

Table S18. Average, minimal and maximal X–Ta–X (X = O, F1 & F2) angle values from the 10 APO_DFT-D3 models of $TaOF_3$. S299

Table S19. Average, minimal and maximal Ta–X–Ta (X = O & F1) angle values from the 10 APO_DFT-D3 models of $TaOF_3$. S299

Table S20. Average, shortest and longest Ta–X (X = O, F1 & F2) bond lengths from the 10 FO_DFT-D3 models of $TaOF_3$. S300

Table S21. Average, minimal and maximal X–Ta–X (X = O, F1 & F2) angle values from the 10 FO_DFT-D3 models of $TaOF_3$. S300

Table S22. Average, minimal and maximal Ta–X–Ta (X = O & F1) angle values from the 10 FO_DFT-D3 models of $TaOF_3$. S301

6. New NbF_5 and TaF_5 correlations ^{19}F σ_{iso} vs δ_{iso} established with VASP S302

Table S23. F site, site multiplicity and Wyckoff symbol, experimental ^{19}F δ_{iso}, calculated ^{19}F σ_{iso}, calculated ^{19}F δ_{iso} and the difference $\Delta\delta_{iso}$ between $\delta_{iso,exp}$ and $\delta_{iso,cal}$ from the APO_DFT-D3 and FO_DFT-D3 structures of NbF_5 and TaF_5. ..... S302

7. $NbOF_3$ and $TaOF_3$ calculated σ_{iso}, σ_{CSA} and η_{CSA} values. S303

Table S24. ^{19}F calculated σ_{iso} of each F atom from the 10 APO_DFT-D3 models of $NbOF_3$ and average σ_{iso} of each F crystallographic site. S303

Table S25. ^{19}F calculated σ_{CSA} of each F atom from the 10 APO_DFT-D3 models of $NbOF_3$ and average absolute value of σ_{CSA} of each F crystallographic site. S304

Table S26. ^{19}F calculated η_{CSA} of each F atom from the 10 APO_DFT-D3 models of $NbOF_3$ and average η_{CSA} of each F crystallographic site. S305

Table S27. ^{19}F calculated σ_{iso} of each F atom from the 10 FO_DFT-D3 models of $NbOF_3$ and average σ_{iso} of each F crystallographic site. S306

Table S28. ^{19}F calculated σ_{CSA} of each F atom from the 10 FO_DFT-D3 models of $NbOF_3$ and average absolute value of σ_{CSA} of each F crystallographic site. S307

Table S29. ^{19}F calculated η_{CSA} of each F atom from the 10 FO_DFT-D3 models of $NbOF_3$ and average η_{CSA} of each F crystallographic site. S308

Table S30. ^{19}F calculated σ_{iso} of each F atom from the 10 APO_DFT-D3 models of $TaOF_3$ and average σ_{iso} of each F crystallographic site. S309

Table S31. ^{19}F calculated σ_{CSA} of each F atom from the 10 APO_DFT-D3 models of $TaOF_3$ and average absolute value of σ_{CSA} of each F crystallographic site. S310

Table S32. ^{19}F calculated η_{CSA} of each F atom from the 10 APO_DFT-D3 models of $TaOF_3$ and average η_{CSA} of each F crystallographic site. S311

Table S33. ^{19}F calculated σ_{iso} of each F atom from the 10 FO_DFT-D3 models of $TaOF_3$ and average σ_{iso} of each F crystallographic site. S312

Table S34. ^{19}F calculated σ_{CSA} of each F atom from the 10 FO_DFT-D3 models of $TaOF_3$ and average absolute value of σ_{CSA} of each F crystallographic site. S313

Table S35. ^{19}F calculated η_{CSA} of each F atom from the 10 FO_DFT-D3 models of $TaOF_3$ and average η_{CSA} of each F crystallographic site. S314

Figure S10. Calculated ^{19}F δ_{iso} of F2 atoms as a function of F2–M (M = Nb, Ta) bond lengths from the APO_DFT-D3 and FO_DFT-D3 models of $NbOF_3$ and $TaOF_3$ S315

8. Hydroxylated $NbOF_3$ structural features S316

Table S36. Average, shortest and longest Nb–F bond lengths from the 10 APO_DFT-D3 models of $NbOF_{0.875}(OH)_{0.125}F_2$. S316

Table S37. Average, shortest and longest Nb–O(OH) bond lengths from the 10 APO_DFT-D3 models of $NbOF_{0.875}(OH)_{0.125}F_2$. S316

Table S38. Average, minimal and maximal X–Nb–X (X = O, OH, F1 & F2) angle values from the 10 APO_DFT-D3 models of $NbOF_{0.875}(OH)_{0.125}F_2$. S317

Table S39. Average, minimal and maximal Nb–X–Nb (X = O, OH & F1) angle values from the 10 APO_DFT-D3 models of $NbOF_{0.875}(OH)_{0.125}F_2$. S317

Table S40. Average, shortest and longest Nb–F bond lengths from the 10 APO_DFT-D3 models of $NbOF_{0.75}(OH)_{0.25}F_2$. S318

Table S41. Average, shortest and longest Nb–O(OH) bond lengths from the 10 APO_DFT-D3 models of $NbOF_{0.75}(OH)_{0.25}F_2$. S318

Table S42. Average, minimal and maximal X–Nb–X (X = O, OH, F1 & F2) angle values from the 10 APO_DFT-D3 models of $NbOF_{0.75}(OH)_{0.25}F_2$. S319

Table S43. Average, minimal and maximal Nb–X–Nb (X = O, OH & F1) angle values from the 10 APO_DFT-D3 models of $NbOF_{0.75}(OH)_{0.25}F_2$. S319

9. Hydroxylated $NbOF_3$ calculated σ_{iso}, σ_{CSA} and η_{CSA} values. S320

Table S44. ^{19}F calculated σ_{iso} of each F atom from the 10 APO_DFT-D3 models of $NbOF_{0.875}(OH)_{0.125}F_2$ and average σ_{iso} of each F crystallographic site. S320

Table S45. ^{19}F calculated σ_{CSA} of each F atom from the 10 APO_DFT-D3 models of $NbOF_{0.875}(OH)_{0.125}F_2$ and average absolute value of σ_{CSA} of each F crystallographic site. S321

Table S46. ^{19}F calculated η_{CSA} of each F atom from the 10 APO_DFT-D3 models of $NbOF_{0.875}(OH)_{0.125}F_2$ and average η_{CSA} of each F crystallographic site. S322

Table S47. ^{19}F calculated σ_{iso} of each F atom from the 10 APO_DFT-D3 models of $NbOF_{0.75}(OH)_{0.25}F_2$ and average σ_{iso} of each F crystallographic site. S323

Table S48. ^{19}F calculated σ_{CSA} of each F atom from the 10 APO_DFT-D3 models of $NbOF_{0.75}(OH)_{0.25}F_2$ and average absolute value of σ_{CSA} of each F crystallographic site. S324

Table S49. ^{19}F calculated η_{CSA} of each F atom from the 10 APO_DFT-D3 models of $NbOF_{0.75}(OH)_{0.25}F_2$ and average η_{CSA} of each F crystallographic site. S325

Figure S11. Calculated ^{19}F δ_{iso} of F2 atoms as a function of F2–M bond lengths from the APO_DFT-D3 models of $NbOF_{0.875}(OH)_{0.125}F_2$ and $NbOF_{0.75}(OH)_{0.25}F_2$. S326

10. Hydroxylated $NbOF_3$: geometries of the O−H···F contacts and calculated δ_{iso} values. S327

Table S50. Geometries of the O−H···F contacts (H−O bond length, H···F distance and O–H···F angle) and calculated ^{1}H and ^{19}F σ_{iso} and δ_{iso} values from the 10 APO_DFT-D3 models of $NbOF_{0.875}(OH)_{0.125}F_2$. S327

Table S51. Geometries of the O−H···F contacts (H−O bond length, H···F distance and O–H···F angle) and calculated ^{1}H and ^{19}F σ_{iso} and δ_{iso} values from the 10 APO_DFT-D3 models of $NbOF_{0.75}(OH)_{0.25}F_2$. S328

References S330

1. ^{19}F MAS NMR spectra and their fits

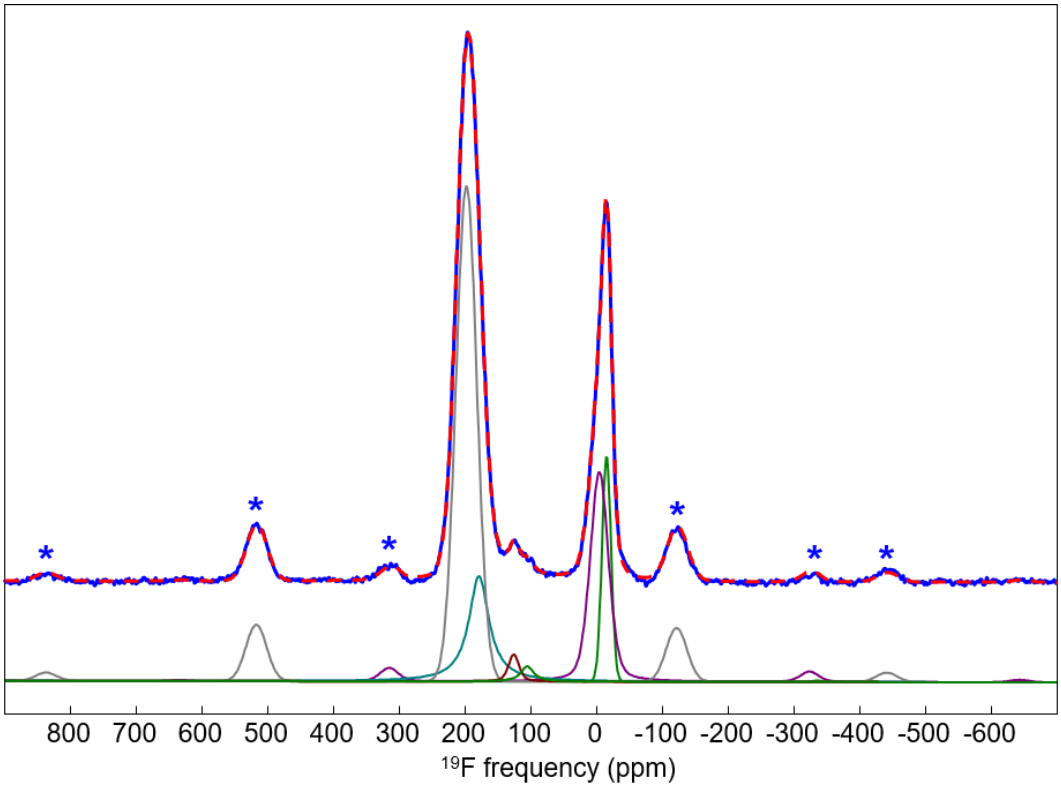


Figure S1. Experimental (blue) and fitted (dashed red) ^{19}F MAS (60 kHz) NMR spectra of $NbOF_3$. The individual resonances used for the fit (**Table S1**) are shown below. The stars indicate spinning sidebands.

Table S1. Experimental ^{19}F δ_{iso} (δ_{iso}, ppm), δ_{CSA} (δ_{CSA}, ppm), η_{CSA}, line width (LW, ppm), relative intensity (I, %) and assignment of each individual resonance used to fit the ^{19}F MAS (60 kHz) NMR spectrum of $NbOF_3$, weighted average ^{19}F δ_{iso} ($<\delta_{iso}>$, ppm), δ_{CSA} ($<\delta_{CSA}>$, ppm) and η_{CSA} ($<\eta_{CSA}>$) of the resonances assigned to the same F atom type (bridging (b), terminal (t)) and sum of the corresponding relative intensities (ΣI, %).

δ_{iso}	δ_{CSA}	η_{CSA}	LW	I	$<\delta_{iso}>$	$<\delta_{CSA}>$	$<\eta_{CSA}>$	ΣI	Assignment
-16.0	98.0	0.35	16.2	8.7	-8.3	-162.4	0.51	29.3	F1 (b)
-5.0	-272.9	0.58	32.6	20.6					
104.5	n. a.	n. a.	23.1	1.2	115.6	n. a.	n. a.	2.6	F2 (t, H-bonded)
125.1	n. a.	n. a.	18.7	1.4					
178.0	-42.0	0.00	36.8	13.2	193.4	-291.6	0.72	68.1	F2 (t)
197.1	-351.9	0.90	37.2	54.9					

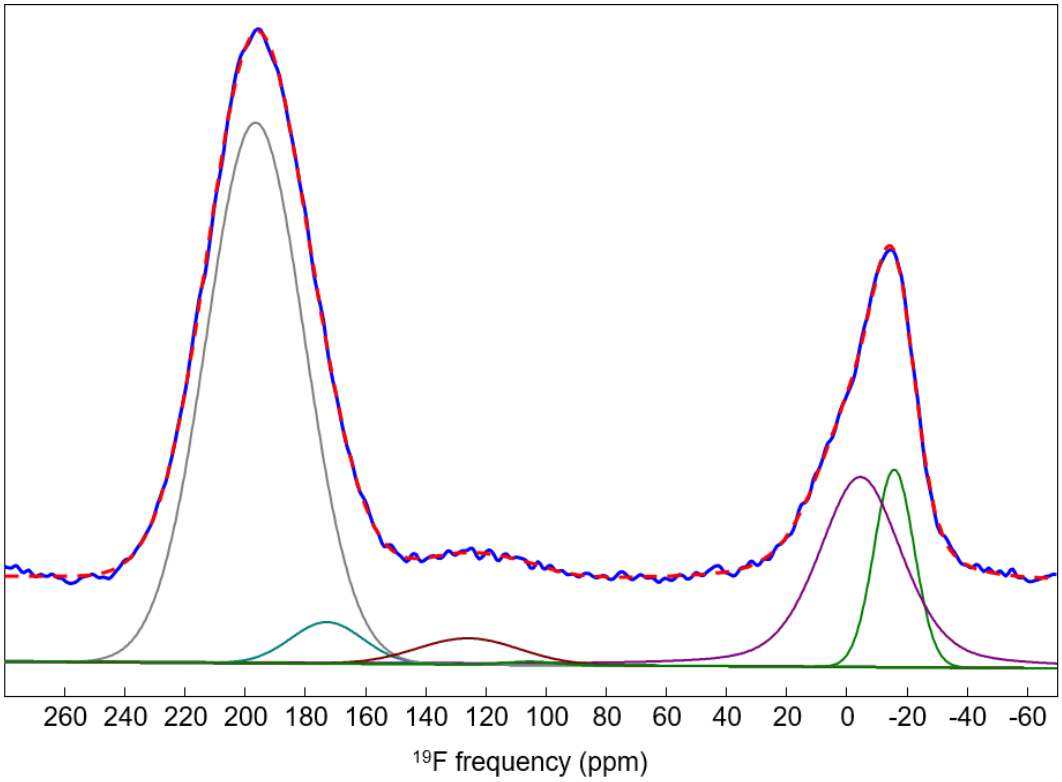


Figure S2. Experimental (blue) and fitted (dashed red) ^{19}F TOP MAS (60 kHz) NMR spectra of $NbOF_3$. The individual resonances used for the fit (**Table S2**) are shown below.

Table S2. Experimental ^{19}F δ_{iso} (δ_{iso}, ppm), line width (LW, ppm), relative intensity (I, %) and assignment of each individual resonance used to fit the ^{19}F TOP MAS (60 kHz) NMR spectrum of $NbOF_3$, weighted average ^{19}F δ_{iso} ($<\delta_{iso}>$, ppm) of the resonances assigned to the same atom type (bridging (b), terminal (t)) and sum of the corresponding relative intensities (ΣI, %).

δ_{iso}	LW	I	$<\delta_{iso}>$	ΣI	Assignment
-15.9	15.6	9.4	-8.2	30.4	F1 (b)
-4.7	32.5	21.1			
104.9	17.6	0.2	124.4	3.2	F2 (t, H-bonded)
125.7	39.9	3.1			
172.7	28.1	3.5	195.2	66.4	F2 (t)
196.4	38.3	62.9			

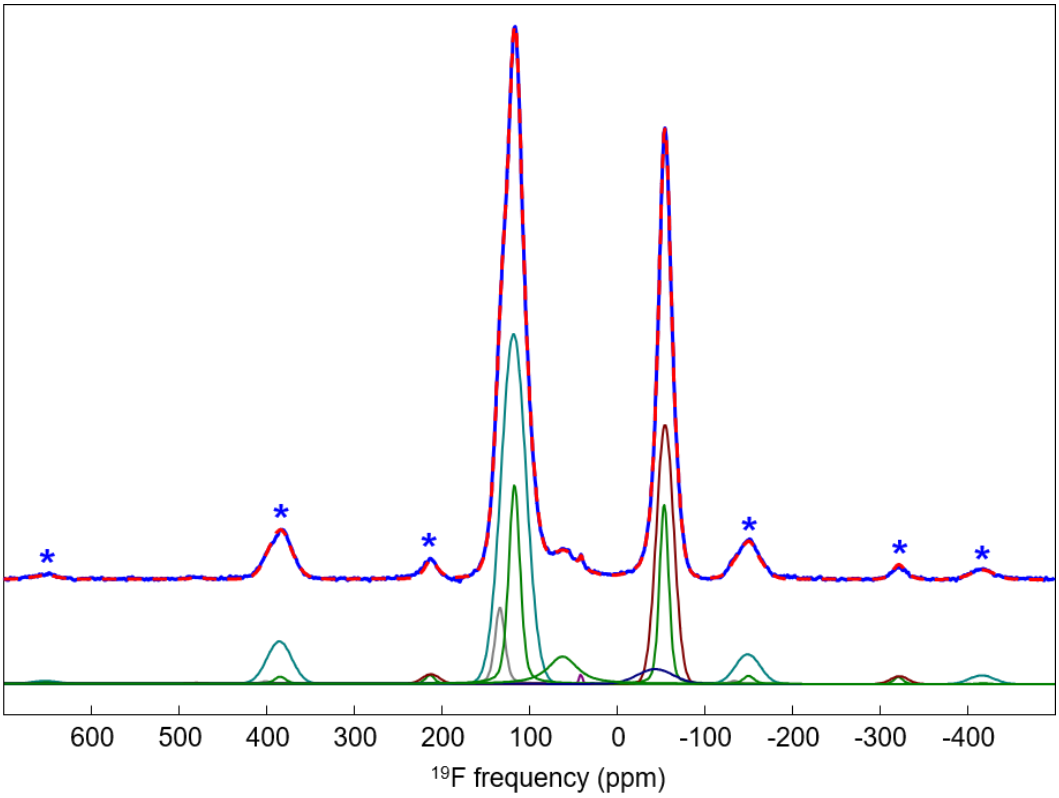


Figure S3. Experimental (blue) and fitted (dashed red) ^{19}F MAS (50 kHz) NMR spectra of $TaOF_3$. The individual resonances used for the fit (**Table S3**) are shown below. The stars indicate spinning sidebands.

Table S3. Experimental ^{19}F δ_{iso} (δ_{iso}, ppm), δ_{CSA} (δ_{CSA}, ppm), η_{CSA}, line width (LW, ppm), relative intensity (I, %) and assignment of each individual resonance used to fit the ^{19}F MAS (50 kHz) NMR spectrum of $TaOF_3$, weighted average ^{19}F δ_{iso} ($<\delta_{iso}>$, ppm), δ_{CSA} ($<\delta_{CSA}>$, ppm) and η_{CSA} ($<\eta_{CSA}>$) of the resonances assigned to the same atom type (bridging (b), terminal (t)) and sum of the corresponding relative intensities (ΣI, %).

δ_{iso}	δ_{CSA}	η_{CSA}	LW	I	$<\delta_{iso}>$	$<\delta_{CSA}>$	$<\eta_{CSA}>$	ΣI	Assignment
-55.5	-177.1	0.45	23.3	20.9	-54.4	-170.0	0.5	32.0	F1 (b)
-54.4	-196.9	0.62	12.4	8.8					
-44.2	0.0	0.00	48.0	2.3					
40.8	n. a.	n. a.	4.6	0.1	61.1	n. a.	n. a.	5.0	F2 (t, H-bonded)
61.5	n. a.	n. a.	40.1	4.9					
116.5	-187.1	0.60	15.0	12.2	118.2	-283.4	0.1	63.0	F2 (t)
117.4	-318.8	0.00	33.2	46.7					
133.0	-166.1	0.15	13.3	4.1					

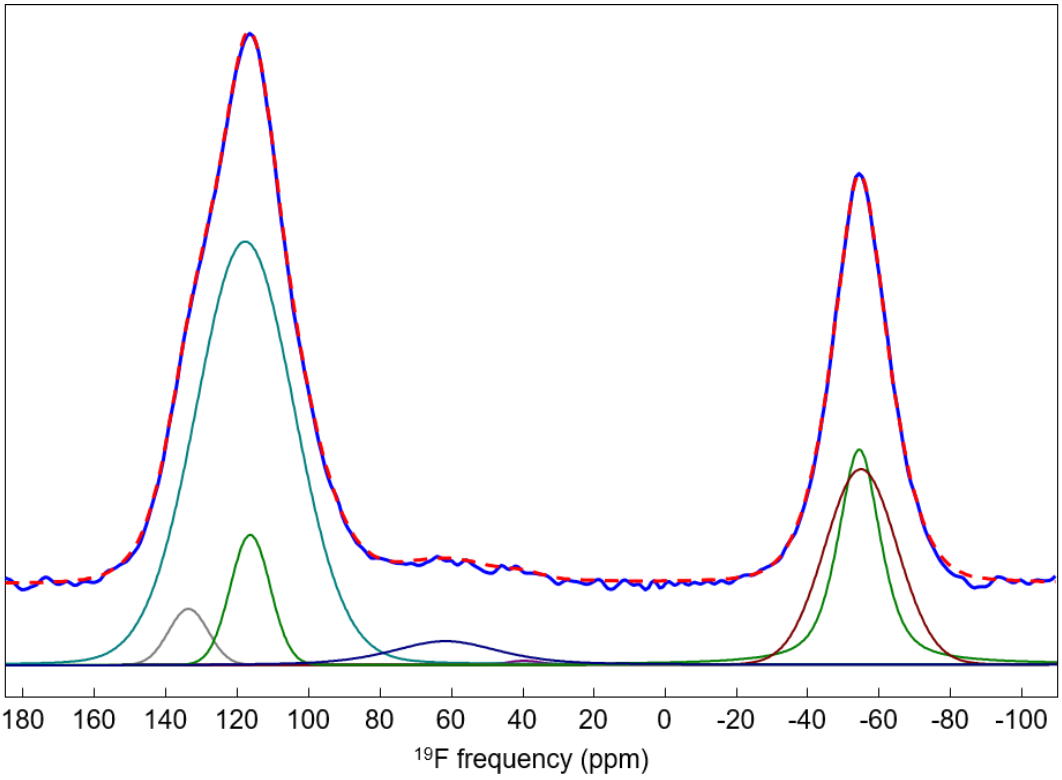


Figure S4. Experimental (blue) and fitted (dashed red) ^{19}F TOP MAS (50 kHz) NMR spectra of $TaOF_3$. The individual resonances used for the fit (**Table S4**) are shown below.

Table S4. Experimental ^{19}F δ_{iso} (δ_{iso}, ppm), line width (LW, ppm), relative intensity (I, %) and assignment of each individual resonance used to fit the ^{19}F TOP MAS (50 kHz) NMR spectrum of $TaOF_3$, weighted average ^{19}F δ_{iso} ($<\delta_{iso}>$, ppm) of the resonances assigned to the same atom type (bridging (b), terminal (t)) and sum of the corresponding relative intensities (ΣI, %).

δ_{iso}	LW	I	$<\delta_{iso}>$	ΣI	Assignment
-54.6	14.0	14.4	-54.9	32.3	F1 (b)
-55.1	23.8	17.9			
39.4	10.9	0.2	60.3	4.0	F2 (t, H-bonded)
61.4	35.7	3.9			
116.2	13.1	6.6	118.2	63.7	F2 (t)
117.6	32.5	54.3			
133.5	13.0	2.8			

2. ^{1}H MAS NMR spectra and their fits

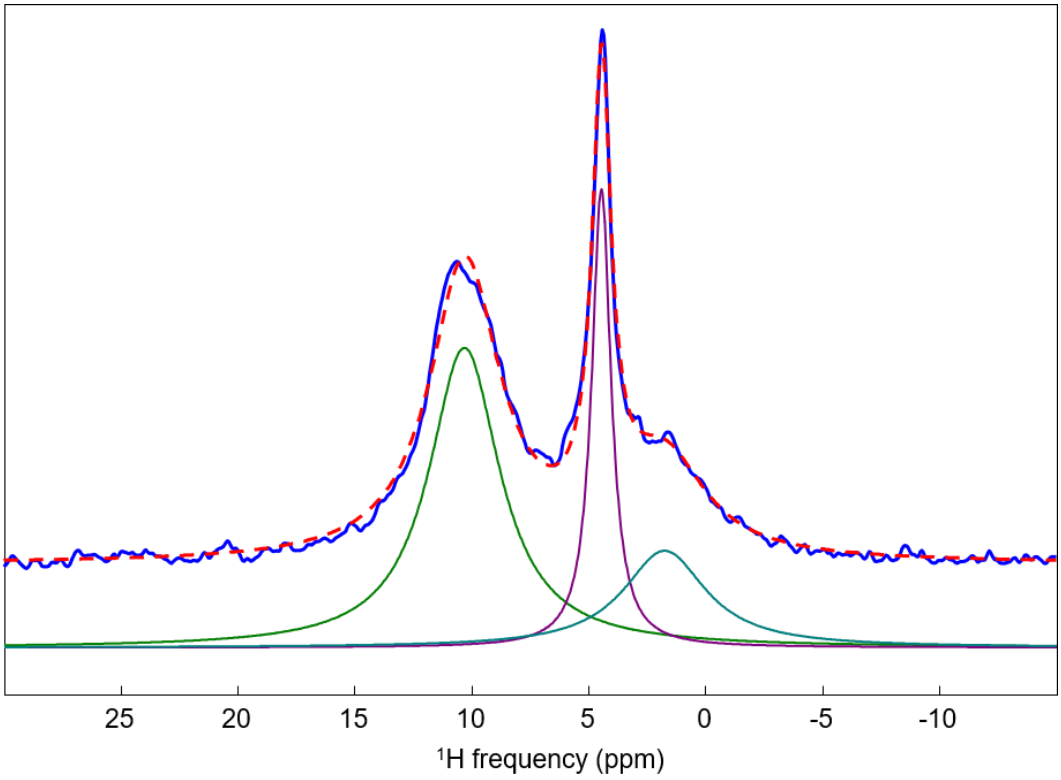


Figure S5. Experimental (blue) and fitted (dashed red) ^{1}H MAS (60 kHz) NMR spectra of $NbOF_3$. The individual resonances used for the fit (**Table S7**) are shown below.

Table S5. Experimental ^{1}H δ_{iso} (δ_{iso}, ppm), line width (LW, ppm) and relative intensity (I, %) of each individual resonance used to fit the ^{1}H MAS (60 kHz) NMR spectrum of $NbOF_3$.

δ_{iso}	LW	I
1.7	4.3	20.6
4.4	1.0	24.0
10.3	3.7	55.4

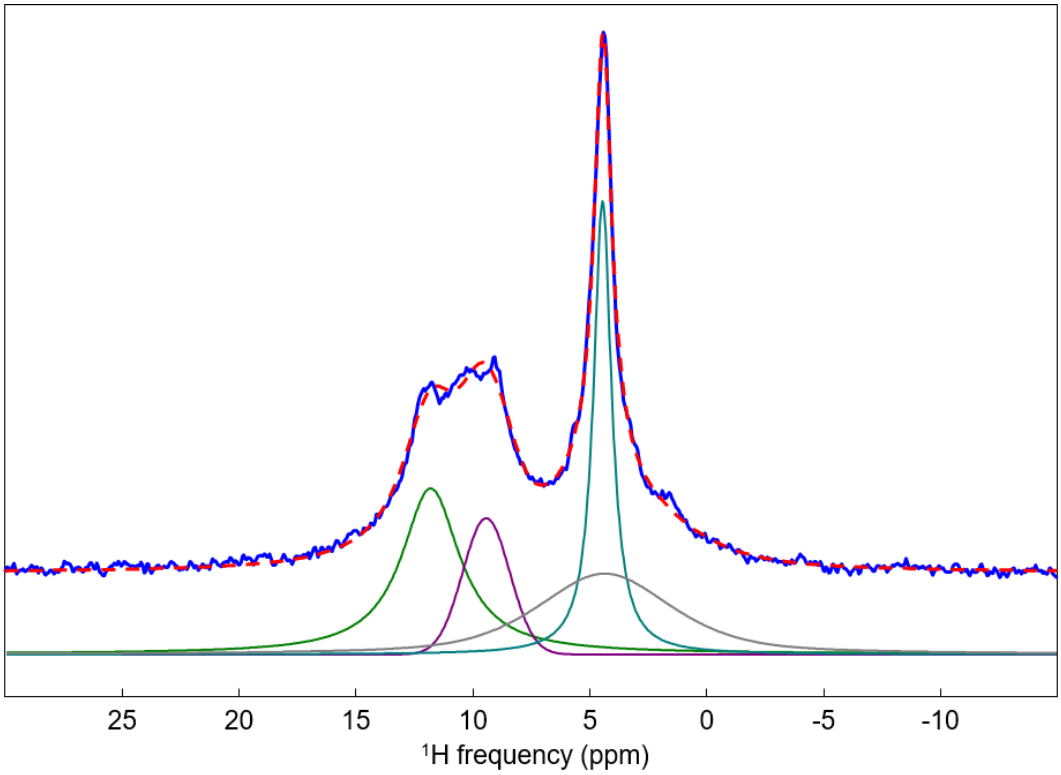


Figure S6. Experimental (blue) and fitted (dashed red) ^{1}H MAS (50 kHz) NMR spectra of $TaOF_3$. The individual resonances used for the fit (**Table S8**) are shown below.

Table S6. Experimental ^{1}H δ_{iso} (δ_{iso}, ppm), line width (LW, ppm) and relative intensity (I, %) of each individual resonance used to fit the ^{1}H MAS (50 kHz) NMR spectrum of $TaOF_3$.

δ_{iso}	LW	I
4.3	6.8	28.0
4.4	0.9	26.9
9.4	2.4	14.2
11.8	3.0	30.9

3. Determination of the OH substitution rate in $NbOF_3$ and $TaOF_3$

Table S7. Assignment, average experimental ^{19}F δ_{iso} ($<\delta_{iso}>$, ppm) and corresponding relative intensity ($<I>$, %), for $NbOF_3$ and $TaOF_3$. The values are estimated by averaging those obtained from the ^{19}F MAS and the ^{19}F TOP MAS NMR spectra (**Tables S1-S4**).

Assignment	$NbOF_3$		$TaOF_3$	
	$<\delta_{iso}>$	$<I>$	$<\delta_{iso}>$	$<I>$
F1	-8.2 (5)	29.9 (6)	-54.7 (3)	32.2 (2)
H-bonded F2	120 (4)	2.9 (3)	60.8 (2)	4.5 (5)
F2	194.3 (9)	67.3 (9)	118.2 (1)	63.4 (4)

Considering the formula $MO1F1_{1-x}(OH)1_xF2_2$ and the relative intensity values, I, of the F1 and F2 sites; the OH substitution rate x is determined from the equation $R(1-x)=2$, with $R=\frac{\sum I_{F2}}{I_{F1}}$, $\sum I_{F2}$, the sum of the I values of the resonances assigned to F2 and I_{F1}, the relative intensity of the resonance assigned to F1 (**Table S6**).

Table S8. Relative intensity ratio (R), OH substitution rate (x) deduced from the ^{19}F MAS and the ^{19}F TOP MAS NMR spectra of $NbOF_3$ and $TaOF_3$, and average R (<R>) and x (<x>) values.

	R	X	<R>	<x>
$NbO1F1_{1-x}(OH)1_xF2_2$	2.409	0.170	2.348(60)	0.148(22)
	2.289	0.126		
$TaO1F1_{1-x}(OH)1_xF2_2$	2.121	0.057	2.108(13)	0.051(6)
	2.096	0.046		

4. Rietveld refinements

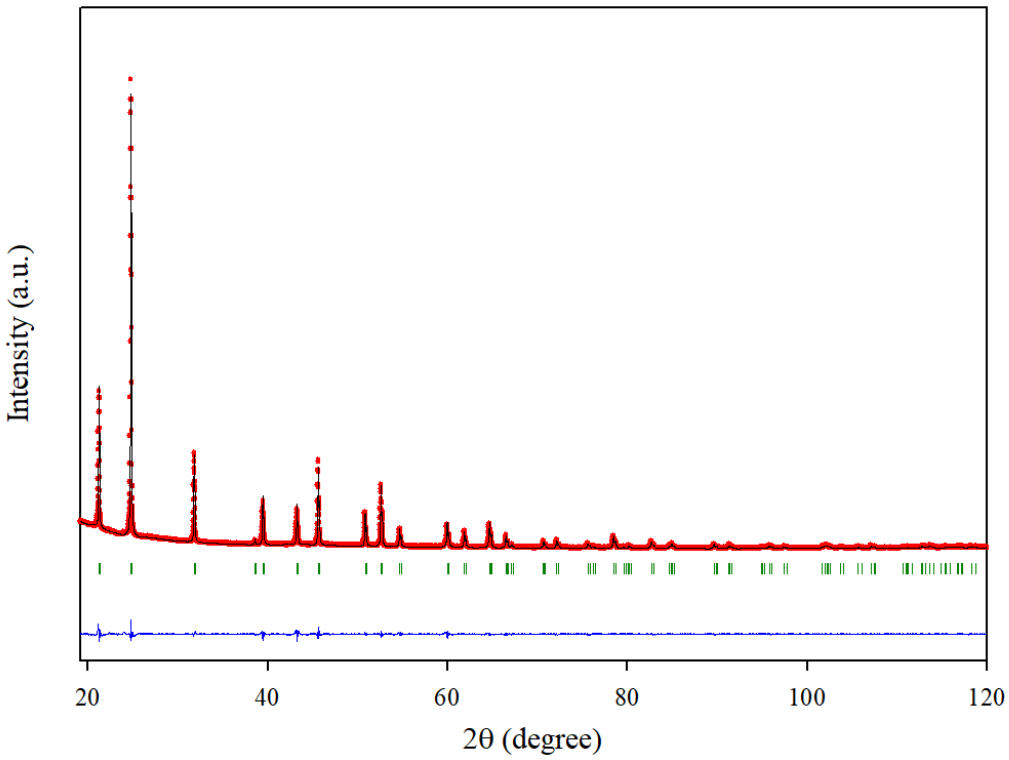


Figure S7. Observed (red), calculated (black) and difference (blue) diffraction patterns of $NbOF_3$. The green vertical markers refer to the Bragg positions. The obtained refinement reliability factors are R_p = 13.6%, R_{wp} = 9.1%, R_{exp} = 3.4%, R_B = 1.9% and R_F = 1.9 %.

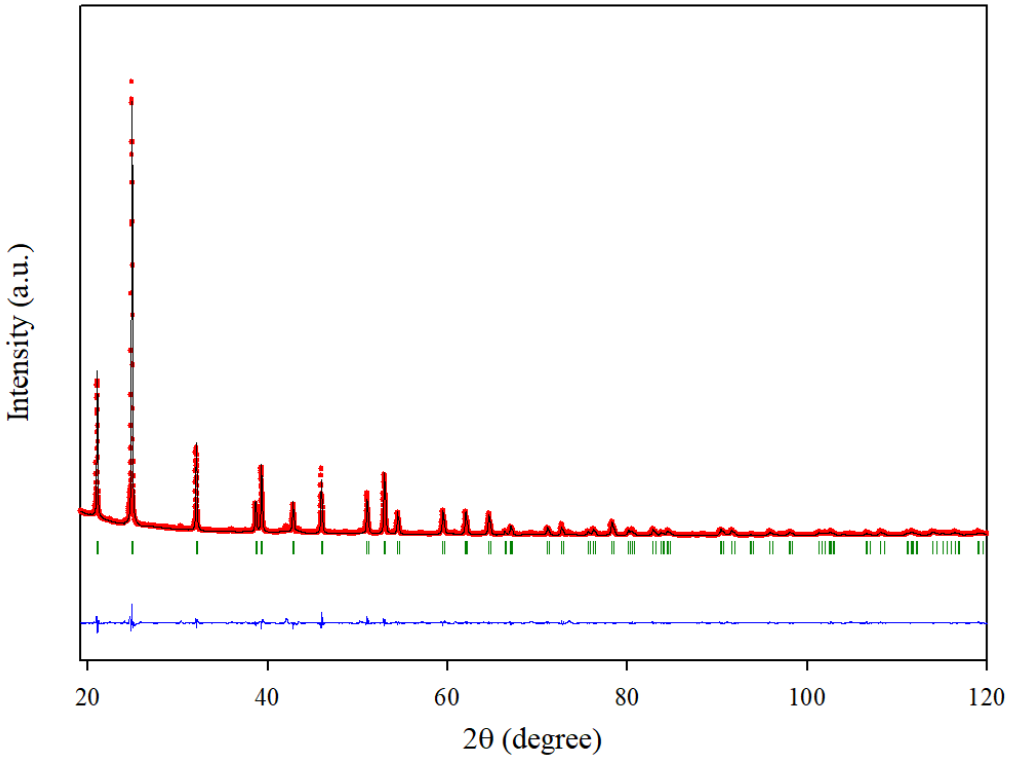


Figure S8. Observed (red), calculated (black) and difference (blue) diffraction patterns of $TaOF_3$. The green vertical markers refer to the Bragg positions. The obtained refinement reliability factors are R_p = 13.2%, R_{wp}= 11.9%, R_{exp} = 2.6%, R_B = 2.2%, R_F = 1.6%.

5. $NbOF_3$ and $TaOF_3$ structural features.

Table S9. Formula, number of F atoms (n_F), number of OH groups (n_{OH}) and number and composition of the MX_6 octahedra in models 1 to 10.

Formula	n_F	n_{OH}	MX_6 octahedra
MOF_3	24	0	MO_2F_4 (x8)
$NbOF_{0.875}(OH)_{0.125}F_2$	23	1	NbO_2F_4 (x6)
			$NbO_2(OH)F_3$ (x2)
$NbOF_{0.75}(OH)_{0.25}F_2$	22	2	NbO_2F_4 (x4)
			$NbO_2(OH)F_3$ (x4)

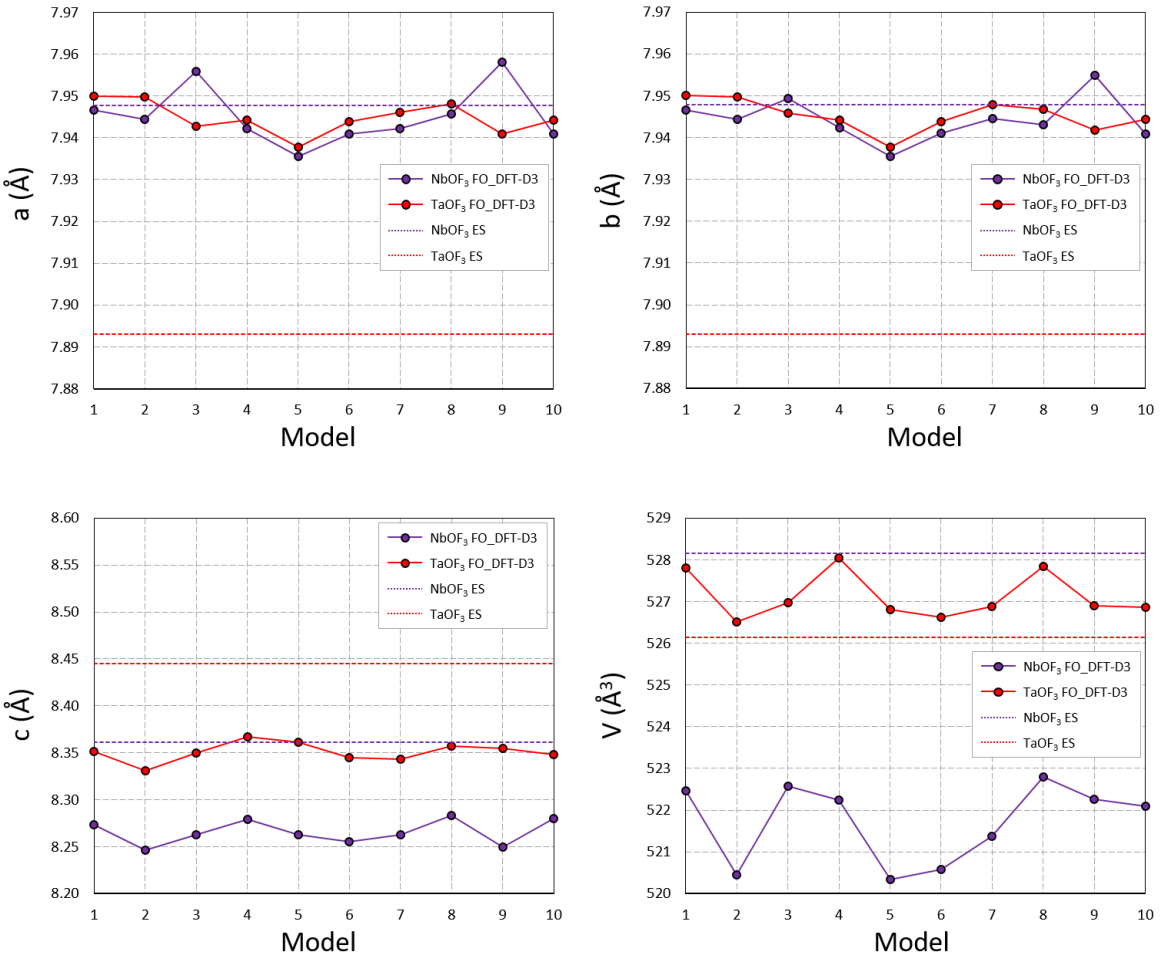


Figure S9. Supercell parameters a, b, c and volume V of each model from the FO_DFT-D3 structures for $NbOF_3$ (in purple) and $TaOF_3$ (in red). The horizontal dashed lines indicate the parameters from the experimental structures.

Table S10. Total energy after relaxation (eV) from the 10 APO_DFT-D3 models of $NbOF_3$, $TaOF_3$, $NbOF_{0.875}(OH)_{0.125}F_2$ and $NbOF_{0.75}(OH)_{0.25}F_2$.

Model	$NbOF_3$	$TaOF_3$	$NbOF_{0.875}(OH)_{0.125}F_2$	$NbOF_{0.75}(OH)_{0.25}F_2$
1	-300.75	-328.75	-306.69	-312.69
2	-300.57	-328.58	-306.56	-312.53
3	-300.66	-328.69	-306.67	-312.70
4	-300.74	-328.77	-306.68	-312.82
5	-300.55	-328.61	-306.67	-312.78
6	-300.56	-328.59	-306.52	-312.54
7	-300.62	-328.63	-306.57	-312.46
8	-300.79	-328.80	-306.73	-312.79
9	-300.62	-328.65	-306.66	-312.74
10	-300.65	-328.68	-306.73	-312.74

Table S11. Average, shortest and longest Nb−X (X = O, F1 & F2) bond lengths (Å) from the 10 APO_DFT-D3 models of $NbOF_3$.

Model	<Nb−O>	$Nb-O_{min}$	$Nb-O_{max}$	<Nb−F1>	$Nb-F1_{min}$	$Nb-F1_{max}$	<Nb−F2>	$Nb-F2_{min}$	$Nb-F2_{max}$
1	1.885	1.885	1.886	2.094	2.094	2.095	1.881	1.881	1.881
2	1.884	1.884	1.884	2.095	2.095	2.095	1.881	1.881	1.881
3	1.888	1.836	1.944	2.094	2.023	2.158	1.881	1.876	1.887
4	1.888	1.881	1.891	2.093	2.085	2.105	1.880	1.875	1.885
5	1.889	1.878	1.900	2.093	2.092	2.093	1.881	1.872	1.890
6	1.887	1.871	1.899	2.094	2.083	2.109	1.881	1.877	1.885
7	1.886	1.872	1.897	2.094	2.085	2.104	1.881	1.877	1.885
8	1.887	1.881	1.890	2.093	2.083	2.105	1.880	1.875	1.884
9	1.890	1.815	1.972	2.094	1.996	2.192	1.881	1.871	1.888
10	1.887	1.878	1.893	2.093	2.089	2.100	1.880	1.871	1.889

Table S12. Average, minimal and maximal X−Nb−X (X = O, F1 & F2) angle values (°) from the 10 APO_DFT-D3 models of $NbOF_3$.

Model	O–Nb–O			F1–Nb–F1			F2–Nb–F2		
	Aver.	min	max	Aver.	min	max	Aver.	min	max
1	96.4	96.4	96.4	84.3	84.3	84.3	161.1	161.1	161.1
2	96.4	96.4	96.4	84.2	84.2	84.2	166.1	166.1	166.1
3	96.4	95.3	97.5	83.2	82.3	84.0	161.6	159.6	163.8
4	96.5	96.4	96.6	83.6	83.5	83.7	160.5	159.7	161.3
5	97.2	97.0	97.5	83.1	82.7	83.5	164.2	163.9	164.6
6	96.2	96.0	96.5	83.4	83.3	83.6	165.1	164.1	166.1
7	96.3	96.1	96.6	83.8	83.4	84.5	164.1	162.4	167.4
8	95.6	89.9	96.6	84.6	83.6	89.0	160.7	158.6	165.5
9	96.8	96.1	97.7	82.9	82.1	83.7	162.1	159.7	164.4
10	96.8	96.1	97.3	83.7	82.9	84.8	162.6	160.2	169.3

Table S13. Average, minimal and maximal Nb−X−Nb (X = O & F1) angle values (°) from the 10 APO_DFT-D3 models of $NbOF_3$.

Model	Nb−O−Nb			Nb−F1−Nb		
	Aver.	min	max	Aver.	min	Max
1	180.0	180.0	180.0	180.0	180.0	180.0
2	180.0	180.0	180.0	180.0	180.0	180.0
3	175.6	173.5	178.6	174.8	170.7	177.9
4	176.7	173.3	180.0	176.4	172.9	180.0
5	172.8	172.6	173.1	173.1	172.7	173.6
6	177.0	173.9	180.0	176.3	172.6	180.0
7	178.4	173.8	180.0	178.1	172.6	180.0
8	178.3	173.3	180.0	178.1	172.7	180.0
9	174.7	171.6	179.6	174.3	171.4	179.7
10	176.3	172.6	179.8	176.4	172.9	179.7

Table S14. Average, shortest and longest Nb−X (X = O, F1 & F2) bond lengths (Å) from the 10 FO_DFT-D3 models of $NbOF_3$.

Model	<Nb−O>	$Nb-O_{min}$	$Nb-O_{max}$	<Nb−F1>	$Nb-F1_{min}$	$Nb-F1_{max}$	<Nb−F2>	$Nb-F2_{min}$	$Nb-F2_{max}$
1	1.885	1.884	1.885	2.094	2.094	2.094	1.880	1.880	1.880
2	1.884	1.884	1.884	2.094	2.094	2.094	1.882	1.882	1.882
3	1.889	1.831	1.953	2.096	2.016	2.170	1.881	1.876	1.887
4	1.886	1.880	1.890	2.091	2.084	2.104	1.880	1.875	1.885
5	1.887	1.876	1.898	2.089	2.087	2.091	1.881	1.872	1.890
6	1.886	1.870	1.898	2.092	2.082	2.106	1.881	1.877	1.886
7	1.885	1.871	1.897	2.093	2.082	2.103	1.881	1.877	1.885
8	1.885	1.879	1.890	2.093	2.084	2.102	1.880	1.875	1.884
9	1.892	1.812	1.980	2.098	1.992	2.205	1.882	1.873	1.889
10	1.886	1.876	1.892	2.091	2.088	2.097	1.880	1.871	1.889

Table S15. Average, minimal and maximal X−Nb−X (X = O, F1 & F2) angle values (°) from the 10 FO_DFT-D3 models of $NbOF_3$.

Model	O−Nb−O			F−Nb−F1			F−Nb−F2		
	Aver.	min	max	Aver.	Min	max	Aver.	min	max
1	96.4	96.4	96.4	84.3	84.3	84.3	161.0	161.0	161.0
2	96.4	96.4	96.4	84.3	84.3	84.3	166.2	166.2	166.2
3	96.4	95.2	97.7	83.2	82.1	84.1	161.4	159.3	163.7
4	96.6	96.5	96.7	83.5	83.4	83.6	160.6	159.9	161.3
5	97.4	97.1	97.7	82.9	82.5	83.2	164.7	164.3	165.1
6	96.3	96.0	96.5	83.3	83.1	83.5	165.3	164.3	166.3
7	96.3	96.1	96.7	83.8	83.2	84.6	164.2	162.5	167.3
8	96.5	96.2	96.6	83.9	83.5	84.5	160.1	159.0	161.8
9	96.8	95.5	97.6	82.8	82.0	84.0	161.6	159.5	163.7
10	96.8	96.0	97.5	83.6	82.7	84.8	162.8	160.2	169.5

Table S16. Average, minimal and maximal Nb−X−Nb (X = O & F) angle values (°) from the 10 FO_DFT-D3 models of $NbOF_3$.

Model	Nb−O−Nb			Nb−F1−Nb		
	Aver.	min	max	Aver.	min	max
1	180.0	180.0	180.0	180.0	180.0	180.0
2	180.0	180.0	180.0	180.0	180.0	180.0
3	175.4	173.5	178.2	174.6	170.6	177.4
4	176.6	173.2	180.0	176.3	172.7	180.0
5	172.7	172.4	172.9	172.9	172.5	173.3
6	176.9	173.8	180.0	176.1	172.2	180.0
7	178.4	173.8	180.0	178.0	172.3	180.0
8	178.3	173.2	180.0	178.1	172.8	180.0
9	174.1	171.3	177.5	173.4	170.7	176.8
10	176.2	172.5	179.8	176.3	172.7	179.6

Table S17. Average, shortest and longest Ta−X (X = O, F1 & F2) bond lengths (Å) from the 10 APO_DFT-D3 models of $TaOF_3$.

Model	<Ta−O>	$Ta-O_{min}$	$Ta-O_{max}$	<Ta−F1>	$Ta-F1_{min}$	$Ta-F1_{max}$	<Ta−F2>	$Ta-F2_{min}$	$Ta-F2_{max}$
1	1.878	1.877	1.879	2.074	2.073	2.075	1.892	1.892	1.892
2	1.877	1.877	1.877	2.075	2.075	2.075	1.893	1.893	1.893
3	1.881	1.875	1.888	2.073	2.062	2.079	1.892	1.887	1.896
4	1.882	1.876	1.884	2.073	2.069	2.083	1.891	1.888	1.895
5	1.884	1.877	1.890	2.073	2.070	2.076	1.892	1.885	1.899
6	1.880	1.873	1.884	2.074	2.069	2.080	1.893	1.889	1.896
7	1.879	1.872	1.884	2.074	2.068	2.081	1.892	1.889	1.895
8	1.880	1.875	1.884	2.073	2.066	2.079	1.891	1.887	1.895
9	1.882	1.875	1.890	2.073	2.065	2.083	1.892	1.884	1.899
10	1.881	1.873	1.886	2.073	2.068	2.080	1.892	1.884	1.898

Table S18. Average, minimal and maximal X−Ta−X (X = O, F1 & F2) angle values (°) from the 10 APO_DFT-D3 models of $TaOF_3$.

Model	O−Ta−O			F−Ta−F1			F−Ta−F2		
	Aver.	min	max	Aver.	min	max	Aver.	min	max
1	96.0	96.0	96.0	84.6	84.6	84.6	161.8	161.8	161.8
2	96.1	96.1	96.1	84.5	84.5	84.5	166.5	166.5	166.5
3	96.7	96.4	96.9	82.8	82.4	83.1	163.2	160.8	165.2
4	96.7	96.6	96.9	82.8	82.7	83.0	161.3	160.7	161.9
5	97.8	97.7	97.9	81.7	81.5	81.7	165.5	165.5	165.6
6	96.5	96.4	96.7	82.8	82.7	82.9	165.9	165.6	166.3
7	96.3	95.9	96.6	83.7	82.7	84.6	164.8	163.2	168.1
8	96.3	95.7	96.7	83.7	82.8	85.0	160.6	159.4	162.8
9	97.2	96.4	98.0	82.2	81.5	83.2	164.2	162.2	167.8
10	96.9	95.8	98.0	83.1	81.5	85.0	163.5	161.1	170.2

Table S19. Average, minimal and maximal Ta−X−Ta (X = O & F1) angle values (°) from the 10 APO_DFT-D3 models of $TaOF_3$.

Model	Ta−O−Ta			Ta−F1−Ta		
	Aver.	Min	max	Aver.	min	max
1	180.0	180.0	180.0	180.0	180.0	180.0
2	180.0	180.0	180.0	180.0	180.0	180.0
3	176.2	172.6	179.9	175.3	171.0	179.7
4	176.2	172.4	180.0	175.5	171.0	180.0
5	172.2	172.1	172.3	171.7	171.5	171.8
6	176.5	172.9	180.0	175.5	171.1	180.0
7	178.2	172.9	180.0	177.7	171.0	180.0
8	178.1	172.5	180.0	177.6	171.0	180.0
9	174.2	172.0	179.8	173.5	171.0	179.7
10	176.0	172.0	179.8	175.6	171.6	179.6

Table S20. Average, shortest and longest Ta−X (X = O, F1 & F2) bond lengths (Å) from the 10 FO_DFT-D3 models of $TaOF_3$.

Model	<Ta−O>	$Ta-O_{min}$	$Ta-O_{max}$	<Ta−F1>	$Ta-F1_{min}$	$Ta-F1_{max}$	<Ta−F2>	$Ta-F2_{min}$	$Ta-F2_{max}$
1	1.887	1.886	1.887	2.094	2.093	2.094	1.890	1.890	1.890
2	1.887	1.887	1.887	2.094	2.094	2.094	1.891	1.891	1.891
3	1.888	1.881	1.897	2.091	2.079	2.095	1.890	1.886	1.894
4	1.889	1.883	1.892	2.090	2.086	2.101	1.889	1.886	1.893
5	1.890	1.883	1.896	2.088	2.085	2.092	1.890	1.883	1.897
6	1.888	1.879	1.893	2.091	2.087	2.094	1.891	1.888	1.894
7	1.887	1.880	1.892	2.092	2.088	2.096	1.890	1.887	1.893
8	1.888	1.883	1.891	2.092	2.084	2.101	1.889	1.885	1.893
9	1.889	1.880	1.898	2.089	2.079	2.100	1.890	1.883	1.897
10	1.888	1.881	1.892	2.091	2.085	2.099	1.890	1.882	1.896

Table S21. Average, minimal and maximal X−Ta−X (X = O, F1 & F2) angle values (°) from the 10 FO_DFT-D3 models of $TaOF_3$.

Model	O−Ta−O			F−Ta−F1			F−Ta−F2		
	Aver.	min	max	Aver.	min	max	Aver.	min	max
1	96.3	96.3	96.3	84.3	84.3	84.3	161.3	161.3	161.3
2	96.3	96.3	96.3	84.3	84.3	84.3	166.0	166.0	166.0
3	96.5	96.3	96.6	83.2	82.9	83.5	162.8	160.5	165.0
4	96.6	96.5	96.6	83.2	83.2	83.3	160.8	160.3	161.4
5	97.3	97.2	97.5	82.3	82.1	82.5	164.8	164.7	164.9
6	96.3	96.2	96.4	83.1	83.0	83.3	165.2	164.8	165.7
7	96.3	96.3	96.4	83.7	83.1	84.4	164.3	162.8	167.4
8	96.4	96.2	96.6	83.8	83.2	84.5	160.3	159.2	162.3
9	96.9	96.3	97.5	82.8	82.3	83.5	163.7	161.6	167.1
10	96.7	96.2	97.4	83.4	82.4	84.4	163.0	160.7	169.1

Table S22. Average, minimal and maximal Ta−X−Ta (X = O & F1) angle values (°) from the 10 FO_DFT-D3 models of $TaOF_3$.

Model	Ta−O−Ta			Ta−F1−Ta		
	Aver.	min	max	Aver.	min	max
1	180.0	180.0	180.0	180.0	180.0	180.0
2	180.0	180.0	180.0	180.0	180.0	180.0
3	175.9	171.9	179.9	176.5	173.3	179.8
4	176.0	172.1	180.0	176.5	173.1	180.0
5	172.3	172.1	172.5	172.7	172.6	172.9
6	176.8	173.6	180.0	176.0	171.9	180.0
7	178.3	173.6	180.0	177.9	171.9	180.0
8	178.2	173.1	180.0	178.0	172.1	180.0
9	174.6	172.6	179.8	174.2	171.8	179.8
10	176.3	172.6	179.8	176.1	172.4	179.8

6. New NbF_5 and TaF_5 correlations ^{19}F σ_{iso} vs δ_{iso} established with VASP

To ensure consistency, new linear regression equations between calculated, with the VASP package [1,2], ^{19}F σ_{iso} and experimental δ_{iso} values [3] were established for NbF_5 and TaF_5.

Table S23. F site, site multiplicity and Wyckoff symbol (Wyck.), experimental ^{19}F δ_{iso} ($\delta_{iso,exp}$, ppm), calculated ^{19}F σ_{iso} (σ_{iso}, ppm), calculated ^{19}F δ_{iso} ($\delta_{iso,cal}$, ppm) and the difference $\Delta\delta_{iso}$ between $\delta_{iso,exp}$ and $\delta_{iso,cal}$ from the APO_DFT-D3 and FO_DFT-D3 structures of NbF_5 and TaF_5.

F site	Wyck.	$\delta_{iso,exp}$	APO_DFT-D3			FO_DFT-D3		
			σ_{iso}	$\delta_{iso,cal}$[(1)]	$\Delta\delta_{iso}$	σ_{iso}	$\delta_{iso,cal}$[(1)]	$\Delta\delta_{iso}$
NbF_5								
F4	8j	-42.1	134.9	-41.8	0.3	132.4	-40.4	1.7
F2	4i	192.9	-92.5	192.7	0.2	-89.8	189.3	3.6
F5	8j	214.8	-113.8	214.6	0.2	-113.2	213.4	1.4
F1	4i	237.8	-134.2	235.7	2.1	-132.1	233.0	4.8
F6	8j	260.0	-159.8	262.1	2.1	-162.1	264.0	4.0
F3	8j	268.1	-165.9	268.3	0.2	-169.9	272.1	4.0
TaF_5								
F4	8	-70.5	183.7	-69.9	0.6	182.3	-69.1	1.4
F2	4	106.3	2.3	105.7	0.6	3.1	104.5	1.8
F5	8	121.6	-13.4	120.9	0.7	-13.8	120.8	0.8
F1	4	135.8	-27.0	134.0	1.8	-25.0	131.7	4.1
F6	8	166.9	-61.5	167.5	0.6	-63.1	168.6	1.7
F3	8	173.8	-70.0	175.7	1.9	-72.3	177.4	3.6

[(1)] For NbF_5 (TaF_5), the calculated ^{19}F δ_{iso} values were deduced from the equations of the linear regressions δ_{iso} (ppm) = -1.031 σ_{iso} + 97.3 (δ_{iso} (ppm) = -0.968 σ_{iso} + 107.9) and δ_{iso} (ppm) = -1.034 σ_{iso} + 96.4 (δ_{iso} (ppm) = -0.968 σ_{iso} + 107.4) for the APO_DFT-D3 and FO_DFT-D3 structures, respectively.

7. $NbOF_3$ and $TaOF_3$ calculated σ_{iso}, σ_{CSA} and η_{CSA} values.

Table S24. ^{19}F calculated σ_{iso} (σ_{iso}, ppm) of each F atom from the 10 APO_DFT-D3 models of $NbOF_3$ and (in bold italic) average σ_{iso} ($<\sigma_{iso}>$, ppm) of each F crystallographic site.

Site	Atom	Model									
		1	2	3	4	5	6	7	8	9	10
F1	F9	111.9	111.3	101.9	110.2	104.7	101.8	104.6	117.1	101.8	114.8
	F10	110.9	111.3	99.0	116.5	104.7	109.9	117.2	105.9	95.5	114.8
	F11	111.9	111.3	120.8	104.2	104.7	116.4	107.1	111.1	109.4	108.2
	F12	110.9	111.3	109.8	116.5	97.4	109.9	111.2	115.0	120.2	100.0
	F13	110.9	111.3	109.8	104.2	97.4	116.4	111.2	109.1	88.3	101.7
	F14	111.9	111.3	99.0	116.5	97.4	101.8	117.2	117.1	89.3	101.7
	F15	110.9	111.3	120.8	116.5	104.7	116.4	106.0	107.6	113.8	100.0
	F16	111.9	111.3	101.9	110.2	97.4	116.4	115.4	111.1	103.5	108.2
	$<\sigma_{iso}>$	***111.4***	***111.3***	***107.9***	***111.8***	***101.1***	***111.1***	***111.2***	***111.7***	***102.7***	***106.2***
F2	F17	-113.1	-108.5	-100.8	-101.7	-88.5	-98.5	-113.5	-116.6	-92.1	-90.0
	F18	-113.1	-108.5	-100.8	-101.7	-88.5	-98.5	-113.5	-116.6	-92.1	-90.0
	F19	-113.1	-108.5	-124.2	-127.6	-111.1	-122.0	-123.1	-128.3	-121.0	-112.6
	F20	-113.1	-108.5	-124.2	-127.6	-111.1	-122.0	-123.1	-128.3	-121.0	-112.6
	F21	-113.1	-108.5	-93.3	-127.6	-111.1	-98.5	-107.5	-116.6	-110.5	-112.4
	F22	-113.1	-108.5	-93.3	-127.6	-111.1	-98.5	-107.5	-116.6	-110.5	-112.4
	F23	-113.1	-108.5	-124.9	-127.6	-88.5	-98.5	-123.1	-102.1	-125.6	-106.3
	F24	-113.1	-108.5	-124.9	-127.6	-88.5	-98.5	-123.1	-102.1	-125.6	-106.3
	F25	-113.1	-108.5	-124.9	-101.7	-111.1	-122.0	-113.5	-112.1	-110.1	-112.4
	F26	-113.1	-108.5	-124.9	-101.7	-111.1	-122.0	-113.5	-112.1	-110.1	-112.4
	F27	-113.1	-108.5	-93.3	-101.7	-137.5	-122.0	-99.4	-128.3	-89.0	-116.8
	F28	-113.1	-108.5	-93.3	-101.7	-137.5	-122.0	-99.4	-128.3	-89.0	-116.8
	F29	-113.1	-108.5	-124.2	-127.6	-137.5	-122.0	-107.5	-112.1	-136.9	-140.2
	F30	-113.1	-108.5	-124.2	-127.6	-137.5	-122.0	-107.5	-112.1	-136.9	-140.2
	F31	-113.1	-108.5	-100.8	-101.7	-111.1	-98.5	-99.4	-102.1	-94.8	-112.6
	F32	-113.1	-108.5	-100.8	-101.7	-111.1	-98.5	-99.4	-102.1	-94.8	-112.6
	$<\sigma_{iso}>$	***-113.1***	***-108.5***	***-110.8***	***-114.6***	***-112.0***	***-110.3***	***-110.9***	***-114.8***	***-110.0***	***-112.9***

Table S25. ^{19}F calculated σ_{CSA} (σ_{CSA}, ppm) of each F atom from the 10 APO_DFT-D3 models of $NbOF_3$ and (in bold italic) average absolute value of σ_{CSA} ($<|\sigma_{CSA}|>$, ppm) of each F crystallographic site.

Site	Atom	Model									
		1	2	3	4	5	6	7	8	9	10
F1	F9	144.1	143.3	-143.2	136.7	139.9	-155.2	-152.8	-137.4	147.9	-132.1
	F10	-151.1	143.3	161.2	-138.0	139.9	134.9	136.9	-146.3	-141.8	-132.1
	F11	144.1	143.3	123.8	-146.8	139.9	137.7	-157.5	-148.3	136.6	-153.8
	F12	-151.1	143.3	-138.5	-138.0	-162.5	134.9	144.3	-130.9	-122.7	-160.1
	F13	-151.1	143.3	-138.5	-146.8	-162.5	137.7	144.3	-149.6	163.0	156.2
	F14	144.1	143.3	161.2	-138.0	-162.5	-155.2	136.9	-137.4	173.2	156.2
	F15	-151.1	143.3	123.8	-138.0	139.9	137.7	152.7	151.4	-143.2	-160.1
	F16	144.1	143.3	-143.2	136.7	-162.5	137.7	-134.0	-148.3	-149.6	-153.8
	$<\|\sigma_{CSA}\|>$	***147.6***	***143.3***	***141.7***	***139.9***	***151.2***	***141.4***	***144.9***	***143.7***	***147.2***	***150.6***
F2	F17	330.7	330.1	319.8	320.5	308.5	318.6	332.6	332.5	311.9	309.0
	F18	330.7	330.1	319.8	320.5	308.5	318.6	332.6	332.5	311.9	309.0
	F19	330.7	330.1	339.7	342.4	331.8	343.4	342.4	341.3	334.1	332.0
	F20	330.7	330.1	339.7	342.4	331.8	343.4	342.4	341.3	334.1	332.0
	F21	330.7	330.1	311.4	342.4	331.8	318.6	329.4	332.5	330.9	330.6
	F22	330.7	330.1	311.4	342.4	331.8	318.6	329.4	332.5	330.9	330.6
	F23	330.7	330.1	340.0	342.4	308.5	318.6	342.4	320.3	339.9	328.8
	F24	330.7	330.1	340.0	342.4	308.5	318.6	342.4	320.3	339.9	328.8
	F25	330.7	330.1	340.0	320.5	331.8	343.4	332.6	329.9	329.6	330.6
	F26	330.7	330.1	340.0	320.5	331.8	343.4	332.6	329.9	329.6	330.6
	F27	330.7	330.1	311.4	320.5	356.8	343.4	318.6	341.3	305.5	334.6
	F28	330.7	330.1	311.4	320.5	356.8	343.4	318.6	341.3	305.5	334.6
	F29	330.7	330.1	339.7	342.4	356.8	343.4	329.4	329.9	352.4	353.4
	F30	330.7	330.1	339.7	342.4	356.8	343.4	329.4	329.9	352.4	353.4
	F31	330.7	330.1	319.8	320.5	331.8	318.6	318.6	320.3	313.8	332.0
	F32	330.7	330.1	319.8	320.5	331.8	318.6	318.6	320.3	313.8	332.0
	$<\|\sigma_{CSA}\|>$	***330.7***	***330.1***	***327.7***	***331.4***	***332.2***	***331.0***	***330.7***	***331.0***	***327.3***	***331.4***

Table S26. ^{19}F calculated η_{CSA} of each F atom from the 10 APO_DFT-D3 models of $NbOF_3$ and (in bold italic) average η_{CSA} ($<\eta_{CSA}>$, ppm) of each F crystallographic site.

Site	Atom	Model									
		1	2	3	4	5	6	7	8	9	10
F1	F9	0.84	0.91	0.86	0.88	1.00	0.84	0.65	0.68	0.62	0.94
	F10	0.58	0.91	0.57	0.67	1.00	0.95	0.81	0.75	0.99	0.94
	F11	0.84	0.91	0.82	0.94	1.00	0.81	0.69	0.63	0.91	0.74
	F12	0.58	0.91	0.93	0.67	0.81	0.95	0.87	0.98	0.98	0.65
	F13	0.58	0.91	0.93	0.94	0.81	0.81	0.87	0.80	0.75	0.80
	F14	0.84	0.91	0.57	0.67	0.81	0.84	0.81	0.68	0.42	0.80
	F15	0.58	0.91	0.82	0.67	1.00	0.81	0.74	0.70	0.77	0.65
	F16	0.84	0.91	0.86	0.88	0.81	0.81	0.88	0.63	0.90	0.74
	$<\eta_{CSA}>$	***0.71***	***0.91***	***0.79***	***0.79***	***0.91***	***0.85***	***0.79***	***0.73***	***0.79***	***0.78***
F2	F17	0.12	0.03	0.21	0.13	0.03	0.06	0.10	0.08	0.05	0.03
	F18	0.12	0.03	0.21	0.13	0.03	0.06	0.10	0.08	0.05	0.03
	F19	0.12	0.03	0.41	0.11	0.11	0.09	0.13	0.10	0.51	0.12
	F20	0.12	0.03	0.41	0.11	0.11	0.09	0.13	0.10	0.51	0.12
	F21	0.12	0.03	0.27	0.11	0.11	0.06	0.06	0.08	0.04	0.10
	F22	0.12	0.03	0.27	0.11	0.11	0.06	0.06	0.08	0.04	0.10
	F23	0.12	0.03	0.26	0.11	0.03	0.06	0.13	0.10	0.43	0.09
	F24	0.12	0.03	0.26	0.11	0.03	0.06	0.13	0.10	0.43	0.09
	F25	0.12	0.03	0.26	0.13	0.11	0.09	0.10	0.15	0.14	0.10
	F26	0.12	0.03	0.26	0.13	0.11	0.09	0.10	0.15	0.14	0.10
	F27	0.12	0.03	0.27	0.13	0.01	0.09	0.02	0.10	0.49	0.04
	F28	0.12	0.03	0.27	0.13	0.01	0.09	0.02	0.10	0.49	0.04
	F29	0.12	0.03	0.41	0.11	0.01	0.09	0.06	0.15	0.08	0.08
	F30	0.12	0.03	0.41	0.11	0.01	0.09	0.06	0.15	0.08	0.08
	F31	0.12	0.03	0.21	0.13	0.11	0.06	0.02	0.10	0.31	0.12
	F32	0.12	0.03	0.21	0.13	0.11	0.06	0.02	0.10	0.31	0.12
	$<\eta_{CSA}>$	***0.12***	***0.03***	***0.29***	***0.12***	***0.06***	***0.08***	***0.08***	***0.11***	***0.25***	***0.08***

Table S27. ^{19}F calculated σ_{iso} (σ_{iso}, ppm) of each F atom from the 10 FO_DFT-D3 models of $NbOF_3$ and (in bold italic) average σ_{iso} ($<\sigma_{iso}>$, ppm) of each F crystallographic site.

Site	Atom	Model									
		1	2	3	4	5	6	7	8	9	10
F1	F9	110.8	109.1	119.4	116.4	104.1	115.3	116.0	116.8	113.6	114.4
	F10	110.8	109.1	119.4	116.4	104.1	115.3	116.0	116.8	110.0	114.4
	F11	110.8	109.1	107.8	116.4	104.1	115.3	114.6	114.8	103.7	107.5
	F12	110.8	109.1	107.8	116.4	104.1	115.3	109.6	110.7	99.7	107.5
	F13	110.4	109.1	99.5	109.6	96.8	108.6	109.6	110.7	92.3	100.7
	F14	110.4	109.1	99.5	109.6	96.8	108.6	106.0	108.6	92.3	100.7
	F15	110.4	109.1	95.1	103.2	96.8	100.4	103.9	106.4	85.5	100.0
	F16	110.4	109.1	95.1	103.2	96.8	100.4	103.9	105.9	83.5	100.0
	$<\sigma_{iso}>$	***110.6***	***109.1***	***105.5***	***111.4***	***100.4***	***109.9***	***110.0***	***111.3***	***97.6***	***105.7***
F2	F17	-112.4	-107.6	-91.9	-100.5	-86.9	-97.1	-98.0	-101.2	-87.6	-88.4
	F18	-112.4	-107.6	-91.9	-100.5	-86.9	-97.1	-98.0	-101.2	-87.6	-88.4
	F19	-112.4	-107.6	-91.9	-100.5	-86.9	-97.1	-98.0	-101.2	-88.7	-105.2
	F20	-112.4	-107.6	-91.9	-100.5	-86.9	-97.1	-98.0	-101.2	-88.7	-105.2
	F21	-112.4	-107.6	-99.7	-100.5	-108.9	-97.1	-106.7	-111.4	-94.7	-110.9
	F22	-112.4	-107.6	-99.7	-100.5	-108.9	-97.1	-106.7	-111.4	-94.7	-110.9
	F23	-112.4	-107.6	-99.7	-100.5	-108.9	-97.1	-106.7	-111.4	-108.7	-110.9
	F24	-112.4	-107.6	-99.7	-100.5	-108.9	-97.1	-106.7	-111.4	-108.7	-110.9
	F25	-112.4	-107.6	-123.6	-126.1	-108.9	-120.3	-112.3	-115.0	-109.0	-111.0
	F26	-112.4	-107.6	-123.6	-126.1	-108.9	-120.3	-112.3	-115.0	-109.0	-111.0
	F27	-112.4	-107.6	-123.6	-126.1	-108.9	-120.3	-112.3	-115.0	-118.5	-111.0
	F28	-112.4	-107.6	-123.6	-126.1	-108.9	-120.3	-112.3	-115.0	-118.5	-111.0
	F29	-112.4	-107.6	-124.0	-126.1	-134.6	-120.3	-122.0	-126.7	-123.6	-115.4
	F30	-112.4	-107.6	-124.0	-126.1	-134.6	-120.3	-122.0	-126.7	-123.6	-115.4
	F31	-112.4	-107.6	-124.0	-126.1	-134.6	-120.3	-122.0	-126.7	-132.1	-138.4
	F32	-112.4	-107.6	-124.0	-126.1	-134.6	-120.3	-122.0	-126.7	-132.1	-138.4
	$<\sigma_{iso}>$	***-112.4***	***-107.6***	***-109.8***	***-113.3***	***-109.8***	***-108.7***	***-109.7***	***-113.6***	***-107.9***	***-111.4***

Table S28. ^{19}F calculated σ_{CSA} (σ_{CSA}, ppm) of each F atom from the 10 FO_DFT-D3 models of $NbOF_3$ and (in bold italic) average absolute value of σ_{CSA} ($<|\sigma_{CSA}|>$, ppm) of each F crystallographic site.

Site	Atom	Model									
		1	2	3	4	5	6	7	8	9	10
F1	F9	144.7	144.9	-141.7	137.0	140.1	-154.0	-150.9	-136.7	149.0	-130.7
	F10	-150.8	144.9	165.0	-136.9	140.1	135.3	137.4	-144.0	145.3	-130.7
	F11	144.7	144.9	125.3	-146.0	140.1	138.6	-157.7	-136.7	144.9	-153.3
	F12	-150.8	144.9	-137.0	-136.9	-159.7	135.3	145.7	-147.7	129.5	-158.2
	F13	-150.8	144.9	-137.0	-146.0	-159.7	138.6	145.7	130.2	168.4	157.0
	F14	144.7	144.9	165.0	-136.9	-159.7	-154.0	137.4	-148.4	176.3	157.0
	F15	-150.8	144.9	125.3	-136.9	140.1	138.6	153.8	151.8	-135.6	-158.2
	F16	144.7	144.9	-141.7	137.0	-159.7	138.6	-132.7	-147.7	155.5	-153.3
	$<\|\sigma_{CSA}\|>$	***147.7***	***144.9***	***142.3***	***139.2***	***149.9***	***141.6***	***145.2***	***142.9***	***150.6***	***149.8***
F2	F17	329.8	328.8	318.4	319.1	306.2	316.7	331.2	331.3	305.8	307.2
	F18	329.8	328.8	318.4	319.1	306.2	316.7	331.2	331.3	305.8	307.2
	F19	329.8	328.8	338.8	341.2	329.6	341.8	341.3	340.4	331.2	330.4
	F20	329.8	328.8	338.8	341.2	329.6	341.8	341.3	340.4	331.2	330.4
	F21	329.8	328.8	309.0	341.2	329.6	316.7	328.1	331.3	328.4	329.1
	F22	329.8	328.8	309.0	341.2	329.6	316.7	328.1	331.3	328.4	329.1
	F23	329.8	328.8	338.6	341.2	306.2	316.7	341.3	319.1	337.8	327.2
	F24	329.8	328.8	338.6	341.2	306.2	316.7	341.3	319.1	337.8	327.2
	F25	329.8	328.8	338.6	319.1	329.6	341.8	331.2	329.0	325.2	329.1
	F26	329.8	328.8	338.6	319.1	329.6	341.8	331.2	329.0	325.2	329.1
	F27	329.8	328.8	309.0	319.1	354.5	341.8	316.9	340.4	304.0	333.1
	F28	329.8	328.8	309.0	319.1	354.5	341.8	316.9	340.4	304.0	333.1
	F29	329.8	328.8	338.8	341.2	354.5	341.8	328.1	329.0	346.8	352.2
	F30	329.8	328.8	338.8	341.2	354.5	341.8	328.1	329.0	346.8	352.2
	F31	329.8	328.8	318.4	319.1	329.6	316.7	316.9	319.1	312.9	330.4
	F32	329.8	328.8	318.4	319.1	329.6	316.7	316.9	319.1	312.9	330.4
	$<\|\sigma_{CSA}\|>$	***329.8***	***328.8***	***326.2***	***330.1***	***330.0***	***329.2***	***329.4***	***329.9***	***324.0***	***329.8***

Table S29. ^{19}F calculated η_{CSA} of each F atom from the 10 FO_DFT-D3 models of $NbOF_3$ and (in bold italic) average η_{CSA} ($<\eta_{CSA}>$, ppm) of each F crystallographic site.

Site	Atom	Model									
		1	2	3	4	5	6	7	8	9	10
F1	F9	0.84	0.90	0.91	0.85	0.95	0.87	0.67	0.69	0.59	0.96
	F10	0.58	0.90	0.54	0.68	0.95	0.91	0.80	0.79	0.93	0.96
	F11	0.84	0.90	0.76	0.97	0.95	0.78	0.70	0.69	0.72	0.75
	F12	0.58	0.90	0.99	0.68	0.86	0.91	0.85	0.64	0.76	0.67
	F13	0.58	0.90	0.99	0.97	0.86	0.78	0.85	0.98	0.67	0.77
	F14	0.84	0.90	0.54	0.68	0.86	0.87	0.80	0.83	0.38	0.77
	F15	0.58	0.90	0.76	0.68	0.95	0.78	0.73	0.70	0.99	0.67
	F16	0.84	0.90	0.91	0.85	0.86	0.78	0.91	0.64	0.87	0.75
	$\boldsymbol{<\eta_{CSA}>}$	***0.71***	***0.90***	***0.80***	***0.80***	***0.90***	***0.84***	***0.79***	***0.74***	***0.74***	***0.79***
F2	F17	0.12	0.02	0.24	0.13	0.04	0.07	0.09	0.07	0.28	0.02
	F18	0.12	0.02	0.24	0.13	0.04	0.07	0.09	0.07	0.28	0.02
	F19	0.12	0.02	0.43	0.10	0.11	0.09	0.13	0.09	0.54	0.12
	F20	0.12	0.02	0.43	0.10	0.11	0.09	0.13	0.09	0.54	0.12
	F21	0.12	0.02	0.32	0.10	0.11	0.07	0.05	0.07	0.28	0.10
	F22	0.12	0.02	0.32	0.10	0.11	0.07	0.05	0.07	0.28	0.10
	F23	0.12	0.02	0.29	0.10	0.04	0.07	0.13	0.10	0.46	0.09
	F24	0.12	0.02	0.29	0.10	0.04	0.07	0.13	0.10	0.46	0.09
	F25	0.12	0.02	0.29	0.13	0.11	0.09	0.09	0.15	0.45	0.10
	F26	0.12	0.02	0.29	0.13	0.11	0.09	0.09	0.15	0.45	0.10
	F27	0.12	0.02	0.32	0.13	0.00	0.09	0.02	0.09	0.52	0.03
	F28	0.12	0.02	0.32	0.13	0.00	0.09	0.02	0.09	0.52	0.03
	F29	0.12	0.02	0.43	0.10	0.00	0.09	0.05	0.15	0.32	0.08
	F30	0.12	0.02	0.43	0.10	0.00	0.09	0.05	0.15	0.32	0.08
	F31	0.12	0.02	0.24	0.13	0.11	0.07	0.02	0.10	0.34	0.12
	F32	0.12	0.02	0.24	0.13	0.11	0.07	0.02	0.10	0.34	0.12
	$\boldsymbol{<\eta_{CSA}>}$	***0.12***	***0.02***	***0.32***	***0.12***	***0.07***	***0.08***	***0.08***	***0.10***	***0.40***	***0.08***

Table S30. ^{19}F calculated σ_{iso} (σ_{iso}, ppm) of each F atom from the 10 APO_DFT-D3 models of $TaOF_3$ and (in bold italic) average σ_{iso} ($<\sigma_{iso}>$, ppm) of each F crystallographic site.

Site	Atom	Model									
		1	2	3	4	5	6	7	8	9	10
F1	F9	168.4	168.0	165.5	167.9	164.4	171.2	165.5	171.1	167.5	169.5
	F10	167.6	168.0	165.7	170.8	164.4	167.4	171.4	165.8	173.0	169.5
	F11	168.4	168.0	173.2	165.0	164.4	171.2	166.4	167.5	161.3	162.8
	F12	167.6	168.0	169.7	170.8	161.2	167.4	167.9	169.8	162.0	162.8
	F13	167.6	168.0	169.7	165.0	161.2	164.4	167.9	166.5	162.4	162.4
	F14	168.4	168.0	165.7	170.8	161.2	171.2	165.5	171.1	169.3	166.4
	F15	167.6	168.0	173.2	170.8	164.4	164.4	171.4	166.3	164.6	166.4
	F16	168.4	168.0	165.5	167.9	161.2	171.2	169.3	167.5	164.6	162.4
	$<\sigma_{iso}>$	***168.0***	***168.0***	***168.5***	***168.6***	***162.8***	***168.5***	***168.2***	***168.2***	***165.6***	***165.3***
F2	F17	-7.9	-5.2	-1.2	-0.7	6.8	1.2	-8.5	-10.7	6.9	7.2
	F18	-7.9	-5.2	-1.2	-0.7	6.8	1.2	-8.5	-10.7	6.9	7.2
	F19	-7.9	-5.2	-14.7	-17.9	-6.5	-14.4	-14.7	-18.1	-14.2	-8.2
	F20	-7.9	-5.2	-14.7	-17.9	-6.5	-14.4	-14.7	-18.1	-14.2	-8.2
	F21	-7.9	-5.2	1.1	-17.9	-6.5	1.2	-5.1	-10.7	-7.0	-6.8
	F22	-7.9	-5.2	1.1	-17.9	-6.5	1.2	-5.1	-10.7	-7.0	-6.8
	F23	-7.9	-5.2	-18.3	-17.9	6.8	1.2	-14.7	-0.5	-18.4	-4.7
	F24	-7.9	-5.2	-18.3	-17.9	6.8	1.2	-14.7	-0.5	-18.4	-4.7
	F25	-7.9	-5.2	-18.3	-0.7	-6.5	-14.4	-8.5	-7.9	-6.9	-6.8
	F26	-7.9	-5.2	-18.3	-0.7	-6.5	-14.4	-8.5	-7.9	-6.9	-6.8
	F27	-7.9	-5.2	1.1	-0.7	-24.6	-14.4	0.9	-18.1	1.6	-11.1
	F28	-7.9	-5.2	1.1	-0.7	-24.6	-14.4	0.9	-18.1	1.6	-11.1
	F29	-7.9	-5.2	-14.7	-17.9	-24.6	-14.4	-5.1	-7.9	-25.9	-26.3
	F30	-7.9	-5.2	-14.7	-17.9	-24.6	-14.4	-5.1	-7.9	-25.9	-26.3
	F31	-7.9	-5.2	-1.2	-0.7	-6.5	1.2	0.9	-0.5	-1.3	-8.2
	F32	-7.9	-5.2	-1.2	-0.7	-6.5	1.2	0.9	-0.5	-1.3	-8.2
	$<\sigma_{iso}>$	***-7.9***	***-5.2***	***-8.3***	***-9.3***	***-7.7***	***-6.6***	***-6.8***	***-9.3***	***-8.2***	***-8.1***

Table S31. ^{19}F calculated σ_{CSA} (σ_{CSA}, ppm) of each F atom from the 10 APO_DFT-D3 models of $TaOF_3$ and (in bold italic) average absolute value of σ_{CSA} ($<|\sigma_{CSA}|>$, ppm) of each F crystallographic site.

Site	Atom	Model									
		1	2	3	4	5	6	7	8	9	10
F1	F9	124.1	123.4	110.1	117.6	120.0	119.9	-110.3	-109.7	117.2	112.6
	F10	-117.3	123.4	128.9	-110.1	120.0	116.9	119.5	110.7	108.1	112.6
	F11	124.1	123.4	108.5	121.4	120.0	119.9	-120.0	-115.5	124.1	131.1
	F12	-117.3	123.4	-112.4	-110.1	124.5	116.9	124.1	113.4	-116.4	131.1
	F13	-117.3	123.4	-112.4	121.4	124.5	120.9	124.1	-116.5	131.6	-115.8
	F14	124.1	123.4	128.9	-110.1	124.5	119.9	128.9	-109.7	-113.3	-118.2
	F15	-117.3	123.4	108.5	-110.1	120.0	120.9	119.5	128.4	121.3	-118.2
	F16	124.1	123.4	110.1	117.6	124.5	119.9	111.5	-115.5	119.9	-115.8
	$<\|\sigma_{CSA}\|>$	***120.7***	***123.4***	***115.0***	***114.8***	***122.3***	***119.4***	***119.7***	***114.9***	***119.0***	***119.4***
F2	F17	268.1	267.8	262.8	262.0	255.1	261.4	269.8	269.7	254.7	254.3
	F18	268.1	267.8	262.8	262.0	255.1	261.4	269.8	269.7	254.7	254.3
	F19	268.1	267.8	275.1	276.1	269.2	276.1	275.1	275.0	276.1	269.5
	F20	268.1	267.8	275.1	276.1	269.2	276.1	275.1	275.0	276.1	269.5
	F21	268.1	267.8	260.8	276.1	269.2	261.4	267.8	269.7	268.8	267.9
	F22	268.1	267.8	260.8	276.1	269.2	261.4	267.8	269.7	268.8	267.9
	F23	268.1	267.8	276.8	276.1	255.1	261.4	275.1	261.3	277.9	267.6
	F24	268.1	267.8	276.8	276.1	255.1	261.4	275.1	261.3	277.9	267.6
	F25	268.1	267.8	276.8	262.0	269.2	276.1	269.8	268.1	268.7	267.9
	F26	268.1	267.8	276.8	262.0	269.2	276.1	269.8	268.1	268.7	267.9
	F27	268.1	267.8	260.8	262.0	284.7	276.1	261.0	275.0	260.9	271.5
	F28	268.1	267.8	260.8	262.0	284.7	276.1	261.0	275.0	260.9	271.5
	F29	268.1	267.8	275.1	276.1	284.7	276.1	267.8	268.1	283.7	282.5
	F30	268.1	267.8	275.1	276.1	284.7	276.1	267.8	268.1	283.7	282.5
	F31	268.1	267.8	262.8	262.0	269.2	261.4	261.0	261.3	263.4	269.5
	F32	268.1	267.8	262.8	262.0	269.2	261.4	261.0	261.3	263.4	269.5
	$<\|\sigma_{CSA}\|>$	***268.1***	***267.8***	***268.9***	***269.0***	***269.6***	***268.7***	***268.4***	***268.5***	***269.3***	***268.8***

Table S32. ^{19}F calculated η_{CSA} of each F atom from the 10 APO_DFT-D3 models of $TaOF_3$ and (in bold italic) average η_{CSA} ($<\eta_{CSA}>$, ppm) of each F crystallographic site.

Site	Atom	Model									
		1	2	3	4	5	6	7	8	9	10
F1	F9	0.68	0.73	0.96	0.60	0.71	0.66	0.98	0.88	0.63	0.86
	F10	0.80	0.73	0.47	0.87	0.71	0.67	0.67	0.91	0.83	0.86
	F11	0.68	0.73	0.82	0.74	0.71	0.66	0.92	0.85	0.86	0.55
	F12	0.80	0.73	1.00	0.87	0.86	0.67	0.70	0.82	0.94	0.55
	F13	0.80	0.73	1.00	0.74	0.86	0.82	0.70	0.99	0.55	0.96
	F14	0.68	0.73	0.47	0.87	0.86	0.66	0.49	0.88	0.98	0.96
	F15	0.80	0.73	0.82	0.87	0.71	0.82	0.67	0.45	0.78	0.96
	F16	0.68	0.73	0.96	0.60	0.86	0.66	0.91	0.85	0.72	0.96
	$<\eta_{CSA}>$	***0.74***	***0.73***	***0.81***	***0.77***	***0.78***	***0.70***	***0.76***	***0.83***	***0.79***	***0.83***
F2	F17	0.11	0.02	0.06	0.12	0.02	0.04	0.08	0.08	0.05	0.04
	F18	0.11	0.02	0.06	0.12	0.02	0.04	0.08	0.08	0.05	0.04
	F19	0.11	0.02	0.13	0.10	0.07	0.05	0.10	0.09	0.10	0.09
	F20	0.11	0.02	0.13	0.10	0.07	0.05	0.10	0.09	0.10	0.09
	F21	0.11	0.02	0.04	0.10	0.07	0.04	0.05	0.08	0.05	0.09
	F22	0.11	0.02	0.04	0.10	0.07	0.04	0.05	0.08	0.05	0.09
	F23	0.11	0.02	0.08	0.10	0.02	0.04	0.10	0.10	0.06	0.08
	F24	0.11	0.02	0.08	0.10	0.02	0.04	0.10	0.10	0.06	0.08
	F25	0.11	0.02	0.08	0.12	0.07	0.05	0.08	0.13	0.12	0.09
	F26	0.11	0.02	0.08	0.12	0.07	0.05	0.08	0.13	0.12	0.09
	F27	0.11	0.02	0.04	0.12	0.01	0.05	0.03	0.09	0.03	0.04
	F28	0.11	0.02	0.04	0.12	0.01	0.05	0.03	0.09	0.03	0.04
	F29	0.11	0.02	0.13	0.10	0.01	0.05	0.05	0.13	0.08	0.07
	F30	0.11	0.02	0.13	0.10	0.01	0.05	0.05	0.13	0.08	0.07
	F31	0.11	0.02	0.06	0.12	0.07	0.04	0.03	0.10	0.08	0.09
	F32	0.11	0.02	0.06	0.12	0.07	0.04	0.03	0.10	0.08	0.09
	$<\eta_{CSA}>$	***0.11***	***0.02***	***0.08***	***0.11***	***0.04***	***0.05***	***0.06***	***0.10***	***0.07***	***0.07***

Table S33. ^{19}F calculated σ_{iso} (σ_{iso}, ppm) of each F atom from the 10 FO_DFT-D3 models of $TaOF_3$ and (in bold italic) average σ_{iso} ($<\sigma_{iso}>$, ppm) of each F crystallographic site.

Site	Atom	Model									
		1	2	3	4	5	6	7	8	9	10
F1	F9	166.6	165.5	171.9	169.3	163.2	168.6	168.9	169.6	171.7	168.6
	F10	166.6	165.5	171.9	169.3	163.2	168.6	168.9	169.6	167.0	168.6
	F11	166.6	165.5	167.2	169.3	163.2	168.6	168.6	169.1	166.8	164.4
	F12	166.6	165.5	167.2	169.3	163.2	168.6	165.9	166.4	163.4	164.4
	F13	166.6	165.5	164.4	167.4	159.2	166.6	165.9	166.4	163.0	160.9
	F14	166.6	165.5	164.4	167.4	159.2	166.6	164.4	165.3	160.6	160.9
	F15	166.6	165.5	164.2	163.8	159.2	162.5	164.1	165.2	160.5	160.7
	F16	166.6	165.5	164.2	163.8	159.2	162.5	163.7	165.0	159.2	160.7
	$<\sigma_{iso}>$	***166.6***	***165.5***	***166.9***	***167.5***	***161.2***	***166.6***	***166.3***	***167.1***	***164.0***	***163.6***
F2	F17	-12.6	-9.7	-2.2	-4.4	4.0	-2.5	-2.9	-4.7	3.5	3.2
	F18	-12.6	-9.7	-2.2	-4.4	4.0	-2.5	-2.9	-4.7	3.5	3.2
	F19	-12.6	-9.7	-2.2	-4.4	4.0	-2.5	-2.9	-4.7	-1.5	-8.4
	F20	-12.6	-9.7	-2.2	-4.4	4.0	-2.5	-2.9	-4.7	-1.5	-8.4
	F21	-12.6	-9.7	-4.8	-4.4	-9.7	-2.5	-9.1	-12.0	-4.2	-10.8
	F22	-12.6	-9.7	-4.8	-4.4	-9.7	-2.5	-9.1	-12.0	-4.2	-10.8
	F23	-12.6	-9.7	-4.8	-4.4	-9.7	-2.5	-9.1	-12.0	-10.4	-10.8
	F24	-12.6	-9.7	-4.8	-4.4	-9.7	-2.5	-9.1	-12.0	-10.4	-10.8
	F25	-12.6	-9.7	-18.7	-22.2	-9.7	-18.5	-12.6	-14.8	-10.5	-11.8
	F26	-12.6	-9.7	-18.7	-22.2	-9.7	-18.5	-12.6	-14.8	-10.5	-11.8
	F27	-12.6	-9.7	-18.7	-22.2	-9.7	-18.5	-12.6	-14.8	-17.8	-11.8
	F28	-12.6	-9.7	-18.7	-22.2	-9.7	-18.5	-12.6	-14.8	-17.8	-11.8
	F29	-12.6	-9.7	-22.7	-22.2	-28.9	-18.5	-19.4	-22.5	-22.3	-14.7
	F30	-12.6	-9.7	-22.7	-22.2	-28.9	-18.5	-19.4	-22.5	-22.3	-14.7
	F31	-12.6	-9.7	-22.7	-22.2	-28.9	-18.5	-19.4	-22.5	-30.3	-30.9
	F32	-12.6	-9.7	-22.7	-22.2	-28.9	-18.5	-19.4	-22.5	-30.3	-30.9
	$<\sigma_{iso}>$	***-12.6***	***-9.7***	***-12.1***	***-13.3***	***-11.0***	***-10.5***	***-11.0***	***-13.5***	***-11.7***	***-12.0***

Table S34. ^{19}F calculated σ_{CSA} (σ_{CSA}, ppm) of each F atom from the 10 FO_DFT-D3 models of $TaOF_3$ and (in bold italic) average absolute value of σ_{CSA} ($<|\sigma_{CSA}|>$, ppm) of each F crystallographic site.

Site	Atom	Model									
		1	2	3	4	5	6	7	8	9	10
F1	F9	125.2	125.4	-113.8	118.5	121.0	122.8	-116.3	-114.4	121.0	113.5
	F10	-121.1	125.4	130.1	-114.8	121.0	117.6	121.5	112.6	-122.7	113.5
	F11	125.2	125.4	109.8	122.7	121.0	121.5	-124.8	-114.4	118.0	-122.1
	F12	-121.1	125.4	-117.3	-114.8	126.0	117.6	125.5	-119.2	109.4	-122.5
	F13	-121.1	125.4	-117.3	122.7	126.0	121.5	125.5	114.5	126.0	132.8
	F14	125.2	125.4	130.1	-114.8	126.0	122.8	121.5	-119.0	133.1	132.8
	F15	-121.1	125.4	109.8	-114.8	121.0	121.5	130.6	129.3	-118.1	-122.5
	F16	125.2	125.4	-113.8	118.5	126.0	121.5	112.7	-119.2	122.7	-122.1
	$<\|\sigma_{CSA}\|>$	***123.2***	***125.4***	***117.7***	***117.7***	***123.5***	***120.8***	***122.3***	***117.8***	***121.4***	***122.8***
F2	F17	272.6	272.4	266.1	265.4	257.4	264.7	273.7	273.8	257.4	257.4
	F18	272.6	272.4	266.1	265.4	257.4	264.7	273.7	273.8	257.4	257.4
	F19	272.6	272.4	279.7	280.3	272.5	280.5	279.9	279.5	280.2	273.3
	F20	272.6	272.4	279.7	280.3	272.5	280.5	279.9	279.5	280.2	273.3
	F21	272.6	272.4	264.0	280.3	272.5	264.7	272.0	273.8	272.4	271.9
	F22	272.6	272.4	264.0	280.3	272.5	264.7	272.0	273.8	272.4	271.9
	F23	272.6	272.4	281.1	280.3	257.4	264.7	279.9	265.2	281.7	271.6
	F24	272.6	272.4	281.1	280.3	257.4	264.7	279.9	265.2	281.7	271.6
	F25	272.6	272.4	281.1	265.4	272.5	280.5	273.7	272.3	272.2	271.9
	F26	272.6	272.4	281.1	265.4	272.5	280.5	273.7	272.3	272.2	271.9
	F27	272.6	272.4	264.0	265.4	288.9	280.5	264.6	279.5	263.9	274.9
	F28	272.6	272.4	264.0	265.4	288.9	280.5	264.6	279.5	263.9	274.9
	F29	272.6	272.4	279.7	280.3	288.9	280.5	272.0	272.3	288.3	287.4
	F30	272.6	272.4	279.7	280.3	288.9	280.5	272.0	272.3	288.3	287.4
	F31	272.6	272.4	266.1	265.4	272.5	264.7	264.6	265.2	266.3	273.3
	F32	272.6	272.4	266.1	265.4	272.5	264.7	264.6	265.2	266.3	273.3
	$<\|\sigma_{CSA}\|>$	***272.6***	***272.4***	***272.7***	***272.9***	***272.8***	***272.6***	***272.6***	***272.7***	***272.8***	***272.7***

Table S35. ^{19}F calculated η_{CSA} of each F atom from the 10 FO_DFT-D3 models of $TaOF_3$ and (in bold italic) average η_{CSA} (<η_{CSA}>, ppm) of each F crystallographic site.

Site	Atom	Model									
		1	2	3	4	5	6	7	8	9	10
F1	F9	0.73	0.79	0.95	0.69	0.80	0.91	0.90	0.83	0.80	0.90
	F10	0.76	0.79	0.57	0.82	0.80	0.76	0.73	0.98	0.87	0.90
	F11	0.73	0.79	0.87	0.83	0.80	0.73	0.88	0.83	0.71	0.93
	F12	0.76	0.79	0.96	0.82	0.95	0.76	0.76	0.81	0.88	0.88
	F13	0.76	0.79	0.96	0.83	0.95	0.73	0.76	0.86	0.95	0.65
	F14	0.73	0.79	0.57	0.82	0.95	0.91	0.73	1.00	0.64	0.65
	F15	0.76	0.79	0.87	0.82	0.80	0.73	0.59	0.56	0.94	0.88
	F16	0.73	0.79	0.95	0.69	0.95	0.73	0.95	0.81	0.87	0.93
	<η_{CSA}>	***0.75***	***0.79***	***0.84***	***0.79***	***0.87***	***0.78***	***0.78***	***0.83***	***0.83***	***0.84***
F2	F17	0.11	0.00	0.07	0.12	0.00	0.04	0.09	0.08	0.05	0.04
	F18	0.11	0.00	0.07	0.12	0.00	0.04	0.09	0.08	0.05	0.04
	F19	0.11	0.00	0.13	0.10	0.08	0.06	0.10	0.09	0.10	0.09
	F20	0.11	0.00	0.13	0.10	0.08	0.06	0.10	0.09	0.10	0.09
	F21	0.11	0.00	0.03	0.10	0.08	0.04	0.04	0.08	0.06	0.09
	F22	0.11	0.00	0.03	0.10	0.08	0.04	0.04	0.08	0.06	0.09
	F23	0.11	0.00	0.08	0.10	0.00	0.04	0.10	0.10	0.07	0.05
	F24	0.11	0.00	0.08	0.10	0.00	0.04	0.10	0.10	0.07	0.05
	F25	0.11	0.00	0.08	0.12	0.08	0.06	0.09	0.13	0.12	0.09
	F26	0.11	0.00	0.08	0.12	0.08	0.06	0.09	0.13	0.12	0.09
	F27	0.11	0.00	0.03	0.12	0.03	0.06	0.03	0.09	0.02	0.05
	F28	0.11	0.00	0.03	0.12	0.03	0.06	0.03	0.09	0.02	0.05
	F29	0.11	0.00	0.13	0.10	0.03	0.06	0.04	0.13	0.08	0.08
	F30	0.11	0.00	0.13	0.10	0.03	0.06	0.04	0.13	0.08	0.08
	F31	0.11	0.00	0.07	0.12	0.08	0.04	0.03	0.10	0.08	0.09
	F32	0.11	0.00	0.07	0.12	0.08	0.04	0.03	0.10	0.08	0.09
	<η_{CSA}>	***0.11***	***0.00***	***0.08***	***0.11***	***0.05***	***0.05***	***0.06***	***0.10***	***0.07***	***0.07***

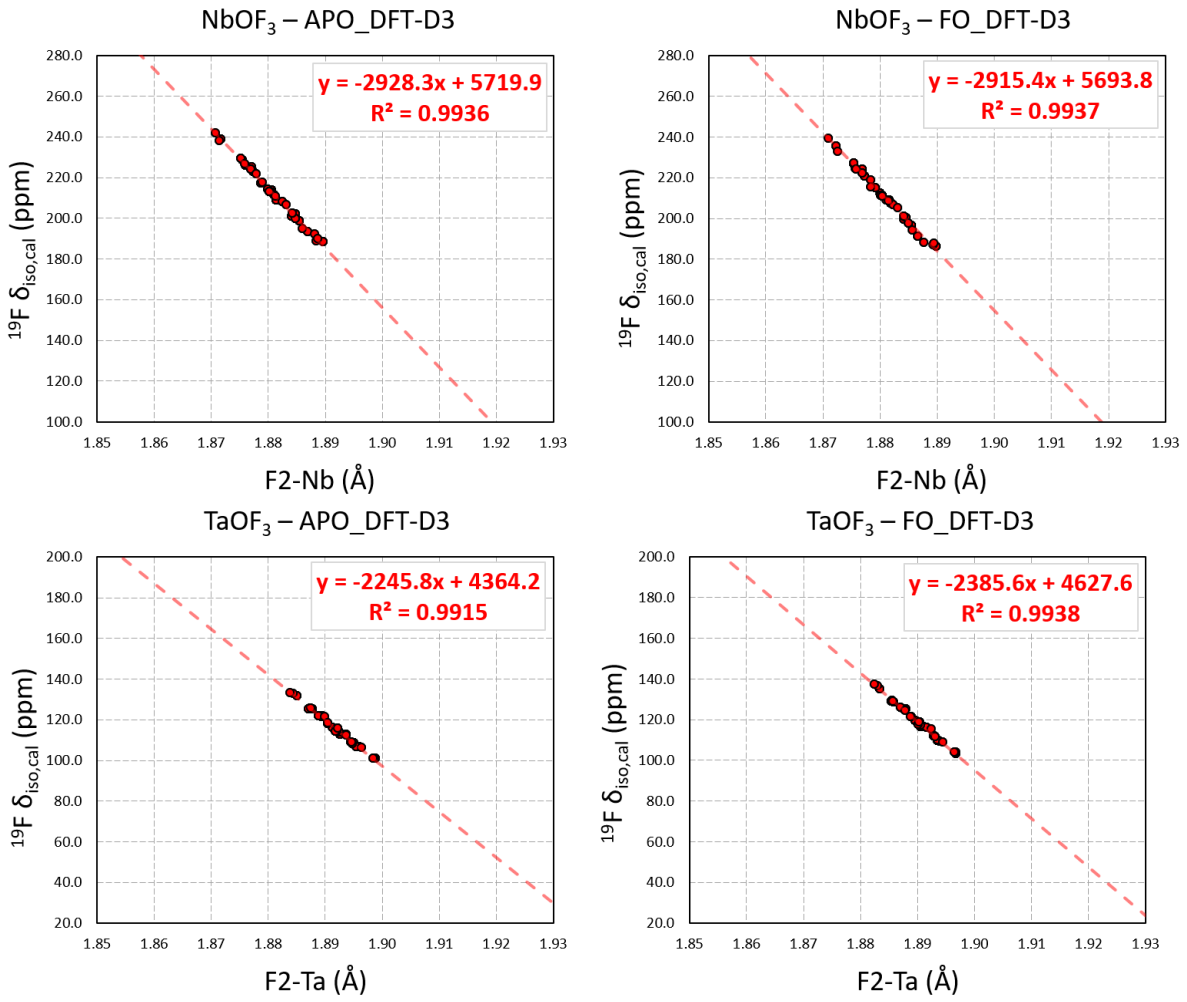


Figure S10. Calculated ^{19}F δ_{iso} of F2 atoms as a function of F2–M (M = Nb, Ta) bond lengths (red dots) from the APO_DFT-D3 and FO_DFT-D3 models of $NbOF_3$ and $TaOF_3$. The dashed lines represent the linear regressions (whose equations are given).

8. Hydroxylated $NbOF_3$ structural features.

Table S36. Average, shortest and longest Nb−F bond lengths (Å) from the 10 APO_DFT-D3 models of $NbOF_{0.875}(OH)_{0.125}F_2$.

Model	<Nb–F1>	$Nb–F1_{min}$	$Nb–F1_{max}$	<Nb–F2>	$Nb–F2_{min}$	$Nb–F2_{max}$
1	2.094	2.078	2.115	1.883	1.874	1.902
2	2.096	2.068	2.126	1.884	1.875	1.903
3	2.097	2.009	2.184	1.885	1.863	1.920
4	2.093	2.083	2.107	1.882	1.868	1.906
5	2.098	1.990	2.204	1.886	1.859	1.920
6	2.094	2.071	2.120	1.884	1.870	1.908
7	2.095	2.082	2.108	1.884	1.871	1.902
8	2.094	2.085	2.103	1.882	1.869	1.901
9	2.098	1.991	2.203	1.885	1.862	1.923
10	2.097	2.000	2.208	1.885	1.859	1.917

Table S37. Average, shortest and longest Nb−O(OH) bond lengths (Å) from the 10 APO_DFT-D3 models of $NbOF_{0.875}(OH)_{0.125}F_2$.

Model	<Nb–O>	$Nb–O_{min}$	$Nb–O_{max}$	<Nb–OH>	$Nb–OH_{min}$	$Nb–OH_{max}$
1	1.886	1.877	1.892	2.118	2.118	2.118
2	1.885	1.877	1.892	2.118	2.118	2.118
3	1.891	1.827	1.974	2.125	2.015	2.236
4	1.888	1.884	1.897	2.116	2.116	2.116
5	1.894	1.823	2.002	2.127	2.013	2.241
6	1.887	1.872	1.897	2.116	2.116	2.116
7	1.886	1.878	1.896	2.113	2.113	2.113
8	1.887	1.877	1.897	2.114	2.114	2.114
9	1.893	1.818	1.985	2.127	2.004	2.250
10	1.890	1.835	1.981	2.130	2.023	2.236

Table S38. Average, minimal and maximal X−Nb−X (X = O, OH, F1 & F2) angle values (°) from the 10 APO_DFT-D3 models of $NbOF_{0.875}(OH)_{0.125}F_2$.

Model	O−Nb−O(OH)			F−Nb−F1			F−Nb−F2		
	Aver.	min	max	Aver.	min	max	Aver.	min	max
1	95.3	91.4	96.6	84.1	83.8	84.5	161.6	160.9	162.5
2	95.4	91.5	96.8	84.0	83.7	84.6	165.9	164.6	168.3
3	95.0	80.8	100.0	83.4	82.6	83.9	161.8	159.1	163.8
4	95.0	90.7	96.4	84.2	83.7	85.1	160.5	159.8	161.2
5	97.0	89.1	101.3	82.7	82.2	83.2	162.4	161.0	163.7
6	94.9	91.4	96.2	84.0	83.5	85.0	165.0	164.0	166.0
7	95.0	91.1	96.3	84.4	84.3	84.7	164.3	162.4	167.7
8	95.0	90.6	96.4	84.5	84.2	84.8	160.2	159.2	162.0
9	95.4	80.4	100.5	82.9	82.2	83.9	161.7	159.5	163.2
10	96.7	89.5	101.0	84.0	83.0	84.7	162.5	159.4	167.0

Table S39. Average, minimal and maximal Nb−X−Nb (X = O, OH & F1) angle values (°) from the 10 APO_DFT-D3 models of $NbOF_{0.875}(OH)_{0.125}F_2$.

Model	Nb–O(OH)–Nb			Nb–F1–Nb		
	Aver.	min	max	Aver.	min	max
1	176.6	162.0	179.6	177.9	175.9	179.3
2	176.5	162.6	179.9	178.6	177.3	179.6
3	172.1	154.7	179.6	173.9	166.5	178.3
4	174.3	160.7	179.4	175.7	173.1	178.9
5	170.1	152.9	178.4	173.3	166.9	178.9
6	174.7	161.3	179.5	175.5	172.9	178.9
7	175.9	161.8	179.6	177.3	174.6	179.6
8	175.6	161.3	179.7	177.2	175.0	179.2
9	170.9	154.2	179.1	172.6	165.4	177.7
10	172.5	153.0	178.9	176.4	167.1	179.8

Table S40. Average, shortest and longest Nb−F bond lengths (Å) from the 10 APO_DFT-D3 models of $NbOF_{0.75}(OH)_{0.25}F_2$.

Model	<Nb−F1>	$Nb-F1_{min}$	$Nb-F1_{max}$	<Nb−F2>	$Nb-F2_{min}$	$Nb-F2_{max}$
1	2.094	2.076	2.115	1.884	1.879	1.890
2	2.095	2.060	2.135	1.886	1.881	1.893
3	2.101	2.005	2.209	1.889	1.868	1.930
4	2.098	2.014	2.193	1.887	1.865	1.927
5	2.102	1.988	2.221	1.889	1.861	1.925
6	2.095	2.080	2.111	1.886	1.881	1.888
7	2.094	2.067	2.127	1.887	1.873	1.909
8	2.100	2.015	2.199	1.888	1.866	1.928
9	2.101	2.002	2.210	1.889	1.863	1.930
10	2.101	2.003	2.214	1.889	1.862	1.929

Table S41. Average, shortest and longest Nb−O(OH) bond lengths (Å) from the 10 APO_DFT-D3 models of $NbOF_{0.75}(OH)_{0.25}F_2$.

Model	<Nb−O>	$Nb-O_{min}$	$Nb-O_{max}$	<Nb−OH>	$Nb-OH_{min}$	$Nb-OH_{max}$
1	1.887	1.882	1.890	2.120	2.120	2.120
2	1.886	1.872	1.894	2.120	2.120	2.120
3	1.895	1.822	1.989	2.123	2.016	2.231
4	1.893	1.827	1.988	2.129	2.004	2.249
5	1.896	1.823	2.003	2.128	2.006	2.251
6	1.886	1.876	1.892	2.114	2.114	2.114
7	1.887	1.876	1.900	2.114	2.107	2.120
8	1.893	1.826	1.978	2.126	2.017	2.231
9	1.895	1.818	2.002	2.127	2.000	2.250
10	1.894	1.827	1.993	2.129	2.014	2.243

Table S42. Average, minimal and maximal X−Nb−X (X = O, OH, F1 & F2) angle values (°) from the 10 APO_DFT-D3 models of $NbOF_{0.75}(OH)_{0.25}F_2$.

Model	O−Nb−O(OH)			F−Nb−F1			F−Nb−F2		
	Aver.	min	max	Aver.	min	max	Aver.	min	Max
1	94.6	91.2	96.5	83.7	83.7	83.7	161.3	160.1	162.5
2	94.9	91.9	96.8	84.1	84.1	84.1	165.8	163.5	168.1
3	94.2	80.3	100.5	83.5	83.1	83.8	162.7	161.0	165.4
4	95.5	80.1	100.7	83.5	83.1	84.1	161.2	157.9	163.6
5	96.8	88.7	101.7	83.2	82.9	83.6	162.4	161.6	163.0
6	94.1	91.3	96.2	85.0	85.0	85.0	164.3	164.2	164.5
7	94.5	91.4	96.4	84.6	84.1	85.2	165.0	162.9	167.7
8	94.2	80.3	100.1	83.5	83.1	84.0	160.8	159.4	163.1
9	95.5	80.1	101.6	83.2	83.0	83.6	162.4	159.9	164.7
10	95.5	81.3	101.5	83.4	82.8	84.2	162.8	159.9	166.1

Table S43. Average, minimal and maximal Nb−X−Nb (X = O, OH & F1) angle values (°) from the 10 APO_DFT-D3 models of $NbOF_{0.75}(OH)_{0.25}F_2$.

Model	Nb–O(OH)–Nb			Nb–F1–Nb		
	Aver.	min	max	Aver.	min	max
1	174.4	163.7	179.4	177.5	177.4	177.9
2	174.5	164.1	179.8	177.7	177.4	178.4
3	169.3	154.7	177.5	172.9	166.3	177.0
4	169.5	153.6	177.3	173.3	165.6	179.2
5	168.0	152.8	178.5	173.6	167.1	177.0
6	173.0	164.1	176.7	175.5	174.6	177.3
7	171.0	154.9	178.3	170.9	166.6	177.1
8	169.6	154.9	178.3	173.2	166.6	177.6
9	168.7	153.3	178.2	173.0	165.3	177.4
10	170.3	153.2	178.6	170.7	165.7	178.2

9. Hydroxylated $NbOF_3$ calculated σ_{iso}, σ_{CSA} and η_{CSA} values.

Table S44. ^{19}F calculated σ_{iso} (σ_{iso}, ppm) of each F atom from the 10 APO_DFT-D3 models of $NbOF_{0.875}(OH)_{0.125}F_2$ and (in bold italic) average σ_{iso} ($<\sigma_{iso}>$, ppm) of each F crystallographic site.

Site	Atom	Model									
		1	2	3	4	5	6	7	8	9	10
F1	F11	115.2	113.8	112.8	115.6	116.5	101.3	118.3	119.8	116.7	107.1
	F12	111.3	110.2	118.2	110.9	92.6	115.8	107.1	110.4	80.1	112.6
	F13	107.7	115.5	99.2	118.7	97.3	106.7	110.5	112.5	98.3	96.0
	F14	111.2	112.2	115.0	103.3	88.6	116.7	110.5	108.3	85.8	105.0
	F15	115.2	113.8	93.9	118.7	102.7	108.7	118.3	114.2	111.9	106.5
	F16	113.5	110.2	113.3	115.6	96.9	115.8	112.5	119.8	114.6	101.9
	F17	111.3	107.9	103.8	107.5	81.6	116.7	112.1	110.4	96.0	113.5
	$<\sigma_{iso}>$	**112.2**	**111.9**	**108.0**	**112.9**	**96.6**	**111.7**	**112.7**	**113.6**	**100.5**	**106.1**
F2	F18	-101.5	-104.4	-81.7	-95.9	-71.2	-113.4	-103.7	-106.2	-75.7	-102.9
	F19	-75.0	-69.0	-73.6	-62.3	-58.7	-99.8	-73.6	-77.1	-64.1	-95.3
	F20	-90.0	-82.9	-126.8	-102.2	-127.7	-111.3	-98.4	-102.8	-124.8	-87.1
	F21	-125.3	-123.2	-133.1	-142.7	-116.4	-113.5	-137.1	-141.9	-128.3	-78.3
	F22	-101.5	-98.1	-81.8	-116.4	-96.1	-113.4	-96.3	-106.2	-94.7	-129.3
	F23	-75.0	-98.6	-84.0	-118.2	-98.2	-99.8	-99.7	-77.1	-96.7	-119.8
	F24	-128.3	-82.9	-14.8	-102.2	-97.9	-58.2	-98.4	-116.4	-9.2	-92.7
	F25	-112.8	-123.2	-153.5	-142.7	-90.3	-96.9	-137.1	-102.8	-155.5	-94.3
	F26	-102.7	-104.4	-107.3	-95.9	-91.3	-137.5	-103.7	-100.7	-89.2	-118.3
	F27	-103.1	-69.0	-97.4	-62.3	-77.7	-111.3	-73.6	-103.2	-76.0	-119.7
	F28	-90.0	-124.3	-104.5	-116.3	-12.4	-113.5	-114.0	-102.8	-102.8	-94.6
	F29	-125.3	-109.6	-95.5	-102.8	-165.6	-96.9	-100.2	-141.9	-93.7	-85.8
	F30	-102.7	-98.1	-109.0	-116.4	-121.6	-137.5	-96.3	-100.7	-122.4	-23.2
	F31	-103.1	-98.6	-110.2	-118.2	-122.8	-93.1	-99.7	-103.2	-123.0	-167.7
	F32	-128.3	-124.3	-119.7	-116.3	-111.0	-58.2	-114.0	-116.4	-116.8	-103.8
	F33	-112.8	-109.6	-108.0	-102.8	-111.1	-93.1	-100.2	-102.8	-105.5	-105.8
	$<\sigma_{iso}>$	**-104.9**	**-101.3**	**-100.1**	**-107.1**	**-98.1**	**-103.0**	**-102.9**	**-106.4**	**-98.6**	**-101.2**

Table S45. ^{19}F calculated σ_{CSA} (σ_{CSA}, ppm) of each F atom from the 10 APO_DFT-D3 models of $NbOF_{0.875}(OH)_{0.125}F_2$ and (in bold italic) average absolute value of σ_{CSA} ($<|\sigma_{CSA}|>$, ppm) of each F crystallographic site.

Site	Atom	Model									
		1	2	3	4	5	6	7	8	9	10
F1	F11	139.6	139.9	147.4	-139.5	125.6	-147.6	134.1	-120.5	124.0	-137.6
	F12	143.7	142.9	122.5	-140.9	150.0	136.6	-149.4	-149.6	174.6	-137.2
	F13	-156.8	137.1	151.4	-121.7	148.6	-139.3	143.1	-135.6	144.3	157.9
	F14	-143.6	143.0	135.1	146.1	164.9	135.8	143.1	-143.3	173.6	153.6
	F15	139.6	139.9	164.1	-121.7	145.7	-149.0	134.1	146.3	137.9	-145.0
	F16	-135.6	142.9	132.8	-139.5	152.6	136.6	147.5	-120.5	135.7	147.8
	F17	143.7	-145.5	136.0	-136.4	174.6	135.8	-139.3	-149.6	149.7	119.9
	$<\|\sigma_{CSA}\|>$	***143.2***	***141.6***	***141.3***	***135.1***	***151.7***	***140.1***	***141.5***	***137.9***	***148.5***	***142.7***
F2	F18	332.9	338.8	314.8	326.8	288.8	334.1	335.9	335.6	305.8	320.6
	F19	280.4	278.9	277.3	273.0	261.9	319.0	281.0	283.8	267.1	315.3
	F20	306.8	305.0	340.8	315.1	343.0	332.6	315.6	315.2	338.1	316.6
	F21	343.2	341.0	346.5	356.2	331.6	336.3	356.0	354.6	342.3	280.5
	F22	332.9	321.2	300.3	331.8	317.4	334.1	318.6	335.6	314.0	344.6
	F23	280.4	322.3	303.3	334.9	318.4	319.0	323.4	283.8	315.5	337.8
	F24	343.7	305.0	245.6	315.1	315.7	325.4	315.6	332.5	242.1	313.0
	F25	331.4	341.0	363.5	356.2	307.2	268.6	356.0	321.8	363.1	316.0
	F26	322.9	338.8	323.9	326.8	317.5	315.4	335.9	318.9	309.6	332.5
	F27	323.7	278.9	293.2	273.0	282.0	357.6	281.0	323.4	279.4	335.0
	F28	306.8	346.2	320.2	335.1	246.3	332.6	331.8	315.2	319.5	311.4
	F29	343.2	330.2	314.1	320.3	370.3	336.3	320.7	354.6	309.9	287.6
	F30	322.9	321.2	324.9	331.8	338.1	315.4	318.6	318.9	335.5	255.2
	F31	323.7	322.3	326.3	334.9	339.7	357.6	323.4	323.4	336.5	377.3
	F32	343.7	346.2	333.2	335.1	325.8	325.4	331.8	332.5	331.3	319.9
	F33	331.4	330.2	325.3	320.3	327.3	268.6	320.7	321.8	319.8	321.4
	$<\|\sigma_{CSA}\|>$	***323.1***	***323.0***	***315.8***	***324.2***	***314.4***	***323.6***	***322.9***	***323.2***	***314.3***	***317.8***

Table S46. ^{19}F calculated η_{CSA} of each F atom from the 10 APO_DFT-D3 models of $NbOF_{0.875}(OH)_{0.125}F_2$ and (in bold italic) average η_{CSA} ($<\eta_{CSA}>$, ppm) of each F crystallographic site.

Site	Atom	Model									
		1	2	3	4	5	6	7	8	9	10
F1	F11	0.60	0.67	0.47	0.67	0.40	0.99	0.59	0.87	0.57	0.99
	F12	0.87	0.93	0.55	0.96	0.78	0.86	0.84	0.63	0.45	0.89
	F13	0.53	0.91	0.56	0.84	0.66	0.94	0.92	0.93	0.84	0.36
	F14	0.71	0.67	0.67	0.93	0.65	0.61	0.92	0.93	0.51	0.47
	F15	0.60	0.67	0.60	0.84	0.79	0.85	0.59	0.67	0.56	0.92
	F16	0.76	0.93	0.74	0.67	0.66	0.86	0.72	0.87	0.82	0.84
	F17	0.87	0.96	0.99	1.00	0.42	0.61	0.83	0.63	0.74	0.78
	$<\eta_{CSA}>$	***0.71***	***0.82***	***0.65***	***0.84***	***0.62***	***0.81***	***0.77***	***0.79***	***0.64***	***0.75***
F2	F18	0.08	0.07	0.34	0.18	0.51	0.04	0.06	0.11	0.40	0.19
	F19	0.31	0.17	0.16	0.11	0.69	0.01	0.30	0.22	0.18	0.18
	F20	0.11	0.02	0.44	0.11	0.44	0.08	0.11	0.10	0.49	0.37
	F21	0.04	0.05	0.41	0.17	0.50	0.10	0.02	0.13	0.44	0.15
	F22	0.08	0.06	0.30	0.12	0.27	0.04	0.06	0.11	0.36	0.18
	F23	0.31	0.05	0.31	0.10	0.29	0.01	0.03	0.22	0.36	0.17
	F24	0.17	0.02	0.29	0.11	0.43	0.12	0.11	0.08	0.41	0.32
	F25	0.14	0.05	0.36	0.17	0.39	0.14	0.02	0.09	0.44	0.32
	F26	0.06	0.07	0.46	0.18	0.48	0.07	0.06	0.17	0.43	0.23
	F27	0.12	0.17	0.68	0.11	0.26	0.02	0.30	0.15	0.61	0.21
	F28	0.11	0.04	0.40	0.11	0.46	0.08	0.04	0.10	0.52	0.46
	F29	0.04	0.05	0.38	0.09	0.49	0.10	0.03	0.13	0.48	0.62
	F30	0.06	0.06	0.49	0.12	0.35	0.07	0.06	0.17	0.43	0.18
	F31	0.12	0.05	0.51	0.10	0.35	0.02	0.03	0.15	0.47	0.25
	F32	0.17	0.04	0.37	0.11	0.51	0.12	0.04	0.08	0.44	0.44
	F33	0.14	0.05	0.35	0.09	0.47	0.14	0.03	0.09	0.49	0.46
	$<\eta_{CSA}>$	***0.13***	***0.06***	***0.39***	***0.12***	***0.43***	***0.07***	***0.08***	***0.13***	***0.43***	***0.30***

Table S47. ^{19}F calculated σ_{iso} (σ_{iso}, ppm) of each F atom from the 10 APO_DFT-D3 models of $NbOF_{0.75}(OH)_{0.25}F_2$ and (in bold italic) average σ_{iso} ($<\sigma_{iso}>$, ppm) of each F crystallographic site.

Site	Atom	Model									
		1	2	3	4	5	6	7	8	9	10
F1	F13	115.6	111.9	108.9	112.5	112.8	113.2	116.3	114.8	113.3	107.9
	F14	115.6	111.9	114.6	110.2	112.8	117.6	108.6	112.8	109.0	102.2
	F15	115.6	109.5	103.0	103.5	88.5	113.2	112.2	99.5	101.0	94.8
	F16	111.3	111.9	103.0	112.4	104.2	117.6	112.2	109.8	101.4	115.8
	F17	115.6	111.9	108.9	118.6	104.2	117.6	116.3	110.3	112.2	96.7
	F18	111.3	109.5	114.6	111.9	88.5	117.6	109.4	114.8	103.3	106.7
	$<\sigma_{iso}>$	**114.1**	**111.1**	**108.8**	**111.5**	**101.8**	**116.2**	**112.5**	**110.3**	**106.7**	**104.0**
F2	F19	-74.0	-70.9	-95.8	-92.0	-82.1	-99.5	-86.3	-109.6	-83.8	-86.1
	F20	-89.7	-85.1	-79.5	-82.2	-63.1	-92.1	-83.3	-89.0	-64.6	-69.7
	F21	-74.0	-70.9	7.4	-111.6	-118.7	-81.4	-88.9	-105.7	6.2	3.7
	F22	-89.7	-85.1	-136.6	-107.6	-108.4	-98.1	-126.5	-104.4	-143.1	-133.6
	F23	-115.0	-111.9	-104.6	-9.5	-118.7	-99.5	-112.0	-99.0	-114.3	-95.5
	F24	-103.2	-99.7	-96.9	-139.1	-108.4	-92.1	-98.3	-95.2	-103.8	-90.9
	F25	-74.0	-70.9	-107.0	-2.5	-82.1	-99.5	-88.9	-99.6	-111.4	-112.3
	F26	-89.7	-85.1	-102.3	-147.8	-63.1	-92.1	-126.5	-84.1	-104.8	-101.4
	F27	-74.0	-70.9	-107.0	-92.7	-97.8	-81.4	-86.3	-119.1	-98.6	-114.6
	F28	-89.7	-85.1	-102.3	-71.4	-85.7	-98.1	-83.3	-107.1	-91.2	-104.3
	F29	-115.0	-111.9	-104.6	-97.5	-1.4	-81.4	-107.7	-5.7	-101.8	-100.5
	F30	-103.2	-99.7	-96.9	-82.8	-156.3	-98.1	-60.4	-142.0	-92.9	-93.7
	F31	-115.0	-111.9	7.4	-132.2	-1.4	-81.4	-112.0	6.4	-2.6	-6.7
	F32	-103.2	-99.7	-136.6	-119.8	-156.3	-98.1	-98.3	-123.2	-154.0	-153.1
	F33	-115.0	-111.9	-95.8	-114.9	-97.8	-99.5	-107.7	-107.6	-91.3	-102.1
	F34	-103.2	-99.7	-79.5	-103.6	-85.7	-92.1	-60.4	-97.1	-76.6	-81.8
	$<\sigma_{iso}>$	**-95.5**	**-91.9**	**-89.4**	**-94.2**	**-89.2**	**-92.8**	**-95.4**	**-92.6**	**-89.3**	**-90.2**

Table S48. ^{19}F calculated σ_{CSA} (σ_{CSA}, ppm) of each F atom from the 10 APO_DFT-D3 models of $NbOF_{0.75}(OH)_{0.25}F_2$ and (in bold italic) average absolute value of σ_{CSA} ($<|\sigma_{CSA}|>$, ppm) of each F crystallographic site.

Site	Atom	Model									
		1	2	3	4	5	6	7	8	9	10
F1	F13	-129.9	140.9	152.1	140.2	125.5	-131.4	134.9	126.4	136.3	142.4
	F14	-129.9	140.9	135.1	127.6	125.5	133.2	138.8	136.7	142.4	155.4
	F15	-129.9	142.7	146.4	146.4	163.3	-131.4	141.1	148.4	158.1	154.1
	F16	143.0	140.9	146.4	127.9	147.5	133.2	141.1	152.0	147.7	126.9
	F17	-129.9	140.9	152.1	120.2	147.5	133.2	134.9	130.1	139.3	151.5
	F18	143.0	142.7	135.1	123.6	163.3	133.2	147.1	126.5	135.7	145.9
	$<\|\sigma_{CSA}\|>$	***134.3***	***141.5***	***144.5***	***131.0***	***145.4***	***132.6***	***139.6***	***136.7***	***143.3***	***146.0***
F2	F19	306.3	305.2	312.7	320.1	298.8	320.4	316.9	325.1	300.3	305.4
	F20	297.4	293.7	277.5	285.2	265.2	315.0	292.1	285.9	266.1	269.4
	F21	306.3	305.2	227.2	335.0	335.2	315.5	308.4	338.0	225.1	227.9
	F22	297.4	293.7	347.8	307.5	324.5	305.6	348.7	302.1	350.3	344.6
	F23	334.5	336.4	319.0	239.0	335.2	320.4	334.9	328.4	328.7	326.5
	F24	322.3	323.0	315.9	348.3	324.5	315.0	322.1	296.2	322.5	290.9
	F25	306.3	305.2	336.5	237.3	298.8	320.4	308.4	318.7	323.7	332.8
	F26	297.4	293.7	303.5	359.2	265.2	315.0	348.7	281.0	299.4	323.4
	F27	306.3	305.2	336.5	311.0	323.4	315.5	316.9	330.6	326.4	329.8
	F28	297.4	293.7	303.5	273.9	289.6	305.6	292.1	323.5	294.0	322.0
	F29	334.5	336.4	319.0	324.2	237.3	315.5	337.9	237.8	320.3	314.8
	F30	322.3	323.0	315.9	285.1	364.1	305.6	268.5	351.9	312.4	290.9
	F31	334.5	336.4	227.2	340.5	237.3	315.5	334.9	225.8	235.1	240.1
	F32	322.3	323.0	347.8	334.0	364.1	305.6	322.1	335.9	362.6	359.5
	F33	334.5	336.4	312.7	333.0	323.4	320.4	337.9	322.9	324.1	332.9
	F34	322.3	323.0	277.5	320.6	289.6	315.0	268.5	315.2	279.1	283.8
	$<\|\sigma_{CSA}\|>$	***315.1***	***314.6***	***305.0***	***309.6***	***304.8***	***314.1***	***316.2***	***307.4***	***304.4***	***305.9***

Table S49. ^{19}F calculated η_{CSA} of each F atom from the 10 APO_DFT-D3 models of $NbOF_{0.75}(OH)_{0.25}F_2$ and (in bold italic) average η_{CSA} ($<\eta_{CSA}>$, ppm) of each F crystallographic site.

Site	Atom	Model									
		1	2	3	4	5	6	7	8	9	10
F1	F13	0.81	0.68	0.35	0.67	0.52	0.99	0.65	0.80	0.37	0.52
	F14	0.81	0.68	0.46	0.57	0.52	0.62	0.91	0.68	0.26	0.37
	F15	0.81	0.79	0.36	0.50	0.32	0.99	0.69	0.47	0.28	0.56
	F16	0.71	0.68	0.36	0.71	0.66	0.62	0.69	0.34	0.38	0.48
	F17	0.81	0.68	0.35	0.94	0.66	0.62	0.65	0.48	0.68	0.39
	F18	0.71	0.79	0.46	0.82	0.32	0.62	0.85	0.87	0.67	0.58
	$<\eta_{CSA}>$	***0.78***	***0.72***	***0.39***	***0.70***	***0.50***	***0.74***	***0.74***	***0.61***	***0.44***	***0.48***
F2	F19	0.14	0.07	0.54	0.44	0.55	0.02	0.05	0.45	0.55	0.51
	F20	0.10	0.10	0.77	0.19	0.68	0.04	0.14	0.67	0.75	0.70
	F21	0.14	0.07	0.22	0.11	0.40	0.04	0.07	0.33	0.56	0.48
	F22	0.10	0.10	0.33	0.29	0.46	0.24	0.02	0.18	0.39	0.30
	F23	0.12	0.03	0.53	0.26	0.40	0.02	0.02	0.40	0.47	0.45
	F24	0.09	0.06	0.50	0.37	0.46	0.04	0.04	0.18	0.46	0.23
	F25	0.14	0.07	0.42	0.06	0.55	0.02	0.07	0.45	0.62	0.22
	F26	0.10	0.10	0.21	0.13	0.68	0.04	0.02	0.67	0.81	0.21
	F27	0.14	0.07	0.42	0.42	0.45	0.04	0.05	0.59	0.46	0.47
	F28	0.10	0.10	0.21	0.61	0.20	0.24	0.14	0.56	0.22	0.44
	F29	0.12	0.03	0.53	0.17	0.35	0.04	0.07	0.20	0.26	0.57
	F30	0.09	0.06	0.50	0.32	0.39	0.24	0.17	0.32	0.24	0.77
	F31	0.12	0.03	0.22	0.54	0.35	0.04	0.02	0.21	0.30	0.29
	F32	0.09	0.06	0.33	0.52	0.39	0.24	0.04	0.35	0.36	0.40
	F33	0.12	0.03	0.54	0.08	0.45	0.02	0.07	0.37	0.31	0.35
	F34	0.09	0.06	0.77	0.09	0.20	0.04	0.17	0.34	0.18	0.18
	$<\eta_{CSA}>$	***0.11***	***0.07***	***0.44***	***0.29***	***0.44***	***0.09***	***0.07***	***0.39***	***0.43***	***0.41***

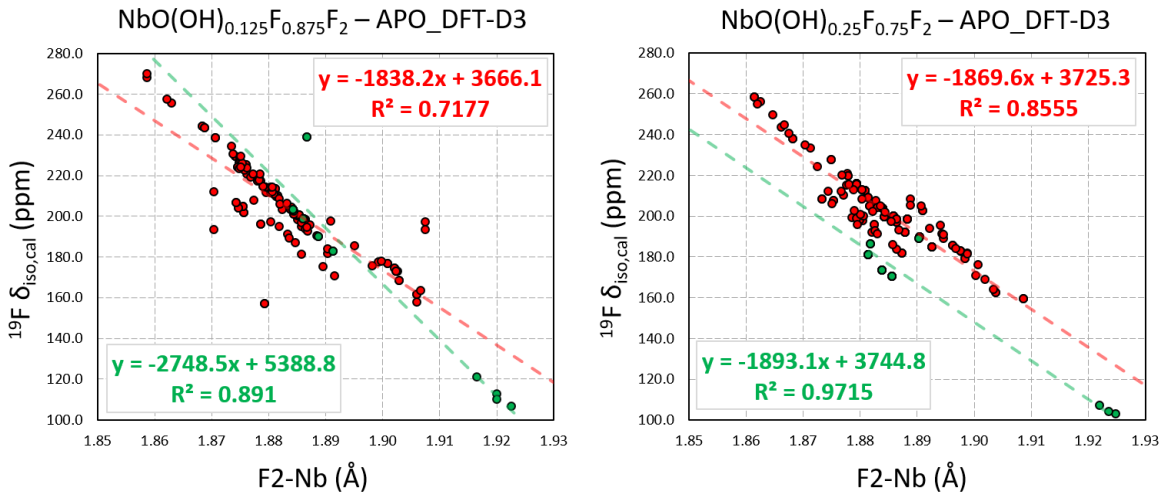


Figure S11. Calculated ^{19}F δ_{iso} of F2 atoms as a function of F2−M (M = Nb, Ta) bond lengths from the APO_DFT-D3 models of $NbOF_{0.875}(OH)_{0.125}F_2$ and $NbOF_{0.75}(OH)_{0.25}F_2$. The red and green dots refer to non H-bonded and H-bonded F2 atoms, respectively. The dashed lines represent the linear regressions (whose equations are given) when considering the dots of the same color.

10. Hydroxylated $NbOF_3$: geometries of the O–H···F contacts and calculated δ_{iso} values.

Table S50. Geometries of the O–H···F contacts (H–O bond length (Å), H···F distance (Å) and O–H···F angle (°)) and calculated ^{1}H and ^{19}F σ_{iso} and δ_{iso} values (σ_{iso} and $\delta_{iso,cal}$, ppm) from the 10 APO_DFT-D3 models of $NbOF_{0.875}(OH)_{0.125}F_2$.

Model	H–O	H···F	O–H···F	^{1}H σ_{iso}	^{1}H $\delta_{iso,cal}$	^{19}F σ_{iso}	^{19}F $\delta_{iso,cal}$
1	0.984	2.068	106.3	20.9	10.1	-75.0	174.6
		2.068	106.3			-75.0	174.6
		2.319	116.4			-90.0	190.1
		2.319	116.4			-90.0	190.1
2	0.987	2.143	120.1	20.7	10.3	-82.9	182.8
		2.143	120.1			-82.9	182.8
		2.144	105.9			-69.0	168.4
		2.144	105.9			-69.0	168.4
3	0.998	1.676	170.6	19.3	11.7	-14.9	112.6
4	0.984	2.140	104.9	21.2	9.8	-102.2	202.6
		2.140	104.9			-102.2	202.6
		2.266	117.2			-62.3	161.5
		2.266	117.2			-62.3	161.5
5	1.001	1.643	177.2	19.0	12.0	-12.4	110.0
6	0.985	2.130	105.6	21.1	9.9	-58.2	157.24
		2.130	105.6			-58.2	157.24
		2.258	117.2			-97.0	197.2
		2.258	117.2			-97.0	197.2
7	0.984	2.083	106.1	20.8	10.2	-73.6	173.1
		2.083	106.1			-73.6	173.1
		2.286	116.9			-98.4	198.7
		2.286	116.9			-98.4	198.7
8	0.984	2.096	105.4	21.1	9.9	-77.1	176.8
		2.096	105.4			-77.1	176.8
		2.280	116.9			-102.8	203.2
		2.280	116.9			-102.8	203.2
9	1.000	1.653	174.8	19.1	11.9	-9.2	106.7
10	0.998	1.674	173.8	19.4	11.6	-23.2	121.2

Table S51. Geometries of the O−H···F contacts (H−O bond length (Å), H···F distance (Å) and O–H···F angle (°)) and calculated ^{1}H and ^{19}F σ_{iso} and δ_{iso} values (σ_{iso} and $\delta_{iso,cal}$, ppm) from the 10 APO_DFT-D3 models of $NbOF_{0.75}(OH)_{0.25}F_2$.

Model	H atom	H–O	H···F	O–H···F	^{1}H σ_{iso}	^{1}H $\delta_{iso,cal}$	^{19}F σ_{iso}	^{19}F $\delta_{iso,cal}$
1	H1	0.988	2.028	121.7	20.5	10.5	-74.0	173.5
			2.028	121.7			-74.0	173.5
			2.173	105.6			-89.7	189.8
			2.173	105.6			-89.7	189.8
	H2	0.988	2.028	121.7	20.5	10.5	-74.0	173.5
			2.028	121.7			-74.0	173.5
			2.173	105.6			-89.7	189.8
			2.173	105.6			-89.7	189.8
2	H1	0.988	2.033	121.5	20.4	10.6	-70.9	170.3
			2.033	121.5			-70.9	170.3
			2.165	106.2			-85.1	185.0
			2.165	106.2			-85.1	185.0
	H2	0.988	2.033	121.5	20.4	10.6	-70.9	170.3
			2.033	121.5			-70.9	170.3
			2.165	106.2			-85.1	185.0
			2.165	106.2			-85.1	185.0
3	H1	1.000	1.662	170.5	19.0	12.0	7.4	89.6
	H2	1.000	1.662	170.5	19.0	12.0	7.4	89.6
4	H1	1.001	1.650	173.7	18.8	12.2	-2.5	99.8
	H2	0.995	1.707	167.5	20.0	11.0	-9.5	107.1
5	H1	1.003	1.633	176.3	18.8	12.3	-1.4	98.7
	H2	1.003	1.633	176.3	18.8	12.3	-1.4	98.7

Table S51. Continued.

Model	H atom	H–O	H···F	O–H···F	^{1}H σ_{iso}	^{1}H $\delta_{iso,cal}$	^{19}F σ_{iso}	^{19}F $\delta_{iso,cal}$
6	H1	0.989	2.019	121.8	20.1	10.9	-81.4	181.2
			2.019	121.8			-81.4	181.2
			2.142	106.3			-98.1	198.4
			2.142	106.3			-98.1	198.4
	H2	0.989	2.019	121.8	20.1	10.9	-81.4	181.2
			2.019	121.8			-81.4	181.2
			2.142	106.3			-98.1	198.4
			2.142	106.3			-98.1	198.4
7	H1	0.986	2.070	107.1	20.7	10.3	-83.3	183.2
			2.070	107.1			-83.3	183.2
			2.288	117.2			-88.9	188.9
			2.288	117.2			-88.9	188.9
	H2	0.984	2.083	106.4	21.2	9.8	-60.4	159.6
			2.083	106.4			-60.4	159.6
			2.459	115.1			-86.3	186.3
			2.459	115.1			-86.3	186.3
8	H1	0.999	1.676	169.9	19.1	11.9	-5.7	103.2
	H2	0.996	1.697	166.4	19.4	11.6	6.4	90.6
9	H1	1.002	1.642	174.7	18.7	12.3	6.2	90.9
	H2	1.001	1.640	174.5	18.7	12.3	-2.6	99.9
10	H1	0.998	1.673	171.1	19.2	11.8	3.7	93.4
	H2	1.001	1.652	173.4	18.9	12.1	-6.7	104.2

References

(1) Kresse, G.; Furthmüller, J. Efficiency of Ab-Initio Total Energy Calculations for Metals and Semiconductors Using a Plane-Wave Basis Set. *Comput. Mater. Sci.* **1996**, *6* (1), 15–50. https://doi.org/10.1016/0927-0256(96)00008-0.

(2) Kresse, G.; Furthmüller, J. Efficient Iterative Schemes for *Ab Initio* Total-Energy Calculations Using a Plane-Wave Basis Set. *Phys. Rev. B* **1996**, *54* (16), 11169–11186. https://doi.org/10.1103/PhysRevB.54.11169.

(3) Biswal, M.; Body, M.; Legein, C.; Sadoc, A.; Boucher, F. NbF_5 and TaF_5: Assignment of ^{19}F NMR Resonances and Chemical Bond Analysis from GIPAW Calculations. *J. Solid State Chem.* **2013**, *207*, 208–217. https://doi.org/10.1016/j.jssc.2013.09.001.

Appendix C

Oxyfluorides Exhibiting Preferential O/F Ordering

Hexagonal-Tungsten-Bronze $TiOF_2$: Synthesis, Crystal Structure and Anionic Short-range Ordering

Madhu Chennabassapa[a], Alexander G. Squires[b,c], Alain Demourgues[a,], Nicolas Penin[a], Etienne Durand[a], Weil Li[d,e], Christophe Legein[f], **Ouail Zakary**[f], Monique Body[f], Thibault Charpentier[g], Olaf J. Borkiewicz[h], Benjamin. J. Morgan[b,c], David O. Scanlon[b,c,i] and Damien Dambournet[d,e,*]*

[a] CNRS, Université de Bordeaux, Bordeaux INP, ICMCB, UMR 5026, F-33600 Pessac, France

[b] Department of Chemistry, University of Bath, BA2 7AY Bath, United Kingdom

[c] The Faraday Institution, Quad One, Harwell Science and Innovation Campus, Didcot OX11 0RA, U.K

[d] Sorbonne Université, CNRS, Physicochimie des Electrolytes et Nanosystèmes Interfaciaux, PHENIX, F-75005 Paris, France

[e] Réseau sur le Stockage Electrochimique de l'Energie (RS2E), FR CNRS 3459, 80039 Amiens Cedex, France

[f] Institut des Molécules et Matériaux du Mans (IMMM), – UMR 6283 CNRS -, Le Mans Université, avenue Avenue Olivier Messiaen, 72805 Le Mans Cedex 9, France

[g] Université Paris-Saclay, CEA, CNRS, NIMBE, CEA, CNRS, Université Paris-Saclay, CEA Saclay, 91191 Gif-sur-Yvette Cedex, France

[h] X-ray Science Division, Advanced Photon Source, Argonne National Laboratory, Illinois 60439, United States

[i] Thomas Young Centre, University College London, Gower Street, London, WC1E 6BT UK

Supporting information

Table of content

1. ^{19}F and ^{1}H MAS NMR spectra and their fits.....S335

Figure S1. Experimental and fitted ^{19}F MAS NMR spectra of HTB-$TiOF_2$.....S335

Table S1. Experimental ^{19}F δ_{iso}, line width, relative intensity and assignment of each individual resonance used to fit the ^{19}F MAS NMR spectrum of HTB-$TiOF_2$, weighted average ^{19}F δ_{iso} of the resonances assigned to the same F atom type and sum of the corresponding relative intensities.....S335

Figure S2. Experimental and fitted ^{1}H MAS NMR spectra of HTB-$TiOF_2$.....S336

Table S2. Experimental ^{19}F δ_{iso}, line width and relative intensity of each individual resonance used to fit the ^{1}H MAS NMR spectrum of HTB-$TiOF_2$.....S336
2. New TiF_4 correlations ^{19}F σ_{iso} vs δ_{iso} established with VASP.....S337
Table S3. Experimental ^{19}F δ_{iso}, calculated ^{19}F σ_{iso} and corresponding calculated ^{19}F $\delta_{iso,cal}$ values and difference $\Delta\delta_{iso}$ for the bridging and terminal F atoms from TiF_4. .....S337
3. $TiOF_{2-x}(OH)_x \cdot 0.33H_2O$ structural features.....S338
Table S4. Model, formula, number of F atoms, number of OH groups and composition of the TiX_6 octahedra. S338
Table S5. Average, shortest and longest Ti–X (X = O & F) bond lengths and their standard deviation from models with the composition $TiOF_{2-x}(OH)_x \cdot 0.33H_2O$ (x = 0, 1/6, 1/3, 1/2, 2/3 and 5/6) S339
4. $TiOF_{2-x}(OH)_x \cdot 0.33H_2O$ calculated σ_{iso} and δ_{iso}.....S340
Table S6. Calculated ^{19}F σ_{iso} and δ_{iso} values, F–Ti bond length and Ti–F–Ti angle of each F atom from the PDF-DFT_2 model. S340
Table S7. Calculated ^{19}F σ_{iso} and δ_{iso} values, F–Ti bond length and Ti–F–Ti angle of each F atom from the PDF-DFT_3 model. S342
Table S8. Calculated ^{19}F σ_{iso} and δ_{iso} values, F–Ti bond length and Ti–F–Ti angle of each F atom from the PDF-DFT_4 model. S344
Table S9. Calculated ^{19}F σ_{iso} and δ_{iso} values, F–Ti bond length and Ti–F–Ti angle of each F atom from the PDF-DFT_5 model. S346
Table S10. Calculated ^{19}F σ_{iso} and δ_{iso} values, F–Ti bond length and Ti–F–Ti angle of each F atom from the PDF-DFT_6 model. S348
Table S11. Calculated ^{19}F σ_{iso} and δ_{iso} values, F–Ti bond length and Ti–F–Ti angle of each F atom from the PDF-DFT_7 model. S350
Figure S3. Experimental and theoretical ^{19}F NMR spectra of HTB-$TiOF_2$. S351
References S352

1. ^{19}F and ^{1}H MAS NMR spectra and their fits

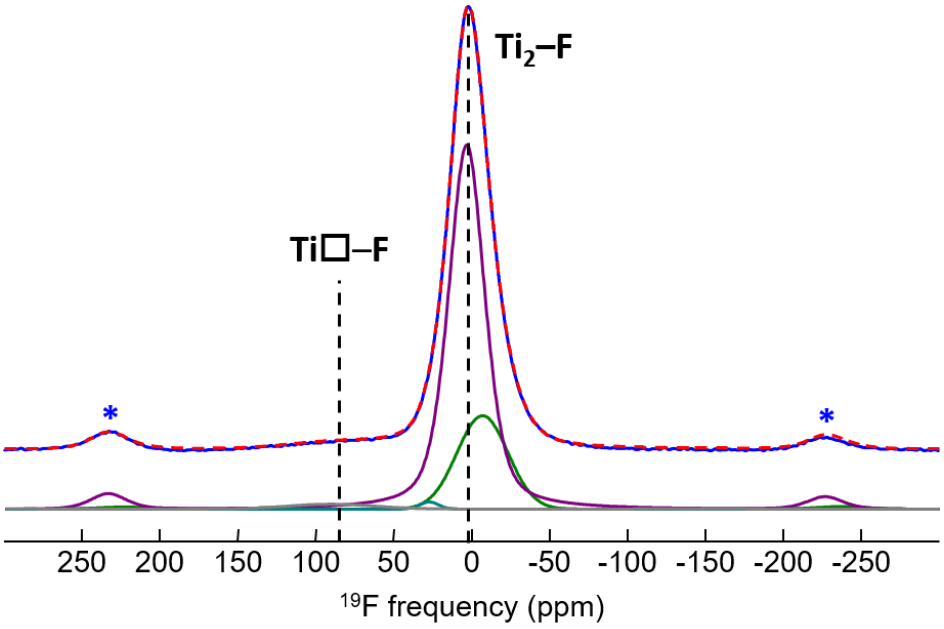


Figure S1. Experimental (blue) and fitted (dashed red) ^{19}F MAS (64 kHz) NMR spectra of HTB-$TiOF_2$. The individual resonances used for the fit (**Table S1**) are shown below. The stars indicate spinning sidebands. The average resonance positions are shown by the dashed black lines and their assignments are given.

Table S1. Experimental ^{19}F δ_{iso} (δ_{iso}, ppm), line width (LW, ppm), relative intensity (I, %) and assignment of each individual resonance used to fit the ^{19}F MAS (64 kHz) NMR spectrum of HTB-$TiOF_2$, weighted average ^{19}F δ_{iso} ($<\delta_{iso}>$, ppm) of the resonances assigned to the same F atom type (Ti_2–F, Ti□–F) and sum of the corresponding relative intensities (ΣI, %).

δ_{iso}	LW	I	$<\delta_{iso}>$	ΣI	Assignment
-6.8	38.4	22.1	1.2	97.9	Ti_2–F
3.3	27.5	75.2			
27.5	14.2	0.7			
90.3	65.3	2.1	90.3	2.1	Ti□–F

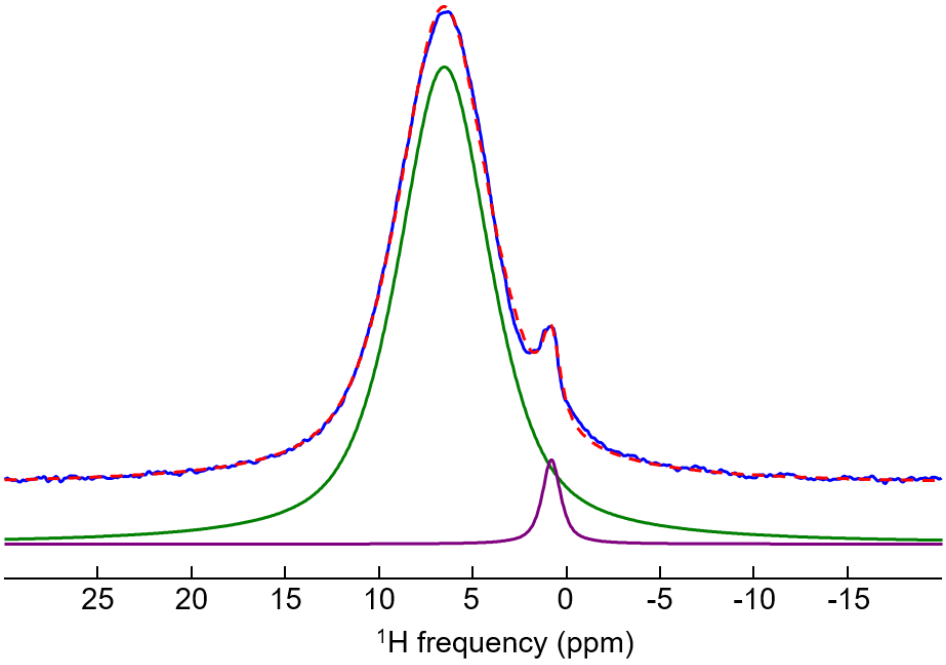


Figure S2. Experimental (blue) and fitted (dashed red) ^{1}H MAS (44 kHz) NMR spectra of HTB-$TiOF_2$. The individual resonances used for the fit (**Table S2**) are shown below.

Table S2. Experimental ^{19}F δ_{iso} (δ_{iso}, ppm), line width (LW, ppm) and relative intensity (I, %) of each individual resonance used to fit the ^{1}H MAS (44 kHz) NMR spectrum of HTB-$TiOF_2$.

δ_{iso}	LW	I
6.6	5.9	96.3
0.8	1.2	3.7

2. New TiF_4 correlations ^{19}F σ_{iso} vs δ_{iso} established with VASP

To ensure consistency, new linear regression equations between calculated, with VASP,[1,2] ^{19}F σ_{iso} and experimental δ_{iso} values[3] were established for TiF_4.

Table S3. Experimental ^{19}F δ_{iso} ($\delta_{iso,exp}$, ppm), calculated ^{19}F σ_{iso} (σ_{iso}, ppm) and corresponding calculated ^{19}F $\delta_{iso,cal}$ ($\delta_{iso,cal}$, ppm) values and difference $\Delta\delta_{iso}$ between $\delta_{iso,cal}$ and $\delta_{iso,exp}$ values for the bridging (Fb) and terminal (Ft) F atoms from TiF_4.

Fb site					Ft site				
	$\delta_{iso,exp}$	σ_{iso}	$\delta_{iso,cal}$***(1)***	$\Delta\delta_{iso}$		$\delta_{iso,exp}^{Ft}$	σ_{iso}^{Ft}	$\delta_{iso,cal}$***(2)***	$\Delta\delta_{iso}$
F1	30.0	17.8	29.5	0.5	F3	426.5	-322.0	426.7	0.2
F2	25.4	22.0	26.0	0.6	F4	479.4	-371.6	481.6	2.2
F5	-2.0	55.4	-1.6	0.4	F7	422.5	-320.1	424.6	2.1
F6	29.4	18.0	29.3	0.1	F8	455.2	-343.0	450.0	5.2
F9	7.6	43.9	7.9	0.3	F10	447.7	-341.3	448.1	0.4
F12	1.7	52.1	1.1	0.6	F11	424.2	-320.1	424.6	0.4

From linear regression equations (1) δ_{iso} (ppm) = –0.828(14) σ_{iso} + 44.2(6) and (2) δ_{iso} (ppm) = –1.107(68) σ_{iso} + 70.4(22.8),, respectively

3. $TiOF_{2-x}(OH)_x \cdot 0.33H_2O$ structural features

Table S4. Model, formula, number of F atoms (n_F), number of OH groups (n_{OH}) and composition of the TiX_6 octahedra.

Model	Form.	n_F	n_{OH}	TiX_6 octahedra
PDF-DFT_2	$TiOF_2 \cdot 0.33H_2O$	24	0	$TiOF_5$ (×2)
				TiO_2F_4 (×8)
				TiO_3F_3 (×2)
PDF-DFT_3	$TiOF_{1.83}(OH)_{0.17} \cdot 0.33H_2O$	22	2	$TiOF_5$ (×1)
				TiO_2F_4 (×6)
				TiO_3F_3 (×1)
				$TiOF_4(OH)$ (×1)
				$TiO_2F_3(OH)$ (×2)
				$TiO_3F_2(OH)$ (×1)
PDF-DFT_4	$TiOF_{1.67}(OH)_{0.33} \cdot 0.33H_2O$	20	4	TiO_2F_4 (×4)
				$TiOF_4(OH)$ (×2)
				$TiO_2F_3(OH)$ (×4)
				$TiO_3F_2(OH)$ (×2)
PDF-DFT_5	$TiOF_{1.50}(OH)_{0.50} \cdot 0.33H_2O$	18	6	TiO_2F_4 (×2)
				$TiOF_4(OH)$ (×1)
				$TiOF_3(OH)_2$ (×1)
				$TiO_2F_3(OH)$ (×5)
				$TiO_2F_2(OH)_2$ (×1)
				$TiO_3F_2(OH)$ (×2)
PDF-DFT_6	$TiOF_{1.33}(OH)_{0.67} \cdot 0.33H_2O$	16	8	TiO_2F_4 (×1)
				$TiOF_4(OH)$ (×1)
				$TiOF_2(OH)_3$ (×1)
				$TiO_2F_3(OH)$ (×4)
				$TiO_2F_2(OH)_2$ (×3)
				$TiO_3F_2(OH)$ (×2)
PDF-DFT_7	$TiOF_{1.17}(OH)_{0.83} \cdot 0.33H_2O$	14	10	$TiOF_4(OH)$ (×1)
				$TiOF_2(OH)_3$ (×1)
				$TiO_2F_3(OH)$ (×4)
				$TiO_2F_2(OH)_2$ (×3)
				$TiO_2F(OH)_3$ (×1)
				$TiO_3F(OH)_2$ (×2)

Table S5. Average, shortest and longest Ti–X (X = O & F) bond lengths (Å) and their standard deviation from models with the composition $TiOF_{2-x}(OH)_x \cdot 0.33H_2O$ (x = 0, 1/6, 1/3, 1/2, 2/3 and 5/6)

Model	<Ti–O>	$Ti–O_{min}$	$Ti–O_{max}$	sdv	<Ti–F>	$Ti–F_{min}$	$Ti–F_{max}$	sdv
PDF-DFT_2	1.811	1.723	1.902	0.049	1.999	1.902	2.159	0.069
PDF-DFT_3	1.838	1.713	2.246	0.101	2.013	1.896	2.191	0.074
PDF-DFT_4	1.867	1.755	2.157	0.113	2.011	1.903	2.194	0.061
PDF-DFT_5	1.887	1.745	2.202	0.117	2.019	1.921	2.182	0.062
PDF-DFT_6	1.912	1.750	2.210	0.125	2.024	1.902	2.198	0.068
PDF-DFT_7	1.927	1.738	2.216	0.131	2.031	1.894	2.232	0.081

4. $TiOF_{2-x}(OH)_x \cdot 0.33H_2O$ calculated σ_{iso} and δ_{iso}

Table S6. Calculated ^{19}F σ_{iso} (σ_{iso}, ppm) and δ_{iso} ($\delta_{iso,cal}$, ppm) values, F–Ti bond length (Å) and Ti–F–Ti angle (°) of each F atom from the PDF-DFT_2 model.

F atom	σ_{iso}	$\delta_{iso,cal}$	F–Ti	Ti–F–Ti
F25	34.1	16.0	1.927	169.2
			2.053	
F26	33.6	16.4	1.927	165.1
			2.062	
F27	30.6	18.9	1.965	150.4
			2.159	
F28	32.3	17.5	1.966	150.1
			2.159	
F29	46.9	5.4	1.961	156.0
			1.969	
F30	8.1	37.5	1.967	137.9
			1.975	
F31	45.1	6.9	1.960	156.2
			1.967	
F32	7.6	37.9	1.967	138.0
			1.975	
F33	35.2	15.0	1.961	164.7
			2.046	
F34	49.2	3.5	1.971	161.8
			2.045	
F35	48.2	4.3	1.970	161.7
			2.044	
F36	35.5	14.9	1.961	165.7
			2.044	
F37	2.1	42.5	1.905	159.2
			2.081	
F38	30.9	18.7	1.984	145.2
			2.026	

Table S6. Continued.

F atom	σ_{iso}	$\delta_{iso,cal}$	F–Ti	Ti–F–Ti
F39	8.0	37.6	1.914	155.0
			2.082	
F40	2.7	42.0	1.967	148.3
			2.007	
F41	3.0	41.7	1.968	149.6
			2.005	
F42	11.2	35.0	1.916	154.1
			2.083	
F43	32.1	17.7	1.983	144.2
			2.027	
F44	-0.7	44.8	1.902	159.7
			2.085	
F45	-14.0	55.8	1.905	151.5
			2.108	
F46	-4.2	47.7	1.912	152.8
			2.073	
F47	-4.5	47.9	1.913	152.5
			2.073	
F48	-11.9	54.1	1.906	151.6
			2.110	

Table S7. Calculated ^{19}F σ_{iso} (σ_{iso}, ppm) and δ_{iso} ($\delta_{iso,cal}$, ppm) values, F–Ti bond length (Å) and Ti–F–Ti angle (°) of each F atom from the PDF-DFT_3 model.

F atom	σ_{iso}	$\delta_{iso,cal}$	F–Ti	Ti–F–Ti
F29	59.2	-4.8	1.952	167.2
			2.048	
F30	65.4	-10.0	1.992	157.6
			2.066	
F31	133.7	-66.4	2.044	141.7
			2.191	
F32	47.0	5.3	1.973	149.0
			2.111	
F33	31.3	18.3	1.936	162.1
			1.957	
F34	24.2	24.2	1.962	137.4
			1.987	
F35	41.5	9.9	1.943	160.2
			1.960	
F36	48.9	3.7	1.978	136.4
			1.981	
F37	59.5	-5.0	1.999	159.2
			2.020	
F38	11.5	34.7	1.900	156.1
			2.094	
F39	56.5	-2.6	1.974	149.0
			2.044	
F40	106.7	-44.1	1.984	148.0
			2.161	
F41	40.3	10.9	1.962	142.1
			2.011	
F42	33.1	16.9	1.951	146.7
			2.033	

Table S7. Continued.

F atom	σ_{iso}	$\delta_{iso,cal}$	F–Ti	Ti–F–Ti
F43	19.2	28.3	1.904	158.4
			2.080	
F44	70.8	-14.4	2.019	145.7
			2.138	
F45	92.2	-32.1	1.958	142.2
			2.184	
F46	-4.7	48.1	1.896	151.6
			2.109	
F47	35.9	14.5	1.926	147.6
			2.093	
F48	57.4	-3.3	1.969	165.0
			2.058	
F49	57.6	-3.5	1.985	165.2
			2.026	
F50	56.0	-2.2	1.971	162.2
			2.057	

Table S8. Calculated ^{19}F σ_{iso} (σ_{iso}, ppm) and δ_{iso} ($\delta_{iso,cal}$, ppm) values, F–Ti bond length (Å) and Ti–F–Ti angle (°) of each F atom from the PDF-DFT_4 model.

F atom	σ_{iso}	$\delta_{iso,cal}$	F–Ti	Ti–F–Ti
F33	61.0	-6.3	1.977	171.3
			2.036	
F34	58.3	-4.1	1.997	164.4
			2.020	
F35	46.9	5.4	2.009	150.3
			2.080	
F36	96.2	-35.4	1.999	146.3
			2.185	
F37	34.9	15.3	1.944	153.4
			1.949	
F38	45.6	6.4	1.973	141.2
			1.990	
F39	54.5	-0.9	1.951	157.4
			1.967	
F40	40.8	10.4	1.970	135.8
			2.003	
F41	69.9	-13.6	1.994	156.6
			2.045	
F42	57.9	-3.7	2.013	150.1
			2.080	
F43	48.3	4.2	1.924	158.0
			2.067	
F44	69.1	-13.0	1.988	143.0
			2.023	
F45	31.5	18.1	1.988	149.4
			1.996	
F46	44.4	7.5	1.954	154.5
			2.043	

Table S8. Continued.

F atom	σ_{iso}	$\delta_{iso,cal}$	F–Ti	Ti–F–Ti
F47	65.4	-9.9	2.022	145.4
			2.054	
F48	51.1	2.0	1.940	147.9
			2.092	
F49	26.8	22.0	1.903	145.1
			2.194	
F50	43.6	8.2	1.955	173.1
			2.047	
F51	54.5	-0.9	1.987	158.5
			2.052	
F52	55.9	-2.0	1.991	175.1
			2.022	

Table S9. Calculated ^{19}F σ_{iso} (σ_{iso}, ppm) and δ_{iso} ($\delta_{iso,cal}$, ppm) values, F–Ti bond length (Å) and Ti–F–Ti angle (°) of each F atom from the PDF-DFT_5 model.

F atom	σ_{iso}	$\delta_{iso,cal}$	F–Ti	Ti–F–Ti
F37	57.9	-3.7	1.966	171.0
			2.053	
F38	48.0	4.5	1.947	155.4
			2.098	
F39	44.6	7.3	1.992	146.8
			2.119	
F40	83.3	-24.8	2.010	148.8
			2.121	
F41	40.1	11.1	1.963	151.5
			1.978	
F42	63.4	-8.3	1.953	155.5
			1.969	
F43	47.4	5.0	1.971	136.3
			2.003	
F44	62.6	-7.6	2.012	155.3
			2.022	
F45	62.0	-7.1	2.021	148.7
			2.050	
F46	58.6	-4.3	1.967	159.8
			2.049	
F47	32.9	17.0	1.988	151.8
			1.996	
F48	61.8	-6.9	1.966	149.5
			2.057	
F49	102.9	-41.0	2.023	138.2
			2.109	
F50	43.2	8.5	1.931	147.6
			2.112	

Table S9. Continued.

F atom	σ_{iso}	$\delta_{iso,cal}$	F–Ti	Ti–F–Ti
F51	40.9	10.4	1.921	148.5
			2.182	
F52	62.0	-7.1	1.981	167.0
			2.077	
F53	58.2	-3.9	2.006	159.4
			2.035	
F54	61.5	-6.7	1.961	168.5
			2.073	

Table S10. Calculated ^{19}F σ_{iso} (σ_{iso}, ppm) and δ_{iso} ($\delta_{iso,cal}$, ppm) values, F–Ti bond length (Å) and Ti–F–Ti angle (°) of each F atom from the PDF-DFT_6 model.

F atom	σ_{iso}	$\delta_{iso,cal}$	F–Ti	Ti–F–Ti
F41	57.7	-3.5	1.969	166.4
			2.064	
F42	50.2	2.7	1.946	150.5
			2.146	
F43	84.0	-25.3	2.047	142.2
			2.112	
F44	80.0	-22.0	2.003	147.4
			2.109	
F45	59.5	-5.0	1.974	149.7
			1.989	
F46	58.1	-3.9	1.961	150.3
			1.968	
F47	44.3	7.6	1.974	140.4
			1.995	
F48	48.5	4.1	1.996	151.4
			2.054	
F49	57.9	-3.7	1.995	154.9
			2.039	
F50	54.1	-0.6	2.005	148.6
			2.006	
F51	73.9	-16.9	1.963	149.3
			2.096	
F52	20.1	27.6	1.902	140.8
			2.198	
F53	57.3	-3.2	1.940	150.8
			2.141	
F54	63.5	-8.4	2.020	166.4
			2.033	

Table S10. Continued.

F atom	σ_{iso}	$\delta_{iso,cal}$	F–Ti	Ti–F–Ti
F55	78.3	-20.6	1.990	159.7
			2.102	
F56	71.7	-15.1	2.007	174.7
			2.033	

Table S11. Calculated ^{19}F σ_{iso} (σ_{iso}, ppm) and δ_{iso} ($\delta_{iso,cal}$, ppm) values, F–Ti bond length (Å) and Ti–F–Ti angle (°) of each F atom from the PDF-DFT_7 model.

F atom	σ_{iso}	$\delta_{iso,cal}$	F–Ti	Ti–F–Ti
F45	61.0	-6.3	1.966	165.6
			2.066	
F46	54.2	-0.6	1.955	149.2
			2.152	
F47	79.8	-21.8	1.996	143.1
			2.150	
F48	78.5	-20.8	1.989	148.3
			2.100	
F49	78.7	-20.9	1.990	146.8
			1.996	
F50	59.9	-5.4	1.963	149.2
			1.967	
F51	47.0	5.3	1.960	139.8
			2.025	
F52	74.4	-17.4	2.030	144.7
			2.037	
F53	66.1	-10.5	1.982	151.2
			2.067	
F54	10.3	35.7	1.894	143.3
			2.232	
F55	86.5	-27.4	1.967	148.4
			2.168	
F56	76.7	-19.3	1.977	162.2
			2.109	
F57	79.6	-21.7	1.988	158.8
			2.116	
F58	71.7	-15.2	1.960	173.1
			2.074	

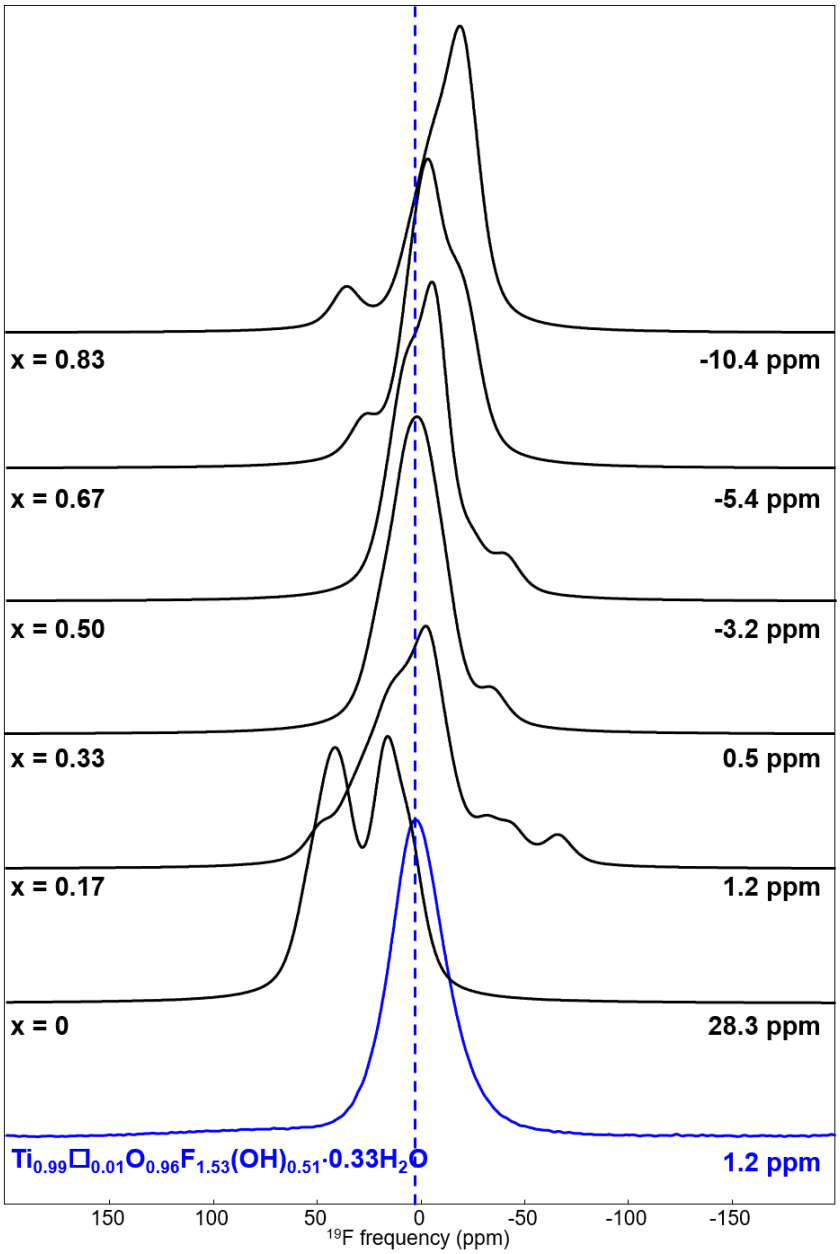


Figure S3. Experimental (blue) and theoretical (black) ^{19}F NMR spectra of HTB-$TiOF_2$. The theoretical spectra are constructed with the ^{19}F δ_{iso} values from the $TiOF_{2-x}(OH)_x \cdot 0.33H_2O$ models. The dashed blue line indicates the weighted average experimental ^{19}F δ_{iso} value, which is given along with the experimental composition. The substitution rate, x, and the average ^{19}F δ_{iso} value of each model are given as well.

References

(1) Kresse, G.; Furthmüller, J. Efficiency of Ab-Initio Total Energy Calculations for Metals and Semiconductors Using a Plane-Wave Basis Set. *Computational Materials Science* **1996**, *6* (1), 15–50. https://doi.org/10.1016/0927-0256(96)00008-0.

(2) Kresse, G.; Furthmüller, J. Efficient Iterative Schemes for *Ab Initio* Total-Energy Calculations Using a Plane-Wave Basis Set. *Phys. Rev. B* **1996**, *54* (16), 11169–11186. https://doi.org/10.1103/PhysRevB.54.11169.

(3) Murakami, M.; Noda, Y.; Takegoshi, K. Terminal and Bridging Fluorine Ligands in TiF_4 as Studied by ^{19}F NMR in Solids. *Solid State Nuclear Magnetic Resonance* **2019**, *101*, 82–88. https://doi.org/10.1016/j.ssnmr.2019.05.007.

Appendix D

“Disordered” Oxyfluorides

Preferential O/F Ordering in the Pyrochlore Oxyfluorides RbM_2O_5F (M = Nb, Ta) Revealed by Multimodal Structural Modeling Approach

Ouail Zakary[a,], Monique Body[a], Christophe Legein[a,*], Vincent Sarou-Kanian[b], Franck Fayon[b], Aydar Rakhmatullin[b], Thibault Charpentier[c]*

[a] Institut des Molécules et Matériaux du Mans (IMMM) – UMR 6283 CNRS, Le Mans Université, avenue Olivier Messiaen, 72085 Le Mans Cedex 9, France

[b] Conditions Extrêmes et Matériaux, Haute Température et Irradiation (CEMHTI), UPR3079 CNRS, Orléans, France

[c] Université Paris-Saclay, CEA, CNRS, NIMBE, 91191, Gif-sur-Yvette cedex, France

Supporting information

Table of content

1. Pyrochlore oxyfluorides S360

Table S1. $A_{2-u}B_2X_{6-v}Y_{1-w}$ oxyfluoride pyrochores without mixed O/F environment around B cation(s). S360

Table S2. $A_{2-m}B_2X_{6-w}Y_{1-n}$ oxyfluoride pyrochores with mixed O/F environment around B cation(s). S361

3. NMR spectra S363

3.1. Experimental and fitted ^{19}F MAS NMR spectra S363

Figure S1. Experimental and fitted ^{19}F MAS NMR spectra of $RbNb_2O_5F$ S363

Table S3. Experimental ^{19}F δ_{iso}, line width and relative intensity of the NMR lines used to fit the ^{19}F MAS NMR spectrum of $RbNb_2O_5F$, and corresponding ^{19}F δ_{iso} weighted average. S363

Figure S2. Experimental and fitted ^{19}F MAS NMR spectra of $RbTa_2O_5F$ S364

Table S4. Experimental ^{19}F δ_{iso}, line width and relative intensity of the NMR lines used to fit the ^{19}F MAS NMR spectrum of $RbTa_2O_5F$, and corresponding ^{19}F δ_{iso} weighted average. S364

2. Rietveld refinements S365

Figure S3. Observed, calculated and difference diffraction patterns of $RbNb_2O_5F$..... S365

Figure S4. Observed, calculated and difference diffraction patterns of $RbTa_2O_5F$ S366

4. Model structural features and energies S367

Table S5. Nb (or Ta) anionic environments from the 20 models of $RbNb_2O_5F$ (or $RbTa_2O_5F$)..... S367

Table S6. Rb anionic environments from the 20 models of $RbNb_2O_5F$ (or $RbTa_2O_5F$). S368

Table S7. Total energy after relaxation from the APO_8b and APO_32e models of $RbNb_2O_5F$ and $RbTa_2O_5F$. S369

5. Linear regressions S370

5.1. ^{19}F linear regression equations S370

Table S8. ^{19}F experimental δ_{iso}, calculated σ_{iso}, calculated δ_{iso} and difference between the $\delta_{iso,cal}$ and $\delta_{iso,exp}$ values S370

5.2. ^{87}Rb linear regression equations S371

Table S9. Fit parameters including δ_{iso}, linewidth, quadripolar coupling constant and asymmetry parameter resonances, used to reconstruct the ^{87}Rb MAS NMR spectrum of RbF..... S371

Figure S6. Experimental and fitted ^{87}Rb MAS NMR spectra of RbF..... S372

Table S10. Compound, ICSD code, space group, number of Rb sites and shifted Monkhorst-Pack k-point mesh of the compounds used for the ^{87}Rb linear regression. S373

Table S11. ^{87}Rb experimental δ_{iso}, calculated σ_{iso}, calculated δ_{iso} and the difference between δ_{iso} and $\delta_{iso,exp}$ values for the listed compounds S373

6. RbM_2O_5F calculated NMR parameters and structural features S375

6.1. Quadrupolar coupling constant values for $RbNb_2O_5F$ models..... S375

Table S12. Calculated C_Q of each Rb and Nb atom from the APO_32e models 1 to 10 of $RbNb_2O_5F$ and average C_Q of all Rb and Nb atoms in a given model. S375

Table S13. Calculated C_Q of each Rb and Nb atom from the APO_32e models 11 to 20 of $RbNb_2O_5F$ and average C_Q of all Rb and Nb atoms in a given model. S376

Table S14. Calculated C_Q of each Rb and Nb atom from the APO_8b models 1 to 10 of $RbNb_2O_5F$ and average C_Q of all Rb and Nb atoms in a given model. S377

Table S15. Calculated C_Q of each Rb and Nb atom from the APO_8b models 11 to 20 of $RbNb_2O_5F$ and average C_Q of all Rb and Nb atoms in a given model. S378

6.2. Asymmetry parameter values for $RbNb_2O_5F$ models S379

Table S16. Calculated η_Q of each Rb and Nb atom from the APO_32e models 1 to 10 of $RbNb_2O_5F$ and average η_Q of all Rb and Nb atoms in a given model. S379

Table S17. Calculated η_Q of each Rb and Nb atom from the APO_32e models 11 to 20 of $RbNb_2O_5F$ and average η_Q of all Rb and Nb atoms in a given model. S380

Table S18. Calculated η_Q of each Rb and Nb atom from the APO_8b models 1 to 10 of $RbNb_2O_5F$ and average η_Q of all Rb and Nb atoms in a given model. S381

Table S19. Calculated η_Q of each Rb and Nb atom from the APO_8b models 11 to 20 of $RbNb_2O_5F$ and average η_Q of all Rb and Nb atoms in a given model. S382

6.3. Magnetic shielding values for $RbNb_2O_5F$ models S383

Table S20. Calculated σ_{iso} of each F, Rb and Nb atom from the APO_32e models 1 to 10 of $RbNb_2O_5F$ and average σ_{iso} of all F, Rb and Nb atoms in a given model. S383

Table S21. Calculated σ_{iso} of each F, Rb and Nb atom from the APO_32e models 11 to 20 of $RbNb_2O_5F$ and average σ_{iso} of all F, Rb and Nb atoms in a given model. S384

Table S22. Calculated σ_{iso} of each F, Rb and Nb atom from the APO_8b models 1 to 10 of $RbNb_2O_5F$ and average σ_{iso} of all F, Rb and Nb atoms in a given model. S386

Table S23. Calculated σ_{iso} of each F, Rb and Nb atom from the APO_8b models 11 to 20 of $RbNb_2O_5F$ and average σ_{iso} of all F, Rb and Nb atoms in a given model. S387

6.4. Quadrupolar coupling constant values for $RbTa_2O_5F$ models S389

Table S24. Calculated C_Q of each Rb atom from the 10 APO_32e models of $RbTa_2O_5F$ and average C_Q of all Rb atoms in a given model S389

Table S25. Calculated C_Q of each Rb atom from the 10 APO_8b models of $RbTa_2O_5F$ and average C_Q of all Rb atoms in a given model S389

6.5. Asymmetry parameter values for $RbTa_2O_5F$ models S390

Table S26. Calculated η_Q of each Rb atom from the 10 APO_32e models of $RbTa_2O_5F$ and average η_Q of all Rb atoms in a given model. S390

Table S27. Calculated η_Q of each Rb atom from the 10 APO_8b models of $RbTa_2O_5F$ and average η_Q of all Rb atoms in a given model. S390

6.6. Magnetic shielding values for $RbTa_2O_5F$ models S391

Table S28. Calculated σ_{iso} of each F and Rb atom from the 10 APO_32e models of $RbTa_2O_5F$ and average σ_{iso} of all F and Rb atoms in a given model. S391

Table S29. Calculated σ_{iso} of each F and Rb atom from the 10 APO_8b models of $RbTa_2O_5F$ and average σ_{iso} of all F and Rb atoms in a given model. S392

7. Structural features of RbM_2O_5F models S393

7.1. $RbNb_2O_5F$ models S393

Table S30. Average, shortest and longest Nb−X (X = O or F) bond lengths and the standard deviation from the average bond length sdv(Nb−X) from the 8 selected APO_32e models of $RbNb_2O_5F$. S393

Table S31. Average, shortest and longest Nb−X (X = O or F) bond lengths and the standard deviation from the average bond length sdv(Nb−X) from the 8 selected APO_8b models of $RbNb_2O_5F$. S393

Table S32. Average, shortest and longest Rb−X (X = O or F) bond lengths and the standard deviation from the average bond length sdv(Rb−X) from the 8 selected APO_32e models of $RbNb_2O_5F$. S394

Table S33. Average, shortest and longest Rb−X (X = O or F) bond lengths and the standard deviation from the average bond length sdv(Rb−X) from the 8 selected APO_8b models of $RbNb_2O_5F$. S394

7.2. $RbTa_2O_5F$ models S395

Table S34. Average, shortest and longest Ta−X (X = O or F) bond lengths and the standard deviation from the average bond length sdv(Ta−X) from the 8 selected APO_32e models of $RbTa_2O_5F$. S395

Table S35. Average, shortest and longest Ta−X (X = O or F) bond lengths and the standard deviation from the average bond length sdv(Ta−X) from the 8 selected APO_8b models of $RbTa_2O_5F$. S395

Table S36. Average, shortest and longest Rb−X (X = O or F) bond lengths and the standard deviation from the average bond length sdv(Rb−X) from the 8 selected APO_32e models of $RbTa_2O_5F$. S396

Table S37. Average, shortest and longest Rb−X (X = O or F) bond lengths and the standard deviation from the average bond length sdv(Rb−X) from the 8 selected APO_8b models of $RbTa_2O_5F$..... S396

References..... S397

1. Pyrochlore oxyfluorides

Table S1. ICSD[1] code, formula and reference of $A_{2-u}B_2X_{6-v}Y_{1-w}$ oxyfluoride pyrochores without mixed O/F environment around B cation(s).

ICSD Code	Formula	Ref.
151522	$(Ca_{1.29}Na_{0.18}U_{0.50}Ce_{0.03})(Ti_{1.09}Nb_{0.79}Zr_{0.14}Fe_{0.04}Ta_{0.01})O_6(O_{0.98}F_{0.02})$	2
31196	$Ca_{1.37}Na_{0.150}Ce_{0.32}Th_{0.08}U_{0.08}Ti_{1.07}Nb_{0.89}Ta_{0.038}O_6O_{0.5}F_{0.5}H_{0.125}$	3
247029	$NdTa_2O_6F$	4
25553	$BiF(Ta_2O_6)$	5
27329	$Hg_2Ni_2F_6O$	6
27330	$Hg_2Zn_2F_6O$	6
50048	$Ca_2(Ta_2O_6)F$	7
157317	$LiCa(Ta_2O_6F)$	8
239231	$(Na_{1.53}Pb_{0.47})Nb_2O_6F$	9
16185	$SrLiTa_2O_6F$	10
24445	$NaCa(Nb_2O_6)F$	11
27815	$(Na_{0.294}Ca_{1.376}Sr_{0.018}Mn_{0.004}Mg_{0.014}Ce_{0.170}La_{0.034}Nd_{0.042}Y_{0.002}U_{0.008}Th_{0.016}Te_{0.002})(Nb_{1.452}Ta_{0.038}Ti_{0.356}Zr_{0.030}Fe_{0.094})O_6O_{0.157}(OH)_{0.050}F_{0.793}$	12
27819	$(Na_{0.738}Ca_{1.056}Sr_{0.034}Ce_{0.038}Fe_{0.022}La_{0.008}Nd_{0.008}Y_{0.006}Th_{0.002})(Nb_{1.856}Ti_{0.122}Zr_{0.018}Fe_{0.004})O_6(OH)_{0.091}F_{0.909}$	12
108945	$(NaY)(TiNb)O_6F$	13
108946	$(NaCe)(TiNb)O_6F$	13
108947	$(NaPr)(TiNb)O_6F$	13
108948	$(NaNd)(TiNb)O_6F$	13
108949	$(NaEu)(TiNb)O_6F$	13
108950	$(NaGd)(TiNb)O_6F$	13
108951	$(NaYb)(TiNb)O_6F$	13
108952	$(CdY)Ti_2O_6F$	13
108953	$(CdNd)Ti_2O_6F$	13
108954	$(CdEu)Ti_2O_6F$	13
108955	$(CdGd)Ti_2O_6F$	13
108956	$(CdYb)Ti_2O_6F$	13

Table S1. (Continued)

ICSD Code	Formula	Ref.
240958	$KCa(Nb_2O_6)F$	14
5269	$Na_{0.82}Ca_{1.06}(Ta_{1.79}Nb_{.21}O_6)F_{0.79}(OH)_{0.21}$	15
156616	$(Na_{0.37}K_{0.02}Ca_{0.73}Sr_{0.07}Mn_{0.04}Pb_{0.01}La_{0.01}Ce_{0.03}Nd_{0.01}U_{0.02})$ $(Nb_{1.72}Ta_{0.02}Ti_{0.16}Si_{0.07}Fe_{0.03})(O_{5.03}(OH)_{0.97})(F_{0.62}(OH)_{0.38})$	16
156617	$(Na_{0.18}K_{0.05}Ca_{0.72}Sr_{0.08}Mn_{0.04}Pb_{0.01}La_{0.01}Ce_{0.04}Nd_{0.01}U_{0.02})$ $(Nb_{1.48}Ta_{0.04}Ti_{0.16}Si_{0.24}Fe_{0.08})(O_{4.63}(OH)_{1.37})(F_{0.46}(OH)_{0.54})$	16
190668	$(Ca_{1.22}Na_{0.54}Mn_{0.06})Sb_2O_6(F_{0.62}(OH)_{0.28}O_{0.10})$	17
17778	$(Bi_{0.80}Na_{0.68}Ca_{0.37})(Ta_{1.42}Ti_{0.30}Nb_{0.21}Sn_{0.07})O_6(O_{0.54}F_{0.39})$	18
182079	$(Na_{1.11}Ca_{0.65}Bi_{0.15})(Ta_2O_6F)$	19
421959	$LiLa_{0.67}Ta_2O_6F$	20
421960	$Li_{1.25}La_{0.58}Nb_2O_6F$	20
181125	$(Na_{0.88}Ca_{0.88}Pb_{0.02})(Ta_{1.70}Nb_{0.14}Si_{0.12}As_{0.04})(O_{5.75}(OH)_{0.25})F_{0.73}$	21
236011	$LiSr_{0.93}Nb_2O_6F_{0.91}$	22
236012	$LiSr_{0.93}Ta_2O_6F_{0.9}$	22
157314	$Ca_{1.5}(Nb_2O_6F)$	8
157316	$Ca_{1.5}(Ta_2O_6F)$	8
230539	$Ca_{1.2}(Nb_{1.7}Ti_{0.3})O_6F$	23
n/a	$NaPbNb_2O_6F$	24
n/a	$KPbNb_2O_6F$	24

Table S2. ICSD[1] code, formula and reference of $A_{2-m}B_2X_{6-w}Y_{1-n}$ oxyfluoride pyrochores with mixed O/F environment around B cation(s).

ICSD Code	Formula	Ref.
9636	$K(Ta_2O_5F)(H_2O)$	25
421274	$KNb_2O_5F(H_2O)_{1.2}$	26
9635	$RbTa_2O_5F$	27
23363	$CsTi_2O_{2.85}F_{3.15}$	28
69625	$Cs(Zn_{.98}Mo_{1.02})O_3F_3$	29
18066	$RbZnTiOF_5$	30
18067	$RbNiWO_3F_3$	30

Table S2. (Continued)

ICSD Code	Formula	Ref.
18068	$RbTa_2O_5F$	30
18069	$RbNb_2O_5F$	30
18072	$CsNiTiOF_5$	30
18073	$CsCuTiOF_5$	30
18074	$CsZnTiOF_5$	30
18075	$CsCoTiOF_5$	30
18076	$CsMnTiOF_5$	30
18077	$CsNiTaO_2F_4$	30
18078	$CsCoTaO_2F_4$	30
18079	$CsNiNbO_2F_4$	30
18081	$CsNiMoO_3F_3$	30
18082	$CsZnMoO_3F_3$	30
18083	$CsMnMoO_3F_3$	30
18084	$CsNiWO_3F_3$	30
18085	$CsZnWO_3F_3$	30
18086	$CsCoWO_3F_3$	30
18087	$CsTiNbO_4F_2$	30
18088	$CsTa_2O_5F$	30
18089	$CsNb_2O_5F$	30
416710	$Cs(Cu_{1.24}V_{0.76})(F_{4.74}O_{0.48})$	31
74283	$Cs_{0.31}(Sb_{0.57}Na_{0.31}Pb_{0.02}Bi_{0.0096})(Ta_{1.88}Nb_{0.12})O_{5.69}(F_{0.5}(OH)_{0.5})$	32
74284	$(Cs_{0.22}K_{0.01})(Na_{0.45}Sb_{0.39}Pb_{0.14}Ca_{0.06}Bi_{0.02})(Ta_{1.95}Nb_{0.05})O_{5.78}((OH)_{0.385}F_{0.385})$	32
161281	$Sn_{1.24}Ti_{1.94}O_{3.66}(OH)_{1.50}F_{1.42}$	33
n/a	$Na_2Nb_2O_5F_2$	34
n/a	$Na_2Ta_2O_5F_2$	34
n/a	$Pb_2Ti_2O_{5.4}F_{1.2}$	35

3. NMR spectra

3.1. Experimental and fitted ^{19}F MAS NMR spectra

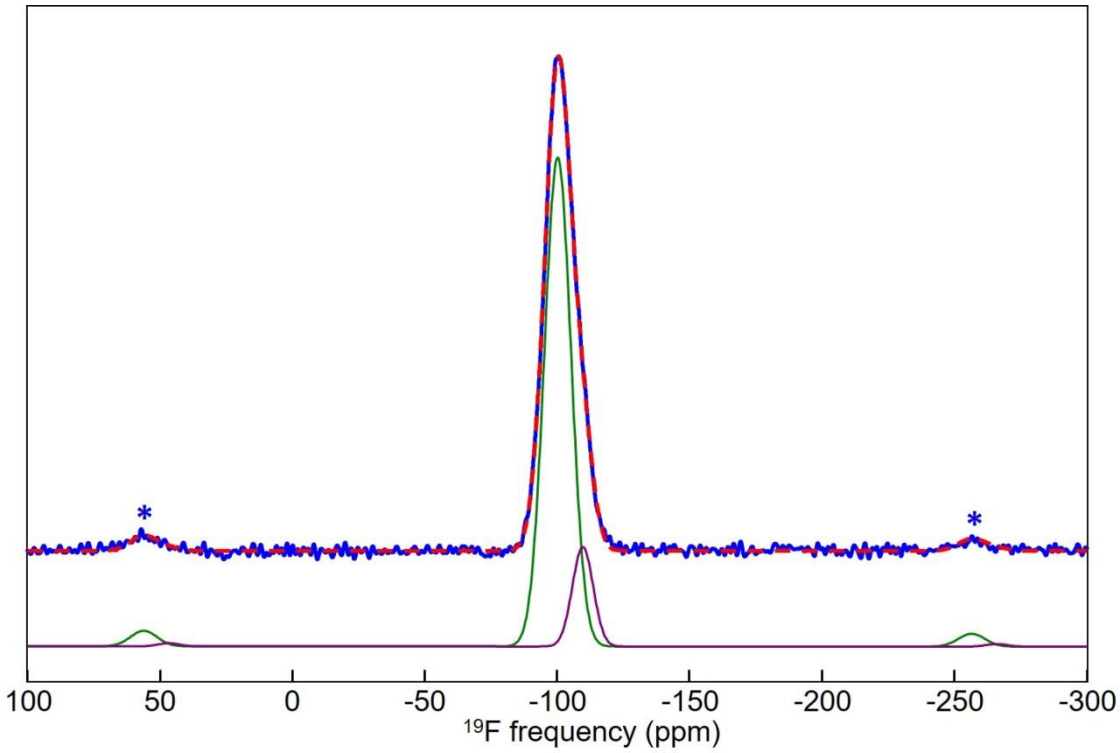


Figure S1. Experimental (blue) and fitted (dashed red) ^{19}F MAS (44 kHz) NMR spectra of $RbNb_2O_5F$. The NMR lines used for the fit (**Table S3**) are shown below. The stars indicate spinning sidebands.

Table S3. Experimental ^{19}F δ_{iso} (ppm), line width (LW, ppm) and relative intensity (I, %) of the NMR lines used to fit the ^{19}F MAS NMR spectrum of $RbNb_2O_5F$, and corresponding ^{19}F δ_{iso} weighted average ($<\delta_{iso}>$, ppm).

δ_{iso}	LW	I	$<\delta_{iso}>$
–100.2	11.8	86.2	–101.5
–109.7	9.2	13.8	

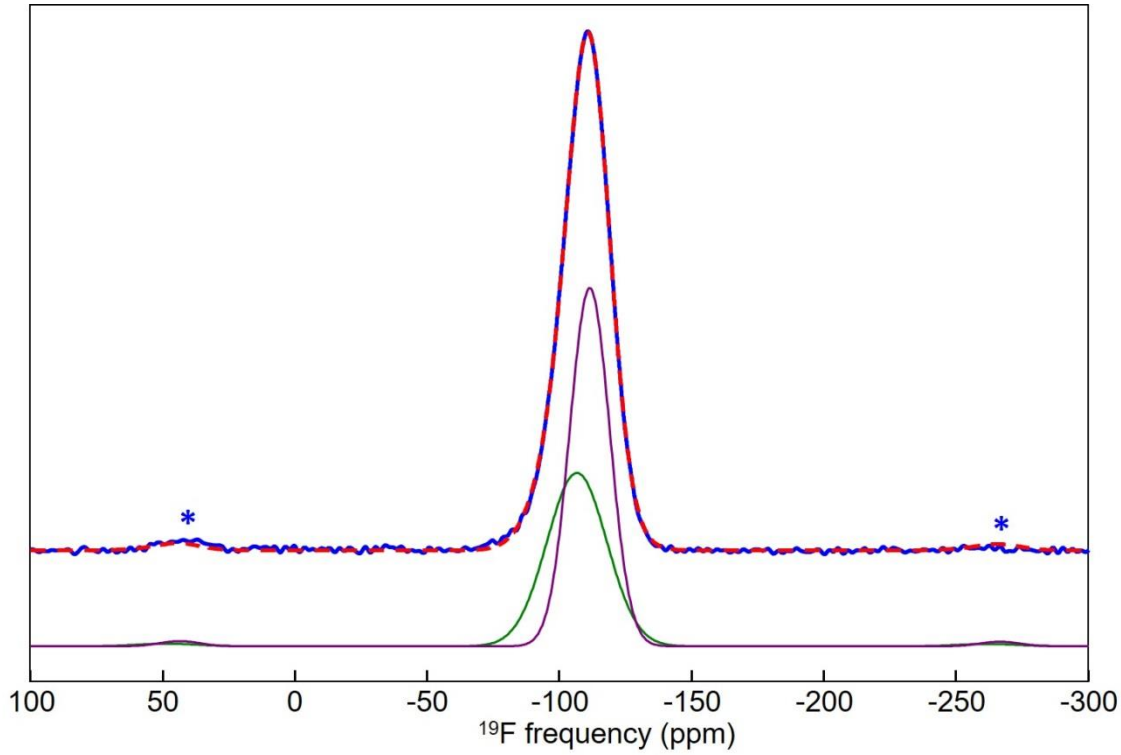


Figure S2. Experimental (blue) and fitted (dashed red) ^{19}F MAS (44 kHz) NMR spectra of $RbTa_2O_5F$. The individual resonances used for the fit (**Table S4**) are shown below. The stars indicate spinning sidebands.

Table S4. Experimental ^{19}F δ_{iso} (ppm), line width (LW, ppm) and relative intensity (I, %) of the NMR lines used to fit the ^{19}F MAS NMR spectrum of $RbTa_2O_5F$, and corresponding ^{19}F δ_{iso} weighted average ($<\delta_{iso}>$, ppm).

δ_{iso}	LW	I	$<\delta_{iso}>$
–106.7	26.5	42.1	–109.5
–111.5	17.7	57.9	

2. Rietveld refinements

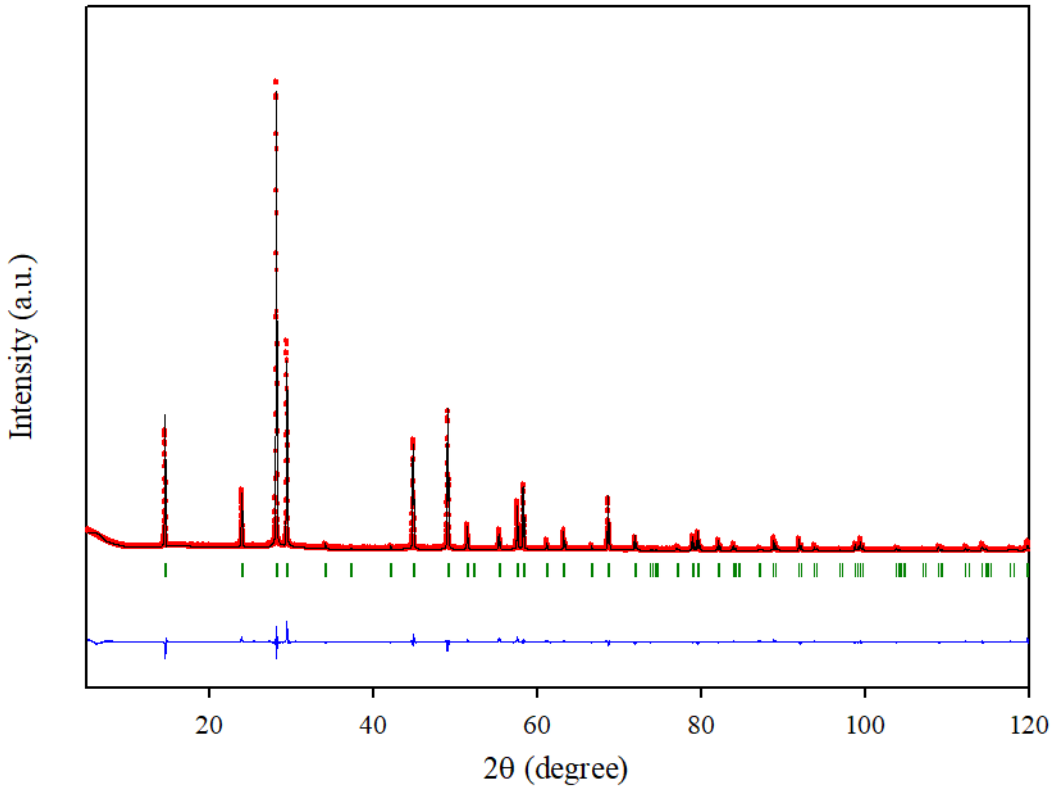


Figure S3. Observed (red), calculated (black) and difference (blue) diffraction patterns of $RbNb_2O_5F$. The green vertical markers refer to the Bragg positions. The obtained refinement reliability factors are R_p = 10.8%, R_{wp} = 8.7%, R_{exp} = 2.3%, R_B = 4.3% and R_F = 3.9 %.

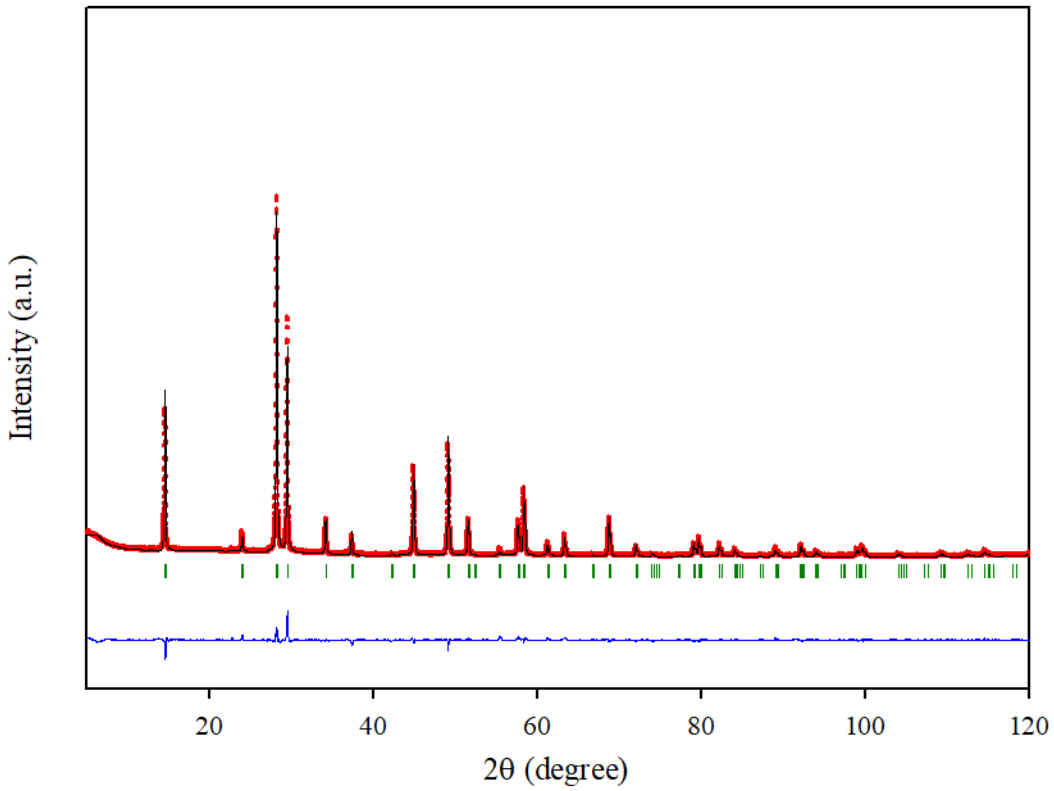


Figure S4. Observed (red), calculated (black) and difference (blue) diffraction patterns of $RbTa_2O_5F$. The green vertical markers refer to the Bragg positions. The obtained refinement reliability factors are R_p = 10.8%, R_{wp}= 10.1%, R_{exp} = 2.1%, R_B = 4.8%, R_F = 3.6%.

4. Model structural features and energies

Table S5. Nb (or Ta) anionic environments from the 20 models of $RbNb_2O_5F$ (or $RbTa_2O_5F$). When these environments change after APO, the new environment is shown in italics.

Model	MO_6	MO_5F	MO_4F_2	MO_3F_3	MO_2F_4	MOF_5	MF_6
1	-	16	-	-	-	-	-
2	-	16	-	-	-	-	-
3	-	16	-	-	-	-	-
4	-	16	-	-	-	-	-
5	1	14	1	-	-	-	-
6	-	16	-	-	-	-	-
7	-	16	-	-	-	-	-
8	-	16	-	-	-	-	-
9	-	16	-	-	-	-	-
10	4	8	4	-	-	-	-
11	5	6	5	-	-	-	-
12	7	3	5	1	-	-	-
13	7	5	2	1	1/*NbO_3F_4*	-	-
14	9	3	2	-	1	1/*NbO_2F_5*	-
15	10	2	-	2	2/1+*$1NbO_3F_4$*	-	-
16	10	2	-	2	2	-	-
17	9	2	4	-	-	-	1/*$NbOF_6$*
18	9	2	4	-	-	-	1/*NbO_2F_6*
19	10	2	-	3	-	1/*NbO_2F_5*	-
20	9	3	2	1	-	-	1/*NbO_2F_6*

Table S6. Rb anionic environments from the 20 models of $RbNb_2O_5F$ (or $RbTa_2O_5F$).

Mod.	RbO_{18}	$RbO_{17}F$	$RbO_{16}F_2$	$RbO_{15}F_3$	$RbO_{14}F_4$	$RbO_{13}F_5$	$RbO_{12}F_6$	$RbO_{11}F_7$	…RbF_{18}
1	-	-	-	8	-	-	-	-	… -
2	-	-	2	4	2	-	-	-	… -
3	-	-	2	4	2	-	-	-	… -
4	-	-	-	8	-	-	-	-	… -
5	-	-	2	4	2	-	-	-	… -
6	-	-	1	6	1	-	-	-	… -
7	-	-	2	4	2	-	-	-	… -
8	-	-	4	-	4	-	-	-	… -
9	-	-	4	-	4	-	-	-	… -
10	-	-	-	8	-	-	-	-	… -
11	-	-	3	2	3	-	-	-	… -
12	-	2	1	2	2	-	1	-	… -
13	-	2	1	2	2	-	1	-	… -
14	1	-	2	1	3	1	-	-	… -
15	1	-	1	2	4	-	-	-	… -
16	1	-	-	4	3	-	-	-	… -
17	-	2	-	2	4	-	-	-	… -
18	-	2	-	4	-	2	-	-	… -
19	1	-	-	4	3	-	-	-	… -
20	1	-	1	2	4	-	-	-	… -

Table S7. Total energy (eV) after relaxation from the APO_8b and APO_32e models of $RbNb_2O_5F$ and $RbTa_2O_5F$.

Model	$RbNb_2O_5F$		$RbTa_2O_5F$	
	DFT_8b	DFT_32e	DFT_8b	DFT_32e
1	–620.35	–620.35	–675.95	–675.95
2	–619.68	–619.77	–675.47	–675.47
3	–618.39	–618.68	–674.32	–674.52
4	–620.04	–620.04	–675.66	–675.66
5	–619.17	–619.17	–674.81	–674.82
6	–619.92	–619.92	–675.55	–675.55
7	–619.19	–619.19	–674.91	–674.91
8	–619.68	–619.82	–675.50	–675.55
9	–617.77	–618.25	–673.81	–674.00
10	–616.79	–617.29	–672.46	–672.72
11	–618.49	–618.49	n/a	n/a
12	–618.99	–618.96	n/a	n/a
13	–618.21	–618.21	n/a	n/a
14	–617.62	–617.62	n/a	n/a
15	–616.79	–617.63	n/a	n/a
16	–617.33	–617.33	n/a	n/a
17	–617.01	–617.23	n/a	n/a
18	–614.94	–617.17	n/a	n/a
19	–617.85	–617.83	n/a	n/a
20	–617.60	–617.60	n/a	n/a

5. Linear regressions

5.1. ^{19}F linear regression equations

For RbF, ^{19}F σ_{iso} values were calculated using VASP (version 6.2.1),[36,37] while the experimental ^{19}F δ_{iso} value was collected from.[38] For MF_5, the experimental ^{19}F δ_{iso} values are gathered from[39] whereas the σ_{iso} values were calculated recently.[40] All these values are gathered in **Table S8** and the resulting linear regression equations are shown in **Figure S5**.

Table S8. ^{19}F experimental δ_{iso} ($\delta_{iso,exp}$, ppm), calculated σ_{iso} (σ_{iso}, ppm), calculated δ_{iso} ($\delta_{iso,cal}$, ppm) and difference between the $\delta_{iso,cal}$ and $\delta_{iso,exp}$ values ($\Delta\delta_{iso}$, ppm). The average $\Delta\delta_{iso}$ are given in bold italics.

Compound	F site	$\delta_{iso,exp}$	σ_{iso}	$\delta_{iso,cal}$	$\Delta\delta_{iso}$
δ_{iso} = –0.959(29) σ_{iso} + 106.1(4.3) (**Figure S5** (a))					
RbF	F1	–90.9	220.9	–105.8	14.9
NbF_5	F4	–42.1	134.9	–23.2	18.9
	F2	192.9	–92.5	194.8	1.9
	F5	214.8	–113.8	215.2	0.4
	F1	237.8	–134.2	234.8	3.0
	F6	260.0	–159.8	259.4	0.6
	F3	268.1	–165.9	265.2	2.9
					6.1
δ_{iso} = –0.935(16) σ_{iso} + 108.9(1.8) (**Figure S5** (b))					
RbF	F1	–90.9	220.9	–97.7	6.8
TaF_5	F4	–70.5	183.7	–62.8	7.7
	F2	106.3	2.3	106.7	0.4
	F5	121.6	–13.4	121.4	0.2
	F1	135.8	–27.0	134.1	1.7
	F6	166.9	–61.5	166.4	0.5
	F3	173.8	–70.0	174.4	0.6
					2.5

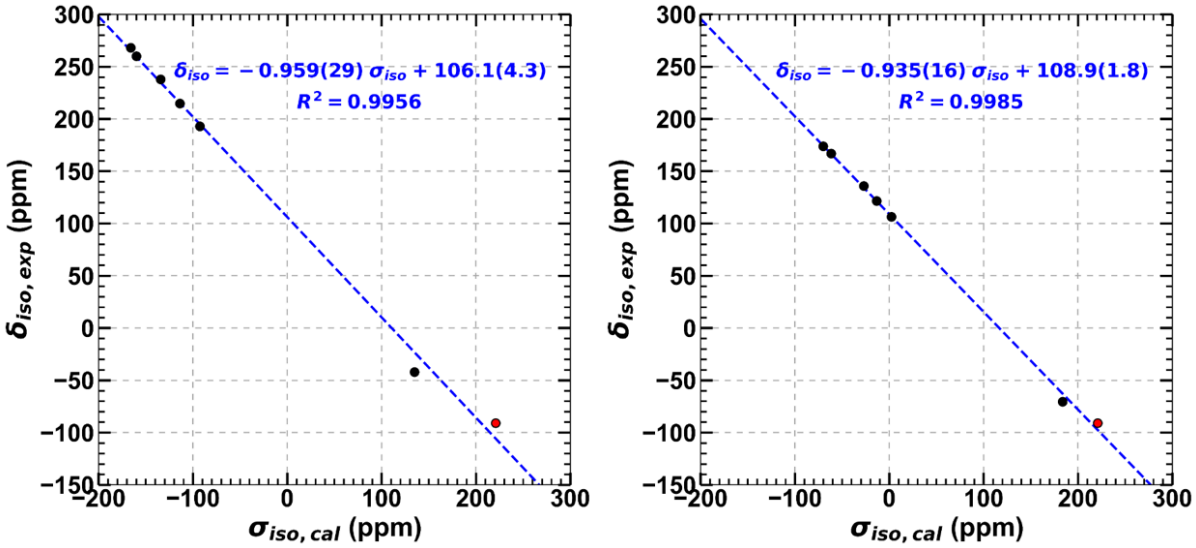


Figure S5. Experimental ^{19}F δ_{iso} as a function of the calculated σ_{iso}. The black dots correspond to NbF_5 (a) and TaF_5 (b) compounds, while the red dot corresponds to the RbF compound. The blue dashed lines represent the linear regressions whose equations and R-squared values are given in the graphs.

5.2. ^{87}Rb linear regression equations

First, a spectrum of RbF was recorded on a Bruker Avance III spectrometer functioning at 7.0 T (^{87}Rb Larmor frequency of 98.2 MHz) using a 2.5 mm CP-MAS probe-head and a spinning frequency of 25 kHz. The 90° pulse was set to 2.25 µs (RF field of 11 kHz) and the recycle delay to 2 s. The spectrum was referenced to 0.1 M/L aqueous solution of RbCl. The spectrum reconstruction is shown in **Figure S6**, whereas the NMR parameters are gathered in **Table S9**.

Table S9. Fit parameters including δ_{iso} (ppm), linewidth (LW, ppm), quadripolar coupling constant (C_Q, MHz) and asymmetry parameter (η_Q) resonances, used to reconstruct the ^{87}Rb MAS (25 kHz) NMR spectrum of RbF.

δ_{iso}	LW	C_Q	η_Q
62.6	4.8	244.8	1.0

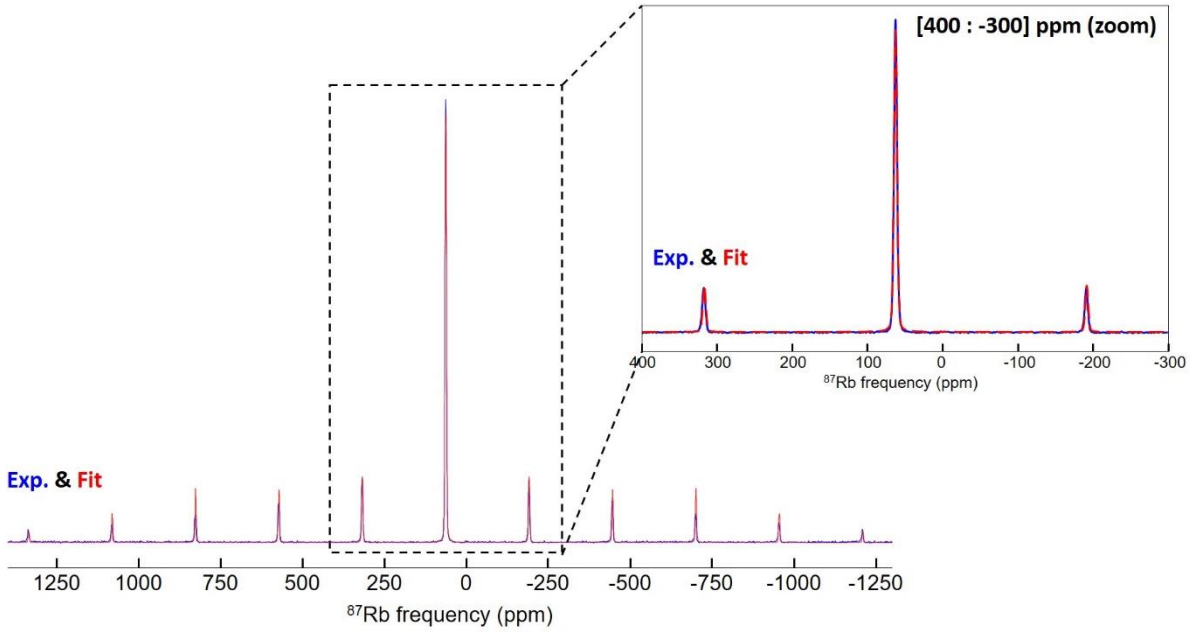


Figure S6. Experimental and fitted ^{87}Rb MAS (25 kHz) NMR spectra of RbF.

The electronic structure of the unit cells of RbF,[41] $RbNO_3$,[42] $RbVO_3$,[43] $RbClO_4$,[44] $RbLaF_4$,[45] Rb_2SO_4[46] and $RbSr_2Nb_3O_{10}$,[47] was obtained through solid-state DFT calculations with periodic boundary conditions using VASP (6.2.1 version)[36,37]. Conjugate gradient algorithm was used for the geometry optimization, all unit cells were geometry optimized except for the highly symmetrical unit cell of RbF. The GGA-PBE approximation was employed to obtain the ground state electronic structure. The PAW potential[48] used for N, O, F, S, Cl, V, Rb, Sr, Nb and La are respectively: N_s_GW, O_s_GW, F_GW, S_GW, Cl_GW, V_sv_GW, Rb_sv_GW, Sr_sv_GW, Nb_sv_GW and La_GW. The wave functions were expanded on a plane-wave basis set with a 550 eV kinetic energy cut-off and shifted Monkhorst-Pack k-point meshes (**Table S10**). The total energy was converged up to a change bellow 10^{-8} eV.

The PAW[49,50] and GIPAW[51,52] approaches were used to calculate the quadrupolar NMR parameters and the magnetic shielding values, respectively. The PAW potentials, plane-wave energy cut-off and the shifted Monkhorst-Pack k-point meshes were set the same as the geometry optimization.

Table S10. Compound, ICSD[1] code, space group (SG), number of Rb sites and shifted Monkhorst-Pack k-point mesh of the compounds used for the ^{87}Rb linear regression.

Compound	ICSD code	SG (No.)	Rb sites	k-point mesh
RbF	n.a.	$Fm\bar{3}m$ (225)	1	8 × 8 × 8
$RbNO_3$	66709	$P3_1$ (144)	3	3 × 3 × 4
$RbVO_3$	1488	*Pbcm* (57)	1	6 × 3 × 6
$RbClO_4$	63363	*Pnma* (62)	1	3 × 5 × 4
$RbLaF_4$	n.a.	*Pnma* (62)	1	5 × 8 × 2
Rb_2SO_4	203159	*Pnma* (62)	2	4 × 3 × 5
$RbSr_2Nb_3O_{10}$	93674	*P*4/*mmm* (123)	1	8 × 8 × 2

Table S11. ^{87}Rb experimental δ_{iso} ($\delta_{iso,exp}$, ppm), calculated σ_{iso} (σ_{iso}, ppm), calculated δ_{iso} (δ_{iso}, ppm) and the difference between δ_{iso} and $\delta_{iso,exp}$ values ($\Delta\delta_{iso}$, ppm) for the listed compounds. The references used are mentioned alongside each $\delta_{iso,exp}$ value. The average $\Delta\delta_{iso}$ is indicated in bold italics.

Compound	Rb site	$\delta_{iso,exp}$	σ_{iso}	δ_{iso}	$\Delta\delta_{iso}$
δ_{iso} = –0.722(32) σ_{iso} + 2297.3(103.0) (**Figure 8**)					
RbF	Rb1	62.6[(a)]	3088.9	67.1	4.5
$RbNO_3$	Rb1	–27.5[(b)][42]	3231.8	–36.1	8.6
	Rb2	–28.7	3219.8	–27.4	1.3
	Rb3	–32.0	3220.5	–27.9	4.1
$RbVO_3$	Rb1	–35.0[(b)][43]	3225.8	–31.7	3.3
$RbClO_4$	Rb1	–13.1[(b)][44]	3198.6	–12.1	1.0
$RbLaF_4$	Rb1	51.0[(a)][45]	3114.2	48.9	2.1
Rb_2SO_4	Rb1	42.3[(b)][44]	3131.0	36.7	5.6
	Rb2	15.8	3169.5	8.9	6.9
$RbSr_2Nb_3O_{10}$	Rb1	–4.1[(b)][47]	3189.3	–5.4	1.3
					3.9

[(a)] and [(b)] correspond to ^{87}Rb δ_{iso} referenced to RbCl and $RbNO_3$, respectively.

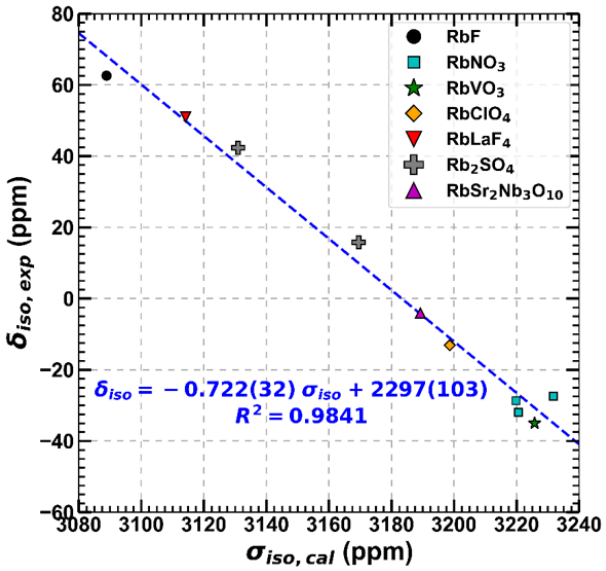


Figure S7. Experimental ^{87}Rb δ_{iso} as a function of the calculated σ_{iso}. The data symbols are identified in the legend located in the upper-right corner of the plot. The blue dashed line represents the linear regression, and its corresponding equation, along with its R-squared value, is given.

6. RbM_2O_5F calculated NMR parameters and structural features

6.1. Quadrupolar coupling constant values for $RbNb_2O_5F$ models

Table S12. Calculated C_Q (C_Q, MHz) of each Rb and Nb atom from the APO_32e models 1 to 10 of $RbNb_2O_5F$ and (in bold italic) average C_Q ($<C_Q>$, MHz) of all Rb and Nb atoms in a given model.

Atom	Model									
	1	2	3	4	5	6	7	8	9	10
Nb49	53.0	44.2	81.6	59.2	142.3	63.7	62.7	66.7	94.8	115.0
Nb50	52.9	77.1	93.7	59.3	113.0	60.1	69.1	61.8	77.6	115.0
Nb51	52.8	77.8	82.4	61.8	75.5	63.2	118.3	73.4	84.8	52.0
Nb52	52.8	59.7	94.2	61.9	85.4	59.1	62.7	56.6	105.4	152.3
Nb53	52.4	44.5	107.4	58.9	83.7	63.3	60.5	65.7	76.0	114.9
Nb54	52.7	79.9	115.4	59.3	92.2	59.9	71.2	62.8	97.3	114.8
Nb55	52.6	78.7	106.9	61.9	36.0	63.4	111.5	58.2	103.0	152.4
Nb56	52.7	69.0	115.5	62.0	87.6	59.4	59.4	74.8	86.0	52.0
Nb57	52.6	44.5	75.9	62.3	81.9	58.4	68.8	57.4	77.8	152.3
Nb58	52.7	60.1	86.1	58.9	83.1	57.4	111.9	66.5	104.0	129.9
Nb59	52.7	69.1	69.3	58.9	76.3	57.7	118.4	68.3	85.6	129.8
Nb60	52.7	44.1	86.6	61.9	49.8	57.7	71.8	73.2	96.8	52.1
Nb61	52.6	76.8	86.5	62.1	74.2	77.9	61.2	59.5	75.8	152.4
Nb62	52.8	79.6	69.8	62.1	100.2	78.2	62.2	74.6	98.4	52.0
Nb63	52.5	78.8	76.2	59.0	86.5	77.1	62.9	61.4	103.1	129.9
Nb64	52.9	78.4	86.0	58.7	95.3	77.8	59.5	60.4	86.4	129.8
$<C_Q>$	***52.7***	***66.4***	***89.6***	***60.5***	***85.2***	***64.6***	***77.0***	***65.1***	***90.8***	***112.3***
Rb65	2.5	2.4	2.7	1.6	1.9	0.9	2.3	2.1	1.2	2.6
Rb66	2.5	2.5	2.3	1.7	2.4	2.7	1.6	1.1	1.9	5.0
Rb67	2.5	1.8	3.5	1.7	3.9	2.8	3.4	1.3	2.2	2.6
Rb68	2.5	3.1	1.6	1.7	4.1	1.9	2.2	2.8	1.4	5.1
Rb69	2.5	2.3	1.7	1.7	3.0	1.9	2.2	2.2	1.4	5.1
Rb70	2.5	2.5	3.5	1.7	2.2	2.7	1.7	1.3	2.2	5.1
Rb71	2.5	1.8	2.1	1.7	4.3	2.8	3.3	0.9	2.2	2.6
Rb72	2.5	3.0	2.7	1.6	3.8	0.2	2.4	2.7	1.4	2.6
$<C_Q>$	***2.5***	***2.4***	***2.5***	***1.7***	***3.2***	***2.0***	***2.4***	***1.8***	***1.7***	***3.9***

Table S13. Calculated C_Q (C_Q, MHz) of each Rb and Nb atom from the APO_32e models 11 to 20 of $RbNb_2O_5F$ and (in bold italic) average C_Q ($\langle C_Q \rangle$, MHz) of all Rb and Nb atoms in a given model.

Atom	Model									
	11	12	13	14	15	16	17	18	19	20
Nb49	88.4	35.0	131.0	113.7	160.6	85.9	92.1	66.5	49.2	35.3
Nb50	50.2	86.2	126.0	63.2	53.4	49.4	127.9	54.5	71.1	30.2
Nb51	49.3	37.3	40.7	67.5	60.2	41.0	37.1	127.4	52.6	127.5
Nb52	99.8	31.4	71.2	109.9	26.6	61.7	74.6	38.9	104.2	57.6
Nb53	56.9	118.2	80.2	138.6	41.2	80.4	115.3	37.2	125.0	130.6
Nb54	42.3	189.6	103.3	140.3	93.5	133.5	112.1	51.3	112.6	40.4
Nb55	121.3	66.1	31.1	118.9	93.6	106.1	30.8	107.3	109.0	92.2
Nb56	157.0	48.0	142.4	74.6	116.4	121.8	114.7	65.7	46.0	131.7
Nb57	79.2	96.4	114.0	83.2	64.6	69.5	121.6	106.9	61.5	142.9
Nb58	63.1	33.6	89.0	66.5	66.3	90.6	39.6	55.0	43.6	51.9
Nb59	89.0	20.6	42.6	67.8	62.7	67.8	117.9	127.5	53.0	53.7
Nb60	99.9	62.5	58.2	103.0	48.2	80.8	58.6	52.5	87.0	53.4
Nb61	122.3	85.0	71.7	67.1	46.2	88.6	50.7	140.0	63.2	91.3
Nb62	159.7	88.6	88.1	84.0	63.7	66.8	126.7	30.6	59.0	30.9
Nb63	88.9	84.3	40.7	43.1	56.1	57.1	58.2	138.7	47.1	128.8
Nb64	73.9	55.3	158.5	57.8	138.1	103.1	93.5	31.0	53.9	39.6
$\langle C_Q \rangle$	***90.1***	***71.1***	***86.8***	***87.5***	***74.5***	***81.5***	***85.7***	***76.9***	***71.1***	***77.4***
Rb65	3.4	3.7	1.8	8.6	3.7	11.4	4.1	8.3	5.5	10.1
Rb66	2.5	2.0	2.2	4.7	4.8	5.2	3.1	2.8	5.9	6.7
Rb67	2.8	3.4	7.5	3.6	3.5	4.9	1.5	2.9	4.3	8.5
Rb68	4.9	1.8	2.8	5.0	8.6	7.9	5.7	8.3	7.1	4.2
Rb69	1.1	5.4	3.7	6.5	6.0	8.7	1.9	4.3	7.2	0.5
Rb70	5.0	4.5	1.4	5.1	4.3	6.4	8.9	8.1	2.8	8.7
Rb71	2.8	5.8	1.5	4.7	3.1	5.3	2.5	2.5	4.3	2.6
Rb72	2.5	3.1	3.7	2.8	1.7	2.7	9.7	5.8	1.6	4.1
$\langle C_Q \rangle$	***3.1***	***3.7***	***3.1***	***5.1***	***4.5***	***6.6***	***4.7***	***5.4***	***4.8***	***5.7***

Table S14. Calculated C_Q (C_Q, MHz) of each Rb and Nb atom from the APO_8b models 1 to 10 of $RbNb_2O_5F$ and (in bold italic) average C_Q ($\langle C_Q \rangle$, MHz) of all Rb and Nb atoms in a given model.

Atom	Model									
	1	2	3	4	5	6	7	8	9	10
Nb49	52.7	43.5	104.9	59.1	142.6	63.2	61.4	66.7	99.2	111.9
Nb50	52.7	81.7	104.9	59.1	113.4	59.8	68.5	66.7	99.2	111.9
Nb51	52.7	83.5	104.9	62.2	76.5	63.2	116.3	66.7	99.2	35.1
Nb52	52.7	69.9	104.9	62.2	85.0	59.8	61.6	66.7	99.2	166.1
Nb53	52.7	43.5	104.9	59.1	83.6	63.2	61.4	66.7	99.2	111.9
Nb54	52.7	81.7	104.9	59.1	91.8	59.8	68.5	66.7	99.2	111.9
Nb55	52.7	83.5	104.9	62.2	35.9	63.2	116.3	66.7	99.2	166.1
Nb56	52.7	69.9	104.9	62.2	87.8	59.8	61.6	66.7	99.2	35.1
Nb57	52.7	43.5	83.4	62.1	81.5	57.9	68.5	66.7	99.2	166.1
Nb58	52.7	69.9	83.4	59.1	83.1	57.9	116.3	66.7	99.2	111.9
Nb59	52.7	69.9	83.4	59.1	76.7	57.9	116.3	66.7	99.2	111.9
Nb60	52.7	43.5	83.4	62.1	50.2	57.9	68.5	66.7	99.2	35.1
Nb61	52.7	81.7	83.4	62.1	73.9	78.4	61.4	66.7	99.2	166.1
Nb62	52.7	81.7	83.4	62.1	100.2	78.4	61.4	66.7	99.2	35.1
Nb63	52.7	83.5	83.4	59.1	86.0	78.4	61.6	66.7	99.2	111.9
Nb64	52.7	83.5	83.4	59.1	96.0	78.4	61.6	66.7	99.2	111.9
$\langle C_Q \rangle$	***52.7***	***69.7***	***94.2***	***60.6***	***85.3***	***64.8***	***77.0***	***66.7***	***99.2***	***106.3***
Rb65	2.5	2.2	0.9	1.7	3.0	1.9	2.1	3.0	0.4	2.8
Rb66	2.5	2.7	3.3	1.7	2.3	2.8	1.7	0.7	1.1	2.8
Rb67	2.5	2.7	0.9	1.7	4.1	1.9	2.0	3.0	0.4	2.8
Rb68	2.5	2.0	3.3	1.7	4.3	2.8	3.4	0.7	1.1	2.8
Rb69	2.5	2.7	3.3	1.7	2.2	2.8	1.7	0.7	1.1	2.8
Rb70	2.5	2.0	3.3	1.7	3.8	2.8	3.4	0.7	1.1	2.8
Rb71	2.5	2.2	1.7	1.7	2.0	0.7	2.0	3.0	0.4	2.8
Rb72	2.5	2.7	1.7	1.7	3.7	0.1	2.1	3.0	0.4	2.8
$\langle C_Q \rangle$	***2.5***	***2.4***	***2.3***	***1.7***	***3.2***	***1.9***	***2.3***	***1.8***	***0.8***	***2.8***

Table S15. Calculated C_Q (C_Q, MHz) of each Rb and Nb atom from the APO_8b models 11 to 20 of $RbNb_2O_5F$ and (in bold italic) average C_Q ($\langle C_Q \rangle$, MHz) of all Rb and Nb atoms in a given model.

Atom	Model									
	11	12	13	14	15	16	17	18	19	20
Nb49	88.6	38.3	130.9	114.0	151.0	85.3	50.8	109.8	57.3	34.6
Nb50	50.4	83.8	125.3	63.2	82.7	49.2	118.3	60.7	57.3	30.8
Nb51	49.6	31.0	40.5	67.6	72.8	40.8	38.7	109.8	50.6	128.7
Nb52	99.6	34.2	69.7	109.5	44.5	62.0	91.8	106.6	105.8	57.4
Nb53	56.5	121.1	81.3	138.5	44.5	80.6	100.4	128.7	119.4	131.1
Nb54	42.2	187.2	103.4	140.5	72.8	133.1	99.2	46.6	119.4	40.3
Nb55	121.2	64.7	31.1	119.3	82.7	106.1	28.6	110.5	105.8	91.3
Nb56	156.6	40.0	142.6	74.8	151.0	121.5	118.3	109.8	50.6	131.1
Nb57	79.9	96.9	114.1	83.0	82.7	69.6	91.8	110.5	61.6	143.0
Nb58	62.9	35.3	89.3	65.4	82.7	90.5	38.7	60.7	45.0	52.9
Nb59	89.0	19.0	41.4	68.0	72.8	67.8	161.6	109.8	45.0	53.6
Nb60	99.8	63.9	58.1	103.2	72.8	80.9	69.3	46.6	87.5	52.9
Nb61	122.5	87.5	71.1	67.0	64.9	88.9	68.8	88.4	63.6	91.3
Nb62	160.0	89.1	88.5	83.9	122.7	66.8	100.4	46.6	58.8	30.8
Nb63	89.0	81.0	40.5	42.9	64.9	57.4	69.3	128.7	49.6	128.7
Nb64	73.6	59.6	158.3	57.9	122.7	102.4	99.2	46.6	49.6	40.3
$\langle C_Q \rangle$	***90.1***	***70.8***	***86.6***	***87.4***	***86.8***	***81.4***	***84.1***	***88.8***	***70.4***	***77.4***
Rb65	1.1	5.0	3.6	6.5	8.8	8.8	2.0	4.6	7.0	0.5
Rb66	2.5	2.1	2.0	4.8	6.0	5.2	2.0	9.3	5.1	6.7
Rb67	5.0	1.3	2.8	5.2	10.8	8.0	3.1	9.3	7.0	4.2
Rb68	2.9	4.4	2.1	4.7	7.7	5.3	1.3	4.6	3.6	2.6
Rb69	5.0	4.5	1.4	5.0	7.7	6.5	7.5	9.3	1.9	8.7
Rb70	2.8	2.8	7.3	3.7	6.0	4.9	3.1	9.3	3.6	8.7
Rb71	3.4	3.5	1.9	8.6	10.8	11.4	1.3	9.3	5.4	10.0
Rb72	2.4	3.6	3.9	2.8	4.1	2.8	7.5	9.3	2.2	4.2
$\langle C_Q \rangle$	***3.1***	***3.4***	***3.1***	***5.1***	***7.7***	***6.6***	***3.5***	***8.1***	***4.5***	***5.7***

6.2. Asymmetry parameter values for $RbNb_2O_5F$ models

Table S16. Calculated η_Q (η_Q, MHz) of each Rb and Nb atom from the APO_32e models 1 to 10 of $RbNb_2O_5F$ and (in bold italic) average η_Q ($<\eta_Q>$, MHz) of all Rb and Nb atoms in a given model.

Atom	Model									
	1	2	3	4	5	6	7	8	9	10
Nb49	0.93	0.29	0.62	0.99	0.29	0.77	0.71	0.54	0.54	0.26
Nb50	0.93	0.74	0.89	0.99	0.15	0.68	0.95	0.79	0.69	0.26
Nb51	0.94	0.31	0.63	0.51	0.16	0.79	0.55	0.51	0.61	0.97
Nb52	0.93	0.77	0.88	0.49	0.40	0.70	0.36	0.88	0.23	0.61
Nb53	0.94	0.33	0.25	1.00	0.14	0.79	0.75	0.81	0.65	0.27
Nb54	0.94	0.83	0.14	0.98	0.26	0.69	0.95	0.58	0.52	0.27
Nb55	0.94	0.47	0.24	0.50	0.96	0.76	0.39	0.67	0.22	0.61
Nb56	0.94	0.34	0.14	0.51	0.58	0.72	0.68	0.51	0.60	0.97
Nb57	0.94	0.34	0.24	0.50	0.40	0.26	0.94	0.83	0.65	0.61
Nb58	0.94	0.77	0.40	0.98	0.59	0.25	0.40	0.77	0.22	0.22
Nb59	0.94	0.35	0.68	0.99	0.96	0.26	0.55	0.54	0.61	0.22
Nb60	0.94	0.28	0.69	0.50	0.53	0.26	0.94	0.53	0.49	0.97
Nb61	0.94	0.75	0.41	0.49	0.69	0.62	0.75	0.73	0.67	0.61
Nb62	0.94	0.82	0.68	0.50	0.81	0.59	0.71	0.50	0.51	0.97
Nb63	0.94	0.48	0.24	0.99	0.27	0.61	0.39	0.82	0.23	0.22
Nb64	0.94	0.30	0.69	0.99	0.52	0.62	0.67	0.60	0.58	0.22
$<\eta_Q>$	***0.94***	***0.51***	***0.49***	***0.74***	***0.48***	***0.59***	***0.67***	***0.66***	***0.50***	***0.52***
Rb65	0.44	0.78	0.87	0.84	0.88	0.16	0.77	0.61	0.96	0.77
Rb66	0.39	0.26	0.41	0.86	0.60	0.69	0.18	0.32	0.84	0.94
Rb67	0.44	0.57	0.30	0.74	0.29	0.69	0.45	0.92	0.16	0.78
Rb68	0.40	0.54	0.98	0.83	0.37	0.76	0.75	0.50	0.95	0.94
Rb69	0.45	0.80	0.94	0.85	0.55	0.80	0.37	0.67	0.67	0.95
Rb70	0.51	0.26	0.28	0.88	0.60	0.66	0.79	0.69	0.76	0.92
Rb71	0.45	0.57	0.36	0.78	0.68	0.75	0.76	0.50	0.31	0.79
Rb72	0.46	0.53	0.89	0.87	0.94	0.69	0.32	0.44	0.73	0.78
$<\eta_Q>$	***0.45***	***0.54***	***0.63***	***0.83***	***0.61***	***0.65***	***0.55***	***0.58***	***0.67***	***0.86***

Table S17. Calculated η_Q (η_Q, MHz) of each Rb and Nb atom from the APO_32e models 11 to 20 of $RbNb_2O_5F$ and (in bold italic) average η_Q ($<\eta_Q>$, MHz) of all Rb and Nb atoms in a given model.

Atom	Model									
	11	12	13	14	15	16	17	18	19	20
Nb49	0.47	0.73	0.33	0.33	0.39	0.76	0.71	0.97	0.38	0.30
Nb50	0.38	0.79	0.52	0.39	0.96	0.92	0.74	0.91	0.30	0.46
Nb51	0.95	0.32	0.88	0.41	0.14	0.99	0.90	0.91	0.72	0.70
Nb52	0.69	0.77	0.69	0.55	0.48	0.93	0.98	0.11	0.56	0.22
Nb53	0.52	0.54	0.40	0.07	0.14	0.25	0.29	0.25	0.67	0.60
Nb54	0.76	0.75	0.28	0.10	0.70	0.34	0.29	0.72	0.71	0.63
Nb55	0.36	0.07	0.98	0.53	0.38	0.15	0.78	0.58	0.55	0.84
Nb56	0.63	0.53	0.83	0.33	0.67	0.22	0.49	0.97	0.98	0.60
Nb57	0.52	0.43	0.43	0.14	0.91	0.87	0.72	0.57	0.72	0.26
Nb58	0.78	0.48	0.46	0.56	0.63	0.35	0.26	0.90	0.53	0.75
Nb59	0.49	1.00	0.70	0.58	0.98	0.86	0.45	0.90	0.91	0.23
Nb60	0.45	0.56	0.47	0.16	0.72	0.12	0.29	0.74	0.11	0.78
Nb61	0.27	0.67	0.24	0.34	0.89	0.63	0.93	0.14	0.89	0.84
Nb62	0.34	0.16	0.08	0.76	0.93	0.59	0.31	0.09	0.20	0.35
Nb63	0.21	0.50	0.87	0.83	0.42	0.44	0.40	0.12	0.83	0.70
Nb64	0.27	0.44	0.14	0.23	0.43	0.72	0.56	0.13	0.96	0.60
$<\eta_Q>$	***0.51***	***0.55***	***0.52***	***0.40***	***0.61***	***0.57***	***0.57***	***0.56***	***0.63***	***0.55***
Rb65	0.94	0.51	0.22	0.05	3.7	0.03	0.90	0.22	0.38	0.18
Rb66	0.71	0.69	0.66	0.19	4.8	0.80	0.97	0.18	0.33	0.97
Rb67	0.92	0.38	0.42	0.77	3.5	0.58	0.15	0.24	0.31	0.11
Rb68	0.48	0.23	0.81	0.38	8.6	0.84	0.56	0.19	0.55	0.46
Rb69	0.67	0.68	0.40	0.10	6.0	0.24	0.95	0.08	0.19	0.88
Rb70	0.19	0.07	0.42	0.18	4.3	0.78	0.19	0.22	0.60	0.16
Rb71	0.34	0.67	0.88	0.35	3.1	0.76	0.70	0.48	0.46	0.35
Rb72	0.77	0.74	0.65	0.59	1.7	0.06	0.41	0.58	0.59	0.55
$<\eta_Q>$	***0.63***	***0.50***	***0.56***	***0.33***	***4.5***	***0.51***	***0.60***	***0.27***	***0.43***	***0.46***

Table S18. Calculated η_Q (η_Q, MHz) of each Rb and Nb atom from the APO_8b models 1 to 10 of $RbNb_2O_5F$ and (in bold italic) average η_Q ($<\eta_Q>$, MHz) of all Rb and Nb atoms in a given model.

Atom	Model									
	1	2	3	4	5	6	7	8	9	10
Nb49	0.94	0.31	0.51	0.98	0.29	0.78	0.74	0.77	0.17	0.54
Nb50	0.94	0.84	0.51	0.99	0.15	0.69	0.99	0.77	0.17	0.54
Nb51	0.94	0.23	0.51	0.49	0.15	0.78	0.53	0.77	0.17	0.96
Nb52	0.94	0.77	0.51	0.49	0.40	0.69	0.55	0.77	0.17	0.76
Nb53	0.94	0.31	0.51	0.99	0.14	0.78	0.74	0.77	0.17	0.54
Nb54	0.94	0.84	0.51	0.98	0.26	0.69	0.99	0.77	0.17	0.54
Nb55	0.94	0.23	0.51	0.49	0.96	0.78	0.53	0.77	0.17	0.76
Nb56	0.94	0.77	0.51	0.49	0.58	0.69	0.55	0.77	0.17	0.96
Nb57	0.94	0.31	0.37	0.49	0.38	0.26	0.99	0.77	0.17	0.76
Nb58	0.94	0.77	0.37	0.98	0.59	0.26	0.53	0.77	0.17	0.54
Nb59	0.94	0.77	0.37	0.99	0.96	0.26	0.53	0.77	0.17	0.54
Nb60	0.94	0.31	0.37	0.49	0.53	0.26	0.99	0.77	0.17	0.96
Nb61	0.94	0.84	0.37	0.49	0.69	0.61	0.74	0.77	0.17	0.76
Nb62	0.94	0.84	0.37	0.49	0.81	0.61	0.74	0.77	0.17	0.96
Nb63	0.94	0.23	0.37	0.98	0.27	0.61	0.55	0.77	0.17	0.54
Nb64	0.94	0.23	0.37	0.99	0.52	0.61	0.55	0.77	0.17	0.54
$<\eta_Q>$	***0.94***	***0.54***	***0.44***	***0.74***	***0.48***	***0.59***	***0.70***	***0.77***	***0.17***	***0.70***
Rb65	0.39	0.18	0.46	0.77	0.59	0.73	0.30	0.97	0.00	0.31
Rb66	0.39	0.66	0.43	0.77	0.64	0.69	0.19	0.00	0.00	0.31
Rb67	0.39	0.93	0.46	0.77	0.38	0.73	0.73	0.97	0.00	0.31
Rb68	0.39	0.05	0.43	0.77	0.69	0.69	0.57	0.00	0.00	0.31
Rb69	0.39	0.66	0.43	0.77	0.61	0.69	0.19	0.00	0.00	0.31
Rb70	0.39	0.05	0.43	0.77	0.29	0.69	0.57	0.00	0.00	0.31
Rb71	0.39	0.18	0.44	0.77	0.84	0.00	0.73	0.97	0.00	0.31
Rb72	0.39	0.93	0.44	0.77	0.97	0.00	0.30	0.97	0.00	0.31
$<\eta_Q>$	***0.39***	***0.45***	***0.44***	***0.77***	***0.63***	***0.53***	***0.45***	***0.49***	***0.00***	***0.31***

Table S19. Calculated η_Q (η_Q, MHz) of each Rb and Nb atom from the APO_8b models 11 to 20 of $RbNb_2O_5F$ and (in bold italic) average η_Q ($<\eta_Q>$, MHz) of all Rb and Nb atoms in a given model.

Atom	Model									
	11	12	13	14	15	16	17	18	19	20
Nb49	0.47	0.68	0.34	0.33	0.13	0.76	0.65	0.96	0.35	0.28
Nb50	0.36	0.83	0.52	0.39	0.30	0.94	0.60	0.80	0.35	0.42
Nb51	0.95	0.62	0.91	0.41	0.45	0.99	0.31	0.96	0.76	0.70
Nb52	0.68	0.52	0.72	0.56	0.51	0.93	0.47	0.21	0.55	0.22
Nb53	0.54	0.47	0.40	0.07	0.51	0.23	0.92	0.04	0.66	0.60
Nb54	0.77	0.77	0.27	0.10	0.45	0.31	0.45	0.43	0.66	0.62
Nb55	0.36	0.10	0.97	0.54	0.30	0.14	0.32	0.10	0.55	0.84
Nb56	0.64	0.73	0.83	0.34	0.13	0.22	0.60	0.96	0.76	0.60
Nb57	0.52	0.38	0.43	0.15	0.30	0.87	0.47	0.10	0.21	0.26
Nb58	0.78	0.38	0.48	0.58	0.30	0.35	0.31	0.80	0.97	0.77
Nb59	0.49	0.93	0.71	0.58	0.45	0.88	0.33	0.96	0.97	0.22
Nb60	0.45	0.57	0.51	0.17	0.45	0.12	0.62	0.43	0.07	0.77
Nb61	0.27	0.65	0.20	0.34	0.11	0.63	0.44	0.10	0.91	0.84
Nb62	0.34	0.18	0.07	0.75	0.65	0.59	0.92	0.43	0.25	0.42
Nb63	0.21	0.57	0.91	0.83	0.11	0.42	0.62	0.04	0.95	0.70
Nb64	0.28	0.48	0.15	0.22	0.65	0.71	0.45	0.43	0.95	0.62
$<\eta_Q>$	***0.51***	***0.55***	***0.53***	***0.40***	***0.36***	***0.57***	***0.53***	***0.48***	***0.62***	***0.55***
Rb65	0.73	0.66	0.40	0.13	0.52	0.23	0.76	0.04	0.12	0.75
Rb66	0.70	0.69	0.70	0.20	0.18	0.79	0.76	0.30	0.42	0.99
Rb67	0.54	0.94	1.00	0.38	0.44	0.84	0.94	0.30	0.12	0.48
Rb68	0.32	0.58	0.75	0.32	0.55	0.78	0.80	0.04	0.78	0.33
Rb69	0.19	0.15	0.41	0.20	0.55	0.78	0.56	0.31	0.95	0.15
Rb70	0.95	0.57	0.40	0.76	0.18	0.58	0.94	0.30	0.78	0.15
Rb71	0.97	0.63	0.24	0.05	0.44	0.01	0.80	0.30	0.49	0.15
Rb72	0.80	0.81	0.64	0.57	0.59	0.07	0.56	0.31	0.69	0.48
$<\eta_Q>$	***0.65***	***0.63***	***0.57***	***0.33***	***0.43***	***0.51***	***0.76***	***0.23***	***0.54***	***0.44***

6.3. Magnetic shielding values for $RbNb_2O_5F$ models

Table S20. Calculated σ_{iso} (σ_{iso}, ppm) of each F, Rb and Nb atom from the APO_32e models 1 to 10 of $RbNb_2O_5F$ and (in bold italic) average σ_{iso} ($<\sigma_{iso}>$, ppm) of all F, Rb and Nb atoms in a given model.

Atom	Model									
	1	2	3	4	5	6	7	8	9	10
F41	198.6	201.8	209.7	214.1	197.1	196.4	184.5	205.4	202.2	160.6
F42	198.7	214.9	210.0	214.3	196.8	220.4	180.9	218.3	213.0	160.9
F43	198.5	214.9	208.0	214.2	200.5	204.1	209.3	198.1	213.9	160.9
F44	198.7	212.2	208.0	214.1	221.0	204.1	206.3	224.2	203.2	171.6
F45	198.7	212.2	191.3	214.0	219.5	203.8	208.8	223.9	184.9	171.5
F46	198.6	201.7	191.3	214.4	164.5	203.8	205.5	199.7	216.8	160.9
F47	198.7	201.1	209.3	214.0	161.2	220.8	206.0	205.6	184.8	171.4
F48	198.6	201.1	210.3	214.0	205.6	195.7	206.1	218.1	214.6	171.6
$<\sigma_{iso}>$	***198.6***	***207.5***	***204.8***	***214.1***	***195.8***	***206.2***	***200.9***	***211.7***	***204.2***	***166.2***
Nb49	408.6	418.2	387.5	427.6	415.0	413.3	411.6	422.2	400.2	405.6
Nb50	408.6	424.2	392.5	427.3	372.0	423.9	390.1	437.8	396.8	405.7
Nb51	408.7	437.3	385.4	414.9	395.5	415.1	392.8	439.6	410.8	404.8
Nb52	408.9	433.4	391.9	415.2	427.3	425.1	432.4	426.8	411.4	382.0
Nb53	409.0	411.0	412.3	427.8	389.8	414.4	409.2	438.6	402.3	405.7
Nb54	408.7	428.6	378.1	427.7	384.6	423.7	380.0	423.8	398.9	405.8
Nb55	408.7	426.2	411.7	415.0	406.4	413.9	400.3	422.5	412.7	381.8
Nb56	408.3	421.8	376.8	415.1	416.5	425.6	428.6	440.4	408.9	405.0
Nb57	409.1	411.2	437.1	415.0	426.5	408.0	390.9	427.3	403.9	381.1
Nb58	408.3	433.3	441.7	428.0	400.2	408.8	399.7	438.1	408.2	378.0
Nb59	409.0	421.6	436.9	427.4	413.2	408.3	393.0	418.6	406.1	378.5
Nb60	408.4	418.2	403.1	415.3	406.9	408.9	378.6	441.2	404.1	404.8
Nb61	408.8	424.8	442.0	414.9	429.0	427.2	408.4	420.5	404.0	381.6
Nb62	408.8	428.8	436.9	414.7	445.2	428.8	412.6	439.1	399.4	404.9
Nb63	409.0	426.0	436.5	427.7	440.0	428.4	433.9	436.7	412.1	378.2
Nb64	408.6	437.5	403.1	428.0	420.2	427.3	427.4	423.1	405.6	378.3
$<\sigma_{iso}>$	***408.7***	***425.1***	***410.9***	***421.4***	***411.8***	***418.8***	***405.6***	***431.0***	***405.3***	***392.6***

Table S20. (Continued)

Atom	Model									
	1	2	3	4	5	6	7	8	9	10
Rb65	3287.9	3288.1	3299.9	3291.6	3269.8	3291.0	3285.7	3298.3	3293.9	3271.5
Rb66	3287.9	3290.6	3286.6	3291.6	3285.3	3291.2	3282.6	3291.8	3290.6	3287.8
Rb67	3287.8	3293.4	3299.3	3291.3	3287.4	3290.7	3301.0	3290.2	3306.3	3271.6
Rb68	3287.9	3292.0	3292.2	3291.4	3288.2	3281.4	3285.3	3294.7	3292.8	3287.7
Rb69	3287.8	3288.1	3292.1	3291.2	3286.9	3281.5	3292.2	3298.0	3293.9	3287.4
Rb70	3287.9	3290.6	3299.0	3291.4	3286.9	3291.2	3273.3	3290.3	3290.5	3287.9
Rb71	3287.9	3293.4	3287.2	3291.3	3290.1	3291.3	3301.4	3292.2	3305.1	3271.5
Rb72	3287.9	3292.1	3299.8	3291.5	3292.7	3305.4	3292.2	3295.8	3293.4	3271.5
<σ_{iso}>	***3287.9***	***3291.0***	***3294.5***	***3291.4***	***3285.9***	***3290.5***	***3289.2***	***3293.9***	***3295.8***	***3279.6***

Table S21. Calculated σ_{iso} (σ_{iso}, ppm) of each F, Rb and Nb atom from the APO_32e models 11 to 20 of $RbNb_2O_5F$ and (in bold italic) average σ_{iso} ($<\sigma_{iso}>$, ppm) of all F, Rb and Nb atoms in a given model.

Atom	Model									
	11	12	13	14	15	16	17	18	19	20
F41	166.7	213.5	138.9	116.0	149.7	138.6	129.0	107.9	152.1	149.2
F42	216.5	227.8	188.9	111.0	237.7	232.7	118.8	139.4	166.2	97.9
F43	209.4	219.5	196.5	143.2	200.3	200.4	51.1	248.9	254.9	241.4
F44	228.3	224.5	212.1	184.8	150.0	207.4	249.6	108.2	190.8	93.4
F45	218.3	227.1	216.0	200.4	240.7	243.7	238.5	218.0	244.7	101.1
F46	170.7	202.9	185.0	188.6	215.6	132.4	-37.4	114.4	190.7	140.9
F47	221.0	204.6	195.1	239.6	233.8	255.2	108.0	75.9	244.8	100.5
F48	189.7	183.3	208.1	229.4	246.3	244.6	53.0	75.4	244.4	241.4
<σ_{iso}>	***202.6***	***212.9***	***192.6***	***176.6***	***209.3***	***206.9***	***113.8***	***136.0***	***211.1***	***145.7***
Nb49	403.2	435.4	417.7	347.9	312.4	348.7	560.7	340.3	385.8	452.1
Nb50	372.6	459.6	335.0	387.8	347.6	384.1	354.1	354.0	374.4	385.4
Nb51	406.3	389.7	360.5	361.6	388.8	386.5	369.0	372.2	351.8	350.7
Nb52	397.3	366.7	363.2	332.2	427.8	359.3	349.3	544.9	335.6	488.0
Nb53	386.9	353.0	427.4	331.3	370.7	400.2	353.2	363.1	330.0	376.4
Nb54	383.0	391.4	362.3	335.8	349.4	325.9	340.4	385.0	324.4	354.1

Table S21. (Continued)

Atom	Model									
	11	12	13	14	15	16	17	18	19	20
Nb55	352.9	388.4	399.4	320.4	400.1	386.8	375.0	340.8	339.0	339.5
Nb56	410.3	387.8	445.4	367.5	315.8	350.7	344.1	340.0	352.4	372.2
Nb57	396.8	381.0	384.7	389.8	374.4	350.3	304.9	341.9	371.3	335.9
Nb58	407.7	380.6	400.3	364.5	366.9	378.3	368.6	353.5	373.2	368.5
Nb59	417.4	390.3	390.8	362.5	366.4	363.9	344.8	371.9	360.1	353.4
Nb60	371.9	416.5	433.8	356.0	372.4	395.9	356.7	383.8	360.9	367.5
Nb61	397.2	404.9	381.8	561.2	417.3	444.0	362.2	329.4	508.0	341.7
Nb62	358.8	437.6	301.4	472.2	481.8	398.7	356.5	376.1	410.0	383.8
Nb63	430.5	366.5	376.5	326.7	411.8	401.6	367.6	392.3	418.3	350.7
Nb64	440.5	387.7	349.0	308.7	380.8	435.8	342.0	376.5	416.1	355.6
<σ_{iso}>	***395.8***	***396.1***	***383.1***	***370.4***	***380.3***	***381.9***	***365.6***	***372.8***	***375.7***	***373.5***
Rb65	3274.3	3278.6	3281.3	3291.6	3288.2	3304.3	3284.2	3290.4	3278.5	3267.5
Rb66	3281.6	3277.0	3286.2	3257.2	3278.3	3279.8	3288.2	3283.2	3284.2	3267.2
Rb67	3292.3	3297.5	3271.7	3279.0	3284.8	3280.4	3269.7	3283.1	3276.1	3278.4
Rb68	3297.4	3299.2	3299.0	3296.0	3292.7	3274.0	3272.2	3291.5	3284.7	3276.5
Rb69	3284.6	3279.1	3276.0	3288.7	3272.8	3286.9	3276.6	3291.7	3291.9	3288.7
Rb70	3296.7	3283.1	3282.2	3292.9	3259.4	3279.7	3274.0	3266.1	3284.4	3277.9
Rb71	3272.7	3291.9	3297.2	3288.1	3267.8	3274.8	3281.2	3285.1	3276.3	3294.3
Rb72	3297.5	3292.5	3290.6	3271.0	3280.9	3261.5	3289.0	3264.4	3281.1	3276.4
<σ_{iso}>	***3287.1***	***3287.4***	***3285.5***	***3283.1***	***3278.1***	***3280.2***	***3279.4***	***3281.9***	***3282.2***	***3278.4***

Table S22. Calculated σ_{iso} (σ_{iso}, ppm) of each F, Rb and Nb atom from the APO_8b models 1 to 10 of $RbNb_2O_5F$ and (in bold italic) average σ_{iso} ($<\sigma_{iso}>$, ppm) of all F, Rb and Nb atoms in a given model.

Atom	Model									
	1	2	3	4	5	6	7	8	9	10
F41	198.6	204.0	211.7	214.2	197.2	196.0	182.7	208.2	203.8	153.4
F42	198.6	204.0	211.7	214.2	197.2	220.9	182.7	208.2	203.8	153.4
F43	198.6	204.0	211.7	214.2	200.4	203.9	206.2	208.2	203.8	153.4
F44	198.6	207.7	211.7	214.2	221.2	203.9	206.3	208.2	203.8	153.4
F45	198.6	207.7	202.5	214.2	219.2	203.9	206.3	208.2	203.8	153.4
F46	198.6	204.0	202.5	214.2	165.0	203.9	206.2	208.2	203.8	153.4
F47	198.6	201.3	202.5	214.2	161.3	220.9	206.3	208.2	203.8	153.4
F48	198.6	201.3	202.5	214.2	205.3	196.0	206.3	208.2	203.8	153.4
$<\sigma_{iso}>$	***198.6***	***204.2***	***207.1***	***214.2***	***195.8***	***206.2***	***200.4***	***208.2***	***203.8***	***153.4***
Nb49	408.6	415.4	396.2	427.6	414.6	414.2	409.2	438.9	414.8	384.2
Nb50	408.6	427.5	396.2	427.7	372.2	424.3	384.2	438.9	414.8	384.2
Nb51	408.6	432.7	396.2	415.3	394.9	414.2	393.7	438.9	414.8	423.2
Nb52	408.6	422.4	396.2	415.3	428.3	424.3	429.1	438.9	414.8	424.6
Nb53	408.6	415.4	396.2	427.7	390.1	414.2	409.2	438.9	414.8	384.2
Nb54	408.6	427.5	396.2	427.6	384.6	424.3	384.2	438.9	414.8	384.2
Nb55	408.6	432.7	396.2	415.3	406.7	414.2	393.7	438.9	414.8	424.6
Nb56	408.6	422.4	396.2	415.3	416.5	424.3	429.1	438.9	414.8	423.2
Nb57	408.6	415.4	443.3	415.3	427.2	408.2	384.2	438.9	414.8	424.6
Nb58	408.6	422.4	443.3	427.6	399.8	408.2	393.7	438.9	414.8	384.2
Nb59	408.6	422.4	443.3	427.7	413.1	408.2	393.7	438.9	414.8	384.2
Nb60	408.6	415.4	443.3	415.3	406.0	408.2	384.2	438.9	414.8	423.2
Nb61	408.6	427.5	443.3	415.3	429.1	427.6	409.2	438.9	414.8	424.6
Nb62	408.6	427.5	443.3	415.3	445.3	427.6	409.2	438.9	414.8	423.2
Nb63	408.6	432.7	443.3	427.6	440.7	427.6	429.1	438.9	414.8	384.2
Nb64	408.6	432.7	443.3	427.7	419.6	427.6	429.1	438.9	414.8	384.2
$<\sigma_{iso}>$	***408.6***	***424.5***	***419.7***	***421.5***	***411.8***	***418.6***	***404.1***	***438.9***	***414.8***	***404.0***

Table S22. (Continued)

Atom	Model									
	1	2	3	4	5	6	7	8	9	10
Rb65	3287.7	3287.4	3290.9	3291.3	3286.9	3281.6	3292.3	3304.8	3297.0	3285.7
Rb66	3287.7	3290.9	3295.9	3291.3	3285.2	3291.1	3276.7	3293.0	3304.1	3285.7
Rb67	3287.7	3299.1	3290.9	3291.3	3288.6	3281.6	3286.5	3304.8	3297.0	3285.7
Rb68	3287.7	3294.8	3295.9	3291.3	3290.0	3291.1	3302.0	3293.0	3304.1	3285.7
Rb69	3287.7	3290.9	3295.9	3291.3	3286.8	3291.1	3276.7	3293.0	3304.1	3285.7
Rb70	3287.7	3294.8	3295.9	3291.3	3287.6	3291.1	3302.0	3293.0	3304.1	3285.7
Rb71	3287.7	3287.4	3310.8	3291.3	3269.9	3290.3	3286.5	3304.8	3297.0	3285.7
Rb72	3287.7	3299.1	3310.8	3291.3	3292.8	3305.5	3292.3	3304.8	3297.0	3285.7
<σ_{iso}>	***3287.7***	***3293.1***	***3298.4***	***3291.3***	***3286.0***	***3290.4***	***3289.4***	***3298.9***	***3300.6***	***3285.7***

Table S23. Calculated σ_{iso} (σ_{iso}, ppm) of each F, Rb and Nb atom from the APO_8b models 11 to 20 of $RbNb_2O_5F$ and (in bold italic) average σ_{iso} ($<\sigma_{iso}>$, ppm) of all F, Rb and Nb atoms in a given model.

Atom	Model									
	11	12	13	14	15	16	17	18	19	20
F41	165.8	213.8	138.3	115.3	140.1	138.6	70.1	-2.1	160.0	148.1
F42	216.9	225.3	189.1	111.7	244.8	233.6	87.4	-7.4	160.0	96.2
F43	208.9	220.5	197.2	143.1	244.8	200.5	69.0	234.6	256.4	241.6
F44	228.5	221.9	212.9	185.0	230.4	206.6	239.8	-2.1	189.1	96.2
F45	218.1	230.7	216.6	200.1	251.8	244.0	239.8	234.6	245.9	100.4
F46	170.6	202.9	185.2	188.6	140.1	132.2	70.1	-7.4	189.1	141.5
F47	221.3	200.9	194.2	239.8	244.8	255.5	87.4	-2.1	245.9	100.4
F48	190.0	181.6	207.6	229.4	244.8	244.3	69.0	-2.1	243.7	241.6
<σ_{iso}>	***202.5***	***212.2***	***192.6***	***176.6***	***217.7***	***206.9***	***116.6***	***55.8***	***211.2***	***145.8***
Nb49	402.9	438.8	418.8	347.7	379.4	349.9	490.2	334.5	389.3	452.6
Nb50	372.5	461.5	334.4	387.8	386.9	384.5	362.7	363.5	389.3	384.9
Nb51	406.4	379.5	361.1	361.1	387.3	386.6	367.4	334.5	347.7	350.4
Nb52	397.0	377.1	363.9	332.2	416.7	358.8	293.6	596.3	342.0	487.8
Nb53	387.2	353.9	425.9	331.5	416.7	400.1	291.5	363.0	329.9	374.6
Nb54	382.8	384.5	361.0	335.8	387.3	326.5	340.5	370.9	329.9	354.5

Table S23. (Continued)

Atom	Model									
	11	12	13	14	15	16	17	18	19	20
Nb55	353.0	396.0	398.5	319.9	386.9	387.2	367.5	364.0	342.0	341.4
Nb56	411.3	373.7	444.0	367.2	379.4	350.3	362.7	334.5	347.7	374.6
Nb57	396.3	379.6	386.8	389.6	386.9	350.2	293.6	364.0	378.4	335.8
Nb58	407.5	377.6	399.7	365.0	386.9	378.9	367.4	363.5	369.1	367.9
Nb59	417.1	388.2	392.0	362.4	387.3	363.1	302.7	334.5	369.1	353.7
Nb60	371.9	409.0	434.6	355.9	387.3	396.5	358.7	370.9	366.6	367.9
Nb61	396.8	400.6	381.5	561.4	401.3	443.8	344.1	368.9	511.6	341.4
Nb62	358.3	434.7	303.3	472.2	425.8	398.7	291.5	370.9	412.0	384.9
Nb63	430.5	364.4	378.4	326.8	401.3	401.6	358.7	363.0	415.2	350.4
Nb64	440.3	382.3	347.5	308.4	425.8	437.0	340.5	370.9	415.2	354.5
$\langle\sigma_{iso}\rangle$	***395.7***	***393.8***	***383.2***	***370.3***	***396.5***	***382.1***	***345.8***	***373.0***	***378.4***	***373.6***
Rb65	3284.4	3273.0	3276.6	3288.5	3303.1	3287.3	3287.4	3259.4	3292.4	3288.6
Rb66	3281.7	3278.9	3285.4	3257.3	3290.6	3279.6	3287.4	3293.7	3283.3	3267.4
Rb67	3297.1	3297.0	3300.0	3295.9	3311.3	3273.6	3266.9	3293.7	3292.4	3276.4
Rb68	3272.5	3295.2	3298.9	3288.1	3286.7	3275.4	3278.7	3259.4	3275.7	3294.6
Rb69	3296.4	3281.5	3282.2	3293.1	3286.7	3279.5	3282.7	3287.5	3284.3	3278.2
Rb70	3291.6	3296.7	3272.9	3278.5	3290.6	3280.4	3266.9	3293.7	3275.7	3278.2
Rb71	3273.8	3277.6	3280.6	3291.6	3311.3	3304.2	3278.7	3293.7	3275.9	3268.6
Rb72	3297.6	3292.2	3288.6	3271.1	3255.2	3261.3	3282.7	3287.5	3281.7	3276.4
$\langle\sigma_{iso}\rangle$	***3286.9***	***3286.5***	***3285.7***	***3283.0***	***3291.9***	***3280.2***	***3278.9***	***3283.6***	***3282.7***	***3278.6***

6.4. Quadrupolar coupling constant values for $RbTa_2O_5F$ models

Table S24. Calculated C_Q (C_Q, MHz) of each Rb atom from the 10 APO_32e models of $RbTa_2O_5F$ and (in bold italic) average C_Q ($\langle C_Q \rangle$, MHz) of all Rb atoms in a given model.

Atom	Model									
	1	2	3	4	5	6	7	8	9	10
Rb65	2.7	3.0	2.6	2.6	2.7	1.8	2.0	2.4	0.8	4.8
Rb66	2.7	2.2	4.0	2.6	2.9	2.9	2.4	0.8	1.6	2.3
Rb67	2.7	2.0	3.2	2.5	3.4	3.0	3.7	0.7	1.6	4.8
Rb68	2.7	2.1	1.0	2.5	4.2	2.0	2.1	2.7	0.9	2.3
Rb69	2.7	2.9	1.1	2.6	3.9	2.0	2.6	2.4	0.8	2.4
Rb70	2.7	2.3	3.2	2.6	3.2	2.9	2.4	0.7	1.7	2.3
Rb71	2.8	2.1	4.0	2.5	4.6	3.0	3.6	0.8	1.7	4.8
Rb72	2.7	2.1	2.6	2.6	4.4	0.1	2.6	2.7	0.8	4.7
$\langle C_Q \rangle$	***2.7***	***2.4***	***2.7***	***2.6***	***3.7***	***2.2***	***2.7***	***1.7***	***1.2***	***3.6***

Table S25. Calculated C_Q (C_Q, MHz) of each Rb atom from the 10 APO_8b models of $RbTa_2O_5F$ and (in bold italic) average C_Q ($\langle C_Q \rangle$, MHz) of all Rb atoms in a given model.

Atom	Model									
	1	2	3	4	5	6	7	8	9	10
Rb65	2.7	3.0	1.9	2.6	4.0	2.0	2.7	3.4	0.5	2.8
Rb66	2.7	2.2	3.1	2.6	3.0	2.9	2.4	0.7	0.2	2.8
Rb67	2.7	2.2	1.9	2.6	4.2	2.0	2.0	3.4	0.5	2.8
Rb68	2.7	2.0	3.1	2.6	4.5	2.9	3.6	0.7	0.2	2.8
Rb69	2.7	2.2	3.1	2.6	3.3	2.9	2.4	0.7	0.2	2.8
Rb70	2.7	2.0	3.1	2.6	3.5	2.9	3.6	0.7	0.2	2.8
Rb71	2.7	3.0	2.1	2.6	2.7	1.7	2.0	3.4	0.5	2.8
Rb72	2.7	2.2	2.1	2.6	4.5	0.0	2.7	3.4	0.5	2.8
$\langle C_Q \rangle$	***2.7***	***2.3***	***2.6***	***2.6***	***3.7***	***2.2***	***2.7***	***2.1***	***0.4***	***2.8***

6.5. Asymmetry parameter values for $RbTa_2O_5F$ models

Table S26. Calculated η_Q (η_Q, MHz) of each Rb atom from the 10 APO_32e models of $RbTa_2O_5F$ and (in bold italic) average η_Q ($<\eta_Q>$, MHz) of all Rb atoms in a given model.

Atom	Model									
	1	2	3	4	5	6	7	8	9	10
Rb65	0.56	0.12	0.44	0.72	0.74	0.04	0.89	0.74	0.14	0.84
Rb66	0.52	0.66	0.41	0.73	0.66	0.86	0.85	0.85	0.41	0.80
Rb67	0.56	0.16	0.33	0.74	0.31	0.84	0.49	0.84	0.46	0.85
Rb68	0.52	0.98	0.61	0.74	0.42	0.44	0.88	0.89	0.15	0.78
Rb69	0.56	0.12	0.77	0.74	0.31	0.41	0.13	0.75	0.24	0.75
Rb70	0.59	0.63	0.34	0.75	0.65	0.86	0.74	0.85	0.37	0.79
Rb71	0.55	0.15	0.41	0.73	0.98	0.90	0.56	0.87	0.44	0.86
Rb72	0.57	0.98	0.44	0.74	0.92	0.69	0.16	0.89	0.08	0.88
$<\eta_Q>$	***0.55***	***0.48***	***0.47***	***0.74***	***0.62***	***0.63***	***0.59***	***0.83***	***0.28***	***0.82***

Table S27. Calculated η_Q (η_Q, MHz) of each Rb atom from the 10 APO_8b models of $RbTa_2O_5F$ and (in bold italic) average η_Q ($<\eta_Q>$, MHz) of all Rb atoms in a given model.

Atom	Model									
	1	2	3	4	5	6	7	8	9	10
Rb65	0.57	0.09	0.78	0.71	0.31	0.37	0.15	0.24	0.00	0.63
Rb66	0.57	0.60	0.34	0.71	0.66	0.86	0.83	0.00	0.00	0.63
Rb67	0.57	0.98	0.78	0.71	0.42	0.37	0.86	0.24	0.00	0.63
Rb68	0.57	0.17	0.34	0.71	0.99	0.86	0.48	0.00	0.00	0.63
Rb69	0.57	0.60	0.34	0.71	0.66	0.86	0.83	0.00	0.00	0.63
Rb70	0.57	0.17	0.34	0.71	0.30	0.86	0.48	0.00	0.00	0.63
Rb71	0.57	0.09	0.01	0.71	0.75	0.00	0.86	0.24	0.00	0.63
Rb72	0.57	0.98	0.01	0.71	0.89	0.00	0.15	0.24	0.00	0.63
$<\eta_Q>$	***0.57***	***0.46***	***0.37***	***0.71***	***0.62***	***0.52***	***0.58***	***0.12***	***0.00***	***0.63***

6.6. Magnetic shielding values for $RbTa_2O_5F$ models

Table S28. Calculated σ_{iso} (σ_{iso}, ppm) of each F and Rb atom from the 10 APO_32e models of $RbTa_2O_5F$ and (in bold italic) average σ_{iso} ($<\sigma_{iso}>$, ppm) of all F and Rb atoms in a given model.

Atom	Model									
	1	2	3	4	5	6	7	8	9	10
F41	221.7	230.2	231.3	231.9	219.6	223.7	208.0	229.3	216.2	196.3
F42	221.8	230.0	231.4	232.2	222.2	235.7	208.4	240.2	232.7	196.4
F43	221.8	230.0	230.8	232.1	229.2	228.4	227.0	224.3	233.2	196.2
F44	221.7	232.8	230.6	232.0	236.4	228.3	227.8	241.7	216.3	185.1
F45	221.8	232.8	232.2	232.1	237.5	228.3	227.9	241.6	216.1	184.8
F46	221.7	230.1	232.4	232.1	187.0	228.3	227.2	224.4	233.2	196.4
F47	221.8	226.9	212.7	232.2	188.9	235.7	227.7	229.2	216.3	185.3
F48	221.8	226.9	212.6	232.1	229.6	223.4	227.6	240.1	232.7	185.3
$<\sigma_{iso}>$	***221.8***	***230.0***	***226.7***	***232.1***	***218.8***	***229.0***	***222.7***	***233.8***	***224.6***	***190.7***
Rb65	3283.9	3283.4	3298.7	3290.4	3274.0	3285.6	3283.2	3299.3	3288.6	3287.7
Rb66	3284.1	3285.8	3296.2	3290.5	3283.0	3286.9	3282.5	3287.5	3297.7	3268.3
Rb67	3284.0	3289.4	3282.5	3290.5	3286.5	3286.5	3297.5	3287.7	3297.6	3288.2
Rb68	3284.0	3294.8	3288.8	3290.5	3284.8	3279.8	3283.3	3297.3	3288.8	3268.4
Rb69	3284.1	3283.6	3288.9	3290.4	3280.9	3279.8	3286.3	3299.3	3288.7	3268.3
Rb70	3283.9	3285.6	3282.3	3290.3	3282.2	3286.6	3283.1	3287.7	3297.4	3268.2
Rb71	3284.0	3289.0	3296.3	3290.4	3282.5	3286.7	3297.9	3287.4	3297.3	3288.1
Rb72	3283.9	3294.8	3298.6	3290.6	3282.6	3306.7	3286.4	3297.2	3288.7	3288.0
$<\sigma_{iso}>$	***3284.0***	***3288.3***	***3291.5***	***3290.4***	***3282.1***	***3287.3***	***3287.5***	***3292.9***	***3293.1***	***3278.2***

Table S29. Calculated σ_{iso} (σ_{iso}, ppm) of each F and Rb atom from the 10 APO_8b models of $RbTa_2O_5F$ and (in bold italic) average σ_{iso} ($<\sigma_{iso}>$, ppm) of all F and Rb atoms in a given model.

Atom	Model									
	1	2	3	4	5	6	7	8	9	10
F41	222.0	230.2	235.4	232.2	219.7	223.7	208.1	234.5	229.8	184.9
F42	222.0	230.2	235.4	232.2	222.0	235.7	208.1	234.5	229.8	184.9
F43	222.0	230.2	235.4	232.2	229.3	228.4	227.1	234.5	229.8	184.9
F44	222.0	233.1	235.4	232.2	236.1	228.4	227.9	234.5	229.8	184.9
F45	222.0	233.1	230.3	232.2	237.4	228.4	227.9	234.5	229.8	184.9
F46	222.0	230.2	230.3	232.2	186.8	228.4	227.1	234.5	229.8	184.9
F47	222.0	227.2	230.3	232.2	189.5	235.7	227.5	234.5	229.8	184.9
F48	222.0	227.2	230.3	232.2	229.8	223.7	227.5	234.5	229.8	184.9
$<\sigma_{iso}>$	***222.0***	***230.2***	***232.9***	***232.2***	***218.8***	***229.0***	***222.6***	***234.5***	***229.8***	***184.9***
Rb65	3284.3	3283.8	3285.4	3290.5	3281.2	3279.9	3286.4	3301.3	3289.5	3280.7
Rb66	3284.3	3285.8	3289.9	3290.5	3283.4	3286.6	3282.8	3287.1	3300.8	3280.7
Rb67	3284.3	3294.9	3285.4	3290.5	3284.9	3279.9	3283.2	3301.3	3289.5	3280.7
Rb68	3284.3	3289.5	3289.9	3290.5	3282.7	3286.6	3297.7	3287.1	3300.8	3280.7
Rb69	3284.3	3285.8	3289.9	3290.5	3282.2	3286.6	3282.8	3287.1	3300.8	3280.7
Rb70	3284.3	3289.5	3289.9	3290.5	3286.2	3286.6	3297.7	3287.1	3300.8	3280.7
Rb71	3284.3	3283.8	3304.7	3290.5	3274.0	3285.0	3283.2	3301.3	3289.5	3280.7
Rb72	3284.3	3294.9	3304.7	3290.5	3282.1	3306.7	3286.4	3301.3	3289.5	3280.7
$<\sigma_{iso}>$	***3284.3***	***3288.5***	***3292.5***	***3290.5***	***3282.1***	***3287.3***	***3287.5***	***3294.2***	***3295.1***	***3280.7***

7. Structural features of RbM_2O_5F models

7.1. $RbNb_2O_5F$ models

Table S30. Average, shortest and longest Nb–X (X = O or F) bond lengths (Å) and the standard deviation from the average bond length sdv(Nb–X) (Å) (X = O and F) from the 8 selected APO_32e models of $RbNb_2O_5F$.

Model	<Nb–O>	$Nb–O_{min}$	$Nb–O_{max}$	<Nb–F>	$Nb–F_{min}$	$Nb–F_{max}$	sdv(Nb–X)
1	1.962	1.854	2.057	2.167	2.166	2.167	0.107
2	1.958	1.842	2.096	2.169	2.150	2.212	0.110
3	1.960	1.847	2.138	2.160	2.118	2.217	0.103
4	1.956	1.849	2.088	2.173	2.169	2.176	0.112
6	1.958	1.846	2.073	2.166	2.144	2.190	0.108
7	1.963	1.862	2.094	2.154	2.125	2.176	0.102
8	1.956	1.844	2.074	2.179	2.160	2.193	0.111
9	1.965	1.850	2.123	2.136	2.111	2.155	0.107

Table S31. Average, shortest and longest Nb–X (X = O or F) bond lengths (Å) and the standard deviation from the average bond length sdv(Nb–X) (Å) (X = O and F) from the 8 selected APO_8b models of $RbNb_2O_5F$.

Model	<Nb–O>	$Nb–O_{min}$	$Nb–O_{max}$	<Nb–F>	$Nb–F_{min}$	$Nb–F_{max}$	sdv(Nb–X)
1	1.963	1.854	2.057	2.167	2.167	2.167	0.107
2	1.953	1.843	2.073	2.169	2.157	2.191	0.099
3	1.948	1.866	2.003	2.147	2.122	2.172	0.084
4	1.956	1.849	2.088	2.173	2.170	2.176	0.112
6	1.958	1.847	2.072	2.166	2.145	2.191	0.108
7	1.963	1.863	2.092	2.154	2.124	2.172	0.101
8	1.948	1.853	2.042	2.170	2.170	2.170	0.100
9	1.951	1.903	1.973	2.123	2.123	2.123	0.069

Table S32. Average, shortest and longest Rb−X (X = O or F) bond lengths (Å) and the standard deviation from the average bond length sdv(Rb−X) (Å) (X = O and F) from the 8 selected APO_32e models of $RbNb_2O_5F$.

Model	<Rb–O>	$Rb–O_{min}$	$Rb–O_{max}$	<Rb–F>	$Rb–F_{min}$	$Rb–F_{max}$	sdv(Rb–X)
1	3.609	2.972	4.256	3.637	3.489	3.716	0.353
2	3.609	2.992	4.231	3.607	3.050	3.911	0.327
3	3.621	3.013	4.277	3.548	2.971	4.184	0.339
4	3.620	3.026	4.098	3.541	3.049	4.254	0.346
6	3.605	2.956	4.318	3.615	3.170	3.839	0.319
7	3.616	2.943	4.300	3.585	2.946	3.823	0.348
8	3.607	3.116	4.164	3.593	3.012	4.168	0.312
9	3.618	3.079	4.336	3.549	2.970	3.879	0.331

Table S33. Average, shortest and longest Rb–X (X = O or F) bond lengths (Å) and the standard deviation from the average bond length sdv(Rb–X) (Å) (X = O and F) from the 8 selected APO_8b models of $RbNb_2O_5F$.

Model	<Rb–O>	$Rb–O_{min}$	$Rb–O_{max}$	<Rb–F>	$Rb–F_{min}$	$Rb–F_{max}$	sdv(Rb–X)
1	3.609	2.971	4.254	3.636	3.495	3.707	0.354
2	3.608	2.977	4.132	3.600	3.207	3.841	0.310
3	3.608	3.062	3.929	3.537	3.161	3.747	0.257
4	3.621	3.026	4.092	3.540	3.048	4.245	0.347
6	3.605	2.956	4.305	3.614	3.165	3.812	0.319
7	3.616	2.949	4.292	3.585	2.971	3.799	0.345
8	3.597	3.172	3.788	3.582	3.226	3.759	0.245
9	3.607	3.180	3.778	3.540	3.130	3.745	0.245

7.2. $RbTa_2O_5F$ models

Table S34. Average, shortest and longest Ta–X (X = O or F) bond lengths (Å) and the standard deviation from the average bond length sdv(Ta–X) (Å) (X = O and F) from the 8 selected APO_32e models of $RbTa_2O_5F$.

Model	<Ta–O>	$Ta–O_{min}$	$Ta–O_{max}$	<Ta–F>	$Ta–F_{min}$	$Ta–F_{max}$	sdv(Ta–X)
1	1.959	1.870	2.031	2.156	2.155	2.157	0.089
2	1.953	1.865	2.040	2.155	2.144	2.173	0.087
3	1.956	1.882	2.016	2.145	2.112	2.170	0.078
4	1.954	1.866	2.033	2.157	2.152	2.161	0.090
6	1.954	1.861	1.861	2.154	2.133	2.179	0.088
7	1.959	1.875	2.031	2.144	2.115	2.162	0.080
8	1.952	1.869	2.035	2.164	2.155	2.173	0.091
9	1.958	1.908	1.992	2.126	2.111	2.142	0.068

Table S35. Average, shortest and longest Ta–X (X = O or F) bond lengths (Å) and the standard deviation from the average bond length sdv(Ta–X) (Å) (X = O and F) from the 8 selected APO_8b models of $RbTa_2O_5F$.

Model	<Ta–O>	$Ta–O_{min}$	$Ta–O_{max}$	<Ta–F>	$Ta–F_{min}$	$Ta–F_{max}$	sdv(Ta–X)
1	1.959	1.870	2.031	2.156	2.156	2.156	0.089
2	1.953	1.865	2.040	2.155	2.145	2.171	0.087
3	1.949	1.879	1.988	2.136	2.115	2.156	0.076
4	1.954	1.866	2.033	2.157	2.153	2.162	0.090
6	1.954	1.861	2.031	2.154	2.133	2.180	0.088
7	1.959	1.875	2.030	2.144	2.114	2.161	0.080
8	1.949	1.873	2.017	2.154	2.154	2.154	0.088
9	1.951	1.904	1.974	2.117	2.117	2.117	0.066

Table S36. Average, shortest and longest Rb−X (X = O or F) bond lengths (Å) and the standard deviation from the average bond length sdv(Rb−X) (Å) (X = O and F) from the 8 selected APO_32e models of $RbTa_2O_5F$.

Model	<Rb–O>	$Rb–O_{min}$	$Rb–O_{max}$	<Rb–F>	$Rb–F_{min}$	$Rb–F_{max}$	sdv(Rb–X)
1	3.602	2.965	4.260	3.629	3.477	3.712	0.354
2	3.598	2.982	4.134	3.595	3.202	3.835	0.308
3	3.613	2.953	4.235	3.540	2.958	3.823	0.331
4	3.598	3.031	4.060	3.582	3.306	4.033	0.309
6	3.598	2.952	4.276	3.602	3.160	3.803	0.316
7	3.609	2.942	4.275	3.578	2.986	3.782	0.345
8	3.596	3.118	4.084	3.580	3.063	4.044	0.297
9	3.611	3.084	4.213	3.539	3.010	3.793	0.325

Table S37. Average, shortest and longest Rb–X (X = O or F) bond lengths (Å) and the standard deviation from the average bond length sdv(Rb–X) (Å) (X = O and F) from the 8 selected APO_8b models of $RbTa_2O_5F$.

Model	<Rb–O>	$Rb–O_{min}$	$Rb–O_{max}$	<Rb–F>	$Rb–F_{min}$	$Rb–F_{max}$	sdv(Rb–X)
1	3.602	2.970	4.241	3.629	3.476	3.705	0.352
2	3.597	2.984	3.597	3.594	3.204	3.830	0.306
3	3.598	3.039	3.918	3.534	3.157	3.742	0.260
4	3.599	3.030	4.061	3.580	3.305	4.036	0.310
6	3.598	2.948	4.272	3.601	3.158	3.797	0.316
7	3.609	2.945	4.268	3.578	2.993	3.777	0.345
8	3.587	3.178	3.783	3.577	3.224	3.753	0.247
9	3.595	3.166	3.770	3.536	3.129	3.739	0.247

References

(1) Levin, I. NIST Inorganic Crystal Structure Database (ICSD), 2020. https://doi.org/10.18434/M32147.

(2) Cámara, F.; Williams, C. T.; Della Ventura, G.; Oberti, R.; Caprilli, E. Non-Metamict Betafite from Le Carcarelle (Vico Volcanic Complex, Italy): Occurrence and Crystal Structure. *Mineral. Mag.* **2004**, *68* (6), 939–950. https://doi.org/10.1180/0026461046860224.

(3) Mazzi, F; Munno, R. Calciobetafite (New Mineral of the Pyrochlore Group) and Related Minerals from Campi Flegrei, Italy; Crystal Structures of Polymignyte and Zirkelite: Comparison with Pyrochlore and Zirconolite. *Am. Mineral.* **1983**, *68*, 262–276.

(4) Janka, O.; Schleid, T. Two Fluoride-Containing Oxotantalates(V) of the Light Lanthanides: $NdFTa_2O_6$ and $La_3Cl_3TaO_5F$. *Solid State Sci.* **2009**, *11* (11), 1992–1997. https://doi.org/10.1016/j.solidstatesciences.2009.07.002.

(5) Dihlström, K.; Westgren, A. Über Den Bau Des Sogenannten Antimontetroxyds Und Der Damit Isomorphen Verbindung $BiTa_2O_6F$. *Z. Für Anorg. Allg. Chem.* **1937**, *235* (1–2), 153–160. https://doi.org/10.1002/zaac.19372350121.

(6) Bernard, D.; Pannetier, J.; Lucas, J. $Hg_2M_2F_6S$ et $Hg_2M_2F_6O$: Deux nouvelles familles de pyrochlores contenant du mercure et des métaux M de transition divalents. *J. Solid State Chem.* **1975**, *14* (4), 328–334. https://doi.org/10.1016/0022-4596(75)90051-1.

(7) Siegrist, T.; Cava, R. J.; Krajewski, J. J. REDUCED ALKALINE EARTH TANTALATES. *Mater. Res. Bull.* **1997**, *32* (7), 881–887. https://doi.org/10.1016/S0025-5408(97)00066-4.

(8) Le Berre, F.; Crosnier-Lopez, M.-P.; Galven, C.; Fourquet, J.-L.; Legein, C.; Body, M.; Buzaré, J.-Y. Ca^{2+}/Vacancies and O^{2-}/F^- Ordering in New Oxyfluoride Pyrochlores $Li_{2x}Ca_{1.5-x}\square_{0.5-x}M_2O_6F$ (M = Nb,Ta) for $0 \leq x \leq 0.5$. *Dalton Trans* **2007**, No. 23, 2457–2466. https://doi.org/10.1039/B701863K.

(9) Yin, R.; Wang, R. C.; Zhang, A.-C.; Hu, H.; Zhu, J. C.; Rao, C.; Zhang, H. CHEMICAL EVOLUTION AND LATE-STAGE RE-EQUILIBRATION OF Zr-Hf-U-BEARING COLUMBITE-GROUP MINERALS IN THE KOKTOKAY NO. 1 GRANITIC PEGMATITE, ALTAI, NORTHWESTERN CHINA. *Can. Mineral.* **2015**, *53* (3), 461–478. https://doi.org/10.3749/canmin.1400091.

(10) Tutov, A.G.; Bader, V.I.; Myl’nikova, I.E. Synthesis and X-Ray Diffraction Study of Single Crystals of a New Pyrochlore Containing Lithium, $SrLiTa_2O_6F$. *Kristallografiya* **1972**, *17*, 406–407.

(11) von Gaertner, H.R. Die Kristallstrukturen von Loparit Und Pyrochlor. *Neues Jahrb. Fuer Mineral. Geol. Palaeontol. Abh. Abt. Mineral. Petrogr.* **1930**, *61*, 1–30.

(12) Perrault, G. La Composition Chimique et La Structure Cristalline Du Pyrochlore d’Oka, P.Q. *Can. Mineral.* **1968**, *9*, 383–402.

(13) Grannec, J.; Baudry, H.; Ravez, J.; Portier, J. Sur de nouveaux composés oxyfluorés des terres rares de structure pyrochlore. *J. Solid State Chem.* **1974**, *10* (1), 66–71. https://doi.org/10.1016/0022-4596(74)90011-5.

(14) Yoo, C.-Y.; Kim, S.-J. $KCaNb_2O_6F$ from a Combined Synchrotron X-Ray and Neutron Powder Diffraction Study. *Acta Crystallogr. Sect. E Struct. Rep. Online* **2007**, *63* (12), i203–i204. https://doi.org/10.1107/S1600536807060436.

(15) Andrade, M. B.; Atencio, D.; Persiano, A. I. C.; Ellena, J. Fluorcalciomicrolite, $(Ca,Na,\square)_2Ta_2O_6F$, a New Microlite-Group Mineral from Volta Grande Pegmatite, Nazareno, Minas Gerais, Brazil. *Mineral. Mag.* **2013**, *77* (7), 2989–2996. https://doi.org/10.1180/minmag.2013.077.7.08.

(16) Bonazzi, P. Single-Crystal Diffraction and Transmission Electron Microscopy Studies of “Silicified” Pyrochlore from Narssarssuk, Julianehaab District, Greenland. *Am. Mineral.* **2006**, *91* (5–6), 794–801. https://doi.org/10.2138/am.2006.1777.

(17) Atencio, D.; Ciriotti, M. E.; Andrade, M. B. Fluorcalcioroméite, $(Ca,Na)_2Sb_2^{5+}(O,OH)_6F$, a New Roméite-Group Mineral from Starlera Mine, Ferrera, Grischun, Switzerland: Description and Crystal Structure. *Mineral. Mag.* **2013**, *77* (4), 467–473. https://doi.org/10.1180/minmag.2013.077.4.06.

(18) Kasatkin, A. V.; Britvin, S. N.; Peretyazhko, I. S.; Chukanov, N. V.; Škoda, R.; Agakhanov, A. A. Oxybismutomicrolite, a New Pyrochlore-Supergroup Mineral from the Malkhan Pegmatite Field, Central Transbaikalia, Russia. *Mineral. Mag.* **2020**, *84* (3), 444–454. https://doi.org/10.1180/mgm.2020.25.

(19) Witzke, T.; Steins, M.; Doering, T.; Schuckmann, W.; Wegner, R.; Pollmann, H. FLUORNATROMICROLITE, $(Na,Ca,Bi)_2Ta_2O_6F$, A NEW MINERAL SPECIES FROM QUIXABA, PARAIBA, BRAZIL. *Can. Mineral.* **2011**, *49* (4), 1105–1110. https://doi.org/10.3749/canmin.49.4.1105.

(20) Galven, C.; Legein, C.; Body, M.; Fourquet, J.; Buzaré, J.; Le Berre, F.; Crosnier-Lopez, M. New Oxyfluoride Pyrochlores $Li_{2-x}La_{(1+x)/3}\square_{(2x-1)/3}B_2O_6F$ (B = Nb, Ta): Average and Local Structure Characterization by XRD, TEM and ^{19}F Solid-State NMR Spectroscopy. *Eur. J. Inorg. Chem.* **2010**, *2010* (33), 5272–5283. https://doi.org/10.1002/ejic.201000599.

(21) Andrade, M. B.; Atencio, D.; Filho, L. A. D. M.; Ellena, J. THE CRYSTAL STRUCTURE OF A MICROLITE-GROUP MINERAL WITH A FORMULA NEAR $NaCaTa_2O_6F$ FROM THE MORRO REDONDO MINE, CORONEL MURTA, MINAS GERAIS, BRAZIL. *Can. Mineral.* **2011**, *49* (2), 615–621. https://doi.org/10.3749/canmin.49.2.615.

(22) Phraewphiphat, T.; Iqbal, M.; Suzuki, K.; Hirayama, M.; Kanno, R. Synthesis and Lithium-Ion Conductivity of $LiSrB_2O_6F$ ($B = Nb^{5+}, Ta^{5+}$) with a Pyrochlore Structure. *J. Jpn. Soc. Powder Powder Metall.* **2018**, *65* (1), 26–33. https://doi.org/10.2497/jjspm.65.26.

(23) Guowu, L.; Guangming, Y.; Fude, L.; Ming, X.; Xiangkun, G.; Baoming, P.; de

Fourestier, J. Fluorcalciopyrochlore, A New Mineral Species From Bayan Obo, Inner Mongolia, P.R. China. *Can. Mineral.* **2016**, *54* (5), 1285–1291. https://doi.org/10.3749/canmin.1500042.

(24) Kim, Sung-Chul; Kang, Jun-Kun; Kim, Seungjoo. Synthesis and Characterization of New Pyrochlore-Type Oxyfluorides, $APbNb_2O_6F$ (A = Na and K). *Bull. Korean Chem. Soc.* **2010**, *31* (2), 497–499. https://doi.org/10.5012/BKCS.2010.31.02.497.

(25) Goodenough, J. B.; Hong, H. Y.-P.; Kafalas, J. A. Fast Na^+-Ion Transport in Skeleton Structures. *Mater. Res. Bull.* **1976**, *11* (2), 203–220. https://doi.org/10.1016/0025-5408(76)90077-5.

(26) Britvin, S. N.; Siidra, O. I.; Lotnyk, A.; Krivovichev, S. V.; Depmeier, W. Niobate and Tantalate Pyrochlores: Soft Synthesis by the Fluoride Route. *Eur. J. Inorg. Chem.* **2010**, *2010* (7), 1082–1088. https://doi.org/10.1002/ejic.200900999.

(27) Goodenough, J. B.; Hong, H. Y.-P.; Kafalas, J. A. Fast Na+-Ion Transport in Skeleton Structures. *Mater. Res. Bull.* **1976**, *11* (2), 203–220. https://doi.org/10.1016/0025-5408(76)90077-5.

(28) Griebler, W. -D.; Babel, D. Röntgenographische Untersuchungen an Titan(III)-Fluorverbindungen Mit Pyrochloverwandten Strukturen. *Z. Für Anorg. Allg. Chem.* **1980**, *467* (1), 187–196. https://doi.org/10.1002/zaac.19804670121.

(29) Mattes, R.; Leimkühler, M.; Nagel, A. Ramanspektren anionen- und kationensubstituierter ternärer Oxide des Molybdäns und Wolframs mit Pyrochlor- und hexagonaler Wolframbronzen-Struktur Einkristallstrukturuntersuchungen an $CsZnMoO_3F_3$, $Rb_{0,3}Nb_{0,3}W_{0,7}O_3$ und $Rb_{0,3}Ga_{0,1}W_{0,9}O_3$. *Z. Für Anorg. Allg. Chem.* **1990**, *582* (1), 131–142. https://doi.org/10.1002/zaac.19905820117.

(30) Babel, D.; Pausewang, G.; Viebahn, W. Die Struktur Einiger Fluoride, Oxide Und Oxidfluoride AMe_2X_6: Der Rb Ni Cr F6-Typ. *Z. Fuer Naturforschung Teil B Anorg. Chem. Org. Chem. Biochem. Biophys. Biol.* **1967**, *22*, 1219–1220.

(31) Baum, E.; Dahlke, P.; Kaiser, V.; Molinier, M.; Schmidt, R. E.; Pebler, J.; Massa, W.; Babel, D. Zur Kristallstruktur von Pyrochloren: Mössbauer-Spektrum von orthorhombischem $CsFe_2F_6$ und röntgenographische Einkristall-Untersuchungen an den kubischen Verbindungen $CsMgGaF_6$, $CsM^{II}V^{III}F_6$ (M^{II} = Mn, Zn), $CsM^{II}Fe^{III}F_6$ (M^{II} = Mn, Cu, Zn) und $Cs_4Cu_5V_{32}O_2F_{19}$. *Z. Für Anorg. Allg. Chem.* **2006**, *632* (14), 2244–2250. https://doi.org/10.1002/zaac.200600138.

(32) Ercit, T. S.; Černý, P.; Hawthorne, F. C. Cesstibtantite—a Geologic Introduction to the Inverse Pyrochlores. *Mineral. Petrol.* **1993**, *48* (2–4), 235–255. https://doi.org/10.1007/BF01163101.

(33) Xie, Y.; Yin, S.; Yamane, H.; Hashimoto, T.; Machida, H.; Sato, T. Microwave Assisted Solvothermal Synthesis of a New Compound, Pyrochlore-Type $Sn_{1.24}Ti_{1.94}O_{3.66}(OH)_{1.50}F_{1.42}$. *Chem. Mater.* **2008**, *20* (15), 4931–4935. https://doi.org/10.1021/cm800277b.

(34) Boivin, E.; Pourpoint, F.; Saitzek, S.; Simon, P.; Roussel, P.; Kabbour, H. An Unusual

O^{2-}/F^- Distribution in the New Pyrochlore Oxyfluorides: $Na_2B_2O_5F_2$ (B = Nb, Ta). *Chem. Commun.* **2022**, *58* (14), 2391–2394. https://doi.org/10.1039/D1CC06760E.

(35) Oka, K.; Hojo, H.; Azuma, M.; Oh-ishi, K. Temperature-Independent, Large Dielectric Constant Induced by Vacancy and Partial Anion Order in the Oxyfluoride Pyrochlore $Pb_2Ti_2O_{6-\delta}F_{2\delta}$. *Chem. Mater.* **2016**, *28* (15), 5554–5559. https://doi.org/10.1021/acs.chemmater.6b02509.

(36) Kresse, G.; Furthmüller, J. Efficiency of Ab-Initio Total Energy Calculations for Metals and Semiconductors Using a Plane-Wave Basis Set. *Comput. Mater. Sci.* **1996**, *6* (1), 15–50. https://doi.org/10.1016/0927-0256(96)00008-0.

(37) Kresse, G.; Furthmüller, J. Efficient Iterative Schemes for *Ab Initio* Total-Energy Calculations Using a Plane-Wave Basis Set. *Phys. Rev. B* **1996**, *54* (16), 11169–11186. https://doi.org/10.1103/PhysRevB.54.11169.

(38) Sadoc, A.; Body, M.; Legein, C.; Biswal, M.; Fayon, F.; Rocquefelte, X.; Boucher, F. NMR Parameters in Alkali, Alkaline Earth and Rare Earth Fluorides from First Principle Calculations. *Phys. Chem. Chem. Phys.* **2011**, *13* (41), 18539. https://doi.org/10.1039/c1cp21253b.

(39) Biswal, M.; Body, M.; Legein, C.; Sadoc, A.; Boucher, F. NbF_5 and TaF_5: Assignment of ^{19}F NMR Resonances and Chemical Bond Analysis from GIPAW Calculations. *J. Solid State Chem.* **2013**, *207*, 208–217. https://doi.org/10.1016/j.jssc.2013.09.001.

(40) Zakary, O.; Body, M.; Charpentier, T.; Sarou-Kanian, V.; Legein, C. Structural Modeling of O/F Correlated Disorder in $TaOF_3$ and $NbOF_{3-x}(OH)_x$ by Coupling Solid-State NMR and DFT Calculations. *Inorg. Chem.* **2023**, *62* (40), 16627–16640. https://doi.org/10.1021/acs.inorgchem.3c02844.

(41) Goldschmidt, V. M. Die Gesetze der Krystallochemie. *Naturwissenschaften* **1926**, *14* (21), 477–485. https://doi.org/10.1007/BF01507527.

(42) Larsen, F. H.; Nielsen, N. Chr. Effects of Finite Rf Pulses and Sample Spinning Speed in Multiple-Quantum Magic-Angle Spinning (MQ-MAS) and Multiple-Quantum Quadrupolar Carr−Purcell−Meiboom−Gill Magic-Angle Spinning (MQ-QCPMG-MAS) Nuclear Magnetic Resonance of Half-Integer Quadrupolar Nuclei. *J. Phys. Chem. A* **1999**, *103* (50), 10825–10832. https://doi.org/10.1021/jp992798i.

(43) Vosegaard, T.; Skibsted, J.; Bildsøe, H.; Jakobsen, H. J. Solid-State NMR of $RbVO_3$. A Comparison of Experiments for Retrieving Chemical Shielding and Quadrupole Coupling Tensorial Interactions. *Solid State Nucl. Magn. Reson.* **1999**, *14* (3–4), 203–210. https://doi.org/10.1016/S0926-2040(99)00021-1.

(44) Vosegaard, T.; Skibsted, J.; Bildsøe, H.; Jakobsen, H. J. Quadrupole Coupling and Anisotropic Shielding from Single-Crystal NMR of the Central Transition for Quadrupolar Nuclei. ^{87}Rb NMR of $RbClO_4$ and Rb_2SO_4. *J. Magn. Reson. A* **1996**, *122* (2), 111–119. https://doi.org/10.1006/jmra.1996.0186.

(45) Rollet, A.-L.; Allix, M.; Veron, E.; Deschamps, M.; Montouillout, V.; Suchomel, M. R.; Suard, E.; Barre, M.; Ocaña, M.; Sadoc, A.; Boucher, F.; Bessada, C.; Massiot, D.;

Fayon, F. Synthesis and Structure Resolution of $RbLaF_4$. *Inorg. Chem.* **2012**, *51* (4), 2272–2282. https://doi.org/10.1021/ic202301e.

(46) Weber, H. J.; Schulz, M.; Schmitz, S.; Granzin, J.; Siegert, H. Determination and Structural Application of Anisotropic Bond Polarisabilities in Complex Crystals. *J. Phys. Condens. Matter* **1989**, *1* (44), 8543–8547. https://doi.org/10.1088/0953-8984/1/44/025.

(47) Wang, X.; Adhikari, J.; Smith, L. J. An Investigation of Distortions of the Dion−Jacobson Phase $RbSr_2Nb_3O_{10}$ and Its Acid-Exchanged Form with ^{93}Nb Solid State NMR and DFT Calculations. *J. Phys. Chem. C* **2009**, *113* (40), 17548–17559. https://doi.org/10.1021/jp902318v.

(48) Kresse, G.; Joubert, D. From Ultrasoft Pseudopotentials to the Projector Augmented-Wave Method. *Phys. Rev. B* **1999**, *59* (3), 1758–1775. https://doi.org/10.1103/PhysRevB.59.1758.

(49) Blöchl, P. E. Projector Augmented-Wave Method. *Phys. Rev. B* **1994**, *50* (24), 17953–17979. https://doi.org/10.1103/PhysRevB.50.17953.

(50) Petrilli, H. M.; Blöchl, P. E.; Blaha, P.; Schwarz, K. Electric-Field-Gradient Calculations Using the Projector Augmented Wave Method. *Phys. Rev. B* **1998**, *57* (23), 14690–14697. https://doi.org/10.1103/PhysRevB.57.14690.

(51) Pickard, C. J.; Mauri, F. All-Electron Magnetic Response with Pseudopotentials: NMR Chemical Shifts. *Phys. Rev. B* **2001**, *63* (24), 245101. https://doi.org/10.1103/PhysRevB.63.245101.

(52) Yates, J. R.; Pickard, C. J.; Mauri, F. Calculation of NMR Chemical Shifts for Extended Systems Using Ultrasoft Pseudopotentials. *Phys. Rev. B* **2007**, *76* (2), 024401. https://doi.org/10.1103/PhysRevB.76.024401.

Résumé en Français

Les composés inorganiques à anions mixtes, connus sous le nom de matériaux hétéroanioniques (HAMs), présentent diverses propriétés physico-chimiques, telles que la supraconductivité à haute température, la conductivité ionique, l'activité photocatalytique, la thermoélectricité et la réponse optique non linéaire. Ils trouvent diverses applications, comme catalyseurs pour la décomposition de l'eau ou comme électrodes de batterie. Les HAMs dérivés des oxydes présentent de nombreux avantages en raison de leur chimie diversifiée, de leur abondance, de leur stabilité et de leur facilité de synthèse. La présence de deux espèces anioniques (ou plus) avec différentes charges, rayons ioniques, électronégativités et polarisabilités dans la structure cristalline permet de modifier la stœchiométrie et la structure locale et entraîne des propriétés distinctes de celles des oxydes analogues. Celles-ci dépendent non seulement de la stœchiométrie et de l'identité des anions constituants, mais aussi de la position de ces anions dans la structure cristalline. Dans certains HAMs, des sites cristallographiques distincts sont totalement occupés par différentes espèces anioniques, produisant une structure cristalline ordonnée. Dans d'autres, ces différentes espèces anioniques occupent les mêmes sites cristallographiques, produisant une structure cristalline désordonnée. Cependant, il existe, entre distribution entièrement ordonnée et aléatoirement désordonnée des anions, de nombreux cas d'ordres anioniques intermédiaires avec des regroupements locaux ou des corrélations étendues, qualifiés de désordre corrélé. Étant donné que les propriétés des HAMs dépendent du positionnement de ces anions, il est essentiel de caractériser précisément la structure de ces matériaux.

Parmi les HAMs dérivés des oxydes, les oxyfluorures représentent la famille la plus importante. Ils sont généralement caractérisés par la diffraction des rayons X et/ou des neutrons, techniques permettant de modéliser l’ordre à longue distance. Étant donné que les facteurs de diffusion des rayons X (ou des neutrons) de O^{2-} et F^{-} sont similaires, les données de diffraction ne permettent pas de les distinguer. Néanmoins, pour les oxyfluorures ordonnées, une description structurale complète peut être obtenue en combinant les données de diffraction et les calculs de somme de valences de liaison (BVS). En revanche, pour les oxyfluorures présentant un désordre anionique aléatoire ou corrélé, les données de diffraction

ne permettent d'obtenir qu'une structure moyenne. Dans de tels cas, une approche multimodale s'appuyant sur des techniques de caractérisation à courte distance est nécessaire pour déterminer la structure locale et un éventuel désordre corrélé, c'est-à-dire un positionnement préférentiel des atomes O et F. La spectroscopie de RMN du solide constitue alors un outil de choix, car elle fournit des caractéristiques structurales précieuses telles que le nombre et les multiplicités relatives des sites occupés par le noyau sondé et permet d'explorer l'environnement chimique local. Les caractéristiques de l'isotope naturel unique du fluor, ^{19}F, à savoir un spin nucléaire de 1/2, une abondance naturelle de 100 %, un rapport gyromagnétique élevé et une large gamme de déplacements chimiques isotropes, δ_{iso}, font de la RMN du solide de ce noyau la technique idéale pour étudier l'ordre O/F dans les oxyfluorures. Néanmoins, le désordre O/F, qu'il soit aléatoire ou corrélé, peut donner lieu à une distribution d'environnements pour les ions F^-, et donc une distribution des valeurs de δ_{iso}. La prédiction de ces valeurs, ainsi que des autres paramètres RMN, au moyen de la DFT, est donc essentielle pour comprendre leurs origines structurales et valider les modèles structuraux.

L'objectif de cette thèse est de décrire l'ordre O/F dans les oxyfluorures inorganiques de métaux de transition, de structures de complexité croissante, depuis les structures ordonnées, en passant par celles présentant un désordre corrélé jusqu'aux structures supposées totalement désordonnées, en utilisant une approche multimodale, qui comprend plusieurs étapes :

- la synthèse des composés d'intérêt sous forme de poudre ;
- leur caractérisation en utilisant la diffraction des rayons X sur poudre (DRXP), la RMN du solide des noyaux ^{1}H et ^{19}F, et éventuellement la RMN haut champ multidimensionnelle des noyaux ^{23}Na, ^{87}Rb et ^{93}Nb ;
- l'étude éventuelle du comportement thermique des composés synthétisés à l'aide de l'analyse ATG/ATD et de la diffraction des rayons X à température contrôlée ;
- la détermination de la structure cristalline par des affinements Rietveld des données de diffraction ;
- la construction de modèles structuraux en appliquant l'approche supermaille, satisfaisant les calculs de sommes de valences de liaison et l'existence éventuelle de désordre corrélé (ordre préférentiel O/F) ;

- l'optimisation DFT des modèles sélectionnés, puis le calcul des paramètres RMN, via les tenseurs de constante d'écran et de gradient de champ électrique en utilisant respectivement les approches GIPAW et PAW ;
- la sélection du(des) modèle(s) final(aux) en comparant les paramètres de RMN théoriques et expérimentaux.

Cette approche a été tout d'abord appliquée à l'étude des oxyfluorures $NaMO_2F_2$ (M = Nb, Ta), en combinant DRXP, RMN de ^{19}F et RMN à haut champ de ^{23}Na et ^{93}Nb et calculs DFT. Pour chaque composé, les positions atomiques dans la structure expérimentale (ES) ont été optimisées (APO), et les paramètres RMN ont été calculés avant et après optimisation. Un meilleur accord avec les données expérimentales est obtenu avec les structures APO. Alors que les composés isotypes du niobium et du tantale au degré V présentent généralement des paramètres de maille très similaires en raison de leurs rayons ioniques de même taille (~0,78 Å en coordinence six), les paramètres de maille de $NaNbO_2F_2$ et $NaTaO_2F_2$ diffèrent sensiblement. Ces différences semblent avoir pour origine l'effet Jahn-Teller au second ordre subi par les ions Nb^{5+} et générant une forte distorsion des octaèdres NbO_4F_2. De plus, des analyses thermiques TGA et TDA mises en œuvre dans le but d'optimiser les conditions de synthèse de ces composés ont montré que $NaNbO_2F_2$ présente un événement endothermique de très faible amplitude lors du chauffage, tandis que son isotype au tantale ne semble pas en présenter. En utilisant la DRXP en température, l'existence de cet événement endothermique a été confirmé par l'évolution des paramètres de maille en fonction de la température. De plus, une analyse approfondie de l'évolution de divers paramètres structuraux avec la température a révélé des tendances distinctes pour les deux composés avec des variations plus fortes des valeurs des angles entre les polyèdres pour $NaTaO_2F_2$ et pour $NaNbO_2F_2$ des variations plus fortes des longueurs de liaison.

Par la suite, l'approche multimodale décrite ci-dessus a été appliquée pour étudier l'ordre O/F dans les oxyfluorures MOF_3 (M = Nb, Ta) et $NbOF_{3-x}(OH)_x$, qui présentent une structure moyenne désordonnée.

L'attribution des résonances RMN de ^{19}F aux sites anioniques des oxyfluorures MOF_3 a été corrigée et leurs structures cristallines réaffinées. Le désordre corrélé O/F résulte de l'existence exclusive d'octaèdres *cis*-MO_2F_4. Ce désordre corrélé, défini par des chaînes –F–M–O–M– le long des directions <100> et <010>, a été modélisé par des supermailles 2×2×1, et confirmé par l'accord remarquable observé entre les valeurs calculées et expérimentales de δ_{iso} de ^{19}F. Ces supermailles optimisées sont des modèles structuraux robustes pour $NbOF_3$ et $TaOF_3$. Les positions atomiques s'écartent, comme prévu, des positions moyennes permettant des longueurs de liaison M−O et M−F différentes d'environ 0,2 Å. De plus, les longueurs de liaison et les angles sont distribuées, comme il se doit dans des composés désordonnés. Enfin, la modélisation structurale de l'oxyfluorure hydroxylé $NbOF_{3-x}(OH)_x$ met en évidence que chaque atome H est fortement lié par liaison hydrogène à un atome F2 ou en contact avec quatre atomes F2. Cette étude prouve l'efficacité de la combinaison des calculs théoriques et de la RMN du solide pour modéliser le désordre corrélé O/F dans les oxyfluorures, même hydroxylés.

Ces résultats ont été valorisés, dans le cadre d'une collaboration, pour mettre en évidence le désordre corrélé dans la phase $TiOF_2$ qui adopte une structure de type bronze hexagonal de tungstène. Sa structure moyenne a été déterminée par des affinements Rietveld des données de diffraction des rayons X et des neutrons. Elle cristallise dans le système orthorhombique avec le groupe d'espace *Pnma*. La formule de ce composé a été estimée comme $Ti_{0.99}\square_{0.01}O_{0.96}F_{1.53}(OH)_{0.51}\cdot 0.33\ H_2O$, et les affinements des données de diffraction mettent en évidence une structure moyenne désordonnée complexe. Néanmoins, l'analyse PDF, combinée aux méthodes d'expansion de cluster paramétrées par DFT menées sur un système stœchiométrique $TiOF_2$, a montré l'existence d'un ordre préférentiel O/F à courte distance caractérisé par une forte préférence pour les octaèdres *cis*-TiO_2F_4. Le modèle DFT a été ensuite évalué en y calculant les valeurs de δ_{iso} de ^{19}F puis en les comparant aux données expérimentales de RMN. Une nouvelle régression linéaire, établie à partir des valeurs de δ_{iso} expérimentales et de constantes d'écran isotropes σ_{iso} calculées pour les atomes F pontants de TiF_4, a été utilisée pour convertir les valeurs calculées de σ_{iso} en valeurs calculées de δ_{iso}. Même si certaines valeurs calculées de δ_{iso} de ^{19}F se situent dans la plage du spectre expérimental, l'accord entre les spectres théoriques et expérimentaux de RMN de ^{19}F n'est pas satisfaisant. Étant donné le taux élevé de groupes OH substituant les atomes F, de nouveaux modèles,

de composition générale $TiOF_{2-x}(OH)_x \cdot 0.33H_2O$, ont été construits pour différents taux de substitution. Un excellent accord entre les spectres théoriques et expérimentaux de RMN ^{19}F a été obtenu pour le modèle de composition $TiOF_{1.67}(OH)_{0.33} \cdot 0.33H_2O$.

Finalement, nous avons modélisé la structure de pyrochlores oxyfluorés RbM_2O_5F (M = Nb, Ta) en utilisant à nouveau l'approche multimodale développée au cours de cette thèse. Les structures moyennes de ces composés présentent un seul site anionique occupé à 83,3 % par O et à 16,7 % par F et le site M est entièrement occupé. En revanche, selon le modèle, le site de Rb a une multiplicité de 32 et n'est occupé qu'à 25 % ou une multiplicité de 8 et est occupé à 100%. Enfin, en appliquant l'approche supermailles, nous avons construit 20 modèles pour chaque structure. Dans cette étude, les valeurs de C_Q se sont avérées être les plus discriminantes. Parmi les 40 modèles testés, seules 16 présentent des valeurs de C_Q calculées compatibles avec les valeurs expérimentales pour ^{87}Rb et ^{93}Nb (lorsqu'ils sont présents). De manière inattendue, la structure des 16 modèles sélectionnés se compose exclusivement d'octaèdres MOF_5 et de cages $RbO_{15}F_3$, $RbO_{14}F_4$ et $RbO_{16}F_2$. Ces résultats suggèrent l'existence d'un ordre préférentiel O/F dans $RbNb_2O_5F$ et $RbTa_2O_5F$.

Enfin, dans ce manuscrit, nous avons dressé un inventaire des équations $\delta_{iso} = -a\,\sigma_{iso} + \sigma_{ref}$ pour ^{19}F indispensables pour convertir les valeurs de σ_{iso} calculées en valeurs calculées de δ_{iso}. La diversité des valeurs de pente et d'ordonnée à l'origine empêche l'établissement d'une équation universelle a fortiori avec une pente égale à 1 pour ce noyau. De plus, nous avons effectué une analyse des divers paramètres à prendre en compte lors du processus de conversion des valeurs calculées de σ_{iso} en valeurs δ_{iso}. Ces paramètres incluent les pseudopotentiels (PAW, GW PAW et USPP), les paramètres de relaxation DFT (E_{cut}, E_{diff} et les k-points), la méthode de calcul des paramètres RMN (méthodes GIPAW et FP-LAPW) et la fonctionnelle d'échange-corrélation (PBE et BJ-LDA) utilisés. Selon le composé étudié, ces paramètres doivent être soigneusement choisis, et les paramètres de relaxation DFT doivent être optimisés. Nous avons aussi fourni une évaluation spéculative de l'effet de la température sur les valeurs de δ_{iso}. Sur la base des régressions linéaires établies dans cette thèse pour ^{19}F, la conversion des valeurs calculées de σ_{iso} en valeurs de δ_{iso} dans un oxyfluorure devrait être effectuée en utilisant une équation de régression linéaire dérivée d'un fluorure ordonné avec plusieurs sites F et le(s) même(s) cation(s).

L'objectif n'est pas d'obtenir une équation avec une pente égale à 1, mais des points bien alignés permettant de calculer des valeurs de δ_{iso} précises.

Il est impératif de reconnaître que bien que cette thèse ait considérablement contribué à la compréhension des oxyfluorures inorganiques et des matériaux hétéroanioniques en général, il reste encore beaucoup à faire. Les composés étudiés dans cette thèse et supposés désordonnés présentent un ordre à courte distance O/F ou un désordre corrélé O/F. De nombreux oxyfluorures inorganiques prétendument désordonnés présentent certainement un désordre corrélé ou sont même ordonnés. Et une question se pose : existe-t-il finalement des oxyfluorures inorganiques où les anions sont distribués complètement aléatoirement ?

COLLEGE DOCTORAL PAYS DE LA LOIRE
ED MATIERE, MOLECULES MATERIAUX ET GEOSCIENCES

Le Mans Université

Titre : Modélisation structurale de l'ordre oxygène-fluor dans des oxyfluorures inorganiques de métaux de transition

Mots clés : Matériaux hétéro-anioniques, Oxyfluorures, Diffraction des rayons X sur poudre, RMN du solide, calculs DFT, Désordre corrélé O/F

Résumé : Les composés inorganiques à anions mixtes, connus sous le nom de matériaux hétéro-anioniques (HAMs), présentent diverses propriétés physico-chimiques, telles que la supraconductivité, la conductivité ionique, l'activité photocatalytique, la thermoélectricité et l'optique non linéaire. Ces HAMs, en particulier ceux dérivés d'oxydes, sont avantageux en raison de leur chimie abondante et de leur synthèse simple. Leurs propriétés dépendent non seulement de la stœchiométrie et de l'identité des anions, mais aussi de leur position dans la structure cristalline. De nombreux cas sont possibles, depuis l'ordre complet jusqu'à une distribution aléatoire des anions, ou des ordres intermédiaires et des corrélations étendues, appelées désordre corrélé.

Cette thèse traite de l'étude de l'ordre O/F dans les oxyfluorures de métaux de transition inorganiques en combinant la diffraction des rayons X sur poudre, la RMN du solide et les calculs ab initio. Cette approche multimodale a été testée sur les composés ordonnés $NaNbO_2F_2$ et $NaTaO_2F_2$, puis utilisée avec succès pour caractériser le désordre corrélé O/F dans les oxyfluorures $TaOF_3$, $NbOF_{3-x}(OH)_x$ et $Ti_{0.99}\square_{0.01}O_{0.96}F_{1.53}(OH)_{0.51}\cdot 0.33H_2O$. De plus, l'effet de l'hydroxylation sur l'environnement local et les déplacements chimiques des atomes de fluor a été modélisé. Enfin, l'existence d'une répartition préférentielle O/F à courte distance a été mise en évidence dans les pyrochlores $RbNb_2O_5F$ et $RbTa_2O_5F$.

Title : Structural modeling of oxygen-fluorine ordering in transition metal inorganic oxyfluorides

Keywords : Heteroanionic materials, Oxyfluorides, X-ray powder diffraction, Solid-state NMR, DFT calculations, O/F correlated disorder

Abstract : Mixed anions inorganic compounds, known as heteroanionic materials (HAMs), exhibit various physicochemical properties, such as superconductivity, ionic conductivity, photocatalytic activity, thermoelectricity, and nonlinear optics. These HAMs, particularly those derived from oxides, are advantageous due to their abundant chemistry and straightforward synthesis. Their properties depend not only on the stoichiometry and identity of the anions but also on their position within the crystal structure. Many cases are possible, ranging from complete order to a random distribution of anions, or intermediate orders and extended correlations, known as correlated disorder.

This thesis deals with the study of the O/F order in inorganic transition metal oxyfluorides by combining powder X-ray diffraction, solid-state NMR, and ab initio calculations. This multimodal approach was first tested on the ordered compounds $NaNbO_2F_2$ and $NaTaO_2F_2$, and then successfully used to describe O/F correlated disorder in $TaOF_3$, $NbOF_{3-x}(OH)_x$, and $Ti_{0.99}\square_{0.01}O_{0.96}F_{1.53}(OH)_{0.51}\cdot 0.33H_2O$. Additionally, the effect of hydroxylation on the local environment and the chemical shifts of fluorine atoms was modeled. Finally, the existence of a preferential short-range O/F ordering was demonstrated in the pyrochlores $RbNb_2O_5F$ and $RbTa_2O_5F$.